frontiers | Research Topics

Recent developments in oxygen minimum zones biogeochemistry

Edited by
Sudheesh Valliyodan, Syed WajihAhmad Naqvi, Gireesh Kumar T. R., Annie Bourbonnais, Mark A. Altabet and Amal Jayakumar

Published in
Frontiers in Marine Science

ISSN 1664-8714
ISBN 978-2-8325-4162-3
DOI 10.3389/978-2-8325-4162-3

About Frontiers

Frontiers is more than just an open access publisher of scholarly articles: it is a pioneering approach to the world of academia, radically improving the way scholarly research is managed. The grand vision of Frontiers is a world where all people have an equal opportunity to seek, share and generate knowledge. Frontiers provides immediate and permanent online open access to all its publications, but this alone is not enough to realize our grand goals.

Frontiers journal series

The Frontiers journal series is a multi-tier and interdisciplinary set of open-access, online journals, promising a paradigm shift from the current review, selection and dissemination processes in academic publishing. All Frontiers journals are driven by researchers for researchers; therefore, they constitute a service to the scholarly community. At the same time, the *Frontiers journal series* operates on a revolutionary invention, the tiered publishing system, initially addressing specific communities of scholars, and gradually climbing up to broader public understanding, thus serving the interests of the lay society, too.

Dedication to quality

Each Frontiers article is a landmark of the highest quality, thanks to genuinely collaborative interactions between authors and review editors, who include some of the world's best academicians. Research must be certified by peers before entering a stream of knowledge that may eventually reach the public - and shape society; therefore, Frontiers only applies the most rigorous and unbiased reviews. Frontiers revolutionizes research publishing by freely delivering the most outstanding research, evaluated with no bias from both the academic and social point of view. By applying the most advanced information technologies, Frontiers is catapulting scholarly publishing into a new generation.

What are Frontiers Research Topics?

Frontiers Research Topics are very popular trademarks of the *Frontiers journals series*: they are collections of at least ten articles, all centered on a particular subject. With their unique mix of varied contributions from Original Research to Review Articles, Frontiers Research Topics unify the most influential researchers, the latest key findings and historical advances in a hot research area.

Find out more on how to host your own Frontiers Research Topic or contribute to one as an author by contacting the Frontiers editorial office: frontiersin.org/about/contact

Recent developments in oxygen minimum zones biogeochemistry

Topic editors

Sudheesh Valliyodan — Central University of Kerala, India
Syed WajihAhmad Naqvi — Indian Institute of Technology Kanpur, India
Gireesh Kumar T. R. — National Institute of Oceanography, Council of Scientific and Industrial Research (CSIR), India
Annie Bourbonnais — University of South Carolina, United States
Mark A. Altabet — University of Massachusetts Dartmouth, United States
Amal Jayakumar — Princeton University, United States

Citation

Valliyodan, S., Naqvi, S. W., Kumar, T. R. G., Bourbonnais, A., Altabet, M. A., Jayakumar, A., eds. (2023). *Recent developments in oxygen minimum zones biogeochemistry*. Lausanne: Frontiers Media SA. doi: 10.3389/978-2-8325-4162-3

Table of contents

frontiers | Frontiers in Marine Science

TYPE Editorial
PUBLISHED 05 December 2023
DOI 10.3389/fmars.2023.1333731

OPEN ACCESS

EDITED AND REVIEWED BY
Eric 'Pieter Achterberg,
Helmholtz Association of German Research Centres (HZ), Germany

*CORRESPONDENCE
Annie Bourbonnais
abourbonnais@seoe.sc.edu

RECEIVED 05 November 2023
ACCEPTED 13 November 2023
PUBLISHED 05 December 2023

CITATION
Bourbonnais A, Valliyodan S, Altabet MA, Jayakumar A, Naqvi SWA and Kumar T. R. G (2023) Editorial: Recent developments in oxygen minimum zones biogeochemistry.
Front. Mar. Sci. 10:1333731.
doi: 10.3389/fmars.2023.1333731

Editorial: Recent developments in oxygen minimum zones biogeochemistry

Annie Bourbonnais[1]*, Sudheesh Valliyodan[2], Mark A. Altabet[3], Amal Jayakumar[4], Syed Wajih Ahmad Naqvi[5] and Gireesh Kumar T. R.[6]

[1]School of the Earth, Ocean, & Environment, University of South Carolina, Columbia, SC, United States, [2]Central University of Kerala, Kasaragod, Kerala, India, [3]School for Marine Science & Technology, University of Massachusetts Dartmouth, New Bedford, MA, United States, [4]Department of Geosciences, Princeton University, Princeton, NJ, United States, [5]Department of Earth Sciences, Indian Institute of Technology, Kanpur, India, [6]National Institute of Oceanography, Council of Scientific and Industrial Research (CSIR), Dona Paula, India

KEYWORDS

oxygen minimum zones, low-oxygen environments, marine biogeochemistry, biogeochemical cycles, microbial ecology, stable isotopes, sensors on autonomous platforms

Editorial on the Research Topic
Recent developments in oxygen minimum zones biogeochemistry

Marine Oxygen Minimum Zones (OMZs) modulate biogeochemical cycles, and directly impact climate dynamics by influencing air-sea fluxes of the potent greenhouse gases methane and nitrous oxide (Levin, 2018). OMZs are formed in regions of weak oxygen (O_2) supply from physical ventilation and high integrated microbial O_2 demand fueled by downward organic flux from overlying surface waters. The ocean's major OMZs are found in the Eastern Tropical South and North Pacific Ocean and the Arabian Sea and Bay of Bengal in the Indian Ocean (Karstensen et al., 2008; Stramma et al., 2008). OMZs are especially prevalent along eastern boundary upwelling systems (EBUS) where high nutrient water is upwelled along the coast to the surface, sustaining high primary productivity (e.g., off Chile, Peru, and South Africa). Other low-O_2 or hypoxic regions (also called dead zones, with hypoxia being less than 2 mg/L O_2) occur in the tropical Atlantic, the Gulf of Mexico, the Baltic Sea and isolated fjords and basins. Recent observations suggest an ongoing expansion and intensification of OMZs. Global warming is recognized as the main driver causing global ocean deoxygenation due to decreased oxygen solubility and increased water-column stratification (Keeling et al., 2010; Helm et al., 2011; Schmidtko et al., 2017). Global warming also causes changes in respiration, ocean circulation and wind patterns, which affect the development of OMZs (Levin, 2018). Declining O_2 concentrations greatly impact marine ecosystems, with consequences for fisheries and the global economy. There is thus a pressing need to better understand future OMZs distribution and biogeochemistry.

This Research Topic presents 14 original research articles with the goal of reviewing current knowledge on OMZ biogeochemistry, the impact of climate change and global warming on OMZ expansion, and novel approaches informing future research directions.

Several contributions to the Research Topic (6 out of 14 manuscripts) cover temporal variability in distribution and volume of OMZs, in both the past and present. Soetaert et al. investigated the mechanisms causing deep-water renewal events in Saanich inlet, a seasonally anoxic basin in British Columbia, Canada, which serves as a natural laboratory to understand OMZs. They found that these events were characterized by a complex layering of water masses with different densities and controlled by a combination of easily predictable (tidal current speeds) and less predictable (the intensity of coastal upwelling) factors.

Muñoz et al. showed a strong temporal variability of the upper part of the OMZ along the Chilean continental margin over the last 2000 years using redox-sensitive metals and $\delta^{15}N$ from sediment cores. The OMZ was more intense before 1400 AD, then oxygenated waters mostly prevailed afterward, including for the last 50 years, except between 1925 and 1970, corresponding with low amplitude of the Pacific Decadal Oscillation and reduced El Niño Southern Oscillation (ENSO). Additionally, Pizarro-Koch et al. observed a strong temporal variability of the subtropical OMZ off central Chile using a coupled physical-biogeochemical regional model during a period dominated by two cold La Niña events (2001 and 2007). Changes in oxygenation were attributed to transport of waters by the oxygen poor Peru-Chile undercurrent, quasi-zonal jets, and mesoscale eddies.

The mechanism explaining the geographic decoupling between the highly productive western boundary and the OMZ in the northeastern part of the Arabian Sea is still a topic up for debate (e.g., Kim et al., 2001; Sarma, 2002; McCreary et al., 2013; Sarma et al., 2020). Zhang et al. attributed this decoupling to the region's ocean circulation and its impact on particle flux. Their model showed enhanced ventilation from the northward circulation of oxygen-rich intermediate waters in the west as well as transport of particulate organic matter (POM) from the productive western region toward the eastern part of the Arabian Sea during summer. Future oxygen evolution in response to climate change in the Arabian Sea is unclear, with contrasting Earth System Model simulations, such as in Vallivattathillam et al., predicting shrinking of the OMZ and other studies observing an expansion (e.g., Lachkar et al., 2019; Lachkar et al., 2021). The findings by Vallivattathillam et al. show the importance of correcting model biases using observational data, especially in regions where local forcing dominates. Lachkar et al. further reviews the current literature on the recent and future evolution of the Arabian Sea OMZ. They discuss the reasons for observed discrepancies in model projections, challenges to predict changes and next research directions.

OMZs greatly impact biogeochemical cycling, with 6 out of 14 submitted manuscripts focused on this topic. Aldunate et al. found that the secondary chlorophyll maximum (SCM) significantly contributed to the particulate organic carbon (POC) pool in the Eastern Tropical North and South Pacific. The SCM develops just below the oxycline in the anoxic portion of OMZs, where nutrient concentrations are generally elevated and light intensity only 1% of incident light. The $\delta^{13}C$ of the POC was enriched by up to 3‰ in the SCM, mostly reflecting net heterotrophy. More depleted $\delta^{13}C$ of POC in the absence of a SCM was attributed to the dominance of chemoautotrophic bacteria (e.g., anammox and sulfur-oxidizing bacteria). Further, Henríquez-Castillo et al. showed, using metagenomics, that gammaproteobacteria of the genus *Alteromonas* are abundant in suboxic waters, peaking at the SCM and significantly impacting carbon cycling in OMZs.

Low-O_2 concentrations in OMZs are the on-switch for hypoxic and anaerobic processes such as nitrogen loss by denitrification and anammox. Up to 30-50% of fixed nitrogen loss occur in OMZs, which represent only 0.1% of total oceanic volume, and affects global marine primary productivity on longer time scales (Codispoti et al., 2001; Gruber and Galloway, 2008; DeVries et al., 2012; Eugster et al., 2013). Chuang et al. used a biogeochemical model in the Benguela Upwelling System and showed the significant role of large sulfur bacteria for benthic nitrogen (and possibly phosphorus) fluxes to the water-column. Denitrification rates were over two times higher than DNRA (dissimilatory nitrate reduction to ammonium) in the presence of these bacteria. Dale et al. used benthic chamber measurements and a numerical model to investigate sedimentary oxygen, carbon, and nutrient fluxes, with a focus on nitrogen, in the Mauritanian upwelling OMZ. The authors estimated a larger net benthic isotope effect of nitrogen loss compared to other marine oxygenated environments, with possible implications for our understanding of the global marine nitrogen budget.

Conversely, OMZs also provides suitable conditions for N_2-fixing organisms, since the key enzyme involved in this process, *nifH*, coding for the Mo-Fe nitrogenase, is inhibited at high oxygen levels. There is however an increasingly recognized discrepancy between low N_2 fixation rates and high diazotrophic diversity in OMZs (Jayakumar and Ward, 2020), including the Northern Benguela Upwelling System (NBUS; Reeder et al.). Reeder and Löscher further explore the causes of this discrepancy by looking at alternative types of nitrogenase, which have been overlooked in previous studies: the Fe-Fe nitrogenase *Anf* and the V-Fe nitrogenase *Vnf*. Diazotrophs with the genetic potential for using these alternative nitrogenases were detected in metagenomes and transcriptomes of OMZs off Peru, the Bay of Bengal and Saanich Inlet. The authors suggest that, while these alternative nitrogenase genes are likely not active in present OMZs due to low trace metal concentrations, their role for N_2 fixation might change under future climate scenarios.

Finally, greenhouse gas production, e.g., nitrous oxide and methane, is enhanced under hypoxic and anoxic conditions, accelerating global warming, putatively creating a positive feedback loop for ocean deoxygenation. Bourbonnais et al. present a N_2O concentration, stable isotopic composition, and isotopomer dataset of unprecedented high spatial and depth resolution in the eastern Pacific Ocean. Different N_2O sources were identified under different oxygen regimes, with the largest N_2O accumulations mostly from denitrification at low oxygen concentrations near the oxycline.

Future research directions emerge from the topics covered in this Research Topic. Novel approaches, such as long-term monitoring using sensors installed on autonomous platforms, which is the goal of programs such as Biogeochemical Argo (BGC-ARGO) or Ocean Observatories Initiative (OOI), will allow

increasing spatial and temporal resolution and extent of observations (e.g., Margolskee et al., 2019; Kwiecinski and Babbin, 2021). In this context, 1 manuscript in the Research Topic (McNeil et al.) presents a gas tension device to study denitrification in the anoxic core of the Eastern Tropical North Pacific OMZ. This device measures total dissolved gas pressure, which allowed obtaining the first autonomous biogenic N_2 profiles in the open ocean. This high-resolution data is necessary to validate numerical models and better understand the evolution of OMZs in the past and future in relation to climate change and global warming. Further, *in-situ* microbial ecology approaches (e.g., Edgcomb et al., 2016) could help better understand biogeochemical cycling and pathways in OMZs and resolve current unknowns, such as the paradigm regarding N_2 fixation in low-oxygen environments.

Author contributions

AB: Writing – original draft. SV: Writing – review & editing. MA: Writing – review & editing. AJ: Writing – review & editing. SN: Writing – review & editing. GT: Writing – review & editing.

Funding

The author(s) declare that no financial support was received for the research, authorship, and/or publication of this article.

Conflict of interest

The authors declare that the research was conducted in the absence of any commercial or financial relationships that could be construed as a potential conflict of interest.

Publisher's note

References

Codispoti, L. A., Brandes, J., Christensen, J. P., Devol, A. H., Naqvi, S. W. A., Paerl, H., et al. (2001). The oceanic fixed nitrogen and nitrous oxide budgets: Moving targets as we enter the anthropocene? *Scientia Marina* 65 (S2), 85–105. doi: 10.3989/scimar.2001.65s285

DeVries, T., Deutsch, C., Primeau, F., Chang, B., and Devol, A. (2012). Global rates of water-column denitrification derived from nitrogen gas measurements. *Nat. Geosci.* 5 (8), 547–550. doi: 10.1038/ngeo1515

Edgcomb, V. P., Taylor, C., Pachiadaki, M. G., Honjo, S., Engstrom, I., and Yakimov, M. (2016). Comparison of Niskin vs. in *situ* approaches for analysis of gene expression in deep Mediterranean Sea water samples. *Deep Sea Res. Part II: Topical Stud. Oceanography* 129, 213–222. doi: 10.1016/j.dsr2.2014.10.020

Eugster, O., Gruber, N., Deutsch, C., Jaccard, S. L., and Payne, M. R. (2013). The dynamics of the marine nitrogen cycle across the last deglaciation. *Paleoceanography* 28 (1), 116–129. doi: 10.1002/palo.20020

Gruber, N., and Galloway, J. N. (2008). An Earth-system perspective of the global nitrogen cycle. *Nature* 451 (7176), 293–296. doi: 10.1038/nature06592

Helm, K. P., Bindoff, N. L., and Church, J. A. (2011). Observed decreases in oxygen content of the global ocean. *Geophysical Res. Lett.* 38 (23), L23602. doi: 10.1029/2011GL049513

Jayakumar, A., and Ward, B. B. (2020). Diversity and distribution of nitrogen fixation genes in the oxygen minimum zones of the world oceans. *Biogeosciences* 17 (23), 5953–5966. doi: 10.5194/bg-17-5953-2020

Karstensen, J., Stramma, L., and Visbeck, M. (2008). Oxygen minimum zones in the eastern tropical Atlantic and Pacific oceans. *Prog. Oceanography* 77 (4), 331–350. doi: 10.1016/j.pocean.2007.05.009

Keeling, R. F., Körtzinger, A., and Gruber, N. (2010). Ocean deoxygenation in a warming world. *Annu. Rev. Mar. Sci.* 2, 199–229. doi: 10.1146/annurev.marine.010908.163855

Kim, H. S., Flagg, C. N., and Howden, S. D. (2001). Northern Arabian Sea variability from TOPEX/Poseidon altimetry data: an extension of the US JGOFS/ONR shipboard ADCP study. *Deep Sea Res. Part II: Topical Stud. Oceanography* 48 (6-7), 1069–1096. doi: 10.1016/S0967-0645(00)00131-4

Kwiecinski, J. V., and Babbin, A. R. (2021). A high-resolution Atlas of the eastern tropical pacific oxygen deficient zones. *Global Biogeochemical Cycles* 35 (12), e2021GB007001. doi: 10.1029/2021GB007001

Lachkar, Z., Lévy, M., and Smith, K. S. (2019). Strong intensification of the Arabian Sea oxygen minimum zone in response to Arabian Gulf warming. *Geophysical Res. Lett.* 46 (10), 5420–5429. doi: 10.1029/2018GL081631

Lachkar, Z., Mehari, M., Al Azhar, M., Lévy, M., and Smith, S. (2021). Fast local warming is the main driver of recent deoxygenation in the northern Arabian Sea. *Biogeosciences* 18 (20), 5831–5849. doi: 10.5194/bg-18-5831-2021

Levin, L. A. (2018). Manifestation, drivers, and emergence of open ocean deoxygenation. *Annu. Rev. Mar. Sci.* 10, 229–260. doi: 10.1146/annurev-marine-121916-063359

Margolskee, A., Frenzel, H., Emerson, S., and Deutsch, C. (2019). Ventilation pathways for the North Pacific oxygen deficient zone. *Global Biogeochemical Cycles* 33 (7), 875–890. doi: 10.1029/2018GB006149

McCreary, J. P. Jr., Yu, Z., Hood, R. R., Vinaychandran, P. N., Furue, R., Ishida, A., et al. (2013). Dynamics of the Indian-Ocean oxygen minimum zones. *Prog. Oceanography* 112, 15–37. doi: 10.1016/j.pocean.2013.03.002

Sarma, V. V. S. S. (2002). An evaluation of physical and biogeochemical processes regulating perennial suboxic conditions in the water column of the Arabian Sea. *Global biogeochemical cycles* 16 (4), 29–21. doi: 10.1029/2001GB001461

Sarma, V. V. S. S., Bhaskar, T. U., Kumar, J. P., and Chakraborty, K. (2020). Potential mechanisms responsible for occurrence of core oxygen minimum zone in the north-eastern Arabian Sea. *Deep Sea Res. Part I: Oceanographic Res. Papers* 165, 103393. doi: 10.1016/j.dsr.2020.103393

Schmidtko, S., Stramma, L., and Visbeck, M. (2017). Decline in global oceanic oxygen content during the past five decades. *Nature* 542 (7641), 335–339. doi: 10.1038/nature21399

Stramma, L., Johnson, G. C., Sprintall, J., and Mohrholz, V. (2008). Expanding oxygen-minimum zones in the tropical oceans. *Science* 320 (5876), 655–658. doi: 10.1126/science.1153847

frontiers | Frontiers in Marine Science

ORIGINAL RESEARCH
published: 19 May 2022
doi: 10.3389/fmars.2022.858308

Carbon Assimilation by the Picoplanktonic Community Inhabiting the Secondary Chlorophyll Maximum of the Anoxic Marine Zones of the Eastern Tropical North and South Pacific

Montserrat Aldunate[1,2,3*†], *Peter von Dassow*[3,4,5], *Cristian A. Vargas*[3,6] *and Osvaldo Ulloa*[1,3]

[1] Department of Oceanography, University of Concepción, Concepción, Chile, [2] Graduate Program in Oceanography, University of Concepción, Concepción, Chile, [3] Millennium Institute of Oceanography (IMO), University of Concepcion, Concepción, Chile, [4] Department of Ecology, Pontificia Universidad Católica de Chile, Santiago, Chile, [5] Department of Integrative Marine Ecology, Stazione Zoologica Anton Dohrn, Naples, Italy, [6] Coastal Ecosystems & Global Environmental Change Lab (ECCALab), Department of Aquatic Systems, Faculty of Environmental Sciences, Universidad de Concepción, Concepción, Chile

Anoxic marine zones (AMZs) constitute pelagic systems distinguished from the oxygen minimum zones (OMZs) by the complete absence of detectable oxygen and the accumulation of nitrite in mid-waters. At the top of the oxygen-depleted layer and below the oxycline, nutrients are abundant; light intensity is very much reduced (<1% of incident light) and a secondary chlorophyll maximum (SCM) is developed. The shoaling of the oxygen-depleted layer, product of the AMZ expansion, could enhance this SCM, which has little-known biogeochemical effects. Here, we show that the SCM is contributing a measurable signal in the particulate organic carbon (POC), enough to alter the $\delta^{13}C_{POC}$ in the top of the oxygen-depleted layer. This data showed significant differences among stations with and without the development of a SCM, being 3.0‰ heavier when a SCM is developed, and indicating photosynthetic activity and/or remineralization in the top of the AMZ. More depleted $\delta^{13}C_{POC}$ values were also found when no SCM was present indicating stronger chemoautotrophic activity, potentially driven by anammox and sulfur-oxidizing bacteria activity. Assimilation rate data show that when sufficient light and *Prochlorococcus* are present, photosynthesis exceeds chemoautotrophic carbon fixation, and can exceed heterotrophic assimilation of glucose or acetate. However, in the majority of the stations, assimilation rates of both glucose and acetate exceeded carbon fixation rates under light stimulation, suggesting that often the SCM is still a net heterotrophic system.

Keywords: autotrophy, secondary chlorophyll maximum, oxygen minimum zones, anoxia, *Prochlorococcus*, heterotrophy

OPEN ACCESS

Edited by:
Syed WajihAhmad Naqvi, Indian Institute of Technology Kanpur, India

Reviewed by:
J Michael Beman, University of California, Merced, United States
Douglas Andrew Campbell, Mount Allison University, Canada
Mangesh Uttam Gauns, Council of Scientific and Industrial Research (CSIR), India

****Correspondence:***
Montserrat Aldunate
montserrat.aldunate@imo-chile.cl

†Present address:
Montserrat Aldunate, Coastal Ecosystems & Global Environmental Change Lab (ECCALab), Department of Aquatic Systems, Faculty of Environmental Sciences, Universidad de Concepción, Concepción, Chile & Millennium Institute of Oceanography (IMO), University of Concepción, Concepción, Chile

Specialty section:
This article was submitted to Marine Biogeochemistry, a section of the journal Frontiers in Marine Science

Received: *19 January 2022*
Accepted: *19 April 2022*
Published: *19 May 2022*

Citation:
Aldunate M, von Dassow P, Vargas CA and Ulloa O (2022) Carbon Assimilation by the Picoplanktonic Community Inhabiting the Secondary Chlorophyll Maximum of the Anoxic Marine Zones of the Eastern Tropical North and South Pacific. Front. Mar. Sci. 9:858308. doi: 10.3389/fmars.2022.858308

INTRODUCTION

Anoxic marine zones (AMZs) are places in the open ocean with contrasting vertical oxygen concentrations. At the surface, there is a photic and oxic layer followed by an abrupt oxycline. At intermediate depths, there is a complete absence of detectable dissolved oxygen, with accumulation of nitrite (Revsbech et al., 2009; Thamdrup et al., 2012; Ulloa et al., 2012), and the occasional presence of H_2S close to the coast (Schunck et al., 2013). Under this anoxic layer, oxygen concentrations increase again. These AMZs are prominent in the Eastern Tropical North and South Pacific (ETNP and ETSP respectively) and in the Arabian Sea (Ulloa et al., 2012). At the top of the anoxic layer, just below a chlorophyll minimum in the oxycline, nutrients are abundant and sunlight levels are very low (<1% of incident light) and in certain cases, a secondary chlorophyll maximum (SCM) develops. This SCM is mainly formed by the picocyanobacteria *Prochlorococcus*, specifically by the ecotypes: LLIV, LLV and LLVI (Lavin et al., 2010), with the last two ecotypes now being renamed as AMZ I and AMZ II respectively, and a recently discovered novel orange-fluorescent ecotype, the ecotype AMZ III, which was traditionally associated with *Synechococcus*-like cells (Ulloa et al., 2021). None of these AMZ ecotypes have yet been successfully cultivated, and photosynthetic picoeukaryotes have not been detected within the SCM (Lavin et al., 2010; Aldunate et al., 2020).

Garcia-Robledo et al. (2017) showed that AMZ *Prochlorococcus* has the ability for carbon fixation through photosynthesis and that this carbon might be recycled through the microbial loop or exported to deeper areas within the AMZs. Furthermore, they also showed that the SCM is producing oxygen, which is not detected because respiration is greater than production. This cryptic oxygen cycle might impact other members of the microbial community, supporting important aerobic metabolisms, such as aerobic respiration and nitrite oxidation (Garcia-Robledo et al., 2017). However, due to the position of the SCM within the water column, it is likely to be transported frequently by internal waves or turbulence to depths where sunlight is scarce for supporting photosynthesis (Cepeda-Morales et al., 2009), decreasing the population or simply dissipating the SCM, and hence stopping the carbon fixation and oxygen production in the top of the anoxic layer. Therefore, it is necessary to understand how the presence or absence of a SCM can influence the net community metabolisms, to explore whether the community is heterotrophic, chemoatotrophic, or net phototrophic.

On the other hand, the expansion of the AMZs (Stramma et al., 2008), and the subsequent shoaling of the upper boundary of the anoxic layer to illuminated waters (Gilly et al., 2013) potentially enhance the SCM. In this way, how the presence/absence of the SCM impacts the carbon metabolism of the AMZ microbial community is still poorly understood.

In this work, we focus on testing the hypothesis that the presence of a SCM has a significant biogeochemical impact in the AMZs. This is expressed in the carbon fractionation and the relative importance of phototrophic vs chemoautotrophic carbon fixation and the light impact in the community organic carbon assimilation. To test this hypothesis, we compared measurements of $\delta^{13}C$ for particulate organic carbon (POC) from the primary and secondary chlorophyll maximum (PCM and SCM respectively) in two AMZs in the Eastern Tropical North and South Pacific oceans during five oceanographic cruises with measurements of $\delta^{13}C$ of POC from the top of the AMZ layer when no SCM was present. To explore the relative importance of carbon fixation through phototrophy vs chemoautotrophy and the potential impact of the light on the community organic carbon assimilation we performed organic and inorganic carbon uptake rates experiments.

MATERIALS AND METHODS

Sampling Site and Field Collection

Samples were obtained from a total of 39 stations in the AMZs of the Eastern Tropical North (ETNP) and South Pacific (ETSP), during five cruises: NH1410 (May 2014) and RB1603 (April 2016) for the ETNP, and NBP1305 (June-July 2013), AT2626 (January 2015) and LowpHOx I (November 2015) for the ETSP (see station map in **Figure 1**; **Table S1**). Samples were collected based on fluorescence and oxygen profiles of each station, taking water from the PCM (fluorescence peak at the surface), the SCM (fluorescence peak at the top of the oxygen-depleted layer) and from the top of the oxygen-depleted layer when no SCM was detected. Samples were collected using a pump profiler system (PPS) that pumps water directly from the desired depth while profiling the water column with an attached CTD system (Seabird SBE-19 plus for ETNP and Seabird SBE-25 for ETSP) providing continuous records of salinity, temperature, depth, dissolved oxygen (Seabird SBE 43 oxygen sensor; all cruises) and *in vivo* fluorescence (WETStar for ETNP cruise and ECO-AFL/FL for ETSP cruises, both WET Labs fluorometers). Discrete nutrient samples were analyzed using standard colorimetric methods according to the manufacturers specifications and the fluorometric method of Holmes et al. (1999). In April 2016 (ETNP; cruise RB1603) seawater was pumped into the laboratory and connected to an auto analyzer for high-resolution profiles of NO_3^-, NO_2^-, and NH_4^+, binned to 1 measurement per meter.

Natural Abundance of $^{13}C/^{12}C$ and Incubation Experiments

Both for the PCM and SCM, natural abundance of $^{13}C/^{12}C$ in suspended POC (0.3 – 3 μm size fraction) was determined by filtering 2-3 L of seawater though a 3-µm pore polycarbonate membrane filter and collecting the microbial biomass on a 0.3 µm nominal pore size glass fiber filter (Sterlitech GF-75; pre-combusted at 500°C for 6 h). The GF-75 filters were dried onboard or frozen in liquid nitrogen. Once in the laboratory, GF-75 filters were fumed with HCl vapors for 8 h to drive off inorganic carbon and then dried and encapsulated in tin capsules. Samples were analyzed at the University of California Davis Stable Isotope Facility by using an Elementar Vario EL Cuve or Micro Cube elemental analyzer (Elementar Analysensysteme GmbH, Hanau, Germany) interfaced to a

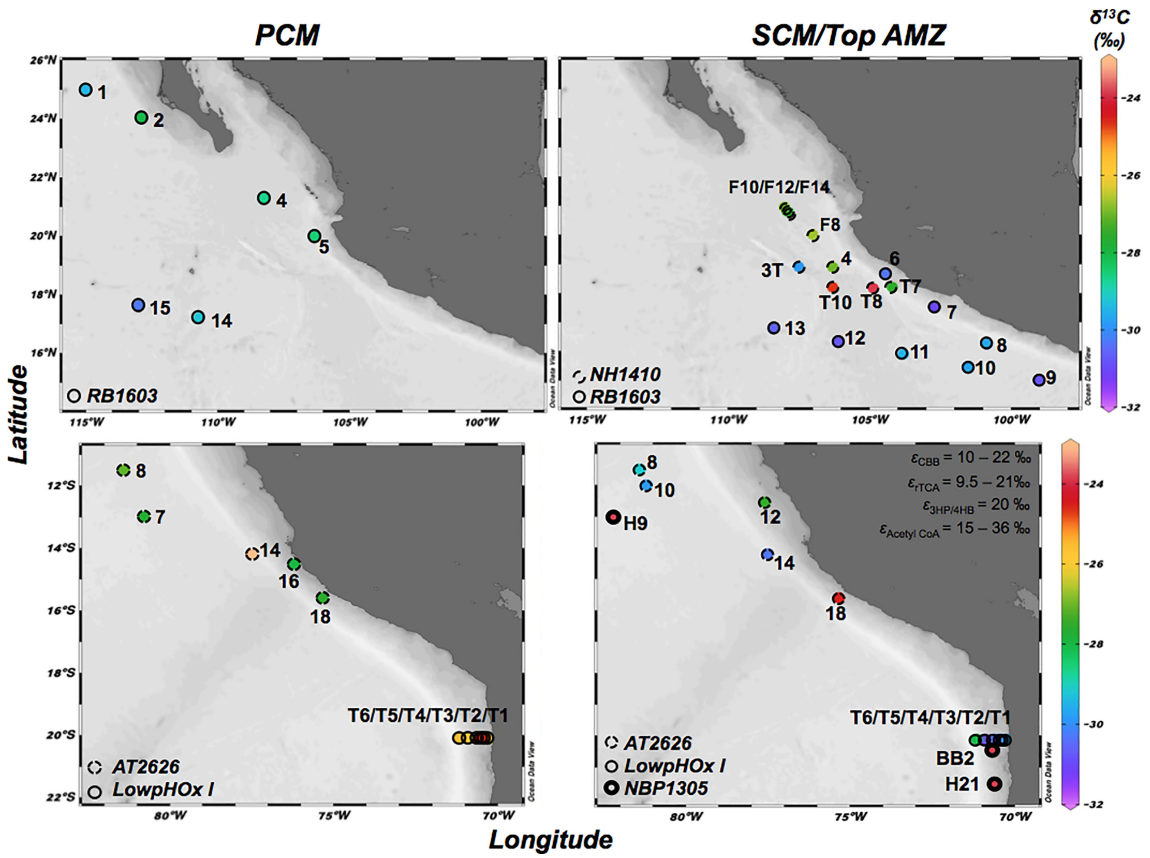

FIGURE 1 | Map with the sampled stations in the ETNP (cruises: NH14010 and RB1603) and the ETSP (cruises: NBP1305, AT2626 and LowpHOx I). Colors indicate $\delta^{13}C$ (‰) of POC (0.3 – 3.0 μm size fraction) in the primary chlorophyll maximum (PCM) (left panels), and in the secondary chlorophyll maximum (SCM) and top AMZ when no SCM was present (right panels). ϵ indicates the isotopic discrimination of the enzymes involved in the Calvin Benson Bassham (CBB) cycle, reductive Tricarboxylic Acid (rTCA) cycle, 3-hydroxypropionate/4-hydroxybutyrate (3HP/4HB) cycles and Acetyl CoA cycle.

PDZ Europa 20–20 isotope ratio mass spectrometer (Sercon Ltd., Cheshire, UK). The standard used was VPDB (Vienna Pee Dee Belemnite) and the long-term precision reported is ±0.2‰ for $\delta\ ^{13}C_{POC}$.

Incubation experiments were performed for determination of uptake rates of organic and inorganic carbon sources in the SCM. Water from the SCM was collected in a 20-L glass bottle and purged for 20 min with a mixture of 800 ppm CO_2 balanced He in order to avoid any oxygen contamination during the sampling and maintain the *in situ* pCO_2/pH. This water was siphoned to 6 – 12 custom-made incubation bottles (1.1 L) and each bottle placed in a water bath inside a temperature-controlled cold van (see diagram in Aldunate et al., 2020). The incubation conditions were set to simulate *in situ* temperature (ranging between 14 and 16°C depending of the station) and light (blue light with intensities of 10 – 30 μmol photons m^{-2} s^{-1}). Three different ^{13}C-labeled compounds (Cambridge Isotope Laboratories) were used to assess the potential carbon uptake rates in the SCM. Final concentrations represented enrichments of 14.9-20.3% for ^{13}C-bicarbonate (HCO_3^-), 17.7% for ^{13}C-glucose and 16.5% for ^{13}C-acetate. After 12 h of incubation, picoplankton from each bottle was concentrated by filtering though a 3-µm pores polycarbonate membrane filter and collecting the microbial biomass on a 0.3 µm nominal pore size glass fiber filter (Sterlitech GF-75; pre-combusted at 500°C for 6 h). Then, filters were fumed with HCl vapors, dried, encapsulated and sent for analysis as described above for $^{13}C/^{12}C$ natural abundance measurements.

Carbon Assimilation Rates Calculations

Assimilation rates ($\rho^{13}C$; mg C L^{-1} h^{-1}) were calculated for each carbon source using the equation (1) (Slawyk et al., 1977):

$$\rho^{13}C = \frac{\left[\frac{(R_{POC} - R_n) \times \left(\frac{POC}{12 \times V_f}\right)}{R_C}\right]}{T} \quad (1)$$

Where R_{POC} represents the ^{13}C enrichment in the filter after incubation (atom %) and R_n represent the natural abundance of ^{13}C (atom %). POC represents the amount of particulate organic carbon recovered in the filter after incubation (µg), V_f represents the incubation volume and T indicates the

incubation time (hours). The excess enrichment of the tracer after its addition at the beginning of the incubation is indicated by R_C (in %) and is calculated using the equation (2):

$$R_C = \frac{\left[\left(\frac{V^{13}C \times 13C}{V_b}\right) + C_i \times C_a\right] \times 100}{C_i + \frac{V^{13}C \times 13C}{Vb}} \quad (2)$$

Where $V^{13}C$ represent the volume of the ^{13}C tracer solution added to the incubation bottle (0.5 mL). 13C represents the concentration in ^{13}C of the added tracer. C_i represents the concentration of the carbon source in the sample before tracer addition; C_a indicates the natural abundance of ^{13}C (in absolute value) and V_b is the volume of sample bottles (1.1 L).

When the tracer additions resulted in initial enrichments exceeding 50%, rates should be considered as potential uptake.

Statistical Analyses

The Kruskal-Wallis test was used to test statistical significance of differences among $\delta^{13}C_{POC}$ from the ETNP SCM, the ETSP SCM and ETSP where there are no SCM, with significance set at 0.05. Correlations between $\delta^{13}C_{POC}$ from the ETNP and ETSP and other environmental variables were calculated using Pearson's correlation analysis, after variables were log-transformed as Log_{10} (X+1). Pearson's correlation coefficients were tested for significance at $\alpha = 0.05$ using XLStat software (AddinSoft SARL).

RESULTS

Environmental Context

The water column structure of the sampled stations exhibited similar patterns between stations, but with some differences (see examples in **Figure 2**). The oxygen profiles showed a superficial oxygenated layer (60-80 m deep), followed by an abrupt oxycline where oxygen dropped to levels below detection by the dissolved oxygen sensors of the CTD at greater depths in the ETNP (90 and 160 m depth) than in the ETSP (70 and 127 m depth). Previous results using the more sensitive dissolved oxygen sensor (STOX sensor; Revsbech et al., 2009; Thamdrup et al., 2012; Garcia-Robledo et al., 2017) as well as the accumulation of nitrite at these depths suggest these layers might be considered anoxic. SCMs were present at the top of the oxygen-depleted layer at average depths of 100 m depth and varied in intensity among stations (see **Figure 2**). Strong SCMs were found both in the ETNP and ETSP (see example in **Figures 2A–C**), and in extreme cases the maximum fluorescence of the SCM could equal or even exceed the surface PCM (not shown). In other stations, we observed a clear SCM in both fluorescence and flow cytometry profiles, but this maximum was smaller than the surface PCM (example in **Figures 2D–F**). Finally, there were stations in the ETSP where no SCM could be detected (example in **Figures 2G–I**; all stations in cruise LowpHOx-I)."

At the depth of the PCM in the surface oxic layer, both nitrate ($\bar{X}$ = 4.5 μM; SD = 4.5 μM) and nitrite ($\bar{X}$ = 0.4 μM; SD = 0.5 μM) concentrations were low, with nitrate accumulating with depth through the oxycline (**Figure 2**; **Table S2**). Once within the oxygen-depleted layer, nitrate showed a slight decrease ($\bar{X}$ = 22.0 μM; SD = 5.4 μM) coupled to nitrite accumulation ($\bar{X}$ = 1.4 μM; SD = 2.3 μM; **Figures 2B, E, H**). Flow cytometry analyses showed marked changes of picophytoplankton with depth (**Figures 2C, F, I**). In the surface oxic layer, the PCM was composed of high abundances of *Prochlorococcus* ($\bar{X}$ = 36.6 x10^3 cell mL^{-1}; SD = 60.4 x10^3 cell mL^{-1}), *Synechococcus* ($\bar{X}$ = 25.1 x10^3 cell mL^{-1}; SD = 32.8 x10^3 cell mL^{-1}) and PPE ($\bar{X}$ = 11.8 x10^3 cell mL^{-1}; SD = 14.7 x10^3 cell mL^{-1}). The abundances of these three groups decreased with depth throughout the oxycline (**Figure 2**; **Table S2**). However, in the stations where a SCM was detected, in the oxygen-depleted layer, *Prochlorococcus* dominated numerically ($\bar{X}$ = 41.0 x10^3 cell mL^{-1}; SD = 25.9 x10^3 cell mL^{-1}), representing on average 93.9% of the picophytoplankton community of the SCM. A less abundant group of orange-fluorescent cells (probably AMZ III *Prochlorococcus*) was also present ($\bar{X}$ = 2.2 x10^3 cell mL^{-1}; SD = 2.6 x10^3 cell mL^{-1}), representing on average 5.1%, of the picophytoplankton community of the SCM, while PPE were very low or undetectable (**Table 1**).

$\delta^{13}C$ of POC at the depth of the PCM and SCM

The natural abundance of $\delta^{13}C_{POC}$ in both the PCM and SCM in the ETNP and ETSP showed a high variability (**Figures 1**, **3**; **Table 2**). $\delta^{13}C_{POC}$ values in the ETNP PCM were in general less variable and more depleted in ^{13}C compared with the ETSP PCM, with averages of -28.7‰ (SD = 1.1‰; n = 8) and -26.1s (SD = 2.5‰ n = 6) respectively (**Figure 3** top panel). On the other hand, $\delta^{13}C_{POC}$ values in the SCM both in the ETNP and ETSP presented similar distributions, ranging from -31.1‰ to -23.9‰ for the ETNP and from -30.4‰ to -23.8‰ for the ETSP. However, the majority of the data is slightly depleted in the ETNP SCM with 50% of the data (n = 17) distributed between -29.9‰ and -27.0‰, compared with the ETSP SCM with 50% or the data (n = 8) between -29.3‰ and -23.9‰. In the case of the samples taken during LowpHOx-I cruise where no SCM was detected (ETSP top AMZ; **Figure 3**), samples were taken from the top of the oxygen-depleted layer. $\delta^{13}C_{POC}$ values were extremely depleted, ranging from -31.0‰ to -28.1‰ (**Figure 3** bottom panel; **Table 2**).

Multiple-pairwise comparisons among $\delta^{13}C_{POC}$ for the ETNP SCM, the ETSP SCM, and ETSP top AMZ (no SCM was developed), indicated that there were no significant differences between $\delta^{13}C_{POC}$ from ETNP SCM vs. ETSP SCM at a 95% confidence level, with the variability among stations only 9% higher in the ETNP SCM. However, significant differences were found between $\delta^{13}C_{POC}$ from ETSP SCM vs. ETSP top AMZ where no SCM was developed, with values 3.3‰ on average heavier and the variability among stations 55% higher when the SCM was developed (**Table 3**). Moreover, no significant correlations were found between $\delta^{13}C_{POC}$ in the SCM and the abundance of *Prochlorococcus* or any other environmental variable evaluated in this study such as nutrients, distance to the coast, among others.

Carbon Assimilation Rates

Uptake rates for inorganic (bicarbonate) and organic (glucose and acetate) carbon sources were measured in incubation

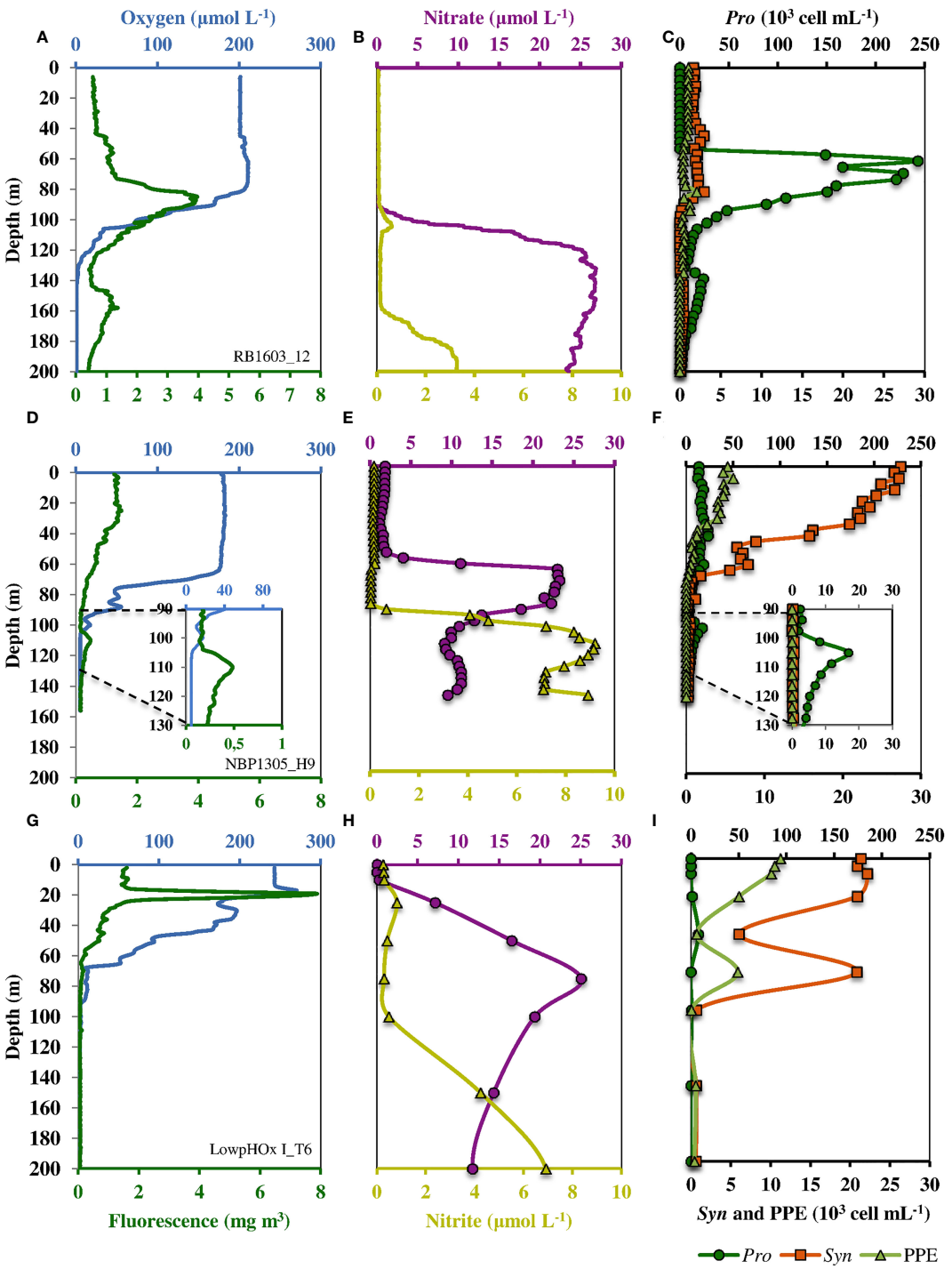

FIGURE 2 | Example vertical structures of water columns and picoplankton with strong, weak, and no SCM at the top of the oxygen-deficient layer in the AMZs. Panels **(A–C)** represents a strong SCM in the ETNP (cruise RB1603, station 12); panels **(D–F)** represent a weak SCM in the ETSP (cruise NBP1305, station H9); and panels **(G–I)** represent an example when no SCM was present in the ETSP (cruise LowpHOx I, station T6). Left panels show oxygen and fluorescence profiles (CTD + fluorometer). Middle panels show nitrate and nitrite profiles measured in continuous flow coupling the PPS and an autoanalyzer **(B)** and a discrete sampling **(E, H)**. Right panels show cell count ($\times 10^3$ cell mL^{-1}) profiles of picophytoplankton components obtained by a high-resolution sampling analyzed by flow cytometry. Dark green circles indicate *Prochlorococcus*, light green triangles indicate PPE, and orange squares represent orange-fluorescent cells.

TABLE 1 | Flow cytometric analysis of the microbial community at the peak depth of the secondary chlorophyll maximum (SCM) for the Eastern Tropical North Pacific (ETNP) and Eastern Tropical South Pacific (ETSP), including: cruise name; station; peak depth of the SCM in meters; *Prochlorococcus* (*Pro*), orange-fluorescent cells (OFC), photosynthetic picoeukaryotes (PPE), non-fluorescent picoplankton (NFP), fluorescent picoplankton (FPP = *Pro* + *Syn* + PPE) abundances (x10^3 cells mL^{-1}); *Pro*, *Syn* and PPE relative abundances (in %) to the fluorescent picoplankton.

Cruise	Station	Depth (m)	*Pro*	*Syn*	PPE (x10^3 cell mL^{-1})	NFP	FPP	*Pro*	OFC (%)	PPE
ETNP										
NH1410	ST04	100	39.2	2.3	0.0	383	41.5	94.4	5.6	0.1
	F8	100	33.6	1.8	0.1	439	35.4	94.9	4.9	0.2
	T7	90	12.1	3.4	0.0	169	15.5	78.3	21.7	0.0
	T8	89	77.1	10.9	0.0	518	88.1	87.6	12.4	0.0
	T10	110	61.1	4.8	0.0	266	65.9	92.7	7.2	0.0
	3T	115	17.6	0.8	0.0	212	18.4	95.4	4.5	0.1
	10F	95	58.4	4.7	0.0	297	63.0	92.6	7.4	0.1
	12F	85	84.7	8.3	0.0	322	93.1	91.1	8.9	0.0
	14F	100	61.4	3.2	0.1	248	64.6	94.9	5.0	0.1
RB1603	ST6	90	52.9	1.3	0.0	556	54.2	97.6	2.4	0.0
	ST7	93	77.5	2.0	0.0	664	79.5	97.5	2.5	0.0
	ST8	97	58.4	1.8	0.0	586	60.3	97.0	3.0	0.0
	ST9	95	40.0	0.9	0.0	535	40.9	97.8	2.2	0.0
	ST10	128	12.8	0.5	0.0	671	13.3	96.3	3.7	0.0
	ST11	115	91.9	0.3	5.1	421	97.4	94.4	0.3	5.3
	ST12	156	22.0	0.2	0.0	402	22.3	98.9	1.1	0.0
	ST13	160	7.1	0.2	0.0	398	7.3	96.6	3.4	0.0
Av.		107								
ETSP										
NBP1305	H 9	113	9.2	0.3	0.0	344	9.5	97.3	2.6	0.1
	H 21	70	7.2	0.7	0.0	436	7.9	91.2	8.8	0.0
	BB2	88	32.7	0.6	0.0	674	33.3	98.2	1.8	0.1
AT2626	ST 08	112	56.50	0.58	2.92	163	60.0	94.2	1.0	4.9
	ST 10	117	46.13	1.30	0.82	196	48.3	95.6	2.7	1.7
	ST 12	127	23.45	0.43	1.47	229	25.3	92.5	1.7	5.8
	ST 14	78	16.25	0.72	1.15	420	18.1	89.7	4.0	6.4
	ST 18	77	26.35	2.27	0.00	504	28.6	92.1	7.9	0.0
Av.		98								
Total Av.		**104**	**41.0**	**2.2**	**0.5**	**402.1**	**43.7**	**93.9**	**5.1**	**1.0**
SD		22	25.9	2.6	1.2	158.2	27.8	4.3	4.6	2.1

Total average are in bold.

experiments in light vs. dark with water samples taken from the SCM (**Figure 4**; **Table S1**). Our results show that bicarbonate (C_i) assimilation in the SCM was highly variable among stations and was always higher in the presence of light (**Figure 4A**). During incubations with light, C_i assimilation rates varied between 4.2 and 150.3 nmol C L^{-1} d^{-1} for the ETNP and between 2.4 and 157.4 nmol C L^{-1} d^{-1} in the ETSP ($\bar{X}$ = 43.7 nmol C L^{-1} d^{-1}; SD = 59.8 nmol C L^{-1} d^{-1}; all stations). Pearson's correlation analysis showed a positive and significant correlation (r = 0.765 p = 0.009) between these rates and the relative abundance of fluorescent cells (*Prochlorococcus* + orange-fluorescent cells) in the total picoplanktonic community (*Prochlorococcus* + orange-fluorescent cells + NFP), with high rates and abundances in the stations T7 in the ETNP (cruise NH1410) and ST8 in the ETSP (cruise AT2626) (**Table S2**). During dark incubations, C_i assimilation rates were very low, but present and ranging between 1.96 and 17.8 nmol C L^{-1} d^{-1} in the ETNP and between 0.5 and 64.8 nmol C L^{-1} d^{-1} in the ETSP ($\bar{X}$ = 4.8 nmol C L^{-1} d^{-1}; SD = 4.5 nmol C L^{-1} d^{-1}; all stations). On average, C_i assimilation rates in the dark were 11.5 times lower (SD =13.9; min = 0.2; max = 44.6) than in the light.

We also performed experiments using organic carbon sources glucose and acetate during the ETNP cruises. In our experiments with glucose, the calculated assimilation rates were also variable among stations and were generally higher in the light (4 out of 6 stations) (**Figure 4B**). Although we found a strong negative correlation between the distance to the coast and the difference between the glucose assimilation rates in light and dark, it was not statistically significant (r = -0.755; p = 0.083). However, there was a strong negative and statistically significant correlation (r = -0.918; p = 0.009) between SCM depth and the difference between glucose assimilation rates in light and dark. That is, there was greater stimulation by light in glucose uptake rates with samples collected from a shallower SCM. The maximum uptake rate recorded was in station T8 (cruise NH1410), with values of 72.1 nmol C L^{-1} d^{-1} in incubations with light and 54.5 nmol C L^{-1} d^{-1} in dark incubations. The lowest uptake rate was recorded in station F8 (cruise NH14010) with values of 1.1 nmol C L^{-1} d^{-1} during incubations with light and 0.8 nmol C L^{-1} d^{-1} during dark incubations (**Figure 4D**). The maximum difference between light and dark uptake rates (19.7 nmol C L^{-1} d^{-1}; being 1.4-fold higher during light incubations) was recorded at station ST6 (cruise RB1603).

We compared C_i and glucose assimilation rates in the only station that we have both measurements (cruise NH1410, St. F8). The results showed that C_i assimilation rate in the SCM

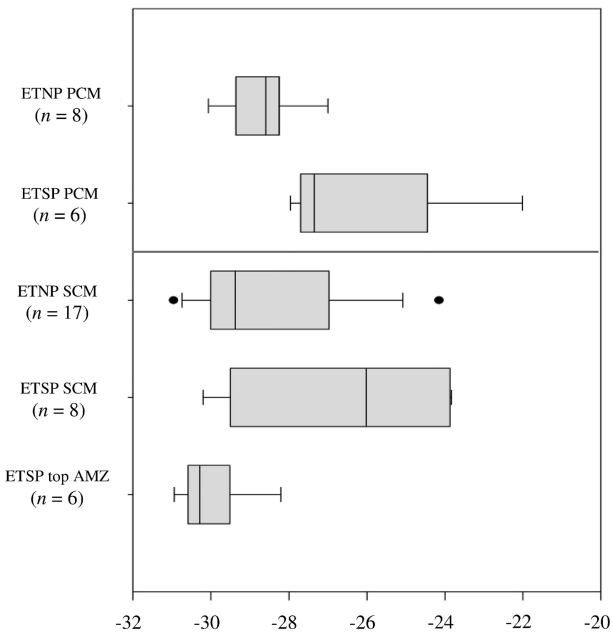

FIGURE 3 | Boxplot of natural abundance of $\delta^{13}C$ (‰) of POC (0.3 – 3.0 μm size fraction) during the ETNP and ETSP cruises. PCM indicates primary chlorophyll maximum (top panel), SCM indicates secondary chlorophyll maximum and "ETSP top AMZ" indicates samples taken at the top of the AMZ when no SCM was present (bottom panel). *n* is the number of measurements per group. The bars indicate the minimum and the maximum values, and the dots indicate the outliers.

exceeded assimilation of glucose by 26.7-fold during light incubations and 2.1-fold during dark incubations (**Figure 4D**). Additionally, we compared C_i and glucose assimilation rates for all stations. Our results showed that C_i assimilation rates ($\bar{X}$ = 43.7 nmol C L^{-1} d^{-1}; SD = 59.8 nmol C L^{-1} d^{-1}; min = 2.4 nmol C L^{-1} d^{-1}; max = 157.4 nmol C L^{-1} d^{-1}) were on average 1.3 times higher than glucose assimilation rates ($\bar{X}$ = 32.4 nmol C L^{-1} d^{-1}; SD = 32.2 nmol C L^{-1} d^{-1}; min = 1.1 nmol C L^{-1} d^{-1}; max = 72.1 nmol C L^{-1} d^{-1}) during light incubations (**Figures 4A, B**). However, during dark incubations, C_i assimilation rates ($\bar{X}$ = 4.8 nmol C L^{-1} d^{-1}; SD = 4.5 nmol C L^{-1} d^{-1}; min = 1.0 nmol C L^{-1} d^{-1}; max = 14.8 nmol C L^{-1} d^{-1}) were on average 5.7 times lower than glucose assimilation rates ($\bar{X}$ = 27.7 nmol C L^{-1} d^{-1}; SD = 22.3 nmol C L^{-1} d^{-1}; min = 0.8 nmol C L^{-1} d^{-1}; max = 54.5 nmol C L^{-1} d^{-1}) (**Figures 4A, B**), showing a prevalence of heterotrophic over autotrophic metabolism at least when no light was present.

Three measurements of acetate assimilation rates were performed in the ETNP (cruise RB1603) (**Figure 4C**). Results showed a high variability among stations, with maximum assimilation rates during light incubations in the station ST9 (203.7 nmol C L^{-1} d^{-1}) and minimum assimilation rates in station ST12 (19.9 nmol C L^{-1} d^{-1}). However, the data is insufficient to identify a pattern between light and dark incubations.

TABLE 2 | Summary of the $\delta^{13}C$ in the particulate organic carbon ($\delta^{13}C$ –POC; ‰) in the primary chlorophyll maximum (PCM) and secondary chlorophyll maximum (SCM) by cruise for the Eastern Tropical North Pacific (ETNP) and Eastern Tropical North Pacific (ETSP).

	PCM					SCM				
	depth (m)	$\delta^{13}C$ (‰)				depth (m)	$\delta^{13}C$ (‰)			
ETNP										
Cruise	**Av.**	**Max.**	**Min.**	**Av.**	**SD**	**Av.**	**Max.**	**Min.**	**Av.**	**SD**
NH1410						98	-23.9	-29.9	-26.9	1.8
RB1603	72	-26.5	-30.3	-28.7	1.1	117	-29.4	-31.1	-30.1	0.6
ETSP										
Cruise										
NBP1305						90	-23.9	-23.9	-23.9	0.0
AT2626	24	-21.7	-28.0	-26.1	2.5	102	-24.5	-30.7	-28.3	2.4
								Anoxic Layer		
LowpHOx I	10	-24.5	-28.1	-25.7	1.3	100	-28.1	-31.0	-30.0	1.0

TABLE 3 | Kruskal-Wallis test for the comparison among δ^{13}C-ETNP SCM, δ^{13}C-ETSP SCM and δ^{13}C-ETSP top AMZ (no SCM). K is Kruskal-Wallis test statistic and DF is degrees of freedom.

Kruskal-Wallis test/Two-tailed test	
K (observed value)	6.385
K (critical value)	5.991
DF	2
p-value	0.041
alpha	0.05

Test interpretation:
H0: The samples come from the same population.
Ha: The samples do not come from the same population.
As the computed p-value is lower than the significance level alpha = 0.05, one should reject the null hypothesis H0, and accept the alternative hypothesis Ha.

DISCUSSION

Our results highlight the importance of picocyanobacteria inhabiting the SCM for modifying the carbon cycle and the isotopic composition of the POC at the top of the oxygen-depleted layer in the AMZs. The structure of the water columns of the stations sampled in both the ETNP and ETSP showed the paradigmatic vertical structure reviewed by Ulloa et al. (2012). The picophytoplanktonic communities inhabiting the SCM in oxygen-depleted subsurface waters differed consistently from those composing the PCM in the oxic surface waters in both abundance and composition similar to previous observations (Goericke et al., 2000; Lavin et al., 2010). Our results show similar trends, with a PCM composed mainly by *Prochlorococcus* (Av. Rel. Ab. = 40.3%) and *Synechococcus*-like orange fluorescent cells (Av. Rel. Ab. = 39.3%), and with an abundant community of PPE (Av. Rel. Ab. = 20.4%). In contrast, the SCM picophytoplanktonic community was dominated numerically by *Prochlorococcus* cells (Av. Rel. Ab. = 94.0%) and to a lesser extent by orange-fluorescent cells (Av. Rel. Ab. = 5.1%) and almost no detectable PPE (Av. Rel. Ab. <1%) (**Table S2**) (Lavin et al., 2010; Garcia-Robledo et al., 2017; Aldunate et al., 2020). The dominant wavelength of light in the SCM (or in the top of the oxygen-depleted layer when no SCM is developed) is blue, with intensities that are in the range of 2-5 μmol photons m^{-2} s^{-1} (Garcia-Robledo et al., 2017). Thus, the great abundance of *Prochorococcus* at such low light levels have been explained by the high concentration of transmembrane divinyl chlorophyll *a* and *b* complexes as their main photosynthetic light-harvesting antennae, very efficient absorbing blue light (Moore and Chisholm, 1999, Goericke et al., 2000). These SCMs, contributed

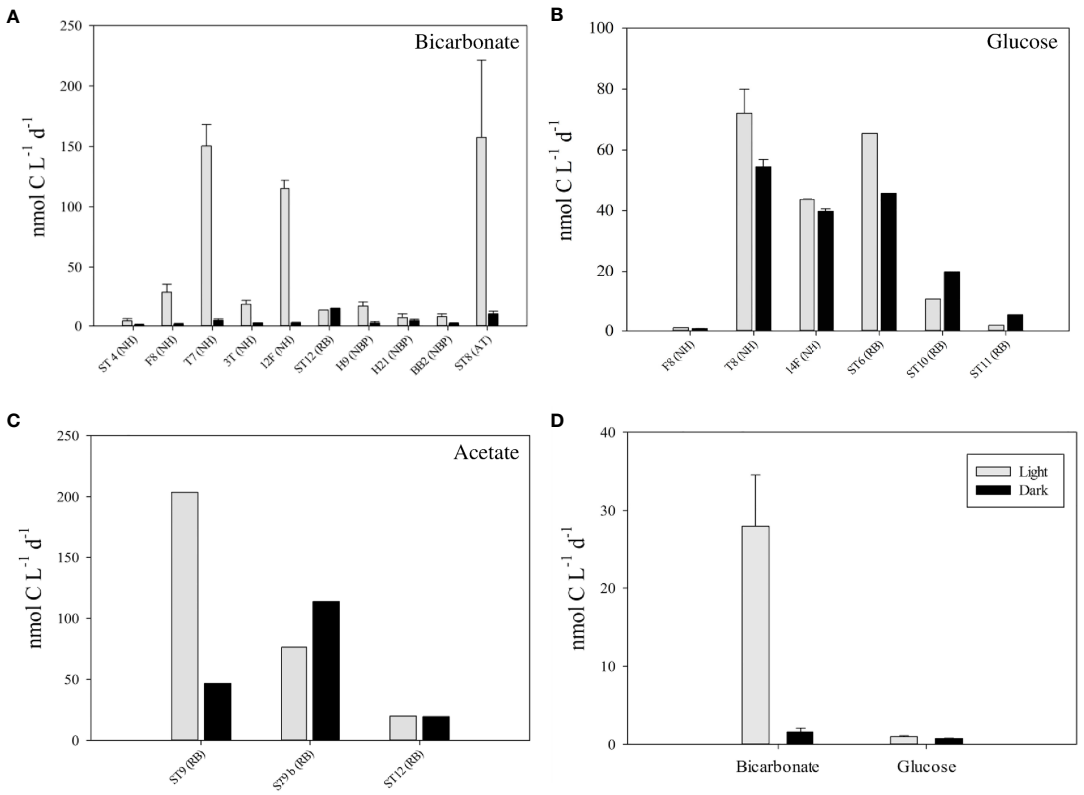

FIGURE 4 | Carbon assimilation rates for bicarbonate **(A)**, glucose **(B)** and acetate **(C)** during light (grey bars) and dark (black bars) incubations for several stations at the depth of the SCM (name of the cruise in parenthesis; NH is NH1410 cruise; RB is RB1603 cruise; AT is AT2626 cruise; NBP is NBP1305 cruise). Panel **(D)** represents C assimilation rates for bicarbonate and glucose during light (grey bars) and dark (black bars) incubations for the SCM at the station F8 in the cruise NH1410. Incubations lasted 12 hours. No incubations were performed in the LowpHOx I cruise.

a measurable signal in POC, enough to alter the $\delta^{13}C_{POC}$ in the top of the oxygen-depleted layer. Also, assimilation rates showed that when sufficient light and *Prochlorococcus* are present, photosynthesis exceeds chemoautotrophic carbon fixation, and can exceed heterotrophic assimilation of glucose or acetate, indicating that chemoautotrophic activity, is normally less important compared with photosynthesis when a SCM, formed by AMZ *Prochlorococcus*, has developed below the oxycline.

Assimilative C Metabolism in the AMZ

POC samples (< 3 μm) represent a mixture of carbon from living and dead phytoplankton, non-fluorescent bacteria, archaea and picoeukaryotes, as well as other components such as organic detritus. $\delta^{13}C_{POC}$ values depend partially on the isotopic composition of the sources of carbon taken up by the microorganisms composing POC (*i.e.* dissolved organic and inorganic carbon) and the isotopic discrimination (ϵ) of the enzymes involved in those processes (Blair et al., 1985).

In the surface, at the depth of the PCM, microorganisms performing the Calvin-Benson-Bassham (CBB) cycle pathway mediated by the enzyme RuBisCO typically dominate the autotrophic community (e.g. Raven, 2009; Hügler and Sievert, 2011; Ruiz-Fernández et al., 2020). This enzyme can generate a large kinetic isotopic fractionation against ^{13}C (ϵ = 10 - 22‰; Hayes, 2001), with plankton reported values of $\delta^{13}C_{POC}$ from -18 to -24‰ in the surface waters (Barros et al., 2010; Podlaska et al., 2012). However, in some stations, the PCM was developed in the upper oxycline (**Figure 2**), where the aerobic ammonium oxidation represents a very important process in our study site, contributing up to 50% of the total dark carbon fixation (Molina and Farías, 2009). This process fixes C_i using 3-hydroxypropionate/4-hydroxybutyrate cycles, and is associated with Thaumarchaeota of the Marine Group I (Ruiz-Fernández et al., 2020). These ammonia-oxidizing archaea, with *Nitrosopumilus maritimus* as a representative, strongly discriminate against de ^{13}C from the C_i (ϵ = 20‰) reaching $\delta^{13}C$-biomass values of approximately -25.8‰ (Könneke et al., 2012). We found natural $\delta^{13}C_{POC}$ values ranging from -30.3‰ to -26.5‰ for the ETNP and from -28.0‰ to -21.7‰ in the ETSP (**Figure 3**). Although within our data there were $\delta^{13}C_{POC}$ values within the expected range for planktonic samples, most of our data showed ^{13}C-depleted values.

Alternative explanations could consider the size fraction of the particles, since most studies consider POC > 0.45, 0.7, 0.8, or 1.0 μm (Close and Henderson, 2020) while this study considered the picoplanktonic fraction (0.3 to 3.0 μm) leaving out larger groups of phytoplankton *e.g.* diatoms, and selecting groups such as *Prochorococcus*, *Synechococcus* and PPE. As large phytoplankton such as diatoms often have higher $\delta^{13}C_{POC}$ values than small phytoplankton and heterotrophic microorganisms (Hansman and Sessions, 2016), the exclusion of these organisms in our POC samples would tend to remove their ^{13}C- enriched signature, explaining in part the depleted $\delta^{13}C_{POC}$ at surface.

In the major AMZs of the world, a partitioning of the marker genes associated with different autotrophic carbon fixation pathways has been reported along the oxygen gradient (Ruiz-Fernández et al., 2020), which fractionate against ^{13}C differentially (Preuß et al., 1989). The oxygen-depleted layer within the AMZs harbors a considerable chemoautotrophic community, including anammox bacteria and sulfur-oxidizers (Stevens and Ulloa, 2008) with metabolisms that strongly fractionate against ^{13}C, producing ^{13}C-depleted biomass (Schouten et al., 2017). Even though the CBB pathway is dominant throughout the entire water column, the reductive Acetyl-CoA pathway is a C-fixing pathway very important in suboxic to oxygen-depleted layers (Ruiz-Fernández et al., 2020), is mainly associated to Planctomycetes of the genus *Candidatus* Scalindua (anammox bacteria), and has a large enzymatic isotope effect (ϵ = 15 - 36‰; Hayes, 2001; Schouten et al., 2017).

The contrasting isotopic data from the stations sampled in the upper part of the oxygen-depleted layer in the presence vs. absence of an SCM can be interpreted as a consequence of the biogeochemical effect of the SCM community in the AMZ. The reduction of inorganic carbon by chemoautotrophs may lead to a significantly greater depletion of ^{13}C than that resulting from photosynthetic fixation (Ruby et al., 1987; Hayes, 2001). Thus, during our study, depleted ^{13}C values in POC were found in the top of the oxygen-depleted layer where the SCM was developed, being markedly more depleted in the top of the oxygen-depleted layer of the ETSP when no SCM was present (**Figure 3**). When the SCM is present, *Prochlorococcus* and anammox bacteria may compete for ammonium, and the cryptic oxygen production by *Prochlorococcus* in the SCM also may repress anammox activity (Aldunate et al., 2020) or autotrophic denitrification (Di Capua et al., 2019). Thus, if no SCM is present, no oxygen is produced in the top of the oxygen-depleted layer and anammox bacteria can be important, explaining more depleted values. On the contrary, when the SCM is present, other (micro)aerobic metabolisms become important such as aerobic respiration and nitrite-oxidation (Garcia-Robledo et al., 2017). A high abundance of transcripts of nitrite oxidizing bacteria (genus Nitrospina) and transcripts encoding nitrite oxidoreductase (nxr) have been found within the SCM (Garcia-Robledo et al., 2017). This is consistent with the metagenomic sequences related to the reductive Tricarboxylic Acid (rTCA) cycle, found in dysoxic to anoxic waters in the AMZ, which are associated to the autotrophic carbon fixation in Nitrospina gracilis, a known aerobic nitrite oxidizer (Ruiz-Fernández et al., 2020). The rTCA pathway has lower enzymatic isotope effect (ϵ = 9.5 - 20.1‰; House et al., 2003; Reid et al., 2013) compared with CBB or Acetyl-CoA pathways. Furthermore, nitrite oxidation rates have been shown to peak in the SCM (Ganesh et al., 2015), and can be being comparable in magnitude with our C*i* fixation rates and with the Ci fixation rates and oxygen production reported by Garcia-Robledo et al., 2017. Actually, it has been shown that nitrite oxidation rates have the potential to consume all the oxygen produced in the SCM (Beman et al., 2021b).

In addition to autotrophs, the oxygen-depleted layer includes heterotrophic microorganisms and part of its isotopic signature comes from the isotopic effect during the assimilation of dissolved organic carbon (DOC). The reported values of

$\delta^{13}C$ -DOC are relatively invariant with depth and geographic region in the ocean, with values in the range of -20‰ to -22‰ (Benner et al., 1997). As the isotopic effect during the assimilation of DOC by heterotrophic microorganisms is very low (0 to 1.9‰; (Fry and Sherr, 1989), it is assumed that the heterotrophic community contribution to POC is only 0.1 to 2‰ heavier that $\delta^{13}C_{DOC}$ (Abelson and Hoering, 1961; Ingram et al., 1973; Monson and Hayes, 1982; Blair et al., 1985). This consideration implies that, the variations that we detect in the $\delta^{13}C_{POC}$ values between one sample and another would reflect the variations in the autotrophic community composing POC (photosynthesis, chemosynthesis). However, the oxidation or remineralization of organic matter releases ^{13}C-depleted carbon back into the inorganic reservoir, making POC heavier (Freeman, 2001). Thus, slightly higher $\delta^{13}C_{POC}$ values in the oxygen-depleted layer, where a SCM is developed (relative to when no SCM is developed) could indicate activity of heterotrophic metabolisms.

This is consistent with the variations in the SCM $\delta^{13}C_{POC}$ isotopic signals vs. the stations where there was no development of a SCM, the $\delta^{13}C_{POC}$ values in the SCM being on average 3.3 ‰ heavier (photosynthesis signal) than when there was no development of a SCM (chemoautotrophy signal). This changes also agrees with the findings of Vargas et al. (2021) for the ETSP off Chile whose results suggest a dynamic shift, in terms of carbon fixation, from a chemoautotrophic dominated oxygen-depleted layer (absence of a SCM), to a largely photoautotrophic/nitrifying system with predominance of heterotrophic processes (development of a SCM). Thus, these results highlight the importance of picocyanobacteria inhabiting the SCM for modifying the carbon cycle and the isotopic composition of the POC at the top of the oxygen-depleted layer in the AMZs.

We were unable to factors that associated with the high variability in $\delta^{13}C_{POC}$ both in the PCM and SCM. Here it may be important to consider that the POC and $\delta^{13}C_{POC}$ integrate recent environmental history in a way that may not correlate well with snapshots of instantaneous environmental variables. For example, $\delta^{13}C_{POC}$ may reflect physical dynamics, such as vertical movements due to internal waves that could alter the light field, affecting the relative rates of photosynthesis compared to other metabolic processes. Alternatively, $\delta^{13}C_{POC}$ could also be affected by trajectories in community dynamics that are not detected by flow cytometry of single time points.

Carbon Assimilation Rates

C_i assimilation was strongly stimulated by light, consistent with the photosynthetic activity of *Prochlorococcus* in the SCM (Garcia-Robledo et al., 2017), presenting higher assimilation rates at the stations with greater relative abundance of *Prochlorococcus* (**Table 1**, **Table S2**). Dark C_i assimilation rates were low at all stations (1 – 15 nmol C L^{-1} d^{-1}), and much lower than the maximum C_i assimilation rate observed in the light (157 nmol C L^{-1} d^{-1}), indicating that chemoautotrophic activity, probably associated with anammox or sulfur-oxidazing bacteria (Stewart et al., 2012), is normally less important compared with photosynthesis when light is available and a SCM formed by AMZ *Prochlorococcus* has developed below the oxycline. In addition, dark C_i assimilation rates could also include C_i assimilation for metabolic pathways involved in heterotrophic growth, such as fatty acid synthesis or gluconeogenesis (Roslev et al., 2004). Nevertheless, at some stations, such as station ST12 (RB) and H21 (NBP), C_i assimilation rates in light and dark incubations showed that the chemoautotrophic activity becomes important when photosynthetic activity is low (**Figure 1A**).

Glucose assimilation rates were variable among stations and were in the range of the values reported in the Pacific Ocean by Rich et al. (1996). Our data showed a strong negative and statistically significant correlation ($r = -0.918$; $p = 0.009$) between SCM depth and the difference between glucose assimilation rates in light and dark. Thus, when the SCM develops in more superficial depths (probably with higher light), glucose assimilation is stimulated by light. On the contrary, when the SCM develops at greater depths (lower light), glucose assimilation is independent of light.

It has been pointed out that microorganisms associated with *Roseobacter* and SAR11 clade contribute a large fraction of the total glucose assimilation when there is a low concentration of this carbon source and Flavobacteria (Bacteroidetes) can be important when this carbon source is more concentrated (Alonso and Pernthaler, 2006). *Roseobacter* and Flavobacteria have been found in the oxic surface waters overlaying the oxygen-depleted layer in the AMZs, and only SAR11 is important in the oxygen-depleted layer where the SCM is developed (Stevens and Ulloa, 2008). Although much of this glucose assimilation may be due to the presence of SAR11, *Prochlorococcus* might also contribute. There is evidence that other ecotypes of *Prochlorococcus* (different from those found in oxygen-depleted SCM) use glucose both in laboratory studies (Gómez-Baena et al., 2008) and in the environment (Van Wambeke et al., 2018). In fact, a study at the North Pacific Subtropical Gyre showed that *Prochlorococcus* glucose assimilation rates peak during the day (our experiments were developed in diel time) while rates in the whole community peak during the night-early morning (Muñoz-Marín et al., 2021). Thus, if glucose is available in the SCM (<1% light environment), *Prochlorococcus* might be using it, competing with SAR11 and other heterotrophic organisms that inhabit the SCM.

Acetate is another important organic carbon source in the ocean and can be produced during the anaerobic degradation of complex organic matter and especially during fermentation (Sansone, 1986; Canfield, 1993; Kristensen et al., 1995). This organic carbon source is especially important in sediments (Boschker, 2001), but also has been reported in the water column (Wu et al., 1997; Zhuang et al., 2019). Maximum assimilation rates have been found in the oxic surface waters and near the suboxic/anoxic interface, suggesting that acetate cycling may be important both in oxic and oxygen-depleted environments (Ho et al., 2002). Acetate is used by both heterotrophic organisms (Zhuang et al., 2019), and by

different phytoplankton groups (Combres et al., 1994; Bouarab et al., 2004; Liang et al., 2009; Zhang and Bryant, 2015; Godrijan et al., 2020), including *Synechococcus* (Ihlenfeldt and Gibson, 1977; Yan et al., 2012). Our results showed variable acetate assimilation rates, with similar variability and magnitude to that shown by Ho et al. (2002) in suboxic/anoxic interface. Although we only have three measurements and a pattern has not been found, speculate that sulfate-reducing bacteria might be important in the assimilation of acetate in darkness (Fauque, 1995), while light might stimulate a photoheterotrophic and/or mixotrophic metabolism by numerically important groups at these depths such as members of the SAR11 clade or *Prochlorococcus*.

SUMMARY AND CONCLUSIONS

It has been suggested that anoxic marine zones are in expansion (Stramma et al., 2008), so the anoxic layer boundaries will move to shallower depths, overlapping more frequently with the photic layer (Gilly et al., 2013). This overlap stimulates the presence of a SCM, which has little-known biogeochemical effects (Garcia-Robledo et al., 2017; Beman et al., 2021a). Our results suggest that the presence of SCM has a biogeochemical effect on the layer where it develops, enough to alter $\delta^{13}C$ of POC in the top of the oxygen-depleted layer and reflected in the significant differences between $\delta^{13}C_{POC}$ values found in samples from below the oxycline in presence vs. absence of a SCM, with the samples from a SCM 3.3‰ heavier on average. The reduction of inorganic carbon by chemoautotrophs may lead to a significantly greater depletion of ^{13}C than that resulting from photosynthetic fixation (Ruby et al., 1987; Hayes, 2001). Therefore, more depleted $\delta^{13}C_{POC}$ values when no SCM was present might indicate a stronger chemoautotrophic activity compared with more enriched values when SCM was present. Anammox bacteria and sulfur-oxidizers are important chemoautotrophic groups inhabiting the oxygen-depleted layer of the AMZ (Stevens and Ulloa, 2008; Stewart et al., 2012; Beman et al., 2021a), with anammox bacteria associated to the Acetyl-CoA carbon fixation pathway (Ruiz-Fernández et al., 2020) that strongly fractionate against ^{13}C, producing ^{13}C-depleted biomass (Schouten et al., 2017). On the other hand, when the SCM is present, photosynthesis and (micro)aerobic metabolisms become important as the aerobic respiration and nitrite-oxidation (Garcia-Robledo et al., 2017). Therefore, picocyanobacteria inhabiting the SCM perform an important role modifying the carbon cycle and the isotopic composition of POC at the top of AMZs.

Our estimates of assimilation of inorganic and organic carbon sources by microbial communities inhabiting the oxygen-depleted SCM have provided useful information about the dominant assimilatory pathways. The layer immediately below the oxycline in AMZs is strongly influenced by the presence or absence of AMZ *Prochlococcus* and their relative abundance in the picoplanktonic community and this is reflected in the enhanced of C_i assimilation rates when light is present. C_i assimilation rates in the dark (chemoautotrophic activity) are probably associated with anammox or sulfur-oxidizing bacteria (Stewart et al., 2012) and do not reach the same maximum magnitudes that photosynthetic carbon fixation can reach when an SCM develops. Glucose assimilation was also stimulated by light (photoheterotrophy) and, although there are a variety of microorganisms that can use light as an energy source to assimilate organic carbon, the most abundant in the oxygen-depleted layer are SAR11 and *Prochlorococcus*. Despite the fact that we only have three measurements of acetate assimilation in the SCM, and a pattern has not been found, we detected stimulation by light in one occasion, suggesting photoheterotrophic and/or mixotrophic metabolisms, which we suggest could performed by numerically important groups at these depths such the SAR11 clade or AMZ *Prochlorococcus*. When there is no light stimulation, the assimilation of acetate might result from organisms such as sulfate-reducing bacteria (Fauque, 1995). Therefore, when light and sufficient *Prochlorococcus* are present, photosynthesis exceeds chemoautotrophic carbon fixation, and can exceed heterotrophic assimilation of glucose or acetate. Furthermore, oxygen produced by *Prochlorococcus* may be suppressing anammox activity, explaining the low chemoautotrophic carbon fixation when SCM is present. However, in the majority of the stations, both the maximum glucose and acetate assimilation rates exceeded carbon fixation rates, supporting that the SCM is often still a net heterotrophic system.

DATA AVAILABILITY STATEMENT

The original contributions presented in the study are included in the article/**Supplementary Material**. Further inquiries can be directed to the corresponding author.

AUTHOR CONTRIBUTIONS

MO, PD and OU contributed the concept and design of the study. MO collected the samples during field samplings, conducted the experiments, and analyzed the samples. MO organized the database and analyzed the datasets. MO drafted the manuscript with contributions from PD and CV. All authors contributed to the manuscript revision, read, and approved the submitted version.

FUNDING

This study was financially supported by the Millennium Science Initiative (grant ICN12_019), the ANID-Chile Fondecyt grant 1161483 to O.U. and ANID graduate fellowship to M.A. Additional support has been provided by ANID Fondecyt Postdoctoral project 3210281 to M.A. during the last stage of this study. ANID-Chile National also supported this study by the Competition for ship time (AUB 150006/12806).

ACKNOWLEDGMENTS

We would like to thank to the chief scientists whose invited to us to participate in the cruises included in this study: Bess Ward and Alan Devol (NPB1305) Frank Stewart (NH1410), Margaret Mulholland (AT2626 and RB1603; NSF OCE-1356056) and Amal Jayakumar (RB1603). We also would like to thank the captain and crew of the *R/V Nathaniel B. Palmer*, the *R/V New Horizon*, the *R/V Atlantis* and NOAA vessel *Ronald Brown* for their help with the sampling. We also want to thank to Gadiel Alarcón, Marguerite Blum and Francisco Chavez for their help with the PPS and Cristian Venegas for flow cytometry analysis.

SUPPLEMENTARY MATERIAL

The Supplementary Material for this article can be found online at: https://www.frontiersin.org/articles/10.3389/fmars.2022.858308/full#supplementary-material

REFERENCES

Abelson, P. H., and Hoering, T. C. (1961). Carbon Isotope Fractionation in Formation of Amino Acids by Photosynthetic Organisms. *Proc. Natl. Acad. Sci.* 47, 623–632. doi: 10.1073/pnas.47.5.623

Aldunate, M., Henríquez-Castillo, C., Ji, Q., Lueders-Dumont, J., Mulholland, M. R., Ward, B. B., et al. (2020). Nitrogen Assimilation in Picocyanobacteria Inhabiting the Oxygen-Deficient Waters of the Eastern Tropical North and South Pacific. *Limnol. Oceanogr.* 65, 437–453. doi: 10.1002/lno.11315

Alonso, C., and Pernthaler, J. (2006). Roseobacter and SAR11 Dominate Microbial Glucose Uptake in Coastal North Sea Waters. *Environ. Microbiol.* 8, 2022–2030. doi: 10.1111/j.1462-2920.2006.01082.x

Barros, G. V., Martinelli, L. A., Oliveira Novais, T. M., Ometto, J. P. H. B., and Zuppi, G. M. (2010). Stable Isotopes of Bulk Organic Matter to Trace Carbon and Nitrogen Dynamics in an Estuarine Ecosystem in Babitonga Bay (Santa Catarina, Brazil). *Sci. Total Environ.* 408, 2226–2232. doi: 10.1016/j.scitotenv.2010.01.060

Beman, J. M., Vargas, S. M., Vazquez, S., Wilson, J. M., Yu, A., Cairo, A., et al. (2021a). Biogeochemistry and Hydrography Shape Microbial Community Assembly and Activity in the Eastern Tropical North Pacific Ocean Oxygen Minimum Zone. *Environ. Microbiol.* 23 (6), 2765–2781. doi: 10.1111/1462-2920.15215

Beman, J. M., Vargas, S. M., Wilson, J. M., Perez-Coronel, E., Karolewski, J. S., Vazquez, S., et al. (2021b). Substantial Oxygen Consumption by Aerobic Nitrite Oxidation in Oceanic Oxygen Minimum Zones. *Nat. Commun.* 12 (1), 7043. doi: 10.1038/s41467-021-27381-7

Benner, R., Biddanda, B., Black, B., and McCarthy, M. (1997). Abundance, Size Distribution, and Stable Carbon and Nitrogen Isotopic Compositions of Marine Organic Matter Isolated by Tangential-Flow Ultrafiltration. *Mar. Chem.* 57, 243–263. doi: 10.1016/S0304-4203(97)00013-3

Blair, N., Leu, A., Munoz, E., Olsen, J., Kwong, E., and Des Marais, D. (1985). Carbon Isotopic Fractionation in Heterotrophic Microbial Metabolism. *Appl. Environ. Microbiol.* 50, 996–1001. doi: 10.1128/aem.50.4.996-1001.1985

Boschker, H. (2001). Bacterial Populations and Processes Involved in Acetate and Propionate Consumption in Anoxic Brackish Sediment. *FEMS Microbiol. Ecol.* 35, 97–103. doi: 10.1016/S0168-6496(00)00116-1

Bouarab, L., Dauta, A., and Loudiki, M. (2004). Heterotrophic and Mixotrophic Growth of Micractinium Pusillum Fresenius in the Presence of Acetate and Glucose:Effect of Light and Acetate Gradient Concentration. *Water Res.* 38, 2706–2712. doi: 10.1016/j.watres.2004.03.021

Canfield, D. E. (1993). "Organic Matter Oxidation in Marine Sediments," in *Interactions of C, N, P and S Biogeochemical Cycles and Global Change* (Berlin, Heidelberg: Springer Berlin Heidelberg), 333–363. doi: 10.1007/978-3-642-76064-8_14

Cepeda-Morales, J., Beier, E., Gaxiola-Castro, G., Lavín, M. F., and Godínez, V. (2009). Effect of the Oxygen Minimum Zone on the Second Chlorophyll Maximum. *Cienc. Marinas* 35 (4), 389–403. doi: 10.7773/cm.v35i4.1622

Close, H. G., and Henderson, L. C. (2020). Open-Ocean Minima in δ13c Values of Particulate Organic Carbon in the Lower Euphotic Zone. *Front. Mar. Sci.* 7, 540165. doi: 10.3389/fmars.2020.540165

Combres, C., Laliberte, G., Reyssac, J. S., and Noue, J. (1994). Effect of Acetate on Growth and Ammonium Uptake in the Microalga Scenedesmus Obliquus. *Physiol. Plant* 91, 729–734. doi: 10.1111/j.1399-3054.1994.tb03012.x

Di Capua, F., Pirozzi, F., Lens, P. N. L., and Esposito, G. (2019). Electron Donors for Autotrophic Denitrification. *Chem. Eng. J.* 362, 922–937. doi: 10.1016/j.cej.2019.01.069

Fauque, G. D. (1995). "Ecology of Sulfate-Reducing Bacteria," in *Sulfate-Reducing Bacteria* (Boston, MA: Springer US), 217–241. doi: 10.1007/978-1-4899-1582-5_8

Freeman, K. H. (2001). "11. Isotopie Biogeochemistry of Marine Organic Carbon," in *Stable Isotope Geochemistry*, vol. 43 . Eds. J. W. Valley and D. R. Cole (Berlin: De Gruyter), 579–606). doi: 10.1515/9781501508745-014

Fry, B., and Sherr, E. B. (1989). "δ13c Measurements as Indicators of Carbon Flow in Marine and Freshwater Ecosystems," in *Stable Isotopes in Ecological Research*, eds. Rundel, P. W., Ehleringer, J. R., and Nagy, K. A. (New York, NY: Springer), 196–229. doi: 10.1007/978-1-4612-3498-2_12

Ganesh, S., Bristow, L. A., Larsen, M., Sarode, N., Thamdrup, B., and Stewart, F. J. (2015). Size-Fraction Partitioning of Community Gene Transcription and Nitrogen Metabolism in A Marine Oxygen Minimum Zone. *ISME J.* 9, 2682–2696. doi: 10.1038/ismej.2015.44

Garcia-Robledo, E., Padilla, C. C., Aldunate, M., Stewart, F. J., Ulloa, O., Paulmier, A., et al. (2017). Cryptic Oxygen Cycling in Anoxic Marine Zones. *Proc. Natl. Acad. Sci.* 114, 8319–8324. doi: 10.1073/pnas.1619844114

Gilly, W. F., Michael Beman, J., Litvin, S. Y., and Robison, B. H. (2013). Oceanographic and Biological Effects of Shoaling of the Oxygen Minimum Zone. *Annu. Rev. Mar. Sci.* 5, 393–420. doi: 10.1146/annurev-marine-120710-100849

Godrijan, J., Drapeau, D., and Balch, W. M. (2020). Mixotrophic Uptake of Organic Compounds by Coccolithophores. *Limnol. Oceanogr.* 11396, 1410–1421. doi: 10.1002/lno.11396

Goericke, R., Olson, R. J., and Shalapyonok, A. (2000). A Novel Niche for Prochlorococcus Sp. In the Low-Light Suboxic Envrionrments in the Arabian Sea and the Eastern Tropical North Pacific. *Deep-Sea Res. I* 47 (7), 1183–1205. doi: 10.1016/S0967-0637(99)00108-9

Gómez-Baena, G., López-Lozano, A., Gil-Martínez, J., Lucena, J. M., Diez, J., Candau, P., et al. (2008). Glucose Uptake and Its Effect on Gene Expression in Prochlorococcus. *PloS One* 3, e3416. doi: 10.1371/journal.pone.0003416

Hansman, R. L., and Sessions, A. L. (2016). Measuring the *in Situ* Carbon Isotopic Composition of Distinct Marine Plankton Populations Sorted by Flow Cytometry. *Limnol. Oceanogr.: Methods* 14 (2), 87–99. doi: 10.1002/lom3.10073

Hayes, J. M. (2001). Fractionation of Carbon and Hydrogen Isotopes in Biosynthetic Processes. *Rev. Mineral. Geochem.* 43, 225–277. doi: 10.2138/gsrmg.43.1.225

Ho, T.-Y., Scranton, M. I., Taylor, G. T., Varela, R., Thunell, R. C., and Muller-Karger, F. (2002). Acetate Cycling in the Water Column of the Cariaco Basin: Seasonal and Vertical Variability and Implication for Carbon Cycling. *Limnol. Oceanogr.* 47, 1119–1128. doi: 10.4319/lo.2002.47.4.1119

Holmes, R. M., Aminot, A., Kérouel, R., Hooker, B. A., and Peterson, B. J. (1999). A Simple and Precise Method For Measuring Ammonium in Marine and Freshwater Ecosystems. *Can. J. Fish. Aquat. Sci.* 56, 1801–1808. doi: 10.1139/f99-128

House, C. H., Schopf, J. W., and Stetter, K. O. (2003). Carbon Isotopic Fractionation by Archaeans and Other Thermophilic Prokaryotes. *Organic Geochemistry* 34 (3), 345–356. doi: 10.1016/S0146-6380(02)00237-1

Hügler, M., and Sievert, S. M. (2011). Beyond the Calvin Cycle: Autotrophic Carbon Fixation in the Ocean. *Annu. Rev. Mar. Sci.* 3 (1), 261–289. doi: 10.1146/annurev-marine-120709-142712

Ihlenfeldt, M. J. A., and Gibson, J. (1977). Acetate Uptake by the Unicellular Cyanobacteria Synechococcus and Aphanocapsa. *Arch. Microbiol.* 113, 231–241. doi: 10.1007/BF00492030

Ingram, L. O., Calder, J. A., Van Baalen, C., Plucker, F. E., and Parker, P. L. (1973). Role of Reduced Exogenous Organic Compounds in the Physiology of the Blue-Green Bacteria (Algae): Photoheterotrophic Growth of a "Heterotrophic" Blue-Green Bacterium. *J. Bacteriol.* 114, 695–700. doi: 10.1128/JB.114.2.695-700.1973

Könneke, M., Lipp, J. S., and Hinrichs, K.-U. (2012). Carbon Isotope Fractionation by the Marine Ammonia-Oxidizing Archaeon Nitrosopumilus Maritimus. *Org. Geochem.* 48, 21–24. doi: 10.1016/j.orggeochem.2012.04.007

Kristensen, E., Ahmed, S. I., and Devol, A. H. (1995). Aerobic and Anaerobic Decomposition of Organic Matter in Marine Sediment: Which is Fastest? *Limnol. Oceanogr.* 40, 1430–1437. doi: 10.4319/lo.1995.40.8.1430

Lavin, P., González, B., Santibáñez, J. F., Scanlan, D. J., and Ulloa, O. (2010). Novel Lineages of Prochlorococcus Thrive Within the Oxygen Minimum Zone of the Eastern Tropical South Pacific. *Environ. Microbiol. Rep.* 2, 728–738. doi: 10.1111/j.1758-2229.2010.00167.x

Liang, Y., Sarkany, N., and Cui, Y. (2009). Biomass and Lipid Productivities of Chlorella Vulgaris Under Autotrophic, Heterotrophic and Mixotrophic Growth Conditions. *Biotechnol. Lett.* 31, 1043–1049. doi: 10.1007/s10529-009-9975-7

Molina, V., and Farías, L. (2009). Aerobic Ammonium Oxidation in the Oxycline and Oxygen Minimum Zone of the Eastern Tropical South Pacific Off Northern Chile (~20°s). *Deep Sea Res. Part II: Topical Stud. Oceanogr.* 56 (16), 1032–1041. doi: 10.1016/j.dsr2.2008.09.006

Monson, K. D., and Hayes, J. (1982). Carbon Isotopic Fractionation in the Biosynthesis of Bacterial Fatty Acids. Ozonolysis of Unsaturated Fatty Acids as a Means of Determining the Intramolecular Distribution of Carbon Isotopes. *Geochim. Cosmochim. Acta* 46, 139–149. doi: 10.1016/0016-7037(82)90241-1

Moore, L. R., and Chisholm, S. W. (1999). Photophysiology of the Marine Cyanobacterium Prochlorococcus: Ecotypic Differences Among Cultured Isolates. *Limnol. Oceanogr.* 44, 628–638. doi: 10.4319/lo.1999.44.3.0628

Muñoz-Marín, M., del, C., Duhamel, S., Björkman, K. M., Magasin, J. D., Díez, J., et al. (2021). Differential Timing for Glucose Assimilation in Prochlorococcus and Coexistent Microbial Populations at the North Pacific Subtropical Gyre. *BioRxiv*, 1–45. doi: 10.1101/2021.10.04.462702

Podlaska, A., Wakeham, S. G., Fanning, K. A., and Taylor, G. T. (2012). Microbial Community Structure and Productivity in the Oxygen Minimum Zone of the Eastern Tropical North Pacific. *Deep Sea Res. Part I Oceanogr. Res. Pap.* 66, 77–89. doi: 10.1016/j.dsr.2012.04.002

Preuß, A., Schauder, R., Fuchs, G., and Stichler, W. (1989). Carbon Isotope Fractionation by Autotrophic Bacteria With Three Different C02 Fixation Pathways. *Z. Für Naturforschung C* 44 (5–6), 397–402. doi: 10.1515/znc-1989-5-610

Raven, J. A. (2009). Contributions of Anoxygenic and Oxygenic Phototrophy and Chemolithotrophy to Carbon and Oxygen Fluxes in Aquatic Environments. *Aquat. Microb. Ecol.* 56 (2–3), 177–192. doi: 10.3354/ame01315

Reid, W. D. K., Sweeting, C. J., Wigham, B. D., Zwirglmaier, K., Hawkes, J. A., McGill, R. A. R., et al. (2013). Spatial Differences in East Scotia Ridge Hydrothermal Vent Food Webs: Influences of Chemistry, Microbiology and Predation on Trophodynamics. *PloS One* 8 (6), e65553. doi: 10.1371/journal.pone.0065553

Revsbech, N. P., Larsen, L. H., Gundersen, J., Dalsgaard, T., Ulloa, O., and Thamdrup, B. (2009). Determination of Ultra-Low Oxygen Concentrations in Oxygen Minimum Zones by the STOX Sensor. *Limnol. Oceanogr. Methods* 7, 371–381. doi: 10.4319/lom.2009.7.371

Rich, J. H., Ducklow, H. W., and Kirchman, D. L. (1996). Concentrations and Uptake of Neutral Monosaccharides Along 140°W in the Equatorial Pacific: Contribution of Glucose to Heterotrophic Bacterial Activity and the DOM Flux. *Limnol. Oceanogr.* 41, 595–604. doi: 10.4319/lo.1996.41.4.0595

Roslev, P., Larsen, M. B., Jørgensen, D., and Hesselsoe, M. (2004). Use of Heterotrophic CO2 Assimilation as a Measure of Metabolic Activity in Planktonic and Sessile Bacteria. *J. Microbiol. Methods* 59 (3), 381–393. doi: 10.1016/j.mimet.2004.08.002

Ruby, E. G., Jannasch, H. W., and Deuser, W. G. (1987). Fractionation of Stable Carbon Isotopes During Chemoautotrophic Growth of Sulfur-Oxidizing Bacteria. *Appl. Environ. Microbiol.* 53, 1940–1943. doi: 10.1128/aem.53.8.1940-1943.1987

Ruiz-Fernández, P., Ramírez-Flandes, S., Rodríguez-León, E., and Ulloa, O. (2020). Autotrophic Carbon Fixation Pathways Along the Redox Gradient in Oxygen-Depleted Oceanic Waters. *Environ. Microbiol. Rep.* 12 (3), 334–341. doi: 10.1111/1758-2229.12837

Sansone, F. J. (1986). Depth Distribution of Short-Chain Organic Acid Turnover in Cape Lookout Bight Sediments. *Geochim. Cosmochim. Acta* 50, 99–105. doi: 10.1016/0016-7037(86)90052-9

Schouten, S., Strous, M., Kuypers, M. M. M., Rijpstra, W. I. C., Baas, M., Schubert, C. J., et al. (2017). Stable Carbon Isotopic Fractionations Associated With Inorganic Carbon Fixation by Anaerobic Ammonium-Oxidizing Bacteria. *Appl. Environ. Microbiol.* 70, 3785–3788. doi: 10.1128/AEM.70.6.3785

Schunck, H., Lavik, G., Desai, D. K., Großkopf, T., Kalvelage, T., Löscher, C. R., et al. (2013). Giant Hydrogen Sulfide Plume in the Oxygen Minimum Zone Off Peru Supports Chemolithoautotrophy. *PloS One* 8 (8), e68661. doi: 10.1371/journal.pone.0068661

Slawyk, G., Collos, Y., and Auclair, J.-C. (1977). The Use of the 13 C and 15 N Isotopes for the Simultaneous Measurement of Carbon and Nitrogen Turnover Rates in Marine Phytoplankton1. *Limnol. Oceanogr.* 22, 925–932. doi: 10.4319/lo.1977.22.5.0925

Stevens, H., and Ulloa, O. (2008). Bacterial Diversity in the Oxygen Minimum Zone of the Eastern Tropical South Pacific. *Environ. Microbiol.* 10, 1244–1259. doi: 10.1111/j.1462-2920.2007.01539.x

Stewart, F. J., Ulloa, O., and DeLong, E. F. (2012). Microbial Metatranscriptomics in a Permanent Marine Oxygen Minimum Zone. *Environ. Microbiol.* 14, 23–40. doi: 10.1111/j.1462-2920.2010.02400.x

Stramma, L., Johnson, G. C., Sprintall, J., and Mohrholz, V. (2008). Expanding Oxygen-Minimum Zones in the Tropical Oceans. *Science* 320 (5876), 655–658. doi: 10.1126/science.1153847

Thamdrup, B., Dalsgaard, T., and Revsbech, N. P. (2012). Widespread Functional Anoxia in the Oxygen Minimum Zone of the Eastern South Pacific. *Deep Sea Res. Part I Oceanogr. Res. Pap.* 65, 36–45. doi: 10.1016/j.dsr.2012.03.001

Ulloa, O., Canfield, D. E., DeLong, E. F., Letelier, R. M., and Stewart, F. J. (2012). Microbial Oceanography of Anoxic Oxygen Minimum Zones. *Proc. Natl. Acad. Sci.* 109, 15996–16003. doi: 10.1073/pnas.1205009109

Ulloa, O., Henríquez-Castillo, C., Ramírez-Flandes, S., Plominsky, A. M., Murillo, A. A., Morgan-Lang, C., et al. (2021). The Cyanobacterium Prochlorococcus has Divergent Light-Harvesting Antennae and may Have Evolved in a Low-Oxygen Ocean. *Proc. Natl. Acad. Sci.* 118 (11), e2025638118. doi: 10.1073/pnas.2025638118

Van Wambeke, F., Gimenez, A., Duhamel, S., Dupouy, C., Lefevre, D., Pujo-Pay, M., et al. (2018). Dynamics and Controls of Heterotrophic Prokaryotic Production in the Western Tropical South Pacific Ocean: Links With Diazotrophic and Photosynthetic Activity. *Biogeosciences* 15, 2669–2689. doi: 10.5194/bg-15-2669-2018

Vargas, C. A., Cantarero, S. I., Sepúlveda, J., Galán, A., De Pol-Holz, R., Walker, B., et al. (2021). A Source of Isotopically Light Organic Carbon in a low-pH Anoxic Marine Zone. *Nat. Commun.* 12 (1), 1604. doi: 10.1038/s41467-021-21871-4

Wu, H., Green, M., and Scranton, M. I. (1997). Acetate Cycling in the Water Column and Surface Sediment of Long Island Sound Following a Bloom. *Limnol. Oceanogr.* 42, 705–713. doi: 10.4319/lo.1997.42.4.0705

Yan, R., Zhu, D., Zhang, Z., Zeng, Q., and Chu, J. (2012). Carbon Metabolism and Energy Conversion of Synechococcus Sp. PCC 7942 Under Mixotrophic Conditions: Comparison With Photoautotrophic Condition. *J. Appl. Phycol.* 24, 657–668. doi: 10.1007/s10811-011-9683-2

Zhang, S., and Bryant, D. A. (2015). Biochemical Validation of the Glyoxylate Cycle in the Cyanobacterium Chlorogloeopsis Fritschii Strain PCC 9212. *J. Biol. Chem.* 290, 14019–14030. doi: 10.1074/jbc.M115.648170

Zhuang, G.-C., Peña-Montenegro, T. D., Montgomery, A., Montoya, J. P., and Joye, S. B. (2019). Significance of Acetate as a Microbial Carbon and Energy Source in the Water Column of Gulf of Mexico: Implications for Marine Carbon Cycling. *Global Biogeochem. Cycles* 33, 223–235. doi: 10.1029/2018GB006129

Conflict of Interest: The authors declare that the research was conducted in the absence of any commercial or financial relationships that could be construed as a potential conflict of interest.

this article, or claim that may be made by its manufacturer, is not guaranteed or endorsed by the publisher.

frontiers | Frontiers in Marine Science

ORIGINAL RESEARCH
published: 26 May 2022
doi: 10.3389/fmars.2022.868261

High Diazotrophic Diversity but Low N_2 Fixation Activity in the Northern Benguela Upwelling System Confirming the Enigma of Nitrogen Fixation in Oxygen Minimum Zone Waters

Christian Furbo Reeder[1], Damian L. Arévalo-Martínez[2,3], Joan A. Carreres-Calabuig[4], Tina Sanders[5], Nicole R. Posth[4] and Carolin Regina Löscher[1,6]*

[1] Nordcee, Department of Biology, University of Southern Denmark, Odense, Denmark, [2] Chemical Oceanography department, GEOMAR Helmholtz Centre for Ocean Research Kiel, Kiel, Germany, [3] Institute for Geosciences, Kiel University, Kiel, Germany, [4] Department of Geosciences and Natural Resource Management (IGN), Geology, University of Copenhagen, Copenhagen, Denmark, [5] Institute for Carbon Cycles, Helmholtz Center Hereon, Geesthacht, Germany, [6] Danish Institute for Advanced Science (DIAS), University of Southern Denmark, Odense, Denmark

OPEN ACCESS

Edited by:
Amal Jayakumar, Princeton University, United States

Reviewed by:
Camila Fernandez, UMR7621 Laboratoire d'océanographie microbienne (LOMIC), France
Maren Voss, Leibniz Institute for Baltic Sea Research (LG), Germany

***Correspondence:**
Christian Furbo Reeder
crfurbo@biology.sdu.dk

Specialty section:
This article was submitted to Marine Biogeochemistry, a section of the journal Frontiers in Marine Science

Received: *02 February 2022*
Accepted: *22 April 2022*
Published: *26 May 2022*

Citation:
Reeder CF, Arévalo-Martínez DL, Carreres-Calabuig JA, Sanders T, Posth NR and Löscher CR (2022) High Diazotrophic Diversity but Low N_2 Fixation Activity in the Northern Benguela Upwelling System Confirming the Enigma of Nitrogen Fixation in Oxygen Minimum Zone Waters. Front. Mar. Sci. 9:868261. doi: 10.3389/fmars.2022.868261

Oxygen minimum zones (OMZs) have been suggested as a suitable niche for the oxygen-sensitive process of biological fixation of dinitrogen (N_2) gas. However, most N_2 fixation rates reported from such waters are low. This low N_2 fixation activity has been proposed to result from the unusual community of N_2 fixers, in which cyanobacteria were typically underrepresented. The Northern Benguela Upwelling System (North BUS) is part of one of the most productive marine ecosystems and hosts a well-developed OMZ. Although previous observations indicated low to absent N_2 fixation rates, the community composition of diazotrophs needed to understand the North BUS has not been described. Here, we present a first detailed analysis of the diazotrophic diversity in the North BUS OMZ and the Angola tropical zone (ATZ), based on genetic data and isotope speciation. Consistent with a previous study, we detected a slight N deficit in the OMZ, but isotope data did not indicate any active or past N_2 fixation. The diazotroph community in the North BUS was dominated by non-cyanobacterial microbes clustering with members of gamma-proteobacteria, as is typical for other OMZ regions. However, we found a strikingly high diversity of Cluster III diazotrophs not yet described in other OMZs. In contrast to previous observations, we could also identify cyanobacteria of the clades *Trichodesmium* sp., UCYN-A and *Cyanothece* sp., in surface waters connected to or above the OMZ, which were potentially active as shown by the presence of genes and transcripts of the key functional marker gene for N_2 fixation, *nifH*. While the detection of diazotrophs and the absence of active N_2 fixation (based on isotopic speciation) are consistent with other OMZ observations, the detected regional variation in the diversity and presence of cyanobacteria indicate that we still are far from understanding the role of diazotrophs in OMZs, which, however, is relevant for understanding the N cycle in OMZ

waters, as well for predicting the future development of OMZ biogeochemistry in a changing ocean.

Keywords: nitrogen fixation, diazotrophs diversity, oxygen minimum zone (OMZ), Benguela coastal upwelling system, Angola Basin

1 INTRODUCTION

Nitrogen (N) is an essential nutrient, and limiting for primary production and carbon (C) uptake from the atmosphere in large parts of the ocean (Redfield, 1958; Capone and Carpenter, 1982; Gruber, 2005). Specialized microbes, so-called diazotrophs, can circumvent this shortage due to their ability to fix dinitrogen gas (N_2). Classically, cyanobacteria were considered the most important diazotrophs in the ocean, i.e., the filamentous genus *Trichodesmium* and unicellular genera, including *Crocosphaera* sp. and *Candidatus* Atelocyanobacteriym thalassa (UCYN-A) (Moisander et al., 2010). However, due to their need for light, their habitat is largely restricted to sunlit surface waters. In recent years, a large diversity of non-cyanobacterial diazotrophs has been discovered, many of them from oxygen minimum zone (OMZ) waters (Fernandez et al., 2011; Hamersley et al., 2011; Jayakumar et al., 2012; Löscher et al., 2014; Turk-Kubo et al., 2014; Cheung et al., 2016; Jayakumar et al., 2017; Jayakumar and Ward, 2020; Löscher et al., 2020). These waters are characterized by massive N loss, creating a theoretical need for N_2 fixation by providing excess phosphorous (Ingall and Jahnke, 1997; Deutsch et al., 2007; Kalvelage et al., 2013). Yet studies have confirmed that N_2 fixation is typically minor in such regions (Wang et al., 2019). In addition, anoxic conditions have been shown to reduce the energy constraints of N_2 fixation as compared to nitrate (NO_3^-) uptake, which suggests that N_2 fixation might be an attractive way of N acquisition in oxygen (O_2)-depleted waters (Großkopf and LaRoche, 2012). Indeed, based on the analysis of the key functional marker gene for N_2 fixation, *nifH*, a broad diversity of mostly non-cyanobacterial diazotrophs was found in OMZ waters of the Eastern Tropical North Pacific (ETNP), the Eastern Tropical South Pacific (ETSP), the Arabian Sea (AS), and the Bay of Bengal (BoB) (Fernandez et al., 2011; Halm et al., 2011; Hamersley et al., 2011; Jayakumar et al., 2012; Bonnet et al., 2013; Farnelid et al., 2013; Löscher et al., 2014; Cheung et al., 2016; Löscher et al., 2016a; Jayakumar et al., 2017; Moisander et al., 2017; Christiansen and Löscher, 2019; Löscher et al., 2020; Li et al., 2021).

A recent report of diazotrophs in OMZ waters revealed a biogeographically distinct and diverse community of N_2 fixers throughout the OMZs of the ETNP, ETSP, and AS (Jayakumar and Ward, 2020), but dominated by only a few operational taxonomic units (OTUs) (Jayakumar and Ward, 2020). Interestingly, despite a certain degree of geographical variation in the overall community structure of N_2 fixers, the identified heterotrophic diazotrophs represented similar metabolic types in all OMZ waters (Jayakumar and Ward, 2020). For instance, proteobacteria-like sequences related to *nifH* Cluster I (Zehr et al., 2003) include alpha-proteobacterial methanotrophs and gamma-proteobacterial N_2 fixers such as *Vibrio diazotrophicus* and *Pseudomonas stutzeri*, which have been reported in the OMZ waters of the ETNP, ETSP, AS and BoB (Fernandez et al., 2011; Löscher et al., 2014; Turk-Kubo et al., 2014; Cheung et al., 2016; Jayakumar et al., 2017). Epsilon-proteobacteria related to *Arcobacter nitrofigilis* (Löscher et al., 2014) and sequences related to *Azotobacter vinelandii* and *Teridinibacter tunerae* have been reported (Turk-Kubo et al., 2014) from the ETSP and BoB (Löscher et al., 2020). Besides Cluster I sequences, delta-proteobacterial *nifH* and other more rare *nifH* types of Clusters II, III, and IV (Zehr et al., 2003) have been identified in OMZs, including anaerobic sulphate-reducers in the ETNP (Jayakumar et al., 2017), the ETSP (Löscher et al., 2014; Turk-Kubo et al., 2014; Christiansen and Löscher, 2019), the AS (Jayakumar et al., 2012) and the BoB (Löscher et al., 2020). Cluster II is rarely found and has only been reported in ETSP (Fernandez et al., 2011). Cluster IV, commonly associated with non-functional *nif*-types or paralogue genes, has been reported from the ETNP (Cheung et al., 2016; Jayakumar et al., 2017), the ETSP (Löscher et al., 2014), the AS (Jayakumar et al., 2012) and BoB OMZ waters (Löscher et al., 2020).

Interestingly, while diazotrophs are usually present and diverse in OMZ waters, they only seem to fix N_2 at minimal rates (Bonnet et al., 2013; Dekaezemacker et al., 2013; Löscher et al., 2016b; Jayakumar et al., 2017; Chang et al., 2019; Löscher et al., 2020). One explanation might be the absence of cyanobacterial N_2 fixers from those waters. Only a few sequences related to cyanobacteria have been reported. This includes *Trichodesmium* (<5 sequences) in the ETNP, ETSP, AS and BoB (Jayakumar et al., 2012; Turk-Kubo et al., 2014; Jayakumar et al., 2017; Löscher et al., 2020), UCYN-B, related to *Crocosphaera* in the ETSP (Löscher et al., 2014) and UCYN-A in the ETSP (Turk-Kubo et al., 2014; Li et al., 2021). In addition, UCYN-B related sequences were detected in the AS based on 16S rRNA analysis (Mazard et al., 2004).

To date, the diazotrophic composition of the OMZ waters in the Northern Benguela upwelling system (North BUS) has not been extensively studied. The Benguela current system spans from 14°S to 35°S is one of four major eastern boundary upwelling regions, and is recognized as the most productive upwelling zone in the global ocean (Bakun, 1996; Carr, 2001). The Benguela current system consists of northern (14–26°S) and southern (26–35°S) sectors with active upwelling which are separated by the Lüderitz upwelling cell (25–27°S). North of 14°S, the coastal areas are part of the Angola tropical zone (ATZ). Upwelling zones in this area are not affected by winds as coastal upwelling zones typically are. North BUS is characterized by equatorward winds, low water temperatures, high phytoplankton biomass, and seasonally O_2 depleted waters with locally intense hydrogen sulfide (H_2S) events and massive N loss (Tyrrell and Lucas, 2002; Kuypers et al., 2005; Monteiro and van der Plas, 2006;

Bartholomae and van der Plas, 2007; Hutchings et al., 2009; Nagel et al., 2013; Vizy et al., 2018). At 17°S, the warm tropical waters coming from the north are mixed with cold waters from the south. This is also known as the Angola-Benguela Frontal Zone (Hutchings et al., 2009). This study focused on the ATZ and North BUS. Waters off North BUS are characterized by N loss, together with increased fluxes of phosphate (PO_4^{3-}) from sediments underlying an OMZ to the water column (Ingall and Jahnke, 1997). Creating a low N:P ratio similar to other OMZ regions, this would classically be considered favorable for N_2 fixation (Wasmund et al., 2005; Flohr et al., 2014). Previous studies have identified N_2 fixation from below the detection limit to up to 8 nmol N L^{-1} d^{-1} in surface waters (>70 m) (Staal et al., 2007; Sohm et al., 2011; Wasmund et al., 2015). While previous studies (Staal et al., 2007; Sohm et al., 2011) might have even overestimated N_2 fixation rates dues to the possible use of contaminated $^{15}N_2$ gas (Dabundo et al., 2014), all rates presented in those studies were comparable to other reports of N_2 fixation in OMZ waters with rates of 0.4 nmol L^{-1} d^{-1} to 3.5 nmol L^{-1} d^{-1} found in the ETNP and ETSP (Fernandez et al., 2011; Bonnet et al., 2013; Löscher et al., 2014; Jayakumar et al., 2017). N_2 fixation was also low or undetectable in the OMZ waters of BoB, (Löscher et al., 2020; Saxena et al., 2020) and has not been measured in the OMZ of the AS, but diazotrophs have been found active (Jayakumar et al., 2012). A similar environment has measured 0.07 nmol L^{-1} d^{-1} in the Southern California Bight (Hamersley et al., 2011) and 0.44 nmol L^{-1} d^{-1} in the Baltic Sea (Farnelid et al., 2013).

The last decade has revealed a distinct diversity of heterotrophic diazotrophs in OMZ waters (Bonnet et al., 2013; Dekaezemacker et al., 2013; Löscher et al., 2016b; Jayakumar et al., 2017; Chang et al., 2019; Löscher et al., 2020). Their role and importance, however, in these OMZ waters are not clear. Understanding the community composition of diazotrophs in these waters is the first step to shed light on their potential contribution to N_2 fixation. Here, we present a first report of the diazotrophic community composition and distribution present in the OMZ of the Northern BUS and the ATZ using a combination of isotope analysis, and sequencing of the biomarker gene, *nifH*. Results were compared and compiled into a statistical analysis with similar sequencing techniques from OMZs in the ETNP, ETSP and AS (Jayakumar and Ward, 2020).

2 MATERIALS AND METHODS

2.1 Seawater Sampling

Samples were collected during the cruise M148/1 on the German research vessel *RV Meteor* from 24th of May to 29th of June 2018. The survey crossed a large area with contrasting environmental properties (e.g., temperature) from the ATZ (South ATZ (10-16°S) and North ATZ (north from 5°S) to North BUS (17-23°S). Details regarding the individual stations can be seen in **Table 1** and the **Supplementary Material, Table S1**. Sampling was carried out by means of a CTD-Rosette system equipped with double sensors for salinity and

TABLE 1 | Overview and description of the *nifH* clone library.

Location	Area	Station	Lon (E°)	Lat (N°)	Depth (m)	O_2 feature	O_2 (µM)	Temp (°C)	Sal	NO_3^- (µM)	NO_2^- (µM)	NH_4^+ (µM)	PO_4^{3-} (µM)	$\delta^{15}N$-NO_3^- [‰]	No. of DNA Seq	No. of cDNA seq
North Angola Tropical Zone	Waters off Angola	42	7	-11.7	97	Oxycline	42.2	24.5	35.6	NA	NA	NA	NA	NA	17	0
		46	11.6	-11.7	9.5	Oxic	222.5	24.3	35.7	NA	NA	NA	NA	NA	90	0
		50	12.5	-11.1	97.2	Oxycline	50.7	15.1	35.6	NA	NA	NA	NA	NA	21	0
		80	13.1	-10.7	143.8	Oxycline	44.3	14.5	35.5	NA	NA	NA	NA	NA	11	0
		80	13.1	-10.7	47.7	Oxycline	69.1	20.7	35.9	10.28	0.266	0.11	0.862	NA	16	0
		80	13.1	-10.7	18.3	Oxic	234.9	22.9	35.5	NA	NA	NA	NA	NA	0	91
	Waters off South Angola	87	11.4	-15	9	Oxic	219.8	24.8	35.8	0	0.001	NA	0.164	NA	74	0
		92	11.8	-15.3	17.3	Oxic	154.9	19.1	35.8	12.6	0.27	0.17	0.924	NA	0	0
South Angola Tropical Zone	Waters off Congo	76	11.2	-6.4	336	Oxycline	27.7	21.6	35.9	1.31	0.079	NA	0.296	NA	56	0
		76	11.2	-6.4	29.7	Oxic	143.4	9.5	34.9	40.98	0	NA	2.506	NA	14	23
		76	11.2	-6.4	9.2	Oxic	211.5	20.5	36	10.1	0.644	NA	0.782	NA	6	34
Northern Benguela Upwelling System	Waters off Namibia	98	11.6	-17.5	37.3	Oxic	101.2	15.1	35.5	29.99	0.646	0.2	1.918	5.17	33	0
		98	11.6	-17.5	7.6	Oxic	103.2	15.1	35.5	NA	NA	0.2	NA	5.24	64	0
		99	12.3	-19	100	Oxycline	23	13.7	35.3	30.3	0.278	0.17	2.38	6.43	85	0
		99	12.3	-19	57.9	Oxycline	35.6	13.7	35.3	28.98	0.103	0.17	2.177	6.33	26	0
		99	12.3	-19	37.6	Oxycline	72.2	13.7	35.3	30.98	0.224	0.17	2.346	6.5	30	0
		102	13.8	-22	95.8	OMZ	3.3	12.8	35.2	7.97	0.508	0.05	1.496	15.87	77	0
		102	13.8	-22	71	Suboxic	10.4	12.8	35.2	22.18	0.514	0.25	2.523	9.8	65	0
		101	13.3	-20.9	17.3	Oxic	123.8	14	35.2	26.8	0.1	0.17	2.1	6.44	0	39
		101	13.3	-20.9	92.5	Suboxic	6.7	12.2	35.1	10.28	1.8	0.64	0.99	6.51	0	4
		103	14.2	-22.7	87.1	OMZ	2.7	12.2	35.1	10.28	1.801	1.9	0.99	11.49	82	0

*From each location, CTD corresponds to sampling station in **Figure 1**. O_2 feature refers to oxic waters (>100 µM), the oxycline (20-100 µM), suboxic waters (5-20 µM) and OMZ waters (<5 µM). The total number of sequences along with the corresponding biogeochemical data from each station is presented.*
NA standard for not available.

temperature (Sea-Bird SBE 43), as well as sensors for turbidity and fluorescence (ECO FLNTURTD, Wetlabs) and O_2 (Sea-Bird Electronics, Bellevue, WA). The O_2 sensor was calibrated by manual Winkler titration. Seawater samples for nutrient analyses were obtained from 10 Niskin bottles attached to the CTD-Rosette. Nitrate (NO_3^-), nitrite (NO_2^-), and PO_4^{3-} concentrations (detection limits: 0.01 µM (NO_3^-, NO_2^-, and PO_4^{3-})) were determined on board with a QuAAtro auto-analyzer (SEAL Analytical GmbH, Germany) immediately after sampling following Grasshoff (1999). Ammonium (NH_4^+) concentrations were measured photometrically following Grasshoff (1999) (detection limit: 0.05 µM (NH_4^+)).

2.2 Nucleic Acid Extraction

Seawater samples for nucleic acid extraction were collected from Niskin bottles in a volume of 0.5 -2 L (exact volumes were recorded) and filtered on Millipore Durapore membrane filters (Millipore, Billaterica, USA) with a pore diameter of 0.2 µm using a gentle vacuum. After a maximum of 20 min of filtration time, filters were stored at -80°C until further analysis. Filters were flash-frozen in liquid nitrogen and nucleic acids (DNA and RNA) were extracted using the Qiagen DNA/RNA AllPrep Kit (Qiagen, Hildesheim, DE) as described in Löscher et al. (2012). The nucleic acid concentration and quality were checked spectrophotometrically on a MySpec spectrofluorometer (VWR, Darmstadt, Germany). Genomic DNA was eliminated from RNA by treating it with DNase I (Invitrogen, Thermo Fisher Scientific United Kingdom). RNA was checked for purity by a *nifH* nested PCR. As no DNA contamination could be seen, RNA was transcribed to cDNA using Qiagen QuantiTect Reverse Transcription Kit (Qiagen, Hildesheim, DE).

2.3 Molecular Methods

Environmental DNA and cDNA samples (48 samples in total) were subjected to *nifH* PCR-amplification using a nested PCR with primers and conditions described by Zani et al. (2000). Both nested PCR runs were carried out with Taq DNA polymerase (Thermo Scientific, Waltham USA). For the first PCR round, Bovine Serum Albumin (BSA, 1.6 µg in 25 µl) (Thermo Scientific, Waltham, USA) were added to the PCR mix. *nifH* amplicons were purified from an agarose gel using the E.Z.N.A. Gel Extraction Kit (Omega Bio-Tek, Norcross, USA). In total, 21 *nifH* products were recovered covering waters from ATZ (northern part off Congo (5°S), southern part off Angola (10-16°S)), North BUS (off Namibia (17-23°S)) (**Figure 1**) and different O_2 ranges (oxic waters >100 µM O_2, oxycline 20-100 µM O_2, suboxic 5-20 µM O_2, and OMZ <5 µM O_2. *nifH* amplicons were Topo TA cloned (Thermo Fisher Scientific,

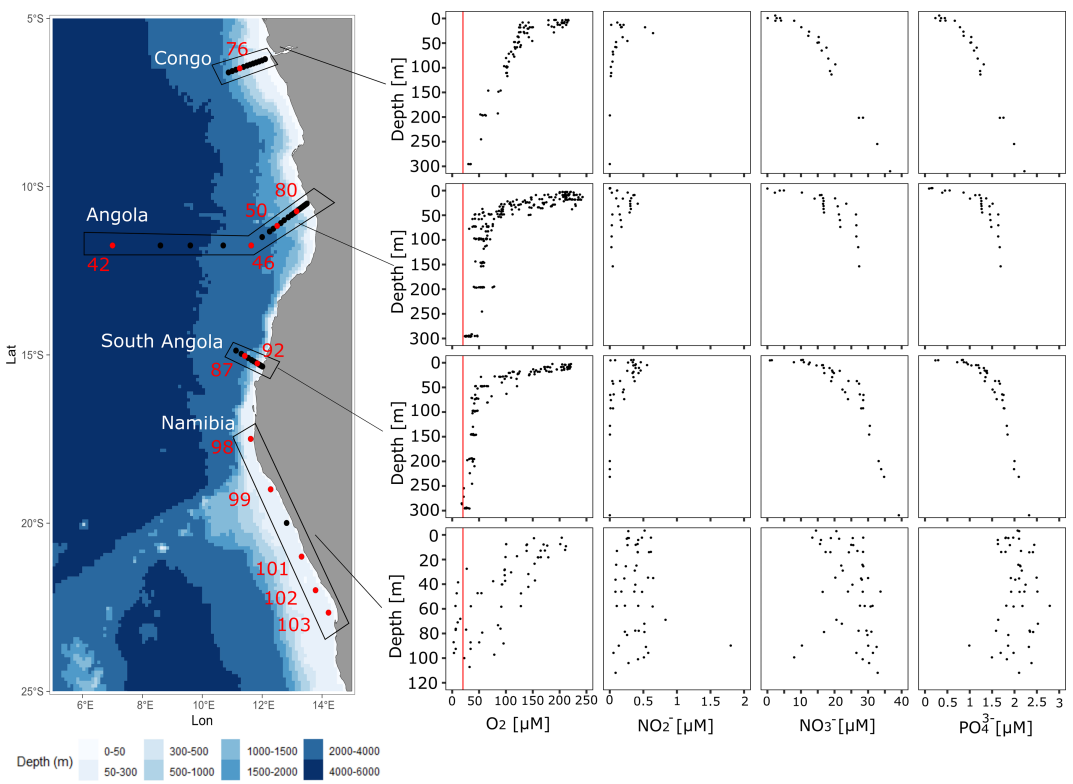

FIGURE 1 | Left panel: Topographical map of the North ATZ (north of 10°S) and South ATZ (between 10 and 15°S) and the North BUS (15-25°S). The four coastal sections of the cruise track are indicated with black dots. Red dots indicate stations from which *nifH* amplicons were generated. Right panels: Oxygen and nutrient depth profiles from each transect as indicated with black boxes on the map. The red line indicates an O_2 concentration of 20 µM.

Waltham, US). Sequencing was carried out as a service of the Institute of Clinical Molecular Biology in Kiel, Germany. In total, 958 *nifH* sequences (191 transcripts and 767 gene sequences) were obtained. Sequences were quality-checked and trimmed to a length of 321 bp in MEGAX (Kumar et al., 2018). The sequences were submitted to NCBI with accession ID OK082431-OK083221, OL412005-OL412134 and OM453718 - OM453821.

2.4 Phylogenetic Analysis and OTU Generation

nifH amplicons were translated into amino acids and aligned in MEGAX (Kumar et al., 2018). Based on the nucleotide alignment OTUs were defined using Mothur (Schloss et al., 2009). For comparability, OTUs were generated following Jayakumar and Ward (2020). Briefly, a distance matrix was created using *pairwise.seqs* followed by assigning sequences to OTUs using *cluster.classic* at the default setting (furthest neighbor clustering algorithm). *nifH* richness was calculated using the command *rarefaction.single*, from each location and O_2 feature. OTUs were defined at a threshold of 0.03% which is similar to the level for species definition used for 16S rDNA (Gaby et al., 2018). Different alignment constraints (delay divergent cut-off (%) at 30, 60, 80, 95) and gap penalties (10 and 20) were tested. There were no observed changes in OTU outcome. In total, 82 OTUs were generated, which were aligned with published *nifH* sequences using *Methanosarcina lacustris* (AAL02156) as the outer group. A maximum-likelihood phylogenetic tree was constructed using the Poisson model with 1000 bootstraps replicate. Finally, a phylogenetic tree was visualized in iTOL (Letunic and Bork, 2019).

2.5 Natural Abundance of $\delta^{15}N$ in the Particulate Organic Material (POM) and NO_3^-

For each sample, 2 L of seawater was filtered onto pre-combusted (450°C, 4-6 hours) 45 mm 0.7 GF/F filters (GE Healthcare Life Sciences, Whatman, USA) at 200 mbar vacuum. Prior to analysis, filters were stored in a -20°C freezer. Natural abundances of $\delta^{15}N$ in POM were determined as follows. Filters were acidified over fuming HCl overnight, oven-dried, and duplicates were analyzed on an Elemental Analyzer Flash EA 1112 series (Thermo Fisher, USA) coupled to an isotope ratio mass spectrometer (Finnigan Delta Plus XP, Thermo Fisher, USA) against a caffeine standard.

Isotope ratios of NO_3^- (plus NO_2^-) were determined by the denitrifier method (Casciotti et al., 2002; Sigman et al., 2001). This method is based on a mass spectrometric measurement of isotopic ratios of N_2O produced by the bacterium *Pseudomonas aureofaciens*. Briefly, 20 nmol of NO_3^- were injected in a 20 mL vial containing *P. aureofaciens*. Two international standards were used (IAEA NO_3^- δ15N= +4.7 ‰, USGS34 $\delta^{15}N$ = −1.8 ‰) for a regression-based correction of isotope values. For further quality assurance, an internal standard was measured with each batch of samples. The standard deviation for $\delta^{15}N$ was better than 0.2 ‰. Samples were measured on a Delta Plus XP mass spectrometer coupled to a Gasbench II (Thermo Fisher, USA).

2.6 Statistical Analysis

The most abundant OTUs from North BUS along with environmental factors (NO_2^-, NO_3^-, PO_4^{3-}, O2, NH_4^+, isotope ($\delta^{15}N - NO_3^-$), depth, temperature, turbulence, salinity and fluorescence) were used for a redundancy analysis (RDA) using the vegan package in R (Oksanen et al., 2020). Briefly, environmental factors from OTUs mixed from different stations were included by taking the average between the stations contributing above 5% to the OTU. Environmental factors were Hellinger-transformed using *decostand*. Then, the most parsimonious RDA model was determined using vegan's function *ordistep*. The RDA model for OTUs derived from this study included depth, $\delta^{15}N - NO_3^-$, salinity, O_2, NH_4^+ and NO_3^- as explanatory variables. Turbulence, fluorescence, NO_2^- and PO_4^{3-} was removed as those parameters turned out to be repetitive. For cross-comparison between OMZ regions, OTUs from the ETNP, ETSP and AS taken from Jayakumar and Ward, 2020 were included in an additional RDA. Compiling OTUs from all OMZ waters, temperature, depth, O_2, NO_2^- and NO_3^- were identified as explanatory variables. Raw data can be accessed in **Table S5**.

3 RESULTS AND DISCUSSION

3.1 Hydrochemistry in the ATZ and North BUS

We investigated the community diversity and distribution of N_2 fixers in the ATZ and the OMZ off the North BUS and compared our results to previous studies on OMZ N_2 fixers. During the time of the cruise, we observed a meridional gradient in O_2 with decreasing concentrations from 5˚S to 16˚S. O_2 concentrations in the ATZ reached a minimum of around 20 µM O_2 at 300 m water depth with an oxycline (20-100 µM O_2) starting at around 50-100 m (**Figure 1**). Only in the Northern BUS, a strong OMZ with O_2 concentrations below 5 µM O_2 could be detected (**Figure 1**).

Along with decreased O_2 concentrations in South ATZ (10-16 °S), a small secondary NO_2^- maximum was detected at a water depth of 75 m (**Figure 1**), possibly indicative for N loss processes, such as denitrification or anammox (Kalvelage et al., 2013). Comparable to the ATZ (5-16 °S), NO_2^- concentrations in the Northern BUS were generally elevated with concentrations of up to 0.8 µM and a single datapoint of 1.8 µM at a depth of 87 m (**Figure 1**; **Table 1**). NO_3^- and PO_4^{3-} showed a vertical distribution with concentrations increasing below the oxycline reaching concentrations of up to 39 µM and 2.5 µM, respectively, in our deepest samples from 300 m water depth in the ATZ. In the Northern Benguela upwelling system OMZ waters, where O_2 concentrations were below 20 µM, some samples showed a decrease of NO_3^- over depth along with increased NO_2^- concentrations, again suggesting beginning denitrification within the water column or the sediment below (**Table 1**; **Figure 1**). Overall, the northern BUS seemed to be N limited compared to the ATZ, as indicated by the negative intercept of the trendline for the N:P ratio

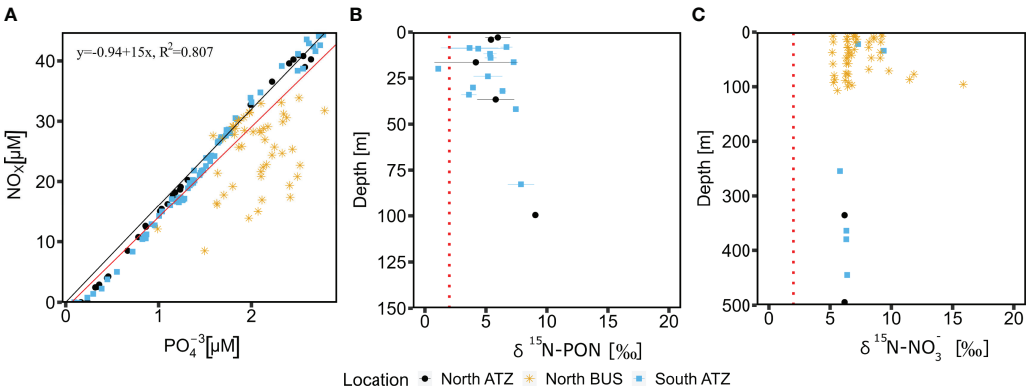

FIGURE 2 | NO_x over PO_4^{3-} concentrations from all sampled stations **(A)**. The N:P ratio is around the Redfield ratio of N:P = 16:1 (black line). The linear regression equation (red line) has a negative intercept suggesting a slight N limitation. Samples from the North BUS OMZ are an exception, as those show an undersaturation of N suggesting active N loss processes. δ^{15}N-PON **(B)** and $\delta^{15}N - NO_3^-$ **(C)** shows no indication of active N_2 fixation but rater N-loss (denitrification, anammox).

(**Figure 2A**). The presence of N loss processes is corroborated by the detected surplus of PO_4^{3-} compared to fixed N assuming Redfield stoichiometry (Redfield et al., 1963) (**Figure 2A**). Alternatively, the surplus might result from enhanced P flux at anoxia (Ingall and Jahnke, 1997).

Classically, a surplus of PO_4^{3-} over fixed nitrogen in combination with low O_2 concentrations would be considered favorable for O_2-sensitive diazotrophs (Wasmund et al., 2005; Deutsch et al., 2007; Flohr et al., 2014). However, our δ^{15}N-PON (3‰ to 7‰) and $\delta^{15}N - NO_3^-$ (5‰ to 17‰) signatures indicates an absence of N_2 fixation (**Figures 2B, C**).Our data rather points towards active denitrification in the north BUS OMZ water, as active N_2 fixation would be expected to result in a lighter δ^{15}N signature of -2‰ – 2‰ (Delwiche and Steyn, 1970; Montoyal et al., 2002; Dähnke and Thamdrup, 2013). Cautiously, one must note that δ^{15}N signatures are a mixed signal of many processes and might be impacted by other factors and processes, including denitrification, annamox or N import *via* dust and rivers. Our measurements are, however, in line with a previous study from the North BUS reporting an isotope enrichment from 1 - 10‰ in the OMZ waters of this region (Nagel et al., 2013) and from other OMZ regions with δ^{15}N-PON signatures from 2‰ - 8‰ (Kumar et al., 2004) or 5-8‰ (Löscher et al., 2020) in the BoB and 4‰ -11.6‰ in the ETNP (Voss et al., 2001).

3.2 Diazotrophic Diversity in the Northern Benguela Upwelling System

While we did not find any clear evidence for active N_2 fixation in either the North/South ATZ or the Northern BUS during our cruise, we found the genetic potential and presence of transcripts for N_2 fixation using the key functional marker gene *nifH*. Altogether, we obtained 958 *nifH* amplicon sequences, which include 191 transcripts from an area covering the North ATZ (waters off Congo 6°S) (133 sequences), the South ATZ (waters off Angola [11°S-15°S)] (320 sequences), the North BUS (waters off Namibia [17-22°S)] (505 sequences) and oxic features, oxic (>100 µM O_2) (435 sequences), oxycline (20-100 µM O_2), suboxic (5-20 µM O_2) and OMZ (<5 µM O_2). See **Tables S1, S2** for details.

Compared to a previous study, which used a similar approach and a higher number of input sequences for *nifH* sequence analysis from OMZs of the ETNP, ETSP, and AS (505 from the North BUS OMZ compared to 787 sequences combined from the ETSP, ETSP and AS, (Jayakumar and Ward, 2020)), we found a higher diversity based on the number of OTUs (in total 82 OTUs combining both ATZ and North BUS compared to 59 OTUs in the previous study) (**Figures S1**, **S2**). This diversity might be somewhat biased as our samples were derived from a wider range of biogeochemical conditions, including the ATZ and the higher obtained total number of sequences. If taking only sequences from the North BUS suboxic (5-20 µM O_2) and OMZ (<5 µM O_2) conditions into account, a similar diversity (41 OTUs in this study and 38 OTUs in Jayakumar and Ward, 2020) can be observed in both studies (**Table S2**; **Figure S1**). Interestingly, we found the highest N_2 fixer diversity in waters of the Northern BUS, which also showed strong OMZ conditions with O_2 concentration below 5 µM O_2 (**Figure 1**; **Table S1**). However, we also recovered more sequences from those waters as compared to our other study sites and compared to the individual OMZs explored by Jayakumar and Ward (2020). The 15 most abundant OTUs and their phylogeny are shown in **Table 2**. Nine of the OTUs were associated with *nifH* Cluster I, which consists of cyanobacteria and proteobacteria mainly (**Table 2**; **Figure 4**). The remaining six OTUs were associated with Cluster III (**Table 2**; **Figure 5**).

3.2.1 Cyanobacterial Diazotrophs in the Northern Benguela Upwelling System

With above 99% coverage and identity, the most abundant OTU (OTU-1), consisting of 284 sequences, was associated with the filamentous cyanobacterium *Trichodesmium IMS101* on DNA and protein level (**Table 2**; **Figure 4**). OTU-1 was mainly found in samples from the South and North ATZ (65% and 22%, respectively) and to a lesser extent in samples from the OMZ in

TABLE 2 | OTU identities of the 15 (out of 83) most abundant OTUs (>10 Seq).

				DNA			
	No. of Seq	***nifH* cluster**	**Phylogenetic affiliation**	**Closets NCBI hit**	**Accession no.**	**Identity (%)**	**Coverage (%)**
OTU1	**284**	1	Cyanobacterium	*Trichodesmium sp IMS101*	AF167538.1	99.69	100
OTU2	**90**	1	Alpha	*Magnetococcus marinus MC-1*	CP000471.1	80.06	99
OTU3	**59**	234	Delta	*Desulfobacter curvatus*	AF065619.1	76.97	93
OTU4	**52**	1	Gamma	*Shewanella dokdonensis*	CP074572.1	81.88	99
OTU5	**35**	1	Gamma	*Marine proteobacterium*	AF046833.1	83.18	100
OTU6	**34**	234	Delta	*Sulfurospirillum sp.*	AP014723.1	74.43	59
OTU7	**33**	1	Alpha	*Bradyrhizobium japonicum*	GQ289567.1	80.75	99
OTU8	**33**	234	Delta	*Solidesulfovibrio carbinolicus*	CP026538.1	83.89	92
OTU9	**30**	1	Cyanobacterium	*Candidatus Atelocyanobacterium Thalassa (UCYN-A)*	KF806612.1	99.38	100
OTU10	**26**	234	Delta	*Pelobacter carbinolicus*	CP000142.2	84.74	100
OTU11	**25**	NA	NA	*Unidentified bacterium*	AF016613.2	98.75	100
OTU12	**18**	234	Delta	*Desulfotomaculum nigrificans*	AY221823.1	84.85	30
OTU13	**18**	234	Delta	*Pseudodesulfovibrio sp. SF6*	AP024485.1	87.54	100
OTU14	**13**	1	Cyanobacterium	*Cyanothece sp. WH8904*	AY620241.1	100	100
OTU15	**10**	1	Actinobacteria	*Frankia sp. D11*	HM026366.1	76.77	61
				Protein			
OTU1	**284**	1	Cyanobacterium	*Trichodesmium erythraeum IMS101*	O34106.1	100	100
OTU2	**90**	1	Gamma	*Azotobacter chroococcum*	AYE20514.1	100	96.26
OTU3	**59**	234	Delta	*Desulfobacteraceae*	RJP85619.1	91.59	100
OTU4	**52**	1	Gamma	*Vibrio sp. HA2012*	WP_100798453.1	100	100
OTU5	**35**	1	Gamma	*Pseudomonas stutzeri*	CBW30543.1	93.46	100
OTU6	**34**	234	Delta	*Solidesulfovibrio carbinolicus*	WP_129352166.1	88.79	100
OTU7	**33**	234	Kiritimatiellaeota	*Pontiellaceae desulfantans*	WP_136081448.1	93.33	100
OTU8	**33**	234	Bacteroidetes	*Lutibacter agarilyticus*	WP_089382364.1	88.79	100
OTU9	**30**	1	Cyanobacterium	*Candidatus Atelocyanobacterium Thalassa (UCYN-A)*	AHH30822.1	98.13	100
OTU10	**26**	234	Delta	*Desulfuromonas sp.*	PLX91276.1	95.33	100
OTU11	**25**	1	Gamma	*Pseudomonas stutzeri*	CBW30543.1	93.69	100
OTU12	**18**	234	Delta	*Desulfobacula sp.*	NJM03842.1	91.59	100
OTU13	**18**	234	Delta	*Maridesulfovibrio frigidus*	WP_031482840.1	95.33	100
OTU14	**13**	1	Cyanobacterium	*Cyanothece sp. UBA12306*	HAC63251.1	97.2	100
OTU15	**10**	1	Planctomycetes	*Planctomyceataceae*	MBV8488868.1	92.52	100

The closets cultivated species and accession number from the NCBI database based on DNA and protein is presented along with phylogenetic affiliation and identity/coverage score. NA standard for not available.

the North BUS (13%, **Figure 3**; **Table S4**). Of those 284 sequences. 23.5% were derived from cDNA and were found in surface waters of the North ATZ (13% cDNA) and the North BUS (10% cDNA) (**Tables S3, S4**). Only below 0.1% were derived from cDNA extracted in the South ATZ (**Tables S3, S4**). Earlier studies found no evidence of *Trichodesmium* sp. and blooms were not detectable by satellite imaging (Shannon and Pillar, 1986; Pitcher et al., 1991; Tyrrell et al., 2003; Westberry and Siegel, 2006; Sohm et al., 2011). More recent studies, however, detected *Trichodesmium* only in low biomass or in a concentration of 1–10 colonies per m^3 (Nagel et al., 2013; Wasmund et al., 2015). Low numbers did not appear to be a result of iron (Fe), vitamin or other trace metal limitations in those earlier studies, but rather of low water temperatures (20-25°C), which limited the growth and activity of *Trichodesmium* (Staal et al., 2007; Wasmund et al., 2015; Tang and Cassar, 2019) (**Figure S3**).

The small unicellular, cosmopolitan cyanobacterium UCYN-A (OTU-9) was detected in the oxic waters of the North ATZ (70%) and North BUS (30%) (**Table 2**; **Figure 3**) with >99% coverage and identity. UCYN-A were not detected in the South ATZ. OTU-9 consisted of 90% transcripts and was found in surface waters down to 30 m water depths (58% cDNA from the North ATZ and 30% from the North BUS), suggesting UCYN-A contributing to N_2 fixation (**Tables S3, S4**). Thus, highlighting the importance of this clade for N_2 fixation. UCYN-A has been found all over the globe, from polar to tropical regions, often playing a major role in N_2 fixation (Short and Zehr, 2007; Martínez-Pérez et al., 2016; Harding et al., 2018; Tang and Cassar, 2019; Gradoville et al., 2020; Mills et al., 2020). Previously, there was one report of UCYN-A from the Benguela upwelling system where it has been found at water depths of 40-110 m off Angola (14.75°S) (Sohm et al., 2011). Otherwise, UCYN-A has not been found in OMZs except for the ETSP and the BoB (Turk-Kubo et al., 2014; Li et al., 2021).

Cyanothece sp. *WH8904* (OTU-14) was detected only in the North BUS and 15% of the sequences were derived from cDNA, suggesting that *Cyanothece* sp. may be active in the North BUS. Additionally, we detected four cyanobacterial OTUs, one clustering closely with *Dolichospermum* spp. (previously known as *Anabaena* sp. [Wacklin et al., 2009)] (OTU-18) and three singletons (OTU-61, OTU-66, OTU-76) related to *Trichodesmium thiebautii* (**Figure 4**). In this study, we found a regional difference in cyanobacterial diazotroph presence and *nifH* gene expression within the Benguela current system (ATZ

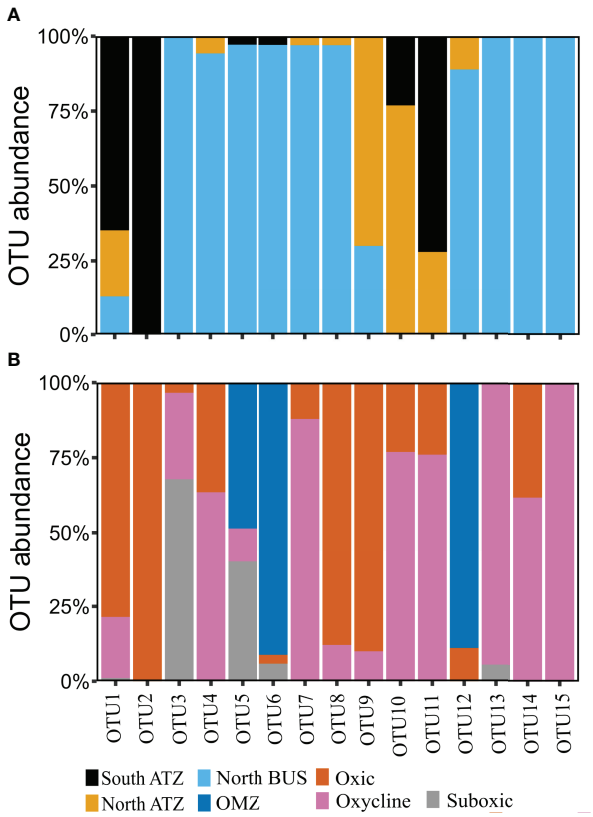

FIGURE 3 | Histogram of the 15 most abundant OTUs (above 10 sequences) divided by location **(A)** and O_2 feature **(B)**. OTUs were defined at a threshold of 3% nucleotide differences and are presented in descending abundance with OTU1 being the most abundant. ATZ stands for Angola Tropical zone and BUS for Benguela Upwelling System.

and North BUS). Moreover, we report for the first time not only the abundance of *nifH* genes but also the detection of *nifH* transcripts related to *Trichodesmium*, *Cyanothece* and UCYN-A in surface waters adjacent to an OMZ.

3.2.2 Heterotrophic Diazotrophs in the Northern Benguela Upwelling System

Besides cyanobacterial N_2 fixers, we found several OTUs related to common OMZ heterotrophic diazotrophs (**Table 2**; **Figure 4**). Based on protein level, several gamma-proteobacteria were detected (OTU-2, 4, 5 and 11) and were related to *Azotobacter* sp., *Vibrio* sp. and *Pseudomonas stutzeri* (*P. stutzeri*) (above 90% identity and coverage) and *nifH* sequences from the BoB OMZ and gamma-proteobacterial sequences from the South Pacific (Moisander et al., 2014). (**Table 2**; **Figure 4**). Related sequences have been reported within both ETNP, ETSP, AS and BOB (e.g., Jayakumar and Ward, 2020). Based on DNA comparison (identity score of 80%), OTU-2 and 7 were related to alpha-proteobacteria, *Magnetococcus marinus* and *Bradyrhizobium* respectively. Based on protein comparison OTU-2 were related to *Azotobacter* sp. with 100% identity. Phylogenetic analysis further establishes OTU-2 being related to gamma-proteobacteria. OTU-7 did not cluster to alpha-proteobacteria or *nifH* cluster I, but rather with *nifH* cluster III sequences related to *Pontiellace*ae.

Like in other OMZ waters, we detected sequences related to *Vibrio* sp. (OTU-4) and *P. stutzeri* (OTU-5) in the North BUS (94% and 97%, respectively). Alpha-proteobacterial sequences have been reported the OMZs of the ETNP, ETSP, AS and BoB (e.g., *M. palustris*, *S. melioti* and *S. azotifegens*), but were not confidently detected in this study, nor were beta-proteobacterial sequences (**Figure 4**) (Halm et al., 2011; Hamersley et al., 2011; Jayakumar et al., 2012; Farnelid et al., 2013; Turk-Kubo et al., 2014; Cheung et al., 2016; Jayakumar et al., 2017). 23 out of 82 OTUs belonged to *nifH* Cluster I. 13 of those OTUs were found in the North BUS (**Figure 4**). These proteobacteria include diazotrophs commonly reported in OMZs (Jayakumar et al., 2012; Löscher et al., 2014; Cheung et al., 2016; Löscher et al., 2020), low O_2 waters of the Southern Californian Bight (Hamersley et al., 2011) and anoxic waters in the Baltic Sea (Farnelid et al., 2013). Gamma-proteobacteria of the Atlantic clade (OTU-11 and -70) (Langlois et al., 2008) (**Figure 4**) were only detected and expressed their *nifH* gene in the ATZ. As previously suggested, they are not commonly active in OMZ or low-O_2 waters (Langlois et al., 2015; Moisander et al., 2017).

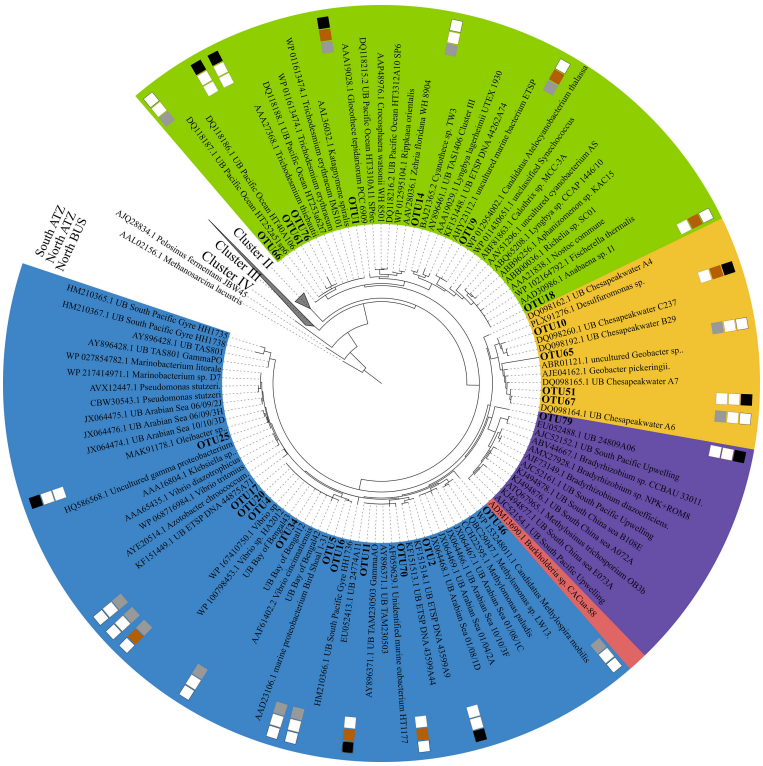

FIGURE 4 | Maximum likelihood tree of Cluster I *nifH* amino acid sequences. The phylogenetic tree is based on a Poisson model with 1000 bootstraps. OTUs are shown in bold nearest to their closest relative. Locations from where sequences were derived from are shown in the outer heatmap, fark brown represents the Northern Angola Tropical Zone, black indicates the Southern Angola Tropical Zone and grey indicates the Northern Benguela Upwelling Zone. Cyanobacteria are shown in green, gamma-proteobacteria are shown in blue, epsilon-proteobacteria are shown in yellow, alpha-proteobacteria are shown in red and beta-proteobacteria are shown in purple.

While gamma-proteobacteria *M. paludis*, a methanotroph (Danilova et al., 2013) have been reported in both ETNP, ETSP and AS (Fernandez et al., 2011; Cheung et al., 2016; Jayakumar and Ward, 2020). We did not find any evidence of methanotrophs in the North BUS. Unlike in the AS and ETNP, we found four OTUs clustering among epsilon-proteobacteria which has also been reported before in ETSP and BoB. However, only two singletons were identified in the North BUS (OTU-65 and 67) (**Table S3**). The more abundant OTU-10 clustered with Chesapeakwater and shares high similarity to *Desulfuromonas* sp. (above 95% identity) and was only found in the ATZ (north 77%, south 23%).

Overall, compared to other OMZ regions (Jayakumar and Ward, 2020), we found a similarly small diversity of heterotrophic diazotrophs in the North BUS OMZ waters. In contrast to most other OMZ waters, we found potentially active UCYN-A and *Trichodesmium* in OMZ-adjacent surface waters. While the role of heterotrophic microbes is unclear, it does not seem that heterotrophic Cluster I diazotrophs play a major role in N_2 fixation in the Northern Benguela upwelling system. Rather, cyanobacterial diazotrophs might play a bigger role due to their presence and activity in the OMZ surface waters.

3.2.3 Delta-Proteobacterial Diazotrophs in the Northern Benguela Upwelling System

In addition to Cluster I diazotrophs, we found a vast diversity of Cluster III sequences (59 OTUs out of 82 OTUs) related to Delta-proteobacteria, Bacteroides, Chlorobi, Spirochaetes, Verrucomicrobiae/Kiritimatiellales and Thiospirochaetes (**Figure 5**). Notably, we did not detect any Cluster II and Cluster IV sequences, which represent e.g., archaeal sequences or non-functional N_2 fixers. Only four out of 59 OTUs consisted of sequences from stations in the ATZ (**Figure 5**). Among the top 15 OTUs associated with Cluster III, only OTU-10 was found in the ATZ (OTU-10: south 23%, north 77%).

OTU-3, 6, 7, 8, 10, 12 and 13 scored above 90% of identity on protein level and closely related to *Desulfobacteraceae* sp., *Solidesulfovibrio* sp., *Pontiellaceae* sp., *Lutibacter* sp., *Desulfuromonas* sp., *Maridesulfovibrio* sp. and *Desulfobacula* sp., respectively (**Table 2**). OTU-3 was mainly found in suboxic waters (68%), while OTU-10 and 13 were found in the oxycline (77% and 94%, respectively), and OTU-6 and 12 were found in the OMZ (91% and 88%) (**Table 2**, **S4** and **Figure 3**, **5**). Despite a wide range of Cluster III sequences, only OTU-13, in the top 15 OTUs, contained transcript sequences (5.5%). OUT-13 were only found in North BUS in oxycline and suboxic

conditions (94.5% and 5.5%, respectively). The low number of *nifH* transcripts is somewhat expected in OMZs as N_2 fixation rates are typically low, too. Although there were few high identity scores (based on DNA) among the top 15 OTUs to known species, four out of six were either on DNA or protein level affiliated with sulphate-reducing microbes (**Table 2**). This speaks for the importance of sulphate reduction associated with N_2 fixation in North BUS. Such co-occurrence resulting in a coupling between sulphate-reduction and N_2 fixation has been previously described in OMZ waters and underlying sediments (Bertics et al., 2013; Gier et al., 2016), mostly represented by sequences clustering closely with *Desulfovibrio* [**Figure 5**, (Fernandez et al., 2011; Löscher et al., 2014; Turk-Kubo et al., 2014)]. Indeed, this coupling seems to be consistence between all OMZ waters stressing the importance of this co-occurrence (Jayakumar and Ward, 2020).

Besides sulphate-reducing clades, we also found sulfide-oxidizing clades, such as *Thiospirochaeta* and *Spirochaetes* (**Figure 5**). OTU-6 consisted mainly of OMZ derived sequences (91%) is related to *Sulfurospirillum* sp., or *Solidesulfovibrio* sp. (**Table 2**), while the phylogenetic analysis determined it as being closely related to the sulfide-oxidizing group Spirochaetes (**Figure 5**). OTU-23, the most abundant OTU related to *Thiospirochaeta*, was only found in the North BUS in the OMZ region. Chlorobi and Spirochaetes identified in our study, have previously been described in the ETNP, ETSP and anoxic waters of the Baltic Sea (Farnelid et al., 2013; Christiansen and Löscher, 2019; Jayakumar and Ward, 2020) (**Figure 5**). Our identified Bacteroidetes sequences were related to sequences from the BoB (**Figure 5**) and have previously been reported in e.g., the sulfidic OMZ off the coast off Peru (Schunck et al., 2013). Also, a recent 16S rRNA-based study from the Southern Benguela upwelling system revealed a similar community with Bacteroides and sulfate-reducing clades present in low-O_2 waters (Rocke et al., 2020). Overall, the diversity of Cluster III microbes could result from locally occurring H_2S events favoring anaerobic sulphate-reducing and sulfide-oxidizing microbes. Like for Cluster I diazotrophs, there is a distinct difference between the North BUS OMZ (waters off Namibia) and the ATZ (waters off Congo and Angola).

3.3 Biogeochemical Controls on Diazotroph Distribution and Diversity

The waters off North BUS were the only ones during this cruise with an OMZ with O_2 concentrations below 5 μM in its core waters. As one main goal of this study was to explore OMZ diazotrophs in North BUS, an RDA based on OTUs (from the top 15), and environmental variables was carried out from those waters specifically. A model containing depth, salinity, the isotope signature of $\delta^{15}N-NO_3^-$, NO_2^-, O_2, NH_4^+ and NO_3^-

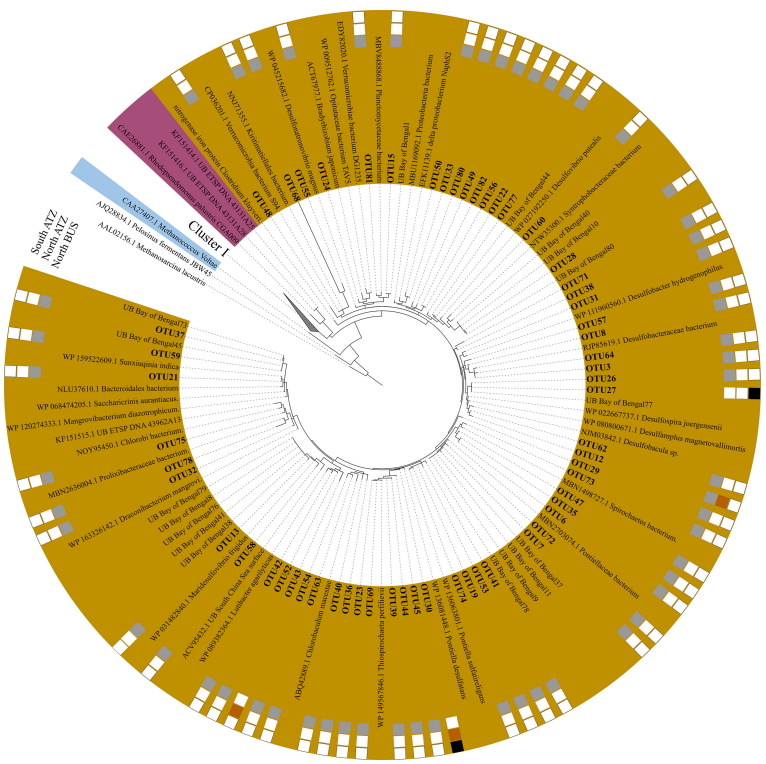

FIGURE 5 | Maximum likelihood tree of Cluster II, III, and IV *nifH*-amino acid sequences. The phylogenetic tree is based on a Poisson model with 1000 bootstraps. OTUs are shown in bold nearest to their next cultivated relatives. Cluster II is shown in purple, Cluster III in brown and Cluster IV in blue.

could explain up to 99% of the total variability (**Figures 6A, B**). While a clear difference in OTUs between the ATZ and the North BUS (**Figure 3**) could be observed, the geographical factors within North BUS seems also evident in the redundancy analysis.

The diazotroph community was divided into three clusters which positively correlated with either O_2 (OTU-4 and 14), NO_3^- (OTU-7, -13 and -15) and $\delta^{15}N - NO_3^-$ along with NH_4^+ (OTU-5, -6 and -12). OTU-4 (*Vibrio* sp.) and 14 (*Cyanothece* sp.) were derived mainly from waters with >20 µM O_2 and positively correlated with O_2. OTU-7 (*Pontiellaceae* sp.), -13 (*Maridesulfovibrio* sp.) and -15 (*Plantomyceataceae* sp.), derived from oxycline features, were positively correlated to depth and NO_3^- and negatively to $\delta^{15}N - NO_3^-$ and NH_4^+. While including the third component (RDA3), OTU-7, -13 and -15 showed the same tendency and were positively correlated to NO_3^- but negatively correlated to O_2, (**Figures 6A, B**). OTU-5 (*P. stutzeri*), -6 (*Solidesulfovibrio* sp.) and -12 (*Desulfobacula* sp.) were identified as suboxic and OMZ-derived OTUs. They correlated positively with $\delta^{15}N - NO_3^-$ along with NH_4^+ and negatively to NO_3^- and O_2. The remaining OTUs (8, 9 and 3) could not be sufficiently explained by our statistical approach. Thus, the diverse explanatory factors for OTU-8 (*Lutibacter* sp.), -9 (UCYN-A), and -3 (*Desulfobacteraceae* sp.) suggest a lack of factors (e.g., organic matter or Fe) that could help to further explain the dataset. Interestingly, our statistical approach suggests that NO_3^- plays a role in separating OTUs derived from oxycline waters (~20-100 µM O_2) from OTUs derived from suboxic/OMZ waters (<5 and 5-20 µM O_2) (**Figures 6A, B**). OTU-5, -6 and -12 correlating to $\delta^{15}N - NO_3^-$ and NH_4^+ indicate that they are present in denitrifying waters enriched $\delta^{15}N - NO_3^-$ and in potentially sulfidic waters typically enriched with NH_4^+. While this correlation does not indicate coupling of denitrification and N_2 fixation in OMZs as previously proposed (Deutsch et al., 2007),

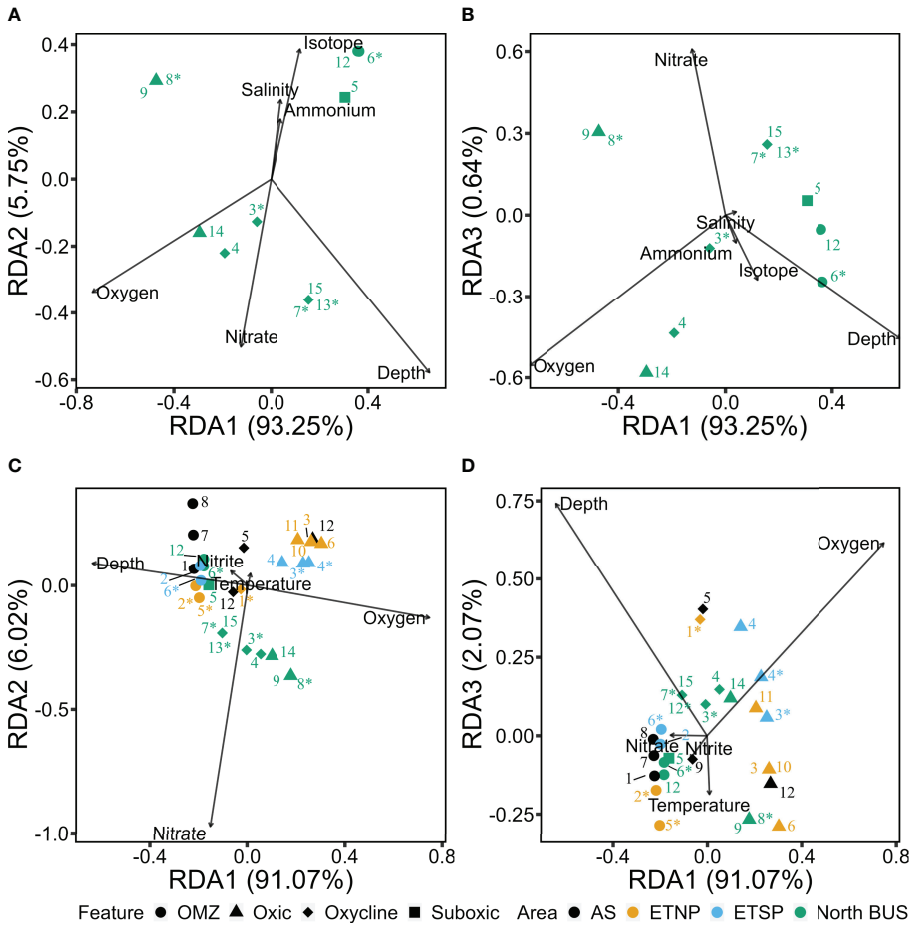

FIGURE 6 | Redundancy analysis (RDA) plot illustrating the relationship between biogeochemical variables and OTUs within the coastal waters the Northern Benguela Upwelling System (North BUS, waters off Namibia) **(A, B)** and between different OMZ areas **(C, D)**. Numbers indicate OTU identifiers, different shapes denote the O_2 feature. Numbers with * are OTUs belonging to Cluster III, other OTUs belong to Cluster I. The Arabian Sea is denoted in black, the ETNP in yellow, the ETSP in blue and waters off Namibia in green. **(A, B)** show only the top 15 abundant OTUs derived majorly from Namibia (>5%). **(C, D)** show OTUs generated from the ETNP, ETSP and AS (Jayakumar and Ward, 2020) along with OTUs from the Northern Benguela Upwelling system.

it suggests a spatial coupling between the habitat of diazotrophs within OMZs and denitrification, and a possible link to sulfate-reduction (Jayakumar and Ward, 2020). Lastly, when comparing across OMZ waters, OTUs derived from OMZ core correlate positively to NO_2^- and negatively to O_2 and NO_3^- (**Figures 6C, D**). OTUs derived from the North BUS correlated positively to NO_3^- (**Figure 6C**). We see between OMZ regions (ETNP, ETSP, AS) a similar pattern where OMZ OTUs correlated positively to NO_2^- and oxic derived OTUs with O_2 or positively with temperature, as it showed collinearity with depth (**Figures 6C, D**).

Compared to other OMZ areas, the most striking difference is the positive correlation between high-NO_3^- and low-O_2 derived OTUs from the North BUS (**Figures 6A, B**). Assimilation of NO_3^- has been suggested to be energetically not of advantage as compared to N_2 fixation in low O_2 environments (Großkopf and LaRoche, 2012). However, it is unclear whether this explains the observed difference between suboxic and OMZ OTUs. The correlation of diazotroph presence to NO_3^- might also be indicative of a correlation with any other compound in the same water mass. As the NO_2^- signal could be sedimentary, it could be similar to a signal of dissolved Fe concentrations from coastal upwelling, or of organic matter possibly stimulating diazotrophic growth (Löscher et al., 2014; Benavides et al., 2015; Benavides et al., 2020). As typical for OMZs, the diazotroph community collected during this cruise consisted mainly of heterotrophic microbes. While we see a segregation of the community in response to macronutrients, it is important to consider that this might rather be an indicator for a general niche within those waters than for NO_3^- directly. It has previously been suggested that heterotrophic N_2 fixation is independent of the Redfield-based N deficiency as long as PO_4^{3-} and iron (Fe) is available (Löscher et al., 2014; Bombar et al., 2016).

Fe can always be considered an important factor for N_2 fixation because the Fe requirement of diazotrophs is 60 times that of other microbes (Berman-Frank et al., 2001). In the Northern BUS, the sedimentary release of Fe is rather low (less than 1 wt.% Fe compared to other OMZ regions between 2-3 wt.% Fe) (Scholz et al., 2016; Böning et al., 2020). This potential Fe limitation might explain why *Trichodesmium* was mainly detected in the ATZ and to a lesser extent the North BUS. It might also explain low N_2 fixation rates (Staal et al., 2007; Sohm et al., 2011; Wasmund et al., 2015) and δ^{15}N-PON, along with $\delta^{15}N - NO_3^-$, being outside of the range indicative for N_2 fixation (**Figure 2**) (Nagel et al., 2013). Sohm et al., 2011 measured up to 2.4 nM Fe in the North BUS and 0.08-0.34 nM in surface waters of the ATZ (north of 14°S). Compared to ETSP OMZ waters with Fe concentrations of 10-60 nmol kg^{-1} and upwelled surface waters with Fe concentrations of up to 267 nmol kg^{-1}, the concentrations measured in the Benguela region indeed appear to be very low (Löscher et al., 2014). On the other hand, nutrient addition experiments did not increase N_2 fixation in Benguela waters (Staal et al., 2007; Wasmund et al., 2015). Thus, other factors that could limit N_2 fixation should be taken into account, such as micronutrients (e.g. molybdenum, zinc, vitamins), macronutrients (e.g., organic matter) or physical factors such as light, temperature, or turbulence (Arrigo, 2005; Saito et al., 2008). Though based on our RDA model, turbulence did not explain the dataset significantly, while temperature only explained a minor part.

4 CONCLUSION

In this study, we explored the diazotrophic community and distribution along the ATZ and the North BUS spanning from the waters off Congo (5°S) to Namibia (23°S). Typically, OMZ regions across the world contain a considerable *nifH* diversity in both surface and OMZ waters, thus it was of little surprise that we could also recover a broad diversity of Cluster I and III diazotrophs. However, in contrast to other OMZs, we did not find any representatives of other *nifH* clusters. Interestingly, *Trichodesmium, Cyanothece* and UCYN-A were both present and potentially active in the ATZ (Coast off Congo and Angola). Moreover, we report a distinct pattern of cyanobacterial in the OMZ waters of the North BUS. While *Trichodesmium* was mainly found in the ATZ; it was, although to a lesser extent, also found potentially active in OMZ surface waters of the North BUS. UCYN-A was detected in the North BUS and the ATZ in both the gene and the transcript pool, even in surface waters of the OMZ waters. Lastly, *Cyanothece* were only found in the North BUS surface waters, potentially active. Cluster I heterotrophic diazotrophs were related to gamma-proteobacteria such as *P. stutzeri, Vibrio* sp., and *Azotobacter* sp. and were mainly found in the North BUS OMZ waters. Unlike in other OMZs, we did not detect any alpha – or beta-proteobacterial diazotrophs. The most striking difference to other OMZs was the vast diversity of Cluster III diazotrophs, consisting of delta-proteobacteria, Bacteroides, Chlorobium, Spirochaetes and Thiospirochaeta. All of them were found in the OMZ environment.

Combining our data with reports from other OMZ regions, we observe a similar pattern with OMZ derived OTUs responding positively to the secondary NO_2^- peak. However, looking at the North BUS OMZ waters, NO_2^- did not play a significant role. Contrary, we did observe a positive correlation with NO_3^- to OTUs derived from low-O_2 waters (~20 µM O_2). While assimilation of NO_3^- is energetically unfavorable in low-O_2 waters, the correlation might indicate a response to either upwelled Fe or organic matter, stimulating diazotrophic growth. OMZ derived OTUs positively correlated with NH_4^+ and $\delta^{15}N - NO_3^-$ which might support the idea of spatially coupled denitrification to N_2 fixation and a link between sulfate-reduction and N_2 fixation.

While we did not measure N_2 fixation rates, earlier reports confirm low rates in waters above 70 m in line with our δ^{15}N isotope speciation data. Like in other OMZs, low or absent rates are related to a specific OMZ diazotroph community with cyanobacteria being underrepresented and heterotrophic diazotrophs fixing N_2 only at low rates. Therefore, the diversity of diazotrophs especially of Cluster III in the North BUS suggests that they find a niche in OMZ waters not because of their ability

to fix N_2, but because of other metabolic capabilities, e.g., sulphate reduction or oxidation. Thus, it is still unclear why those microbes keep their genetic ability to fix N_2, as they rarely seem to use it.

DATA AVAILABILITY STATEMENT

The sequences were submitted to NCBI with accession ID OK082431-OK083221, OL412005-OL412134 and OM453718 - OM453821.

AUTHOR CONTRIBUTIONS

CL, CR, and DA-M designed the study. JC-C, TS, CR, and DA-M carried out field and laboratory experiments. CR performed statistical and molecular analysis. JC-C and TS carried out isotopic measurement. CR wrote the manuscript with contributions from all co-authors. All authors contributed to the article and approved the submitted version.

FUNDING

Financial support was provided by the German Federal Ministry of Education and Research within the collaborative project 'Southwest African Coastal Upwelling System and Benguela Niños II (SACUS)', the Villum Foundation (grants #16518 to Don Canfield and #29411 to CL), grants #15397 to NP.

ACKNOWLEDGMENTS

We are grateful to Captain Rainer Hammacher and his crew and the Chief Scientist of M148, Marcus Dengler, for excellent collaboration and centralized services. We thank Hanna Campen (GEOMAR) and Danial Bastian (Hereon) for nutrient and oxygen analyses. Likewise, we thank Erik Laursen (SDU) for assistance with molecular analyses and Zarah Kofoed (SDU) for assistance with isotopic measurements. The ship time on board R/V METEOR was provided by the German Research Council (DFG) within the core program METEOR/MERIAN. We also thank Amal Jayakumar and Bess Ward for sharing metadata and for helpful and straightforward communication. We further acknowledge the Nordcee labs, GEOMAR, and DIAS for core support.

SUPPLEMENTARY MATERIAL

The Supplementary Material for this article can be found online at: https://www.frontiersin.org/articles/10.3389/fmars.2022.868261/full#supplementary-material

REFERENCES

Arrigo, K. R. (2005). Marine Microorganisms and Global Nutrient Cycles. *Nature* 438, 122. doi: 10.1038/nature04265

Bakun, A. (1996). "Patterns in the Ocean: Ocean Processes and Marine Population Dynamics," in *Calif. Sea Grant, Coop. with Cent. Investig. Biol* (La Paz, Mexico: California Sea Grant, in cooperation with Centro de Investigaciones Biologicas del Noroeste), 332 pp.

Bartholomae, C., and van der Plas, A. (2007). Towards the Development of Environmental Indices for the Namibian Shelf, With Particular Reference to Fisheries Management. *Afr. J. Mar. Sci.* 29, 25–35. doi: 10.2989/AJMS.2007.29.1.2.67

Benavides, M., Duhamel, S., Van Wambeke, F., Shoemaker, K. M., Moisander, P. H., Salamon, E., et al. (2020). Dissolved Organic Matter Stimulates N2 Fixation and nifH Gene Expression in Trichodesmium. *FEMS Microbiol. Lett.* 367, 1–8. doi: 10.1093/femsle/fnaa034

Benavides, M., Moisander, P. H., Berthelot, H., Dittmar, T., Grosso, O., and Bonnet, S. (2015). Mesopelagic N2 Fixation Related to Organic Matter Composition in the Solomon and Bismarck Seas (Southwest Pacific). *PLoS One* 10, 1–20. doi: 10.1371/journal.pone.0143775

Berman-Frank, I., Cullen, J. T., Shaked, Y., Sherrell, R. M., and Falkowski, P. G. (2001). Iron Availability, Cellular Iron Quotas, and Nitrogen Fixation in Trichodesmium. *Limnol. Oceanogr.* 46, 1249–1260. doi: 10.4319/lo.2001.46.6.1249

Bertics, V. J., Löscher, C. R., Salonen, I., Dale, A. W., Gier, J., Schmitz, R. A., et al. (2013). Occurrence of Benthic Microbial Nitrogen Fixation Coupled to Sulfate Reduction in the Seasonally Hypoxic Eckernförde Bay, Baltic Sea. *Biogeosciences* 10, 1243–1258. doi: 10.5194/bg-10-1243-2013

Bombar, D., Paerl, R. W., and Riemann, L. (2016). Marine Non-Cyanobacterial Diazotrophs: Moving Beyond Molecular Detection. *Trends Microbiol.* 24, 916–927. doi: 10.1016/j.tim.2016.07.002

Böning, P., Schnetger, B., Belz, L., Ferdelman, T., Brumsack, H. J., and Pahnke, K. (2020). Sedimentary Iron Cycling in the Benguela Upwelling System Off Namibia. *Earth Planet. Sci. Lett.* 538, 116212. doi: 10.1016/j.epsl.2020.116212

Bonnet, S., Dekaezemacker, J., Turk-Kubo, K. A., Moutin, T., Hamersley, R. M., Grosso, O., et al. (2013). Aphotic N2 Fixation in the Eastern Tropical South Pacific Ocean. *PLoS One* 8, 1–14. doi: 10.1371/journal.pone.0081265

Capone, D., and Carpenter, E. J. (1982). Nitrogen Fixation in the Marine Environment *Science (New York, N.Y.)* 4565, 1140–1142. doi: 10.1126/science.217.4565.1140

Carr, M. E. (2001). Estimation of Potential Productivity in Eastern Boundary Currents Using Remote Sensing. *Deep. Res. Part II. Top. Stud. Oceanogr.* 49, 59–80. doi: 10.1016/S0967-0645(01)00094-7

Casciotti, K. L., Sigman, D. M., Galanter Hastings, M., Böhlke, J. K., and Hilkert, A. (2002) Measurement of the Oxygen Isotopic Composition of Nitrate in Seawater and Freshwater Using the Denitrifier Method. *Anal. Chem.* 74 (19), 4905–4912, doi: 10.1021/ac020113w.

Chang, B. X., Jayakumar, A., Widner, B., Bernhardt, P., Mordy, C. W., Mulholland, M. R., et al. (2019). Low Rates of Dinitrogen Fixation in the Eastern Tropical South Pacific. *Limnol. Oceanogr.* 64, 1913–1923. doi: 10.1002/lno.11159

Cheung, S., Xia, X., Guo, C., and Liu, H. (2016). Diazotroph Community Structure in the Deep Oxygen Minimum Zone of the Costa Rica Dome. *J. Plankt. Res.* 38, 380–391. doi: 10.1093/plankt/fbw003

Christiansen, C. F., and Löscher, C. R. (2019). Facets of Diazotrophy in the OMZ Off Peru Revisited- What We Couldn't See From a Single Marker Gene Approach. *BioarXiv*. doi: 10.1101/558072

Dabundo, R., Lehmann, M. F., Treibergs, L., Tobias, C. R., Altabet, M. A., Moisander, P. H., et al. (2014). The Contamination of Commercial15n2 Gas Stocks With15n-Labeled Nitrate and Ammonium and Consequences for Nitrogen Fixation Measurements. *PLoS One* 9, e110335. doi: 10.1371/journal.pone.0110335

Dähnke, K., and Thamdrup, B. (2013). Nitrogen Isotope Dynamics and Fractionation During Sedimentary Denitrification in Boknis Eck, Baltic Sea. *Biogeosci. Discuss.* 10, 681–709. doi: 10.5194/bgd-10-681-2013

Danilova, O. V., Kulichevskaya, I. S., Rozova, O. N., Detkova, E. N., Bodelier, P. L. E., Trotsenko, Y. A., et al. (2013). Methylomonas Paludis Sp. Nov., the First

Acidtolerant Member of the Genus Methylomonas, From an Acidic Wetland. *Int. J. Syst. Evol. Microbiol.* 63, 2282–2289. doi: 10.1099/ijs.0.045658-0

Dekaezemacker, J., Bonnet, S., Grosso, O., Moutin, T., Bressac, M., and Capone, D. G. (2013). Evidence of Active Dinitrogen Fixation in Surface Waters of the Eastern Tropical South Pacific During El Niño and La Niña Events and Evaluation of its Potential Nutrient Controls. *Global Biogeochem. Cycle.* 27, 768–779. doi: 10.1002/gbc.20063

Delwiche, C. C., and Steyn, P. L. (1970). Nitrogen Isotope Fractionation in Soils and Microbial Reactions. *Environ. Sci. Technol.* 4, 929–935. doi: 10.1021/es60046a004

Deutsch, C., Sarmiento, J. L., Sigman, D. M., Gruber, N., and Dunne, J. P. (2007). Spatial Coupling of Nitrogen Inputs and Losses in the Ocean. *Nature* 445, 163–167. doi: 10.1038/nature05392

Farnelid, H., Bentzon-Tilia, M., Andersson, A. F., Bertilsson, S., Jost, G., Labrenz, M., et al. (2013). Active Nitrogen-Fixing Heterotrophic Bacteria at and Below the Chemocline of the Central Baltic Sea. *ISME. J.* 7, 1413–1423. doi: 10.1038/ismej.2013.26

Fernandez, C., Farías, L., and Ulloa, O. (2011). Nitrogen Fixation in Denitrified Marine Waters. *PLoS One* 6, e20539. doi: 10.1371/journal.pone.0020539

Flohr, A., van der Plas, A. K., Emeis, K. C., Mohrholz, V., and Rixen, T. (2014). Spatio-Temporal Patterns of C : N : P Ratios in the Northern Benguela Upwelling System. *Biogeosciences* 11, 885–897. doi: 10.5194/bg-11-885-2014

Gaby, J. C., Rishishwar, L., Valderrama-Aguirre, L. C., Green, S. J., Valderrama-Aguirre, A., Jordan, I. K., et al. (2018). Diazotroph Community Characterization *via* a Highthroughput nifH Amplicon Sequencing and Analysis Pipeline. *Appl. Environ. Microbiol.* 84, e01512–e01517. doi: 10.1128/AEM.01512-17

Gier, J., Sommer, S., Löscher, C. R., Dale, A. W., Schmitz, R. A., and Treude, T. (2016). Nitrogen Fixation in Sediments Along a Depth Transect Through the Peruvian Oxygen Minimum Zone. *Biogeosciences* 13, 4065–4080. doi: 10.5194/bg-13-4065-2016

Gradoville, M. R., Farnelid, H., White, A. E., Turk-Kubo, K. A., Stewart, B., Ribalet, F., et al. (2020). Latitudinal Constraints on the Abundance and Activity of the Cyanobacterium UCYN-A and Other Marine Diazotrophs *Methods of Seawater Analysis*, in the North Paci Fi C. *Limnol. Oceanogr.* 9999, 1–18. doi: 10.1002/lno.11423

Grasshoff, G., Kremling, K., and Erhardt, M. (1999). (Weinheim: Wiley VCH, Weinheim), 3rd Edn., ISBN 3527295895.

Großkopf, T., and LaRoche, J. (2012). Direct and Indirect Costs of Dinitrogen Fixation in Crocosphaera Watsonii WH8501 and Possible Implications for the Nitrogen Cycle. *Front. Microbiol.* 3. doi: 10.3389/fmicb.2012.00236

Gruber, N. (2005). A Bigger Nitrogen Fix. *Nature* 436, 786–787. doi: 10.1038/436786a

Halm, H., Lam, P., Ferdelman, T. G., Lavik, G., Dittmar, T., Laroche, J., et al. (2011). Heterotrophic Organisms Dominate Nitrogen Fixation in the South Pacific Gyre. *ISME. J.* 6, 1238–1249. doi: 10.1038/ismej.2011.182

Hamersley, M. R., Turk, K. A., Leinweber, A., Gruber, N., Zehr, J. P., Gunderson, T., et al. (2011). Nitrogen Fixation Within the Water Column Associated With Two Hypoxic Basins in the Southern California Bight. *Aquat. Microb. Ecol.* 63, 193–205. doi: 10.3354/ame01494

Harding, K., Turk-Kubo, K. A., Sipler, R. E., Mills, M. M., Bronk, D. A., and Zehr, J. P. (2018). Symbiotic Unicellular Cyanobacteria Fix Nitrogen in the Arctic Ocean. *Proc. Natl. Acad. Sci. U. S. A.* 115, 13371–13375. doi: 10.1073/pnas.1813658115

Hutchings, L., van der Lingen, C. D., Shannon, L. J., Crawford, R. J. M., Verheye, H. M. S., Bartholomae, C. H., et al. (2009). The Benguela Current: An Ecosystem of Four Components. *Prog. Oceanogr.* 83, 15–32. doi: 10.1016/j.pocean.2009.07.046

Ingall, E., and Jahnke, R. (1997). Influence of Water-Column Anoxia on the Elemental Fractionation of Carbon and Phosphorus During Sediment Diagenesis. *Mar. Geol.* 139, 219–229. doi: 10.1016/S0025-3227(96)00112-0

Jayakumar, A., Al-Rshaidat, M. M. D., Ward, B. B., and Mulholland, M. R. (2012). Diversity, Distribution, and Expression of Diazotroph nifH Genes in Oxygen-Deficient Waters of the Arabian Sea. *FEMS Microbiol. Ecol.* 82, 597–606. doi: 10.1111/j.1574-6941.2012.01430.x

Jayakumar, A., Chang, B. X., Widner, B., Bernhardt, P., Mulholland, M. R., and Ward, B. B. (2017). Biological Nitrogen Fixation in the Oxygen-Minimum Region of the Eastern Tropical North Pacific Ocean. *ISME. J.* 11, 2356–2367. doi: 10.1038/ismej.2017.97

Jayakumar, A., and Ward, B. B. (2020). Diversity and Distribution of Nitrogen Fixation Genes in the Oxygen Minimum Zones of the World Oceans. *Biogeosciences* 17, 5953–5966. doi: 10.5194/bg-17-5953-2020

Kalvelage, T., Lavik, G., Lam, P., Contreras, S., Arteaga, L., Löscher, C. R., et al. (2013). Nitrogen Cycling Driven by Organic Matter Export in the South Pacific Oxygen Minimum Zone. *Nat. Geosci.* 6, 228–234. doi: 10.1038/ngeo1739

Kumar, S., Ramesh, R., Bhosle, N. B., Sardesai, S., and Sheshshayee, M. S. (2004). Natural Isotopic Composition of Nitrogen in Suspended Particulate Matter in the Bay of Bengal. *Biogeosci. Discuss* 1, 63–70. doi: 10.5194/bgd-1-87-2004

Kumar, S., Stecher, G., Li, M., Knyaz, C., and Tamura, K. (2018). MEGA X: Molecular Evolutionary Genetics Analysis Across Computing Platforms. *Mol. Biol. Evol.* 35, 1547–1549. doi: 10.1093/molbev/msy096

Kuypers, M. M. M., Lavik, G., Woebken, D., Schmid, M., Fuchs, B. M., Amann, R., et al. (2005). Massive Nitrogen Loss From the Benguela Upwelling System Through Anaerobic Ammonium Oxidation. *Proc. Natl. Acad. Sci. U. S. A.* 102, 6478–6483. doi: 10.1073/pnas.0502088102

Langlois, R., Großkopf, T., Mills, M., Takeda, S., and LaRoche, J. (2015). Widespread Distribution and Expression of Gamma A (UMB), an Uncultured, Diazotrophic, γ-Proteobacterial nifH Phylotype. *PLoS One* 10, 1–18. doi: 10.1371/journal.pone.0128912

Langlois, R. J., Hümmer, D., and LaRoche, J. (2008). Abundances and Distributions of the Dominant nifH Phylotypes in the Northern Atlantic Ocean. *Appl. Environ. Microbiol.* 74, 1922–1931. doi: 10.1128/AEM.01720-07

Letunic, I., and Bork, P. (2019). Interactive Tree of Life (iTOL) V4: Recent Updates and New Developments. *Nucleic Acids Res.* 47, 256–259. doi: 10.1093/nar/gkz239

Li, L., Wu, C., Huang, D., Ding, C., Wei, Y., and Sun, J. (2021). Integrating Stochastic and Deterministic Process in the Biogeography of N2-Fixing Cyanobacterium Candidatus Atelocyanobacterium Thalassa. *Front. Microbiol.* 12. doi: 10.3389/fmicb.2021.654646

Löscher, C. R., Bange, H. W., Schmitz, R. A., Callbeck, C. M., Engel, A., Hauss, H., et al. (2016a). Water Column Biogeochemistry of Oxygen Minimum Zones in the Eastern Tropical North Atlantic and Eastern Tropical South Pacific Oceans. *Biogeosciences* 13, 3585–3606. doi: 10.5194/bg-13-3585-2016

Löscher, C. R., Bourbonnais, A., Dekaezemacker, J., Charoenpong, C. N., Altabet, M. A., Bange, H. W., et al. (2016b). N2 Fixation in Eddies of the Eastern Tropical South Pacific Ocean. *Biogeosciences* 13, 2889–2899. doi: 10.5194/bg-13-2889-2016

Löscher, C. R., Großkopf, T., Desai, F. D., Gill, D., Schunck, H., Croot, P. L., et al. (2014). Facets of Diazotrophy in the Oxygen Minimum Zone Waters Off Peru. *ISME. J.* 8, 1–13. doi: 10.1038/ismej.2014.71

Löscher, C. R., Kock, A., Könneke, M., LaRoche, J., Bange, H. W., and Schmitz, R. A. (2012). Production of Oceanic Nitrous Oxide by Ammonia-Oxidizing Archaea. *Biogeosciences* 9, 2419–2429. doi: 10.5194/bg-9-2419-2012

Löscher, C. R., Mohr, W., Bange, H. W., and Canfield, D. E. (2020). No Nitrogen Fixation in the Bay of Bengal? *Biogeosciences* 17, 851–864. doi: 10.5194/bg-17-851-2020

Martínez-Pérez, C., Mohr, W., Löscher, C., Dekaezemacker, J., Littmann, S., Yilmaz, P., et al. (2016). The Small Unicellular Diazotrophic Symbiont, UCYN-A, is a Key Player in the Marine Nitrogen Cycle. *Nat. Microbiol.* 1, 16163. doi: 10.1038/nmicrobiol.2016.163

Mazard, S. L., Fuller, N. J., Orcutt, K. M., Bridle, O., and Scanlan, D. J. (2004). PCR Analysis of the Distribution of Unicellular Cyanobacterial Diazotrophs in the Arabian Sea. *Appl. Environ. Microbiol.* 70, 7355–7364. doi: 10.1128/AEM.70.12.7355-7364.2004

Mills, M. M., Turk-Kubo, K. A., van Dijken, G. L., Henke, B. A., Harding, K., Wilson, S. T., et al. (2020). Unusual Marine Cyanobacteria/Haptophyte Symbiosis Relies on N2 Fixation Even in N-Rich Environments. *ISME. J.* 14, 2395–2406. doi: 10.1038/s41396-020-0691-6

Moisander, P. H., Beinart, R. A., Hewson, I., White, A. E., Johnson, K. S., Carlson, C. A., et al. (2010). Unicellular Cyanobacterial Distributions Broaden the Oceanic N2 Fixation Domain *Am. Assoc. Adv. Sci.* 327, 1512–1514. doi: 10.1126/science.1185468

Moisander, P. H., Benavides, M., Bonnet, S., Berman-Frank, I., White, A. E., and Riemann, L. (2017). Chasing After non-Cyanobacterial Nitrogen Fixation in Marine Pelagic Environments. *Front. Microbiol.* 8. doi: 10.3389/fmicb.2017.01736

Moisander, P. H., Serros, T., Paerl, R. W., Beinart, R. A., and Zehr, J. P. (2014). Gammaproteobacterial Diazotrophs and nifH Gene Expression in Surface

Waters of the South Pacific Ocean. *ISME. J.* 8, 1962–1973. doi: 10.1038/ismej.2014.49

Monteiro, P. M. S., and van der Plas, A. K. (2006). 5 Low Oxygen Water (LOW) Variability in the Benguela System: Key Processes and Forcing Scales Relevant to Forecasting. *Larg. Mar. Ecosyst.* 14, 71–90. doi: 10.1016/S1570-0461(06)80010-8

Montoyal, J. P., Carpenter, E. J., and Capone, D. G. (2002). Nitrogen Fixation and Nitrogen Isotope Abundances in Zooplankton of the Oligotrophic North Atlantic. *Limnol. Oceanogr.* 47, 1617–1628. doi: 10.4319/lo.2002.47.6.1617

Nagel, B., Emeis, K. C., Flohr, A., Rixen, T., Schlarbaum, T., Mohrholz, V., et al. (2013). N-Cycling and Balancing of the N-Deficit Generated in the Oxygen Minimum Zone Over the Namibian Shelf - An Isotope-Based Approach. *J. Geophys. Res. Biogeosci.* 118, 361–371. doi: 10.1002/jgrg.20040

Oksanen, F. J., Blanchet, G., Friendly, M., Roeland Kindt, P., Legendre, D., McGlinn, P. R., et al. (2020). *Vegan: Community Ecology Package*. version 2.5.7, Available at: http://cran.r-project.org/, http://vegan.r-forge.r-project.org/

Pitcher, G. C., Walker, D. R., Mitchell-Innes, B. A., and Moloney, C. L. (1991). Short-Term Variability During an Anchor Station Study in the Southern Benguela Upwelling System: A Simulation Model. *Prog. Oceanogr.* 28, 39–64. doi: 10.1016/0079-6611(91)90023-F

Redfield, A. (1958). The Biological Control of Chemical Factors in the Environment *Sigma Xi, The Scientific Research Honor Society* 46, 205–221. doi: 10.1515/9783112312308-007

Redfield, A. C., Ketchum, B. H., and Richards, F. A. (1963). The Influence of Organisms on the Composition of Sea Water. *sea* 2, 26–77.

Rocke, E., Cheung, S., Gebe, Z., Dames, N. R., Liu, H., and Moloney, C. L. (2020). Marine Microbial Community Composition During the Upwelling Season in the Southern Benguela. *Front. Mar. Sci.* 7. doi: 10.3389/fmars.2020.00255

Saito, M. A., Tyler, G. J., and Ritt, J. T. (2008). Some Thoughts on the Concept of Colimitation : Three Definitions and the Importance of Bioavailability. *Limnol. Oceanogr.* 53, 276–290. doi: 10.4319/lo.2008.53.1.0276

Saxena, H., Sahoo, D., Khan, M. A., Kumar, S., Sudheer, A. K., and Singh, A. (2020). Dinitrogen Fixation Rates in the Bay of Bengal During Summer Monsoon. *Environ. Res. Commun.* 2, 051007. doi: 10.1088/2515-7620/ab89fa

Schloss, P. D., Westcott, S. L., Ryabin, T, Hall, J. R., Hartmann, M, Hollister, E. B., et al. (2009). Introducing Mothur. *Appl. Env. Microbiol.* 75, 7537-7541. doi: 10.1128/AEM.01541-09.

Scholz, F., Löscher, C. R., Fiskal, A., Sommer, S., Hensen, C., Lomnitz, U., et al. (2016). Nitrate-Dependent Iron Oxidation Limits Iron Transport in Anoxic Ocean Regions. *Earth Planet. Sci. Lett.* 454, 272–281. doi: 10.1016/j.epsl.2016.09.025

Schunck, H., Lavik, G., Desai, D. K., Großkopf, T., Kalvelage, T., Löscher, C. R., et al. (2013). Giant Hydrogen Sulfide Plume in the Oxygen Minimum Zone Off Peru Supports Chemolithoautotrophy. *PLoS One* 8, e68661. doi: 10.1371/journal.pone.0068661

Shannon, L. V., and Pillar, S. C. (1986). "The Benguela Ecosystem. Part III. Plankton," in *Oceanogr. Mar. Biol* London: CRC Press, 65–170 .

Short, S. M., and Zehr, J. P. (2007). Nitrogenase Gene Expression in the Chesapeake Bay Estuary. *Environ. Microbiol.* 9, 1591–1596. doi: 10.1111/j.1462-2920.2007.01258.x

Sigman, D. M., Casciotti, K. L., Andreani, M., Barford, C., Galanter, M., and Böhlke, J. K. (2001). A Bacterial Method for the Nitrogen Isotopic Analysis of Nitrate in Seawater and Freshwater. *Anal. Chem.* 73 (17), 4145–4153. doi: 10.1021/ac010088e.

Sohm, J. A., Hilton, J. A., Noble, A. E., Zehr, J. P., Saito, M. A., and Webb, E. A. (2011). Nitrogen Fixation in the South Atlantic Gyre and the Benguela Upwelling System. *Geophys. Res. Lett.* 38, 1–7. doi: 10.1029/2011GL048315

Staal, M., Hekkert, S. T. L., Brummer, G. J., Veldhuis, M., Sikkens, C., Persijn, S., et al. (2007). Nitrogen Fixation Along a North-South Transect in the Eastern Atlantic Ocean. *Limnol. Oceanogr.* 52, 1305–1316. doi: 10.4319/lo.2007.52.4.1305

Tang, W., and Cassar, N. (2019). Data-Driven Modeling of the Distribution of Diazotrophs in the Global Ocean. *Geophys. Res. Lett.* 46, 12258–12269. doi: 10.1029/2019GL084376

Turk-Kubo, K. A., Karamchandani, M., Capone, D. G., and Zehr, J. P. (2014). The Paradox of Marine Heterotrophic Nitrogen Fixation: Abundances of Heterotrophic Diazotrophs do Not Account for Nitrogen Fixation Rates in the Eastern Tropical South Pacific. *Environ. Microbiol.* 16, 3095–3114. doi: 10.1111/1462-2920.12346

Tyrrell, T., and Lucas, M. I. (2002). Geochemical Evidence of Denitrification in the Benguela Upwelling System. *Cont. Shelf. Res.* 22, 2497–2511. doi: 10.1016/S0278-4343(02)00077-8

Tyrrell, T., Marañón, E., Poulton, A. J., Bowie, A. R., Harbour, D. S., and Woodward, E. M. S. (2003). Large-Scale Latitudinal Distribution of Trichodesmium Spp. In the Atlantic Ocean. *J. Plankt. Res.* 25, 405–416. doi: 10.1093/plankt/25.4.405

Vizy, E. K., Cook, K. H., and Sun, X. (2018). Decadal Change of the South Atlantic Ocean Angola–Benguela Frontal Zone Since 1980. *Clim. Dyn.* 51, 3251–3273. doi: 10.1007/s00382-018-4077-7

Voss, M., Dippner, J. W., and Montoya, J. P. (2001). Nitrogen Isotope Patterns in the Oxygen-Deficient Waters of the Eastern Tropical North Pacific Ocean. *Deep. Res. Part I. Oceanogr. Res. Pap.* 48, 1905–1921. doi: 10.1016/S0967-0637(00)00110-2

Wacklin, P., Hoffmann, L., and Komárek, J. (2009). Nomenclatural Validation of the Genetically Revised Cyanobacterial Genus Dolichospermum (Ralfs Ex Bornet Et Flahault) Comb, Nova. *Fottea* 9, 59–64. doi: 10.5507/fot.2009.005

Wang, W. L., Moore, J. K., Martiny, A. C., and Primeau, F. W. (2019). Convergent Estimates of Marine Nitrogen Fixation. *Nature* 566, 205–211. doi: 10.1038/s41586-019-0911-2

Wasmund, N., Lass, H. U., and Nausch, G. (2005). Distribution of Nutrients, Chlorophyll and Phytoplankton Primary Production in Relation to Hydrographic Structures Bordering the Benguela-Angolan Frontal Region. *Afr. J. Mar. Sci.* 27, 177–190. doi: 10.2989/18142320509504077

Wasmund, N., Struck, U., Hansen, A., Flohr, A., Nausch, G., Grüttmüller, A., et al. (2015). Missing Nitrogen Fixation in the Benguela Region. *Deep. Res. Part I. Oceanogr. Res. Pap.* 106, 30–41. doi: 10.1016/j.dsr.2015.10.007

Westberry, T. K., and Siegel, D. A. (2006). Spatial and Temporal Distribution of Trichodesmium Blooms in the World's Oceans. *Glob. Biogeochem. Cycle.* 20, GB4016. doi: 10.1029/2005GB002673

Zani, S., Mellon, M. T., Collier, J. L., and Zehr, J. P. (2000). Expression of nifH Genes in Natural Microbial Assemblages in Lake George, New York, Detected by Reverse Transcriptase PCR. *Appl. Environ. Microbiol.* 66, 3119. doi: 10.1128/AEM.66.7.3119-3124.2000

Zehr, J. P., Jenkins, B. D., Short, S. M., and Steward, G. F. (2003). Nitrogenase Gene Diversity and Microbial Community Structure: A Cross-System Comparison. *Environ. Microbiol.* 5, 539–554. doi: 10.1046/j.1462-2920.2003.00451.x

Conflict of Interest: The authors declare that the research was conducted in the absence of any commercial or financial relationships that could be construed as a potential conflict of interest.

frontiers | Frontiers in Marine Science

ORIGINAL RESEARCH
published: 04 July 2022
doi: 10.3389/fmars.2022.875582

Nitrogenases in Oxygen Minimum Zone Waters

Christian Furbo Reeder[1] *and Carolin Regina Löscher*[1,2]*

[1] Nordcee, Department of Biology, University of Southern Denmark, Odense, Denmark, [2] Danish Institute for Advanced Study, University of Southern Denmark, Odense, Denmark

Biological dinitrogen (N_2) fixation is the pathway making the large pool of atmospheric N_2 available to marine life. Besides direct rate measurements, a common approach to explore the potential for N_2 fixation in the ocean is a screening-based targeting the key functional marker gene *nifH*, coding for a subunit of the nitrogenase reductase. As novel sequencing techniques improved, our understanding of the diversity of marine N_2 fixers grew exponentially. However, one aspect of N_2 fixation in the ocean is often underexplored, which are the two alternative types of the key enzyme of N_2 fixation, the nitrogenase. Altogether there are three isoenzymes, the most common Mo-Fe nitrogenase Nif, the Fe-Fe nitrogenase Anf, and the V-Fe nitrogenase Vnf, which differ regarding their genetic organization, as well as their metal co-enzymes. While Mo is only available in the presence of at least traces of oxygen (O_2), V and Fe are available if O_2 is absent. Therefore, low O_2 and anoxic ocean environments could be an ideal place to explore the diversity of the different isotypes of the nitrogenases. Most phylogenetic studies, however, were only based on the functional marker gene *nifH*, encoding for a subunit of the Nif nitrogenase, and thus limited in representing the diversity of alternative nitrogenases. Here, we screened metagenomes and -transcriptomes from O_2 minimum zones off Peru, from the Bay of Bengal, and the anoxic Saanich Inlet to explore the diversity of genes involved in N_2 fixation. We identified genes related to all three nitrogenases, and a generally increased diversity as compared to our previous *nifH* based on studies from OMZ waters. While we could not confirm gene expression of alternative nitrogenases from our transcriptomic, we detected diazotrophs harboring the genetic potential for alternative nitrogenases. We suggest that alternative nitrogenases may not be used under conditions present in those waters, however, depending on trace metal availability they may become active under future ocean deoxygenation.

Keywords: alternative nitrogenases, nitrogen fixation, oxygen minimum zone (OMZ), diazotrophs diversity, bioinfomatic analysis

OPEN ACCESS

Edited by:
Annie Bourbonnais,
University of South Carolina,
United States

Reviewed by:
Takuhei Shiozaki,
The University of Tokyo, Japan
Anthony Bertagnolli,
Montana State University,
United States
Shunyan Cheung,
University of California, Santa Cruz,
United States

***Correspondence:**
Carolin Regina Löscher
cloescher@biology.sdu.dk

Specialty section:
This article was submitted to Marine Biogeochemistry, a section of the journal Frontiers in Marine Science

Received: *14 February 2022*
Accepted: *25 May 2022*
Published: *04 July 2022*

Citation:
Reeder CF and Löscher CR (2022) Nitrogenases in Oxygen Minimum Zone Waters. Front. Mar. Sci. 9:875582. doi: 10.3389/fmars.2022.875582

INTRODUCTION

Biological fixation of dinitrogen gas (N_2) is quantitatively the most important external supply of nitrogen (N) to the Ocean. Only certain N_2 fixing microbes, called diazotrophs, can perform this highly energy costly enzymatic reaction. First pioneering studies involving large scale sequencing surveys, based on the then-available Sanger sequencing technique, identified the paraphyletic nature

of diazotrophs throughout the archaeal and bacterial kingdoms (Zehr et al., 1998; Zani et al., 2000; Zehr and Turner, 2001). More recent studies using high throughput sequencing approaches [e.g., (Farnelid et al., 2011; Cheung et al., 2016; Gaby et al., 2018)] broadened the tree of diazotrophs and more clades could be added to the diversity of N_2 fixers in the Ocean, however, it appears that the initial trees did not fundamentally change concerning their main cluster structure.

One major reason may be in the nature of the available genetic screening methods, which are mostly based on selectively targeting the *nifH* gene, defined as a key functional marker for the operon encoding for the enzyme dinitrogenase reductase (Yun and Szalay, 1984). The operon contains, however, two additional structural genes, *nifD* and *nifK*, altogether the *nif* regulon comprises seven operons (Brill, 1980). *nifH* genes are often represented in small numbers in the marine realm, and PCR-based detection requires subsequent amplification steps thus introducing certain biases. Thus, to approach the diversity of diazotrophs in the environment, it may be helpful to consider other parts of the *Nif* operon to obtain a more complete picture. An additional problem regarding the molecular screening for nitrogenases is that the common nitrogenase (encoded by *nif*) is only one out of three nitrogenases (Bishop et al., 1980; Joerger et al., 1988; Kennedy et al., 1991).

Two alternative nitrogenases were described, one of which is the Anf nitrogenase, which is characterized by an iron-iron (Fe) co-enzyme, the other nitrogenase, Vnf, is a vanadium (V)-Fe nitrogenase. The classic Nif nitrogenase has a Fe-Molybdenum (Mo) cofactor. The difference regarding those metal cofactors is of particular interest in anoxic or generally O_2 depleted environments. Mo –in contrast to Fe and V- is only available when at least traces of O_2 are present (Bertine and Turekian, 1973; Collier, 1985; Morford and Emerson, 1999; Anbar and Knoll, 2002). This is important with regard to the predicted loss of O_2 in today's Oceans in a warming world (Stramma et al., 2008; Keeling et al., 2010; Schmidtko et al., 2017) which might possibly lead to Mo not always being available, disabling Nif nitrogenases and facilitate the use of alternative nitrogenases. The reason for the evolutionary development of three different nitrogenases is still debated. The general conclusion, however, is that the two alternative nitrogenases originated from *nif* (Raymond et al., 2004; Boyd et al., 2011; Boyd and Peters, 2013; Boyd et al., 2015), which is supported, e.g., by a similar genetic structure and alternative nitrogenases being dependent on *nif*-machinery for biosynthesis (Kennedy and Dean, 1992).

Alternative nitrogenases are frequently detected and active in terrestrial environments (Bellenger et al., 2020). However, information on the ecological role of alternative nitrogenases and their activity and presence in marine settings is scarce. A previous study based on whole-genome mining and PacBio from coastal environments identified a 20 fold increase in diversity of diazotrophs when including genes encoding for alternative nitrogenases *anf* and *vnf* (McRose et al., 2017) suggesting the importance of those nitrogenases for obtaining a conclusive picture of the diazotroph community in an environment. The contribution of alternative nitrogenases to N_2 fixation in environments including cyanolichens, microbial mats, anaerobic sediments has been further corroborated by studies based on isotope fractionation using an isotopic acetylene reduction assay able to distinguish canonical Mo and alternative nitrogenase activities based on carbon isotope fractionation during acetylene reduction to ethylene (Zhang et al., 2016). Based on this assay, Zhang et al., 2016 determined alternative nitrogenases to contribute 20-55% to bulk N_2 fixation rates in salt marshes.

Due to the above-mentioned potential advantage of diazotrophs with alternative nitrogenases, marine OMZs might turn into suitable niches for those microbes. In the light of Ocean deoxygenation (Stramma et al., 2008; Keeling et al., 2010; Schmidtko et al., 2017) and increasing frequency of regional severe anoxic and sulfidic events (Lennartz et al., 2014) diazotrophs possessing those alternative nitrogenases may therefore increasingly obtain advantage, because Mo may become limiting under anoxia, thus disabling the functionality of the *nif*-nitrogenase (Helz et al., 1996; Bellenger et al., 2020; Bennett and Canfield, 2020). Still, information on the presence and distribution of alternative nitrogenases in OMZ waters is to date not available.

In this study, we explored the presence of the three different nitrogenases in OMZs with different intensities. We compared nitrogenases in the OMZ off Peru, which is one of the most prominent examples for expanding and progressing deoxygenation (Stramma et al., 2010) and displays coastal sulfidic anoxia (Schunck et al., 2013; Löscher et al., 2015; Callbeck et al., 2018), Saanich Inlet (SI), a seasonally anoxic fjord (Carter, 1932; Carter, 1934; Anderson and Devol, 1973; Torres-Beltrán et al., 2017), and the Bay of Bengal (BoB) OMZ as part of the Northern Indian Ocean, which has been described to maintain traces of oxygen in its OMZ core waters (Bristow et al., 2017).

MATERIALS AND METHODS

We re-analyzed metagenomic and -transcriptomic datasets collected on a cruise to the eastern tropical South Pacific in 2009/2010. The cruise was carried out in the framework of the collaborative research center SFB 754 'Climate-biogeochemistry interactions in tropical Oceans' on the German research vessel RV Meteor. The samples were collected as previously described (Schunck et al., 2013; Löscher et al., 2014) on the shelf on station #19, 12°21.88′S, 77°10.00′W, where the water column was anoxic from 20 m down to the sediment (124 m) and hydrogen sulfide (H_2S) was present in the anoxic zone reaching concentrations up to 5 µmol L^{-1}. Metagenomic dataset for from BoB were collected from Löscher et al., 2020 with location 17°N, 88.2°E. Metagenomic dataset from SI (48.5° N, 123.5°W) are accessible through JGI IMG/G portal as indicated in Hawley et al., 2017.

Seawater Sampling

Samples for salinity, O_2 and nutrient analysis, including nitrate, nitrite, ammonia, and phosphate (NO_3^-, NO_2^-, NH_4^+ and PO_4^{3-}),

respectively were collected from a pump-CTD system. On M77/3 this allowed to combine the classical conductivity-temperature-density sensor measurements with O_2, fluorescence, turbidity, and acoustic doppler counter profiler measurements, and importantly with continuous water sampling over a water column of maximum 350 m depth in high resolution. Seabird sensor O_2 measurements were calibrated with Winkler method measurements; salinity and nutrients were measured directly after sampling according to Grasshoff et al., 1999 using an autoanalyzer. Samples for nucleic acid extraction were prefiltered through 10 µm pore size filters (Whatman Nuclepore Track-Etch) and cells were collected on 0.22 µm pore size filters (Durapore Membrane filters, Millipore) using a vacuum pump, with filtration times not exceeding 20 min. Filters were frozen and stored at -80°C.

Molecular Methods

Molecular analysis for this study is based on a publicly available metagenomic and –transcriptomic dataset, originally presented in Schunck et al., 2013 with a focus on chemolithoautotrophic lifestyles in sulfidic OMZ waters. Sequencing resulted in 1,888,768 (DNA) and 1,560,959 (RNA) sequences with an average length of 392 base pairs, accounting for 757,439,211 and 599,103,110 base pairs of sequence information, respectively. Sequence datasets are publicly available from the metagenomics analysis server (MG-RAST) under accession numbers 4460677.3, 4450892.3, 4450891.3, 4460736.3, 4461588.3, 4460676.3, 4452038.3, 4460734.3, 4452039.3, 4452042.3, 4460735.3, 4460734.3 and 4452043.3.

Bioinformatic Methods

Metagenomic and transcriptomic raw-reads from the Peruvian shelf, BoB and SI were uploaded and processed on MG-RAST, an open-submission portal for analyzing metagenomic/transcriptomic dataset, such as annotation and functional reconstruction (Keegan et al., 2016). We screened for nitrogenase genes using COG (Cluster of Orthologous genes) database and were subsequently exported. A total of 8677 nif-related and 1112 alternative-related genes were exported from SI, 529 nif-related and 124 alternative-related genes from the Peruvian Shelf, and 116 nif-related and 27 alternative-related genes from the BoB. Exported nitrogenase genes were subject to a BLAST search on the NCBI Genbank database to create a reference library. Mega 7 was used for phylogenetic analysis (Neighbor-joining method) using the reference library and exported nitrogenase genes (Kumar et al., 2016). Clades were defined based on phylogenetic analysis. In order to constrain differences to our previous study of the same samples (Löscher et al., 2014), which were based on *nifH* Sanger sequencing, we constructed Neighbor-joining trees. Gene/transcript relative abundances were estimated by normalizing counts of nitrogenase genes to the housekeeping gene, *rpoB*.

In order to identify parameters determining the distribution of N_2 fixers in these sulfidic waters, we applied simple correlation analysis and a principal component analysis (PCA, **Table S1** and **Figure S2**). This dataset was compared to a metagenomic dataset available from the BoB from a situation with an OMZ with only traces of O_2 left in its core waters, low productivity and a typical OMZ diazotroph community as identified by Sanger sequencing of *nifH* (Löscher et al., 2020), and from the SI from Oct 2011 where O_2 concentrations were below 5 µmol L^{-1} (Hawley et al., 2017).

RESULTS AND DISCUSSION

Hydrochemistry Features

In this study, we used full metagenomes and –transcriptomes from an environment sharing certain characteristics with an ancient Ocean, in order to explore the functional diversity of N_2 fixers, and the expression of genes involved in it. We compared the results of this presumably unbiased dataset to previous PCR-based studies targeting the classical functional marker for N_2 fixation, *nifH*. Sampling took place on the shelf off Peru, in a patch of water that was sulfidic at the time. Sulfidic conditions were reported in other studies as well (Galán et al., 2014; Callbeck et al., 2018), thus this condition could be a permanent feature. The distribution of nutrients and chemical properties can be seen in Schunck et al., 2013. Briefly, the path which was sulfidic during our cruise is visibly O_2 depleted even in this integrated plot. The water column was anoxic from 18 m downwards and hydrogen sulfide (H_2S) was detected along the vertical profile from 27 m downwards (**Figures 3C, D**). At the same depth (27 m) NO_3^- and NO_2^- were depleted and $NH_4^+$was accumulated throughout the anoxic water column (**Figure 1**). Iron (Fe) concentrations were reportedly high reaching concentrations up to about 267 nmol kg^{-1} in the water column, mostly in the bioavailable form of Fe(II) (Schlosser et al., 2018) in line with earlier reports from that same area (Hong and Kester, 1986).

Composition of Diazotrophs off the Peruvian Shelf

In our previous study from 2014 (Löscher et al., 2014) based on Sanger sequencing of the *nifH* gene, we identified a community of seven previously unknown and two described clades of N_2 fixers in the OMZ waters off Peru. Organisms matching those clades could be recovered from our metagenomes, thus supporting our previous study regarding the validity of sequence presence (**Figure 2**). In addition to those previously described N_2 fixers, we identified several diazotroph clades on the genus level from the combined metagenomes and transcriptomes, thus suggesting that the previously used Sanger sequencing did not entirely cover the present diversity. Taking all *nif, anf*, and *vnf* genes into consideration, we identified additional N_2 fixers amongst ß-, ɣ-, and ɗ- Proteobacteria, green and purple sulfur bacteria, Firmicutes, Verrumicrobia, Crenarchaeota and Euryarchaeota.

Importantly, we could not identify the traditionally genetic marker gene for nitrogenases (*nifH*), but rather, rather *nifA*, were the most abundant nitrogenase gene identified (**Tables S2A, B**). This, indeed, leaves us wondering how far any of the genes identified in this or other studies are translated into functional nitrogenases. N_2 fixation has been shown to occur in those OMZ

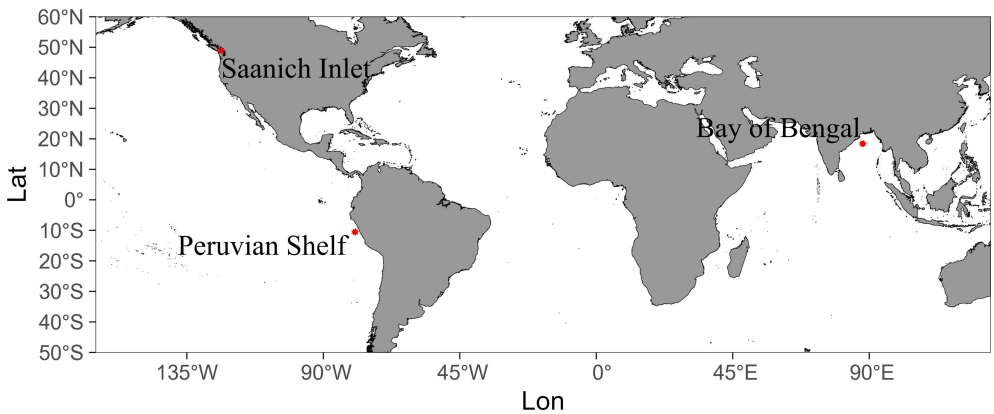

FIGURE 1 | Location of stations from where samples were analyzed from. Stations are indicated by a red star. Peruvian Shelf at 12.2°S, 77°W. Saanich inlet at 48.5°N, 123.5°W. Bay of Bengal at 17°N, 88.2°E.

waters, however, rates deviated strongly and ranged from below the detection limit (Bonnet et al., 2013; Dekaezemacker et al., 2013; Turk-Kubo et al., 2014) to comparably high rates of up to 24.8 ± 8.4 nmol N L^{-1} d^{-1} (Löscher et al., 2014; Löscher et al., 2016) (**Figure 3D**). The latter, however possibly having been corrupted by the use of a potentially contaminated gas stock (Dabundo et al., 2014). In our previous studies, we could not clearly correlate a specific clade of N_2 fixers to the high rates in N_2 fixation in the euphotic zone in the sulfidic patch. Our data, however, shows the presence of N_2 fixers within the genera of both Burkholderiales, Rhizobiales, and Myxococcales in the euphotic zone (**Figure 3A** and **Figure S1**), possibly contributing to N_2 fixation in surface waters.

There were two descriptions of this area developing sulfidic anoxia (Schunck et al., 2013; Callbeck et al., 2018). Historical reports of Peruvian fishermen on the characteristic smell and black fishing gear (Schunck et al., 2013), and at least two earlier descriptions of sulfidic anoxia in those waters point towards re-occurring sulfidic anoxia in this region (Burtt, 1852; Dugdale et al., 1977). We identified clades typically observed in anoxic environments, such as clades related to Desulfovibrio and Chlorobiales (Farnelid et al., 2013; Löscher et al., 2014; Jayakumar and Ward, 2020). A large fraction, of N_2 fixers in those sulfidic waters, as previously described (Fernandez et al., 2011; Löscher et al., 2014), are microbes involved in sulfur cycling, and similar to those found in organic carbon-rich sediments [e.g., (Bertics et al., 2013; Gier et al., 2016)]. While those N_2 fixers do not seem to be quantitatively important for N_2 fixation rates, they still find a niche and might become more important in the future with intensifying, expanding OMZs and more frequent events of sulfidic anoxia (Stramma et al., 2008; Lennartz et al., 2014).

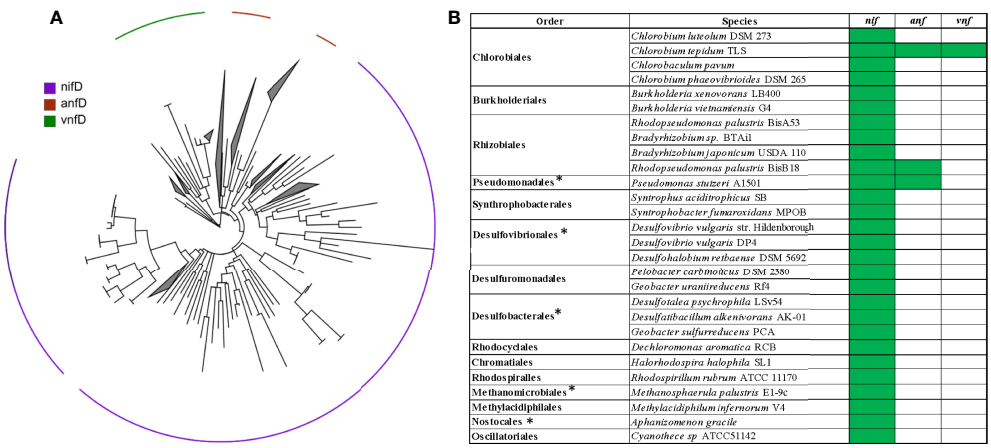

Order	Species	*nif*	*anf*	*vnf*
Chlorobiales	*Chlorobium luteolum* DSM 273			
	Chlorobium tepidum TLS			
	Chlorobaculum pavum			
	Chlorobium phaeovibrioides DSM 265			
Burkholderiales	*Burkholderia xenovorans* LB400			
	Burkholderia vietnamiensis G4			
Rhizobiales	*Rhodopseudomonas palustris* BisA53			
	Bradyrhizobium sp. BTAil			
	Bradyrhizobium japonicum USDA 110			
	Rhodopseudomonas palustris BisB18			
Pseudomonadales*	*Pseudomonas stutzeri* A1501			
Synthrophobacterales	*Syntrophus aciditrophicus* SB			
	Syntrophobacter fumaroxidans MPOB			
Desulfovibrionales*	*Desulfovibrio vulgaris* str. Hildenborough			
	Desulfovibrio vulgaris DP4			
	Desulfohalobium retbaense DSM 5692			
Desulfuromonadales	*Pelobacter carbinolicus* DSM 2380			
	Geobacter uraniireducens Rf4			
Desulfobacterales*	*Desulfotalea psychrophila* LSv54			
	Desulfatibacillum alkenivorans AK-01			
	Geobacter sulfurreducens PCA			
Rhodocyclales	*Dechloromonas aromatica* RCB			
Chromatiales	*Halorhodospira halophila* SL1			
Rhodospiralles	*Rhodospirillum rubrum* ATCC 11170			
Methanomicrobiales*	*Methanosphaerula palustris* E1-9c			
Methylacidiphilales	*Methylacidiphilum infernorum* V4			
Nostocales *	*Aphanizomenon gracile*			
Oscillatoriales	*Cyanothece sp.* ATCC51142			

FIGURE 2 | Presence of nitrogenase genes in the metagenomes and -transcriptomes. **(A)** The maximum likelihood tree shows the detected diversity based on *nifD*, *anfD*, and *vnfD*. **(B)** Species closest related to the detected diazotrophs, the presence of *nif, anf*, and *vnf* is indicated in green. Note that the majority of diazotrophs possesses *nif*-nitrogenase genes only. * mark genera, of which we found representatives in our previous *nifH*-based study.

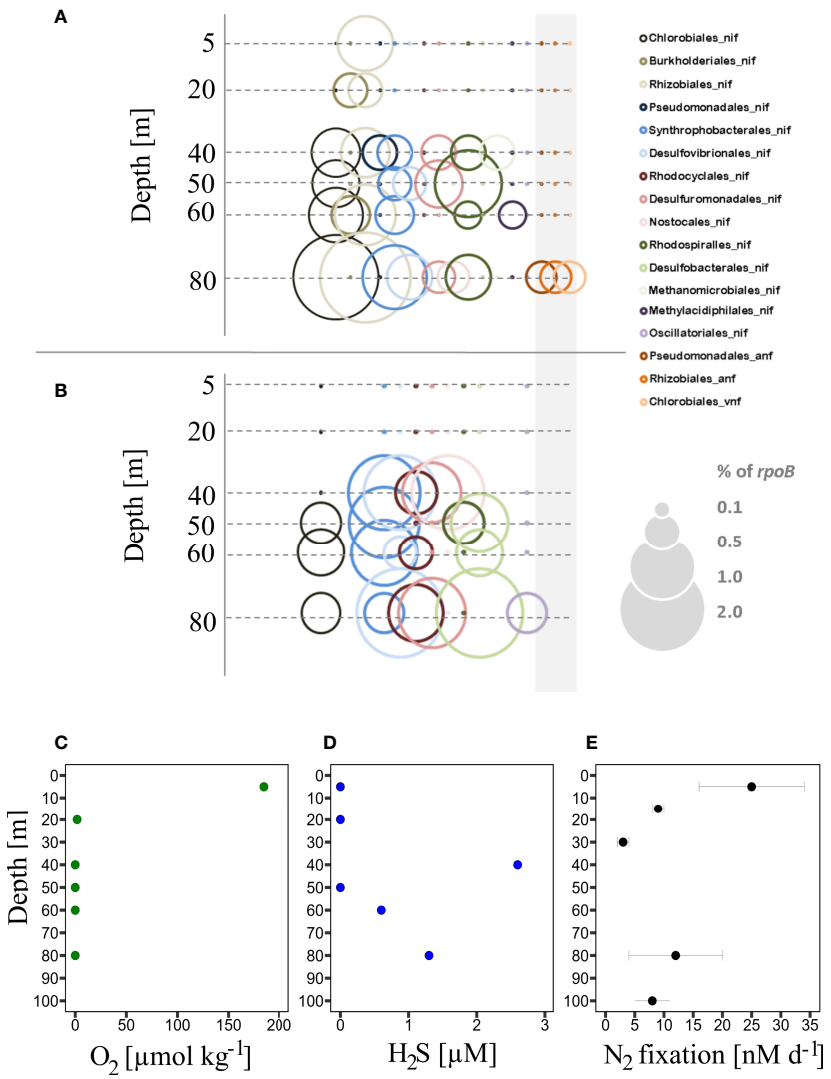

FIGURE 3 | Phylogenetic representation of organisms possessing nitrogenase genes of the *nif*, *anf*, or *vnf* type (all genes of the operons pooled) in metagenomes **(A)** and -transcriptomes **(B)** from the sulfidic station. Genera identified from annotations of protein-coding genes (in the NCBI database) in both our metagenomes and –transcriptomes. Nitrogenase gene abundances and expression are shown relative to the putative single copy per organism of RNA polymerase subunit B (*rpoB*). The grey rectangle indicates the alternative nitrogenases *anf* and *vnf*, note that no expression of either of them was found. Vertical profiles from the Peruvian Shelf of O_2 **(C)**, H_2S **(D)** and N_2 fixation rate **(E)** are modified from Löscher et al., 2014.

Activity of Diazotrophs off the Peruvian Shelf

The metatranscriptomic analysis showed no expression of genes coding for either of the two alternative nitrogenases. *nif* transcripts could be detected at water depths below 40 m downwards (**Figure 3B**) affiliated with the genera of Chlorobiales, Syntrophobacterales, Desulfovibrionales, Rhodocyclales, Desulfuromonadales, and Desulfobacterales. The presence and transcriptional activity of the sulfate-reducing Desulfovibrionales and Desulfobacterales, as well as the sulfur-respiring Desulfuromonadales, is in line with our previous study, as well as with a sediment-focused study on N_2 fixation from the same area, where those clades have been identified important amongst N_2 fixers (Gier et al., 2016).

Green sulfur bacteria (Chlorobiales), sulfate-reducing Syntrophobacterales, and Rhodocyclales (mostly classified closest to Dechloromonas clades, which can denitrify) have, however, previously never been described to play any role in N_2 fixation in the Peruvian OMZ. Except for the identified Rhodocyclales, all those newly identified N_2 fixing clades are capable of metabolizing sulfur compounds, thus hinting towards a link between N_2 fixation and sulfur cycling. However, a statistical correlation to the concentration of H_2S could only be observed for transcripts of Desulfovibrionales and

Desulfuromonadales, thus speaking for a potential link of N_2 fixation and H_2S turnover only in those clades (**Figure 3D**, **Table S1**).

Previous studies reported both, massive denitrification rates, as well as extreme nitrous oxide production from the sulfidic shelf area off Peru (Kalvelage et al., 2013; Arévalo-Martínez et al., 2015). We identified Rhodocyclales, in our dataset related to Dechloromonas, which are described as denitrifiers, producing the greenhouse gas nitrous oxide as an end-product in their denitrification chain (Horn et al., 2005). Principle component analysis revealed transcript abundances of Rhodocyclales to be linearly correlated to nitrous oxide concentrations (**Table S1B**) which supports the idea of spatially coupled denitrification and N_2 fixation, as previously suggested (Deutsch et al., 2007). However, this correlation is limited by sampling size and further, nitrous oxide concentrations are a result of combined multiple processes. Thus, a connection between denitrification and N_2 fixation remains speculative and will still require a deeper focused analysis in those waters in the future. *nif* transcripts of Desulfovibrionales and Desulfobacterales were dominant at 80 m depth, which is where N_2 fixation was at its maximum at anoxic conditions. Those clades were identified as well *via nifH* amplicon-based screening and peaked in abundance at the same depth in our previous study, however, only in the gene, but not in the transcript pool.

Based on the dominant abundance of transcripts related to Desulfovibrionales and Desulfobacterales, those clades seem to play an important role in N_2 fixation in those sulfidic waters, possibly contributing to the described N_2 fixation rates. In this sense, using full metagenomes/-transcriptomes did, compared to the *nifH*-only based approach, only provide novel insights into identifying active diazotrophs to a certain extent. The power of a metagenome/-transcriptome based approach seems to rather be important in exploring the diversity of possibly underrepresented clades, as well as clades discriminated against by the common *nifH* primers (Zehr et al., 1998).

Alternative Nitrogenases and Diazotrophs Across OMZ Waters

In addition to *nif*, we identified alternative nitrogenases in OMZ waters off Peru, SI and the BoB. We detected *anf* genes associated with Pseudomonadales and Rhizobiales, and Chlorobiales, and *vnf* genes associated with Rhizobiales, Chlorobiales, and low abundances of Rhodospririllales, Acidothiobacillales, Methylacidiphilales and Desulfovibrionales (**Figures 2**, **3A** and **Figures S1**).If compared to other O_2 depleted ocean water bodies with available full metagenomic datasets (BoB, SI), the diversity of alternative nitrogenases seems similar, with Pseudomonadales, Rhizobiales and Chlorobiales consistently present in the *anf* pool, and Rhizobiales, Chlorobiales, and Rhodospirillales dominating the *vnf* pool of sequences (**Figure S1**). Because alternative N_2 fixers always also have genes coding for the *nif* nitrogenase, it cannot be expected that the diversity of alternative nitrogenase genes exceeds the diversity of *nif* genes.

One obvious effect of the limitations of *nifH*-based mining is the previous lack of a description of alternative nitrogenases. In our samples, we could identify at least some clades possessing genes for *anf* and *vnf* consistently through OMZs of different intensity thus raising the question of whether those genes are maintained in the genome for at least occasional use when Mo is limiting for the expression of n*if*. This, however, cannot be answered from our dataset and is generally a question we can only speculate about.

The turnover of trace metals, in general, is largely redox sensitive (Morford and Emerson, 1999), and has been reported to be impacted by ENSO-dependent changes in redox conditions at the sediment-water interface in this area. With a cyclic alternation between oxic conditions favoring V and Mo fluxes to the water column and anoxic conditions re-precipitating V and Mo to the sediment, both V and Mo accumulate in shelf sediments in the Peruvian OMZ (Scholz et al., 2011). Further, a reduction of V to V(III) by H_2S has been demonstrated experimentally, thus explaining the redox-dependent accumulation in sulfate-reducing sediments (Wanty and Goldhaber, 1992). Under sulfidic conditions, Mo(VI) is reduced to Mo(IV) and precipitated to the sediments (Crusius et al., 1996). While this precipitation at anoxic and sulfidic conditions in principle removes Mo and V from the water column, it promotes the formation of a reservoir of those trace metals in the sediments (Bennett and Canfield, 2020), enabling their availability in the water column *via* upwelling at least occasionally when redox conditions allow for it. Given the decrease in Mo and V availability at anoxic-sulfidic conditions, possessing the genes for an additional Fe-Fe nitrogenase may thus be advantageous, both regarding ocean anoxic events in Earth history and future ocean deoxygenation likewise. Thus, one could suggest that while *anf* and *vnf* may presently not play a major role for N_2 fixation in OMZs they may become important under a possible future euxinia scenario.

It has only recently been shown that even under Mo limitation alternative N_2 fixers will try to acquire enough of this trace metal to still sustain their *nif* nitrogenase instead of expressing the alternative nitrogenases (Philippi et al., 2021). Thus, the presence of alternative nitrogenases, while being a given, is not explainable for us right now. Thou, they may play a substantial role in N_2 fixation in costal sediment environments, particular in sediments (Zhang et al., 2016; McRose et al., 2017).

CONCLUSION

This study addresses the diazotrophic community, based on a whole-metagenome and – transcriptome screening. It reports an increased diversity of N_2 fixing microbes in the sulfidic shelf water off Peru, as compared to the previous target-gene based studies from the same waters. In addition to a generally higher diversity, genes encoding for alternative nitrogenases, which were previously not subject of any study on N_2 fixation in those OMZs, were detected. The ecological meaning and evolutionary history of those alternative nitrogenases are debated, however, their presence in OMZ waters would possibly become relevant under scenarios of extreme and

persistent anoxia, which may become important in a future ocean challenged by progressive deoxygenation.

DATA AVAILABILITY STATEMENT

The datasets presented in this study can be found in online repositories. The names of the repository/repositories and accession number(s) can be found in the article/**Supplementary Material**

AUTHOR CONTRIBUTIONS

CL and CR designed the study. CR carried out bioinformatic analysis. CL and CR wrote the manuscript. All authors contributed to the article and approved the submitted version.

FUNDING

The cruise was funded by the German Research Foundation within the Collaborative Research Center SFB754. Funding was further received from the European Union in the framework of the H2020 program (Marie Curie IF, # 704272 to CL), and from the Villum Foundation (Grant No. 16518 to D. Canfield and Grant No. 29411 to CL).

ACKNOWLEDGMENTS

We acknowledge the captain, crew and the chief scientist, Martin Frank, of the RV Meteor cruise M77/3. We thank the Peruvian government for giving access to their territorial waters. G. Klockgether, A. Ellrott, V. León Fernández, and P. Fritsche, we thank you for technical support during the cruise. We further thank Will Bennett for helpful discussion of trace metal availability.

SUPPLEMENTARY MATERIAL

The Supplementary Material for this article can be found online at: https://www.frontiersin.org/articles/10.3389/fmars.2022.875582/full#supplementary-material

REFERENCES

Anbar, A. D., and Knoll, A. H. (2002). Proterozoic Ocean Chemistry and Evolution: A Bioinorganic Bridge? *Science* 297, 1137–1142. doi: 10.1126/science.1069651

Anderson, J. J., and Devol, A. H. (1973). Deep Water Renewal in Saanich Inlet, an Intermittently Anoxic Basin. *Estuar. Coast. Mar. Sci.* 1, 1–10. doi: 10.1016/0302-3524(73)90052-2

Arévalo-Martínez, D. L., Kock, A., Löscher, C. R., Schmitz, R. A., and Bange, H. W. (2015). Evidence of Massive Nitrous Oxide Emissions From the Tropical South Pacific Ocean. *Nat. Geosci.* 8, 530–533. doi: 10.1038/ngeo2469

Bellenger, J. P., Darnajoux, R., Zhang, X., and Kraepiel, A. M. L. (2020). Biological Nitrogen Fixation by Alternative Nitrogenases in Terrestrial Ecosystems: A Review. *Biogeochemistry* 149, 53–73. doi: 10.1007/s10533-020-00666-7

Bennett, W. W., and Canfield, D. E. (2020). Redox-Sensitive Trace Metals as Paleoredox Proxies: A Review and Analysis of Data From Modern Sediments. *Earth-Sci. Rev.* 204, 103175. doi: 10.1016/j.earscirev.2020.103175

Bertics, V. J., Löscher, C. R., Salonen, I., Dale, A. W., Gier, J., Schmitz, R. A., et al. (2013). Occurrence of Benthic Microbial Nitrogen Fixation Coupled to Sulfate Reduction in the Seasonally Hypoxic Eckernförde Bay, Baltic Sea. *Biogeosciences* 10, 1243–1258. doi: 10.5194/bg-10-1243-2013

Bertine, K. K., and Turekian, K. K. (1973). Molybdenum in Marine Deposits. *Geochim. Cosmochim. Acta* 37, 1415–1434. doi: 10.1016/0016-7037(73)90080-X

Bishop, P. E., Jarlenski, D. M., and Hetherington, D. R. (1980). Evidence for an Alternative Nitrogen Fixation System in Azotobacter Vinelandii. *Proc. Natl. Acad. Sci. U. S. A.* 77, 7342–7346. doi: 10.1073/pnas.77.12.7342

Bonnet, S., Dekaezemacker, J., Turk-Kubo, K. A., Moutin, T., Hamersley, R. M., Grosso, O., et al. (2013). Aphotic N2 Fixation in the Eastern Tropical South Pacific Ocean. *PloS One* 8, 1–14. doi: 10.1371/journal.pone.0081265

Boyd, E. S., Anbar, A. D., Miller, S., Hamilton, T. L., Lavin, M., and Peters, J. W. (2011). A Late Methanogen Origin for Molybdenum-Dependent Nitrogenase. *Geobiology* 9, 221–232. doi: 10.1111/j.1472-4669.2011.00278.x

Boyd, E. S., Garcia Costas, A. M., Hamilton, T. L., Mus, F., and Peters, J. W. (2015). Evolution of Molybdenum Nitrogenase During the Transition From Anaerobic to Aerobic Metabolism. *J. Bacteriol.* 197 (9), 1690–1699. doi: 10.1128/JB.02611-14

Boyd, E. S., and Peters, J. W. (2013). New Insights Into the Evolutionary History of Biological Nitrogen Fixation. *Front. Microbiol.* 4. doi: 10.3389/fmicb.2013.00201

Brill, W. J. (1980). Biochemical Genetics of Nitrogen Fixation. *Microbiol. Rev.* 44, 449–467. doi: 10.1128/mr.44.3.449-467.1980

Bristow, L. A., Callbeck, C. M., Larsen, M., Altabet, M. A., Dekaezemacker, J., Forth, M., et al. (2017). N2 Production Rates Limited by Nitrite Availability in the Bay of Bengal Oxygen Minimum Zone. *Nat. Geosci.* 10, 24–29. doi: 10.1038/ngeo2847

Burtt, J. L. (1852). On Fish Destroyed by Sulphuretted Hydrogen in the Bay of Callao. *Am. J. Sci.* 2, 433–434.

Callbeck, C. M., Lavik, G., Ferdelman, T. G., Fuchs, B., Gruber-Vodicka, H. R., Hach, P. F., et al. (2018). Oxygen Minimum Zone Cryptic Sulfur Cycling Sustained by Offshore Transport of Key Sulfur Oxidizing Bacteria. *Nat. Commun.* 9, 1729. doi: 10.1038/s41467-018-04041-x

Carter, N. M. (1932). The Oceanography of the Fjords of Southern British Columbia. *J. Fish. Res. Bd. Canada Prog. Rept. Pac. Coast. Sta* 12, 7–11.

Carter, N. M. (1934). Physiography and Oceanography of Some British Columbia Fjords. *J. Proc. Fifth. Pac. Sci. Cong.* 1, 721.

Cheung, S., Xia, X., Guo, C., and Liu, H. (2016). Diazotroph Community Structure in the Deep Oxygen Minimum Zone of the Costa Rica Dome. *J. Plankton. Res.* 38, 380–391. doi: 10.1093/plankt/fbw003

Collier, R. W. (1985). Molybdenum in the Northeast Pacific Ocean. *Limnol Oceanogr.* 30, 1351–1354. doi: 10.4319/lo.1985.30.6.1351

Crusius, J., Calvert, S., Pedersen, T., and Sage, D. (1996). Rhenium and Molybdenum Enrichments in Sediments as Indicators of Oxic, Suboxic and Sulfidic Conditions of Deposition. *Earth Planet. Sci. Lett.* 145, 65–78. doi: 10.1016/s0012-821x(96)00204-x

Dabundo, R., Lehmann, M. F., Treibergs, L., Tobias, C. R., Altabet, M. A., Moisander, P. H., et al. (2014). The Contamination of Commercial 15n2 Gas Stocks With 15N–Labeled Nitrate and Ammonium and Consequences for Nitrogen Fixation Measurements. *PloS One* 9, e110335. doi: 10.1371/journal.pone.0110335

Dekaezemacker, J., Bonnet, S., Grosso, O., Moutin, T., Bressac, M., and Capone, D. G. (2013). Evidence of Active Dinitrogen Fixation in Surface Waters of the Eastern Tropical South Pacific During El Niño and La Niña Events and Evaluation of its Potential Nutrient Controls. *Global Biogeochem. Cycles* 27, 768–779. doi: 10.1002/gbc.20063

Deutsch, C., Sarmiento, J. L., Sigman, D. M., Gruber, N., and Dunne, J. P. (2007). Spatial Coupling of Nitrogen Inputs and Losses in the Ocean. *Nature* 445, 163–167. doi: 10.1038/nature05392

Dugdale, R. C., Goering, J. J., Barber, R. T., Smith, R. L., and Packard, T. T. (1977). Denitrification and Hydrogen Sulfide in the Peru Upwelling Region During 1976. *Deep. Res.* 24, 601–608. doi: 10.1016/0146-6291(77)90530-6

Farnelid, H., Andersson, A. F., Bertilsson, S., Al-Soud, W. A., Hansen, L. H., Sørensen, S., et al. (2011). Nitrogenase Gene Amplicons From Global Marine Surface Waters Are Dominated by Genes of Non-Cyanobacteria. *PloS One* 6, e19223. doi: 10.1371/journal.pone.0019223

Farnelid, H., Bentzon-Tilia, M., Andersson, A. F., Bertilsson, S., Jost, G., Labrenz, M., et al. (2013). Active Nitrogen-Fixing Heterotrophic Bacteria at and Below the Chemocline of the Central Baltic Sea. *ISME J.* 7, 1413–1423. doi: 10.1038/ismej.2013.26

Fernandez, C., Farías, L., and Ulloa, O. (2011). Nitrogen Fixation in Denitrified Marine Waters. *PloS One* 6, e20539. doi: 10.1371/journal.pone.0020539

Gaby, J. C., Rishishwar, L., Valderrama-Aguirre, L. C., Green, S. J., Valderrama-Aguirre, A., Jordan, I. K., et al. (2018). Diazotroph Community Characterization *via* a Highthroughput nifH Amplicon Sequencing and Analysis Pipeline. *Appl. Environ. Microbiol.* 84, e01512–17. doi: 10.1128/AEM.01512-17

Galán, A., Faúndez, J., Thamdrup, B., Santibáñez, J. F., and Farías, L. (2014). Temporal Dynamics of Nitrogen Loss in the Coastal Upwelling Ecosystem Off Central Chile: Evidence of Autotrophic Denitrification Through Sulfide Oxidation. *Lmnol. Ocean.* 59, 1865–1878. doi: 10.4319/lo.2014.59.6.1865

Gier, J., Sommer, S., Löscher, C. R., Dale, A. W., Schmitz, R. A., and Treude, T. (2016). Nitrogen Fixation in Sediments Along a Depth Transect Through the Peruvian Oxygen Minimum Zone. *Biogeosciences* 13, 4065–4080. doi: 10.5194/bg-13-4065-2016

Grasshoff, G., Kremling, K., and Erhardt, M. (1999). *Methods of Seawater Analysis. 3ed* (Weinheim: Wiley VCH).

Hawley, A. K., Torres-Beltrán, M., Zaikova, E., Walsh, D. A., Mueller, A., Scofield, M., et al. (2017). A Compendium of Multi-Omic Sequence Information From the Saanich Inlet Water Column. *Sci. Data* 4, 170160. doi: 10.1038/sdata.2017.160

Helz, G. R., Miller, C. V., Charnock, J. M., Mosselmans, J. F. W., Pattrick, R. A. D., Garner, C. D., et al. (1996). Mechanism of Molybdenum Removal From the Sea and its Concentration in Black Shales: EXAFS Evidence. *Geochim. Cosmochim. Acta* 60, 3631–3642. doi: 10.1016/0016-7037(96)00195-0

Hong, H., and Kester, D. R. (1986). Redox State of Iron in the Offshore Waters of Peru1. *Limnol. Oceanogr.* 31, 512–524. doi: 10.4319/lo.1986.31.3.0512

Horn, M. A., Ihssen, J., Matthies, C., Schramm, A., Acker, G., and Drake, H. L. (2005). Dechloromonas Denitrificans Sp. Nov., Flavobacterium Denitrificans Sp. Nov., Paenibacillus Anaericanus Sp. Nov. And Paenibacillus Terrae Strain MH72, N2O-Producing Bacteria Isolated From the Gut of the Earthworm Aporrectodea Caliginosa. *Int. J. Syst. Evol. Microbiol.* 55, 1255–1265. doi: 10.1099/ijs.0.63484-0

Jayakumar, A., and Ward, B. B. (2020). Diversity and Distribution of Nitrogen Fixation Genes in the Oxygen Minimum Zones of the World Oceans. *Biogeosciences* 17, 5953–5966. doi: 10.5194/bg-17-5953-2020

Joerger, R. D., Bishop, P. E., and Evans, H. J. (1988). Bacterial Alternative Nitrogen Fixation Systems. *CRC Crit. Rev. Microbiol.* 16, 1–14. doi: 10.3109/10408418809104465

Kalvelage, T., Lavik, G., Lam, P., Contreras, S., Arteaga, L., Löscher, C. R., et al. (2013). Nitrogen Cycling Driven by Organic Matter Export in the South Pacific Oxygen Minimum Zone. *Nat. Geosci.* 6, 228–234. doi: 10.1038/ngeo1739

Keegan, K. P., Glass, E. M., and Meyer, F. (2016). MG-RAST, a Metagenomics Service for Analysis of Microbial Community Structure and Function. *Methods Mol. Biol.* 1399, 207–233. doi: 10.1007/978-1-4939-3369-3_13

Keeling, R. F., Körtzinger, A., and Gruber, N. (2010). Ocean Deoxygenation in a Warming World. *Ann. Rev. Mar. Sci.* 2, 199–229. doi: 10.1146/annurev.marine.010908.163855

Kennedy, C., Bali, A., Blanco, G., Contreras, A., Drummond, M., Merrick, M., et al. (1991). "Regulation of Expression of Genes for Three Nitrogenases in Azotobacter Vinelandii," in *Nitrogen Fixation* (Dordrecht: Springer Netherlands), 13–23. doi: 10.1007/978-94-011-3486-6_2

Kennedy, C. I., and Dean, D. (1992). The Nifu, niPS and nifV Gene Products are Required for Activity of All Three Nitrogenases of Azotobacter Vinelandii. *Molec. Gen. Genet.* 231, 494–498. doi: 10.1007/BF00292722

Kumar, S., Stecher, G., and Tamura, K. (2016). MEGA7: Molecular Evolutionary Genetics Analysis Version 7.0 for Bigger Datasets. *Mol. Biol. Evol.* 33, 1870–1874. doi: 10.1093/molbev/msw054

Lennartz, S. T., Lehmann, A., Herrford, J., Malien, F., Hansen, H. P., Biester, H., et al. (2014). Long-Term Trends at the Boknis Eck Time Series Station (Baltic Sea), 1957-2013: Does Climate Change Counteract the Decline in Eutrophication? *Biogeosciences* 11, 6323–6339. doi: 10.5194/bg-11-6323-2014

Löscher, C. R., Bange, H. W., Schmitz, R. A., Callbeck, C. M., Engel, A., Hauss, H., et al. (2015). Water Column Biogeochemistry of Oxygen Minimum Zones in the Eastern Tropical North Atlantic and Eastern Tropical South Pacific Oceans. *Biogeosci. Discuss.* 12, 4495–4556. doi: 10.5194/bgd-12-4495-2015

Löscher, C., Bourbonnais, A., Dekaezemacker, J., Charoenpong, C., Altabet, M., Bange, H., et al. (2016). N2 Fixation in Eddies of the Eastern Tropical South Pacific Ocean. *Biogeosciences* 13, 2889–2899. doi: 10.5194/bg-13-2889-2016

Löscher, C. R., Großkopf, T., Desai, F., Gill, D., Schunck, H., Croot, P., et al. (2014). Facets of Diazotrophy in the Oxygen Minimum Zone Off Peru. *ISME J.* 8, 2180–2192. doi: 10.1038/ismej.2014.71

Löscher, C. R., Mohr, W., Bange, H. W., and Canfield, D. E. (2020). No Nitrogen Fixation in the Bay of Bengal? *Biogeosciences* 17, 851–864. doi: 10.5194/bg-17-851-2020

McRose, D. L., Zhang, X., Kraepiel, A. M. L., and Morel, F. M. M. (2017). Diversity and Activity of Alternative Nitrogenases in Sequenced Genomes and Coastal Environments. *Front. Microbiol.* 8. doi: 10.3389/fmicb.2017.00267

Morford, J. L., and Emerson, S. (1999). The Geochemistry of Redox Sensitive Trace Metals in Sediments. *Geochim. Cosmochim. Acta* 63, 1735–1750. doi: 10.1016/S0016-7037(99)00126-X

Philippi, M., Kitzinger, K., Berg, J. S., Tschitschko, B., Kidane, A. T., Littmann, S., et al. (2021). Purple Sulfur Bacteria Fix N2 *via* Molybdenum-Nitrogenase in a Low Molybdenum Proterozoic Ocean Analogue. *Nat. Commun.* 12, 1–12. doi: 10.1038/s41467-021-25000-z

Raymond, J., Siefert, J. L., Staples, C. R., and Blankenship, R. E. (2004). The Natural History of Nitrogen Fixation. *Mol. Biol. Evol.* 21, 541–554. doi: 10.1093/molbev/msh047

Schlosser, C., Streu, P., Frank, M., Lavik, G., Croot, P. L., Dengler, M., et al. (2018). H2S Events in the Peruvian Oxygen Minimum Zone Facilitate Enhanced Dissolved Fe Concentrations. *Sci. Rep.* 8, 12642. doi: 10.1038/s41598-018-30580-w

Schmidtko, S., Stramma, L., and Visbeck, M. (2017). Decline in Global Oceanic Oxygen Content During the Past Five Decades. *Nature* 542, 335–339. doi: 10.1038/nature21399

Scholz, F., Hensen, C., Noffke, A., Rohde, A., Liebetrau, V., and Wallmann, K. (2011). Early Diagenesis of Redox-Sensitive Trace Metals in the Peru Upwelling Area – Response to ENSO-Related Oxygen Fluctuations in the Water Column. *Geochim. Cosmochim. Acta* 75, 7257–7276. doi: 10.1016/j.gca.2011.08.007

Schunck, H., Lavik, G., Desai, D. K., Großkopf, T., Kalvelage, T., Löscher, C. R., et al. (2013). Giant Hydrogen Sulfide Plume in the Oxygen Minimum Zone Off Peru Supports Chemolithoautotrophy. *PloS One* 8, e68661. doi: 10.1371/journal.pone.0068661

Stramma, L., Johnson, G. C., Sprintall, J., and Mohrholz, V. (2008). Expanding Oxygen-Minimum Zones in the Tropical Oceans. *Science* 320, 655–658. doi: 10.1126/science.1153847

Stramma, L., Schmidtko, S., Levin, L. A., and Johnson, G. C. (2010). Ocean Oxygen Minima Expansions and Their Biological Impacts. *Deep. Res. Part I-Oceanogr. Res. Pap.* 57, 587–595. doi: 10.1016/j.dsr.2010.01.005

Torres-Beltrán, M., Hawley, A. K., Capelle, D., Zaikova, E., Walsh, D. A., Mueller, A., et al. (2017). A Compendium of Geochemical Information From the Saanich Inlet Water Column. *Sci. Data* 4, 1–11. doi: 10.1038/sdata.2017.159

Turk-Kubo, K. A., Karamchandani, M., Capone, D. G., and Zehr, J. P. (2014). The Paradox of Marine Heterotrophic Nitrogen Fixation: Abundances of Heterotrophic Diazotrophs do Not Account for Nitrogen Fixation Rates in the Eastern Tropical South Pacific. *Environ. Microbiol.* 16, 3095–3114. doi: 10.1111/1462-2920.12346

Wanty, R. B., and Goldhaber, M. B. (1992). Thermodynamics and Kinetics of Reactions Involving Vanadium in Natural Systems: Accumulation of Vanadium in Sedimentary Rocks. *Geochim. Cosmochim. Acta* 56, 1471–1483. doi: 10.1016/0016-7037(92)90217-7

Yun, A. C., and Szalay, A. A. (1984). Structural Genes of Dinitrogenase and Dinitrogenase Reductase are Transcribed From Two Separate Promoters in the

Broad Host Range Cowpea Rhizobium Strain Irc78. *Proc. Natl. Acad. Sci. U. S. A.* 81, 7358–7362. doi: 10.1073/pnas.81.23.7358

Zani, S., Mellon, M. T., Collier, J. L., and Zehr, J. P. (2000). Expression of nifH Genes in Natural Microbial Assemblages in Lake George, New York, Detected by Reverse Transcriptase PCR. *Appl. Environ. Microbiol.* 66, 3119–3124. doi: 10.1128/AEM.66.7.3119-3124.2000

Zehr, J. P., Mellon, M. T., and Zani, S. (1998). New Nitrogen-Fixing Microorganisms Detected in Oligotrophic Oceans by Amplification of Nitrogenase (Nifh) Genes. *Appl. Environ. Microbiol.* 64, 3444–3450. doi: 10.1128/AEM.64.9.3444-3450.1998

Zehr, J. P., and Turner, P. J. (2001). "Nitrogen Fixation: Nitrogenase Genes and Gene Expression," in *Methods in Microbiology*, vol. 30. (San Diego: Academic Press Inc), 271–286.

Zhang, X., McRose, D. L., Darnajoux, R., Bellenger, J. P., Morel, F. M. M., and Kraepiel, A. M. L. (2016). Alternative Nitrogenase Activity in the Environment and Nitrogen Cycle Implications. *Biogeochemistry* 127, 189–198. doi: 10.1007/s10533-016-0188-6

Conflict of Interest: The authors declare that the research was conducted in the absence of any commercial or financial relationships that could be construed as a potential conflict of interest.

Publisher's Note: All claims expressed in this article are solely those of the authors and do not necessarily represent those of their affiliated organizations, or those of the publisher, the editors and the reviewers. Any product that may be evaluated in this article, or claim that may be made by its manufacturer, is not guaranteed or endorsed by the publisher.

frontiers | Frontiers in Marine Science

TYPE Original Research
PUBLISHED 20 September 2022
DOI 10.3389/fmars.2022.993667

OPEN ACCESS

EDITED BY
Amal Jayakumar,
Princeton University, United States

REVIEWED BY
Clara A. Fuchsman,
University of Maryland, College Park, United States
Ram Murti Meena,
National Institute of Oceanography, India
J. Michael Beman,
University of California, Merced, United States

*CORRESPONDENCE
Carlos Henríquez-Castillo
carlos.henriquez@ceaza.cl

†These authors share first authorship

SPECIALTY SECTION
This article was submitted to Marine Biogeochemistry, a section of the journal Frontiers in Marine Science

RECEIVED 13 July 2022
ACCEPTED 30 August 2022
PUBLISHED 20 September 2022

CITATION
Henríquez-Castillo C, Plominsky AM, Ramírez-Flandes S, Bertagnolli AD, Stewart FJ and Ulloa O (2022) Metaomics unveils the contribution of *Alteromonas* bacteria to carbon cycling in marine oxygen minimum zones.
Front. Mar. Sci. 9:993667.
doi: 10.3389/fmars.2022.993667

Metaomics unveils the contribution of *Alteromonas* bacteria to carbon cycling in marine oxygen minimum zones

Carlos Henríquez-Castillo[1,2*†], Alvaro M. Plominsky[3†], Salvador Ramírez-Flandes[4,5], Anthony D. Bertagnolli[6,7], Frank J. Stewart[6,7] and Osvaldo Ulloa[4,5]

[1]Laboratorio de Fisiología y Genética Marina, Centro de Estudios Avanzados en Zonas Áridas, Coquimbo, Chile, [2]Facultad de Ciencias del Mar, Universidad Católica del Norte, Coquimbo, Chile, [3]Marine Biology Research Division, Scripps Institution of Oceanography, University of California, San Diego, La Jolla, CA, United States, [4]Instituto Milenio de Oceanografía, Universidad de Concepción, Concepción, Chile, [5]Departamento de Oceanografía, Universidad de Concepción, Concepción, Chile, [6]Department of Microbiology and Cell Biology, Montana State University, Bozeman, MT, United States, [7]School of Biological Sciences and Center for Microbial Dynamics and Infection, Georgia Institute of Technology, Atlanta, GA, Bozeman, United States

Gammaproteobacteria of the genus *Alteromonas* are prominent members of pelagic marine microbial communities, playing critical roles in the aerobic degradation of particulate organic matter. Comparative genomic studies of these microorganisms have mainly focused on the metabolic and genomic plasticity of strains isolated primarily from oxygenated environments. In this study, we show that *Alteromonas* significantly contribute to marine microbial communities from suboxic waters ($[O_2] < 5$ uM) in both the free-living (FL) and particle-attached (PA) fractions, but considerably decrease in abundance in the anoxic waters. The highest proportion of *Alteromonas* transcripts was found within the secondary fluorescence maximum (SFM) of Oxygen Minimum Zones (OMZs). This metatranscriptomic information suggests an *in situ* coupling of *Alteromonas* iron (Fe) and carbon metabolisms, and a relevant role of the glyoxylate cycle across the different layers of the OMZs. This study demonstrates that *Alteromonas* is an abundant and active member of the OMZ microbial communities, with a potentially significant impact on the carbon cycling in these ecosystems. These results provide valuable environmental evidence to support previous culture-based studies assessing the physiology and ecology of these ubiquitous marine heterotrophs under low-oxygen conditions.

KEYWORDS

Oxygen Minimum Zones, environmental genomics, biogeochemical cycles, single-cell genomics, *Alteromonas*

Introduction

Bacteria of the gammaproteobacterial genus *Alteromonas* are ecologically relevant copiotrophs that inhabit almost every marine environment, from surface waters to bathypelagic depths (Mikhailov et al., 2006; Nayfach et al., 2016). Members of this genus are considered r-strategists that can proliferate when organic nutrients are available (Math et al., 2012) and are typically associated with particles or aggregates (López-Pérez and Rodríguez-Varela, 2016). A study from Lekunberri et al. (2013) found that the relative abundance of *Alteromonas* increased with depth in the tropical Atlantic. Also, Schattenhofer et al. (2009) showed that *Alteromonas* was more abundant in the euphotic layer than in mesopelagic waters in a latitudinal Atlantic transect. Similar results were reported by Dobal-Amador et al. (2016) off the Galician coast of Spain. In terms of activity, *Alteromonas* has repeatedly accounted for most of the increase in cell abundance and activity in a variety of microcosms (Jin et al., 2016; Aguayo et al., 2020).

Alteromonas ecotypes can occupy diverse niches, with such plasticity linked to the presence of genes associated with genomic islands or mobile elements (López-Pérez and Rodriguez-Valera, 2016; López-Pérez et al., 2017; Koch et al., 2020). Surface ecotypes are enriched in genes involved in degrading simple carbohydrates, amino acids, and regulatory elements (e.g., two-component systems). Contrastingly, deep ecotypes seem specialized to microaerophilic conditions and the degradation of complex organic matter while attached to sinking particles (Ivars-Martinez et al., 2008a). Regarding metabolic activity, coastal and oceanic *Alteromonas* have shown strain-specific responses to Fe-limitation according to their different strategies for carbon metabolism and energy acquisition (Fourquez et al., 2014).

Eastern boundary oceanic ecosystems are among the most productive on Earth. In these regions, reduced circulation and high productivity at the surface contribute to enhanced oxygen consumption and the formation of oxygen minimum zones (OMZs) at intermediate depths (Messié and Chavez, 2015). Within the OMZs from the Eastern Tropical North and South Pacific (ETNP and ETSP, respectively) and the Arabian Sea, dissolved oxygen concentrations often drop below the detection limit of the most sensitive modern sensors (< 1–10 nM) (Revsbech et al., 2009). Thus, these areas have also been called 'Anoxic Marine Zones' (AMZs; Ulloa et al., 2012) and can be distinguished by a peak in the accumulation of nitrite, which typically occurs within their anoxic core when O_2 falls below the nanomolar detection limit (Thamdrup et al., 2012). These systems are characterized by a remarked redox gradients that profoundly impacts the composition and activities of microbial communities at the base of marine food webs (Medina et al., 2017). Notably, AMZs may have a secondary fluorescence maximum (SFM) within the lower euphotic depths that overlap with the anoxic layer (Tiano et al., 2014; Banse et al., 2017; Garcia-Robledo et al., 2017). Studies in the ETNP suggest two important aspects regarding the presence of the anoxic SFM: the covariation of oxygen in its spatial distribution, and the association between the SFM and the 26.0 kg m^{-3} isopycnal (Cepeda-Morales et al., 2009; Márquez-Artavia et al., 2019). This phenomenon is also linked to the presence of unique ecotypes of the cyanobacterium *Prochlorococcus* (Lavin et al., 2010; Ulloa et al., 2021), whose oxygenic photosynthesis drives a cryptic oxygen cycle in these anoxic waters, and provides organic matter to the microbial community (Garcia-Robledo et al., 2017, Fuchsman et al., 2019).

However, the biogeography, genomic potential, and environmental impact of *Alteromonas* in these marine regions has been briefly documented regarding their representatives inhabiting the oxic layers of the OMZs (Ivars-Martinez 2008a, Ivars-Martinez 2008b, López-Pérez et al., 2017; Koch et al., 2020). Moreover, there is an overall lack of information regarding the abundance, metabolic potential, and *in situ* transcriptional activity of *Alteromonas* representatives across the redox gradients of low-oxygen environments, such as OMZs. This study addressed these aspects of the *Alteromonas* populations inhabiting the Pacific Ocean AMZs by using various 16S rRNA gene amplicon-based ecological analysis, as well as metabolic assessments based on single-cell genome and metatranscriptomic sequencing. Through these multi-omic approaches we demonstrate that *Alteromonas* spp. are an abundant, and active group of the AMZ microbial communities, especially within the SFM, with potentially major impacts on carbon cycling in these ecosystems.

Material and methods

16S rRNA gene amplicon processing

Samples from the ETSP-AMZ were collected during the LowPhOx I and II cruises (November 2015 and February 2018, respectively). Additional samples corresponding to the SFM of both the ETNP and ETSP AMZs were collected during four cruises: NH1410 (May 2014) and RB1603 (April 2016) for the ETNP, and NBP1305 (June 2013) and AT2626 (January 2015) for the ETSP (Padilla et al., 2016; Padilla et al., 2017; Aldunate et al., 2020). Samples were collected based on the fluorescence and oxygen profiles of each station, sampling water from the surface, oxycline, the SFM, and the core of the anoxic layer. The collection of water samples was performed using a pump profiler system, an instrument that pumps water directly from the desired depth while profiling the water column with an attached conductivity-temperature-depth (CTD) system (Seabird SBE-19 plus for ETNP and Seabird SBE-25 for ETSP). For the LowpHOx II cruise, seawater samples were collected using 10L Niskin bottles. Seawater was sequentially

filtered through 20 µm, 3 µm, and 0.2 µm pore size diameter filters (Millipore, Darmstadt, Germany). Total DNA was extracted from the 0.2 - 3 µm (Free-Living) and 3 - 20 µm (Particle-Attached) fractions with the Phenol: Chloroform protocol described by Sambrook and Russell, 2006. Additional metabarcoding samples from the ETNP-AMZ and from Golfo Dulce (GD), an anoxic tropical basin with a O_2/H_2S interphase, were obtained from the NCBI SRA repository. These samples corresponded to two size fractions, from 0.22 to 1.6 µm (here also considered as Free-Living) and from 1.6 to 30 µm (here also considered as Particle-Attached) for samples from the ETNP (Ganesh et al., 2015), and only for 0.22-1.6 for GD samples (Padilla et al., 2016). Accession numbers are in Table S1. All samples analyzed here were sequenced using the modified universal F515 (5'-GTGYCAGCMGCCGCGGTAA-3', Parada et al., 2016) and 806R (5'-GGACTACNVGGGTWTCTAAT-3', Apprill et al., 2015) primer pairs (Walters et al., 2016), which amplify the hyper-variable V4 region of the 16S rRNA gene, and the Illumina MiSeq platform. All amplicon sequence data were analyzed together using the DADA2 package (v1.11.3) (Callahan et al., 2016) implemented in R (v3.4.4). The primers were removed using cutadapt (v1.2.1) (Martin, 2011), and the sequences from each pair were trimmed to 210 and 190 bases respectively and quality filtered (truncLen=c(210, 190), maxEE=1, maxN=0, truncQ=11, rm.phix=TRUE). Amplicon Sequence Variants (ASVs) were inferred from de-replicated sequences. Chimeras were removed using the "consensus" removal method. Taxonomic assignment was performed using the Silva v132 16S rRNA gene database (Quast et al., 2013). The relative abundance of ASVs in each sample and community analysis (Observed species, alpha-diversity indices) calculated from subsampled datasets were performed in the R environment with the phyloseq package (McMurdie and Holmes, 2013). Inference of microbial interaction networks was performed through statistical co-occurrence using FlashWeave with the sensitive option (Tackmann et al., 2019).

Clustering and correlations analysis

The ASVs count table was normalized using the variance stabilization transformation through the DESeq package (Bolaños et al., 2020). Hierarchical clustering was performed using the Euclidean distance of the normalized count table, and the WardD2 method was applied for the linkage. A principal component analysis was also performed using the normalized count table. Inference of microbial interaction networks was performed through statistical co-occurrence using FlashWeave (Tackmann et al., 2019) with the sensitive option. We used the function envfit to fit environmental variables onto ordination. All these analyses were performed in the R environment.

Single Amplified Genomes (SAGs)

Samples were collected on 19th November, 2010, during the BiGRAPA cruise from the Secondary Fluorescence Maximum (53 m depth) of the ETSP-AMZ off the coast of Iquique, Chile (Table S3). Single-cell sorting, whole-genome amplification, 16S rRNA real-time PCR screening, and PCR product sequencing were performed at the Bigelow Laboratory for Ocean Sciences, Single Cell Genomics Center (SCGC, www.bigelow.org/scgc), as described previously (Stepanauskas et al., 2017). This procedure identified 19 SAGs affiliated to *Alteromonas*, based on the 16S rRNA partial sequences obtained during the SAG screening (Plominsky et al., 2018). Single cells were sequenced utilizing the HiSeq 2000 platform (Canada's Michael Smith Genome Sciences Centre). Artifactual sequences were filtered from the raw data, and draft SAGs were assembled using SPAdes 3.5 with default parameters (Bankevich et al., 2013). SAG contigs >1Kbp in length were decontaminated using ProDeGe (Tennessen et al., 2016) and uploaded for gene prediction and annotation through the IMG/MER pipeline (Markowitz et al., 2009). SAG completeness and contamination were estimated by the presence of conserved single-copy genes using CheckM v1.0.7 (Parks et al., 2015). Average nucleotide identity (ANI) was computed using fastANI (Jain et al., 2018).

Pangenome analysis

Based on 16S rRNA and ANI comparisons, contigs from similar SAGs (>97% similarity) were analyzed as *Alteromonas* OMZ "populations". The operational definition of "population" is described in Delmont and Eren (2018), as an agglomerate of naturally occurring microbial cells, genomes of which are similar enough to align to the same genomic reference with high sequence identity as defined by the read recruitment stringency. Reference *Alteromonas* genomes (76) were downloaded from the IMG/MER platform and the NCBI SRA repository (accession numbers available in Table S3). Pangenome analysis was performed using the Anvi'o software v5 (Eren et al., 2015) by clustering based on the presence/absence of genes in each genome with the mcl algorithm (inflation = 8) through Euclidean distance and the wardD2 linkage method. Annotation of predicted genes was performed using DIAMOND (Buchfink et al., 2015) with the sensitive option to find homologs in different databases, including the Kyoto Encyclopedia of Genes and Genomes (KEGG) (Kanehisa and Goto, 2000), Pfam (Mistry et al., 2021), the Clusters of Orthologous Groups (COGs) (Tatusov et al., 2000). The distribution of genes, COG categories, KEGG Orthologs, and Pfam modules across genomes were analyzed in the R environment. A phylogenetic tree was generated using 137 single-copy genes obtained with the Anvi'o function anvi-get-sequences-for-hmm-hits with the -return-best-hit option. The

phylogenetic tree was inferred from the concatenated alignment of the single-copy genes using IQ-TREE (Nguyen et al., 2015).

Metatranscriptome read recruitments

Metatranscriptomes from OMZs were downloaded from the NCBI SRA (reported in Stewart et al., 2012; Padilla et al., 2016 and Garcia-Robledo et al., 2017; Table S6). Raw metatranscriptomic sequences were quality filtered using Trimmomatic (Bolger et al., 2014) and the protein-encoding genes were functionally predicted using the KEGG database. The *Alteromonas* genomes and SAGs were used to recruit reads from the metatranscriptomic dataset using DIAMOND, with a cutoff nucleotide identity of 97% over a minimum alignment length of 100 nucleotides and a bitscore >50. The relative recruitment over each *Alteromonas* genome was calculated based on the number of KOs detected in the metatranscriptome associated with the *Alteromonas* genomes and normalized to the total number of KO predicted in each Metatranscriptome multiplied by 100. Protein-coding gene abundances (those with a KO) were normalized by the fraction of KEGG assigned to *Alteromonas* from the total KEGG assigned in each metatranscriptome.

Results

Distribution of *Alteromonas* along the OMZ redox gradient and among biomass size fractions

The diversity of *Alteromonas* Amplicon Sequence Variants (ASVs) in the free-living (FL) and the particle-attached (PA) biomass fractions was assessed in geographically diverse locations across the ETNP and ETSP AMZs (Figure 1A). The sections sampled were classified according to their water chemistry (Oxygen and Nitrite concentrations) and collection depth as Surface (depths of 0 – 30 m); SFM (within the Secondary Fluorescence Maximum); Oxycline ($[O_2] > 5$ uM); Suboxic ($[O_2] < 5$ uM); Anoxic Core ($[O_2] < 5$ uM and > 1 μM Nitrite); and Mesopelagic (depths below 500 m; $[O_2] > 5$ uM) (Table S1).

A PCA based on all ASVs from all study sites revealed a clear partitioning of samples (Figure 1B) based on these chemical/depth classifications (PERMANOVA, Pr(>r) = 0.001). Here, all communities from low-oxygen waters ($[O_2] < 5$ μM) within the AMZs (i.e., "Suboxic", "SFM", and "Anoxic-Core") clustered together regardless of their geographic origin and were distinct from the low-oxygen communities from the sulfidic, coastal

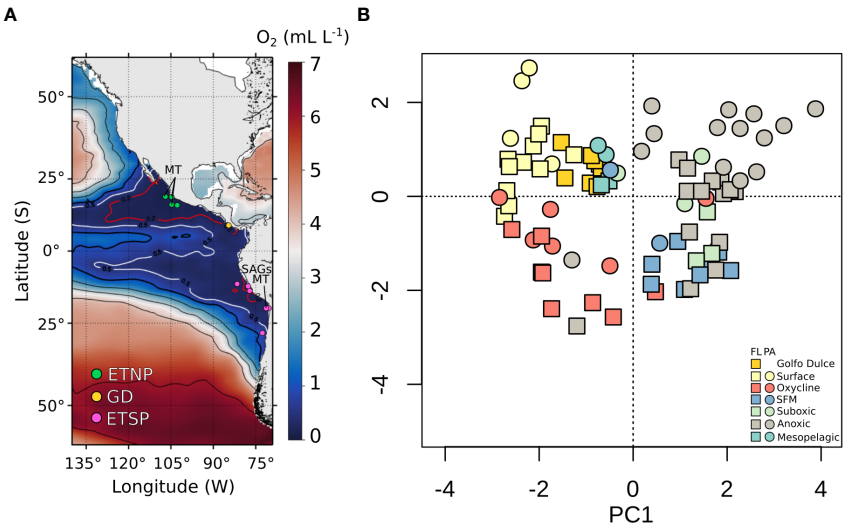

FIGURE 1
Geographic distribution of samples and prokaryotic community structure across OMZs of the Pacific Ocean. Geographic and depth distribution of samples across OMZs of the Pacific Ocean. **(A)** Map of the Eastern Pacific Ocean showing the stations utilized in this study (white filled circles). Colors and the contour lines correspond to the oxygen concentrations in mL L^{-1} at 325 meters depth (mean depth of the OMZ core, CARS 2009). **(B)** Principal component analysis of the bacterial community composition according to 16S rRNA gene metabarcoding data. The ASVs counts table was normalized using the variance-stabilizing transformation performed by DESeq. The two principal components were plotted. Samples were colored based on the water chemistry and collection depths. Surface: samples from depths of 0 -~30m; SFM Secondary Fluorescence Maximum; Oxycline: $[O_2] > 5$ uM); Suboxic: $[O_2] < 5$ uM); Anoxic: $[O_2] < 5$ uM, and > 4 μM of Nitrite. ETNP, Eastern Tropical North Pacific; GD, Golfo Dulce; ETSP, Eastern Tropical South Pacific; FL, Free-Living; PA, Particle-Attached.

OMZ of Golfo Dulce, Costa Rica (Hierarchical Cluster, Figure 2). Samples from the FL fraction corresponding to the SFM, Suboxic, and Anoxic Core formed distinct sub-clusters, whereas all PA communities sampled from low-oxygen waters ([O_2] < 5 μM) clustered together regardless of their nitrite levels or depth (Figure 2). The FL fraction from low-oxygen waters was dominated by bacteria classified as SAR406, SUP05, SAR324, and SAR11 clades I and II (Figure S1A). In contrast, the PA fraction was dominated by bacteria classified as *Alteromonas*, UBA10353 marine group, NS9 Marine group, SAR406, *Oleibacter*, and archaea of Marine group III Euryarchaeota (Figure S1B).

ASVs assigned to the *Alteromonas* genus reached up to ~22% of the prokaryotic community in the sites/depths studied here (Figure 2B). A single ASV (ASV 8) represented more than the 90% of the *Alteromonas*-related ASVs, while three other ASVs (ASV 79, 112, and 210) were consistently detected in these sampling locations but at lower proportions (Figure 2). *Alteromonas* ASVs were less abundant in the FL fraction than in the PA fraction at all depths, except at the SFM, where abundances in the FL and PA fractions were similar (Figure 2B). The overall higher abundance of *Alteromonas* within the PA fraction here was statistically significant ($p < 0.0001$, Mann-Whitney test Figure 2B, inset), with the highest abundances of *Alteromonas* detected in mesopelagic (3.2 - 21.87%) and suboxic (2.62 - 13.5%) waters (Figure 2B) in the PA fraction. Network analysis of samples from low-oxygen waters (n = 49) revealed that while the ASV_8 was widely distributed across the oxygen gradient and size fractions, the ASV 79 was exclusively represented in the PA fraction, and the ASV 112 was restricted to hypoxic but not anoxic waters. These two ASVs co-occurred with carbon degraders as *Oleibacter* and *Thalassolituus* and host-associated bacteria including Sva0996 marine group, Absconditabacteriales_(SR1), and Margulisbacteria among others (Table S2).

Genomic potential of *Alteromonas* Single-cell Amplified Genomes from the ETSP OMZ.

A total of 19 *Alteromonas* Single-cell Amplified Genomes (SAGs) were generated from samples collected at the ETSP SFM (20.0834° S 70.7997° W, at 53 m depth, and 3.6 μM O_2) (Table S3). These SAGs, with estimated completeness that ranged from 30% to 77%, corresponded to two well-defined populations based on their average nucleotide identity (ANI > 95%) (Figure S2). SAGs from AMZ population 1 (n=6) shared 100% 16S rRNA gene sequence identity with the dominant *Alteromonas* spp. ASV_8 and were phylogenetically related to

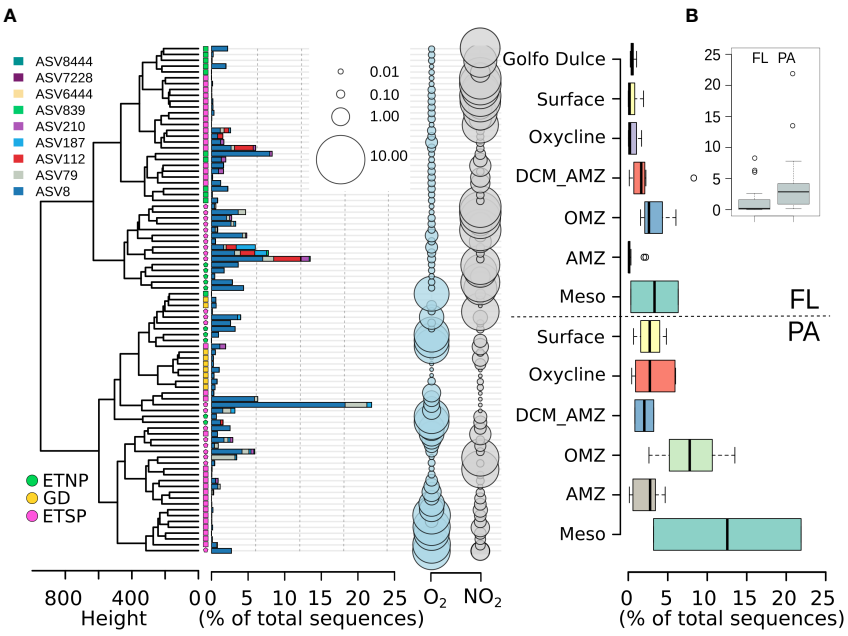

FIGURE 2
Alteromonas-related ASV abundances over the redox gradient of OMZ waters of the Pacific Ocean. **(A)** *Alteromonas* ASVs per sample as a percentage of the total reads in each sample. The color code corresponds to the different geographic locations. Samples from the free-living (FL) fraction are marked with squares. Particle-attached (PA) samples are marked with circles. Oxygen concentrations are presented in mL L^{-1}, and nitrite concentrations are presented in μM. **(B)** Barplot corresponds to the percentage of reads classified as *Alteromonas* relative to the total number of reads in each sample. ETNP, Eastern Tropical North Pacific; GD, Golfo Dulce; ETSP, Eastern Tropical South Pacific; O2, Oxygen; NO2, Nitrite; SFM, Secondary Fluorescence Maximum; Meso, Mesopelagic.

10.3389/fmars.2022.993667

the *A. macleodii* ecotype. In contrast, SAGs from AMZ population 2 (n=13) shared 100% 16S rRNA gene sequence identity with *Alteromonas* spp. ASV_79 were affiliated with the *A. naphtalenivorans* SN2 ecotype (Figure S3; Table S4).

Comparative genomics of representative *Alteromonas* spp. genomes (n=76) and the SAGs (two populations) revealed that the pangenome of this bacterial genus contained a core set of 3787 genes (Figure 3). This also confirmed that the SAGs from AMZ population 1 are related to the *A. macleodii* ecotype, with a similar gene composition to that of *Alteromonas* HOT1A3, EZ55, and MED G140, presenting only 34 predicted genes that were unique of this population. SAGs from AMZ population 2 were related to the SN2 ecotype and the *Alteromonas stellipolaris* strains PQQ42, PQQ44, LMG21856, among others, and had 224 predicted genes unique to this population. Functional analysis of the unique genes present in SAGs from AMZ population 1 revealed that those with an assigned KO function were a multidrug efflux pump and two-component systems, among others (Table S5). Instead, the unique genes with a predicted KO function from AMZ population 2 are involved in cell wall biosynthesis, processing and transport of peptides and aminoacids, and genes for stability and defense mechanisms that are also found in other organisms from the

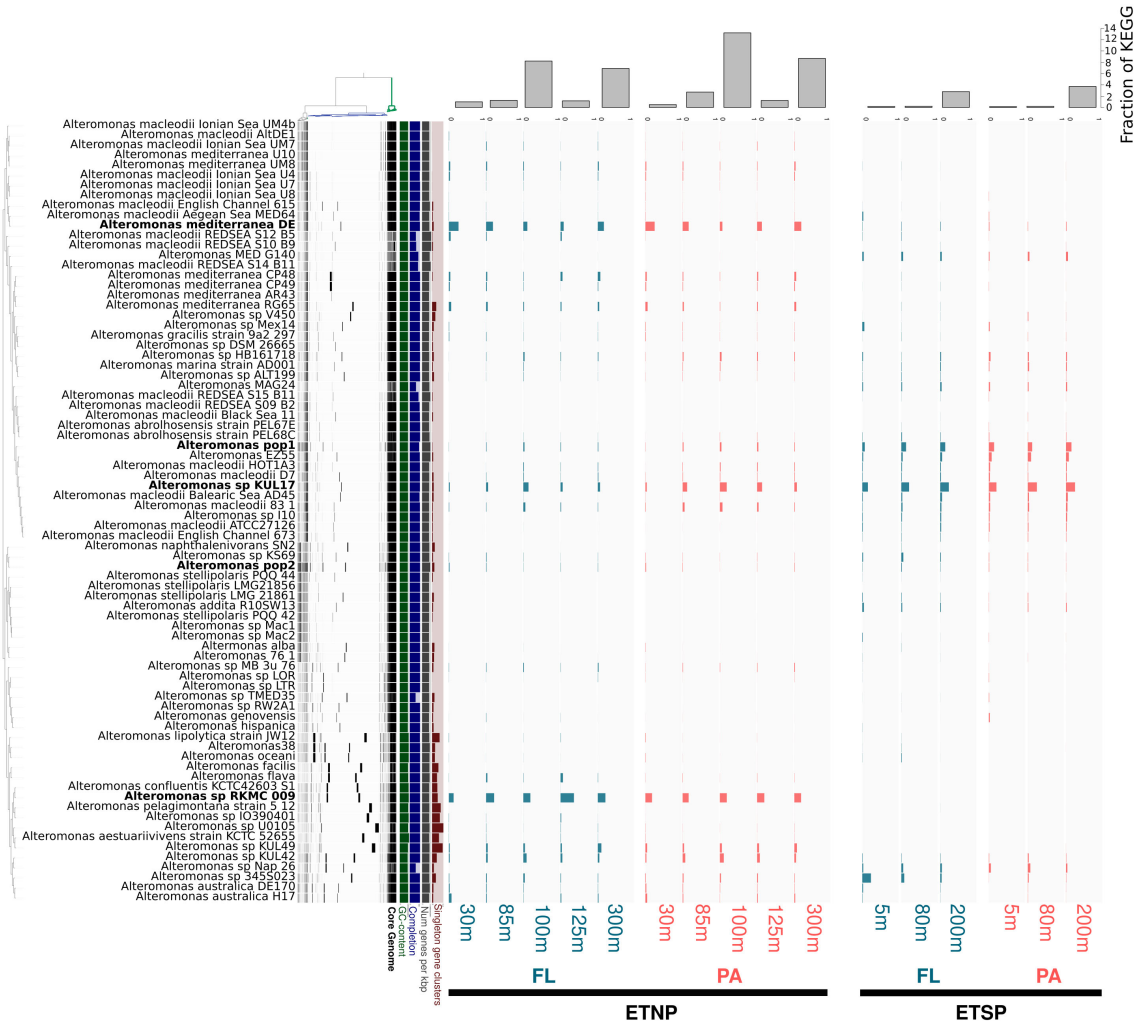

FIGURE 3
Pangenomic analysis of the *Alteromonas* genomes and percentage recruitment of OMZ metatranscriptome read fragments. Pangenomic analysis of the *Alteromonas* genomes and fragment recruitment of OMZ metatranscriptomes. A. The dendrogram at the left shows the clustering of 76 isolated genomes and the two SAGs populations based on the distribution of 7,385 genes (black bars) recovered from the pangenomic analysis (Euclidean distance and ward D2 clustering). The barplots corresponds to metatranscriptome reads recruited to each genome represented as a fraction of the total *Alteromonas* recruited reads in the metatranscriptome. ETNP, Eastern Tropical North Pacific; ETSP, Eastern Tropical South Pacific; FL, Free-Living; PA, Particle-Attached. The upper barplot corresponds to the relative recruit over all the *Alteromonas* genomes, calculated based on the number of KOs detected in the Metatranscriptome that are present in the *Alteromonas* genomes and normalized to the total number of KO predicted in each Metatranscriptome (fraction of KEGG).

order Altermonadales, such as *Colwellia sppp.*, and *Paraglaciecola* spp (Table S5).

Environmental transcriptomic activity of *Alteromonas* in OMZs

To further evaluate the *in situ* activity and the functional role of *Alteromonas* lineages across the OMZ redox gradient and between the FL and PA biomass fractions, we mapped AMZ metatranscriptomic reads against 76 reference *Alteromonas* genomes from public repositories in addition to the SAGs from the ETSP SFM. Overall, the proportion of *Alteromonas* transcripts was highest in ETNP compared to the ETSP (Table S6). The higher representation of *Alteromonas* was observed at 100 m depth of the ETNP (SFM) in the PA fraction where they accounted for 1.8% of the total reads and 13.23% of the reads assignable to KEGG functions.

A differential reprentation of *Alteromonas* ecotypes was detected among the different AMZ sites and depths (Figure 3; Table S6). Of all the genomes used as references, *Alteromonas* strain RKMC-009 recruited the most metatranscriptomic reads at the ETNP, especially between 85 m and 125 m depth in the FL fraction (constituting up to 37% of all the *Alteromonas*-recruited reads) (Figure 3), and a homogeneous representation in the PA fraction with an average recruitment of 18% of all the *Alteromonas*-recruited reads). Other genome that recruited a high percentage of transcripts in the ETNP corresponded to the *Alteromonas* strains DE, with a peak in abundance in the surface chlorophyll maxima (25% of the *Alteromonas*-recruited reads in both the FL and PA fraction), *Alteromonas* KUL17 dominated in terms of transcript abundances at the ETSP in both the FL and PA fraction (22% of the *Alteromonas*-recruited reads). *Alteromonas* SAGs from population 1 represented up to 15% of the *Alteromonas*-recruited reads in the ETSP, where *Alteromonas* sp. 345S023 was the genome that recruited the most transcripts from the surface waters at the ETSP (Figure 3).

Regarding their functional representation, the most abundant and prevalent *Alteromonas* transcripts in the ETNP and ETSP AMZs encoded the glucose-1-phosphate thymidylyltransferase (*rfb*A, *rff*H; K00973) and a pre-protein translocase, respectively. The iron complex outer membrane receptor protein (TC.FEV.OM; K02014) was also highly represented in both AMZs (Table S7). No differences in functional representation were detected in *Alteromonas* representatives between FL and PA metatranscriptomes (Table S7). The most abundant functional transcripts encoded iron complex outer membrane receptor protein, a solute:Na^+

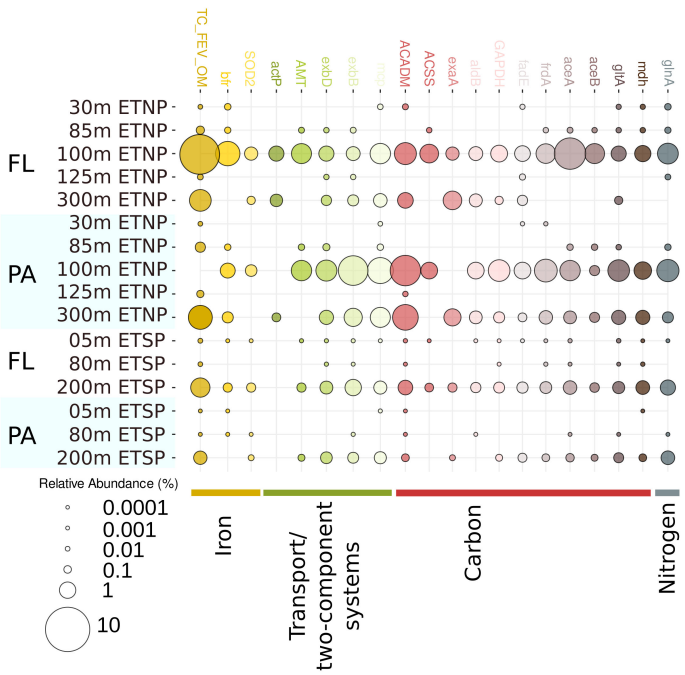

FIGURE 4
Percentage recruitment of ETNP and ETSP OMZs metatranscriptome read fragments to key *Alteromonas* functional genes. *Alteromonas* genomes and SAGs populations were used to recruit reads from the metatranscriptomic data from both the ETNP and ETSP using a cutoff of 97% nucleotide identity over a minimum alignment length of 100 nucleotides. the top 20 KEGG orthologs (KOs) were selected. FL, Free-living; PA, Particle-attached. Values for each KO were normalized by the fraction of KEGG assigned to *Alteromonas* from the total KEGG assigned in each metatranscriptome.

symporter, a biopolymer transport protein ExbB threonine synthase, and the glutamine Synthetase. Iron metabolism-related transcripts encoding the Fe-II oxidizing enzyme bacterioferritin (K03594) and a superoxide dismutase from the Fe-Mn family (K04564) and to a lesser extent, the periplasmic protein TonB (K03832) were also detected, coinciding with the high level of transcripts for the iron complex outer membrane receptor protein (Figure 4; Table S7).

In addition to glucose-1-phosphate thymidylyltransferase, the most abundant *Alteromonas* transcripts related to carbon metabolism encoded isocitrate lyase (K01637), malate synthase (K01638), aconitate hydratase 2 (K01682), and succinate dehydrogenase/fumarate reductase (K00239) (Table S7). Levels of these transcripts were the highest within the AMZ SFM (Figure 4) from the ETNP.

Other enzymes related to aminoacid metabolism and catabolism, including glutamine synthetase (K01915), ketol-acid reductoisomerase (K00053), and acyl-CoA dehydrogenase (K06445), were also highly transcribed in the SFM in the ETNP. The most abundant nitrogen metabolism-related transcript encoded an ammonium transporter (amt, K03320). Transcripts encoding type I and type III cytochrome c oxidases peaked in abundance in the SFM and at the anoxic core in the coastal station (Table S7). Accordingly, transcripts for a major ammonium assimilation pathway for (the glutamine synthetase/glutamate synthase [GS/GOGAT] pathway) were also highly abundant at the ETNP (Figure 4, Table S7).

Finally, transcripts encoding alcohol dehydrogenase (K00114), a cold-shock protein (K03704) and a methyl-accepting chemotaxis protein (K03406) were also abundant at anoxic depths (Figure 4).

Discussion

Alteromonas bacteria constitute a relevant fraction of microbial communities inhabiting the Pacific Ocean AMZ

Although *Alteromonas* is one of the most prevalent bacterial taxa in the oceans (Nayfach et al., 2016), there is still a lack of knowledge regarding the distribution, diversity, and ecology of these bacteria in oxygen-deficient marine environments. A high representation of *Alteromonas* have been reported in the Sansha Yongle Blue Hole, an O_2 - deficient environment in the South China (He et al., 2020), and in the Arabian Sea OMZ (Bandekar et al., 2018). This study reports a field-based analysis of the diversity and distribution of *Alteromonas* lineages across various redox gradients and depths in the Pacific Ocean AMZs. Based on 16S rRNA gene amplicon data from both free-living (FL) and particle-attached (PA) biomass fractions, we show that *Alteromonas* is a quantitatively relevant member of the microbial community across all the AMZ waters of the eastern boundary of the Pacific Ocean, especially within the PA fraction where it can reach more than 20% of total prokaryotic 16S rRNA gene sequences (Figure 2).

A single ASV, related to *Alteromonas* AMZ population 1 SAGs and the *A. macleodii* ecotype, dominated in all the oxygen-deficient marine environments included in this study (Figure 1A). The abundance of *Alteromonas* in the FL fraction of the SFM and suboxic waters was significantly higher than in the anoxic core of the AMZ (Figure 2B). The absence of detectable concentrations of nitrite in both the SFM and Suboxic samples suggests the presence of low, though undetectable, amounts of oxygen. A cryptic oxygen cycle linked to oxygenic cyanobacterial lineages has been demonstrated to occur within SFM depths of the Eastern Pacific AMZs (Lavin et al., 2012; Garcia-Robledo et al., 2017). Accordingly, the abundance of genes and transcripts of aerobic respiration and nitrification spike in the *Prochlorococcus*-enriched AMZ-SFM (Bertagnolli and Stewart, 2018). Cryptic oxygen supply by the AMZ *Prochlorococcus* lineages, can potentially allow *Alteromonas* and other heterotrophs to degrade complex carbohydrates fueled by aerobic respiration and/or supplemented by facultative anaerobic respiration of nitrate, nitrite, or sulfur compounds in these scarcely oxygenated waters.

The *Alteromonas* populations support their higher abundance in the Particle-Attached fraction

The genomic versatility among and within *Alteromonas* ecotypes presumably contributes to the success of these bacteria under diverse environmental conditions (Math et al., 2012; López-Pérez and Rodriguez-Valera, 2016; Koch et al., 2020). Most *Alteromonas* ecotypes, including those explored in our study, contain genes supporting aerobic respiration and the degradation of organic matter under low-oxygen conditions (Figure S4). These genes are assembled in a cluster flanked by a universal stress protein-coding gene and encode an anaerobic transcriptional regulator, the *cbb3-type* cytochrome c oxidase, a bacterioferritin a P-type Cu^{+2} transporting ATPase, and glutamate synthase (NADPH) large chain subunit (Figure S4). Most of these genes are transcribed in the oxygen-deficient-waters studied here (Table S7; Figure 4). The decrease in the representation of *Alteromonas* ASVs in the anoxic core, especially in the FL fraction, coincides with the drop of the oxygen concentrations below the detection limit of current sensors (<10 nM oxygen) and where anaerobic processes largely replace oxygenic respiration, as shown by the accumulation of nitrite (Figure 2).

The relatively high proportional abundance of *Alteromonas* in the PA fraction at the anoxic core is more challenging to

explain. This taxonomic signal may be somewhat refractory, representing organisms that were active on particles at oxic depths but are relatively inactive when those particles sink into the anoxic core of the AMZ. Alternatively, since the *Alteromonas* transcripts from low-oxygen waters PA fractions (Figure 4 and Table S6) included a high-affinity terminal oxidases and a nitrite reductases, among other transcribed genes, these populations may be utilizing the undetectable traces of oxygen or conducting anaerobic metabolism. Finally, the higher abundances of Alteromonas in both the FL and PA fraction in the mesopelagic waters below the AMZ indicate an abundance of usable organic matter at these depths. Previously sediment trap data indicated reduced degradation of sinking particles in AMZs (Keil et al., 2016; Cram et al., 2022), which would allow these particles to be a source of energy for aerobic heterotrophs such as Alteromonas in these deeper waters.

Our results show that in these low oxygen waters, *Alteromonas* ecotypes have higher abundances in association with particles or cell-cell aggregates. Indeed, a high abundance of traditionally biofilm-associated marine bacteria (i.e., *Oleibacter Marinus* and *Marinobacter hydrocarbonoclasticus*) was found in the OMZ PA fraction (Table S2). Such microorganisms specialize in degrading hydrophobic organic compounds that can represent a significant fraction of organic matter in marine waters (Mounier et al., 2014). It remains unclear if AMZ *Alteromonas* are filling a similar metabolic niche on particles or are potentially interacting with these or other PA-associated taxa. In surface waters a single *Alteromonas* strain is able to consume as much DOC as diverse free-living microbial communities (Pedler et al., 2014). Here, the enrichment of *Alteromonas* in the SFM is consistent with a potential association between *Alteromonas* and picocyanobacteria (Aharonovich and Sher, 2016; Hennon et al., 2018). In such associations, *Alteromonas* has been shown to alleviate oxidative stress and nutrient limitation during extended periods of darkness (Coe et al., 2016; Biller et al., 2018). For example, *Alteromonas* may secrete asparagine and glutamine, which has been shown to coincide with the up-regulation of related importers by the co-cultured *Prochlorococcus* (Koch et al., 2020).

Alteromonas bacteria are transcriptionally active members of the AMZ microbial communities

A differential representation of *Alteromonas* species was observed between the ETSP and ETNP AMZ transcripts. Although both AMZs often present similar oxygen and nitrate profiles through depth (Tiano et al., 2014), the differences in nitrite and ammonium between the two AMZs at the sampling time could have an influence over the representation of the different ecotypes, and the abundance of the gene transcripts (Table S7). AMZ *Alteromonas* transcripts were dominated by sequences most closely related to those of *Alteromonas* strain RKMC-009, isolated from the sponge *Xestospongia muta* (MacIntyre et al., 2019) and of the *Alteromonas* DE, with a differential representation between the ETSP and the ETNP (Figure 3). Interestingly, the unique KOs and COGs assigned to strains RKMC-009 and DE were only sparsely represented in the metatranscriptomic dataset analyzed. A similar trend was observed for all the prevalent *Alteromonas* genotypes, suggesting a disconnect between their representation and their unique genomic functions (Tables S5, S6). The genome of RKMC-009 contains the highest amount of carbohydrate-active enzymes among the *Alteromonas* genomes analyzed here (CAZymes, n = 142, with 31 unique genes related to carbohydrate transport and metabolism), in addition to unique genes associated with inorganic ion transport and metabolism. This genomic characteristic suggests that the ability of RKMC-009 to degrade diverse polysaccharides may extend to its AMZ *Alteromonas* relatives and underlie their success in these environments. The *Alteromonas* DE ecotype, described initially from deep-sea sites in the Mediterranean (Ivars-Martinez et al., 2008a) was transcriptionally active in all the samples analyzed. This "deep" strain is adapted to live on large particles that sink to meso- and bathy-pelagic depths. However, *Alteromonas* DE relatives are also present in surface habitats (Lopez-Pérez et al., 2012), as also demonstrated here, and are not an obligate bathytype (Ivars-Martinez, et al., 2008). The SAGs from AMZ population 1 recruited their highest proportion of reads from the ETSP AMZ transcriptomes. These SAGs are closely related to *Alteromonas KUL17*, which is one of the most represented genomes in the transcriptomes. This bacterium was isolated from a mollusk and can utilize diverse carbon sources for growth, including ulvan and L-rhamnose (He et al., 2017). The SAGs from AMZ population 2 were phylogenetically related to both *Alteromonas SN2* (isolated from a crude oil-contaminated marine tidal flat; Jin et al., 2012) and *Alteromonas 76-1* (isolated from an alginate-supplemented microcosm at the Patagonian continental shelf; Koch et al., 2019) and had low transcriptional representation in the samples studied here (Figure 3). The low recruitment by AMZ *Alteromonas* SAGs, particularly from the population 2 might be explained by the low overall representation of *Alteromonas* in metatranscriptomic samples from the ETSP, were the SAGs were collected, but also by the lack of metatranscriptomic samples from the SFM in this area. This remains to be explored in future research.

Metabolic contributions of *Alteromonas* bacteria to the AMZ microbial communities

Regarding carbon metabolism, two key glyoxylate shunt genes were found at high proportional abundance in the *Alteromonas*-associated transcript pool, particularly in the SFM (Figure 4). These encode the enzymes isocitrate lyase (which utilizes isocitrate from the Citric Acid Cycle and catalyzes its transformation into succinate

and glyoxylate) and malate synthase (which catalyzes the formation of malate from glyoxylate and Acetyl-CoA). Along with citrate synthase, aconitase, and phosphoenolpyruvate carboxykinase, these enzymes compose the glyoxylate shunt. This pathway is likely a relevant carbon acquisition pathway for marine heterotrophic bacteria including other prevalent marine bacteria, including *Photobacterium* spp. and Alphaproteobacterial of the SAR11 group (Beier et al., 2015; Koedooder et al., 2018).

With respect to the nitrogen metabolism, the high abundance of genes for the GS/GOGAT pathway in the ETNP (Figure 4, Table S7) is similar to results described by Jin et al. (2016) when exposing the *Alteromonas* SN2 marine ecotype to different environmental conditions. Accordingly, the aforementioned study reported a higher transcription of genes related to glyoxylate metabolism and glutamate synthesis (glutamate dehydrogenase) in a tidal flat habitat that experiences low-oxygen conditions.

Interestingly, a high proportion of transcripts were found to encode for an extracellular iron-complex binding protein, bacterioferritin, a superoxide dismutase from the Fe-Mn family (Figure 4), and, to a lesser extent, TonB-dependent transporters. This could be due to their high representation in the *Alteromonas* RKMC-009 genome but also with the over-expression observed in cultures of *Alteromonas macleodii* (Fourquez et al., 2014), Candidatus *Pelagibacter ubique* (SAR11 clade), and *Photobacterium angustum* under iron-limitation (Fourquez et al., 2014; Koedooder et al., 2018; Manck et al., 2020). Iron-related TonB-dependent transporters and extracellular iron-complex binding proteins are responsible for iron and carbon acquisition, while ferritin can be used to store iron (Andrews et al., 2003; Manck et al., 2020).

Iron is tightly linked to carbon metabolism due to its central role as a cofactor in the citric acid cycle and respiratory chain enzymes. Dissolved iron concentrations in the ocean are generally low (Moore and Braucher, 2007) and can significantly vary across OMZs (Kondo and Moffett, 2015; Vedamati et al., 2014). In low-oxygen water columns, dissolved iron concentration depends on diverse factors, potentially including conditions in the underlying sediment and in some cases connectivity with the continental shelf (Schlosser et al., 2018; Croot et al., 2019). At both the ETSP and ETNP OMZs analyzed here, total dissolved Fe and labile inorganic Fe complexes concentrations increase with depth at all stations, coincident with an increase in genes encoding Fe-proteins involved in dissimilatory nitrogen metabolisms (Glass et al., 2015). Over the ETSP continental shelf, dissolved iron concentrations increase markedly at ~100 m depth, and are almost entirely composed of reduced Fe(II) species (Heller et al., 2017). A minimum in dissolved iron concentration (dFe) that overlaps with the deep chlorophyll maximum (DCM) have been reported throughout the open ocean, which marks the lower limit of the euphotic zone (Hawco et al., 2021). However, measurements of iron concentration and speciation in the SFM from anoxic waters remain relatively sparse. Additional studies of iron and other trace metal concentrations in SFM from AMZs are needed given their potential relevance in the C-metabolism of highly abundant heterotrophs, such as *Alteromonas*. The seemingly coupled transcription of *Alteromonas* carbon and iron metabolism genes in our data supports the aforementioned culture-based physiological and genomic studies linking iron-depletion stress under anaerobic conditions and the carbon metabolism of these ubiquitous marine heterotrophs. Since heterotrophic bacteria play a significant role in the incorporation of new iron into the marine environment (Manck et al., 2022), our results raise the hypothesis that natural *Alteromonas* populations may overcome iron fluctuations in coastal low-oxygen environments (such as AMZs) by the uptake of larger organically complex iron substrates.

Conclusions

Our results reveal a significant representation of *Alteromonas* in the SFM of marine low-oxygen environments in both the free-living and particle-associated microbial communities. These *Alteromonas* populations co-occur with other critical microbial players in the carbon cycle, including complex-carbon degraders (i.e., *Marinobacter*) and primary producers (i.e., *Prochlorococcus*). In contrast to our current knowledge of the nitrogen, sulfur, and oxygen cycles in OMZs (Ganesh et al., 2014; Ganesh et al., 2015; Glass et al., 2015; Garcia-Robledo et al., 2016; Garcia-Robledo et al., 2017; Fuchsman et al., 2017; Saunders et al., 2019; Raven et al., 2021), the carbon cycle has been poorly characterized in these low-oxygen environments. Recently couplings between carbon, sulfur, and nitrogen metabolisms have been proposed (Plominsky et al., 2018), along with the partitioning of different carbon fixation pathways along the AMZ redox gradient (Ruiz-Fernández et al., 2020). Considering all the caveats regarding metatranscriptomic fragment recruitment, the data presented here suggests an *in situ* coupling of *Alteromonas* iron and carbon metabolisms and the potential importance of its glyoxylate cycle in the AMZs. Also, the peak transcription of iron complex outer membrane receptors, SOD2 and glutamine synthase at the SFM suggest a possible interplay between AMZ *Alteromonas* and co-occurring *Prochloroccocus* populations in subsurface waters, similar to the described for surface ecotypes when co-cultured. Our results indicate that *Alteromonas* may contribute significantly to the carbon metabolism in AMZs, particularly in the SFM in coastal areas, where similar functional features were transcribed in both the FL and the PA size fractions. These findings set the foundation for further studies assessing the *Alteromonas* ecotypes from other OMZ systems and their connections with the vertical gradients of carbon, nitrogen, oxygen, and trace metals.

Data availability statement

The datasets presented in this study can be found in online repositories. The names of the repository/repositories and accession number(s) can be found in the article/ Supplementary Material.

Author contributions

CH-C, OU, and SR-F conceived the research. CH-C, AMP, and SR-F perform the analysis. CH-C and AMP wrote the manuscript with contribution from all the authors. All authors approved the final submitted manuscript

Funding

This work was supported by the Chilean Agency for Research and Development (grant FONDECYT-POSTDOCTORADO 3180724 and ICN12_019-IMO).

Acknowledgments

The authors want to thank the crew of the R/V Cabo de Hornos from the Chilean Navy and to the IMO staff, particularly to Eduardo Navarro and Cristian Venegas for their support in the sampling during the lowphox I & II cruises. We also thank Montserrat Aldunate for their invaluable contribution, collecting the samples during the cruises: NH1410, RB1603, NBP1305 and AT2626 and to Matías Pizarro-Koch for his support with the oceanographic data.

Conflict of interest

The authors declare that the research was conducted in the absence of any commercial or financial relationships that could be construed as a potential conflict of interest.

Publisher's note

Supplementary material

The Supplementary Material for this article can be found online at: https://www.frontiersin.org/articles/10.3389/fmars.2022.993667/full#supplementary-material

References

Aguayo, P., Campos, V. L., Henríquez, C., Olivares, F., De Ia Iglesia, R., Ulloa, O., et al. (2020). The influence of pCO2-driven ocean acidification on open ocean bacterial communities during a short-term microcosm experiment in the Eastern tropical south pacific (ETSP) off northern Chile. *Microorganisms* 8 (12), 1924. doi: 10.3390/microorganisms8121924

Aharonovich, D., and Sher, D. (2016). Transcriptional response of *Prochlorococcus* to co-culture with a marine alteromonas: Differences between strains and the involvement of putative infochemicals. *ISME J.* 10 (12), 2892. doi: 10.1038/ismej.2016.70

Aldunate, M., Henríquez-Castillo, C., Ji, Q., Lueders-Dumont, J., Mulholland, M. R., Ward, B. B., et al. (2020). Nitrogen assimilation in picocyanobacteria inhabiting the oxygen-deficient waters of the eastern tropical north and south pacific. *Limnol. Oceanogr.* 65 (2), 437–453. doi: 10.1002/lno.11315

Andrews, S. C., Robinson, A. K., and Rodríguez-Quiñones, F. (2003). Bacterial iron homeostasis. *FEMS Microbiol. Rev.* 27 (2-3), 215–237. doi: 10.1016/S0168-6445(03)00055-X

Apprill, A., McNally, S., Parsons, R., and Weber, L. (2015). Minor revision to V4 region SSU rRNA 806R gene primer greatly increases detection of SAR11 bacterioplankton. *Aquat. Microb. Ecol.* 75 (2), 129–137. doi: 10.3354/ame01753

Bandekar, M., Ramaiah, N., Jain, A., and Meena, R. M. (2018). Seasonal and depth-wise variations in bacterial and archaeal groups in the Arabian Sea oxygen minimum zone. *Deep Sea Res. Part II Top. Stud. Oceanogr.* 156, 4–18. doi: 10.1016/j.dsr2.2017.12.015

Bankevich, A., Nurk, S., Antipov, D., Gurevich, A. A., Dvorkin, M., Kulikov, A. S., et al. (2012). SPAdes: A new genome assembly algorithm and its applications to single-cell sequencing. *J. Comput. Biol.* 19 (5), 455–477. doi: 10.1089/cmb.2012.0021

Banse, K., Naqvi, S. W. A., and Postel, J. R. (2017). A zona incognita surrounds the secondary nitrite maximum in open-ocean oxygen minimum zones. *Deep Sea Res. Part I Oceanogr. Res. Pap.* 127, 111–113.

Beier, S., Gálvez, M. J., Molina, V., Sarthou, G., Quéroué, F., Blain, S., et al. (2015). The transcriptional regulation of the glyoxylate cycle in SAR11 in response to iron fertilization in the southern ocean. *Environ. Microbiol. Rep.* 7, 427–434. doi: 10.1111/1758-2229.12267

Bertagnolli, A. D., and Stewart, F. J. (2018). Microbial niches in marine oxygen minimum zones. *Nat. Rev. Microbiol.* 16 (12), 723–729. doi: 10.1038/s41579-018-0087-z

Biller, S. J., Coe, A., Roggensack, S. E., and Chisholm, S. W. (2018). Heterotroph interactions alter *Prochlorococcus* transcriptome dynamics during extended periods of darkness. *Msystems* 3 (3). doi: 10.1128/mSystems.00040-18

Bolaños, L. M., Karp-Boss, L., Choi, C. J., Worden, A. Z., Graff, J. R., Haëntjens, N., et al. (2020). Small phytoplankton dominate western north Atlantic biomass. *ISME J.*, 1–12.

Bolger, A. M., Lohse, M., and Usadel, B. (2014). Trimmomatic: A flexible trimmer for illumina sequence data. *Bioinformatics* 30 (15), 2114–2120. doi: 10.1093/bioinformatics/btu170

Bruland, K. W., Rue, E. L., Smith, G. J., and DiTullio, G. R. (2005). Iron, macronutrients and diatom blooms in the Peru upwelling regime: Brown and blue waters of Peru. *Mar. Chem.* 93 (2-4), 81–103. doi: 10.1016/j.marchem.2004.06.011

Buchfink, B., Xie, C., and Huson, D. H. (2015). Fast and sensitive protein alignment using DIAMOND. *Nat. Methods* 12, 59–60. doi: 10.1038/nmeth.3176

Callahan, B. J., McMurdie, P. J., Rosen, M. J., Han, A. W., Johnson, A. J. A., and Holmes, S. P. (2016). DADA2: High-resolution sample inference from illumina amplicon data. *Nat. Methods* 13 (7), 581–583. doi: 10.1038/nmeth.3869

Cepeda-Morales, J., Beier, E., Gaxiola-Castro, G., Lavín, M. F., and Godínez, V.M (2009) Effect of the oxygen minimum zone on the second chlorophyll maximum. *Ciencias Marinas,* 35 (4), 389–403.

Coe, A., Ghizzoni, J., LeGault, K., Biller, S., Roggensack, S. E., and Chisholm, S. W. (2016). Survival of *Prochlorococcus* in extended darkness. *Limnol. Oceanogr.* 61 (4), 1375–1388. doi: 10.1002/lno.10302

Cram, J. A., Fuchsman, C. A., Duffy, M. E., Pretty, J. L., Lekanoff, R. M., Neibauer, J. A., et al. (2022). Slow particle remineralization, rather than suppressed disaggregation, drives efficient flux transfer through the Eastern tropical north pacific oxygen deficient zone. *Global Biogeochem. Cycles* 36, e2021GB007080. doi: 10.1029/2021GB007080

Croot, P. L., Heller, M. I., and Wuttig, K. (2019). Redox processes impacting the flux of iron (II) from shelf sediments to the OMZ along the Peruvian shelf. *ACS Earth Space Chem.* 3 (4), 537–549. doi: 10.1021/acsearthspacechem.8b00203

Delmont, T. O., and Eren, A. M. (2018). Linking pangenomes and metagenomes: the prochlorococcus metapangenome. *PeerJ* 6, e4320. doi: 10.7717/peerj.4320

Dobal-Amador, V., Nieto-Cid, M., Guerrero-Feijoo, E., Hernando-Morales, V., Teira, E., and Varela, M. M. (2016). Vertical stratification of bacterial communities driven by multiple environmental factors in the waters (0–5000 m) off the Galician coast (NW Iberian margin). *Deep-Sea Res. Pt I* 114, 1–11. doi: 10.1016/j.dsr.2016.04.009

Eren, A. M., Esen, Ö.C., Quince, C., Vineis, J. H., Morrison, H. G., Sogin, M. L., et al. (2015). Anvi'o: an advanced analysis and visualization platform for 'omics data. *PeerJ* 3, e1319. doi: 10.7717/peerj.1319

Fourquez, M., Devez, A., Schaumann, A., Guéneuguès, A., Jouenne, T., Obernosterer, I., et al. (2014). Effects of iron limitation on growth and carbon metabolism in oceanic and coastal heterotrophic bacteria. *Limnol. Oceanogr.* 59 (2), 349–360. doi: 10.4319/lo.2014.59.2.0349

Fuchsman, C. A., Devol, A. H., Saunders, J. K., McKay, C., and Rocap, G. (2017). Niche partitioning of the n cycling microbial community of an offshore oxygen deficient zone. *Front. Microbiol.* 8, 2384. doi: 10.3389/fmicb.2017.02384

Fuchsman, C. A., Palevsky, H. I., Widner, B., Duffy, M., Carlson, M. C., Neibauer, J. A, et al. (2019). Cyanobacteria and cyanophage contributions to carbon and nitrogen cycling in an oligotrophic oxygen-deficient zone. *ISME* 13 (11), 2714–2726

Ganesh, S., Bristow, L. A., Larsen, M., Sarode, N., Thamdrup, B., and Stewart, F. J. (2015). Size-fraction partitioning of community gene transcription and nitrogen metabolism in a marine oxygen minimum zone. *ISME J.* 9, 2682–2696. doi: 10.1038/ismej.2015.44

Ganesh, S., Parris, D. J., DeLong, E. F., and Stewart, F. J. (2014). Metagenomic analysis of size-fractionated picoplankton in a marine oxygen minimum zone. *ISME J.* 8, 187–211. doi: 10.1038/ismej.2013.144

Garcia-Robledo, E., Borisov, S., Klimant, I., and Revsbech, N. P. (2016). Determination of respiration rates in water with sub-micromolar oxygen concentrations. *Front. Mar. Sci.* 3, 1–13. doi: 10.3389/fmars.2016.00244

Garcia-Robledo, E., Padilla, C. C., Aldunate, M., Stewart, F. J., Ulloa, O., Paulmier, A., et al. (2017). Cryptic oxygen cycling in anoxic marine zones. *P Natl. Acad. Sci. U.S.A.* 114 (31), 8319–8324. doi: 10.1073/pnas.1619844114

Glass, J. B., Kretz, C. B., Ganesh, S., Ranjan, P., Seston, S. L., Buck, K. N., et al. (2015). Meta-omic signatures of microbial metal and nitrogen cycling in marine oxygen minimum zones. *Front. Microbiol.* 6, 998. doi: 10.3389/fmicb.2015.00998

Hawco, N. J., Fu, F., Yang, N., Hutchins, D. A., and John, S. G. (2021). Independent iron and light limitation in a low-light-adapted *Prochlorococcus* from the deep chlorophyll maximum. *ISME J.* 15 (1), 359–362. doi: 10.1038/s41396-020-00776-y

He, C., Muramatsu, H., Kato, S. I., and Ohnishi, K. (2017). Characterization of an *Alteromonas* long-type ulvan lyase involved in the degradation of ulvan extracted from ulva ohnoi. *Biosci. Biotech. Bioch.* 81 (11), 2145–2151. doi: 10.1080/09168451.2017.1379352

He, P., Xie, L., Zhang, X., Li, J., Lin, X., Pu, X, et al. (2020). Microbial diversity and metabolic potential in the stratified Sansha Yongle Blue Hole in the South China Sea. *Scientific rep* 10 (1), 1–17. doi: 10.1038/s41598-020-62411-2

Hennon, G. M., Morris, J. J., Haley, S. T., Zinser, E. R., Durrant, A. R., Entwistle, E., et al. (2018). The impact of elevated CO2 on *Prochlorococcus* and microbial interactions with 'helper' bacterium *Alteromonas*. *ISME J.* 12 (2), 520. doi: 10.1038/ismej.2017.189

Heller, M. I., Lam, P. J., Moffett, J. W., Till, C. P., Lee, J. M., Toner, B. M, et al. (2017). Accumulation of Fe oxyhydroxides in the Peruvian oxygen deficient zone implies non-oxygen dependent Fe oxidation. *Geochimica et Cosmochimica Acta* 211, 193. doi: 10.1016/j.gca.2017.05.019

Ivars-Martinez, E., D'auria, G., Rodriguez-Valera, F., Sánchez-Porro, C., Ventosa, A., Joint, I., et al. (2008b). Biogeography of the ubiquitous marine bacterium *Alteromonas macleodii* determined by multilocus sequence analysis. *Mol. Ecol.* 17 (18), 4092–4106. doi: 10.1111/j.1365-294X.2008.03883.x

Ivars-Martinez, E., Martin-Cuadrado, A. B., D'auria, G., Mira, A., Ferriera, S., Johnson, J., et al. (2008a). Comparative genomics of two ecotypes of the marine planktonic copiotroph *Alteromonas macleodii* suggests alternative lifestyles associated with different kinds of particulate organic matter. *ISME J.* 2 (12), 1194. doi: 10.1038/ismej.2008.74

Jain, C., Rodriguez-R, L. M., Phillippy, A. M., Konstantinidis, K. T., and Aluru, S. (2018). High throughput ANI analysis of 90K prokaryotic genomes reveals clear species boundaries. *Nat. Commun.* 9 (1), 1–8. doi: 10.1038/s41467-018-07641-9

Jin, H. M., Im Jeong, H., Kim, K. H., Hahn, Y., Madsen, E. L., and Jeon, C. O. (2016). Genome-wide transcriptional responses of *Alteromonas naphthalenivorans* SN2 to contaminated seawater and marine tidal flat sediment. *Sci. Rep.* 6, 21796. doi: 10.1038/srep21796

Jin, H. M., Kim, J. M., Lee, H. J., Madsen, E. L., and Jeon, C. O. (2012). *Alteromonas* as a key agent of polycyclic aromatic hydrocarbon biodegradation in crude oil-contaminated coastal sediment. *Environ. Sci. Technol.* 46, 7731–7740. doi: 10.1021/es3018545

Kanehisa, M., and Goto, S. (2000). KEGG: Kyoto encyclopedia of genes and genomes. *Nucleic Acids Res.* 28 (1), 27–30. doi: 10.1093/nar/28.1.27

Keil, R. G., Neibauer, J. A., Biladeau, C., van der Elst, K., and Devol, A. H. (2016). A multiproxy approach to understanding the "enhanced" flux of organic matter through the oxygen-deficient waters of the Arabian Sea. *Biogeosciences* 13, 2077–2092. doi: 10.5194/bg-13-2077-2016

Koch, H., Freese, H. M., Hahnke, R. L., Simon, M., and Wietz, M. (2019). Adaptations of *Alteromonas* sp. 76-1 to polysaccharide degradation: A CAZyme plasmid for ulvan degradation and two alginolytic systems. *Front. Microbiol.* 10, 504.

Koch, H., Germscheid, N., Freese, H. M., Noriega-Ortega, B., Lücking, D., Berger, M., et al. (2020). Genomic, metabolic and phenotypic variability shapes ecological differentiation and intraspecies interactions of *Alteromonas macleodii*. *Sci. Rep.* 10 (1), 1–4. doi: 10.1038/s41598-020-57526-5

Kondo, Y., and Moffett, J.W. (2015). Iron redox cycling and subsurface offshore transport in the eastern tropical South Pacific oxygen minimum zone. *Marine Chemistry* 168, 95–103. doi: 10.1016/j.marchem.2014.11.007

Koedooder, C., Guéneuguès, A., Van Geersdaële, R., Vergé, V., Bouget, F.-Y., and Labreuche, Y. (2018). The role of the glyoxylate shunt in the acclimation to iron limitation in marine heterotrophic bacteria. *Front. Mar. Sci.* 5, 435. doi: 10.3389/fmars.2018.00435

Lavin, P., González, B., Santibáñez, J. F., Scanlan, D. J., and Ulloa, O. (2010). Novel lineages of *Prochlorococcus* thrive within the oxygen minimum zone of the eastern tropical south pacific. *Env. Microbiol. Rep.* 2 (6), 728–738. doi: 10.1111/j.1758-2229.2010.00167.x

Lekunberri, I., Sintes, E., De Corte, D., Yokokawa, T., and Herndl, G. J. (2013). Spatial patterns of bacterial and archaeal communities along the romanche fracture zone (tropical Atlantic). *FEMS Microbiol. Ecol.* 85 (3), 537–552. doi: 10.1111/1574-6941.12142

López-Pérez, M., and Rodriguez-Valera, F *The Family Alteromon-adaceae, in: The Prokaryotes: Gammaproteobacteria*, edited by:E. Rosenberg, E. F. DeLong, S. Lory, E. Stackebrandt and F Thompson. Berlin, Heidelberg:Springer Berlin Heidelberg

López-Pérez, M., Gonzaga, A., Martin-Cuadrado, A. B., Onyshchenko, O., Ghavidel, A., and Ghai, R. (2012). Genomes of surface isolates of *Alteromonas* macleodii: The life of a widespread marine opportunistic copiotroph. *Scientific reports* 2 (1), 11–11. doi: 10.1038/srep00696

López-Pérez, M., Ramon-Marco, N., and Rodriguez-Valera, F. (2017). Networking in microbes: Conjugative elements and plasmids in the genus *Alteromonas*. *BMC Genomics* 18 (1), 36. doi: 10.1186/s12864-016-3461-0

López-Pérez, M., and Rodriguez-Valera, F. (2016). Pangenome evolution in the marine bacterium *Alteromonas*. *Genome Biol. Evol.* 8 (5), 1556–1570. doi: 10.1093/gbe/evw098

MacIntyre, L. W., Haltli, B. A., and Kerr, R. G. (2019). Draft genome sequence of alteromonas sp. strain RKMC-009, isolated from xestospongia muta *via in situ* culturing using an isolation chip diffusion chamber. *Microbiol. Resour. Announc.* 8 (25), e00508–e00519.

Manck, L. E., Espinoza, J. L., Dupont, C. L., and Barbeau, K. A. (2020). Transcriptomic study of substrate-specific transport mechanisms for iron and carbon in the marine copiotroph *Alteromonas macleodii*. *mSystems* 5 (2). doi: 10.1128/mSystems.00070-20

Manck, L. E., Park, J., Tully, B. J., Poire, A. M., Bundy, R. M., Dupont, C. L., et al. (2022). Petrobactin, a siderophore produced by *Alteromonas*, mediates community iron acquisition in the global ocean. *ISME J.* 16 (2), 358–369. doi: 10.1038/s41396-021-01065-y

Markowitz, V. M., Mavromatis, K., Ivanova, N. N., Chen, I. M. A., Chu, K., and Kyrpides, N. C. (2009). IMG ER: A system for microbial genome annotation expert review and curation. *Bioinformatics* 25 (17), 2271–2278. doi: 10.1093/bioinformatics/btp393

Martin, M. (2011). Cutadapt removes adapter sequences from high-throughput sequencing reads. *EMBnet. J.* 17 (1), 10–12. doi: 10.14806/ej.17.1.200

Márquez-Artavia, A., Sánchez-Velasco, L., Barton, E. D., Paulmier, A., Santamaría-Del-Ángel, E., Beier, E., et al. (2019). A suboxic chlorophyll-a maximum persists within the Pacific oxygen minimum zone off Mexico. *Deep Sea Res. Part II: Topical Studies in Oceanography* 169 (1), 104686.

Math, R. K., Jin, H. M., Kim, J. M., Hahn, Y., Park, W., Madsen, E. L., et al. (2012). Comparative genomics reveals adaptation by *Alteromonas* sp. SN2 to marine tidal-flat conditions: cold tolerance and aromatic hydrocarbon metabolism. *PloS One* 7 (4), e35784.

McMurdie, P. J., and Holmes, S. (2013). Phyloseq: An r package for reproducible interactive analysis and graphics of microbiome census data. *PloS One* 8 (4), e61217. doi: 10.1371/journal.pone.0061217

Medina, L. E., Taylor, C. D., Pachiadaki, M. G., Henríquez-Castillo, C., Ulloa, O., and Edgcomb, V. P. (2017). A review of protist grazing below the photic zone emphasizing studies of oxygen-depleted water columns and recent applications of *in situ* approaches. *Front. Mar. Sci.* 4, 105. doi: 10.3389/fmars.2017.00105

Messié, M., and Chavez, F. P. (2015). Seasonal regulation of primary production in eastern boundary upwelling systems. *Prog. Oceanogr.* 134, 1–18. doi: 10.1016/j.pocean.2014.10.011

Mikhailov, V. V., Romanenko, L. A., and Ivanova, E. P. (2006). *The genus alteromonas and related proteobacteria. the prokaryotes: A handbook on the biology of bacteria* Vol. 6 (New York, USA: Springer-Verlag), 597–645.

Mistry, J., Chuguransky, S., Williams, L., Qureshi, M., Salazar, G. A., Sonnhammer, E. L., et al. (2021). Pfam: The protein families database in 2021. *Nucleic Acids Res.* 49 (D1), D412–D419. doi: 10.1093/nar/gkaa913

Moore, J. K., and Braucher, O. (2007). Observations of dissolved iron concentrations in the world ocean: Implications and constraints for ocean biogeochemical models. *Biogeosciences* 4 (2), 1241–1277. doi: 10.5194/bgd-4-1241-2007

Mounier, J., Camus, A., Mitteau, I., Vaysse, P. J., Goulas, P., Grimaud, R., et al. (2014). The marine bacterium marinobacter hydrocarbonoclasticus SP17 degrades a wide range of lipids and hydrocarbons through the formation of oleolytic biofilms with distinct gene expression profiles. *FEMS Microbiol. Ecol.* 90 (3), 816–831. doi: 10.1111/1574-6941.12439

Nayfach, S., Rodriguez-Mueller, B., Garud, N., and Pollard, K. S. (2016). An integrated metagenomics pipeline for strain profiling reveals novel patterns of bacterial transmission and biogeography. *Genome Res.* 26 (11), 1612–1625. doi: 10.1101/gr.201863.115

Nguyen, L. T., Schmidt, H. A., Von Haeseler, A., and Minh, B. Q. (2015). IQ-TREE: a fast and effective stochastic algorithm for estimating maximum-likelihood phylogenies. *Mol. Biol. Evol.* 32 (1), 268–274. doi: 10.1093/molbev/msu300

Padilla, C. C., Bertagnolli, A. D., Bristow, L. A., Sarode, N., Glass, J. B., Thamdrup, B., et al. (2017). Metagenomic binning recovers a transcriptionally active gammaproteobacterium linking methanotrophy to partial denitrification in an anoxic oxygen minimum zone. *Front. Mar. Sci.* 4, 23. doi: 10.3389/fmars.2017.00023

Padilla, C. C., Bristow, L. A., Sarode, N., Garcia-Robledo, E., Ramírez, E. G., Benson, C. R., et al. (2016). NC10 bacteria in marine oxygen minimum zones. *ISME J.* 10 (8), 2067. doi: 10.1038/ismej.2015.262

Parada, A. E., Needham, D. M., and Fuhrman, J. A. (2016). Every base matters: assessing small subunit rRNA primers for marine microbiomes with mock communities, time series and global field samples. *Environ. Microbiol.* 18 (5), 1403–1414. doi: 10.1111/1462-2920.13023

Parks, D. H., Imelfort, M., Skennerton, C. T., Hugenholtz, P., and Tyson, G. W. (2015). CheckM: assessing the quality of microbial genomes recovered from isolates, single cells, and metagenomes. *Genome Res.* 25 (7), 1043–1055. doi: 10.1101/gr.186072.114

Pedler, B. E., Aluwihare, L. I., and Azam, F. (2014). Single bacterial strain capable of significant contribution to carbon cycling in the surface ocean. *P Natl. Acad. Sci. U.S.A.* 111 (20), 7202–7207. doi: 10.1073/pnas.1401887111

Plominsky, A. M., Trefault, N., Podell, S., Blanton, J. M., de la Iglesia, R., Allen, E. E., et al. (2018). Metabolic potential and *in situ* transcriptomic profiles of previously uncharacterized key microbial groups involved in coupled carbon, nitrogen and sulfur cycling in anoxic marine zones. *Environ. Microbiol.* 20 (8), 2727–2742. doi: 10.1111/1462-2920.14109

Quast, C., Pruesse, E., Yilmaz, P., Gerken, J., Schweer, T., Yarza, P., et al. (2013). The SILVA ribosomal RNA gene database project: improved data processing and web-based tools. *Nucl. Acids Res.* 41 (D1), D590–D596.

Raven, M. R., Keil, R. G., and Webb, S. M. (2021). Microbial sulfate reduction and organic sulfur formation in sinking marine particles. *Science* 3, 178–181. doi: 10.1126/science.abc6035

Revsbech, N. P., Larsen, L. H., Gundersen, J., Dalsgaard, T., Ulloa, O., and Thamdrup, B. (2009). Determination of ultra-low oxygen concentrations in oxygen minimum zones by the STOX sensor. *Limnol. Oceanogr-Meth.* 7 (5), 371–381. doi: 10.4319/lom.2009.7.371

Ruiz-Fernández, P., Ramírez-Flandes, S., Rodríguez-León, E., and Ulloa, O. (2020). Autotrophic carbon fixation pathways along the redox gradient in oxygen-depleted oceanic waters. *Environ. Microbiol. Rep.* 12 (3), 334–341. doi: 10.1111/1758-2229.12837

Sambrook, J., and Russell, D. W. (2006). Purification of nucleic acids by extraction with phenol: chloroform. *Cold Spring Harbor Protoc.* 2006 (1), pdb–prot4455.

Saunders, J. K., Fuchsman, C. A., Mckay, C., and Rocap, G. (2019). Complete arsenic-based respiratory cycle in the marine microbial communities of pelagic oxygen-deficient zones. *Proc. Natl. Acad. Sci. U.S.A.* 116, 9925–9930. doi: 10.1073/pnas.1818349116

Schattenhofer, M., Fuchs, B. M., Amann, R., Zubkov, M. V., Tarran, G. A., and Pernthaler, J. (2009). Latitudinal distribution of prokaryotic picoplankton populations in the Atlantic ocean. *Environ. Microbiol.* 11 (8), 2078–2093. doi: 10.1111/j.1462-2920.2009.01929.x

Schlosser, C., Streu, P., Frank, M., Lavik, G., Croot, P. L., Dengler, M., et al. (2018). H2S events in the Peruvian oxygen minimum zone facilitate enhanced dissolved fe concentrations. *Sci. Rep.* 8 (1), 12642.

Stepanauskas, R., Fergusson, E. A., Brown, J., Poulton, N. J., Tupper, B., Labonté, J. M., et al. (2017). Improved genome recovery and integrated cell-size analyses of individual uncultured microbial cells and viral particles. *Nat. Commun.* 8 (1), 1–10.

Stewart, F. J., Ulloa, O., and DeLong, E. F. (2012). Microbial metatranscriptomics in a permanent marine oxygen minimum zone. *Environ. Microbiol.* 14 (1), 23–40. doi: 10.1111/j.1462-2920.2010.02400.x

Tackmann, J., Rodrigues, J. F. M., and von Mering, C. (2019). Rapid inference of direct interactions in large-scale ecological networks from heterogeneous microbial sequencing data. *Cell Syst.* 9 (3), 286–296. doi: 10.1016/j.cels.2019.08.002

Tatusov, R. L., Galperin, M. Y., Natale, D. A., and Koonin, E. V. (2000). The COG database: A tool for genome-scale analysis of protein functions and evolution. *Nucleic Acids Res.* 28 (1), 33–36. doi: 10.1093/nar/28.1.33

Tennessen, K., Andersen, E., Clingenpeel, S., Rinke, C., Lundberg, D. S., Han, J., et al. (2016). ProDeGe: A computational protocol for fully automated decontamination of genomes. *ISME J.* 10 (1), 269–272. doi: 10.1038/ismej.2015.100

Thamdrup, B., Dalsgaard, T., and Revsbech, N.P. (2012). Widespread functional anoxia in the oxygen minimum zone of the Eastern South Pacific. *Deep Sea Res. Part I Oceanogr. Res. Pap.* 65, 36–45

Tiano, L., Garcia-Robledo, E., Dalsgaard, T., Devol, A. H., Ward, B. B., Ulloa, O., et al. (2014). Oxygen distribution and aerobic respiration in the north and south eastern tropical pacific oxygen minimum zones. *Deep Sea Res. Part I Oceanogr. Res. Pap.* 94, 173–183. doi: 10.1016/j.dsr.2014.10.001

Ulloa, O., Canfield, D. E., DeLong, E. F., Letelier, R. M., and Stewart, F. J. (2012). Microbial oceanography of anoxic oxygen minimum zones. *P Natl. Acad. Sci. U.S.A.* 109 (40), 15996–16003. doi: 10.1073/pnas.1205009109

Ulloa, O., Henríquez-Castillo, C., Ramírez-Flandes, S., Plominsky, A. M., Murillo, A. A., Morgan-Lang, C., et al. (2021). The cyanobacterium prochlorococcus has divergent light-harvesting antennae and may have evolved in a low-oxygen ocean. *P Natl. Acad. Sci. U.S.A.* 118 (11), e2025638118. doi: 10.1073/pnas.2025638118

Vedamati, J., Goepfert, T., and Moffett, J. W. (2014). Iron speciation in the eastern tropical south pacific oxygen minimum zone off peru. *Limnol. Oceanogr.* 59, 1945–1957. doi: 10.4319/lo.2014.59.6.1945

Walters, W., Hyde, E. R., Berg-Lyons, D., Ackermann, G., Humphrey, G., Parada, A., et al. (2016). Improved bacterial 16S rRNA gene (V4 and V4-5) and fungal internal transcribed spacer marker gene primers for microbial community surveys. *Msystems* 1 (1), e00009–e00015. doi: 10.1128/mSystems.00009-15

frontiers | Frontiers in Marine Science

TYPE Original Research
PUBLISHED 06 October 2022
DOI 10.3389/fmars.2022.927921

OPEN ACCESS

EDITED BY
Sudheesh Valliyodan,
Central University of Kerala, India

REVIEWED BY
Shiba Shankar Acharya,
Presidency University, India
Anju Mallissery,
University of Haifa, Israel

*CORRESPONDENCE
Fei Chai
fchai@sio.org.cn
Wentao Ma
wtma@sio.org.cn

SPECIALTY SECTION
This article was submitted to Marine Biogeochemistry, a section of the journal Frontiers in Marine Science

RECEIVED 25 April 2022
ACCEPTED 14 September 2022
PUBLISHED 06 October 2022

CITATION
Zhang Z, Ma W and Chai F (2022) Role of ocean circulation and settling of particulate organic matter in the decoupling between the oxygen minimum zone and the phytoplankton productive zone in the Arabian Sea: A modeling study.
Front. Mar. Sci. 9:927921.
doi: 10.3389/fmars.2022.927921

Role of ocean circulation and settling of particulate organic matter in the decoupling between the oxygen minimum zone and the phytoplankton productive zone in the Arabian Sea: A modeling study

Zhiwei Zhang[1,2], Wentao Ma[2,3]* and Fei Chai[1,2]*

[1]School of Oceanography, Shanghai Jiao Tong University, Shanghai, China, [2]State Key Laboratory of Satellite Ocean Environment Dynamics, Second Institute of Oceanography, Ministry of Natural Resources, Hangzhou, China, [3]Southern Marine Science and Engineering Guangdong Laboratory (Zhuhai), Zhuhai, China

The oxygen minimum zone has a significant effect on primary production, marine biodiversity, food web structure, and marine biogeochemical cycle. The Arabian Sea oxygen minimum zone (ASOMZ) is one of the largest and most extreme oxygen minimum zones in the world, with a positional decoupling from the region of phytoplankton blooms. The core of the ASOMZ is located to the east of the high primary production region in the western Arabian Sea. In this study, a coupled physical–biogeochemical numerical model was used to quantify the impact of ocean circulation and settling of particulate organic matters (POMs) on the decoupling of the ASOMZ. Model results demonstrate that the increased (decreased) dissolved oxygen replenishment in the western (central) Arabian Sea is responsible for decoupling. The oxygen-rich intermediate water (200–1,000 m) from the southern Arabian Sea enters the Arabian Sea along the west coast and hardly reaches the central Arabian Sea, resulting in a significant oxygen replenishment in the western Arabian Sea high-productivity region (Gulf of Aden) but only a minor contribution in the central Arabian Sea. Besides that, the POMs that are remineralized to consume central Arabian Sea dissolved oxygen comprises not only local productivity in winter bloom but also the transport from the western Arabian Sea high-productivity region (Oman coast) in summer bloom. More dissolved oxygen replenishment in the western Arabian Sea, and higher dissolved oxygen consumption and fewer dissolved oxygen replenishment in the central Arabian Sea could contribute to the decoupling of the ASOMZ and phytoplankton productive zone.

KEYWORDS

Arabian Sea oxygen minimum zone, dissolved oxygen (DO), oxygen-rich intermediate water, sinking velocity, source regions of POM, decoupling

1 Introduction

Oxygen levels in both open and coastal oceans have declined for the past 50 years (Diaz and Rosenberg, 2008; Stramma et al., 2008; Keeling et al., 2010; Ito et al., 2017; Schmidtko et al., 2017; Breitburg et al., 2018). Ocean deoxygenation, one of the most important changes occurring in the marine ecosystem (Zhang et al., 2010; Rabalais et al., 2014; Levin and Breitburg, 2015), can lead to the expansion of low-oxygen waters, which are known as oxygen minimum zones (OMZs; dissolved oxygen, DO< 60 mmol·m^{-3}; Stramma et al., 2008; Breitburg et al., 2018; Bindoff et al., 2019). The major OMZs in the global oceans mainly occur in upwelling-dominated regions, poorly ventilated regions, and large river estuaries, such as the Gulf of California (Lluch-Cota et al., 2007), eastern Tropical North Pacific (Karstensen et al., 2008), eastern Tropical South Pacific (Ulloa et al., 2012; Tiano et al., 2014), Arabian Sea (Kamykowski and Zentara, 1990; McCreary et al., 2013; Lachkar et al., 2018), Bay of Bengal (Sarma, 2002; Al Azhar et al., 2017), Gulf of Mexico (Rabalais et al., 2002; Bianchi et al., 2010), and Changjiang River Estuary (Zhang et al., 2010; Zhou et al., 2017; Zhang et al., 2018). The expansion of OMZ causes not only a decrease in the oxygen level in the water column but also an increase in the rate of anammox and denitrification, which effectively removes nitrate from the water column (Gilly et al., 2013). Considering that upwelled nutrients are important for surface primary production, the variability in OMZ will constrain primary production, marine biodiversity, food web structure, and marine biogeochemical cycles (Rabalais et al., 2002; Naqvi et al., 2006; Vaquer-Sunyer and Duarte, 2008; Levin et al., 2009; Bianchi et al., 2012; Breitburg et al., 2018; Laffoley and Baxter, 2019).

The Arabian Sea OMZ (ASOMZ) is one of the largest and most extreme OMZs in the world, with suboxic areas (DO< 4 mmol·m^{-3}) in the majority of its northern and northeastern intermediate water depths ranging from 200 to 1,000 m (Morrison et al., 1998). Over the Arabian Sea, monsoon winds alternately blow from the northeast and the southwest during winter and summer, respectively. Although the monsoon winds cause significant spatial and temporal variability in ocean dynamics and biological activity, the annual cycle of the ASOMZ is weak. The ASOMZ in the western Arabian Sea retreats slightly eastward during the summer monsoon and expands slightly westward during the winter monsoon. On the other hand, the ASOMZ in the eastern Arabian Sea expands slightly southward during the summer monsoon and retreats northward during the winter monsoon (Resplandy et al., 2012; Rixen et al., 2014; Shenoy et al., 2020).

The western Arabian Sea has high productivity due to upwelling in the summer monsoon and the northern Arabian Sea has high productivity due to strong mixing in the winter monsoon, while the eastern/central Arabian Sea has significantly lower productivity due to nutrient limitation (McCreary et al., 2009; Anju et al., 2020). The ASOMZ is distinguished by the fact that its core area (DO< 4 mmol·m^{-3}) is located far from the upwelling-dominated high primary productivity region in the western Arabian Sea and is most developed in the eastern and central Arabian Sea (Naqvi, 1991). To explain the occurrence of the ASOMZ away from the high-productivity region, previous studies showed that advection of sea water and settling of particulate organic matters (POMs) might play dominant roles. The northward advection of oxygen-rich water (e.g., the Indian Ocean Central Water; ICW) from the southern boundary of the Arabian Sea replenishes the dissolved oxygen in the west (Sarma, 2002; Resplandy et al., 2012; Rixen et al., 2014). The settling of POM in the upwelling region was found to be associated with little remineralization in the upper ocean (Honjo et al., 1999; Naqvi et al., 2010). These POMs are small and slow-sinking enough to be transported northward and eastward before being remineralized (Wiggert and Murtugudde, 2007; Hood et al., 2009; McCreary et al., 2013; Acharya and Panigrahi, 2016). Other explanations include the lack of mesoscale mixing in the eastern Arabian Sea, which results in poorly ventilated subsurface waters (McCreary et al., 2013; Schmidt et al., 2020); Persian Gulf water (PGW) and Red Sea Water (RSW) ventilating the upper ASOMZ (e.g., Lachkar et al., 2019); the cross-shelf transport of organic matter from the eastern Arabian Sea shelf, which increases oxygen consumption in the eastern Arabian Sea (Sarma et al., 2020); iron limitation in the western Arabian Sea, which leads to an eastward shift in the utilization of upwelled nutrients and intensifies the OMZ (Moffett and Landry, 2020); and the regulation of westward Rossby waves (Kim et al., 2001; Shenoy et al., 2020).

The above studies have revealed the potential mechanisms affecting the location of the ASOMZ's core area. However, the quantitative effects of sea water advection and settling of POM are still not well worked out due to limited *in situ* observation data and simplified physical–biogeochemical models (Acharya and Panigrahi, 2016). Another unknown is source regions of POM detected in the western and central Arabian Sea. This study therefore set up a control experiment and some sensitivity experiments to investigate the decoupling of the ASOMZ by analyzing the sea water advection and settling of POM through a coupled physical–biogeochemical numerical model. Besides that, the main pathway of water masses and its impact on the ASOMZ through Lagrangian particle tracking experiment are investigated. Another purpose of this study is to estimate the proportion of POM originating from different seasons and regions by using ideal POM sinking experiments, and to explore why there is a significant seasonal cycle of chlorophyll in the surface and a weaker ASOMZ variation in the intermediate layer.

Details of the coupled numerical model, experiment setting, and observation data are described in *Section 2*. Model validation, physical and biological factors affecting the ASOMZ, and variation of microbial hypoxic and suboxic zones in the ASOMZ are given in *Section 3*. We also discuss

source regions of POM, and the decoupling of the ASOMZ mechanisms in *Section 4*. Finally, the conclusions are drawn in *Section 5*.

2 Methods and data

2.1 Numerical model

The physical–biogeochemical numerical model used here includes a circulation model component, the Regional Ocean Modeling System (Shchepetkin and McWilliams, 2003; Shchepetkin and McWilliams, 2005), coupled with a biogeochemical model, the carbon silicate, nitrogen ecosystem (CoSiNE) model (Chai et al., 2002), for the entire Indian Ocean. The model uses the non-local K-profile parameterization (KPP) scheme for vertical mixing (Large et al., 1994) and the Smagorinsky scheme (Smagorinsky, 1963) for horizontal mixing. The tracer advections with third-order upstream-bias and fourth-order centered difference schemes are applied in the horizontal and vertical directions, respectively. The model domain extends from 31°S to 32°N and from 30°E to 120°E, with a horizontal resolution of 1/12°. It has 40 non-uniform sigma layers that are refined near the surface. Ten tidal constituents (M2, S2, N2, K2, K1, O1, P1, Q1, MM, and MF) are considered in the equilibrium tide module (Liang et al., 2019) and imposed at the open boundaries using the data obtained from TPXO7.2 (Egbert and Erofeeva, 2002).

Temperature and salinity boundary and initial conditions are from the climatological monthly dataset of the Simple Ocean Data Assimilation (SODA; Carton and Giese, 2008), while nitrate, silicate, phosphate, and oxygen are from the World Ocean Atlas (WOA) 2018 (Garcia et al., 2019). The air–sea heat flux is calculated with a bulk formula (Ahsan and Blumberg, 1999) through the climatological monthly mean data from the European Center for Medium-Range Weather Forecasts (ECMWF) ERA-5 reanalysis products, including wind, air temperature, air pressure, solar shortwave radiation flux, solar longwave radiation flux, and relative humidity with a spatial resolution of 0.25° × 0.25°. Monthly mean discharges of major rivers in the Indian Ocean are considered, deriving from the Global Runoff Data Centre (GRDC, http://grdc.bafg.de) and Global River Discharge Database (https://sage.nelson.wisc.edu/riverdata/).

The CoSiNE model used in this study is based on a newly developed version (Ma et al., 2019). The CoSiNE model has been successfully applied in different regions (Liu and Chai, 2009; Xiu and Chai, 2011; Xiu and Chai, 2014; Ma et al., 2019; Zhang et al., 2021). It contains 16 state variables including four inorganic nutrients (nitrate [NO_3], ammonium [NH_4], silicate [$Si(OH)_4$], and phosphate [PO_4]), two phytoplankton groups (small phytoplankton [P1] and diatoms [P2]) and their corresponding chlorophyll components ([Chl1] and [Chl2]), two size classes of zooplankton (microzooplankton [Z1] and mesozooplankton [Z2]), three kinds of particles (small particulate organic nitrogen [SDet], large PON [LDet], and biogenic silica [bSi]), dissolved oxygen [DO], dissolved inorganic carbon [TCO2], and total alkalinity [TALK] (see schematic diagram in Ma et al., 2019). Detailed key control equations are presented in the Ma et al. (2019) Supplement.

The budget of the dissolved oxygen is diagnosed as follows,

$$\int \frac{\partial DO}{\partial t} dv = -\int \left(u\frac{\partial DO}{\partial x} + v\frac{\partial DO}{\partial y} + w\frac{\partial DO}{\partial z} \right) dV + \int \left[\frac{\partial}{\partial x}\left(Kh\frac{\partial DO}{\partial x} \right) + \frac{\partial}{\partial y}\left(Kh\frac{\partial DO}{\partial y} \right) + \frac{\partial}{\partial z}\left(Kv\frac{\partial DO}{\partial z} \right) \right] dV + PP + WCR + Nitrif + Flux_{air-sea} \quad (1)$$

where DO represents dissolved oxygen concentration ($mmol \cdot m^{-3}$), PP is oxygen produced from primary production, WCR stands for water column respiration by POM and excretion of zooplankton, $Nitrif$ is oxygen consumption due to nitrification, and $Flux_{air\text{-}sea}$ indicates gas exchange across the air–sea interface. K_h and K_v are the horizontal and vertical diffusivity, respectively. The first two terms on the right-hand side are advection and diffusion induced by oxygen changes, respectively.

2.2 Numerical experiment settings

To obtain a relatively steady sate, the model was first spun up for 15 years with the climatological forcing. For dissolved oxygen, the model drift decreased significantly at the end of the spin-up period (Figure S1). After that, another 5-year simulation with climatological forcing was conducted for control run after the spin-up (Table 1). The results from the last year of the 5-year integration were used for analysis if not specifically stated in the text. In addition, four basic numerical experiments were carried out (Table 1). The stronger branch of the ICW (DO = 50 $mmol \cdot m^{-3}$, WOA2018) enters the western Arabian Sea *via* the Somali Coastal Current (You, 1997; Schott and McCreary, 2001). The other branch of the ICW transports dissolved oxygen at a lower level (~30 $mmol \cdot m^{-3}$) into the eastern Arabian Sea along with the West Indian Coastal Current (Schmidt et al., 2020; Shenoy et al., 2020; Sudheesh et al., 2022). The dissolved oxygen on the section along 7°N was set to 15 $mmol \cdot m^{-3}$ (lower than a third of the observed value in the western Arabian Sea) throughout intermediate water layer (200–1,000 m) in Exp1. In Exp2, the model was forced with higher dissolved oxygen (100 $mmol \cdot m^{-3}$, roughly twice the observed value) water entering the Arabian Sea, with other conditions remaining unchanged from Exp1. In Exp3, the sinking velocity of POM was reduced by a factor of 2 on the original basis (Exp0), from 5.0 to 2.5 $m \cdot day^{-1}$. In Exp4, the sinking velocity of POM was increased by a factor of 2 on the original basis (Exp0), from 5.0 to 10.0 $m \cdot day^{-1}$.

Several other experiments were also conducted (Table 1). First, the online Lagrangian particle tracking experiment in the ROMS model was conducted for 12 years, with 31,305 particles

TABLE 1 Numerical experiment settings.

	Name	Description
Control Run	Exp0	5-year simulation with climatological forcing
Basic Experiment	Exp1	Lower dissolved oxygen (15 mmol·m^{-3}) water entering the Arabian Sea from 7°N
	Exp2	Higher dissolved oxygen (100 mmol·m^{-3}) water entering the Arabian Sea from 7°N
	Exp3	The sinking velocity of POM is reduced by a factor of 2 in the control run (Exp0), from 5 to 2.5 m·day^{-1}
	Exp4	The sinking velocity of POM is increased by a factor of 2 in the control run (Exp0), from 5 to 10 m·day^{-1}
Lagrangian Particles Experiment	Ltest1	31,305 particles released at 0.25° interval along the 10°N transect in the Arabian Sea at depths ranging from 0 to 2,000 m
POM Ideal Sinking Experiment	Dtest1	POM released in the surface grid of the Persian Gulf
	Dtest2	POM released in the surface grid of the central Arabian Sea
	Dtest3	POM released in the surface grid of the eastern Arabian Sea continental shelf
	Dtest4	POM released in the surface grid of the Gulf of Aden
	Dtest5	POM released in the surface grid of the Oman Coast

uniformly released along the transect of 10°N in the Arabian Sea at an interval of 0.25° at depths ranging from 0 to 2,000 m. Specifically, the depths of particles release were at 0 m, 10 m, 30 m, and 50–150 m with an interval of 25 m, 150–250 m with an interval of 50 m, 300–1,000 m with an interval of 100 m, and 1,000–2,000 m with an interval of 250 m. Particles were released on the first day of June, July, and August during the summer monsoon in the first model year due to the Somali Coastal Current peaks in summer.

Second, idealized experiments were performed to trace the source of the POM. In each experiment, the POM was arranged in the surface layer in one of five high-productivity regions (within a 2° × 2° box; see Figure S2; Table 1), representing the Persian Gulf, central Arabian Sea, eastern continental shelf of the Arabian Sea, Gulf of Aden, and Oman coast, respectively. The idealized POM was essentially a passive tracer with specific sinking velocity, but no degradation or other removal processes. The POM was ideally set to a fixed value (here was 1,000 mmol·N·m^{-3}) to represent an end number. The fraction of POM from various regions was used to track down the source. The POM was released in December and June, representing the high productivity during the winter and summer monsoons, respectively.

2.3 *In situ* observation and satellite data

The *in situ* observation data of sea surface temperature (SST), sea surface salinity (SSS), dissolved oxygen, and nitrate are from the I07N cruise supported by the Global Ocean Ship-Based Hydrographic Investigation Program (GO-SHIP) in April–June 2018. Although the cruise crosses the entire western Indian Ocean, only a portion of the stations in the Arabian Sea are selected (Figure 1). These data can be accessed from the Clivar and Carbon Hydrographic Data Office (CCHDO).

The sea surface climatological current is from the Drifter-Derived Climatology of Global Near-Surface Currents, with a resolution of 0.25° (Laurindo et al., 2017). Sea surface height (SSH) anomalies are from the SSALTO/DUACS multi-mission altimeter products from the Archiving, Validation and Interpretation of Satellite Oceanographic (AVISO) data with a horizontal resolution of 0.25°. Climatological monthly mean chlorophyll concentration data are from the Moderate Resolution Imaging Spectroradiometer (MODIS) with a horizontal resolution of 4 km. SST data are from the Optimum Interpolation Sea Surface Temperature (OISST) with a horizontal resolution of 0.25° from September 1981 to the present (Reynolds et al., 2007).

3 Results

3.1 Model validation

Available *in situ* and satellite-based observations are used to validate the performance of the model in the Arabian Sea, including key physical and biogeochemical properties in terms of seasonal variability. Sea surface currents, SSH anomalies, SST, and SSS are compared to evaluate the physical model. Comparison with surface drifter climatological current (Laurindo et al., 2017) shows that the model reproduces the main patterns of the surface circulations during the summer and winter monsoons (Figure S3). For example, the model successfully reproduces the counterclockwise circulation during the winter monsoon and the clockwise circulation during the summer monsoon, as shown in Schott and McCreary (2001). In particular, the model captures the strength and seasonal reversal of the Somali Coastal Current. Modeled temporal and spatial distributions of SSH anomalies during the summer and winter monsoons are consistent with AVISO data (Figure S4).

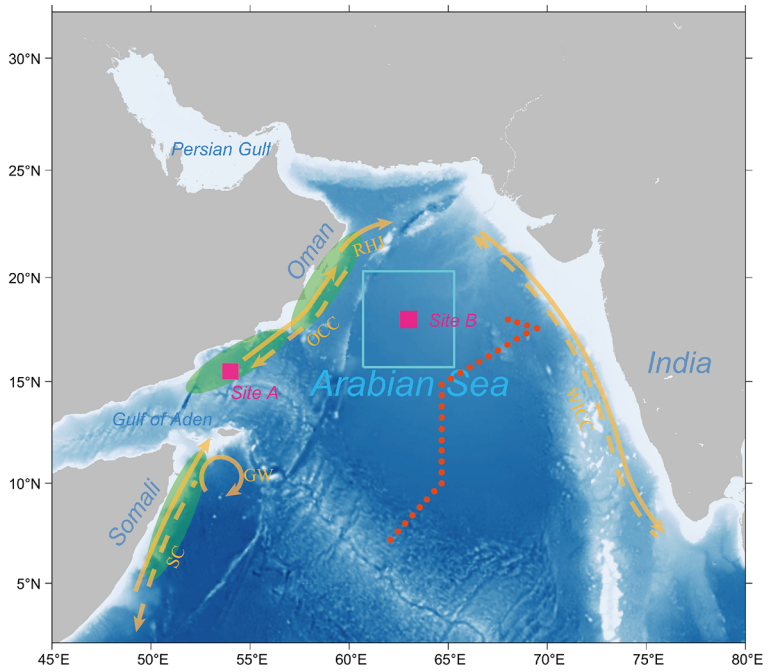

FIGURE 1
Map of the Arabian Sea and its adjacent seas. Coastal upwelling systems (green shading) and coastal circulations, after Schott and McCreary (2001). The solid (dashed) arrows represent the Somali Coastal Current (SC), the Great Whirl (GW), the Oman Coastal Current (OCC), Ras al Hadd Jet (RHJ), and the West Indian Coastal Current (WICC) in the winter (summer) monsoon state. Red dots represented the cruise track of the I07N cruise supported by the GO-SHIP in April–June 2018. Two squares represent the two sites (i.e., sites A and B) selected for analysis.

The main patterns of SST and SSS are also successfully captured by the model (Figures S5, S6). In particular, the model successfully reproduces the upwelling region off the coasts of Oman and Somalia, which are characterized by low SST during the summer monsoon. The north–south temperature gradient off the Persian Gulf during the winter monsoon is also presented in the model. The model, however, depicts temporal and spatial distributions of higher SSS in the northern and central Arabian Sea. Normalized Taylor diagrams (Taylor, 2001) are used in each season to assess model's skills in salinity, nitrate, and oxygen relative to the WOA 2018 data, in temperature relative to the OISST data, and in chlorophyll relative to the MODIS data (Figure 2). Skill score (Murphy, 1988) of the simulated results are calculated to quantify the performance. SS is graded as excellent if it is greater than 0.65, very good when it is between 0.5 and 0.65, good when between 0.2 and 0.5, and poor if it is less than 0.2. Statistical analysis indicates that the simulated and observed SST have similar standard deviations; and the RMSE reaches 0.11°C, 0.12°C, 0.13°C, and 0.12°C during different seasons, respectively, and correlation coefficient (CC) reaches 0.99 in different seasons (Figure 2). All of the SSs fall in the excellent category (0.99, 0.98, 0.98, and 0.98). Similarly, SSS's RMSE reaches 0.26, 0.25, 0.21, and 0.23 psu, respectively, and CC reaches ~0.97 in all seasons. The SS of SSS also falls in the excellent category (0.93, 0.94, 0.96, and 0.94). Consequently, these results indicate that the model adequately reproduces the features of temperature and salinity, paving the way for further analysis.

The high chlorophyll concentrations in the northern and western Arabian Sea during the summer and winter monsoons are consistent with MODIS chlorophyll concentrations (Figure S7). The high chlorophyll concentrations off the Indian west coast during the summer and winter monsoons are also reproduced. However, chlorophyll concentrations off the Oman coast are obviously underestimated in the model during the winter monsoon. The reason for this could be that the sinking velocity of POM in the model is relatively faster, resulting in less remineralization and insufficient recycle of nitrogen to support phytoplankton growth (Anderson et al., 2007). The reason could also be that weak winter mixing reduces the nutrient supply to the surface layer. The model also underestimates the chlorophyll concentrations off the Somalia coast during the summer monsoon. It could be due to silicate limiting diatom growth (Anju et al., 2020). From the statistical results, RMSE reaches ~0.95 $mg{\cdot}m^{-3}$ in different seasons, and CC shows acceptable results (Figure 2). Overall, the fidelity of the modeled chlorophyll concentration in the Arabian Sea is acceptable, as it is similar to the results of the state-of-the-art models in the Indian Ocean and Arabian Sea (e.g., Resplandy

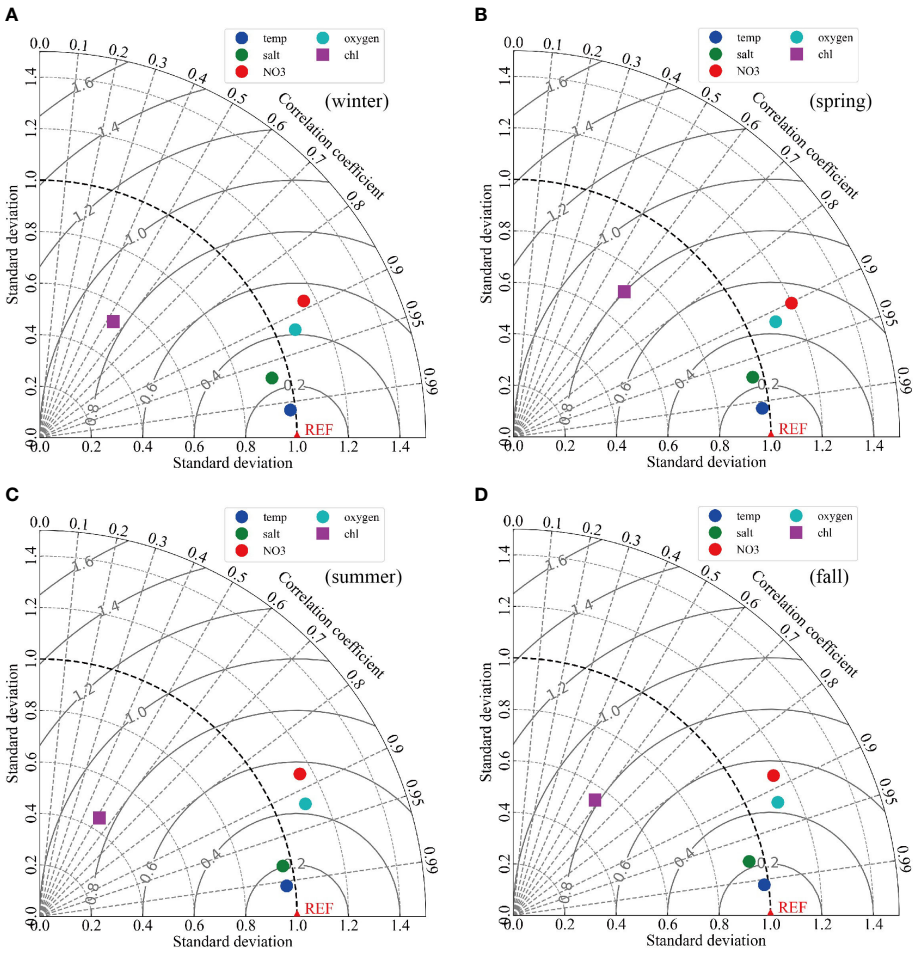

FIGURE 2
Normalized Taylor diagram for statistical comparison of observed and modeled variables of temperature (blue), salinity (green), nitrate (red), oxygen (cyan), and chlorophyll (purple) in winter **(A)**, spring **(B)**, summer **(C)**, and fall **(D)**. The observation data of temperature, salinity, nitrate, and oxygen are in the upper 800 m from the WOA 2018 dataset, and the chlorophyll data are from the MODIS.

et al., 2012; Lachkar et al., 2016; Lachkar et al., 2018; Lachkar et al., 2019; Lachkar et al., 2021).

The temporal and spatial distributions of nitrate during the summer and winter monsoons are successfully reproduced in the model, comparing with the WOA 2018 data (Figure S8). In particular, the high surface concentration off the Oman coast upwelling region in the summer monsoon is successfully simulated. The statistical results also indicate the model's performance is acceptable with RMSE of ~0.75 mmol·m^{-3} and CC of ~0.88 in different seasons (Figure 2). Moreover, the dissolved oxygen concentrations are relative accurately simulated during the summer and winter monsoons (Figure S9). In particular, the model generally reproduces the location, size, and intensity of the ASOMZ. However, the location of the ASOMZ is relatively closer to the western side of the Arabian Sea compared to its location based on the WOA 2018 dataset. The east–west vertical distribution of dissolved oxygen reveals similar phenomena that the suboxic area (DO< 4 mmol·m^{-3}) in the ASOMZ is larger than the observed. This could be due to the biases of chlorophyll concentration in the central Arabian Sea. Such biases may also arise from the underestimated eddy activity in the model, leading to underestimated OMZ ventilation as shown in Lachkar et al. (2016). The underestimated injection of ventilated oxygen-rich Persian Gulf waters into the northern Arabian Sea in the upper ASOMZ might also play a role (Lachkar et al., 2019). Although the model overestimated the intensity of the ASOMZ, the temporal and spatial distributions are still acceptable, both vertically and horizontally. Statistical analysis presents relatively good results with RMSE of ~0.49 mmol·m^{-3} and CC of ~0.92 in different seasons. Also, the SS of dissolved oxygen is in the excellent category at ~0.77 in different seasons. These results show that the model is capable of reproducing observed measurements in the region of interest in a statistical sense.

Simulated SST, SSS, nitrate, and dissolved oxygen are also compared to cruise observation data in 2018 (Figures 1, 3, S10, S11). Although the cruise covers 124 stations along the transection of the western Indian Ocean, only stations in the Arabian Sea (Stations 95–124) from 7° to 18°N are selected to evaluate the model performance. The scatter diagram associated with statistics analysis reveals that the model successfully captures the main physical and chemical characteristics in the Arabian Sea (Figure 3). The RMSE reaches 0.18 psu for salinity, 0.76°C for temperature, 6.22 mmol·m^{-3} for nitrate, and 21.55 mmol·m^{-3} for dissolved oxygen. Correspondingly, the CC shows good results with the values of 0.95, 1, 0.95, and 0.96, respectively, for the four variables. The SSs are all in the excellent category (0.89, 0.99, 0.84, and 0.93) during different seasons. The vertical distributions of temperature, salinity, nitrate, and dissolved oxygen successfully reproduce main physical and chemical patterns in the Arabian Sea. However, the vertical distribution of dissolved oxygen reveals that the modeled results are lower than the cruise results, with the area of suboxic province being smaller and the depth being shallower. It is attributed to the location of the ASOMZ in the model being further west than observed.

In conclusion, the model performs reasonably well in terms of large-scale features of the circulations, and seasonal variations in nitrate and chlorophyll, despite some biases. The location and structure of the observed ASOMZ are generally reproduced in the model.

3.2 Characteristics of the ASOMZ

The temporal and spatial distributions of dissolved oxygen in the Arabian Sea exhibit weak seasonal variation in both vertical and horizontal directions (Figures S9C, D), as concluded in Resplandy et al. (2012). The southern boundary of the ASOMZ (DO = 20 mmol·m^{-3}) extends to ~8°N at the east

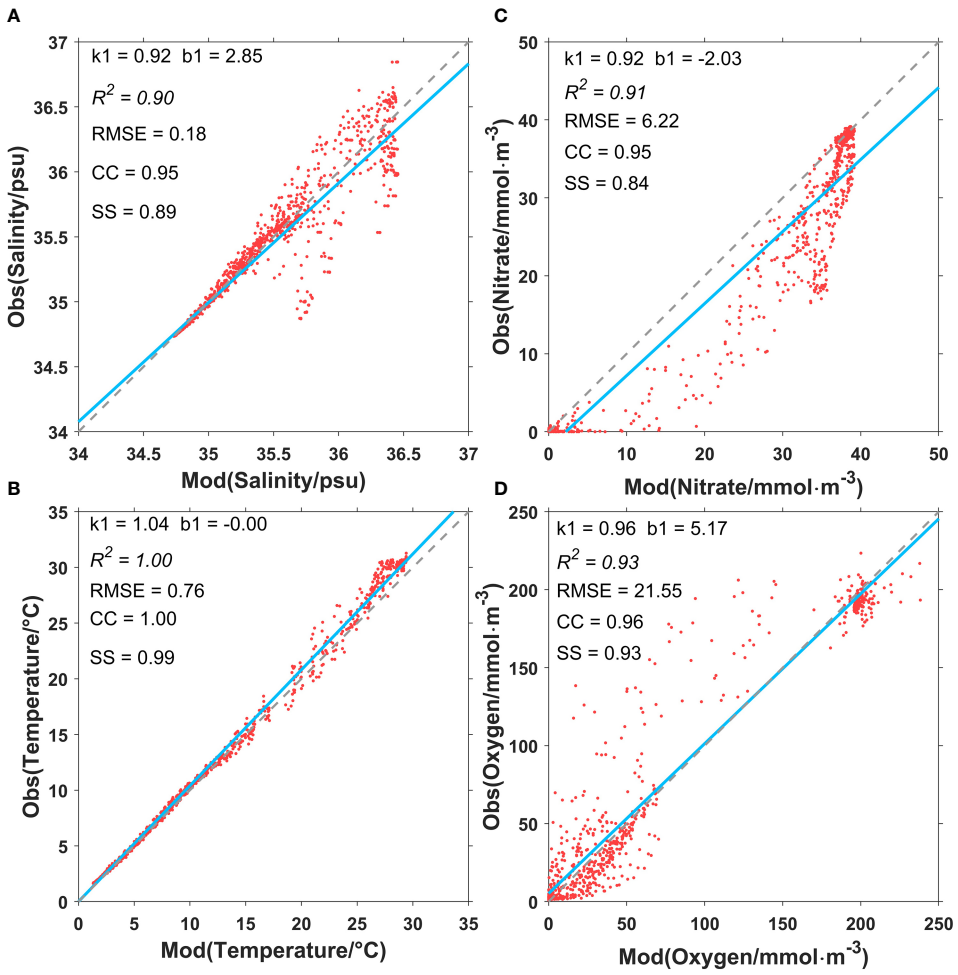

FIGURE 3
Model-data point-to-point comparison for salinity **(A)**, temperature **(B)**, nitrate **(C)**, and dissolved oxygen **(D)** in the upper 1500 m. The observation data are the I07N cruise data in 2018. RMSE, root-mean-square error; CC, correlation coefficient; SS, skill score.

and ~11°N at the west from the winter monsoon to summer monsoon. The suboxic area in the central Arabian Sea reaches ~59°E to the east during the winter monsoon and ~58°E during the summer monsoon. Similarly, a weak seasonal variation in the vertical distribution of dissolved oxygen can be seen in Figure S9.

A budget analysis of dissolved oxygen was performed for the entire Arabian Sea (areas north of 10°N) intermediate water (200–1,000 m), also known as the main layer of the ASOMZ (Figure 4). Considering that there is no phytoplankton production of oxygen and no air–sea exchange in the intermediate water (200–1,000 m), the terms PP and $Flux_{air\text{-}sea}$ in Eq. 1 can be ignored. The ASOMZ mainly gains and loses dissolved oxygen *via* horizontal advection (Hadv) and oxygen consumption (WCR), respectively. Similar conclusions were derived by other authors (Resplandy et al., 2012). The Hadv accounts for about 71% of the total dissolved oxygen gain, while the WCR accounts for about 70% of the total loss. Moreover, the Hadv is about three times larger during the summer monsoon than during the winter monsoon, while the vertical diffusion term (Vdiff) acts as a local oxygen loss during the winter monsoon. Both oxygen consumption and nitrification (Nitrif), which function as local oxygen loss, are relatively stable throughout the year. The roles of horizontal advection and oxygen consumption on the ASOMZ region will be described in detail in the following sections.

3.3 Physical factors affecting the ASOMZ

3.3.1 Transit time and pathway of oxygen-rich water

Previous studies suggested that the oxygen-rich water from the southern boundary of the Arabian Sea promotes the eastward migration of the ASOMZ (Resplandy et al., 2012; McCreary et al., 2013; Rixen et al., 2014). In view of this, a Lagrangian particle tracking experiment (details in *Section 2.2*) was conducted to identify the transit time and pathway of the oxygen-rich water mass from the southern boundary. The transit time of particles, defined here as the time when half of the particles in the same water layer reach the central Arabian Sea (cyan box in Figure 1), is shown in Figure 5. Given that the ASOMZ is mainly distributed in the intermediate depth (200–1,000 m) and ~6% of particles (approximately 50% of the total particles released in the intermediate layer) takes about 5 years to enter the central Arabian Sea, the integration time for the four basic numerical experiments is set to 5 years each.

The model results indicate that particles released on the west side (50°–55°E) of the southern boundary along 10°N tend to travel in the western Arabian Sea and are more likely to enter the box. The particles in the upper layer (0–200 m) are more easily impacted by wind-generated circulation due to the faster velocities. As a result, they enter the central Arabian Sea earlier than their counterparts released between 1,000 and 2,000 m where particles rarely enter the central box (Figure 6). The particles released on the east side (70°–76°E) tend to travel along the eastern Arabian Sea.

3.3.2 Effect of oxygen-rich water from the southern boundary

The Lagrangian particle tracking experiments indicate that the southern oxygen-rich water entering the Arabian Sea has a significant impact on dissolved oxygen concentration, consistent with previous studies (Resplandy et al., 2012; McCreary et al., 2013; Rixen et al., 2014; Acharya and Panigrahi, 2016). Two numerical experiments associated with southern oxygen-rich water were conducted to investigate the role of oxygen-rich

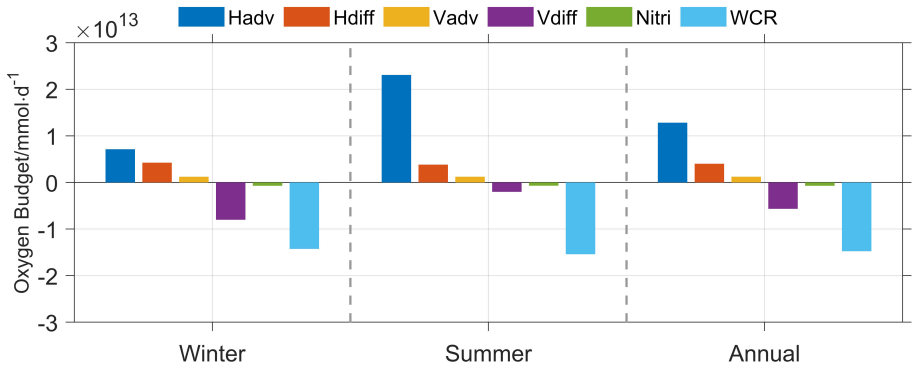

FIGURE 4
Modeled oxygen budget of dissolved oxygen concentration for intermediate water column (200–1,000 m) in the Arabian Sea Oxygen Minimum Zone. Abbreviations in the legend are for horizontal advection (Hadv), vertical advection (Vadv), horizontal diffusion (Hdiff), vertical diffusion (Vdiff), nitrification (Nitri), and water column respiration (WCR). Note that the positive value in the budget represents a net gain of dissolved oxygen while the negative value represents a net loss.

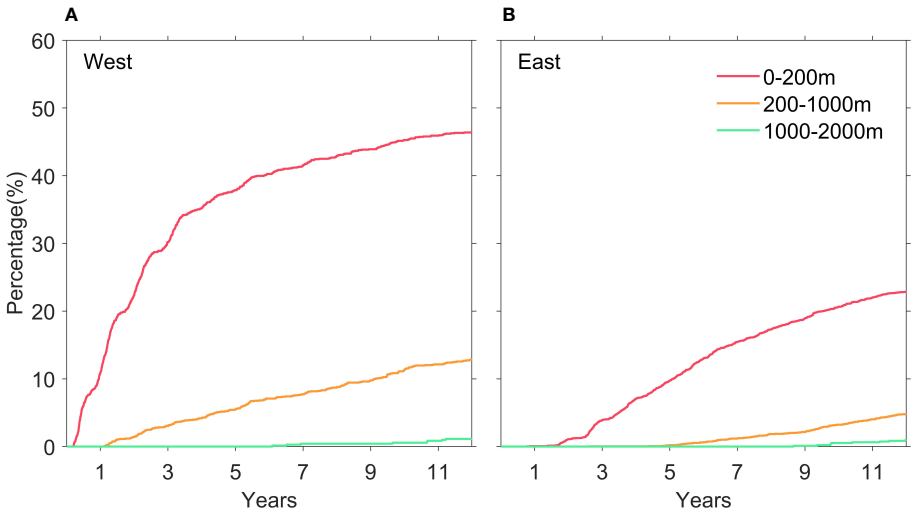

FIGURE 5
Transit time for particles to travel from different sources (**A**, west of southern boundary at 10°N in the Arabian Sea; **B,** east of southern boundary at 10°N in the Arabian Sea) to the central Arabian Sea. The percentage of transit time represents proportion of particles to the number of particles in the water layer where they are located. The transit time of particles, defined here as the time when half of the particles in the same water layer reach the central Arabian Sea.

water from the southern boundary of the Arabian Sea (described in detail in *Section 2.2*). Water mass entering the Arabian Sea was set to a low dissolved oxygen concentration (15 mmol·m^{-3}) in Exp1 and to a high concentration (100 mmol·m^{-3}) in Exp2.

Figure 7 depicts annual mean horizontal distributions of dissolved oxygen averaged between 200 and 1,000 m and vertical distributions along 17°N from three experiments (Exp0, Exp1, and Exp2). When water with lower dissolved oxygen concentration enter the Arabian Sea *via* the Somali Coastal Current (Exp1), the suboxic area expands significantly westward to around 58°E (compared to 59°E in Exp0). Note that the suboxic area is significantly reduced in Exp2, with the boundary contracts to about 60°E in the west and about 22°N in the north (compared to 25°N in Exp0) when high dissolved oxygen water flows in.

In particular, the inflow with low dissolved oxygen concentration causes a dramatic decrease in dissolved oxygen in the Gulf of Aden from ~14.4 to ~6.0 mmol·m^{-3}. The vertical profile of dissolved oxygen shows that the volume of suboxic water in the Gulf of Aden increases significantly as the depth range is extended from 150–400 m to 150–600 m (Figure 7). In Exp2, the dissolved oxygen concentration in the Gulf of Aden dramatically increases from ~14.4 to ~39.2 mmol·m^{-3}. The volume of suboxic water is also reduced significantly and the microbial hypoxic zone, defined by Rixen et al. (2020) as the layer with DO< 20 mmol·m^{-3} and anammox occurred, is uplifted from ~800 to ~400 m (Figure 7). The eastern Arabian Sea is also affected by the oxygen-rich water from the southern boundary, albeit less significantly than the western part. Only the water mass ranging from 150 to 300 m shows a significant increase in dissolved oxygen concentration from ~4 to ~35 mmol·m^{-3} (Figure 7F).

To better understand the impact of oxygen-rich water from the southern boundary of the Arabian Sea, two representative sites are selected (sites A and B in Figure 1) to represent the region with high primary production and high dissolved oxygen concentration in the Gulf of Aden and that with low dissolved oxygen concentration in the central Arabian Sea, respectively. The presence of the Somali Coastal Current influences the oxygen-rich water at site A near the Gulf of Aden. Figure 8 depicts current flux and associated dissolved oxygen flux averaged between 200 and 1,000 m in the Somali Coastal Current at 11.8°N on the western side of the Arabian Sea. The results indicate that the current is a net inflow into the Arabian Sea during the summer and peaked in August. Correspondingly, the dissolved oxygen flux also peaks in the same month with the value of ~8.5 × 10^{7} mmol·s^{-1} in Exp1, nearly one-fourth of that in Exp0 (~3.7 × 10^{8} mmol·s^{-1}), and ~9.9 × 10^{8} mmol·s^{-1} in Exp2. It is noteworthy that the southern boundary of the western Arabian Sea shifts from gain to loss when the oxygen-rich water from the southern boundary becomes low oxygen water. The annual mean flux of dissolved oxygen changes from ~2.7 × 10^{7} mmol·s^{-1} in Exp0 to −1.1 × 10^{6} mmol·s^{-1} in Exp1. However, it increases about threefold from ~2.7 × 10^{7} mmol·s^{-1} in Exp0 to ~9.5 × 10^{7} mmol·s^{-1} in Exp2 with higher oxygen-rich water from the southern boundary entering the Arabian Sea. As a result, the dissolved oxygen concentration at site A increases significantly after the replenished flux reaches the site in August (Figure 9A), whereas it decreases significantly with lower oxygen water

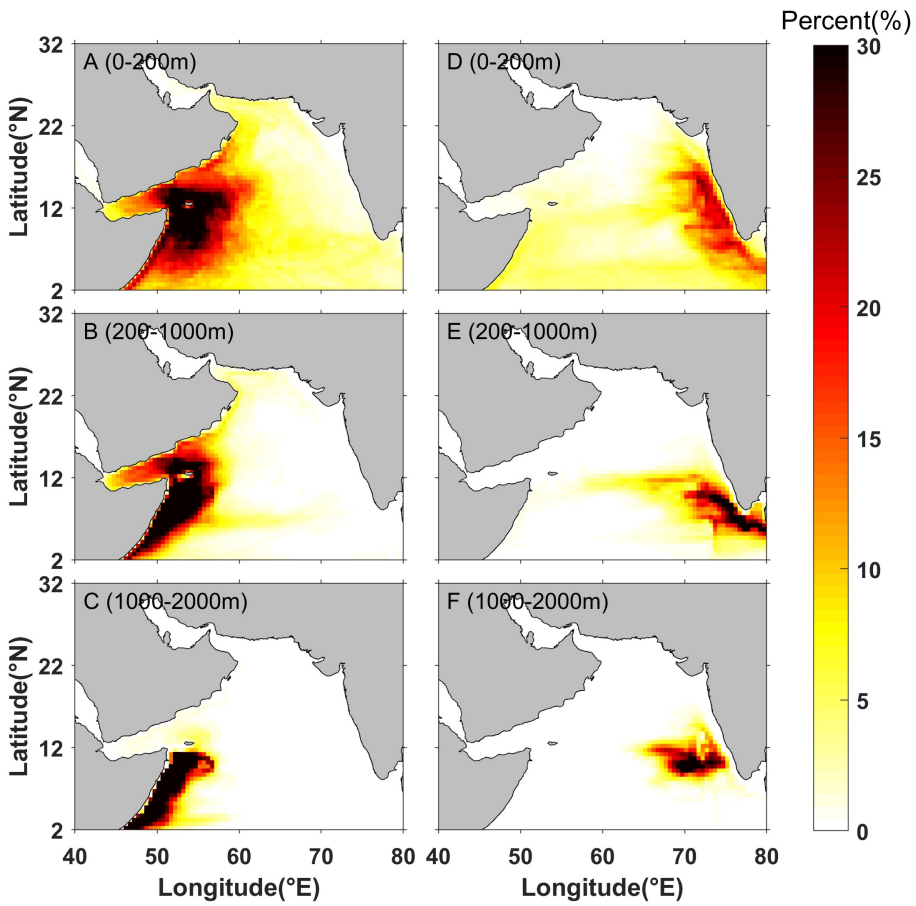

FIGURE 6
Transport pathways of particles 5 years after being released in different sources (**A–C**, released in the west of southern boundary at 10°N in the Arabian Sea; **D–F**, released in the east), and being released at different depths (**A, D** released at depths ranging from 0 to 200 m; **B, E** released at depths ranging from 200 to 1,000 m; **C, F** released at depths ranging from 1,000 to 2,000 m).

flowing in. The annual mean dissolved oxygen concentration at site A increases significantly from ~14.4 to ~39.2 mmol·m^{-3} with higher oxygen-rich water, while it decreases significantly to ~6.0 mmol·m^{-3} with lower oxygen-rich water.

Site B, located in the central Arabian Sea, is hardly affected by the oxygen-rich water from the southern boundary (Figure 9). Despite variation in the oxygen level of water from the southern boundary, the dissolved oxygen concentration in the central Arabian Sea remains nearly constant. Previous Lagrangian particle tracking experiments also demonstrates that it is difficult for the water masses below 200 m from the southern boundary to enter the central Arabian Sea, but it can reach the northern Arabian Sea along the coast (Figure 6; You, 1997; Schott and McCreary, 2001; Rixen et al., 2014). Therefore, it can be concluded that the dissolved oxygen carried by oxygen-rich water from the southern boundary of the Arabian Sea plays an important role in regulating dissolved oxygen concentration in the western Arabian Sea, but has little effect on the central Arabian Sea.

3.4 Biological factors affecting the ASOMZ

The oxygen budget analysis indicates that the horizontal advection term acts as the main oxygen gain, and the oxygen consumption term is the main oxygen loss. The role of horizontal advection is demonstrated in the previous section. In this section, we investigate the effect of oxygen consumption.

Previous studies showed that oxygen consumption in the OMZ is mainly consumed by the remineralization of POM (McCreary et al., 2013; Acharya and Panigrahi, 2016), while the sinking velocity is the vital important factor to affect the

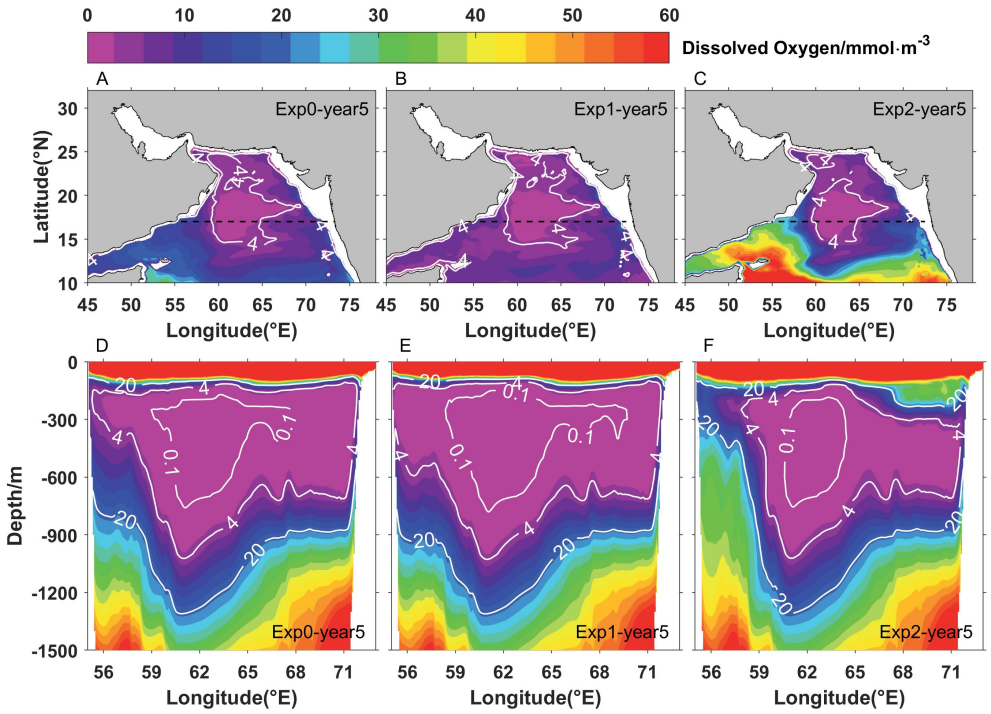

FIGURE 7
Annual mean horizontal distributions of dissolved oxygen **(A–C)** averaged between 200 and 1,000 m and vertical distributions of dissolved oxygen **(D–F)** in the upper 1,500 m at 17°N from three experiments (Exp0, Exp1, and Exp2) after 5 years of integration.

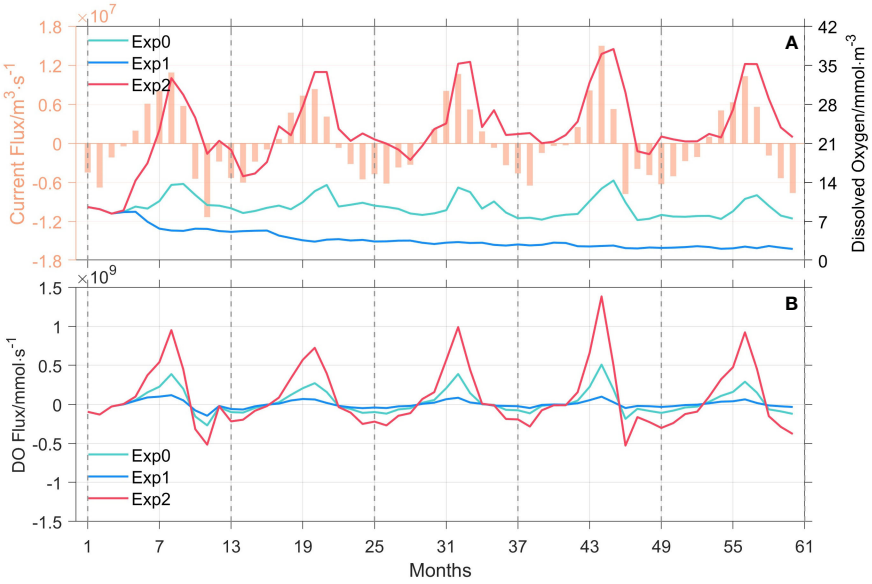

FIGURE 8
Current flux (**A**, orange bar, left *y*-axis) and dissolved oxygen concentration (**A**, line, right *y*-axis) near 11.8°N in the western side of the Arabian Sea (50°–55°E). Associated dissolved oxygen flux **(B)** averaged between 200 and 1,000 m near 11.8°N in the western side of the Arabian Sea from three experiments (Exp0, Exp1, and Exp2).

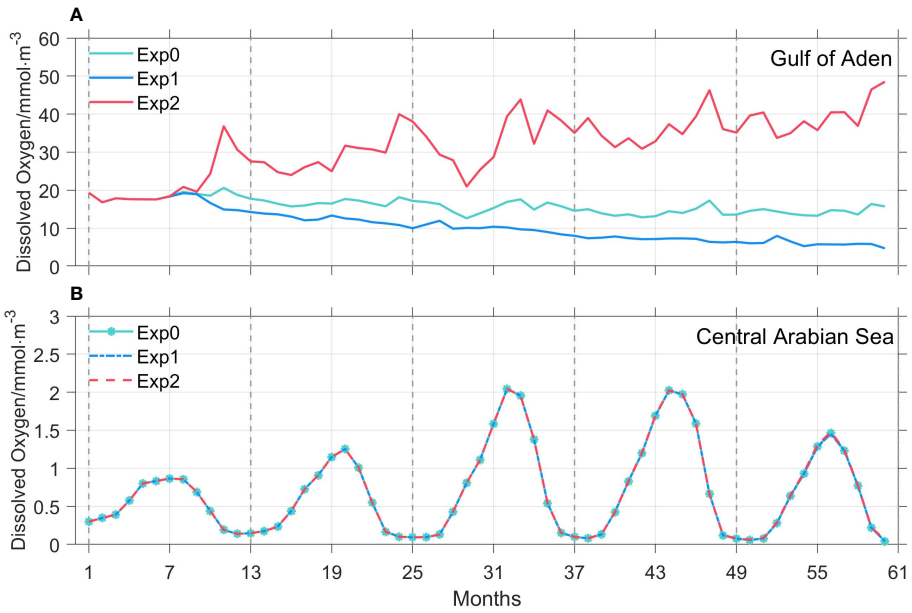

FIGURE 9
Time series of averaged dissolved oxygen concentration at site A (**A**; Gulf of Aden) and site B (**B**; central Arabian Sea) from three experiments (Exp0, Exp1, and Exp2).

fraction of POM remineralized in this zone. Consequently, two numerical experiments associated with different sinking velocity were conducted (see *Section 2.2*).

Unlike the experiments in which oxygen-rich water from the southern boundary of the Arabian Sea has a significant impact only in the high primary productivity region (Gulf of Aden) in the western Arabian Sea, variation in sinking velocity of POM affects the entire ASOMZ. Figure 10 depicts the annual mean horizontal distributions of dissolved oxygen averaged between 200 and 1,000 m and vertical distributions in the upper 1,500 m at 17°N in the three experiments (Exp0, Exp3, and Exp4). When the sinking velocity is reduced by a factor of 2 (Exp3), the suboxic area of the Arabian Sea contracts to approximately 60°E in the west, ~20°N in the north, and ~15°N in the south. The dissolved oxygen concentration at site A (Gulf of Aden) increases from ~14.4 to ~20.0 mmol·m^{-3}, while the concentration in site B (the central Arabian Sea) also increases from ~0.6 to ~1.2 mmol·m^{-3}. The vertical profile of dissolved oxygen also shows that the suboxic volume retreats from ~55°E to ~57°E in the Gulf of Aden. In the central Arabian Sea, the suboxic zone reduces from ~1,000 to ~900 m and microbial hypoxic zone reduces from ~1,300 to ~1,200 m.

When the sinking velocity is increased by a factor of 2 (Exp4), the suboxic area extends westward to ~58°E, southward to ~13°N, and northeastward to the coast of Pakistan. The dissolved oxygen concentration at site A decreases from ~14.4 to ~10.8 mmol·m^{-3}, and the concentration at site B also decreases from ~0.6 to ~0.5 mmol·m^{-3} (Figure 12). The vertical distribution of dissolved oxygen shows that the suboxic zone extends from ~1,000 to ~1,200 m and the microbial hypoxic zone extends from ~1,300 to ~1,400 m in the central Arabian Sea. The microbial hypoxic zone in the Gulf of Aden extends from 800 to 1,000 m, despite little change in the suboxic region.

POM consumed more dissolved oxygen at shallow depths when sinking velocity of POM decreased (Exp3), resulting in a shoaling of the ASOMZ (Mathew et al., 2021). On the contrary, the ASOMZ retracted vertically when sinking velocity increased (Exp4, Figures 10D-F). Depth variation of the upper boundary of the ASOMZ (DO = 60 mmol·m^{-3}) in sites A and B also shows this feature (Figure 11). The depth of upper boundary of the ASOMZ in the central Arabian Sea decreases from 60 to 45 m in late summer when the sinking velocity of POM decreased, and the boundary increases from 60 to 90 m when sinking velocity of POM increased. The depth of upper boundary in the Gulf of Aden becomes a little shallow in Exp3 and deepens to ~60 m in Exp4. Besides that, it is interesting to note that the variation of the depth of the upper boundary of the ASOMZ has significant seasonal cycle (Sudheesh et al., 2022). The upper boundary of the ASOMZ in the central Arabian Sea reaches the shallowest depth (~60 m) in late summer due to more POM, which generates from the high primary production in the summer monsoon, and consumes a large amount of dissolved oxygen in the upper water column. Then, it gradually deepens to ~85 m during the winter monsoon.

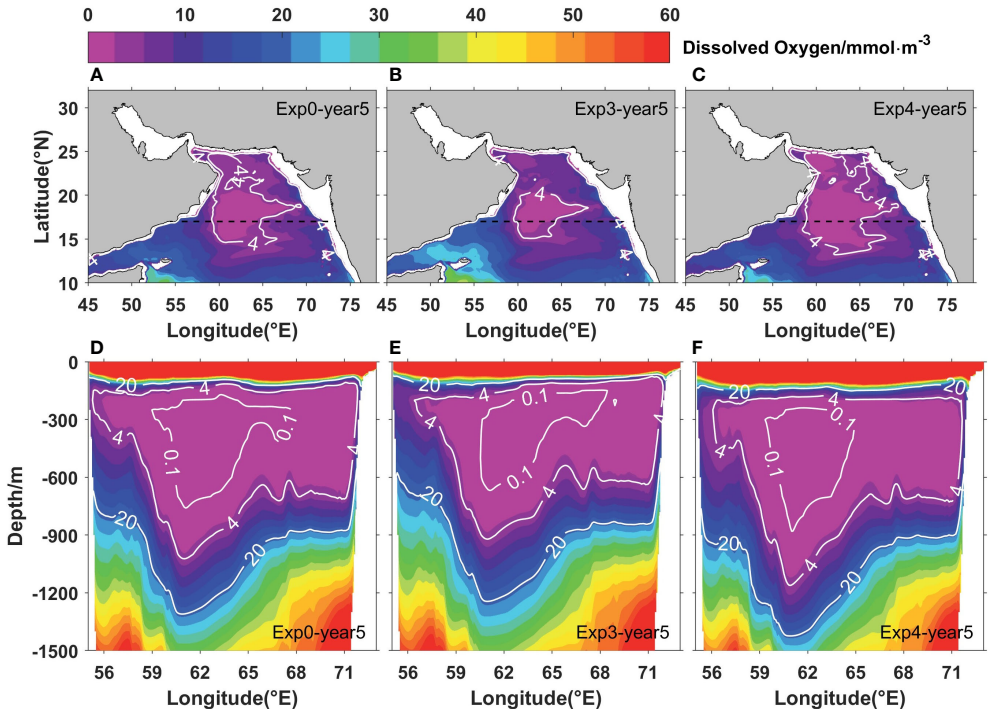

FIGURE 10
Annual mean horizontal distributions of dissolved oxygen **(A–C)** averaged between 200 and 1,000 m and vertical distributions of dissolved oxygen **(D–F)** in the upper 1,500 m at 17°N from three experiments (Exp0, Exp3, and Exp4) after 5 years of integration.

3.5 Variation of the ASOMZ

Previous studies demonstrated that both horizontal advection and oxygen consumption affect the ASOMZ. Therefore, we used sensitivity experiments (Exp0–Exp4) to calculate changes in the area and volume of the ASOMZ (Figure 13). For the microbial hypoxic zone (averaged DO between 200 and 1,000 m< 20 mmol·m^{-3}), its area expands to ~2.3 × 10^{12} m^2 as lower oxygen water enters the Arabian Sea, and then maintains it stably due to the whole Arabian Sea becomes a microbial hypoxic zone. Nevertheless, as more oxygen-rich water enters the Arabian Sea such that the annual mean dissolved oxygen flux rises approximately threefold, the microbial hypoxic area gradually drops to ~1.65 × 10^{12} m^2 after 5 years of integration, which is only ~72% of the control (Exp0). For the case of changes in oxygen consumption caused by variation of sinking velocity, when the sinking velocity is reduced to 2.5 m·day^{-1} and the POM flux at 200 m (F_{POM200}; Figure 12) decreases by ~45% from ~1.45 × 10^4 mg·C·m^{-2}·year^{-1} (Exp0) to ~7.95 × 10^3 mg·C·m^{-2}·year^{-1} (Exp3), the microbial hypoxic area gradually drops to ~2.11 × 10^{12} m^2, which is ~92% of the control (Exp0). When sinking velocity is increased to 10 m·day^{-1} and the F_{POM200} increases by 18% (Exp4), the microbial hypoxic area gradually expands to ~2.3 × 10^{12} m^2 and remains stable. A similar feature is observed in the variation of OMZ volume. The microbial hypoxic volume increases to ~3.80 × 10^{15} m^3 (Exp1) and ~3.62 × 10^{15} m^3 (Exp4), or increases by ~10% and ~5% compared to Exp0, respectively. The microbial hypoxic volume drops to ~2.68 × 10^{15} m^3 (Exp2) and ~3.11 × 10^{15} m^3 (Exp3), or decreases by ~22% and ~9% compared to Exp0, respectively.

For the suboxic zone (DO< 4 mmol·m^{-3}), a similar feature is more pronounced: the suboxic area (DO averaged between 200 and 1,000 m) gradually expands to ~8.09 × 10^{11} m^2 with lower oxygen water entering the Arabian Sea (Exp1), while it drops to ~4.83 × 10^{11} m^2 with higher oxygen-rich water entering the Arabian Sea (Exp2), or increases by ~19% and decreases by ~29% compared to Exp0, respectively. Meanwhile, the suboxic volume climbs to ~2.33 × 10^{15} m^3 (Exp1) and falls to ~1.35 × 10^{15} m^3 (Exp2), or increases by ~26% and decreases ~27% compared to Exp0, respectively. On the other hand, the variation of sinking velocity suggests that the suboxic area drops to ~3.82 × 10^{11} m^2 when sinking velocity decreases by a factor of 2 (Exp3), yet it expands to ~8.98 × 10^{11} m^2 when sinking velocity increases by a factor of 2 (Exp4), or decreases by ~44% and increases by ~32% compared to Exp0, respectively. Moreover, the suboxic volume decreases to ~1.59 × 10^{15} m^3 in Exp3 compared to Exp0, or decreases by ~14%, and the suboxic volume remains virtually the same in Exp4 because the average dissolved

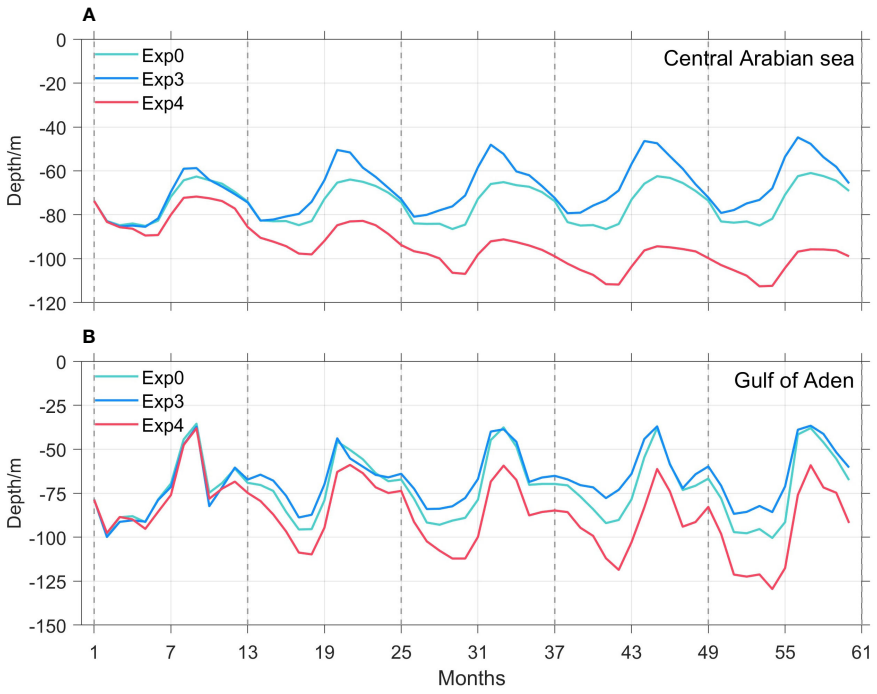

FIGURE 11
Time series of the upper boundary of the ASOMZ at site A (**A**; central Arabian Sea) and site B (**B**; Gulf of Aden) from three experiments (Exp0, Exp3, and Exp4).

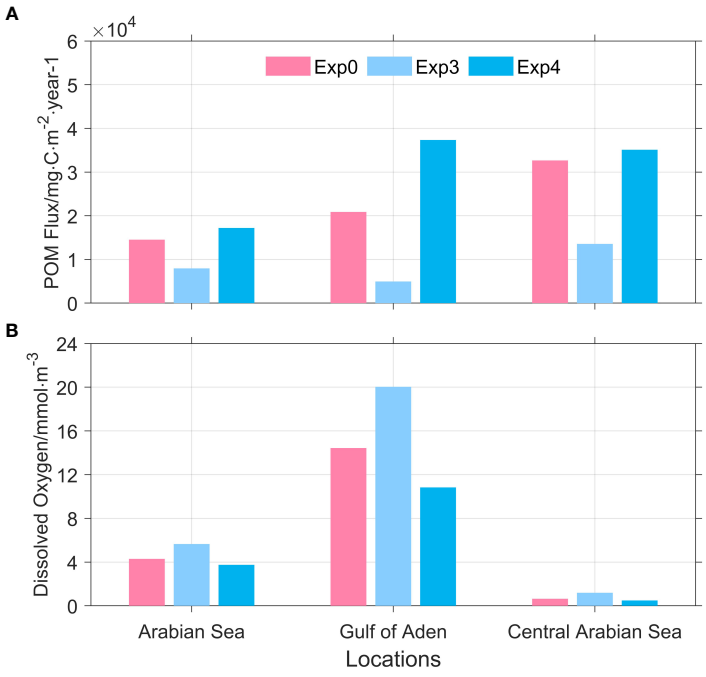

FIGURE 12
POM flux at 200 m **(A)**, dissolved oxygen average concentration ranging from 200 to 1,000 m **(B)** in the Arabian Sea (left column), site A (middle column; Gulf of Aden) and site B (right column; central Arabian Sea) from three experiments (Exp0, Exp3, and Exp4).

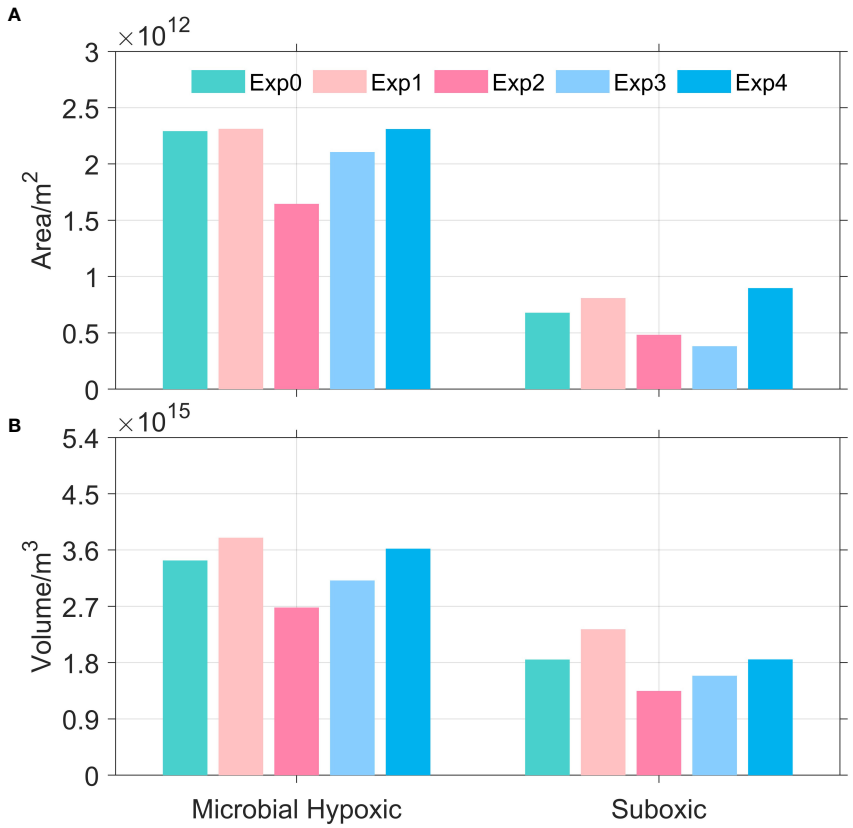

FIGURE 13
Changes in area **(A)** and volume **(B)** of microbial hypoxic zone (DO< 20 mmol·m^{-3}; left column) and suboxic zone (DO< 4 mmol·m^{-3}; right column) from five experiments (Exp0 to Exp4).

oxygen concentration of the Arabian Sea at the intermediate depth is nearly 4 mmol·m^{-3}.

4 Discussion

4.1 Source regions of POM

To better understand the effect of POM sinking on the formation of the ASOMZ, some idealized experiments to trace the source of the POM were performed (details in *Section 2.2* and supplement; see Table 1). To further study the contribution of different source regions in the central Arabian Sea, the POM results were adjusted according to the concentration of chlorophyll in the source regions. The POM in the Gulf of Aden is primarily derived from local productivity, particularly the bloom in the summer, while ~15% of POM from the winter bloom off the Oman coast is detected in the Gulf of Aden (Figure 14). The summer bloom off the Oman coast contributed ~14% of summer POM in the central Arabian Sea, and all winter POM in the central Arabian Sea are from the local winter bloom productivity. On the other hand, although the surface primary production of the central Arabian Sea is low in the summer monsoon, POM from the western Arabian Sea high primary productivity region (Oman Coast) due to the offshore Ekman transport still consumes dissolved oxygen in the central Arabian Sea intermediate layer (Rixen et al., 2006). Combined oxygen consumption of POM from summer bloom and winter bloom could be one of the reasons for the significant seasonal cycle of chlorophyll in the surface layer and the weaker seasonal variation of ASOMZ distribution in the intermediate layer.

After the winter bloom, when the sinking velocity is decreased by a factor of 2 (Exp3), the POM in the Gulf of Aden is mainly derived from local productivity (~65%) and Oman coast (~34%), and the POM in the central Arabian Sea is entirely derived from local productivity. However, part of the POM detected in the Gulf of Aden come from the primary production off the Oman coast after 6 months of POM release under the influence of winter circulation. Meanwhile, majority of the POM (~53%) in the central Arabian Sea is from the summer bloom off the Oman coast due to Ekman transport, followed by POM originated from the Gulf of Aden and local productivity indigenous output. Furthermore, when the sinking velocity is doubled (Exp4), the

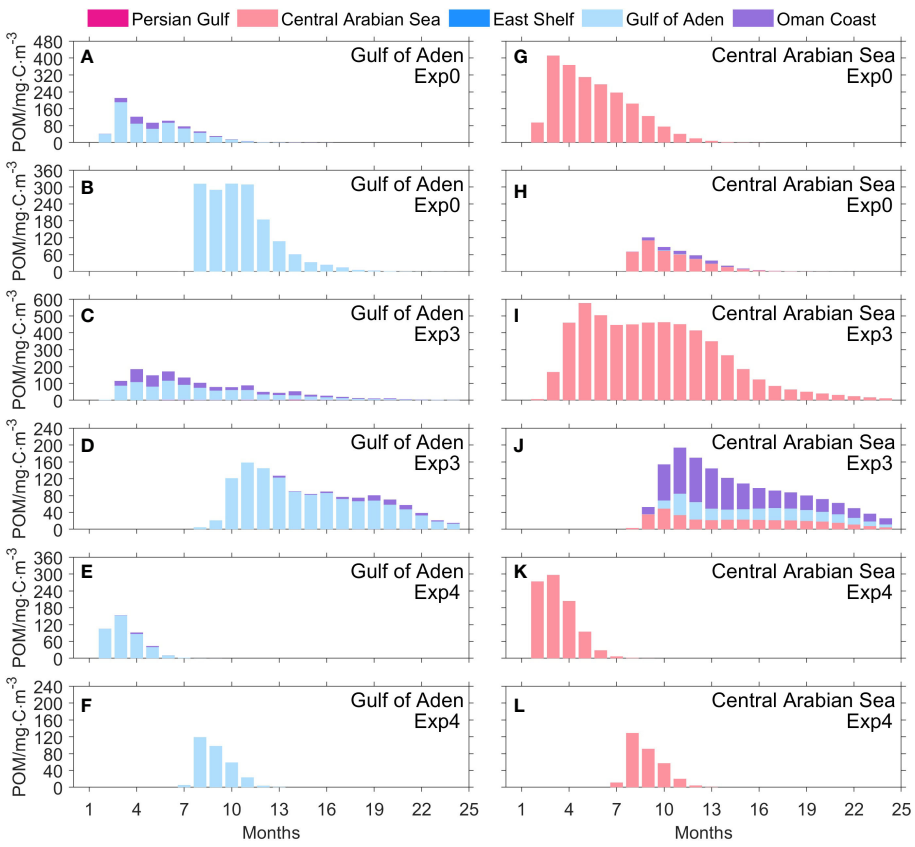

FIGURE 14
Variations and source regions of POM concentration at site A (**A–F**; Gulf of Aden) and site B (**G–L**; central Arabian Sea). POM was released from the five locations (Figure S2) with constant values in different released seasons (**A, C, E, G, I, K**, POM released in December; **B, D, F, H, J, L**, POM released in June). The POM model results were adjusted according to the concentration of chlorophyll in the source regions.

POM is primarily sourced from local productivity, regardless of the summer or winter monsoon season and regardless of the location, in both the Gulf of Aden and the central Arabian Sea. These results of the change in sinking velocity represent the transport of POM of different sizes generated by various community compositions (Wiggert and Murtugudde, 2007; Hood et al., 2009; McCreary et al., 2013; Acharya and Panigrahi, 2016; Chowdhury et al., 2021). Huge species produce large POM with fast sinking velocity, while small species produce small POM with slow sinking velocity. However, it is worth noting that POM originating from other regions will be smaller than the estimated value mentioned above in reality due to remineralization, fragmentation, and other removal processes.

4.2 Mechanism of the ASOMZ's decoupling

The Lagrangian particle experiments suggest that oxygen-rich water from the southern boundary of the Arabian Sea has a significant effect on regulating the dissolved oxygen concentration in the high primary productivity region (Gulf of Aden) on the western side of the Arabian Sea during the summer monsoon (Figure S7), especially in the intermediate water (200–1,000 m) where the ASOMZ is located (Figure S9). The POM detected in the Gulf of Aden is mainly derived from local primary productivity and indigenous output. It will be remineralized in the sinking process over the next few months, which continuously consumes dissolved oxygen in the Gulf of Aden (Figure 14). Meanwhile, during the summer monsoon, the oxygen-rich intermediate water is replenished to relieve dissolved oxygen depletion in high primary productivity regions, resulting in higher dissolved oxygen concentration on the western side of the Arabian Sea (Gulf of Aden) relative to the other regions (Figure 10). Otherwise, if the dissolved oxygen replenishment from the southern oxygen-rich intermediate water gradually decreased with global climate change, the dissolved oxygen concentration in the high primary productivity region would gradually decrease. In that case, the ASOMZ may move westward.

The Lagrangian particle experiments also suggest that it is difficult for the oxygen-rich water from the southern boundary of the Arabian Sea to enter the central Arabian Sea, and that the component that could enter the central Arabian Sea is the low oxygen water after passing through the high primary productivity regions (Figure 6). As a result, oxygen-rich water from the southern boundary of the Arabian Sea is not effective at replenishing dissolved oxygen in the central Arabian Sea. The dissolved oxygen concentration in the central Arabian Sea is more influenced by sinking POM and its remineralization process. The POM, affecting the central Arabian Sea, mainly originates from the high primary productivity regions on the western side of the Arabian Sea during the summer monsoon and its local production in the central Arabian Sea during the winter monsoon (Figure 14).

4.3 Limitations of this study

This study still has several limitations. For instance, the 15-year model spin-up may not be long enough to decrease the dissolved oxygen drift to exactly zero. As a result, it may lead to long-term accumulated errors that the simulated dissolved oxygen has an overall bias in the long-term integration. However, only the model results of the last year are used for analysis. Besides that, 15-year model spin-up is not particularly short due to technical difficulty. Hence, we expect the major conclusions of this study to stay unchanged under a longer spin-up time. Similarly, the 5-year simulation for sensitivity experiments, which is derived from the particles transit time, may not be long enough to fully address the ventilation of the ASOMZ. It may underestimate the dissolved oxygen concentration in the central Arabian Sea when analyzing sensitivity experiments. In the following study, longer spin-up may be needed for model drift stability and longer simulation time of the Lagrangian particle tracking experiment may be needed for more transit time of oxygen-rich water masses from the southern boundary of the Arabian Sea. Consequently, simulation time of sensitivity experiments may be extended for ventilation of the ASOMZ.

Besides that, several studies suggest that Persian Gulf water (PGW) and Red Sea Water (RSW) play a significant role in ventilating the ASOMZ (e.g., Lachkar et al., 2019). These oxygen-rich water masses can reach the western side of the Arabian Sea to replenish the dissolved oxygen depletion there (Schmidt et al., 2020). However, considering that the flow of PGW (~0.1 Sv) and RSW (~0.3 Sv) is much smaller than the Somali coastal current (~10 Sv, Schott et al., 1990; Schott and McCreary, 2001), they are not included in this study for this reason. Moreover, some new mechanisms have also not been considered in this study, for instance, the contribution of poorly ventilated waters to the ASOMZ due to the lack of mesoscale mixing (McCreary et al., 2013; Schmidt et al., 2020) and the effect of oxygen consumption by remineralization of organic matter originating from the eastern Arabian Sea shelf on ASOMZ (Sarma et al., 2020). In addition, increased primary productivity due to the eastward transport of excess upwelled nutrients induced by iron limitation in the western Arabian Sea thus intensifies the OMZ in the central/northern Arabian Sea (Moffett and Landry, 2020). Consequently, the lack of iron in the model may lead to higher primary productivity in the western Arabian Sea, and less nutrients are transported to the central/northern Arabian Sea, weakening the intensity of the ASOMZ there.

Notwithstanding these limitations, analysis of the inflow of oxygen-rich water and sinking velocity of POM in this study further deepens the understanding of the position decoupling of ASOMZ and phytoplankton productive zone.

5 Conclusions

In this study, we investigated the effects of the oxygen-rich water from the southern boundary of the Arabian Sea and the sinking velocity of POM on the decoupling of the ASOMZ, through a coupled physical–biogeochemical model. The oxygen budget analysis confirms that horizontal advection acts as the main (~71%) oxygen gain and oxygen consumption acts as the main (~70%) oxygen loss. The results of Lagrangian particle experiments suggest that the oxygen-rich intermediate water (200–1,000 m) from the southern boundary of the Arabian Sea enters the Arabian Sea along the west coast, but hardly enters the central Arabian Sea.

Sensitivity tests suggest that if annual mean dissolved oxygen flux increased by threefold, the dissolved oxygen concentration in the Gulf of Aden would increase by three times, and it would remain fairly steady in the central Arabian Sea. Unlike oxygen-rich water, variation in sinking velocity of POM affects the entire ASOMZ. Reduced sinking velocity of POM would alleviate the depletion of dissolved oxygen in the central Arabian Sea, and POM from the western Arabian Sea could have higher probability to reach the central Arabian Sea.

The oxygen-rich water from the southern boundary of the Arabian Sea effectively mitigates the dissolved oxygen consumption caused by remineralization of POM in the western Arabian Sea high primary productivity regions. However, not only the central Arabian Sea is less ventilated by the oxygen-rich water from the southern boundary of the Arabian Sea, but also the POMs are remineralized to consume local dissolved oxygen, which are from the high primary productivity regions (Oman Coast) on the west side and transported to the central Arabian Sea in summer bloom and are from local productivity in winter bloom. In other words, more dissolved oxygen replenishment occurs in the western Arabian Sea, and more dissolved oxygen consumption and fewer dissolved oxygen replenishment take place in the central Arabian Sea, which are responsible for the position decoupling of the ASOMZ and phytoplankton productive zone. This also explains why the ASOMZ variation is weaker than the significant seasonal cycle of surface chlorophyll in the Arabian Sea.

Data availability statement

Publicly available datasets were analyzed in this study. This data can be found here: *In-situ* Observation data used in this study is provided by the project "the I07N cruise supported by the Global Ocean Ship-Based Hydrographic Investigation Program (GO-SHIP)", from the Clivar and Carbon Hydrographic Data Office (CCHDO; https://cchdo.ucsd.edu). The sea surface wind and heat flux data obtained from ECMWF are available at http://apps.ecmwf.int/datasets/. Initial and open ocean boundary conditions are provided by SODA at https://www.soda.umd.edu/. Tidal constituents are obtained from the TPXO7.2 (https://www.tpxo.net/). Monthly mean discharges of major rivers are derived from the Global Runoff Data Centre (GRDC, http://grdc.bafg.de) and Global River Discharge Database (https://sage.nelson.wisc.edu/riverdata/). WOA18 datasets are available online (https://www.ncei.noaa.gov/access/world-ocean-atlas-2018/). The sea-surface climatological current is from the Drifter-Derived Climatology of Global Near-Surface Currents (https://www.aoml.noaa.gov/phod/gdp/animations.php). Sea-surface height (SSH) anomalies are from the SSALTO/DUACS multimission altimeter products from the Archiving, Validation and Interpretation of Satellite Oceanographic data (AVISO; http://www.aviso.altimetry.fr). Mean chlorophyll concentration data are from the Moderate Resolution Imaging Spectroradiometer (MODIS; https://modis.gsfc.nasa.gov). SST data are from the Optimum Interpolation Sea Surface Temperature, (OISST; https://www.ncei.noaa.gov/products/optimum-interpolation-sst).

Author contributions

ZZ: investigation and writing. WM and FC: design of the study and review of the manuscript. All authors contributed to the article and approved the submitted version.

Funding

This study was jointly supported by the Southern Marine Science and Engineering Guangdong Laboratory (Zhuhai) (Grant No. SML2020SP008), the Strategic Priority Research Program, Chinese Academy of Sciences, China (Grant No. XDB42000000), the National Natural Science Foundation of China (Nos. 41876123, 42276063), and Global Change and Air–Sea Interaction Program Phase II ["Joint Advanced Marine and Ecological Studies in the Bay of Bengal and the eastern equatorial Indian Ocean (JAMES)", Grant No. GASI-01-EIND-STwin].

Conflict of interest

The authors declare that the research was conducted in the absence of any commercial or financial relationships that could be construed as a potential conflict of interest.

Publisher's note

All claims expressed in this article are solely those of the authors and do not necessarily represent those of their affiliated organizations, or those of the publisher, the editors and the reviewers. Any product that may be evaluated in this article, or claim that may be made by its manufacturer, is not guaranteed or endorsed by the publisher.

Supplementary material

The Supplementary Material for this article can be found online at: https://www.frontiersin.org/articles/10.3389/fmars.2022.927921/full#supplementary-material

References

Acharya, S. S., and Panigrahi, M. K. (2016). Eastward Shift and maintenance of Arabian Sea oxygen minimum zone: Understanding the paradox. *Deep Sea Res. Part I: Oceanogr. Res. Pap.* 115, 240–252. doi: 10.1016/j.dsr.2016.07.004

Ahsan, A. Q., and Blumberg, A. F. (1999). Three-dimensional hydrothermal model of Onondaga lake, new York. *J. Hydraul. Eng.* 125 (9), 912–923. doi: 10.1061/(ASCE)0733-9429(1999)125:9(912)

Al Azhar, M., Lachkar, Z., Levy, M., and Smith, S. (2017). Oxygen minimum zone contrasts between the Arabian Sea and the bay of Bengal implied by differences in remineralization depth. *Geophys. Res. Lett.* 44 (21), 11,106–111,114. doi: 10.1002/2017GL075157

Anderson, T. R., Ryabchenko, V. A., Fasham, M. J., and Gorchakov, V. A. (2007). Denitrification in the Arabian Sea: A 3D ecosystem modelling study. *Deep Sea Res. Part I: Oceanogr. Res. Pap.* 54 (12), 2082–2119. doi: 10.1016/j.dsr.2007.09.005

Anju, M., Sreeush, M. G., Valsala, V., Smitha, B. R., Hamza, F., Bharathi, G., et al. (2020). Understanding the role of nutrient limitation on plankton biomass over Arabian Sea via 1-d coupled biogeochemical model and bio-argo observations. *J. Geophys. Res.: Oceans* 125 (6), e2019JC015502. doi: 10.1029/2019JC015502

Bianchi, T. S., DiMarco, S. F., Cowan, J.Jr., Hetland, R. D., Chapman, P., Day, J., et al. (2010). The science of hypoxia in the northern gulf of Mexico: A review. *Sci. Total Environ.* 408 (7), 1471–1484. doi: 10.1016/j.scitotenv.2009.11.047

Bianchi, D., Dunne, J. P., Sarmiento, J. L., and Galbraith, E. D. (2012). *Data-based estimates of suboxia, denitrification, and N2O production in the ocean and their sensitivities to dissolved O2* (Global Biogeochemical Cycles). 26(2). doi: 10.1029/2011GB004209

Bindoff, N. L., Cheung, W. W., Kairo, J. G., ArÃstegui, J., Guinder, V. A., and Hallberg, R. (2019). "Changing ocean, marine ecosystems, and dependent communities," in H.-O. Pörtner, D.C. Roberts, V. Masson-Delmotte, P. Zhai, M. Tignor, E. Poloczanska, et al. (Eds.) *IPCC special report on the ocean and cryosphere in a changing climate*, Switzerland: Intergovernmental Panel on Climate Change 477–587.

Breitburg, D., Levin, L. A., Oschlies, A., GrÃ©goire, M., Chavez, F. P., and Conley, D. J. (2018). Declining oxygen in the global ocean and coastal waters. *Science* 359 (6371), eaam7240. doi: 10.1126/science.aam7240

Carton, J. A., and Giese, B. S. (2008). A reanalysis of ocean climate using simple ocean data assimilation (SODA). *Monthly weather Rev.* 136 (8), 2999–3017. doi: 10.1175/2007MWR1978.1

Chai, F., Dugdale, R., Peng, T.-H., Wilkerson, F., and Barber, R. (2002). One-dimensional ecosystem model of the equatorial pacific upwelling system. part I: Model development and silicon and nitrogen cycle. *Deep Sea Res. Part II: Topical Stud. Oceanogr.* 49 (13-14), 2713–2745. doi: 10.1016/S0967-0645(02)00055-3

Chowdhury, M., Biswas, H., Mitra, A., Silori, S., Sharma, D., and Bandyopadhyay, D. (2021). Southwest monsoon-driven changes in the phytoplankton community structure in the central Arabian Se–2018): After two decades of JGOFS. *Prog. Oceanogr.* 197, 102654. doi: 10.1016/j.pocean.2021.102654

Diaz, R. J., and Rosenberg, R. (2008). Spreading dead zones and consequences for marine ecosystems. *Science* 321 (5891), 926–929. doi: 10.1126/science.1156401

Egbert, G. D., and Erofeeva, S. Y. (2002). Efficient inverse modeling of barotropic ocean tides. *J. Atmospheric Oceanic Technol.* 19 (2), 183–204. doi: 10.1175/1520-0426(2002)019<0183:EIMOBO>2.0.CO;2

Garcia, H., Weathers, K., Paver, C., Smolyar, I., Boyer, T., Locarnini, M., et al. (2019). *World ocean atlas 2018, volume 3: Dissolved oxygen, apparent oxygen utilization, and dissolved oxygen saturation*. NOAA Atlas NESDIS 83, 38pp. Available at: https://archimer.ifremer.fr/doc/00651/76337/

Gilly, W. F., Beman, J. M., and Litvin, S. Y. (2013). Oceanographic and biological effects of shoaling of the oxygen minimum zone. *Annu. Rev. Of Mar. Sci.* 5 (1), 393–420. doi: 10.1146/annurev-marine-120710-100849

Honjo, S., Dymond, J., Prell, W., and Ittekkot, V. (1999). Monsoon-controlled export fluxes to the interior of the Arabian Sea. *Deep Sea Res. Part II: Topical Stud. Oceanography* 46 (8-9), 1859–1902. doi: 10.1016/S0967-0645(99)00047-8

Hood, R. R., Wiggert, J. D., and Naqvi, S. W. A. (2009). Indian Ocean research: Opportunities and challenges. *Geophysical Monograph Ser.*, 409–429. doi: 10.1029/2008GM000714

Ito, T., Minobe, S., Long, M. C., Deutsch, C., Shenoy, D. M., Suresh, I., et al. (2017). Upper ocean O2 trends: 1958-2015 variability of dissolved oxygen in the Arabian Sea oxygen minimum zone and its driving mechanisms. *Geophys. Res. Lett.* 44 (9), 4214–4223. doi: 10.1002/2017GL073613

Kamykowski, D., and Zentara, S.-J. (1990). Hypoxia in the world ocean as recorded in the historical data set. *Deep Sea Res. Part A. Oceanogr. Res. Pap.* 37 (12), 1861–1874. doi: 10.1016/0198-0149(90)90082-7

Karstensen, J., Stramma, L., and Visbeck, M. (2008). Oxygen minimum zones in the eastern tropical Atlantic and pacific oceans. *Prog. In Oceanogr.* 77 (4), 331–350. doi: 10.1016/j.pocean.2007.05.009

Keeling, R. F., Kortzinger, A., and Gruber, N. (2010). Ocean deoxygenation in a warming world. *Annu. Rev. Mar. Sci.* 2, 199–229. doi: 10.1146/annurev.marine.010908.163855

Kim, H. S., Flagg, C. N., and Howden, S. D. (2001). Northern Arabian Sea variability from TOPEX/Poseidon altimetry data: An extension of the US JGOFS/ONR shipboard ADCP study. *Deep Sea Res. Part II: Topical Stud. Oceanography* 48 (6-7), 1069–1096. doi: 10.1016/S0967-0645(00)00131-4

Lachkar, Z., Levy, M., and Smith, S. (2018). Intensification and deepening of the Arabian Sea oxygen minimum zone in response to increase in Indian monsoon wind intensity. *Biogeosciences* 15 (1), 159–186. doi: 10.5194/bg-15-159-2018

Lachkar, Z., Levy, M., and Smith, K. S. (2019). Strong intensification of the Arabian Sea oxygen minimum zone in response to Arabian gulf warming. *Geophys. Res. Lett.* 46 (10), 5420–5429. doi: 10.1029/2018GL081631

Lachkar, Z., Mehari, M., Al Azhar, M., Levy, M., and Smith, S. (2021). Fast local warming is the main driver of recent deoxygenation in the northern Arabian Sea. *Biogeosciences* 18 (20), 5831–5849. doi: 10.5194/bg-18-5831-2021

Lachkar, Z., Smith, S., Levy, M., and Pauluis, O. (2016). Eddies reduce denitrification and compress habitats in the Arabian Sea. *Geophys. Res. Lett.* 43 (17), 9148–9156. doi: 10.1002/2016GL069876

Laffoley, D., and Baxter, J. M. (2019). *Ocean deoxygenation: Everyone's problem-causes, impacts, consequences and solutions* (Switzerland: IUCN Gland).

Large, W. G., McWilliams, J. C., and Doney, S. C. (1994). Oceanic vertical mixing: A review and a model with a nonlocal boundary layer parameterization. *Rev. geophys.* 32 (4), 363–403. doi: 10.1029/94RG01872

Laurindo, L. C., Mariano, A. J., and Lumpkin, R. (2017). An improved near-surface velocity climatology for the global ocean from drifter observations. *Deep Sea Res. Part I: Oceanogr. Res. Pap.* 124, 73–92. doi: 10.1016/j.dsr.2017.04.009

Levin, L. A., and Breitburg, D. L. (2015). Linking coasts and seas to address ocean deoxygenation. *Nat. Climate Change* 5 (5), 401–403. doi: 10.1038/nclimate2595

Levin, L. A., Whitcraft, C. R., Mendoza, G. F., Gonzalez, J. P., and Cowie, G. (2009). Oxygen and organic matter thresholds for benthic faunal activity on the Pakistan margin oxygen minimum zone (700¨C1100 m). *Deep Sea Res. Part II: Topical Stud. Oceanogr.* 56 (6-7), 449–471. doi: 10.1016/j.dsr2.2008.05.032

Liang, L., Xue, H., and Shu, Y. (2019). The Indonesian throughflow and the circulation in the banda Sea: A modeling study. *J. Geophys. Res.: Oceans* 124 (5), 3089–3106. doi: 10.1029/2018JC014926

Liu, G., and Chai, F. (2009). Seasonal and interannual variability of primary and export production in the south China Sea: A three-dimensional physicalâ€"biogeochemical model study. *ICES J. Mar. Sci.* 66 (2), 420–431. doi: 10.1093/icesjms/fsn219

Lluch-Cota, S. E., Aragon-Noriega, E. A., Arreguin-Sanchez, F., Aurioles-Gamboa, D., Bautista-Romero, J. J., Brusca, R. C., et al. (2007). The gulf of California: review of ecosystem status and sustainability challenges. *Prog. In Oceanogr.* 73 (1), 1–26. doi: 10.1016/j.pocean.2007.01.013

Mathew, T., Prakash, S., Shenoy, L., Chatterjee, A., Bhaskar, T. U., and Wojtasiewicz, B. (2021). Observed variability of monsoon blooms in the north-central Arabian Sea and its implication on oxygen concentration: A bio-argo study. *Deep Sea Res. Part II: Topical Stud. Oceanogr.* 184, 104935. doi: 10.1016/j.dsr2.2021.104935

Ma, W., Xiu, P., Chai, F., and Li, H. (2019). Seasonal variability of the carbon export in the central south China Sea. *Ocean Dynam.* 69 (8), 955–966. doi: 10.1007/s10236-019-01286-y

McCreary, J., Murtugudde, R., Vialard, J., Vinayachandran, P., Wiggert, J. D., and Hood, R. R. (2009). Biophysical processes in the Indian ocean. *Indian Ocean biogeochem. proc. Ecol. variability* 185, 9–32.

McCreary, J. J.P., Yu, Z., Hood, R. R., Vinaychandran, P., Furue, R., Ishida, A., et al. (2013). Dynamics of the Indian-ocean oxygen minimum zones. *Prog. In Oceanogr.* 112, 15–37. doi: 10.1016/j.pocean.2013.03.002

Moffett, J. W., and Landry, M. R. (2020). Grazing control and iron limitation of primary production in the Arabian Sea: Implications for anticipated shifts in southwest monsoon intensity. *Deep Sea Res. Part II: Topical Stud. Oceanogr.* 179, 104687. doi: 10.1016/j.dsr2.2019.104687

Morrison, J. M., Codispoti, L., Gaurin, S., Jones, B., Manghnani, V., and Zheng, Z. (1998). Seasonal variation of hydrographic and nutrient fields during the US JGOFS Arabian Sea process study. *Deep Sea Res. Part II: Topical Stud. Oceanogr.* 45 (10-11), 2053–2101. doi: 10.1016/S0967-0645(98)00063-0

Murphy, A. H. (1988). Skill scores based on the mean square error and their relationships to the correlation coefficient. *Monthly weather Rev.* 116 (12), 2417–2424. doi: 10.1175/1520-0493(1988)116<2417:SSBOTM>2.0.CO;2

Naqvi, S., Naik, H., Pratihary, A., D'souza, W., Narvekar, P., and Jayakumar, D. (2006). Coastal versus open-ocean denitrification in the Arabian Sea. *Biogeosciences* 3 (4), 621–633. doi: 10.5194/bg-3-621-2006

Naqvi, W. A. (1991). Geographical extent of denitrification in the Arabian Sea in relation to some physical processes. *Oceanologica Acta* 14 (3), 281–290. Available at: https://archimer.ifremer.fr/doc/00101/21257/

Naqvi, S. W. A., Moffett, J. W., Gauns, M. U., Narvekar, P. V., Pratihary, A. K., Naik, H., et al. (2010). The Arabian Sea as a high-nutrient, low-chlorophyll region during the late Southwest Monsoon. *Biogeosciences* 7, 2091–2100. doi: 10.5194/bg-7-2091-2010

Rabalais, N. N., Cai, W.-J., Carstensen, J., Conley, D. J., Fry, B., and Hu, X. (2014). Eutrophication-driven deoxygenation in the coastal ocean. *Oceanography* 27 (1), 172–183. doi: 10.5670/oceanog.2014.21

Rabalais, N. N., Turner, R. E., and Wiseman, W. J.Jr. (2002). Gulf of Mexico hypoxia, aka the dead zone. *Annu. Rev. Ecol. Systematics* 33 (1), 235–263. doi: 10.1146/annurev.ecolsys.33.010802.150513

Resplandy, L., Levy, M., Bopp, L., Echevin, V., Pous, S., Sarma, V., et al. (2012). Controlling factors of the oxygen balance in the Arabian sea's OMZ. *Biogeosciences* 9 (12), 5095–5109. doi: 10.5194/bg-9-5095-2012

Reynolds, R. W., Smith, T. M., Liu, C., Chelton, D. B., Casey, K. S., and Schlax, M. G. (2007). Daily high-resolution-blended analyses for sea surface temperature. *J. Climate* 20 (22), 5473–5496. doi: 10.1175/2007JCLI1824.1

Rixen, T., Baum, A., Gaye, B., and Nagel, B. (2014). Seasonal and interannual variations in the nitrogen cycle in the Arabian Sea. *Biogeosciences* 11 (20), 5733–5747. doi: 10.5194/bg-11-5733-2014

Rixen, T., Cowie, G., Gaye, B., Goes, J., do RosÃ¡rio Gomes, H., and Hood, R. R. (2020). Reviews and syntheses: Present, past, and future of the oxygen minimum zone in the northern Indian ocean. *Biogeosciences* 17 (23), 6051–6080. doi: 10.5194/bg-17-6051-2020

Rixen, T., Goyet, C., and Ittekkot, V. (2006). Diatoms and their influence on the biologically mediated uptake of atmospheric CO2 in the Arabian Sea upwelling system. *Biogeosciences* 3 (1), 1–13. doi: 10.5194/bg-3-1-2006

Sarma, V. (2002). An evaluation of physical and biogeochemical processes regulating perennial suboxic conditions in the water column of the Arabian Sea. *Global Biogeochem. Cycles* 16 (4), 29–21-29-11. doi: 10.1029/2001GB001461

Sarma, V., Bhaskar, T. U., Kumar, J. P., and Chakraborty, K. (2020). Potential mechanisms responsible for occurrence of core oxygen minimum zone in the

north-eastern Arabian Sea. *Deep Sea Res. Part I: Oceanogr. Res. Pap.* 165, 103393. doi: 10.1016/j.dsr.2020.103393

Schmidt, H., Czeschel, R., and Visbeck, M. (2020). Seasonal variability of the Arabian Sea intermediate circulation and its impact on seasonal changes of the upper oxygen minimum zone. *Ocean Sci.* 16 (6), 1459–1474. doi: 10.5194/os-16-1459-2020

Schmidtko, S., Stramma, L., and Visbeck, M. (2017). Decline in global oceanic oxygen content during the past five decades. *Nature* 542 (7641), 335–339. doi: 10.1038/nature21399

Schott, F. A., and McCreary, J. J.P. (2001). The monsoon circulation of the Indian ocean. *Prog. In Oceanogr.* 51 (1), 1–123. doi: 10.1016/S0079-6611(01)00083-0

Schott, F., Swallow, J. C., and Fieux, M. (1990). The Somali Current at the equator: Annual cycle of currents and transports in the upper 1000 m and connection to neighbouring latitudes. *Deep Sea Res. Part A. Oceanographic Res. Papers* 37 (12), 1825–1848. doi: 10.1016/0198-0149(90)90080-F

Shenoy, D. M., Suresh, I., Uskaikar, H., Kurian, S., Vidya, P. J., Shirodkar, G., et al. (2020). Variability of dissolved oxygen in the Arabian Sea Oxygen Minimum Zone and its driving mechanisms. *J. Marine Syst.* 204, 103310. doi: 10.1016/j.jmarsys.2020.103310

Shchepetkin, A. F., and McWilliams, J. C. (2003). A method for computing horizontal pressure gradient force in an oceanic model with a nonaligned vertical coordinate. *J. Geophys. Res.: Oceans* 108 (C3), 3090. doi: 10.1029/2001JC001047

Shchepetkin, A. F., and McWilliams, J. C. (2005). The regional oceanic modeling system (ROMS): A split-explicit, free-surface, topography-following-coordinate oceanic model. *Ocean Model.* 9 (4), 347–404. doi: 10.1016/j.ocemod.2004.08.002

Smagorinsky, J. (1963). General circulation experiments with the primitive equations: I. *basic experiment Monthly weather Rev.* 91 (3), 99–164. doi: 10.1175/1520-0493(1963)091<0099:GCEWTP>2.3.CO;2

Stramma, L., Johnson, G. C., Sprintall, J., and Mohrholz, V. (2008). Expanding oxygen-minimum zones in the tropical oceans. *Science* 320 (5876), 655–658. doi: 10.1126/science.1153847

Sudheesh, V., Gupta, G. V. M., Reddy, Y., Bepari, K. F., Chari, N. V. H. K., and Sherin, C. K. (2022). Oxygen minimum zone along the eastern Arabian Sea: Intra-annual variation and dynamics based on ship-borne studies. *Prog. Oceanogr.* 201, 102742. doi: 10.1016/j.pocean.2022.102742

Taylor, K. E. (2001). Summarizing multiple aspects of model performance in a single diagram. *J. Geophysical Research: Atmospheres* 106 (D7), 7183–7192. doi: 10.1029/2000JD900719

Tiano, L., Garcia-Robledo, E., Dalsgaard, T., Devol, A. H., Ward, B. B., and Ulloa, O. (2014). Oxygen distribution and aerobic respiration in the north and south eastern tropical pacific oxygen minimum zones. *Deep Sea Res. Part I: Oceanogr. Res. Pap.* 94, 173–183. doi: 10.1016/j.dsr.2014.10.001

Ulloa, O., Canfield, D. E., DeLong, E. F., Letelier, R. M., and Stewart, F. J. (2012). Microbial oceanography of anoxic oxygen minimum zones. *Proc. Natl. Acad. Sci.* 109 (40), 15996–16003. doi: 10.1073/pnas.1205009109

Vaquer-Sunyer, R., and Duarte, C. M. (2008). Thresholds of hypoxia for marine biodiversity. *Proc. Natl. Acad. Sci.* 105 (40), 15452–15457. doi: 10.1073/pnas.0803833105

Wiggert, J. D., and Murtugudde, R. G. (2007). The sensitivity of the southwest monsoon phytoplankton bloom to variations in aeolian iron deposition over the Arabian Sea. *J. Geophysical Research: Oceans* 112 (C5). doi: 10.1029/2006JC003514

Xiu, P., and Chai, F. (2011). Modeled biogeochemical responses to mesoscale eddies in the south China Sea. *J. Geophys. Res.: Oceans* 116 (C10), C10006. doi: 10.1029/2010jc006800

Xiu, P., and Chai, F. (2014). Connections between physical, optical and biogeochemical processes in the pacific ocean. *Prog. In Oceanogr.* 122, 30–53. doi: 10.1016/j.pocean.2013.11.008

You, Y. (1997). Seasonal variations of thermocline circulation and ventilation in the Indian ocean. *J. Geophys. Res.: Oceans* 102 (C5), 10391–10422. doi: 10.1029/96JC03600

Zhang, J., Gilbert, D., Gooday, A., Levin, L., Naqvi, S., and Middelburg, J. (2010). Natural and human-induced hypoxia and consequences for coastal areas: synthesis and future development. *Biogeosciences* 7 (5), 1443–1467. doi: 10.5194/bg-7-1443-2010

Zhang, H.-R., Wang, Y., Xiu, P., Qi, Y., and Chai, F. (2021). The roles of iron limitation in phytoplankton dynamics in the western and eastern subarctic pacific. *Front. Mar. Sci.*, 8, 735826. doi: 10.3389/fmars.2021.735826

Zhang, W., Wu, H., and Zhu, Z. (2018). Transient hypoxia extent off changjiang river estuary due to mobile changjiang river plume. *J. Geophys. Res.: Oceans* 123 (12), 9196–9211. doi: 10.1029/2018JC014596

Zhou, F., Chai, F., Huang, D., Xue, H., Chen, J., and Xiu, P. (2017). Investigation of hypoxia off the changjiang estuary using a coupled model of ROMS-CoSiNE. *Prog. In Oceanogr.* 159, 237–254. doi: 10.1016/j.pocean.2017.10.008

frontiers | Frontiers in Marine Science

TYPE Original Research
PUBLISHED 11 October 2022
DOI 10.3389/fmars.2022.1001146

OPEN ACCESS

EDITED BY
Sudheesh Valliyodan,
Central University of Kerala, India

REVIEWED BY
Alyse K. Hawley,
University of British Columbia, Canada
Mónica Torres-Beltrán,
Autonomous University of Baja California, Mexico

*CORRESPONDENCE
Roberta C. Hamme
rhamme@uvic.ca

SPECIALTY SECTION
This article was submitted to Marine Biogeochemistry, a section of the journal Frontiers in Marine Science

RECEIVED 22 July 2022
ACCEPTED 15 September 2022
PUBLISHED 11 October 2022

CITATION
Soetaert G, Hamme RC and Raftery E (2022) Renewal of seasonally anoxic Saanich Inlet is temporally and spatially dynamic.
Front. Mar. Sci. 9:1001146.
doi: 10.3389/fmars.2022.1001146

Renewal of seasonally anoxic Saanich Inlet is temporally and spatially dynamic

Grayson Soetaert, Roberta C. Hamme* and Erinn Raftery

School of Earth and Ocean Sciences, University of Victoria, Victoria, BC, Canada

Injection of oxygenated water into anoxic basins sets off a cascade of biogeochemical reactions and ecosystem shifts. The dynamic nature of these events can create spatial variability in the resulting water mass that strongly affects subsequent observations. Their irregularity can also make their prediction for experiment planning challenging. Our study focuses on Saanich Inlet, one of the most accessible and well-studied anoxic basins in the world. In the late summer and early fall, dense water can cross the sill into this fjord, in discrete events, bringing oxygen and nitrate to the deep waters of the inlet. We assess the potential strength of these renewal events using density measured at a bottom mooring on the sill. We find that the occurrence and potential strength of renewals is primarily controlled by tidal current speeds, which can be well predicted. However, the intensity of coastal upwelling, which brings dense water into the estuarine system, plays a significant secondary control, reducing predictability. We also demonstrate that renewals do not result in a homogeneous water mass filling the deep inlet. Instead, high frequency measurements from a profiling mooring in the centre of the inlet reveal that different densities intruding over the several-day renewal period create a complex layering of waters containing different proportions of new oxic and old anoxic waters. Finally, we show that not every instance of high density water observed over the sill results in flushing of the deepest waters inside the inlet. We hypothesize that each renewal improves the chance of a subsequent renewal in the same season by reducing the density contrast between waters entering and already inside the inlet. Consideration of the temporal and spatial complexity of these renewal dynamics is necessary to support studies using Saanich Inlet as a natural laboratory for exploring oxygen deficient systems.

KEYWORDS

anoxic, renewal, flushing, intermittent anoxia, Saanich Inlet, tides and currents, oxygen deficient zones

1 Introduction

Carefully planned field work can be thwarted by unexpected conditions at the site, a particular problem in dynamic Saanich Inlet. This glacially carved fjord with a long, shallow sill at the mouth lies in SW British Columbia, Canada (Figure 1A). Restricted deep-water circulation and high surface productivity (Takahashi et al., 1977; Timothy and Soon, 2001; Grundle et al., 2009) cause anoxia in the deep waters over most of the year (Carter, 1934; Richards, 1965). Its proximity to several major oceanographic institutions, particularly Fisheries and Oceans Canada's Institute of Ocean Sciences right on its shore, and the installation in 2006 of a cabled observatory have made Saanich Inlet perhaps the most accessible and well-studied anoxic basin

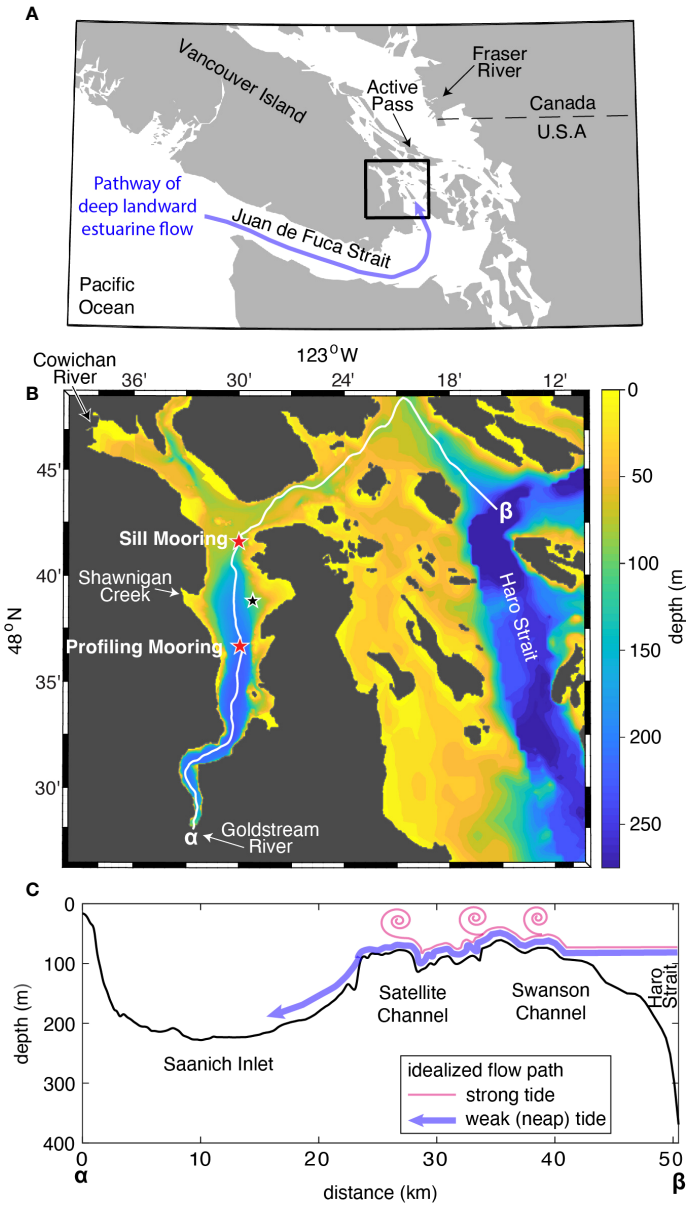

FIGURE 1
(A) Map of Salish Sea region on the west coast of North America. Blue line shows idealized conception of the landward pathway seawater follows in the estuarine system. Black box shows location of next panel. **(B)** Map of Saanich Inlet and its connection through Satellite Channel and Swanson Channel to Haro Strait. Red stars mark the locations of the sill mooring and profiling mooring. Smaller black star marks the location of a bottom mooring in Patricia Bay. White line marks the location of the deepest part of the channel (thalweg) **(C)** Cross-section along the thalweg from the southern end of Saanich Inlet (α, distance 0) to Haro Strait (β). Colored lines show idealized conception of bottom water flowing over the sill during neap tidal current speeds (blue) and higher tidal currents (pink).

in the world. Indeed, Saanich Inlet has come to serve as a natural laboratory to investigate biogeochemical processes and ecological communities in Oxygen Deficient Zones (ODZs) (e.g. Emerson et al., 1979; Tunnicliffe, 1981; Juniper and Brinkhurst, 1986; Zaikova et al., 2010). However, this basin experiences discrete deep-water renewal events during the late summer and early fall of many years, which bring oxygen, nitrate, and other oxidized compounds to the deep-waters (Herlinveaux, 1962; Richards, 1965; Anderson and Devol, 1973), interrupting anoxia and creating much more dynamic conditions than ODZs typically experience. In 2014, we began planning the Saanich Inlet Redox Experiment, for which a team intended to sample the inlet every two weeks from oxygenated to sulfidic conditions. However, the intermittent nature of the renewal process and particularly its poorly understood interannual variability was frustrating to the planning process. This paper grew out of a desire to better predict and understand both the occurrence of large renewal events in Saanich Inlet and their impact on the resulting water mass structure. We hope it will aid others in planning their field programs in the region and serve as a basis to investigate the controls and complexity of water mass renewal in other restricted basins.

The mechanism of renewal events in Saanich Inlet is similar to several other fjord systems and has been studied previously. Circulation of dense waters that could flush out the deep inlet is blocked by a shallow (~70 m), rather long (~10 km) sill at the mouth of the inlet (Figure 1B). In order for a renewal event to occur, waters denser than those in the deep inlet must flow over the sill and move into or under the water mass already present. Dense water arrives at the Saanich Inlet sill via the estuarine circulation of the Salish Sea, which pulls salty, dense waters landward (Figure 1A) as the fresher surface water (dominated by Fraser River outflow) flows seaward (Waldichuk, 1957; Masson, 2002; Masson, 2006). During late spring through early fall (Bylhouwer et al., 2013), intermittent upwelling off the coast of Vancouver Island supplies especially dense water (Freeland and Denman, 1982) to this deep landward estuarine flow. Indeed, Anderson and Devol (1973) suggested that Saanich Inlet renewal events occur primarily during the late upwelling season due to this supply of denser water. The estuarine circulation of the Salish Sea is forced through narrow straits and over multiple sills (Victoria Sill, Swanson and Satellite Channels, Boundary Pass), mixing the deeper salty water with the fresher water above. Tides drag these layers of water back and forth over the sills creating even more intense mixing (Gargett, 1994; Farmer et al., 1994; Camargo et al., 2014) and reducing the density of the bottom landward flow. The 14-d spring-neap cycle in tides strongly modulates this mixing (Gargett et al., 2003), so that it is more intense under faster flowing tidal current speeds - spring tides - and less intense during slower tidal current speeds - neap tides (Figure 1C). Stucchi and Giovando (1984) show that observations of high salinity water over the Saanich Inlet sill follow periods of low tidal current speeds, demonstrating the link between neap tides and dense water flowing over the Saanich Inlet sill. Thus, for Saanich Inlet and similar systems, deep water renewal only occurs during the lowest tidal current speeds (Geyer and Cannon, 1982; Griffin and LeBlond, 1990; LeBlond et al., 1991; Masson and Cummins, 2000; Masson, 2002; Manning et al., 2010; Thomson et al., 2020).

Note that the shallow waters of Saanich Inlet experience their own unique estuarine circulation, involving a fortnightly variation in the circulation direction (see Gargett et al., 2003). The vast majority of freshwater supplied to Saanich Inlet comes from outside the inlet (Fraser River, Cowichan River). When mixing over the sill is weak (neap tides), this freshwater flows into the inlet through the mouth creating a reverse estuarine flow and near surface downwelling. In contrast, when mixing is strong (spring tides), the near-surface salinity gradient changes, normal estuarine flow is established, and upwelling supplies nutrients to the surface driving Saanich Inlet's high productivity. Although both this circulation and the deep renewal process are driven by the spring-neap tidal cycle, the shallow circulation dominates the upper waters, well above sill depth, and has little direct impact on the renewal process we focus on in this paper.

The impact of renewal events on the resulting water mass within Saanich Inlet has been explored in low frequency shipboard observations. Dense waters flowing along the bottom of Saanich can lift less dense anoxic waters to shallower depths where they may persist for weeks to a month before being fully flushed out by the shallower circulation (Richards, 1965; Anderson and Devol, 1973). Compared to the very stratified upper water column, the new deep waters can appear relatively homogeneous in properties such as temperature, salinity, oxygen, nutrients, and dissolved N_2 gas (Manning et al., 2010). After renewal events cease, the biogeochemistry of the inlet typically evolves toward more reducing conditions (oxygen and nitrate are consumed and sulfide begins to accumulate). Deep Saanich Inlet is known for its low turbulence levels (Gargett et al., 2003), but slow mixing nevertheless reduces the salinity and temperature contrast between the deep waters and the waters above over time (Manning et al., 2010).

In this paper, we clarify the importance of competing factors on the potential for renewal events and show that renewals create complex layering of water masses within Saanich Inlet and likely other similar systems. In Section 2, we present the methods used in our study. While the effect of tidal current speeds on the deep-water renewal process has been a keystone in predicting renewal events in Saanich Inlet for some time and upwelling dynamics have been previously hypothesized to have a controlling factor, in Section 3.1 we quantitatively examine the relative influence of these two factors in controlling the potential for deep-water renewal events. In Section 3.2, we use new high frequency observations to demonstrate the complexity of the water

mass produced in the deep inlet by renewals. In Section 3.3, we point out how conditioning of the inlet by renewals is an important factor in allowing dense water that has moved over the sill to actually flush the deep inlet. Finally, in Section 4, we emphasize how the results of this study can be used to allow researchers studying Saanich Inlet to time their expeditions and interpret their results in terms of the complexity of water masses emplaced by renewals. These findings will also help elucidate the main controls over dense water flowing over sills and the complexity of water masses produced in other fjord systems.

2 Materials and methods

2.1 Sill mooring

We used autonomous observations collected by Ocean Networks Canada (ONC) at a bottom mooring on the Saanich Inlet sill to examine the potential for deep-water renewal. Data from 10 deployments during 2012-2020 of a bottom mooring located at 90±3 m depth at the southern terminus of the Saanich Inlet sill (at 48.688°N 123.500°W, Figure 1B) were obtained from https://www.oceannetworks.ca. Each deployment lasted 4-8 months with gaps of a few weeks to years between deployments. Data were collected every 5-15 minutes during each deployment. (See Supplementary Material Table S1 for details on each deployment). Salinity, temperature, and pressure data came from a SeaBird SBE16plus or SBE19plus V2 while oxygen data in 2016 came from an Aanderaa Optode 4175C sensor. No further calibrations were applied other than those by Ocean Networks Canada based on factory calibration. This lack of additional calibration is justified for oxygen, since we use that data only qualitatively as a measure of relative change. A 50-hour triangular filter was further applied to the potential density and to the oxygen data, primarily to remove the short-term influence of the semi-diurnal tides.

Potential renewal events were identified in each year when minima in smoothed tidal current speeds were below 1.1 m s^{-1} during 1 July - 30 November at Active Pass (NE of Saanich Inlet, Figure 1A). This period encompasses when renewals have been observed historically (see also Section 4). We quantified the potential strength of a renewal event as the change in potential density between a pre-event baseline and the 25-hr averaged potential density maxima during the event. The pre-event baseline was defined as the average potential density over 2-4 days prior to the associated minimum in the smoothed tidal current speed, which ensured sufficient data for a robust average while avoiding variability in the timing of the increase at the start of the renewal event. This potential renewal strength is a metric of the potential for renewal to occur based on the availability of dense water supplied over the sill, rather than of actual displacement of water within the inlet itself.

2.2 Ship-based CTD profiles

We also examined a collection of CTD casts spanning 1976 to 2019 within Saanich Inlet. These casts came from four sources: Fisheries and Oceans Canada obtained from Frank Whitney (personal communication), the Hallam Lab at the University of British Columbia obtained from Céline Michiels (personal communication) but since available from Torres-Beltrán et al. (2017), the Juniper Lab at University of Victoria obtained from Kim Juniper (personal communication), and the University of Victoria's Ocean Science Minor program. Individual profile data were chosen within 48.55°N-48.70°N and 123.40°W-123.55°W and binned into 1-m depth intervals. Density as σ_θ was calculated for each profile from temperature, salinity, and pressure using the 1983 equation of state (Fofonoff and Millard, 1983).

Profiles that spanned a potential renewal event were hand-selected. Profile timing was plotted on smoothed tidal current speeds at Active Pass. Event start profiles were selected if they preceded a minimum in the smoothed tidal current speed by no more than 10 days. Event end profiles were selected if they were no more than 2 weeks after the same minimum in smoothed tidal current speed. For events where more than one profile could be considered the event end, the profile which exhibited the highest change in density was chosen. By only choosing profiles that spanned a single tidal current minimum, we excluded the possibility that the change between profiles reflected more than one event. Finally, to quantify the strength of the renewal event, the average density change below 140 m was calculated between the event end and start profiles. The 140 m depth was chosen because waters above this depth often result from the uplift of the basin's older water mass as the new water enters.

2.3 Profiling mooring

We used autonomous observations collected by ONC from a profiling mooring in the central inlet to examine the impact of deep-water renewals on the water column properties in Saanich Inlet. The ONC Buoy Profiler System was designed to profile four times per day near the deepest part of Saanich Inlet (at 48.622°N 123.499°W, 215 m bottom depth, Figure 1B). High frequency temperature, conductivity, pressure, and oxygen data from a SeaBird SBE19plus and SBE43 were downloaded directly from the ONCSensorDataService for the Nov 2015 - Dec 2016 deployment. Temperature and oxygen were both corrected for time lags from the conductivity sensor arising from system plumbing/sensor response time, and then salinity was calculated from conductivity and temperature. Downcasts were averaged in 1 dbar pressure bins. Communication problems, a faulty depth sensor on the winch prior to 8 Sep 2016, and power outages caused some casts to be aborted, resulting in data gaps of

a few hours to a week. A corroded bulkhead connector on the CTD pump caused slower response times for sensors from at least 25 Oct 2016. We also used profiling mooring oxygen data in a qualitative manner and did not apply any further calibration.

2.4 Ancillary data

We combined observations from Saanich Inlet with tidal current predictions, coastal upwelling indices, and river discharge data to interpret the dynamics. Tidal current speeds at nearby Active Pass (NE of Saanich Inlet, 48.867°N, 123.307° W, Figure 1A) were predicted with a 15-min frequency for each year separately from 1975 to 2072 using the XTide database (Flater, 2001) queried using the T-Tide MATLAB Analysis Toolbox (Pawlowicz, 2002). Active Pass is the closest current speed prediction site in the database, and is used here as a proxy for tidal currents in Satellite and Swanson Channels. The absolute values of these current speeds were smoothed with a centred 50-hr triangular filter to highlight the spring-neap cycle. Other nearby tidal predictions were also considered (see Supplementary Material Section S2). Predictions for year 2038 and later were calculated using an updated version of the tidal equilibrium arguments and node factors obtained from https://flaterco.com/xtide/files.html. We obtained daily values of the Bakun Index at 48°N, 125°W as an upwelling metric representative of the conditions off the continental shelf. For each potential renewal event, an average of the Bakun Index was taken for 30 days prior to the minimum tidal current speed associated with that event, to account for lags in transfer of dense water by coastal upwelling into the estuarine system. Daily river discharge data for the Cowichan and Fraser Rivers during 2012-2019 was obtained from Environment and Climate Change Canada.

3 Results and discussion

3.1 Tidal currents and upwelling control potential strength and timing of renewals

An increase in potential density followed most strong minima in smoothed tidal current speeds (Figure 2 shows an example for 2020). To avoid bias in the following analysis, events resulting in decreased potential density were not removed from the data. Two minima in smoothed tidal current speeds occur every month (neap tides), but one is typically stronger, i.e. reaches lower speeds, than the other. The observed density increases over the sill create the possibility for renewal of the deep inlet. Fifty-two of these potential renewal events were observed in July through November of 2012-2020 (Supplementary Figure S2). Additional events occurred during this time, but were not observed due to data gaps. Clear increases in density at the sill mooring typically began up to two days

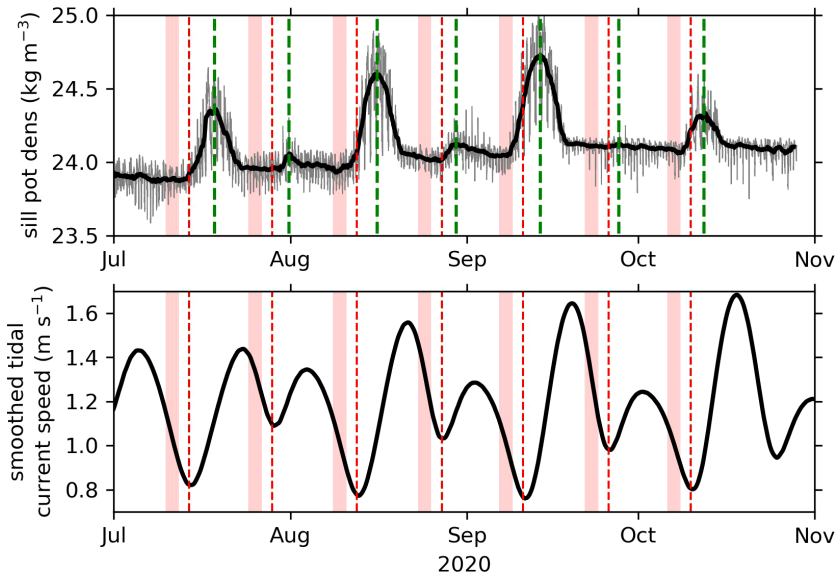

FIGURE 2
Relationship between potential density at the sill mooring and tidal current speeds for the 2020 renewal season. (upper panel) Potential density observed at the sill mooring (σ_θ, kg m^{-3}). Thin gray line is the 10-min frequency data. Thick black line is smoothed with a 50-hr triangular filter. Vertical dashed green lines mark the times of the maximum smoothed density. (lower panel) Predicted absolute tidal current speeds at Active Pass smoothed with a 50-hr triangular filter (see Section 2.3). (both panels) Vertical red dashed lines mark the times of the minima in smoothed tidal current speed associated with an event. Lighter red bars indicate the pre-event window for calculation of the baseline potential density.

before the minimum in tidal current speeds, while maximum densities were observed 2-5 days following the minimum. The potential density observed at high frequency (every 5-15 minutes at the sill mooring, grey line in Figure 2A) showed large semi-diurnal variability (two maxima and two minima per day, see Section 3.3).

The strength of these possible renewal events was strongly related to the minimum smoothed tidal current speed and to coastal upwelling strength (Figure 3). Note how the largest density change events (density change > 0.3 kg m^{-3}) occur at smoothed tidal current speeds less than 0.9 m s^{-1}, while the three events with a density change greater than 0.6 kg m^{-3} all occurred at smoothed tidal current speeds less than 0.8 m s^{-1}. In this region, the tides drag stratified waters back and forth over the complex topography of the sill, mixing the different density waters together (Farmer et al., 1994; Gargett et al., 2003). Lower tidal current speeds allow for the high density of water masses at the bottom to be preserved as they flow over the long and shallow Saanich Inlet sill, because less mixing occurs with lower density shallower waters (Stucchi and Giovando, 1984; Griffin and LeBlond, 1990; LeBlond et al., 1991; Masson, 2002).

However, tidal current speeds are not the only control. When smoothed tidal current speeds are lower than 0.9 m s^{-1}, there are many events where the change in density is less than 0.3 kg m^{-3} (points in the lower left quadrant of Figure 3). These small density change despite low tidal current events occurred when the Bakun Index was near or below zero, i.e. when downwelling was dominant off the coast of Vancouver Island. The Bakun Index (Bakun, 1973) is an upwelling metric that uses observations of sea level pressure (to estimate wind stress) and latitude to estimate Ekman transport as a proxy for coastal upwelling. Positive values indicate primarily upwelling conditions off the coast and negative values indicate downwelling. While upwelling off the coast of Vancouver Island is driven by more than wind dynamics (see last paragraph in this section), the Bakun Index still functions as a good proxy for upwelling/downwelling strength. Downwelling conditions on the coast supply lower density water to the deep estuarine flow into the Salish Sea (Figure 1A), while upwelling conditions supply higher density water (Freeland and Denman, 1982; Mackas et al., 1987; Kämpf and Chapman, 2016). Our results show that the density of water supplied outside of the Saanich Inlet sill, regulated by coastal upwelling *vs.* downwelling, plays an additional controlling role in the potential strength of a given renewal event. If tidal current speeds are low enough to facilitate a strong density change over the sill, downwelling conditions can still suppress the magnitude of the density change.

A multiple linear regression analysis shows that both tidal current speeds and upwelling dynamics are significant controls on the potential strength of renewals but that tidal current speeds are most important. The collection of 52 possible renewal events was fit to:

$$\Delta\sigma_\theta = A * TidalCurrent + B * BakunIndex + Intercept$$

where $\Delta\sigma_\theta$ is the change in density observed at the sill mooring for each event, *TidalCurrent* is the associated minimum in the smoothed tidal current speed, and *BakunIndex* is the 30-d average of the upwelling Bakun index prior to the event. *A*, *B*, and *Intercept* parameters were determined by minimizing the

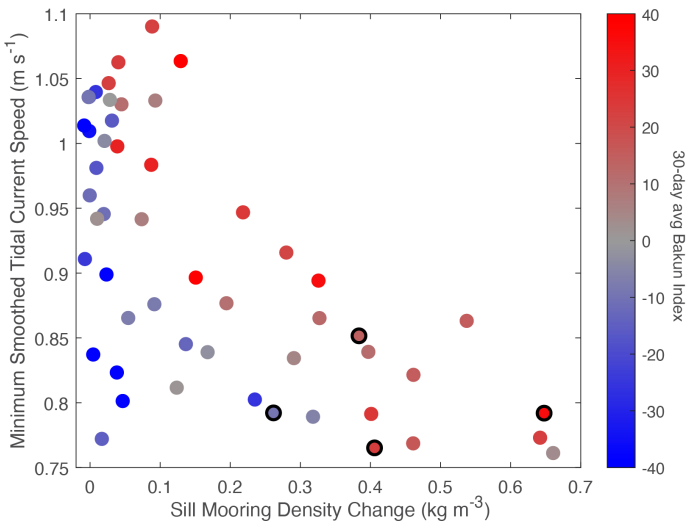

FIGURE 3
The minimum in the smoothed tidal current speed vs. the potential strength of a renewal event (change in potential density ($\Delta\sigma_\theta$) observed at the Saanich Inlet sill mooring). Each renewal event is coloured by the average of the Bakun Index over the 30 days prior to the minimum smoothed tidal current speed. Events in 2016 (see next section) are outlined in black.

sum of the least squares between the predicted and actual $\Delta\sigma_\theta$. When the independent variables of such a model are uncorrelated (as is the case for the minimum tidal current speed and the Bakun Index with an $r^2 < 0.0001$ between them), their respective normalized coefficients (*A* and *B*) represent the relative power of each variable in determining the result, potential strength of renewals in this case. To normalize the coefficients, each coefficient was multiplied by the standard deviation of its respective variable and divided by the standard deviation of the change in density. The relatively high r^2 value of 0.65 for the multiple linear regression (Table 1) demonstrates that these two factors control a high proportion of the potential strength of renewals in Saanich Inlet. Both the minimum smoothed tidal current speed and the Bakun Index are important factors in determining the potential strength of a given renewal event (Table 1), but the larger magnitude normalized coefficient of -0.64 indicates that current speed is the dominant factor. The sign of the coefficient is negative, because low tidal current speeds correlate with high density changes. However, the reasonably high normalized coefficient for the Bakun Index shows that upwelling dynamics have a controlling factor on the potential strength of deep-water renewal events that shouldn't be dismissed. We found similar results using shorter averaging periods for the Bakun Index of 14 and 7 days, suggesting that it is the overall seasonal cycle that matters most for this variable. Multiple regression analysis using other upwelling indices yielded similar results but with slightly lower coefficients (see Supplementary Material Section S4).

In addition to the analysis of the sill mooring data, we also examined a 50-yr dataset of CTD casts from within Saanich Inlet for the impact of tides and upwelling on renewal. Nineteen renewal events were identified based on our selection procedure (Section 2.2). The strongest observed changes in density occurred for renewal events at low tidal current speeds (<0.8 m s^{-1}) when upwelling, as indicated by a positive Bakun Index, was prevalent (Figure 4). However, the suppression of renewal events by downwelling is less clear here, possibly because the data available from individual profiles captured few events during times of downwelling. A similar multiple linear regression analysis suggested that tidal current speeds and the Bakun Index explain much less of the variance in the strength of renewal events from CTD data compared to the sill mooring analysis (Table 2). The normalized coefficients still demonstrate an important control by smoothed tidal current speeds, but no significant dependence on the Bakun Index could be detected. Several factors may explain the overall lower correlation. First, the timing of the CTD casts relative to renewals was much more variable. There was never more than a five day difference between the smoothed tidal current speed minimum and the maximum density observed at the sill mooring. However, event start profiles varied from days to hours prior to the minimum tidal current speed, while CTD profiles spanning an event were on average 11 days apart, ranging from 3 to 18 days. The geomorphology of Saanich Inlet is such that new water is introduced during a deep-water renewal event along the western edge of the basin, driven by the Coriolis force (Hamme et al., 2015). This spatial distribution leads to an east-west gradient in water mass properties within the deep-waters of Saanich Inlet, which then drives lateral mixing following deep-water renewal events. The inconsistent duration between profiles is likely to mean that some profiles capture renewal events before and some after the lateral mixing with older water. Similarly, a very short duration between profiles could mean that the full impact of the renewal event was not captured. Second, we show in Section 3.3 that when waters within deep Saanich Inlet are denser, this situation preconditions the inlet to experience stronger renewals. The multiple linear regression analysis presented here does not consider the average density of the deep water but only the density change from one profile to another.

TABLE 1 Multiple linear regression analysis results for the dependence of the potential renewal strength on the minimum smoothed tidal current speed and the Bakun Index.

Variable	Normalized coefficient	r^2
Min. Tidal Current Speed	-0.64	0.65
Bakun Index	0.48	

We considered whether river discharge into the region represented a significant third control on the potential strength of renewals, but found its inclusion did not improve predictions. The Cowichan River feeds into the northwest segment of the inlet (Figure 1B) and reaches a peak discharge of ~100 m^3 s^{-1} in the winter season due to local rainfall (Pike et al., 2018). The Fraser River is the primary freshwater input to the Salish Sea (Figure 1A) and reaches a peak discharge near 7000 m^3 s^{-1} in the summer due to snow melt (Griffin and LeBlond, 1990; Johannessen and McCarter, 2010). The discharge of Goldstream River at the southern part (head) of the inlet and Shawnigan Creak nearer the mouth are negligible at 5 and 8 m^3 s^{-1}, respectively (Herlinveaux, 1962; Campbell and Belcic, 2006). Freshwater input drives the estuarine circulation, which draws dense seawater landward along the bottom of the region's straits, supplying the renewals. Although river discharge and upwelling have no direct effect on each other, upwelling conditions on the coast are somewhat correlated with discharge from both rivers, because all three have a strong seasonal cycle (r^2 of 0.26 between Fraser River discharge and the Bakun Index and 0.47 between Cowichan River discharge and the Bakun Index). We performed a cross-validation analysis to show that the addition of river discharge records as additional explanatory variables did not improve predictions from the multiple linear regression (see Supplementary Material Section S5).

El Niño Southern Oscillation (ENSO) and coastal trapped waves also impact the density of waters entering the estuarine system, and may affect the potential strength of renewals in Saanich Inlet, but we could not assess the potential impact.

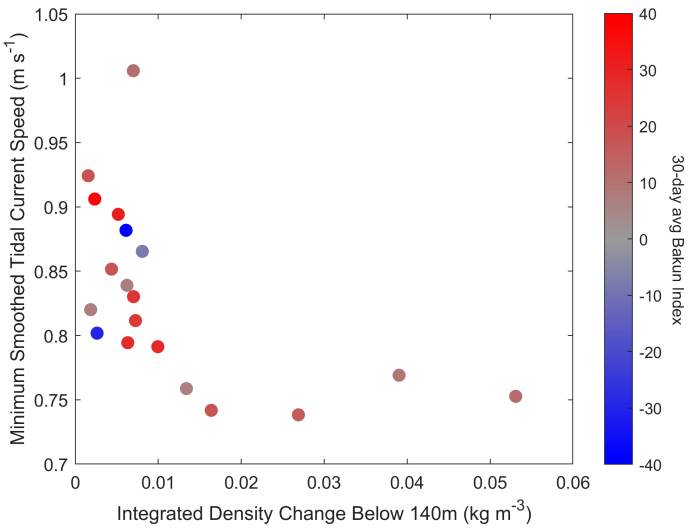

FIGURE 4
The minimum in the smoothed tidal current speed *vs.* the potential strength of a renewal event (change in potential density ($\Delta\sigma_\theta$) below 140m observed through CTD casts in Saanich Inlet). Each renewal event is coloured by the average of the Bakun Index over the 30 days prior to the minimum smoothed tidal current speed.

Indeed, Masson (2002) suggested that El Niño conditions can lead to a shutdown of the deep-water renewal process in the Strait of Georgia, to the northeast of Saanich Inlet. Regional shifts in winds, Ekman transport, and associated upwelling strength occur during the warm and cool phases of ENSO (Alexander et al., 2002; Alexander and Scott, 2008); these effects should be included in the wind-based Bakun Index. However, coastal trapped waves also depress the pycnocline off the coast of British Columbia during El Nino, leading to upwelling of lower density water (Miller et al., 1997; Fiedler et al., 2013; Ray et al., 2020). Our time series from the sill mooring (2012-2020) is too short to investigate an interannual variation like ENSO, so its impact on Saanich Inlet remains unquantified. More generally, coastal trapped waves play an important role in upwelling dynamics in this region, independent of the winds and apart from their interaction with ENSO (Freeland and Denman, 1982; Frischknecht et al., 2015; Engida et al., 2016). However, a time series of the occurrence of these waves is not available for analysis.

TABLE 2 Multiple linear regression analysis results for the dependence of the potential renewal strength on the minimum smoothed tidal current speed and the Bakun Index as observed through CTD casts in Saanich Inlet.

Variable	Normalized coefficient	r^2
Min. Tidal Current Speed	-0.46	0.22
Bakun Index	0.05	

3.2 Renewals create complex water mass layering

Summer and fall of 2016 experienced four distinct renewal events, captured in unprecedented detail by the profiling mooring in the central inlet (Figure 5). Each pulse of higher density water observed at the sill mooring began approximately a day before the lowest average smoothed tidal current speeds (beginning of pink bars/vertical lines in Figure 5) and lasted for 6-9 days. The higher density water was oxygen rich compared to bottom water over the sill either before or after the event (Figure 5C). Oxygen concentration over the sill actually experienced a maximum every 14 days, but density only showed significant increases during the weaker neaps in tidal current speed.

These four renewal events in 2016 had very different effects on the deepest waters of the inlet. The profiling mooring observed no changes to water properties below 160 m during July (Supplementary Figure S3), suggesting that the July renewal did not penetrate to the bottom of the inlet. In contrast, the next three renewal events affected depths all the way to the bottom, bringing new warmer, denser, saltier, and more oxygen rich waters to these depths (Figures 5D-F). The profiling mooring executed very few profiles during the August renewal (Supplementary Figure S4), so we do not consider this event further and instead focus on the September and October renewals.

Water intruded at different densities and then mixed in several stages during the September renewal (Figure 6). New,

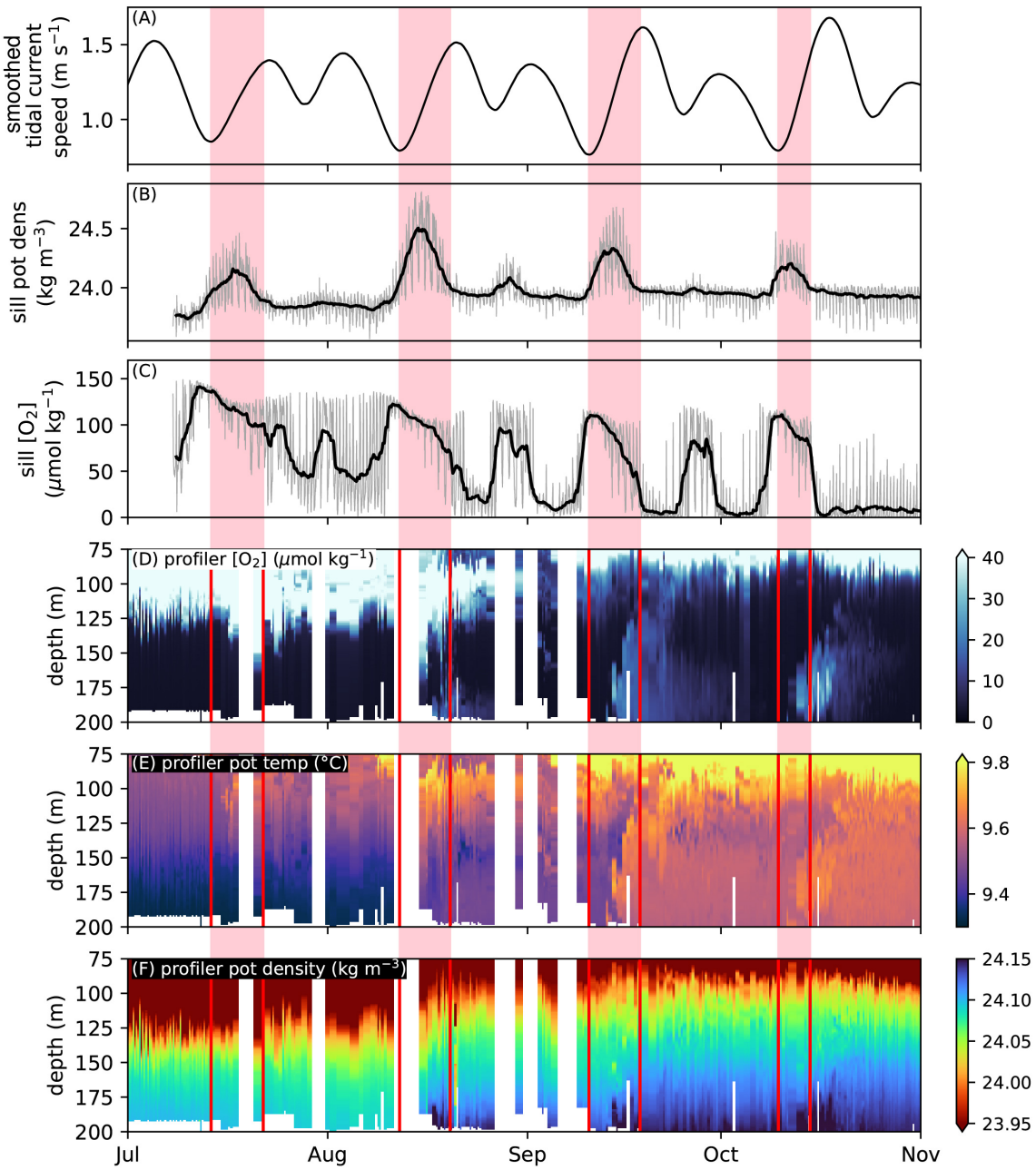

FIGURE 5
Overview of 2016 renewal season. **(A)** Smoothed tidal current speeds at Active Pass (m s^{-1}). **(B)** Potential density (σ_θ kg m^{-3}) at the sill mooring. **(C)** Oxygen concentration (μmol kg^{-1}) at the sill mooring. **(B, C)** Grey lines show 10-min frequency data. Black lines show 50-hr triangular filter. **(D)** Oxygen concentration (μmol kg^{-1}) at the profiling mooring. **(E)** Potential temperature (°C) at the profiling mooring. **(F)** Potential density (σ_α kg m^{-1}) at the profiling mooring. **(A-F)** Pink bars/red lines indicate the renewal event from the minimum in smoothed tidal current speed in **(A)** to the approximate return of the sill mooring density to the baseline in **(B)**. **(D-F)** Only waters deeper than 75 m are shown.

warmer, saltier, and oxygen-rich water first intruded to a depth of ~130 m during 9-12 Sept. Data from the profiling mooring is missing 5-8 Sept, so we cannot precisely quantify the date of the first change, but the minimum in tidal current speed is near this time on 10 Sept. In the next three days (13-15 Sept), new water is observed intruding below 160 m. This new water mass appears to displace the previous water mass upward (note the shoaling partway through the September renewal of the lower temperature, low oxygen water mass and the persistence of that signal at shallower depths for a week in Figure 5). New

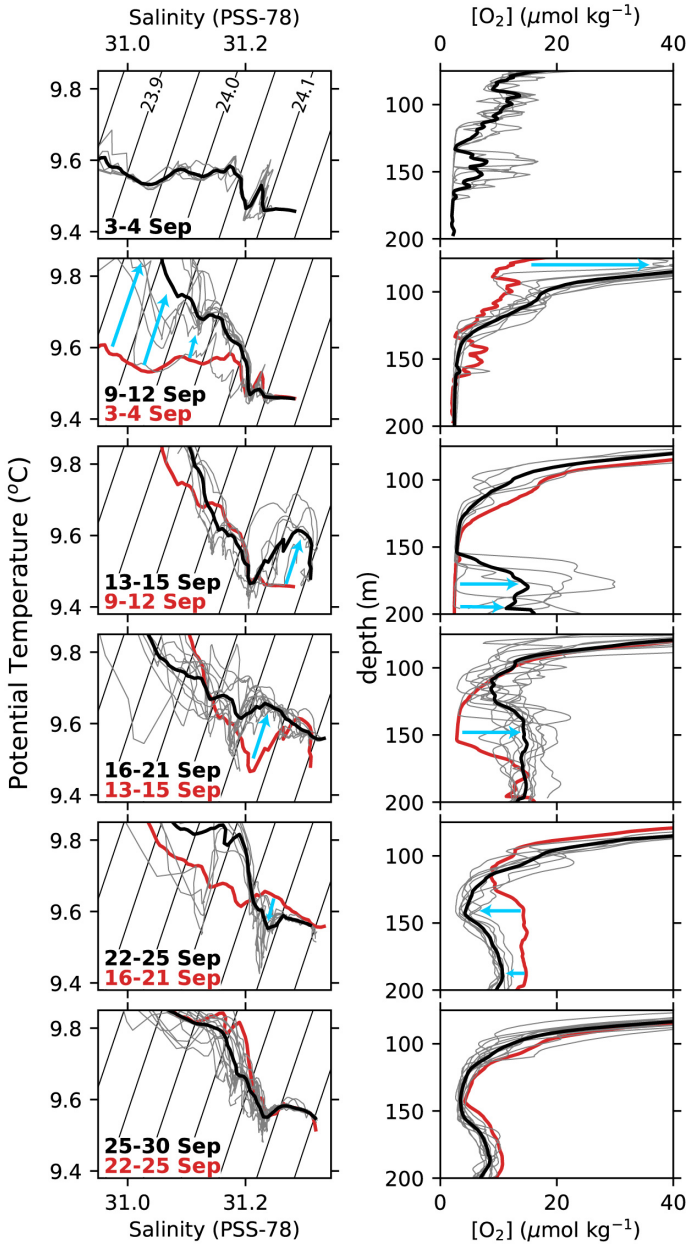

FIGURE 6
Detailed profiles over the Sept 2016 renewal event. Left hand panels show T-S diagrams with potential temperature on the y-axis and salinity on the x-axis. Black contours are lines of constant potential density (σ_θ kg m^{-3}, labeled in the top panel). Right hand panels show depth profiles of O_2 concentration deeper than 75 m. In each panel thin grey lines show individual profiles collected by the profiling mooring during the dates shown in black text, while the thick blackline is the average of the individual profiles. Thick red line shows the average of individual lines from the panel above (during the dates shown in red text). Blue arrows highlight changes between the red and black dates. Missing dates indicate missing data.

water is not observed at 130-160 m until 16 Sept. Density over the sill returned to pre-renewal levels by 18 Sept. During 22-25 Sept, the profiling mooring then captured the relaxation of properties at 120-160 m toward pre-renewal conditions. New water enters the inlet from the north hugging the western side of the inlet, then mixes laterally with older anoxic water present on the eastern side of the inlet (Hamme et al., 2015). Here we see evidence of that mixing process, as waters become cooler and less oxygen rich at 120-160 m following the main September renewal period.

The October renewal showed contrasting behavior (Figure 7). New water appeared first at the deepest depths

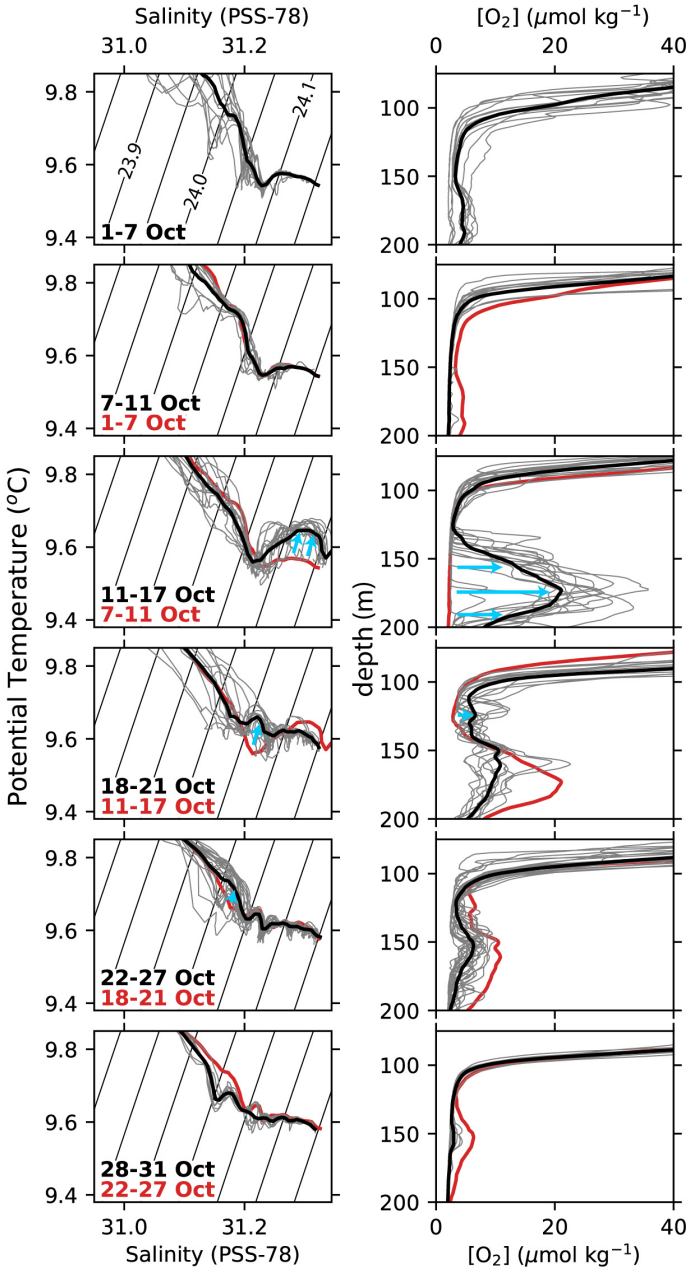

FIGURE 7
Same as Figure 6 but for October 2016.

(>130 m) beginning on 11 Oct, two days after the lowest tidal current speeds. The largest changes in water properties were centered at 160-180 m, but small changes were observed down to the deepest depths. By 18 Oct, changes were observed above 130 m, and the properties of water at deeper depths relaxed partly back to early October observations, again likely by lateral mixing with older waters.

The result of each renewal, and indeed the entire renewal season, was not a new homogeneous water mass filling the deep Saanich Inlet. Instead, the progressive intrusion of waters of different densities at different depths resulted in a layered injection of warmer, saltier waters carrying oxygen. The V-shaped cross-section of the inlet (Figure 1B) means that these injections of new water encounter varying volumes of old, anoxic water. Lateral mixing (Hamme et al., 2015) finally creates layers containing different proportions of new oxygenated waters and old anoxic waters present in the inlet since renewal events of the previous year, which are likely laterally homogeneous while

remaining vertically distinct. We suspect that this behavior is characteristic of renewal events in Saanich Inlet generally, but the profiling mooring dataset from 2016 is the first profile data with such high temporal resolution where the phenomenon can be clearly observed.

3.3 Renewals condition the deep waters to promote subsequent renewals

The very different behavior of these 2016 renewals - July did not reach bottom, September began at shallower depths, October began at the deeper depths - suggests variability in the conditions of renewal that affect the resulting waters masses in Saanich Inlet. Of the four renewal periods, July had the highest smoothed tidal current speeds (minimum at 0.85 m s^{-1} compared to 0.76-0.79 m s^{-1} for the other three renewals). Despite higher current speeds, the maximum density observed over the sill in July was similar to that in October (though lower than both August and September) and sustained for longer than in October. Note that the lower density change in October despite the low tidal current speeds is explained by the reduction in coastal upwelling at that time (30-d mean Bakun Index of -10 for the October 2016 event *vs.* 13-35 for the other events that year).

We suggest that each renewal within a single season conditions the inlet to promote further renewals. In July, the density of the water column within the inlet is at its lowest value at every depth (Figure 5F). This low density means that new dense water flowing over the sill encounters and mixes with low density water within the inlet, creating a mixed water mass with lower density than if that same entering water had encountered higher density inlet water. As each subsequent renewal emplaces higher density water within the inlet, water entering at the next renewal encounters a smaller density contrast, remains at higher density as it flows into the inlet, and is more likely to reach the deepest depths. The idea that higher density water within the inlet promotes renewals may seem counter-intuitive, but the notion that water entering the inlet experiences significant mixing is supported by the higher density of inflowing water (values as high as 24.4 σ_θ observed at the sill mooring for brief periods in July) compared to the maximum density where changes are observed at the profiling mooring (24.05 σ_θ in July).

The differences between the September and October renewals, with the October renewal characterized by density changes at the bottom first, may be partially explained by this same effect, but here the density of the inflowing water appears to be an additional factor. The density of the water observed over the sill during renewal events is variable, largely in phase with the semi-diurnal tidal cycle, higher density during flood tide and lower density during ebb tide (Figure 8). This relationship between density over the sill and the semi-diurnal tides was first hypothesized by Anderson and Devol (1973) and makes sense as flood tide brings water outside the inlet toward the inlet and ebb removes lower density water from the inlet. The start of the October renewal was characterized by unusually high densities, while the density observed over the sill during the September renewal built slowly over several days. Lower density water entering at the start of the September renewal would have intruded at shallower depths than the unusually high density water entering at the start of the October renewal.

4 Conclusions and implications for prediction

Being able to predict renewal events that flush the deep waters of Saanich Inlet is important to experiment planning in this accessible, natural laboratory used to investigate processes and organisms in oxygen deficient zones (e.g., Manning et al., 2010; Bourbonnais et al., 2013; Hawley et al., 2014; Chu and Tunnicliffe, 2015; Capelle et al., 2019; Torres-Beltrán et al., 2019; Ji et al., 2020). Understanding Saanich Inlet renewal events may also help to understand such events in other fjords, especially ones marked by periodic low oxygen conditions (Levings, 1980; Newton et al., 2007). Probably due to its location separated from the coast by many kilometers of straits and sills where mixing is enhanced, renewals in Saanich Inlet may be more strongly controlled by tidal current speeds than basins where only a single sill or a short distance separates them from coastal waters. For example, Barkley Sound on the west coast of Vancouver Island appears strongly controlled by upwelling alone (Pawlowicz, 2017). Upwelling supplying dense waters has also been the primary explanation for basin renewal events in Santa Barbara Basin (Bograd et al., 2002). Effingham Inlet, near Barkley Sound, displays fortnightly variations in water intrusions but a clear link to spring-neap timing has not been identified (Thomson et al., 2017). In contrast, reduced mixing during neap tides has been shown to play an important role in the occurrence of intrusions of high density waters into the nearby Strait of Georgia and into Puget Sound, a region of the southern Salish Sea with several sills separating it from the open ocean (Geyer and Cannon, 1982; Cannon et al., 1990; Griffin and LeBlond, 1990; Lavelle et al., 1991; LeBlond et al., 1991; Masson and Cummins, 2000; Masson, 2002; Leonov and Kawase, 2009). Our study establishes the link between the strength of the neap and the likelihood of renewal, which likely characterizes these other fjords of the Salish Sea. Note that the studies mentioned above that focus on upwelling alone are based on low temporal resolution sampling (monthly or quarterly) and could miss a potential role of tidal currents that our high resolution data reveals. However, renewals of other intermittently anoxic basins, for example the deep Baltic Sea, have been firmly tied to specific wind conditions in the region (Schinke and Matthäus, 1998), demonstrating that tidal currents do not play a role everywhere.

Our analysis reveals that the density of water flowing over the Saanich Inlet sill is controlled by tidal current speeds and

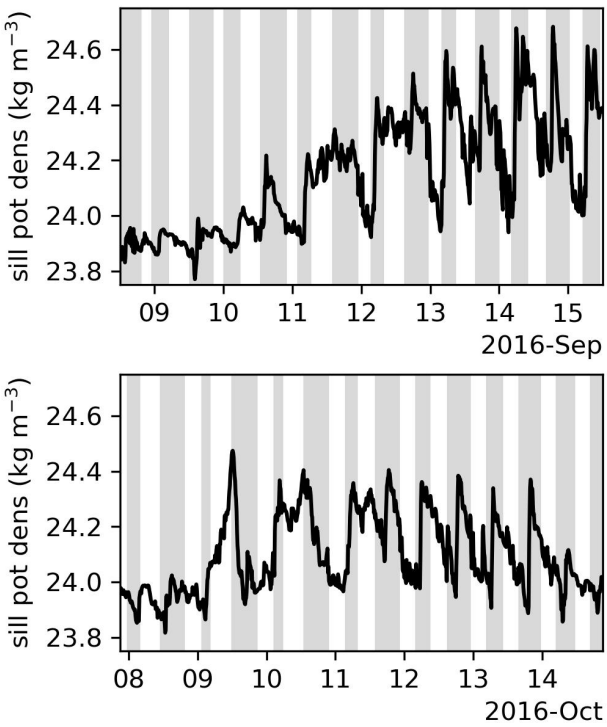

FIGURE 8
Potential density (σ_θ kg m^{-3}) at the sill mooring, 10-min frequency data. Upper panel shows data from one week in September 2016 while lower panels shows one week in October 2016. Each time period begins two days before the minimum in smoothed tidal current speed predicted at Active Pass. Grey bars in background mark flood tide/white marks ebb tide.

upwelling dynamics. Tidal current speeds have a larger role in determining the potential strength of a renewal event but unfavourable upwelling dynamics (i.e. downwelling conditions) can lead to weaker renewals. This dominance by currents suggests that, in general, the predictable tidal current speeds at Active Pass can be used to plan cruises in Saanich Inlet, and that variations in tidal current speeds should be a primary avenue for investigation of other silled basins. However, the seasonally and interannually varying upwelling dynamics off the west coast of Vancouver Island inject a factor of unpredictability. We go on to show that the actual flushing of the deep waters within the inlet is affected by previous flushing events, so that each renewal within a single season conditions the inlet to subsequent renewals by lowering the density contrast between the waters flowing over the sill and those already within the inlet. This conditioning suggests that a series of events with high density water flowing over the sill is necessary to replace a large proportion of the deep waters in the inlet.

Although tidal current speeds in the region are very predictable for many years into the future, they vary strongly both seasonally and interannually, causing renewals to typically be observed in Saanich Inlet in late summer and early fall and creating the potential for some years to experience much stronger renewals than others (e.g., Capelle et al., 2018). Bylhouwer et al. (2013) show that upwelling near the mouth of the Juan de Fuca Strait typically begins in mid-May, ends in mid-September, and fully transitions to downwelling by mid-November. The lowest tidal current speeds in the region are not typically observed until mid-July and last until mid-November (Figure 9A). Based on this timing, we conclude that the greatest possibility for full-bottom water renewals exists from mid-July to mid-October, with greater likelihood towards the end of this period given the pre-conditioning of the water column by earlier renewals. Experiments that require a well developed anoxic water column with significant sulfide concentrations should be planned for the period from winter to very early summer. Significant sulfide concentrations are typically observed by mid-January, especially farther south within the inlet (observations by the University of Victoria Ocean Science Minor program), and continue accumulating until the next renewal. Note that occasional mid-water renewal events have been observed in winter and spring, but these have not flushed the very deepest waters (e.g., Manning et al., 2010).

Based only on tidal current speeds, there are large differences in the potential for renewals between years, even within the late summer/early fall period (compare 2007 with several strong minima in smoothed tidal current speeds with 2014 where such strong minima are not observed, black vs. red lines in Figure 9A).

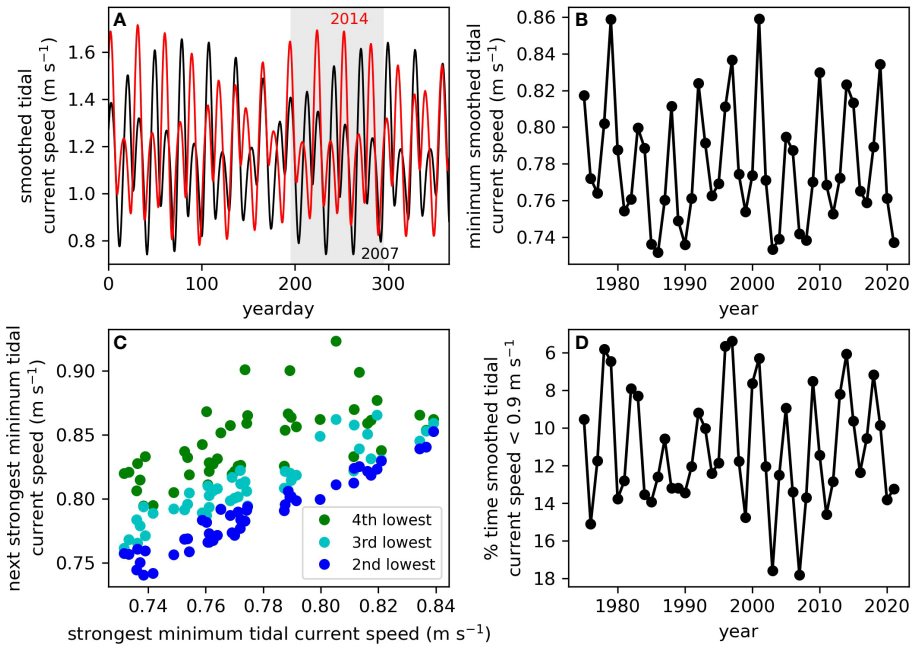

FIGURE 9
Interannual variability in tidal current speed. **(A)** Predicted smoothed tidal current speeds in 2007 with strong minimums (black) and in 2014 with weak minimums (red). Grey background shows the summer/fall renewal period considered in the rest of the panels. **(B)** Minimum smoothed tidal current speed predicted during the renewal season in a given year. **(C)** Correlation between the minimum smoothed tidal current speed during the renewal season in a given year and the 2nd (blue), 3rd (cyan), and 4th (green) lowest events in the same season and year. **(D)** Percentage of time smoothed tidal current speed is below 0.9 m s^{-1} during the renewal season in a given year. Note the y-axis is reversed to show the correspondence with the panel above.

The strongest minima in smoothed tidal current speed varies between 0.73 and 0.86 m s^{-1} among different years (Figure 9B). Moreover, years with one strong minima are likely to experience several strong minima as shown by the high correlation between the strongest minima in each year and the 2nd, 3rd, and 4th strongest minima in the same year (Figure 9C). Similarly, years with a strong minima are also likely to have a larger percentage of the renewal season at lower current speeds (Figure 9D). Experiments that rely on a strong flushing of the deep Saanich Inlet should be planned for those years that experience the strongest reductions in tidal current speeds (see Supplementary Material Figure S5 for predictions for the next 50 years) and targeted for just past the lowest tidal current speeds in August and September. Over the next decade, 2025 is an example of a year likely to experience strong renewals based on very low tidal current speeds, whereas 2032 is an example of a year that may experience no renewal at all (Supplementary Material Figure S5). Note that factors that cannot be predicted so far in advance may strongly enhance or hinder renewals, particularly upwelling strength, which may be affected not only by local winds but also by coastal trapped waves and ENSO, but also potentially river discharge. Future climate change may also impact upwelling and the estuarine circulation of the Salish Sea in ways that affect renewal strength in Saanich Inlet but are not easily predicted.

Finally, we emphasize that renewals do not result in deep Saanich Inlet being filled with a new homogeneous water mass. Several previous studies have shown that renewal events do not completely replace the previously anoxic waters in the inlet, but instead create mixtures of old and new water in varying proportions (Anderson and Devol, 1973; Lee et al., 1999; Manning et al., 2010). Here we show that renewal events result in a complex layering of water masses, with each layer containing different proportions of old and new water. This layering is caused by the variations in the density of water flowing over the sill during a renewal event and by the V-shape of the inlet with different volumes of old water encountered at each depth. Such layering of water masses with different physical and biogeochemical properties as the result of each renewal event has strong implications for ecosystem shifts and process rates in these different layers (companion paper) and is likely to characterize other systems with occasional renewal events as well.

Data availability statement

The 2012-2020 sill mooring and 2016 profiling mooring datasets analyzed for this study are openly available from Ocean Networks Canada at https://data.oceannetworks.ca/, and are

presented as a dataset collection at https://doi.org/10.26152/rk52-qy70. Bakun Index values were obtained from the Environmental Resource Division of the National Oceanic and Atmospheric Administration (NOAA), https://oceanview.pfeg.noaa.gov/products/upwelling/dnld. Daily river discharge data for the Cowichan and Fraser Rivers was extracted from the Environment and Climate Change Canada Historical Hydrometric Data web site, https://wateroffice.ec.gc.ca/mainmenu/historical_data_index_e.html.

Author contributions

GS analyzed the sill mooring data (Section 3.1) and drafted the first version of much of the manuscript. ER analyzed and presented the initial interpretation of the profiling mooring data. RH expanded the profiling mooring analysis, drafted the first version of Sections 3.2 and 3.3, and revised the manuscript. All authors contributed to revising the figures and manuscript and approved the submitted version.

Funding

Funding for this work came from the Natural Sciences and Engineering Research Council of Canada (NSERC) under DG 328290-2012 and University of Victoria internal funding to RH, a Jamie Cassels Undergraduate Research Award to GS, and an NSERC Undergraduate Student Research Award to ER.

Acknowledgments

We are grateful to the following people whose work helped make this paper possible: Adam Monahan for statistical advice, Caitie Frenkle for initial analysis of the profiling mooring data, Akash Sastri (ONC) for facilitating the deployment of the profiling mooring and initial work with the data, Rowan Fox for code to download and process the profiling mooring data, Frank Whitney for emphasizing the importance of interannual tidal variations to Saanich Inlet renewals at the 2016 Saanich Inlet Symposium, Petra Clementson and Pandora Gibbs for work creating and updating the Saanich Inlet CTD profile database, Alice Olga Victoria Bui (ONC) for communicating key metadata, Melissa Cuthill (ONC) for creating the data citation, and Frank Whitney, Brett Jameson, and Philippe Tortell for comments on a draft of the manuscript.

Conflict of interest

The authors declare that the research was conducted in the absence of any commercial or financial relationships that could be construed as a potential conflict of interest.

Publisher's note

Supplementary material

The Supplementary Material for this article can be found online at: https://www.frontiersin.org/articles/10.3389/fmars.2022.1001146/full#supplementary-material

References

Alexander, M. A., Bladé, I., Newman, M., Lanzante, J. R., Lau, N.-C., and Scott, J. D. (2002). The atmospheric bridge: The influence of ENSO teleconnections on air–sea interaction over the global oceans. *J. Climate* 15, 2205–2231. doi: 10.1175/1520-0442(2002)015<2205:TABTIO>2.0.CO;2

Alexander, M. A., and Scott, J. D. (2008). The role of Ekman ocean heat transport in the northern hemisphere response to ENSO. *J. Climate* 21, 5688–5707. doi: 10.1175/2008JCLI2382.1

Anderson, J. J., and Devol, A. H. (1973). Deep water renewal in Saanich Inlet, an intermittently anoxic basin. *Estuar. Coast. Mar. Sci.* 1, 1–10. doi: 10.1016/0302-3524(73)90052-2

Bakun, A. (1973). *Coastal upwelling indices, West Coast of North America 1946-1971*. (Seattle, WA, USA:Department of Commerce, National Oceanic and Atmospheric Administration, National Marine Fisheries Service) SSRF–671, 103pp.

Bograd, S. J., Schwing, F. B., Castro, C. G., and Timothy, D. A. (2002). Bottom water renewal in the Santa Barbara Basin. *J. Geophys. Res.: Oceans* 107, 9–1. doi: 10.1029/2001JC001291

Bourbonnais, A., Lehmann, M. F., Hamme, R. C., Manning, C. C., and Juniper, S. K. (2013). Nitrate elimination and regeneration as evidenced by dissolved inorganic nitrogen isotopes in Saanich Inlet, a seasonally anoxic fjord. *Mar. Chem.* 157, 194–207. doi: 10.1016/j.marchem.2013.09.006

Bylhouwer, B., Ianson, D., and Kohfeld, K. (2013). Changes in the onset and intensity of wind-driven upwelling and downwelling along the North American Pacific coast. *J. Geophys. Res.: Oceans* 118, 2565–2580. doi: 10.1002/jgrc.20194

Camargo, D., Murowinski, E., Lueck, R., and Wolk, F. (2014). "Turbulence over the sill of Saanich Inlet, BC, Canada," in *Proceedings of the 17th Physics of Estuaries and Coastal Seas (PECS) conference*. Available at: https://rocklandscientific.com/wp-content/uploads/2015/01/xabs_183_Camargo_etal.pdf.

Campbell, C., and Belcic, B. (2006). *Shawnigan-Goldstream water allocation plan*. (Victoria, BC, Canada:Water Stewardship Division, Ministry of Environment, Province of British Columbia).

Cannon, G., Holbrook, J., and Pashinski, D. (1990). Variations in the onset of bottom-water intrusions over the entrance sill of a fjord. *Estuaries* 13, 31–42. doi: 10.2307/1351430

Capelle, D., Hallam, S., and Tortell, P. (2019). Time-series CH_4 measurements from Saanich Inlet, BC, a seasonally anoxic fjord. *Mar. Chem.* 215:1–10. doi: 10.1016/j.marchem.2019.103664

Capelle, D. W., Hawley, A. K., Hallam, S. J., and Tortell, P. D. (2018). A multi-year time-series of N_2O dynamics in a seasonally anoxic fjord: Saanich inlet, British Columbia. *Limnol. Oceanography* 63, 524–539. doi: 10.1002/lno.10645

Carter, N. M. (1934). Physiography and oceanography of some British Columbia fjords. *Proc. Fifth Pacif. Sci. Cong* 1, 721.

Chu, J. W., and Tunnicliffe, V. (2015). Oxygen limitations on marine animal distributions and the collapse of epibenthic community structure during shoaling hypoxia. *Global Change Biol.* 21, 2989–3004. doi: 10.1111/gcb.12898

Emerson, S., Cranston, R., and Liss, P. (1979). Redox species in a reducing fjord: equilibrium and kinetic considerations. *Deep Sea Res. Part A* 26, 859–878. doi: 10.1016/0198-0149(79)90101-8

Engida, Z., Monahan, A., Ianson, D., and Thomson, R. E. (2016). Remote forcing of subsurface currents and temperatures near the northern limit of the California Current System. *J. Geophys. Res.: Oceans* 121, 7244–7262. doi: 10.1002/2016JC011880

Farmer, D., D'Asaro, E., Trevorrow, M., and Dairiki, G. (1994). Three-dimensional structure in a tidal convergence front. *Continental Shelf Res.* 15, 1649–1673. doi: 10.1016/0278-4343(94)00084-Z

Fiedler, P., Mendelssohn, R., Palacios, D., and Bograd, S. (2013). Pycnocline variations in the Eastern Tropical and North Pacific 1958–2008. *J. Climate* 26, 583–599. doi: 10.1175/JCLI-D-11-00728.1

Flater, D. (2001) *XTide*. Available at: https://flaterco.com/xtide/.

Fofonoff, N. P., and Millard, R. C. (1983). Algorithms for the computation of fundamental properties of seawater. *UNESCO Tech. Papers Mar. Sci* 44, 53pp. (Paris, France:UNESCO). doi: 10.25607/OBP-1450

Freeland, H. J., and Denman, K. L. (1982). A topographically controlled upwelling center off southern Vancouver Island. *J. Mar. Res.* 40, 1069–1093.

Frischknecht, M., Münnich, M., and Gruber, N. (2015). Remote versus local influence of ENSO on the California Current System. *J. Geophys. Res.: Oceans* 120, 1353–1374. doi: 10.1002/2014JC010531

Gargett, A. E. (1994). Observing turbulence with a modified acoustic Doppler current profiler. *J. Atmospheric Oceanic Technol.* 11, 1592–1610. doi: 10.1175/1520-0426(1994)011<1592:OTWAMA>2.0.CO;2

Gargett, A. E., Stucchi, D., and Whitney, F. (2003). Physical processes associated with high primary production in Saanich Inlet, British Columbia. *Estuarine Coast. Shelf Sci.* 56, 1141–1156. doi: 10.1016/S0272-7714(02)00319-0

Geyer, W., and Cannon, G. (1982). Sill processes related to deep water renewal in a fjord. *J. Geophys. Res.: Oceans* 87, 7985–7996. doi: 10.1029/JC087iC10p07985

Griffin, D. A., and LeBlond, P. H. (1990). Estuary/ocean exchange controlled by spring-neap tidal mixing. *Estuarine Coast. Shelf Sci.* 30, 275–297. doi: 10.1016/0272-7714(90)90052-S

Grundle, D. S., Timothy, D. A., and Varela, D. E. (2009). Variations of phytoplankton productivity and biomass over an annual cycle in Saanich Inlet, a British Columbia fjord. *Continental Shelf Res.* 29, 2257–2269. doi: 10.1016/j.csr.2009.08.013

Hamme, R. C., Berry, J. E., Klymak, J. M., and Denman, K. L. (2015). In situ O_2 and N_2 measurements detect deep-water renewal dynamics in seasonally-anoxic Saanich Inlet. *Continental Shelf Res.* 106, 107–117. doi: 10.1016/j.csr.2015.06.012

Hawley, A. K., Brewer, H. M., Norbeck, A. D., Paša-Tolić, L., and Hallam, S. J. (2014). Metaproteomics reveals differential modes of metabolic coupling among ubiquitous oxygen minimum zone microbes. *Proc. Natl. Acad. Sci.* 111, 11395–11400. doi: 10.1073/pnas.1322132111

Herlinveaux, R. (1962). Oceanography of Saanich Inlet in Vancouver Island, British Columbia. *J. Fish. Board Canada* 19, 1–37.

Ji, Q., Jameson, B. D., Juniper, S. K., and Grundle, D. S. (2020). Temporal and vertical oxygen gradients modulate nitrous oxide production in a seasonally anoxic fjord: Saanich inlet, British Columbia. *J. Geophys. Res.: Biogeosci.* 125, e2020JG005631. doi: 10.1029/2020JG005631

Johannessen, S. C., and McCarter, B. (2010). Ecosystem status and trends report for the Strait of Georgia ecozone. *Fish. Oceans Canada Can. Sci. Advisory Secretariat* 1919-50442010/010, 51pp.

Juniper, S. K., and Brinkhurst, R. O. (1986). Water-column dark CO_2 fixation and bacterial-mat growth in intermittently anoxic Saanich Inlet, British Columbia. *Mar. Ecol. Prog. Ser.* 33, 41–50.

Kämpf, J., and Chapman, P. (2016). *Upwelling systems of the world* (Switzerland: Springer).

Lavelle, J. W., Cokelet, E. D., and Cannon, G. A. (1991). A model study of density intrusions into and circulation within a deep, silled estuary: Puget Sound. *J. Geophys. Res.* 96, 16779. doi: 10.1029/91jc01450

LeBlond, P. H., Ma, H., Doherty, F., and Pond, S. (1991). Deep and intermediate water replacement in the Strait of Georgia. *Atmosphere-Ocean* 29, 288–312. doi: 10.1080/07055900.1991.9649406

Lee, B.-S., Bullister, J. L., and Whitney, F. A. (1999). Chlorofluorocarbon CFC-11 and carbon tetrachloride removal in Saanich Inlet, an intermittently anoxic basin. *Mar. Chem.* 66, 171–185. doi: 10.1016/S0304-4203(99)00039-0

Leonov, D., and Kawase, M. (2009). Sill dynamics and fjord deep water renewal: idealized modeling study. *Continental Shelf Res.* 29, 221–233. doi: 10.1016/j.csr.2008.04.005

Levings, C. D. (1980). Demersal and benthic communities in Howe Sound basin and their responses to dissolved oxygen deficiency. *Fisheries and Aquatic Sciences no. 951,*. (Vancouver, BC, Canada:Department of Fisheries and Oceans).

Mackas, D. L., Denman, K. L., and Bennett, A. F. (1987). Least squares multiple tracer analysis of water mass composition. *J. Geophys. Res.: Oceans* 92, 2907–2918. doi: 10.1029/JC092iC03p02907

Manning, C. C., Hamme, R. C., and Bourbonnais, A. (2010). Impact of deep-water renewal events on fixed nitrogen loss from seasonally-anoxic Saanich Inlet. *Mar. Chem.* 122, 1–10. doi: 10.1016/j.marchem.2010.08.002

Masson, D. (2002). Deep water renewal in the Strait of Georgia. *Estuarine Coast. Shelf Sci.* 54, 115–126. doi: 10.1006/ecss.2001.0833

Masson, D. (2006). Seasonal water mass analysis for the Straits of Juan de Fuca and Georgia. *Atmosphere-Ocean* 44, 1–15. doi: 10.3137/ao.440101

Masson, D., and Cummins, P. F. (2000). Fortnightly modulation of the estuarine circulation in Juan de Fuca Strait. *J. Mar. Res.* 58, 439–463. doi: 10.1357/002224000321511106

Miller, A., White, W., and Cayan, D. (1997). North Pacific thermocline variations on ENSO timescales. *J. Phys. Oceanography* 27, 2023–2039. doi: 10.1175/1520-0485(1997)027<2023:NPTVOE>2.0.CO;2

Newton, J., Bassin, C., Devol, A., Kawase, M., Ruef, W., Warner, M., et al. (2007). "Hypoxia in Hood Canal: An overview of status and contributing factors," in *Proceedings of the 2007 Georgia Basin Puget Sound Research Conference*. Seattle, WA, USA:University of Washing.

Pawlowicz, R. (2002). Observations and linear analysis of sill-generated internal tides and estuarine flow in Haro Strait. *J. Geophys. Res.* 107, 1–13. doi: 10.1029/2000jc000504

Pawlowicz, R. (2017). Seasonal cycles, hypoxia, and renewal in a coastal fjord (Barkley Sound, British Columbia). *Atmosphere-Ocean* 55, 264–283. doi: 10.1080/07055900.2017.1374240

Pike, R., Goetz, J., Spittlehouse, D. L., and Young, E. (2018). Cowichan River: A summary of historical disturbances, water use pressures and streamflow trends. *Tech. rep., Water Science Series WSS2017-05.* (Victoria B.C, Canada:Prov. B.C).

Ray, S., Siedlecki, S., Alexander, M., Bond, N., and Hermann, A. (2020). Drivers of subsurface temperature variability in the Northern California Current. *J. Geophys. Res.: Oceans* 125, e2020JC016227. doi: 10.1029/2020JC016227

Richards, F. A. (1965). "Anoxic basins and fjords," in *Chemical Oceanography vol. I*. Eds. J. P. Riley and G. Skirrow (New York, USA:Academic Press), 611–645.

Schinke, H., and Matthäus, W. (1998). On the causes of major Baltic inflows–an analysis of long time series. *Continental Shelf Res.* 18, 67–97. doi: 10.1016/S0278-4343(97)00071-x

Stucchi, D., and Giovando, L. (1984). "Deep water renewal in Saanich Inlet, B.C," in *Proceedings of a Multidisciplinary Symposium on Saanich Inlet*, vol. 38, 7–15. (Sidney, BC, Canada:Department of Fisheries and Oceans Canada).

Takahashi, M., Seibert, D., and Thomas, W. (1977). Occasional blooms of phytoplankton during summer in Saanich Inlet, BC, Canada. *Deep Sea Res.* 24, 775–780. doi: 10.1016/0146-6291(77)90499-4

Thomson, R., Kulikov, E., Spear, D., and Johannessen, S. (2020). A role for gravity currents in cross-sill estuarine exchange and subsurface inflow to the southern Strait of Georgia. *J. Geophys. Res.: Oceans* 125, 1–24. doi: 10.1029/2019JC015374

Thomson, R. E., Spear, D. J., Krassovski, M. V., Hourston, R. A., Juhász, T. A., and Mihály, S. F. (2017). Buoyancy-driven coastal current blocks ventilation of an anoxic fjord on the Pacific coast of Canada. *J. Geophys. Res.: Oceans* 122, 2976–2998. doi: 10.1002/2016JC012512

Timothy, D. A., and Soon, M. Y. (2001). Primary production and deep-water oxygen content of two British Columbian fjords. *Mar. Chem.* 73, 37–51. doi: 10.1016/S0304-4203(00)00071-2

Torres-Beltrán, M., Hawley, A. K., Capelle, D., Zaikova, E., Walsh, D. A., Mueller, A., et al. (2017). A compendium of geochemical information from the Saanich Inlet water column. *Sci. Data* 4, 1–11. doi: 10.1038/sdata.2017.159

Torres-Beltrán, M., Mueller, A., Scofield, M., Pachiadaki, M. G., Taylor, C., Tyshchenko, K., et al. (2019). Sampling and processing methods impact microbial community structure and potential activity in a seasonally anoxic fjord: Saanich Inlet, British Columbia. *Front. Mar. Sci.* 6. doi: 10.3389/fmars.2019.00132

Tunnicliffe, V. (1981). High species diversity and abundance of the epibenthic community in an oxygen-deficient basin. *Nature* 294, 354–356. doi: 10.1038/294354a0

Waldichuk, M. (1957). Physical oceanography of the Strait of Georgia, British Columbia. *J. Fish. Board Canada* 14, 321–486. doi: 10.1139/f57-013

Zaikova, E., Walsh, D. A., Stilwell, C. P., Mohn, W. W., Tortell, P. D., and Hallam, S. J. (2010). Microbial community dynamics in a seasonally anoxic fjord: Saanich Inlet, British Columbia. *Environ. Microbiol.* 12, 172–191. doi: 10.1111/j.1462-2920.2009.02058.x

frontiers | Frontiers in Marine Science

TYPE Original Research
PUBLISHED 16 November 2022
DOI 10.3389/fmars.2022.929913

OPEN ACCESS

EDITED BY
Annie Bourbonnais,
University of South Carolina,
United States

REVIEWED BY
Volker Brüchert,
Stockholm University, Sweden
Gwénaëlle Chaillou,
Université du Québec à Rimouski,
Canada

*CORRESPONDENCE
Pei-Chuan Chuang
pchuang@geomar.de

SPECIALTY SECTION
This article was submitted to Marine Biogeochemistry, a section of the journal Frontiers in Marine Science

RECEIVED 27 April 2022
ACCEPTED 15 September 2022
PUBLISHED 16 November 2022

CITATION
Chuang P-C, Anderson CH, Kossack M, Fabian J, Su C-C, Vosteen P, Zabel M, Scholz F, Schulz-Vogt HN, Sommer S and Dale AW (2022) Nutrient turnover by large sulfur bacteria on the Namibian mud belt during the low productivity season. *Front. Mar. Sci.* 9:929913. doi: 10.3389/fmars.2022.929913

Nutrient turnover by large sulfur bacteria on the Namibian mud belt during the low productivity season

Pei-Chuan Chuang[1]*, Chloe H. Anderson[2], Michael Kossack[2], Jenny Fabian[3], Chih-Chieh Su[4], Paul Vosteen[1], Matthias Zabel[2], Florian Scholz[1], Heide N. Schulz-Vogt[3], Stefan Sommer[1] and Andrew W. Dale[1]

[1]GEOMAR Helmholtz Centre for Ocean Research Kiel, Kiel, Germany, [2]MARUM – Center for Marine Environmental Sciences, University of Bremen, Bremen, Germany, [3]Leibniz Institute for Baltic Sea Research Warnemünde, Rostock, Germany, [4]Institute of Oceanography, National Taiwan University, Taipei, Taiwan

Surface sediments of the coastal mud belt in the Benguela Upwelling System (BUS) off Namibia host extensive communities of chemotrophic large sulfur bacteria (LSB) of the family *Beggiatoaceae* such as *Thiomargarita* spp. and *Candidatus Maribeggiatoa* spp. In order to understand the role of these bacteria in N and P cycling, biogeochemical data from three sites in the mud belt were simulated with a biogeochemical model including LSB catabolic pathways. Organic carbon remineralization was dominated by the reduction of sulfate to hydrogen sulfide (5.0–7.7 mmol C m^{-2} d^{-1}). At the two stations where LSB were observed, produced hydrogen sulfide was almost completely oxidized by LSB using nitrate as the electron acceptor. Modeled rates of nitrate reduction to N_2 by LSB were over two times higher than nitrate reduction to ammonium. This points toward a potential negative feedback by LSB on primary production. Furthermore, loss of fixed N strongly enriched the benthic fluxes in P relative to N. Although the model included intracellular polyphosphate accumulation by LSB and subsequent breakdown to phosphate, a clear link between polyphosphate dynamics and hydroxyapatite precipitation and burial could not be clearly substantiated. This is partly due to simplifying assumptions in the model and analytical uncertainties in distinguishing between authigenic hydroxyapatite and allochthonous hydroxyapatite (e.g., fish bones), both of which are major components of particulate P in the BUS. Our modeling suggests a significant control of LSB on benthic N and P fluxes to the water column. Given the extensive coverage of LSB on the shelf (>30,000 km^2), more accurate forecasts of nutrient cycling and primary production in the BUS necessitate a closer inspection of benthic P sources and sinks in the mud belt and a clearer understanding of the controls on the end product of nitrate reduction by LSB.

KEYWORDS

nutrient turnover, sediments, large sulfur bacteria, Benguela Upwelling System (BUS), hydrogen sulfide oxidation, DNRA, polyphosphate

Introduction

The major nutrients nitrogen (N) and phosphorus (P) are required for the growth of all organisms, and their availability largely controls the productivity of marine ecosystems. On long kyr time scales, changes in the oceanic N and P inventories can have major impacts on the global carbon cycle (Gruber, 2008; Wallmann et al., 2016). Today, eastern boundary upwelling systems including the California, Humboldt, Canary, and Benguela current systems play a significant role in the marine C cycle, accounting for 10% to 20% of total marine primary production and global fish catches despite covering less than 1% of the ocean surface (Carr, 2001; Capone and Hutchins, 2013; Malone et al., 2017). Among the four major upwelling systems, the Benguela Upwelling System (BUS), located along the coasts of Angola, Namibia, and South Africa (14°S–34°S), has the highest primary production at 0.37 Gt C yr^{-1} (Carr, 2001).

In the northern part of the BUS, especially offshore Namibia between 20°S and 25°S, a perennial oxygen minimum zone (OMZ) in subsurface waters along the coast has been present for millennia (West et al., 2004; Hutchings et al., 2009). The lack of oxygen is driven by intense respiration of phytodetritus in the water column and sediments (Brüchert et al., 2006; Mohrholz et al., 2008). In austral summer, the dominant water mass is the poleward-propagating and warm South Atlantic Central Water (SACW) from the Angola Gyre, which is nutrient-rich and oxygen-poor (~20–70 μM; Mohrholz et al., 2008). In austral winter, cross-shelf circulation intensifies and brings equatorward subtropical Eastern SACW (ESACW) that is more oxygenated (~250–300 μM) and lower in nutrients. The combination of nutrient supply, high particle fluxes to the seafloor, and low O_2 levels has resulted in an extensive mud belt on the Namibian shelf of over 700 km in length that is characterized by extraordinary particulate organic carbon (POC) contents exceeding 15% dry weight (Inthorn et al., 2006; Meisel et al., 2011) and high rates of benthic carbon respiration.

Respiration of carbon in the sedimentary mud belt is mainly carried out anaerobically by bacterial sulfate reduction, resulting in elevated concentrations of dissolved hydrogen sulfide (H_2S) in sediment porewaters (Brüchert et al., 2003; Brüchert et al., 2006). The flux of H_2S from the sediment to the bottom water is largely controlled by the activity of colorless large sulfur bacteria (LSB) of the family *Beggiatoaceae* such as chemotrophic *Thiomargarita* spp. and *Candidatus Maribeggiatoa* spp. that oxidize H_2S to gain energy (Schulz et al., 1999; Brüchert et al., 2003). These bacteria are aerobic or microaerophilic and present throughout the mud belt, covering an area >30,000 km^2 (Brüchert et al., 2006). If the efficiency of the microbial filter is inhibited, H_2S can escape the sediment and produce plumes of elemental sulfur in the water column that are detectable by satellite imagery (Ohde and Dadou, 2018). These sulfidic events appear to correlate with the seasonal variability of the OMZ and generally occur in late austral summer (February–March) and early austral autumn (April–May) (Ohde and Dadou, 2018). Given its toxicity, sulfide accumulation in the water column can cause massive fish mortality (Brüchert et al., 2003; Brüchert et al., 2006; Ohde and Dadou, 2018). A firm understanding of the factors leading to benthic H_2S emissions is therefore of prime importance.

LSB oxidize sulfide using nitrate (NO_3^-) stored in their intracellular vacuoles, producing either ammonium (NH_4^+) or N_2 as the N end product (Otte et al., 1999; Winkel et al., 2016). These pathways are referred to as dissimilatory nitrate reduction to ammonium (DNRA) or dinitrogen ($DNRN_2$). DNRA and $DNRN_2$ are of environmental significance since the former recycles fixed N between NO_3^- and NH_4^+, whereas the latter leads to a net loss of fixed N as N_2 gas. The environmental factors that determine the relative rates of these processes are generally unknown but may be related to the relative abundance of electron acceptors (Kraft et al., 2014). DNRA can have further significance for the overall N loss from the ecosystem. For instance, a significant fraction of NH_4^+ consumed in the water column offshore Peru by anammox can be supplied by DNRA in the sediments (Kalvelage et al., 2013; Dale et al., 2016a). In the BUS water column, massive N loss is known to occur through anammox and denitrification, but the contribution of benthic NH_4^+ to pelagic N loss is not well resolved (Kuypers et al., 2005; Nagel et al., 2013). A greater quantitative understanding of dissimilatory nitrate reduction is essential for closing nutrient budgets and for predicting benthic-pelagic feedback across the mud belt (Brüchert et al., 2003; Borchers et al., 2005; Dale et al., 2009).

In addition to their influence on benthic N cycling, LSB may be instrumental in controlling porewater PO_4^{3-} concentrations and benthic P fluxes (Schulz and Schulz, 2005; Goldhammer et al., 2010; Brock and Schulz-Vogt, 2011; Goldhammer et al., 2011; Dale et al., 2013; Langer et al., 2018). LSB, in addition to other microorganisms, are thought to accumulate polyphosphate under oxic or hypoxic conditions (Schulz and Schulz, 2005; Brock and Schulz-Vogt, 2011). Polyphosphates are long chains of orthophosphate units linked by high energy phosphoanhydride bonds (Gächter and Meyer, 1993). Hydrolysis of polyphosphate under unfavorable anoxic or sulfidic conditions provides an energy source for the bacteria and releases PO_4^{3-} to the porewater (Jones et al., 2016). This mechanism has been suggested to drive a sink for P *via* the precipitation of authigenic hydroxyapatite (Schulz and Schulz, 2005).

The importance of the BUS to the Namibian economy justifies a closer inspection and understanding of N and P sources and sinks. In this study, we examine this aspect from a benthic perspective with a particular focus on LSB. Due to the complexities of the coupled C, S, and nutrient cycles, we use a numerical model to assess how LSB influence nutrient turnover and sediment–water exchange fluxes. To date, only a limited number of studies have quantified the biogeochemical turnover

rates of N and P in Namibian shelf and the linkages with LSB (Brüchert et al., 2003; Schulz and Schulz, 2005; Dale et al., 2009; Goldhammer et al., 2010; Neumann et al., 2016). In this study, new data from sediments of the Namibian mud belt are used to estimate the relative importance of $DNRN_2$ versus DNRA and the impact on the N and P fluxes communicated to the water column.

Study site and methods

Study area

Data are presented from three stations in the northern BUS: within and at the edge of the mud belt at 23°S and within the mud belt at 25°S (Figure 1). Upwelling at 23°S is strong but only seasonally active, whereas at 25°S–27°S upwelling persists throughout the year (Mohrholz et al., 2008; Hutchings et al., 2009). The inner shelf mud belt covers a total area of 30,000 km^2 (Brüchert et al., 2006). It is composed of organic- and diatom-rich mud with minimal dilution by terrigenous sediment (Calvert and Price, 1983; Borchers et al., 2005). Microbial sulfate reduction rates can be exceptional (>60 mmol m^{-2} d^{-1}), with dissolved H_2S levels occasionally exceeding 15 mM a few cm below the sediment surface (Brüchert et al., 2006). At St. 14, *Ca. Maribeggiatoa* spp. and *Thiomargarita* spp. were prevalent, whereas at St. 41, *Thiomargarita* spp. were dominant (Fabian et al., in prep). At St. 12, no conspicuous LSB were observed. Observations of the filamentous LSB *Ca. Marithioploca* spp. have also been reported (Gallardo et al., 1998; Flood et al., 2021), but are probably not widely distributed, and no specimens were observed at the sites studied here or detected based on 16S-RNA (data not shown). During the fieldwork, the water mass on the inner shelf was dominated by ESACW that prevented anoxic conditions in the bottom waters (Zabel et al., 2019). Bottom waters were nonetheless low in O_2 (26–53 µM), with NO_3^- and PO_4^{3-} concentrations of ~24 µM for NO_3^- and ~1 µM for PO_4^{3-}, respectively (Supplementary Table 1).

Sampling and analytical methods

Sediment data presented in this study were collected from St. 12 (23°S), St. 14 (23°S), and St. 41 (25°S) (Figure 1). Although several other sites were sampled throughout the mud belt, the sediments at these three stations presented clear and contrasting geochemical trends that are suitable for modeling. Sediments were collected with a multiple-corer (MUC) and a gravity corer (GC) during R/V *Meteor* cruise 157 between 4 August and 16 September, 2019, which corresponds to the low productivity season (Zabel et al., 2019). Sampling and analytical methods are described in detail by Zabel et al. (2019). After core retrieval, all cores were transferred to a cool room on board (4°C). Gravity

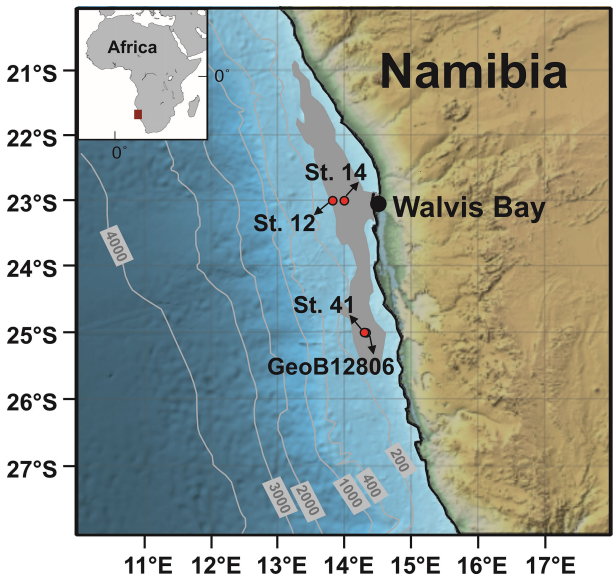

FIGURE 1
Sampling locations on the Namibian mud belt (bathymetry contours in m). The approximate extension of mud belt shown in gray is based on Inthorn et al. (2006) and Zabel et al. (2012) for surface sediments with total organic carbon (TOC) concentrations higher than 5 wt%. St. 12 (23° 00′S; 13°52.0′E; water depth = 151 m) is located at the edge of the mud belt. St. 14 (23°00′S; 14°02.9′E; water depth = 138 m), St. 41 (25°00′S; 14°22.6′E; water depth = 140 m), and GeoB12806 (25°00.4′S; 14°23.5′E; water depth = 133 m) are located inside the mud belt.

cores were 3–5 m long and were cut into 1m sections on the deck prior to subsampling. The MUC deployments recovered approximately 40 cm of sediment at each site.

MUC cores were subsampled into Falcon tubes in a glove bag under argon at a resolution of 1 to 4 cm. Porewater samples were collected by centrifugation and filtered (0.2 µm cellulose-acetate filters) inside the glove bag. Wet sediments were sampled into pre-weighed plastic cups for water content and porosity determinations at a resolution of 1 to 4 cm. Porewater samples from GCs were extracted using rhizon samplers (5 cm length, 0.2 µm porous polymer) at 15 to 40 cm intervals. Wet sediments for porosity were sampled at a resolution of 1 m.

Dissolved iron (Fe^{2+}), phosphate (PO_4^{3-}), and ammonium (NH_4^+) were analyzed immediately onboard. The remaining samples and porewater aliquots were refrigerated for analysis at the home laboratories following the cruise. Fe^{2+} was analyzed photometrically (Hach Lange DR 5000 photometer) at 565 nm following the method of Collins et al. (1959). Aliquots of 1 ml of acidified sample (20 µl of 1% ascorbic acid) were added to 50 µl of a ferrospectral reagent (Merck Chemicals) in disposable polystyrene cuvettes (Stookey, 1970) for analyses. Samples with high Fe^{2+} concentrations were diluted with oxygen-free artificial seawater. PO_4^{3-} concentrations were determined photometrically *via* the molybdenum blue method using a Hach Lange DR 5000 photometer (Grasshoff et al., 1999). Highly sulfidic samples were spiked with 20 µl of 30% HCl and bubbled with argon for 1 minute to limit sulfide interference for PO_4^{3-} analysis. NH_4^+ was measured by flow injection using a polytetrafluoroethylene (PTFE) tape gas separator technique after Hall and Aller (1992). The precisions of the Fe^{2+}, PO_4^{3-}, and NH_4^+ analyses were 1%, 7% and 6%, respectively.

Shore-based analyses at MARUM (Bremen, Germany) included sulfate (SO_4^{2-}), hydrogen sulfide (H_2S), and cations. SO_4^{2-} was determined by ion chromatography (Metrohm 861 Advanced Compact IC, Metrohm A Supp 5 column, 0.8 ml min^{-1}, conductivity detection after chemical suppression). Total dissolved H_2S was measured photometrically using the methylene blue method in samples that were fixed on board with zinc acetate (ZnAc) (Cline, 1969). The analytical precision for SO_4^{2-} and H_2S analysis was 2%. Dissolved calcium (Ca^{2+}) and magnesium (Mg^{2+}) were determined in samples acidified by suprapure concentrated HNO_3 (10 µl per ml of sample) by inductively coupled plasma optical emission spectroscopy (ICP-OES; axial plasma observation; Agilent 720) with a precision of 2%.

Porewater data from site GeoB12806 collected during R/V *Meteor* cruise M76/1 in April/May 2008 were used in addition to data from St. 41 to help constrain the model, as the locations of these two stations are nearly identical (Figure 1). Sampling and analytical methods were presented in Goldhammer et al. (2011) with the exception of total alkalinity. Total alkalinity was determined by titration of 1 ml of porewater with 0.01 or 0.05 M of HCl to pH 3.8 (Grasshoff et al., 1999).

A comparison of porewater data from the GCs and MUCs suggested a loss of surface sediments from the GCs during penetration of the core into the sediment of 20 cm (St. 12), 37 cm (St. 14), 34 cm (St. 41), and 27 cm (GeoB12806). The data presented here have been corrected accordingly.

Cells of *Thiomargarita* spp. were collected from a 1 ml sediment subsample upon visual identification using a stereomicroscope. To estimate the biovolume of all *Thiomargarita* spp. cells in the 1 ml sediment sample, the cells were first divided into different size classes. Then, the number of cells (c) and the average cell radius ($\bar{r}$) were determined for each size class (a) to calculate the total biovolume of all cells per size class assuming a spherical cell structure (Eq. (1)). Finally, the total biovolume of all cells per 1 ml of sediment was determined as the sum of the biovolumes of all size classes (n):

$$\textbf{Biovolume} = \sum_{a=1}^{n} \frac{4}{3} \cdot \pi \cdot \bar{r}_a^3 \cdot c_a \quad (1)$$

The concentration of intracellularly stored nitrate was determined by nitrate analysis on an autoanalyzer from 200 collected cells after washing them three times in sterile filtered seawater and subjecting them to a cycle of shock freezing and thawing to break the cell walls. From these data, the NO_3^- stored within the large sulfur bacteria (NO_{3bac}^-) could be calculated.

Porosity was determined from the water loss after freeze-drying assuming a seawater density of 1.023 g cm^{-3} and a particle density of 2.5 g cm^{-3}. The freeze-dried solid phase was analyzed for POC, total particulate nitrogen (TN), and total particulate sulfur (TS) using an element analyzer (Euro EA, HEKAtech). POC was determined after acidifying the sample with 0.25 N of HCl to remove carbonate. POC content refers to the dry weight percent (wt%) of C (detection limit<0.1 wt% and relative error of 3%). Total iron (TFe) concentration in the solid phase was determined by ICP-OES following digestion in nitric acid, hydrofluoric acid, and perchloric acid (Scholz et al., 2011). For quality control of the procedure, the certified reference material MESS-3 (Canadian Research Council) was digested and analyzed along with the sediment samples. The measured TFe in the reference material was always within the certified range.

A five-step sequential extraction scheme modified after Ruttenberg (1992); Schenau and De Lange (2000), and Küster-Heins et al. (2010) was used for the speciation of particulate P. Approximately 125 mg freeze-dried sediment sample was successively washed with 25 ml of 1) 2 M of NH_4Cl (pH 7; 4 h; repeated 8 to 10 times), 2) CDB (citrate-dithionite-bicarbonate) buffer solution (pH 7.5; 8 h), 3) 1 M of sodium acetate buffer solution (pH 4; 6 h), 4) 1 M of HCl (24 h), and 5) 1 M of HCl (24 h) after ignition for 3 h at 550°C. The extracted P components include biogenic P in fish scales, bones, and teeth that are mainly composed of hydroxyapatite (P_{Hydap}) from step 1, iron-bound P (P_{Fe}) from step 2, authigenic apatite ($P_{Authigenic}$) from step 3 typically corresponding to carbonate fluorapatite,

detrital P ($P_{Detrital}$) from step 4, and organic P (P_{org}) from step 5. The sum of these fractions gives the total P content (P_{total}). The P concentration of the solutions was determined by ICP-OES with a precision of<5%. TS, TFe, and P phases are reported in μmol (g dry weight)$^{-1}$ of S, Fe, and P, respectively.

Freeze-dried sediment samples were used for determining ^{210}Pb activity. At St. 12, samples (>5 g) were measured for a total ^{210}Pb by a low-background coaxial Ge(Li) detector *via* its gamma peak at 46.5 keV at Kiel University, Germany (e.g., Bohlen et al., 2011). As there were limited amounts of sediment available for St. 14 and St. 41, samples (0.5 to 3.5 g) were measured by using the well-type HPGe gamma spectrometry system (GWL-100230) at the Institute of Oceanography, National Taiwan University (Geilert et al., 2018). Excess ^{210}Pb ($^{210}Pb_{xs}$) was calculated by subtracting ^{214}Pb from the total ^{210}Pb. The activities of radionuclides were decay-corrected to the sampling date. All radionuclide data were calculated on a salt-free dry-weight basis.

Mass accumulation and sedimentation rate

Mass accumulation rates (MAR in g cm^{-2} yr^{-1}) were derived from the $^{210}Pb_{xs}$ data below the mixed layer. The mixed layer was estimated by visual inspection as the depth where a change in the $^{210}Pb_{xs}$ content was discernible (Figure 2). Below this depth, particles are transported downwards by burial and compaction (e.g., de Haas et al., 1997). The slope of the regression line of ln($^{210}Pb_{xs}$) activity versus depth was used to determine MAR (Huh et al., 2009). Assuming steady-state sediment accumulation, the sedimentation rate (ω_{acc} in cm yr^{-1}), or burial velocity, was then calculated using the porosity (φ_∞) of the compacted sediment (0.89 at St. 12, 0.95 at St. 14, and 0.93 at St. 41) and a dry sediment density (ds) of 2.5 g cm^{-3}:

$$\omega_{acc} = \frac{MAR}{ds \times (1 - \varphi_\infty)} \quad (2)$$

φ_∞ was determined from the porosity data in the same core where ^{210}Pb was measured. We assumed that the derived ω_{acc} values are valid over the depth of our main model simulation (100 cm, see below), which implies steady-state sediment accumulation over the time period during which the top meter was deposited (~1 kyr). Strictly, however, ^{210}Pb-derived sedimentation rates are reliable over the lifetime of the radiotracer (~100 yr).

The $^{210}Pb_{xs}$ data were further used to determine sediment mixing rates either by animals (i.e., bioturbation) or by current-induced disturbance of the surface layer. The mixing coefficient, $D_B(0)$ (cm^2 yr^{-1}), was obtained by inverse modeling of the $^{210}Pb_{xs}$ data following Dale et al. (2021).

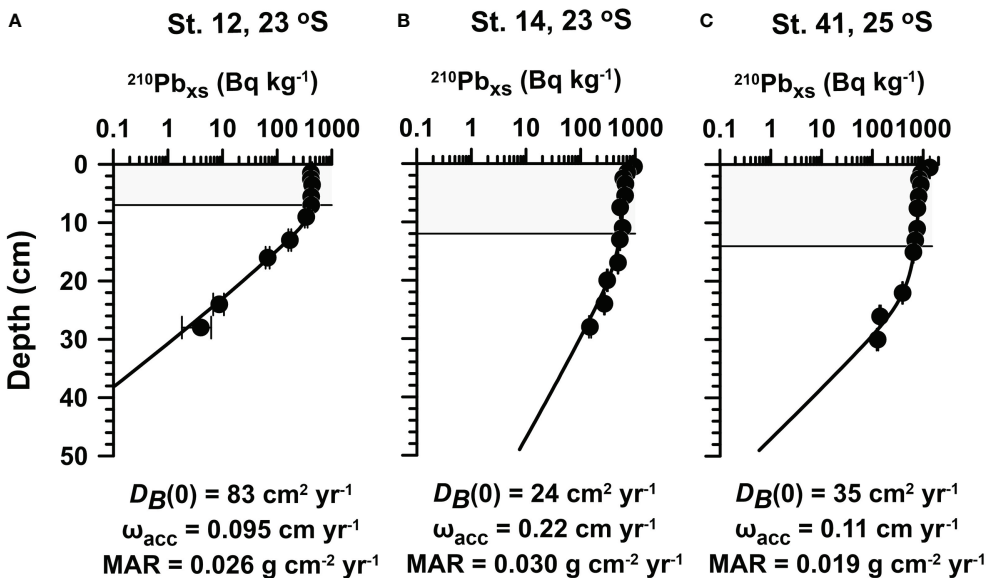

FIGURE 2
Measured (symbols) and modeled (curves) excess ^{210}Pb ($^{210}Pb_{xs}$) at **(A)** St. 12, **(B)** St. 14, and **(C)** St. 41. Mass accumulation rates (MAR), sedimentation accumulation rates (ω_{acc}), and bioturbation coefficients [$D_B(0)$] were calculated as described in *Sampling and analytical methods*. The mixed layer depth is indicated by the gray shaded area.

Reaction-transport model

To quantify the turnover of C, S, N, and P in the mud belt sediments, a steady-state, vertically resolved 1-D reaction-transport model (RTM) was applied to simulate the geochemical data. The model was based on previous studies of biogeochemical cycles in low-oxygen environments (Dale et al., 2009; Bohlen et al., 2011; Dale et al., 2016a; Dale et al., 2016b; Dale et al., 2019), yet now including two pathways of DNRA and a more comprehensive P cycle, as detailed below.

The RTM includes the biogeochemical network in Figure 3 and simulates the distributions of 15 dissolved species including O_2, NO_2^-, NO_3^-, SO_4^{2-}, H_2S, CH_4, NH_4^+, dissolved inorganic carbon (DIC), PO_4^{3-}, TA (total alkalinity), Ca^{2+}, Mg^{2+}, Fe^{2+}, H_2, and NO_3^- stored within the large sulfur bacteria (NO_{3bac}^-). It further includes 16 solid species, consisting of four fractions of reactive POC, organic sulfur (S_{org}), particulate organic nitrogen (N_{org}), two reactive iron (oxyhydr)oxide fractions (i.e., highly reactive ($Fe(OH)_{3HR}$) and moderately reactive ($Fe(OH)_{3MR}$)) and unreactive iron fraction (Fe_U), and pyrite (FeS_2). Five particulate P fractions are considered: P_{org}, P_{Fe}, intracellular polyphosphate (P_{poly}), fish bones deposited on the seafloor (P_{Fish}), and authigenic hydroxyapatite (P_{HAp}). The operationally defined $P_{Authigenic}$ fraction is not included since it is negligible in the cores studied (Supplementary Figure 1), which suggests that carbonate fluorapatite is of minor importance. On the Namibian margin, the dominant authigenic phase is hydroxyapatite (Schulz and Schulz, 2005). In the model, measured P_{Hydap} is compared to the sum of the simulated P_{Fish} and P_{HAp} fractions since these two components cannot be clearly separated analytically. Solids are transported through the sediment column by accumulation (burial) and mixing by animals (bioturbation). Solutes are transported by molecular diffusion, (bio)irrigation, and bioturbation. A complete description of the model is given in the Supplementary Material and Supplementary Tables 2–6. It should be remembered that the steady-state model represents only a snapshot of the reaction rates and fluxes based on the measured geochemical data at the time of sampling. Based on previous non-steady-state modeling of OMZ sediments offshore Peru, we estimate that the seasonality in benthic fluxes varies within 20%–30% of the annual mean (Dale et al., 2017). This can be taken as a rough estimate of the accuracy of our model simulation results.

The primary redox reactions that describe POC remineralization (Supplementary Table 5, R1–R6) by various electron acceptors include aerobic respiration, NO_3^- and NO_2^- reduction, iron reduction, sulfate reduction, and methanogenesis. The total POC degradation rate (R_{POC}) is the sum of the degradation rates of the four POC fractions (POC_i, i =1–4), each assigned with a different first-order reactivity constant (k_{POCi}, i = 1–4), i.e. a multi-G model (Jørgensen, 1978; Westrich and Berner, 1984). This number of fractions is arbitrary and is the minimum required to capture the evolving trends in the solid phase and solution chemistry at the study sites. POC degradation rates were constrained from the measured NH_4^+, SO_4^{2-}, POC, and TA data and benthic flux data of O_2, H_2S, NH_4^+, and PO_4^{3-}.

The model includes a range of secondary redox reactions (i.e. those not directly coupled to degradation of POC) including aerobic and anaerobic oxidation of NH_4^+, NO_2^-, H_2S, and Fe^{2+}, reductive dissolution of Fe oxides coupled to oxidation of hydrogen sulfide, FeS_2 precipitation; and anaerobic oxidation of methane by SO_4^{2-} (AOM). Hydroxyapatite is oversaturated in mud belt porewaters (Goldhammer et al., 2010), and its precipitation is modeled as a first-order kinetic process that is dependent on the porewater PO_4^{3-} concentration (Supplementary Table 6; R23) and is constrained with the measured data (Figure 4). P_{org} and P_{Fish} are added to the sediment from the water column and undergo simple first-order dissolution. P_{Fe} arrives at the seafloor with iron (oxyhydr)oxides and is also formed authigenically during the precipitation of iron (oxyhydr)oxides (e.g., Slomp et al., 1996). P_{Fe} is considered for both

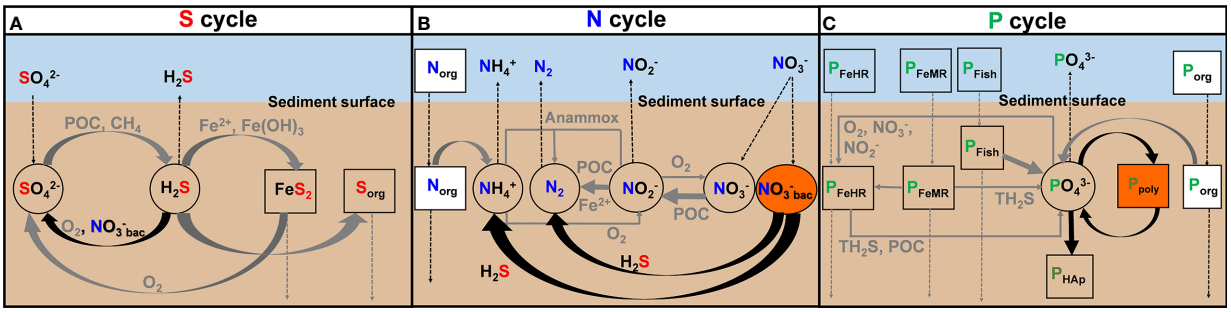

FIGURE 3
Schematic diagram of key biogeochemical processes of **(A)** S, **(B)** N, and **(C)** P cycles in Namibian mud belt sediments considered in the model, including pathways of biological NO_3^- (NO_{3bac}^-) reduction by giant sulfur bacteria. The thick black arrows highlight the important reactions related to giant sulfur bacteria.

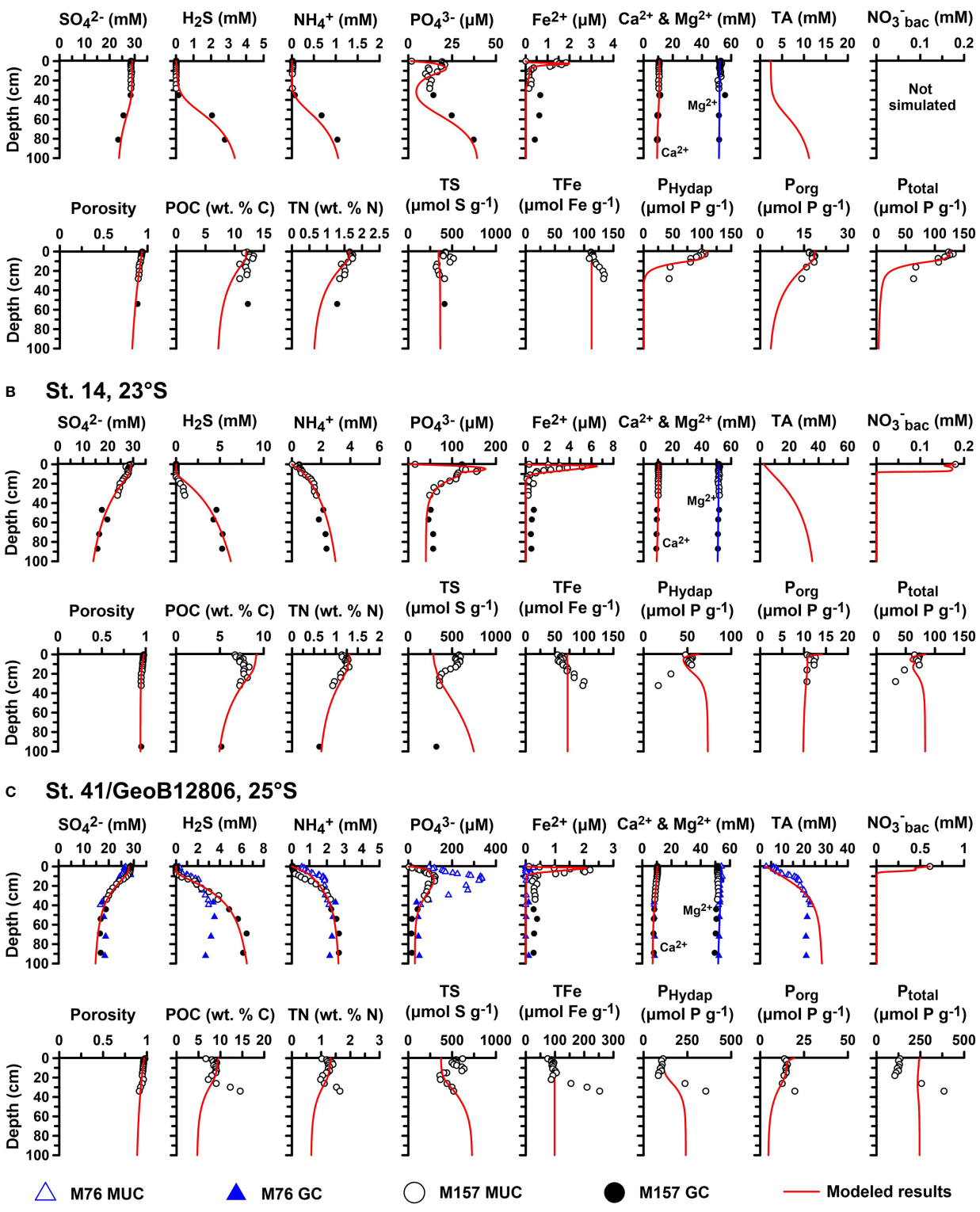

FIGURE 4
Modeled (curves) and measured (symbols) depth profiles of solutes, porosity, and solid species in the upper 100 cm at **(A)** St. 12, **(B)** St. 14, and **(C)** St. 41/GeoB12806. Sediments were collected with a multiple-corer (MUC) (open symbols) and a gravity corer (GC) (filled symbols) during R/V *Meteor* cruises 157 (circles) and 76 (triangles).

highly reactive and moderately reactive fractions (P_{FeHR} and P_{FeMR}). The kinetic rate constants for these processes were either constrained from the data or taken from the literature (Supplementary Table 4).

The key reactions associated with the LSB are H_2S oxidation and the associated P recycling (Figure 3). The model does not differentiate between the different species of large sulfur bacteria since these microorganisms share similar biogeochemistry (Otte et al., 1999; Schulz and Jørgensen, 2001; Mußmann et al., 2007; Winkel et al., 2016). Two pathways of H_2S oxidation coupled to nitrate reduction were considered (Winkel et al., 2016). The first is the DNRA:

$$H_2S + NO^-_{3bac} + H_2O \rightarrow SO^{2-}_4 + NH^+_4 \quad (3)$$

and the second is $DNRN_2$:

$$\frac{5}{8}H_2S + NO^-_{3bac} \rightarrow \frac{1}{2}N_2 + \frac{1}{2}H_2O + \frac{5}{8}SO^{2-}_4 + \frac{1}{4}H^+ \quad (4)$$

Fewer moles of H_2S are required to reduce 1 mole of nitrate with N_2 as the end product versus NH^+_4. $DNRN_2$ also leads to a net loss of 0.25 alkalinity equivalents, whereas DNRA has no net alkalinity change. The rates of DNRA and $DNRN_2$ were constrained by the porewater H_2S depletion in the upper sediment layers, NH^+_4 concentrations, and NO^-_{3bac} in surface sediments. The rate of PO^{3-}_4 uptake and storage as P_{poly} in LSB was dependent on NO^-_{3bac} contents and ambient PO^{3-}_4 concentrations. Since it is unclear whether P_{poly} is extracted from the leaching steps (Goldhammer et al., 2010), the modeled P_{poly} pool was added to the sum of other modeled P species and compared to total extracted P fractions (P_{total}).

LSB require a continuous source of NO^-_3 to sustain their metabolic activity. Some members of the *Beggiatoaceae* like *Ca. Maribeggiatoa* spp. are motile and can take up NO^-_3 from the bottom water by extending their filaments through the sediment surface (Schulz and Jørgensen, 2001). However, the exact mechanism by which *Thiomargarita* spp. access NO^-_3 is poorly understood. Since *Thiomargarita* spp. are probably non-motile, it has been argued that passive mixing of the sediment by strong bottom currents is required for them to replenish their intracellular reservoir (Schulz and Jørgensen, 2001). The rate of mixing of sediments required to simulate H_2S depletion in surface sediments would be equivalent to ca. 3 $cm^2\ d^{-1}$ over the upper 10 cm (Dale et al., 2009). This mixing intensity would result in homogenous $^{210}Pb_{xs}$ contents within the mixed layer, which is inconsistent with the observed more gradual decrease in $^{210}Pb_{xs}$ in the mixed layer (see *Results*). Consequently, without further information on how *Thiomargarita* spp. capture NO^-_3, NO^-_{3bac} was transported into the sediment assuming a non-local source term analogous to that described by Dale et al. (2009) (see Supplementary Table 2).

The total model length was 650 cm, although the focus here is on the upper 100 cm where reaction rates are the highest. By simulating a depth larger than the section of interest, we avoid artifacts caused by imposing lower boundary conditions for solutes at 100 cm. From 100 down to 650 cm, the model is only fit to the SO^{2-}_4, H_2S, NH^+_4, and POC data with the aim of providing a more robust assessment of the slowly degrading organic matter fractions in the top 100 cm (Dale et al., 2011). The kinetic rate constants for organic matter degradation become more uncertain with depth below 100 cm since sediment accumulation cannot be assumed to have been at a steady state over 650 cm. For this reason, we relegate model simulation plots below 100 cm to the Supplementary Material.

The model was solved using MATHEMATICA software and run to steady state. Upper boundary conditions for all species are listed in Supplementary Table 1 and comprise fixed concentrations for solutes and fluxes for solids. At 650 cm, a zero-gradient Neumann boundary was imposed for all species, except for H_2S and NH^+_4 at St. 12 where a non-zero gradient was configured from the measured concentration gradients.

Results

Sediment biogeochemistry

Sediment geochemical data in the top 100 cm at the four sites are shown in Figure 4, and SO^{2-}_4, H_2S, NH^+_4, and POC data within the upper 650 cm are shown in Supplementary Figure 2.

The upper sediments were characterized by a high-water content. Porosity decreased slightly from 0.98 to approximately 0.9 at St. 14 and St. 41 and from 0.93 to approximately 0.82 for St. 12 (Figure 4). $^{210}Pb_{xs}$ distributions indicated a surface mixed layer of 7 cm, 12 cm, and 14 cm at St. 12, St. 14, and St. 41, respectively (Figure 2). A rather high mixing coefficient was determined for St. 12 (83 $cm^2\ yr^{-1}$), with lower values at St. 14 (24 $cm^2\ yr^{-1}$) and St. 41 (35 $cm^2\ yr^{-1}$). MAR ranged from 0.019 to 0.030 g $cm^{-2}\ yr^{-1}$ across the sites. As expected from the respective locations, sedimentation rates were the highest at St. 14 (0.22 cm yr^{-1}) compared to St. 41 (0.11 cm yr^{-1}) and St. 12 (0.095 cm yr^{-1}). These are in the same order as those determined at other sites on the Namibian shelf and slope (~0.1 cm yr^{-1}, Dale et al., 2009; Emeis et al., 2009).

POC contents were within previously reported values for the mud belt (Figure 4), ranging from 5% to 15% (Inthorn et al., 2006). TN contents displayed similar trends as POC. Mean C/N ratios were 8.9, 7.5, and 8.4 at St. 12, St. 14, and St. 41, respectively (Supplementary Figure 1). TS contents varied between 317 and 636 μmol g^{-1}. Total iron (TFe) increased with depth from 112 to 135 μmol g^{-1} at St. 12 and from 55 to 100 μmol g^{-1} at St. 14, whereas it decreased with depth from 158 to 132 μmol g^{-1} at St. 41/GeoB12806. P_{total} concentrations were lowest at St. 14 (< 70 μmol g^{-1}) and highest at St. 41 (>300 μmol g^{-1}) and showed either a general decrease (St. 12 and St. 14) or increase (St. 41) in the top 30 cm (Supplementary Figure 1). More than 68% (St. 12), 52% (St. 14), and 77% (St. 41) of P

extracted from the solid phase were composed of P_{Hydap}. P_{org} was the next most abundant phase, with $P_{Authigenic}$, P_{Fe}, and $P_{Detrital}$ being of minor importance. P_{org} concentrations were fairly similar at all sites with little down-core variability (15–20 μmol g^{-1}). Mean organic C:P_{org} ratios were 592, 537, and 507 at St. 12, St. 14, and St. 41, respectively. The mean ratios of C to total reactive P ($P_{reactive} = P_{Hydap} + P_{Fe} + P_{Authigenic} + P_{org}$) were 102, 106 and 54. Overall, more than 95% of P was $P_{reactive}$.

Thiomargarita spp. were present at St. 14 and St. 41 and at other stations in the mud belt but absent at St. 12 (Zabel et al., 2019). The total biovolume of *Thiomargarita* spp. at St. 14 (0.2 μl ml^{-1} of sediment) was lower than at St. 41 (2.5 μl ml^{-1} of sediment). The opposite is true regarding intracellular NO_3^- concentrations at these sites, which were 445 mmol L^{-1} of biovolume at St. 14 and 188 mmol L^{-1} of biovolume at St. 41. These values were converted to porewater equivalents using a porosity of 0.9. The average NO_{3bac}^- concentrations on a porewater basis at St. 14 and St. 41 were 0.10 and 0.52 mmol L^{-1} of porewater, respectively. For all sampling stations at 23°S and 25°S where *Thiomargarita* spp. were observed, the mean NO_{3bac}^- was 0.18 mmol L^{-1} of porewater and 0.61 mmol L^{-1} of porewater, respectively. These data are used in the model as boundary conditions for intracellular NO_3^- (Supplementary Table 1).

In general, SO_4^{2-} concentrations decreased over the upper 100 cm due to microbial degradation of organic matter (Figure 4). At St. 12, SO_4^{2-} concentrations in the top 30 cm were unusually constant and close to seawater values. NH_4^+ and H_2S concentrations at St. 12 showed a similar behavior to SO_4^{2-} with very low concentrations in the top 30 cm. At St. 14, NH_4^+ increased immediately below the sediment surface, whereas H_2S remained at μM levels down to 15 cm, below which H_2S increased to 5 mM at 40 cm. The two proximate sites St. 41 and GeoB12806 showed a mixed picture, with higher NH_4^+ and H_2S concentrations immediately detectable below the sediment surface at St. GeoB12806. At St. 41, NH_4^+ and H_2S concentrations were low in the upper 10 cm but then increased to similar levels as at St. GeoB12806. The gravity core data below 100 cm show that NH_4^+ and H_2S concentrations continued to increase at St. 14 and St. 41, whereas at St. 12, they both decreased steadily toward the bottom of the core (Supplementary Figure 2). High levels of total alkalinity in excess of 20 mM were measured at St. GeoB12806, presumably due to the anaerobic breakdown of organic matter by sulfate reduction.

Plots of NH_4^+ versus SO_4^{2-} were used to estimate the molar ratio of NH_4^+ produced versus SO_4^{2-} reduced, $r_{N:S}$, at St. 14 and St. 41, assuming that sulfate reduction is the dominant carbon respiration pathway (Burdige, 2006; Burdige and Komada, 2013; Dale et al., 2021). The changes in porewater NH_4^+ and SO_4^{2-} concentrations were calculated relative to the bottom water concentrations (shown as the capital delta, Δ, in Figure 5). The left-hand side of the following equation is the slope of the linear regression of the data shown in Figure 5:

$$\frac{d\mathrm{NH}_4^+}{d\mathrm{SO}_4^{2-}} = -r_{N:S} \cdot \frac{D_{\mathrm{SO}_4^{2-}}}{D_{\mathrm{NH}_4^+}} \quad (5)$$

where D_i is the bulk molecular diffusion coefficient of solute *i* (Supplementary Table 3). For Redfield C/N stoichiometry of 16, and assuming that the organic carbon being oxidized has an oxidation state of zero, the expected slope between NH_4^+ and SO_4^{2-} is 0.3 (Dale et al., 2021). $r_{N:S}$ values in the mud belt were higher and decreased with sediment depth. At St. 14, $r_{N:S}$ decreased from 0.49 to 0.37, and at St. 41, $r_{N:S}$ decreased from 0.43 to 0.15.

Dissolved Fe^{2+} concentrations displayed a surface peak of up to 5 μM at all stations. The Fe^{2+} peak was more pronounced at St. GeoB12806 compared to St. 41. Below 10 cm, Fe^{2+} levels were <1 μM. The Fe^{2+} peaks were coincident with local maxima in PO_4^{3-} concentrations, which reached the highest levels of ca. 340 μM at St. GeoB12806. Ca^{2+} and Mg^{2+} showed little change from bottom water values over depth at St. 12 and St. 14, indicating little or no net carbonate precipitation, whereas at St. 41, Ca^{2+} and Mg^{2+} decreased to 8.3 and 50.0 mM at 100 cm.

Diagenetic model simulations

Baseline model simulations showed a very good correspondence with the field data over the upper 100 cm (Figure 4) and over 650 cm for SO_4^{2-}, H_2S, NH_4^+, and POC (Supplementary Figure 2). This was mainly achieved by adjusting the rate constants for POC degradation and the boundary fluxes of POC at the seafloor. The unchanging concentrations of SO_4^{2-}, H_2S, and NH_4^+ down to 35 cm at St. 12 (Figure 4A) could only be simulated assuming intense (bio) irrigation of porewater solutes, as discussed later. The model was able to reproduce the surface Fe^{2+} and PO_4^{3-} peaks, and the measured particulate P fractions were reasonably well simulated (Figures 4B, C).

The total modeled flux of POC (i.e. the rain rate) to the seafloor required to achieve a good correspondence between porewater and solid phase data and the model was 17.5, 9.0, and 12.8 mmol m^{-2} d^{-1} at St. 12, St. 14, and St. 41/GeoB12806, respectively (Table 1). According to the model, the most reactive POC fraction was highly labile, with first-order degradation constants of 33, 30, and 12 yr^{-1} at St. 12, St. 14, and St. 41, respectively, corresponding to half-lives of 8, 8, and 21 days. This fraction is completely oxidized within the mixed layer. The less reactive fractions have half-lives (calculated from the rates constants) of 30–9,000 years and are degraded over greater depths. Depth-integrated rates of POC mineralization were 8.7, 6.1, and 9.1 mmol m^{-2} d^{-1} of C at St. 12, St. 14, and St. 41/GeoB12806 (Supplementary Table 7; Supplementary Figure 3). Sulfate reduction (R5, Supplementary Table 7; Supplementary Figure 3) was the major POC remineralization

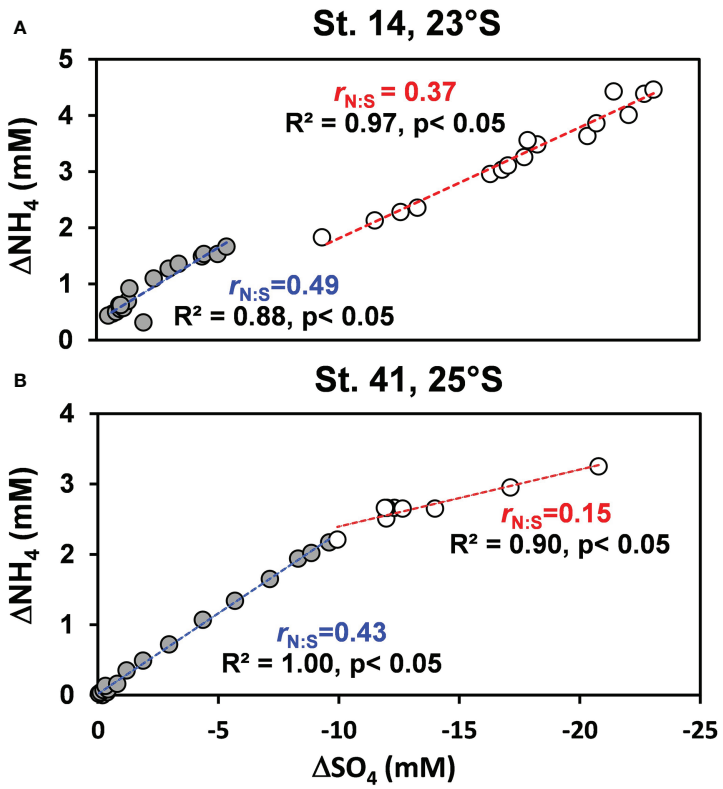

FIGURE 5
NH_4^+ – SO_4^{2-} property–property plots for the changes in porewater NH_4^+ and SO_4^{2-} concentrations relative to the bottom water concentrations (shown as the capital delta, Δ) at **(A)** St. 14 and **(B)** St. 41. The slope of the correlation ($d NH_4^+/d SO_4^{2-}$) is used to calculate $r_{N:S}$ (Eq. (5)). The data for each regression were chosen by eye from the conceivable changes in slope. In panel **(A)**, the filled circles represent data from 0.5 to 32 cm, and the open circles below 47 cm. In panel **(B)**, the filled circles represent data from 0.5 to 34 cm, and the open circles below 44 cm.

pathway and the major sink for sulfate (5.0–7.7 mmol C m^{-2} d^{-1}). The other POC remineralization pathways were negligible by comparison (Supplementary Table 7).

The model predicted that the H_2S produced by sulfate reduction at St. 14 and St. 41 was mainly consumed by DNRA and $DNRN_2$ in the upper 10 cm (Supplementary Figure 4). Depth profiles of ΣDNRA + $DNRN_2$ rates at St. 14 and St. 41 (Supplementary Figure 4) were almost identical to total H_2S oxidation rates, demonstrating that these pathways were mainly responsible for H_2S oxidation. The sum of these two rates (R15 + R16) was 1.9 and 3.4. mmol m^{-2} d^{-1} of H_2S, respectively, (Supplementary Figure 3D). At St. 12, where no LSB were observed, the model predicted that a small fraction of H_2S was oxidized aerobically, with the bulk of H_2S inferred to be lost to the overlying water by (bio)irrigation (model data not shown). At St. 14 and St. 41, POC degradation and DNRA contributed equally to NH_4^+ production (Supplementary Figure 3). At these stations, $DNRN_2$ was twice as high as DNRA and thus the major nitrate reduction pathway.

Depth-integrated rates of biogenic P_{Fish} dissolution were similar at the three stations (R29; 0.33 –0.43 mmol P m^{-2} d^{-1}; Supplementary Table 7; Supplementary Figure 3). Organic P dissolution rates were comparatively lower (0.031–0.19 mmol P m^{-2} d^{-1}), and rates of iron-associated P turnover were negligible. Although P_{Fish} dissolution rates were similar across the sites, peak PO_4^{3-} concentrations were <25 μM at St. 12, but 150 μM at St. 14 and >100 μM at St. 41 (Figure 4). The model is able to reproduce the PO_4^{3-} peaks at St. 14 and at St. 41 as well as the particulate P contents when P_{poly} accumulation and breakdown were included in the model. P_{poly} turnover was apparently rapid (1.8 mmol P m^{-2} d^{-1} at St. 14). By contrast, P_{HAp} precipitation rates ranged from <0.01 mmol P m^{-2} d^{-1} at St. 12 to 0.24 mmol P m^{-2} d^{-1} at St. 41.

NH_4^+, PO_4^{3-}, and H_2S modeled fluxes ranged from −0.3 to −1.6, −0.3 to −0.5, and −0.0013 to −2.97 mmol m^{-2} d^{-1} at St. 12, St. 14, and St. 41, respectively (Supplementary Table 8). By comparison, the fluxes of NO_3^- + NO_2^- (hereafter ΣNO_3^-) ranged from 0.86 to 5.18 mmol N m^{-2} d^{-1} (Supplementary Table 8), showing that the sediments were a net sink for ΣNO_3^-. The modeled flux ratios of ΣNO_3^-: PO_4^{3-} were thus negative (approximately −1.1 to −2.1). Including the intracellular uptake of ΣNO_3^- leads to even lower ratios of −2.2 to −18.5

TABLE 1 Organic carbon budget at the three sites in the northern BUS compared with published data.

Site	Rain rate (mmol C m^{-2} d^{-1})	POC accumulation (mmol C m^{-2} d^{-1})	CBE (%)	Primary production (mmol C m^{-2} d^{-1})	POC accumulation / Primary production (%)
St. 12, 23°S	17.5[a]	14.6[b]	84[c]	208[d]	7.0
St. 14, 23°S	9.0[a]	7.0[b]	78[c]	208[d]	3.4
St. 41 and GeoB12806, 25°S	12.8[a]	8.5[b]	67[c]	208[d]	4.1
Northern BUS (<500 m) [e]	13.7[f]	6.8[g]	50[c]	137	5.0
Namibian shelf (100 m) [h]	100	60	60	150	40
Peruvian shelf (<200 m) [i]	33	11	33	111	10
Global coastal ocean (<200 m)	13.3[j]	4[j]	30[j]	26–41[k]	10–15

[a]Model results (this study).
[b]Model results at 10 cm (this study).
[c]Obtained by dividing the POC accumulation rate by the rain rate.
[d]Monteiro (2010).
[e]Emeis et al. (2018).
[f]Sediment trap data at 23°S and 60 m water depth.
[g]At 5 cm depth.
[h]Brüchert et al. (2003).
[i]Mean values from Dale et al. (2015).
[j]Burdige et al. (2007) for muddy sediments.
[k]Assuming a primary production of 3,100–4,900 Tg C yr^{-1} in the coastal ocean (<200m depth) (Buitenhuis et al., 2013) and a seafloor area<200 m of 27.1 × 10^{12} m^2 (Burdige et al., 2007).

(Supplementary Table 8). Modeled flux ratios of total dissolved inorganic N (NH_4^+ + NO_3^- + NO_2^-): PO_4^{3-} ranged from −1.1 to 4.6 and DIC: PO_4^{3-} from 12 to 31 (Supplementary Table 8). These are much lower than the respective Redfield ratios of 16 and 106 and demonstrate strong enrichment of dissolved P from the sediment to the water column relative to N and C (Supplementary Table 8). The highest predicted benthic O_2 flux was 2.5 mmol O_2 m^{-2} d^{-1} at St. 12, and the lowest value was calculated for St. 14 (0.71 mmol O_2 m^{-2} d^{-1}). Modeled fluxes compare well with flux measurements made using benthic chambers during the same campaign and with *ex situ* diffusive fluxes (Figure 6). Clearly though, the variability in measured fluxes is high.

Discussion

POC degradation and burial

High biological productivity has led to the formation of an extensive mud belt parallel to the coastline in the northern BUS that consists of organic-rich diatom ooze interspersed with fish debris and phosphorite deposits (Bremner, 1980; Emeis et al., 2004). Our model-derived POC rain rates (~9 to 18 mmol C m^{-2} d^{-1}) compare well with previously reported values from sediment traps of 13.7 mmol C m^{-2} d^{-1} (Table 1). This is approximately 10% of primary production (137 mmol C m^{-2} d^{-1}; Emeis et al., 2018). Consequently, POC accumulation rates in the sediment (~7 to 15 mmol C m^{-2} d^{-1}; Table 1) are equivalent to 3%–7% of primary production, which can be interpreted as the overall preservation efficiency of newly synthesized POC (Table 1). This is similar to other reports from the Namibian and Peruvian shelf (Dale et al., 2015; Emeis et al., 2018), but far lower than the 40% estimated for the 100m isobath in the mud belt by Brüchert et al. (2003). This might be because POC rain rates and burial rates were not directly measured by these workers but inferred from other data. It should be noted that the mean measured sulfate reduction rates reported by Brüchert et al. (2003) for the 100 m isobath (20 mmol S m^{-2} d^{-1}) require carbon rain rates of at least 40 mmol m^{-2} d^{-1} of POC according to the reaction stoichiometry, a factor of 2–4 higher than those at our sites. Although temporal variability cannot be dismissed, these discrepancies underscore the heterogeneity of benthic carbon turnover in the mud belt and, possibly, highly patchy preservation efficiencies of new production. Spatial heterogeneity of benthic carbon remineralization is further evident in the banded distribution of organic carbon across the mud belt and in the wide range of benthic solute fluxes (Bremner, 1983; Neumann et al., 2016; Sommer et al., in prep.).

The carbon burial efficiency (CBE, %) with regard to the deposition of POC at the seafloor can be estimated as POC accumulation rate / rain rate × 100%. CBEs for our sites were calculated using the POC accumulation rates at 10 cm depth (for comparison with similar data from Peru, see Table 1) and the model-derived rain rate. This calculation assumes that the organic matter reaching the seafloor has been deposited vertically from the photic zone. The derived CBEs were rather similar: 84%, 78%, and 67% at St. 12, St. 14, and St. 41, respectively (Table 1). CBEs calculated from sediment trap data were lower at 50% (Emeis et al., 2018).

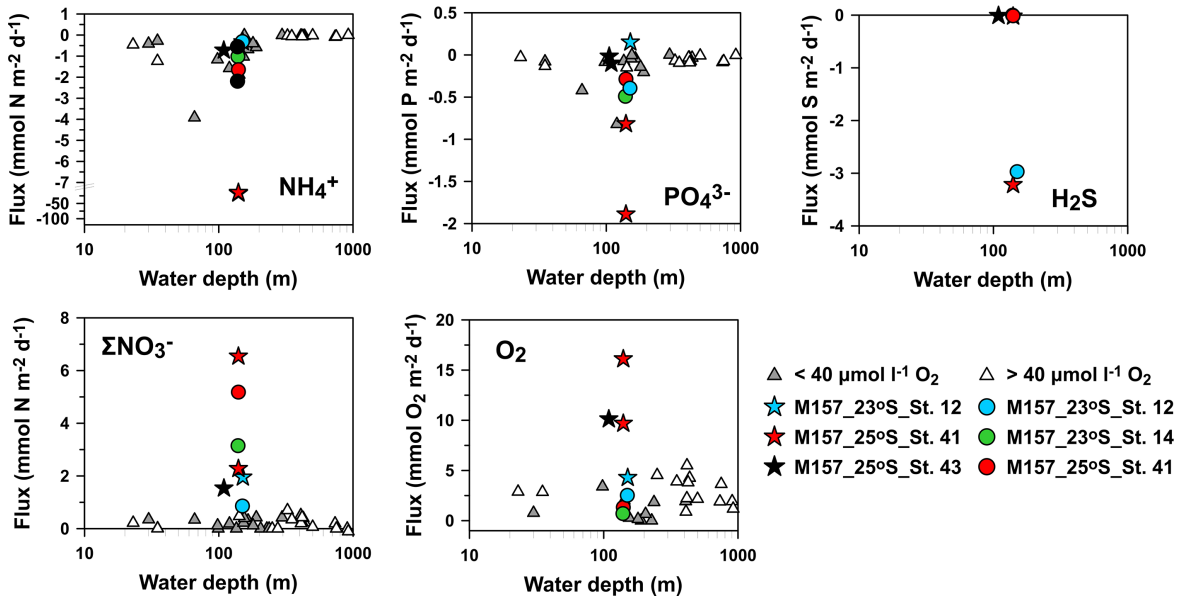

FIGURE 6
Comparison of modeled benthic fluxes (circles) with *in situ* benthic fluxes measured using benthic chambers during M157 (stars; Sommer et al., in prep.) and *ex situ* diffusive fluxes (triangles; Neumann et al., 2016) versus water depth (logarithmic scale). Ranges of modeled benthic fluxes for St. 14 (green bars) and St. 41 (red bars) reflect a sensitivity analysis with and without sulfide oxidation by large sulfur bacteria (LSB). Note the axis break for NH_4^+. Positive fluxes are directed into the sediment and vice versa. Note that red and green circles overlap in the H_2S plot.

Amino acid degradation indices (DI; Dauwe et al., 1999) in surface sediments of nearby stations have been published (Nagel et al., 2016), where high DI values indicate good preservation of organic matter. Based on values at nearby sites, the DI is approximately 0.9 at St. 14, 0.7 at St. 41, and 0.4 at St. 12, suggesting that organic matter is more degraded at St. 12. Similar logic can be inferred from the lower C:N ratios in surface sediments at St. 14 and St. 41 (~7) compared to St. 12 (~9) (Supplementary Figure 1). Based on these results, the decrease in CBE from the mud belt sites to St. 12 might have been expected to be more pronounced.

Additional controlling factors for carbon preservation include oxygen availability and bioturbation. Exposure of organic particles to oxygen is understood to promote carbon degradation (Hedges and Keil, 1995; Hartnett et al., 1998). Bioturbation can further enhance the oxygen exposure time through continual sediment reworking. Faunal community analysis suggests that the macrofaunal biomass is higher at St. 12 at the western edge of the mud belt compared to St. 14 and other mud belt sites along 23°S (M. Zettler, pers. comm). This agrees with mixing rates inferred from $^{210}Pb_{xs}$, which were the highest at St. 12 (Figure 2). Bottom water O_2 levels at the edge of the mud belt also tend to be greater than sites closer to land (Nagel et al., 2016). These observations dovetail with the findings from the DI and C/N ratios, whereby the conditions at St. 12 ought to be conducive to a lower CBE compared to St. 14 and St. 41. We speculate that the CBE calculation at St. 12 is confounded by the lateral transport of organic particles in the bottom nepheloid layers (Inthorn et al., 2006; Mollenhauer et al., 2007). Offshore particle transport leads to an incremental deposition of older, reworked material, as described for deeper water on the margin (Inthorn et al., 2006) and for the Peruvian margin and the Californian basins (Berelson et al., 1996; Arthur et al., 1998; Dale et al., 2015). Since this material is inherently less reactive than material deposited vertically from the photic zone, POC accumulation rates will be skewed upwards, along with the calculated CBE (i.e. at the western-most St. 12).

The CBEs in the central mud-belt are markedly higher than 33% determined at similar water depths on the Peruvian inner shelf (Figure 7 and Table 1). DI values on the Peruvian shelf (~0.2 to 0.6) and total hydrolyzable amino acid contents are low compared to deeper waters in the permanently anoxic OMZ (Lomstein et al., 2009). This suggests that the organic matter on the Peruvian inner shelf is in a more advanced degradation compared to the central Namibian mud belt. The relatively low CBE on the Peruvian shelf is suspected to be caused by periodic oxygenation of bottom waters during the passage of coastal trapped waves that can raise O_2 levels above 100 µM and increase the oxygen exposure time of organic particles on the seafloor (Gutiérrez et al., 2008; Dale et al., 2015). Oxygenation is further associated with a shift in the macrofaunal community from tube-dwelling, interface feeders to burrowing, deposit feeders, and a further increase in oxygen exposure time

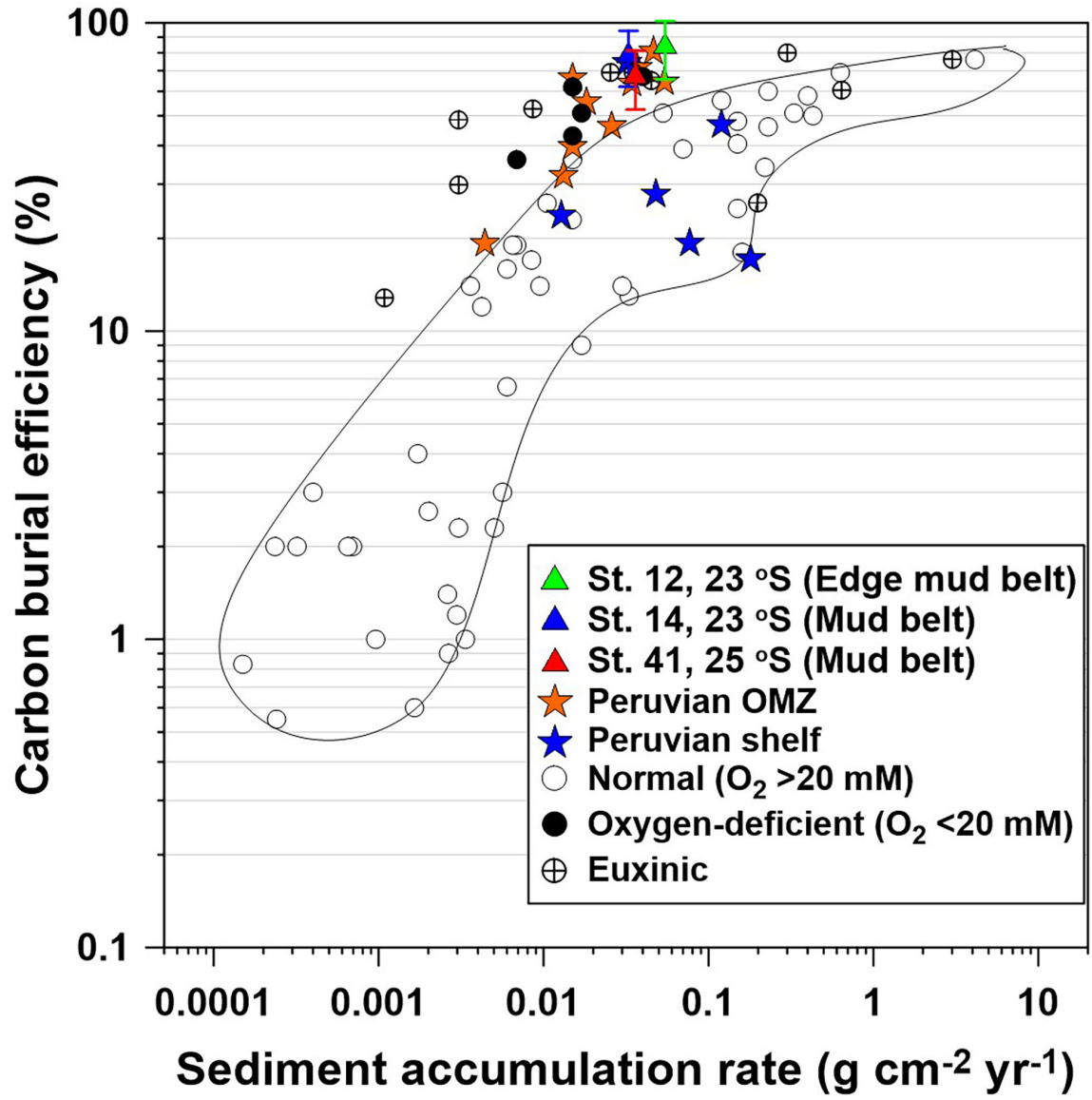

FIGURE 7
Carbon burial efficiency (CBE) versus sediment accumulation rate in contemporary ocean sediments. Blue and orange stars indicate CBE at 10 cm depth for the shelf sites of the Peruvian margin (from Dale et al., 2015). Open and filled circles represent sites from published studies with bottom water O_2 >20 and<20 μM, respectively; the former is enclosed by the solid line. Euxinic settings are also indicated (see Dale et al. (2015) for data sources). Green, blue, and red triangles are data from this study for CBE calculated at 10 cm depth (see text). Error bars were calculated using standard error propagation rules assuming a 20% uncertainty in ω_{acc} and particulate organic carbon (POC) content at 10 cm.

(Gutiérrez et al., 2008). In Namibia, such vigorous ventilation events are less frequent (Schmidt and Eggert, 2016; Pitcher et al., 2021), and organic matter preservation in the mud belt might instead be driven by the long-term redox state of the bottom waters. Nevertheless, due to the high porewater H_2S levels in the mud belt, sulfurization of organic carbon very likely further increases carbon preservation (Wakeham et al., 1995; Brüchert et al., 2000), although its quantitative significance is largely unknown (Dale et al., 2009). At Peru, porewaters tend to be depleted in H_2S in the upper 10 to 20 cm due to very efficient oxidation by gliding *Marithioploca* spp. (Dale et al., 2016a).

Coupled S and N cycling by LSB

Persistently low O_2 levels in bottom waters on the Namibian shelf preclude aerobic respiration as the major POC degradation pathway in mud belt sediments. Instead, sulfate reduction is the

major redox process for carbon mineralization (Brüchert et al., 2003). The sulfide produced by microbial sulfate reduction provides an energy source for LSB that thrive by oxidizing sulfide *via* dissimilatory nitrate reduction pathways (Schulz et al., 1999; Brüchert et al., 2003). These bacteria exert an important control on the distribution of H_2S in the porewater and its flux to the water column. At St. 14 and St. 41 where LSB were observed, porewaters were depleted in H_2S down to ca. 15 cm, which agrees with the depth distribution of LSB observed by Schulz et al. (1999). Benthic H_2S fluxes were negligible at St. 14 and St. 41. Benthic H_2S fluxes were also negligible in the mud belt at 23.5°S (St. 226680), even though sulfate reduction rates were fivefold higher (Table 2; Dale et al., 2009). Consequently, the H_2S oxidation efficiency by LSB at these locations is close to 100%. However, the picture across the mud belt is much more variable. Using data from 25 to 125 m water depth on the Namibian margin, Brüchert et al. (2003) reported significant fluxes of H_2S from the sediment (−1 to −32 mmol S m^{-2} d^{-1}), with a mean H_2S oxidation efficiency of only 16%. Sommer et al. (in prep.) also measured significant variability in benthic H_2S fluxes in the mud belt.

H_2S fluxes tend to be correlated with the distribution of LSB (Brüchert et al., 2006). These workers noted that some *Beggiatoaceae* strains, e.g., *Ca. Maribeggiatoa* spp., are more efficient at detoxifying H_2S compared to others, e.g., *Thiomargarita* spp., which are "leaky" with regard to benthic H_2S emissions. Different physiological adaptations may partly explain this behavior. The H_2S oxidation potential of *Thiomargarita* spp. depends on the amount of NO_3^- stored within their vacuoles that, in turn, is thought to rely on physical resuspension events for replenishment (Schulz and Jørgensen, 2001). Being both filamentous and motile, *Ca. Maribeggiatoa* spp. have an ecological advantage over *Thiomargarita* spp., since they can access the seawater NO_3^- pool directly by extending their filaments into the bottom water and by gliding vertically through the sediment. Therefore, *Ca. Maribeggiatoa* spp. are able to oxidize H_2S to greater depths below the sediment surface (Schulz and Jørgensen, 2001). The impact of filamentous *Marithioploca* in the Peruvian OMZ is even more striking. They are able to maintain H_2S-free porewater down to 30 cm or more despite similar rates of sulfate reduction as in the mud belt (Henrichs and Farrington, 1984; Fossing et al., 1995; Dale et al., 2016a). The dominant microbial community at any particular location could help to explain why sulfidic events in the Peruvian OMZ are rare compared to the northern BUS. It is thus essential that ecosystem models are able to incorporate the regional distribution of LSB communities into their predictions (Schmidt and Eggert, 2016).

Although *Thiomargarita* spp. were observed in our sediment samples, rates of DNRA and $DNRN_2$ by LSB were not measured directly but estimated *via* curve fitting of modeled and measured

TABLE 2 Depth-integrated modeled rates of sulfate reduction, H_2S oxidation, and the benthic H_2S flux in sediments inhabited by LSB.

Site	Bottom waterO_2	Sulfate reduction	H_2S flux	H_2S oxidation	H_2S oxidation by LSB	LSB oxidation efficiency	H_2S oxidation by LSB / Sulfate reduction
	(μM)	(mmol S m^{-2} day^{-1})				(%)	(%)
St. 14	26.3	2.5	−0.0013	1.98	1.93	97	77
St. 41	52.6	3.9	−0.0130	3.47	3.43	99	88
St. 226680 [a]	2.0	17.3	−0.0300	17.2	16.9	98	98
Namibian shelf [b]	<14.8	23.1 (6.3–62.7)	−7.7 (−1.2 to −32.2)	15.3 (5.5–46.8)	1.5 (0.7–3.7)	16 (0.44–54)	9.8 (0.16–25.69)

[a]Dale et al. (2009).
[b]The average values calculated from stations located between 25 and 125 m of water depth in Brüchert et al. (2003). The range of values is given in brackets.

TABLE 3 Modeled benthic fluxes for St. 14 and St. 41 derived from sensitivity analysis with and without sulfide oxidation by LSB.

	NH_4^+		PO_4^{3-}		H_2S		ΣNO_3^-		O_2	
	(mmol N m^{-2} d^{-1})		(mmol P m^{-2} d^{-1})		(mmol S m^{-2} d^{-1})		(mmol N m^{-2} d^{-1})		(mmol O_2 m^{-2} d^{-1})	
	St. 14	St. 41	St. 14	St. 41	St. 14	St. 41	St. 14	St. 41	St. 14	St. 41
Baseline model	−1.02	−1.64	−0.49	−0.28	−0.0013	−0.013	3.15	5.18	0.71	1.32
R_{DNRA} = 0	−0.55	−0.80	−0.49	−0.28	−0.0017	−0.019	3.35	5.58	0.68	1.36
R_{DNRN2} = 0	−2.19	−3.58	−0.49	−0.31	−0.0025	−0.049	2.35	3.73	0.74	1.54
R_{DNRA} = R_{DNRN2} = 0	−0.56	−0.84	−0.50	−0.35	−1.59	−2.97	0.41	0.41	0.82	1.75

Benthic fluxes results are derived from sensitivity analysis shown in Supplementary Figure 5.

porewater data. Sensitivity tests show that the predicted H_2S oxidation rates by LSB are well constrained by the measured NH_4^+ and H_2S data (Supplementary Figure 5). NH_4^+ increases markedly if the H_2S concentrations are instead fit to the data by assuming that DNRA is the only S oxidation pathway by LSB, which justifies including DNRA in the model. Turning off DNRA and $DNRN_2$ raises the concentrations of H_2S over the whole sediment core but lowers the concentrations of NH_4^+. At the same time, the NO_3^- uptake decreases to 0.41 mmol m^{-2} d^{-1} and NH_4^+ fluxes decrease to −0.56 and −0.84 mmol m^{-2} d^{-1} at St. 14 and St. 41, whereas H_2S fluxes increase to −1.6 and −3.0 mmol m^{-2} d^{-1} (Table 3).

Further evidence of DNRA is provided by the measured $r_{N:S}$ ratios (Figure 5). These can be used to derive the C-to-N ratio of organic matter undergoing degradation, $r_{C:N}$ (Dale et al., 2021), and compared to measured ratios in the sediment cores. Assuming a POC oxidation state of zero, $r_{C:N}$ is equal to $2/r_{N:S}$, where the factor 2 denotes the moles of POC oxidized per mole of SO_4^{2-} reduced during microbial sulfate reduction (Supplementary Table 5). This gives $r_{C:N}$ values of 4.1 and 4.7 for the upper sections of the sediment at St. 14 and St. 41, respectively (Figure 5). The measured C:N ratios in the upper sections (top ca. 30 cm) are far higher and range from ~7 to 11 (Supplementary Figure 1). The excess NH_4^+ in the porewater can be attributed to DNRA (Dale et al., 2016a).

Unfortunately, we could not apply this approach to quantify $DNRN_2$ due to the analytical challenges of measuring dissolved N_2, in sediment porewaters (Prokopenko et al., 2011). Genomic investigations of several LSB species underline their ability to oxidize H_2S through chemotrophic denitrification (Mußmann et al., 2007; Winkel et al., 2016). This includes species of the genera *Thiomargarita* spp. and *Ca. Maribeggiatoa* spp., which were most abundant in the investigated sediments (Fabian et al., data unpublished). So far, a genome of the Namibian species *Thiomargarita namibiensis* has not been published. Incubation experiments of isolated organisms tentatively suggest that they are able to switch between DNRA and $DNRN_2$ (Schulz, 2006, Fabian et al., unpublished). Nevertheless, little is known about the conditions under which each metabolism becomes active in *Thiomargarita* cells (Sweerts et al., 1990; Otte et al., 1999).

Working with mats of filamentous LSB in the Guaymas Basin, Schutte et al. (2018) proposed that the availability of H_2S and NO_3^- determines whether denitrification ($DNRN_2$) or DNRA dominates within a single organism. In situations with a high supply of H_2S relative to NO_3^-, microorganisms gain more energy per NO_3^- reduced by carrying out DNRA (Schutte et al., 2018). H_2S can be oxidized more efficiently *via* $DNRN_2$ if NO_3^- supply is plentiful, for example, close to the sediment–water interface (compare Eq. (3) and (4)). The ratios between $DNRN_2$ and DNRA at St. 14 and St. 41 are on the same order of magnitude as determined for the microbial mats in the Guaymas Basin (~2–3). Although the sensitivity analysis confirms the need to include $DNRN_2$ in the model to capture the trends in porewater data and benthic fluxes, more direct measurements of this process are needed to ascribe $DNRN_2$ to *Thiomargarita* spp. in the mud belt and quantify the rate more accurately. It is important that this effort is made since NO_3^- turnover is dominated by $DNRN_2$ at the sites studied here (see Supplementary Figure 3D, R16). Given that $DNRN_2$ results in a loss of bioavailable inorganic N, changes in the relative proportion of $DNRN_2$ versus DNRA could have broader implications for the N:P ratio of regenerated nutrients released from the seabed and the oxygen budget of the OMZ (see below).

Unexplained H_2S depletion at St. 12

Our model predicts similar rates of sulfate reduction at St. 12 and St. 41 (Supplementary Figure 3B, R5). Given that the sediments of St. 12 were not colonized with LSB, the pore waters ought to be enriched with H_2S to a similar degree as St. 41. Dissolved H_2S concentrations at St. 12 were nearly negligible down to 35 cm depth. This lack of H_2S accumulation in the sediment porewater, along with SO_4^{2-} and NH_4^+ concentrations that were close to bottom water values, is suggestive of a rapid exchange of porewater and seawater at this site. These trends were simulated using a pseudo-(bio)irrigation exchange process applied over the upper sediment layers. This has the effect of bringing SO_4^{2-} into the sediment whilst simultaneously flushing H_2S out as soon as it is produced by sulfate reduction, along with NH_4^+ produced by ammonification. Similar trends have been reported elsewhere including the Namibian continental slope (Fossing et al., 2000). Bioirrigation by animals can be ruled out because burrowing and tube-dwelling animals at this site were not observed below ca. 5cm depth (Zettler, pers. comm.). Seawater infiltration through tubes and cracks created by methane gas bubbles rising through the soft surface sediments can create similar porewater patterns to those at St. 12 (Haeckel et al., 2007; Brüchert et al., 2009; Chuang et al., 2013). Although free gas is widespread in the mud belt and ebullition has been observed as acoustic backscattering (Emeis et al., 2004; Currie et al., 2018), there was no evidence in acoustic Parasound data for free gas directly beneath the coring site at St. 12. Non-steady-state deposition of a sediment layer due to mass wasting from shallower waters is an unlikely alternative explanation because the mud belt is rather flat. The $^{210}Pb_{xs}$ data also show a gradual decrease below the mixed layer (7 cm) rather than a homogeneous signal expected from turbidite deposition. For similar reasons, mixing of the upper 35 cm by bottom currents can be excluded. Although the model is able to simulate the field data at St. 12, the mechanistic explanation for the trends in H_2S, SO_4^{2-}, and NH_4^+ concentrations remains open to interpretation.

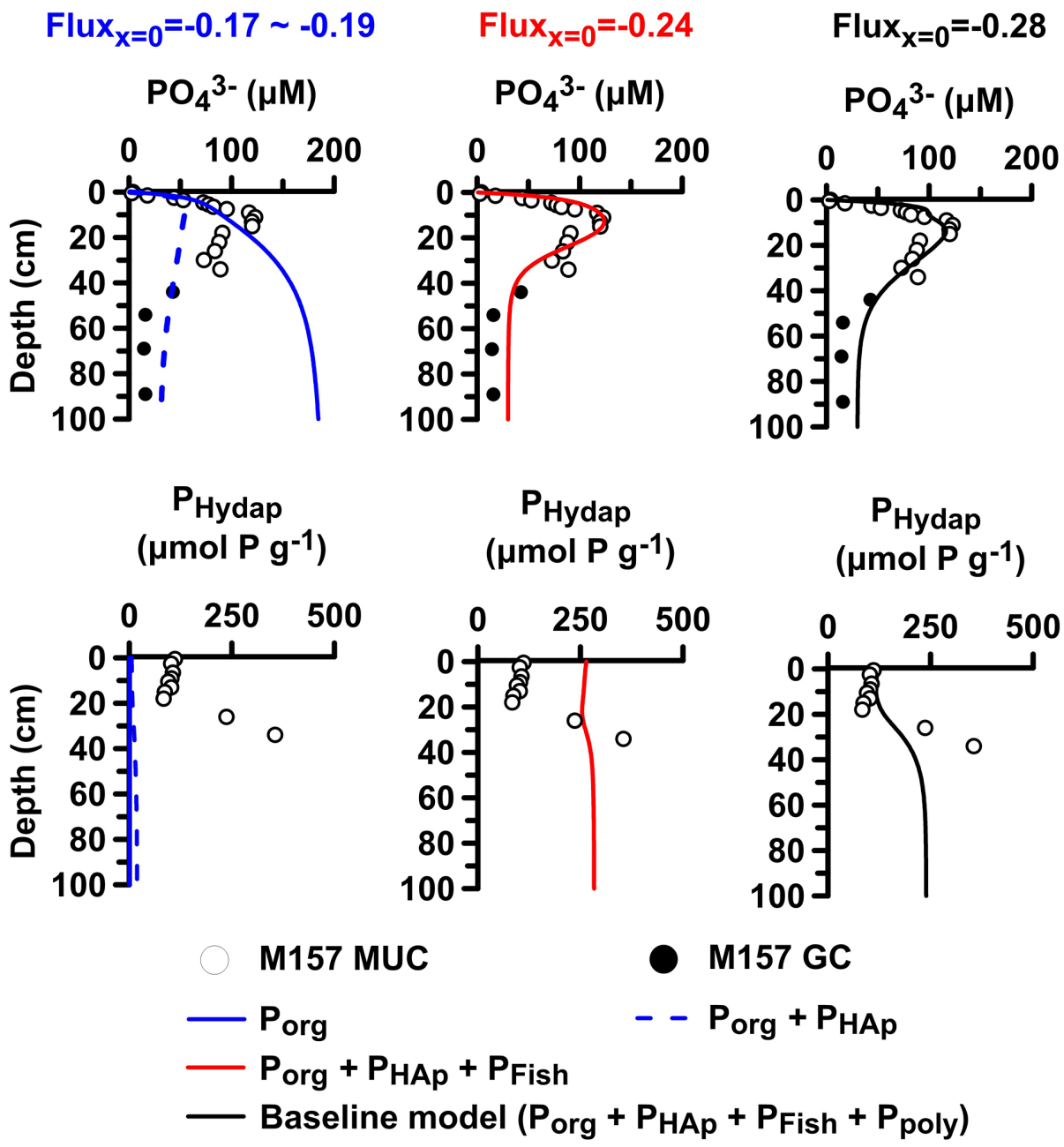

FIGURE 8
Model sensitivity analysis of porewater PO_4^{3-} and P_{Hydap} at St. 41 for increasing model complexity (see text). Baseline model values are shown as black curves and measured data as symbols. P_{Fe} is included in the plots, but since it makes a negligible contribution to total P, the corresponding data are not shown explicitly. The changing PO_4^{3-} benthic at each step is shown above each plot.

Phosphorus cycling in the mud belt

Continental margins are major sites of phosphorus removal from the global ocean (Wallmann, 2010; Ruttenberg, 2014). In the mud belt, biogenic P_{Fish} and P_{org} are the most important P phases delivered to the sediments (Supplementary Figure 3), similar to the Peruvian OMZ (Suess, 1981; Lomnitz et al., 2016). Our model predicts that the dissolution of these components is important in the northern BUS sediments, in addition to P_{poly} turnover. P_{Fe} has a negligible impact on PO_4^{3-} levels (Supplementary Figure 3) due to low reactive iron content in the sediment (Brüchert et al., 2003; Dale et al., 2009). Thus, the coincident subsurface peaks in porewater PO_4^{3-} and Fe^{2+} are not

evidence for the control of PO_4^{3-} levels by iron mineral dissolution. P_{Fe} plays a more significant role below the OMZ where bottom water O_2 levels are higher and sediments are less reducing (Küster-Heins et al., 2010).

Preferential dissolution of P_{org} relative to POC results in low organic C:P remineralization ratios (Goldhammer et al., 2011) and high residual particulate organic C:P ratios exceeding 500 that are characteristic of anoxic sediments (Slomp and Van Cappellen, 2007). The burial efficiency of P_{org} is only 2%–13% (Supplementary Table 8), which is similar to <2%–11% for other anoxic settings (Dale et al., 2016b). However, since a fraction of P liberated from P_{Fish} and P_{org} is precipitated as hydroxyapatite, $C:P_{reactive}$ is much lower (54–106). This "sink-switching" enhances the permanent burial of P (Ruttenberg and Berner, 1993; Slomp et al., 1996). Nonetheless, the benthic fluxes remain highly P-enriched relative to both dissolved C and N. This behavior, in addition to nitrogen removal in the water column (Kuypers et al., 2005), contributes to the low observed N:P ratios (e.g., 4.6:1) in bottom waters (van der Plas et al., 2007).

Model sensitivity tests can illustrate this interplay more clearly (Figure 8). If PO_4^{3-} is released exclusively from P_{org} remineralization, PO_4^{3-} concentrations increase continuously with depth, and the observed subsurface PO_4^{3-} peak is not simulated (solid blue lines) (Van Cappellen and Berner, 1988). Including hydroxyapatite precipitation brings down the overall PO_4^{3-} concentrations but results in negligible P_{Hydap} content (blue dashed lines). The benthic PO_4^{3-} flux in this case (–0.17 mmol m^{-2} d^{-1}) is lower than the baseline model result of –0.28 mmol m^{-2} d^{-1}. With P_{Fish} dissolution included, the PO_4^{3-} peak and flux can be correctly simulated but at the cost of overestimating P_{Hydap} in the upper 20 cm where the PO_4^{3-} peak is located (red curves). Further inclusion of P_{poly} dynamics lowers P_{Hydap} to match the observations and increases the PO_4^{3-} flux slightly (black curves). Indirect evidence in support of this finding is provided by observed fish bones and scales at St. GeoB12806 (Zabel et al., 2012) in addition to measured hydroxyapatite precipitation rates in mud belt sediments of 0.21–0.78 mmol P m^{-2} d^{-1} (Goldhammer et al., 2010) that agree with those in the example in Figure 8 (0.28 mmol P m^{-2} d^{-1} at St. 41).

In the current model configuration, intracellular P_{poly} accumulation and breakdown of LSB dwarf other P cycling pathways, although the net rate of P_{poly} build-up and breakdown is small (Supplementary Figure 3). Modeled intracellular P_{poly} accumulation rates (0.21–1.83 mmol P m^{-2} d^{-1}, Supplementary Table 7) are similar to P uptake rates by LSB of 0.25–1.2 mmol P m^{-2} d^{-1} in the incubation experiments by Goldhammer et al. (2010). These might be minimum estimates because the presence of polyphosphate kinase 1 (*ppk1*) and exopolyphosphatase (*ppx*) in mud belt samples indicates the potential for a wide range of microorganisms to synthesize and hydrolyze P_{poly} in addition to LSB (Zoss et al., 2019). It will remain difficult to pinpoint the significance of P_{poly} until its abundance and turnover can be better quantified. Standard operationally-defined wet chemical extractions do not include P_{poly} explicitly, and it is currently unclear whether it is wholly or partially recovered in these approaches (Goldhammer et al., 2010). Advanced analytical techniques such as ^{31}P NMR and Raman spectroscopy are more promising since they are able to quantify P_{poly} contents in biogenic material such as intracellular polyphosphate inclusions, dissolved organics, and sinking particles (Diaz et al., 2008; Fernando et al., 2019).

For these reasons, the linkage between microbial P uptake and P_{poly} accumulation remains speculative, especially with regard to settings exposed to variable redox conditions and our understanding of the environmental tipping points for microbial P release (Langer et al., 2018). Sudden onset of anoxic conditions can trigger massive P release from LSB and induce the spontaneous precipitation of hydroxyapatite (Schulz and Schulz, 2005). The same dynamic was invoked to explain large enrichments in porewater PO_4^{3-} following the onset of seasonal hypoxia in Eckernförde Bay (Dale et al., 2013). Supporting experimental evidence has been provided by Langer et al. (2018), who used $^{18}O–H_2O$ labeling experiments with the *Beggiatoa* sp. strain 35Flor to elucidate a metabolically active P_{poly} pool under both oxic and anoxic conditions with higher P_{poly} enrichments under oxic conditions. These workers, and others (Brock and Schulz-Vogt, 2011), further showed that high sulfide levels are an additional stress-inducing factor leading to a loss of intracellular P. This is clearly of particular relevance for the mud belt. The role of H_2S on microbial P dynamics has not been considered in the model due to a lack of empirical data on the relevant H_2S threshold concentrations for intracellular P breakdown.

Conclusions and future perspectives

Ocean deoxygenation has become a widespread phenomenon throughout the world, and global ocean deoxygenation has strong impact on ocean productivity, nutrient cycling, carbon cycling, and marine habitats (Breitburg et al., 2018). With the model developed in this study, we have been able to provide some clarity on potential feedback between the activity of LSB and the recycling fluxes of N and P from the sediment to the water column. The novel findings with regard to N and P cycling are two-fold: i) N turnover by $DNRN_2$ is quantitatively more significant than the sum of DNRA and denitrification, and ii) the nutrient fluxes are strongly enriched in P relative to N, in part due to the activity of LSB. This points toward a potential negative feedback by LSB on primary production close to the coast. Given that *Beggiatoaceae* communities cover an area of the shelf > 30,000 km^2 (Brüchert et al., 2006), this underscores the need to correctly account for benthic N turnover by LSB in regional models of the northern BUS. Our model predictions would profit from experimental studies quantifying rates of $DNRN_2$ and DNRA by *Beggiatoaceae*

strains commonly found in the BUS and the environmental conditions under which they might switch between these pathways.

The conceptual P cycle in the model is consistent with available empirical observations from the mud belt. However, the impact of LSB on hydroxyapatite precipitation and P burial could not be clearly substantiated. The model is tuned to simulate the data under a set of simplifying assumptions concerning the P cycle. The natural benthic P cycle is complex, and the model treats key P turnover pathways in a basic manner (e.g., P_{poly} dynamics) or ignores them altogether (e.g., nucleation of apatite precursors). Unfortunately, there are little published data to significantly improve the conceptual P model from its current incarnation. Significant advances could be made with better analytical separation between authigenic hydroxyapatite and allochthonous hydroxyapatite (e.g., fish bones), both of which are major components of particulate P in OMZs. Additional and potentially large uncertainties are further associated with C, S, and nutrient cycling under seasonally changing bottom water redox regimes. Regional ecosystem models could be used to test plausible scenarios of how seasonal dynamics of LSB modify nutrient budgets in the water column.

Data availability statement

The data presented in this study is archived at the PANGAEA World Data Center:Porewater data: https://doi.pangaea.de/10.1594/PANGAEA.913247, https://doi.pangaea.de/10.1594/PANGAEA.913250, https://doi.pangaea.de/10.1594/PANGAEA.945658, https://doi.pangaea.de/10.1594/PANGAEA.945659. Sequential extraction of P components: https://doi.pangaea.de/10.1594/PANGAEA.945664, https://doi.pangaea.de/10.1594/PANGAEA.945660, https://doi.pangaea.de/10.1594/PANGAEA.945665. Sediment data are uploaded to PANGAEA World Data Center and can be found in the Supplementary Material.

Author contributions

P-CC and AWD designed the study, carried out the model simulations, and wrote the manuscript. All authors contributed to the review and editing of the manuscript. Geochemical data were provided by CHA, MK, JF, C-CS, PV, MZ, FS, HNS-V, and SS. All authors contributed to the article and approved the submitted version.

Funding

This study was funded through the project EVAR (03F0814) of the German Federal Ministry of Education and Research (BMBF) (https://www.ebus-climate-change.de/home).

Acknowledgments

We thank the captain, crew, and the scientific shipboard party of R/V *Meteor* cruise M157. A. Bleyer, B. Domeyer, and R. Surberg are acknowledged for biogeochemical analysis. We also thank the assistance of Feng-Hsin Hsu and Yao-Li Chang at the Institute of Oceanography, National Taiwan University, for ^{210}Pb analyses. We acknowledge Silvana Pape for invaluable technical and analytical support for the SEDEX P sequential extraction and sediment geochemical analysis.

Conflict of interest

The authors declare that the research was conducted in the absence of any commercial or financial relationships that could be construed as a potential conflict of interest.

Publisher's note

Supplementary material

The Supplementary Material for this article can be found online at: https://www.frontiersin.org/articles/10.3389/fmars.2022.929913/full#supplementary-material

References

Arthur, M. A., Dean, W. E., and Laarkamp, K. (1998). Organic carbon accumulation and preservation in surface sediments on the Peru margin. *Chem. Geol.* 152, 273–286. doi: 10.1016/S0009-2541(98)00120-X

Berelson, W. M., McManus, J., Coale, K. H., Johnson, K. S., Kilgore, T., Burdige, D., et al. (1996). Biogenic matter diagenesis on the sea floor: A comparison between two continental margin transects. *J. Mar. Res.* 54, 731–762. doi: 10.1357/0022240963213673

Bohlen, L., Dale, A. W., Sommer, S., Mosch, T., Hensen, C., Noffke, A., et al. (2011). Benthic nitrogen cycling traversing the Peruvian oxygen minimum zone. *Geochimica. Cosmochimica. Acta* 75, 6094–6111. doi: 10.1016/j.gca.2011.08.010

Borchers, S. L., Schnetger, B., Böning, P., and Brumsack, H.-J. (2005). Geochemical signatures of the Namibian diatom belt: Perennial upwelling and intermittent anoxia. *Geochem. Geophys. Geosy.* 6. doi: 10.1029/2004GC000886

Breitburg, D., Levin, L. A., Oschlies, A., Grégoire, M., Chavez, F. P., Conley, D. J., et al. (2018). Declining oxygen in the global ocean and coastal waters. *Science* 359, eaam7240. doi: 10.1126/science.aam7240

Bremner, J. M. (1980). Physical parameters of the diatomaceous mud belt off south West Africa. *Mar. Geol.* 34, :M67–M76. doi: 10.1016/0025-3227(80)90064-X

Bremner, J. M. (1983). "Biogenic sediments on the south West African (Namibian) continental margin," in *Coastal upwelling: Its sedimentary record, part b: Sedimentary records of ancient coastal upwelling*. Eds. J. Thiede and E. Suess (New York: Plenum Press), pp 73–pp104.

Brock, J., and Schulz-Vogt, H. N. (2011). Sulfide induces phosphate release from polyphosphate in cultures of a marine beggiatoa strain. *ISME J.* 5, 497–506. doi: 10.1038/ismej.2010.135

Brüchert, V., Currie, B., and Peard, K. R. (2009). Hydrogen sulphide and methane emissions on the central Namibian shelf. *Prog. Oceanogr.* 83, 169–179. doi: 10.1016/j.pocean.2009.07.017

Brüchert, V., Currie, B., Peard, K. R., Lass, U., Endler, R., Dübecke, A., et al. (2006). *An integrated assessment of shelf anoxia and water column hydrogen sulphide in the Benguela coastal upwelling system off Namibia*. In L. N. Neretin (Ed.) Past and present water column anoxia (pp. 161–194). Dordrecht: Springer.

Brüchert, V., Jørgensen, B. B., Neumann, K., Riechmann, D., Schlösser, M., and Schulz, H. (2003). Regulation of bacterial sulfate reduction and hydrogen sulfide fluxes in the central namibian coastal upwelling zone. *Geochimica. Cosmochimica. Acta* 67, 4505–4518. doi: 10.1016/S0016-7037(03)00275-8

Brüchert, V., Pérez, M.E., and Lange, C.B. (2000). Coupled primary production, benthic foraminiferal assemblage, and sulfur diagenesis in organic-rich sediments of the Benguela upwelling system. *Marine Geology* 163, 27–40. doi: 10.1016/S0025-3227(99)00099-7

Buitenhuis, E. T., Hashioka, T., and Quéré, C. L. (2013). Combined constraints on global ocean primary production using observations and models. *Global Biogeochem. Cycles* 27, 847–858. doi: 10.1002/gbc.20074

Burdige, D. J. (2006). *Geochemistry of marine sediments* (Princeton, NJ: Princeton Univ. Press).

Burdige, D. J. (2007). Preservation of organic matter in marine sediments: controls, mechanisms, and an imbalance in sediment organic carbon budgets? *Chem. Rev.* 107, 467–485. doi: 10.1021/cr050347q

Burdige, D. J., and Komada, T. (2013). Using ammonium pore water profiles to assess stoichiometry of deep remineralization processes in methanogenic continental margin sediments. *Geochem. Geophys. Geosy.* 14, 1626–1643. doi: 10.1002/ggge.20117

Calvert, S. E., and Price, N. B. (1983). "Geochemistry of Namibian shelf sediments," in *Coastal upwelling its sediment record: Part a: Responses of the sedimentary regime to present coastal upwelling*. Eds. E. Suess and J. Thiede (Boston, MA: Springer US), 337–375.

Capone, D. G., and Hutchins, D. A. (2013). Microbial biogeochemistry of coastal upwelling regimes in a changing ocean. *Nat. Geosci.* 6, 711–717. doi: 10.1038/ngeo1916

Carr, M.-E. (2001). Estimation of potential productivity in Eastern boundary currents using remote sensing. *Deep Sea Res. Part II: Topical Stud. Oceanogr.* 49, 59–80. doi: 10.1016/S0967-0645(01)00094-7

Chuang, P.-C., Dale, A. W., Wallmann, K., Haeckel, M., Yang, T. F., Chen, N.-C., et al. (2013). Relating sulfate and methane dynamics to geology: Accretionary prism offshore SW Taiwan. *Geochem. Geophys. Geosy.* 14, 2523–2545. doi: 10.1002/ggge.20168

Cline, J. D. (1969). Spectrophotometric determination of hydrogen sulfide in natural waters. *Limnol. Oceanogr.* 14, 454–458. doi: 10.4319/lo.1969.14.3.0454

Collins, P. F., Diehl, H., and Smith, G. F. (1959). 2,4,6-tripyridyl-s-triazine as reagent for iron. determination of iron in limestone, silicates, and refractories. *Anal. Chem.* 31, 1862–1867. doi: 10.1021/ac60155a056

Currie, B., Utne-Palm, A. C., and Salvanes, A. G. V. (2018). Winning ways with hydrogen sulphide on the Namibian shelf. *Front. Mar. Sci.* 5. doi: 10.3389/fmars.2018.00341

Dale, A. W., Bertics, V. J., Treude, T., Sommer, S., and Wallmann, K. (2013). Modeling benthic–pelagic nutrient exchange processes and porewater distributions in a seasonally hypoxic sediment: evidence for massive phosphate release by beggiatoa? *Biogeosciences* 10, 629–651. doi: 10.5194/bg-10-629-2013

Dale, A. W., Bourbonnais, A., Altabet, M., Wallmann, K., and Sommer, S. (2019). Isotopic fingerprints of benthic nitrogen cycling in the Peruvian oxygen minimum zone. *Geochimica. Cosmochimica. Acta* 245, 406–425. doi: 10.1016/j.gca.2018.10.025

Dale, A. W., Boyle, R. A., Lenton, T. M., Ingall, E. D., and Wallmann, K. (2016b). A model for microbial phosphorus cycling in bioturbated marine sediments: Significance for phosphorus burial in the early Paleozoic. *Geochimica. Cosmochimica. Acta* 189, 251–268. doi: 10.1016/j.gca.2016.05.046

Dale, A. W., Brüchert, V., Alperin, M., and Regnier, P. (2009). An integrated sulfur isotope model for Namibian shelf sediments. *Geochimica. Cosmochimica. Acta* 73, 1924–1944. doi: 10.1016/j.gca.2008.12.015

Dale, A. W., Graco, M., and Wallmann, K. (2017). Strong and Dynamic Benthic-Pelagic Coupling and Feedbacks in a Coastal Upwelling System (Peruvian Shelf). *Front. Mar. Sci.* 4, 29. doi: 10.3389/fmars.2017.00029

Dale, A. W., Sommer, S., Bohlen, L., Treude, T., Bertics, V. J., Bange, H. W., et al. (2011). Rates and regulation of nitrogen cycling in seasonally hypoxic sediments during winter (Boknis eck, SW Baltic sea): Sensitivity to environmental variables. *Estuarine Coast. Shelf Sci.* 95, 14–28. doi: 10.1016/j.ecss.2011.05.016

Dale, A. W., Sommer, S., Lichtschlag, A., Koopmans, D., Haeckel, M., Kossel, E., et al. (2021). Defining a biogeochemical baseline for sediments at carbon capture and storage (CCS) sites: An example from the north Sea (Goldeneye). *Int. J. Greenhouse Gas Control* 106, 103265. doi: 10.1016/j.ijggc.2021.103265

Dale, A. W., Sommer, S., Lomnitz, U., Bourbonnais, A., and Wallmann, K. (2016a). Biological nitrate transport in sediments on the Peruvian margin mitigates benthic sulfide emissions and drives pelagic n loss during stagnation events. *Deep Sea Res. Part I: Oceanogr. Res. Pap.* 112, 123–136. doi: 10.1016/j.dsr.2016.02.013

Dale, A. W., Sommer, S., Lomnitz, U., Montes, I., Treude, T., Liebetrau, V., et al. (2015). Organic carbon production, mineralisation and preservation on the Peruvian margin. *Biogeosciences* 12, 1537–1559. doi: 10.5194/bg-12-1537-2015

Dauwe, B., Middelburg, J. J., Herman, P. M. J., and Heip, C. H. R. (1999). Linking diagenetic alteration of amino acids and bulk organic matter reactivity. *Limnol. Oceanogr.* 44, 1809–1814. doi: 10.4319/lo.1999.44.7.1809

de Haas, H., Boer, W., and Van Weering, T. C. E. (1997). Recent sedimentation and organic carbon burial in a shelf sea: the north Sea. *Mar. Geol.* 144, 131–146. doi: 10.1016/S0025-3227(97)00082-0

Diaz, J., Ingall, E., Benitez-Nelson, C., Paterson, D., de Jonge, M. D., McNulty, I., et al. (2008). Marine polyphosphate: A key player in geologic phosphorus sequestration. *Science* 320, 652–655. doi: 10.1126/science.1151751

Emeis, K. C., Brüchert, V., Currie, B., Endler, R., Ferdelman, T., Kiessling, A., et al. (2004). Shallow gas in shelf sediments of the Namibian coastal upwelling ecosystem. *Cont. Shelf Res.* 24, 627–642. doi: 10.1016/j.csr.2004.01.007

Emeis, K., Eggert, A., Flohr, A., Lahajnar, N., Nausch, G., Neumann, A., et al. (2018). Biogeochemical processes and turnover rates in the northern benguela upwelling system. *J. Mar. Syst.* 188, 63–80. doi: 10.1016/j.jmarsys.2017.10.001

Emeis, K.-C., Struck, U., Leipe, T., and Ferdelman, T. G. (2009). Variability in upwelling intensity and nutrient regime in the coastal upwelling system offshore Namibia: results from sediment archives. *Int. J. Earth Sci.* 98, 309–326. doi: 10.1007/s00531-007-0236-5

Fernando, E. Y., McIlroy, S. J., Nierychlo, M., Herbst, F.-A., Petriglieri, F., Schmid, M. C., et al. (2019). Resolving the individual contribution of key microbial populations to enhanced biological phosphorus removal with raman–FISH. *ISME J.* 13, 1933–1946. doi: 10.1038/s41396-019-0399-7

Flood, B. E., Louw, D. C., van der Plas, A. K., and Bailey, J. V. (2021). Giant sulfur bacteria (*Beggiatoaceae*) from sediments underlying the benguela upwelling system host diverse microbiomes. *PloS One* 16 (11), e0258124. doi: 10.1371/journal.pone.0258124

Fossing, H., Ferdelman, T. G., and Berg, P. (2000). Sulfate reduction and methane oxidation in continental margin sediments influenced by irrigation (South-East Atlantic off Namibia). *Geochimica. Cosmochimica. Acta* 64, 897–910. doi: 10.1016/S0016-7037(99)00349-X

Fossing, H., Gallardo, V. A., Jørgensen, B. B., Hüttel, M., Nielsen, L. P., Schulz, H., et al. (1995). Concentration and transport of nitrate by mat-forming sulphur bacterium thioploca. *Nature* 374, 713–715. doi: 10.1038/374713a0

Gächter, R., and Meyer, J. S. (1993). The role of microorganisms in mobilization and fixation of phosphorus in sediments. *Hydrobiologia* 253, 103–121. doi: 10.1007/BF00050731

Gallardo, V. A., Klingelhoeffer, E., Arntz, W., and Graco, M. (1998). First report of the bacterium thioploca in the benguela ecosystem off Namibia. *J. Mar. Biol. Assoc. United Kingdom* 78, 1–4. doi: 10.1017/S0025315400044945

Geilert, S., Hensen, C., Schmidt, M., Liebetrau, V., Scholz, F., Doll, M., et al. (2018). On the formation of hydrothermal vents and cold seeps in the guaymas basin, gulf of California. *Biogeosciences* 15, 5715–5731. doi: 10.5194/bg-15-5715-2018

Goldhammer, T., Brüchert, V., Ferdelman, T. G., and Zabel, M. (2010). Microbial sequestration of phosphorus in anoxic upwelling sediments. *Nat. Geosci.* 3, 557. doi: 10.1038/ngeo913

Goldhammer, T., Brunner, B., Bernasconi, S. M., Ferdelman, T. G., and Zabel, M. (2011). Phosphate oxygen isotopes: Insights into sedimentary phosphorus cycling from the benguela upwelling system. *Geochimica. Cosmochimica. Acta* 75, 3741–3756. doi: 10.1016/j.gca.2011.04.006

K. Grasshoff, K. Kremling and M. Ehrhardt (Eds.) (1999). *Methods of seawater analysis, 3rd edn* (Weinheim, New York: Wiley-VCH).

Gruber, N. (2008). "The marine nitrogen cycle: Overview and challenges," in *Nitrogen in the marine environment, 2nd Edn*. Eds. D. G. Capone, D. A. Bronk, M. R. Mulholland and E. J. Carpenter (San Diego: Academic Press), 1–50.

Gutiérrez, D., Enríquez, E., Purca, S., Quipúzcoa, L., Marquina, R., Flores, G., et al. (2008). Oxygenation episodes on the continental shelf of central Peru: Remote forcing and benthic ecosystem response. *Prog. Oceanogr.* 79, 177–189. doi: 10.1016/j.pocean.2008.10.025

Haeckel, M., Boudreau, B. P., and Wallmann, K. (2007). Bubble-induced porewater mixing: A 3-d model for deep porewater irrigation. *Geochimica. Cosmochimica. Acta* 71, 5135–5154. doi: 10.1016/j.gca.2007.08.011

Hall, P. O. J., and Aller, R. C. (1992). Rapid, small-volume, flow injection analysis for ΣCO2 and NH4+ in marine and freshwaters. *Limnol. oceanogr.* 37, 1113–1119. doi: 10.4319/lo.1992.37.5.1113

Hartnett, H. E., Keil, R. G., Hedges, J. I., and Devol, A. H. (1998). Influence of oxygen exposure time on organic carbon preservation in continental margin sediments. *Nature* 391, 572–575. doi: 10.1038/35351

Hedges, J. I., and Keil, R. G. (1995). Sedimentary organic matter preservation: an assessment and speculative synthesis. *Mar. Chem.* 49, 81–115. doi: 10.1016/0304-4203(95)00008-F

Henrichs, S. M., and Farrington, J. W. (1984). Peru Upwelling region sediments near 15 °S. 1. remineralization and accumulation of organic matter. *Limnol. Oceanogr.* 29, 1–19. doi: 10.4319/lo.1984.29.1.0001

Huh, C.-A., Lin, H.-L., Lin, S., and Huang, Y.-W. (2009). Modern accumulation rates and a budget of sediment off the gaoping (Kaoping) river, SW Taiwan: A tidal and flood dominated depositional environment around a submarine canyon. *J. Mar. Syst.* 76, 405–416. doi: 10.1016/j.jmarsys.2007.07.009

Hutchings, L., van der Lingen, C. D., Shannon, L. J., Crawford, R. J. M., Verheye, H. M. S., Bartholomae, C. H., et al. (2009). The benguela current: An ecosystem of four components. *Prog. Oceanogr.* 83, 15–32. doi: 10.1016/j.pocean.2009.07.046

Inthorn, M., Wagner, T., Scheeder, G., and Zabel, M. (2006). Lateral transport controls distribution, quality, and burial of organic matter along continental slopes in high-productivity areas. *Geology* 34, 205–208. doi: 10.1130/G22153.1

Jones, D. S., Flood, B. E., and Bailey, J. V. (2016). Metatranscriptomic insights into polyphosphate metabolism in marine sediments. *ISME J.* 10, 1015–1019. doi: 10.1038/ismej.2015.169

Jørgensen, B. B. (1978). A comparison of methods for the quantification of bacterial sulfate reduction in coastal marine sediments II. Calculation from mathematical models. *Geomicrobiol. J.* 1, 29–47. doi: 10.1080/01490457809377722

Kalvelage, T., Lavik, G., Lam, P., Contreras, S., Arteaga, L., Löscher, C. R., et al. (2013). Nitrogen cycling driven by organic matter export in the south pacific oxygen minimum zone. *Nat. Geosci.* 6, 228–234. doi: 10.1038/ngeo1739

Kraft, B., Tegetmeyer, H. E., Sharma, R., Klotz, M. G., Ferdelman, T. G., Hettich, R. L., et al. (2014). The environmental controls that govern the end product of bacterial nitrate respiration. *Science* 345, 676. doi: 10.1126/science.1254070

Küster-Heins, K., Steinmetz, E., De Lange, G. J., and Zabel, M. (2010). Phosphorus cycling in marine sediments from the continental margin off Namibia. *Mar. Geol.* 274, 95–106. doi: 10.1016/j.margeo.2010.03.008

Kuypers, M. M. M., Lavik, G., Woebken, D., Schmid, M., Fuchs, B. M., Amann, R., et al. (2005). Massive nitrogen loss from the benguela upwelling system through anaerobic ammonium oxidation. *Proc. Natl. Acad. Sci. United States America* 102, 6478–6483. doi: 10.1073/pnas.0502088102

Langer, S., Vogts, A., Schulz-Vogt, H. N., and Bowman, G. R. (2018). Simultaneous visualization of enzymatic activity in the cytoplasm and at polyphosphate inclusions in beggiatoa sp. strain 35Flor incubated with 18O-labeled water. *mSphere* 3, e00489–e00418. doi: 10.1128/mSphere.00489-18

Lomnitz, U., Sommer, S., Dale, A. W., Löscher, C. R., Noffke, A., Wallmann, K., et al. (2016). Benthic phosphorus cycling in the Peruvian oxygen minimum zone. *Biogeosciences* 13, 1367–1386. doi: 10.5194/bg-13-1367-2016

Lomstein, B. A., Niggemann, J., Jørgensen, B. B., and Langerhuusa, A. T. (2009). Accumulation of prokaryotic remains during organic matter diagenesis in surface sediments off Peru. *Limnol. Oceanogr.* 54, 1139–1151. doi: 10.4319/lo.2009.54.4.1139

Malone, T., Azzaro di Rosamarina, M., Bode, A., Brown, E., Duce, R., Kamykowski, D., et al. (2016). *Primary production, cycling of nutrients, surface layer and plankton*. in The First Global Integrated Marine Assessment: World Ocean Assessment I, ed Oceans and Law of the Sea, United Nations (Cambridge: Cambridge University Press), 119–148. doi: 10.1017/9781108186148.009.

Meisel, S., Struck, U., and Emeis, K.-C. (2011). Nutrient dynamics and oceanographic features in the central Namibian upwelling region as reflected in δ15N-signals of suspended matter and surface sediments. *Fossil Rec.* 14, 153–169. doi: 10.5194/fr-14-153-2011

Mohrholz, V., Bartholomae, C. H., van der Plas, A. K., and Lass, H. U. (2008). The seasonal variability of the northern benguela undercurrent and its relation to the oxygen budget on the shelf. *Cont. Shelf Res.* 28, 424–441. doi: 10.1016/j.csr.2007.10.001

Mollenhauer, G., Inthorn, M., Vogt, T., Zabel, M., Sinninghe Damsté, J. S., and Eglinton, T. I. (2007). Aging of marine organic matter during cross-shelf lateral transport in the benguela upwelling system revealed by compound-specific radiocarbon dating. *Geochem. Geophys. Geosy.* 8. doi: 10.1029/2007GC001603

Monteiro, P. M. S. (2010). "The benguela current system," in *Carbon and nutreint fluxes in continental margins - a global synthesis*. Eds. K.-K. Liu, L. Atkinson, R. A. Quinones and L. Talaue-McManus (Springer).

Mußmann, M., Hu, F. Z., Richter, M., De Beer, D., Preisler, A., Jørgensen, B. B., et al. (2007). Insights into the genome of large sulfur bacteria revealed by analysis of single filaments. *PloS Biol.* 5, 1923–1937. doi: 10.1371/journal.pbio.0050230

Nagel, B., Emeis, K.-C., Flohr, A., Rixen, T., Schlarbaum, T., Mohrholz, V., et al. (2013). N-cycling and balancing of the n-deficit generated in the oxygen minimum zone over the Namibian shelf–an isotope-based approach. *J. Geophys. Res.: Biogeosci.* 118, 361–371. doi: 10.1002/jgrg.20040

Nagel, B., Gaye, B., Lahajnar, N., Struck, U., and Emeis, K.-C. (2016). Effects of current regimes and oxygenation on particulate matter preservation on the Namibian shelf: Insights from amino acid biogeochemistry. *Mar. Chem.* 186, 121–132. doi: 10.1016/j.marchem.2016.09.001

Neumann, A., Lahajnar, N., and Emeis, K.-C. (2016). Benthic remineralisation rates in shelf and slope sediments of the northern benguela upwelling margin. *Cont. Shelf Res.* 113, 47–61. doi: 10.1016/j.csr.2015.12.009

Ohde, T., and Dadou, I. (2018). Seasonal and annual variability of coastal sulphur plumes in the northern benguela upwelling system. *PloS One* 13, e0192140–e0192140. doi: 10.1371/journal.pone.0192140

Otte, S., Kuenen, J. G., Nielsen, L. P., Paerl, H. W., Zopfi, J., Schulz, H. N., et al. (1999). Nitrogen, carbon, and sulfur metabolism in natural thioploca samples. *Appl. Environ. Microbiol.* 65, 3148–3157. doi: 10.1128/AEM.65.7.3148-3157.1999

Pitcher, G. C., Aguirre-Velarde, A., Breitburg, D., Cardich, J., Carstensen, J., Conley, D. J., et al. (2021). System controls of coastal and open ocean oxygen depletion. *Prog. Oceanogr.* 197, 102613. doi: 10.1016/j.pocean.2021.102613

Prokopenko, M. G., Sigman, D. M., Berelson, W. M., Hammond, D. E., Barnett, B., Chong, L., et al. (2011). Denitrification in anoxic sediments supported by biological nitrate transport. *Geochim. Cosmochim. Acta* 75, 7180–7199. doi: 10.1016/j.gca.2011.09.023

Ruttenberg, K. C. (1992). Development of a sequential extraction method for different forms of phosphorus in marine sediments. *Limnol. Oceanogr.* 37, 1460–1482. doi: 10.4319/lo.1992.37.7.1460

Ruttenberg, K. C (2014) "10.13 - the global phosphorus cycle," in *Treatise on geochemistry, 2nd ed.* Eds. H. D. Holland and K. K Turekian (Oxford: Elsevier), 499–558.

Ruttenberg, K. C., and Berner, R. A. (1993). Authigenic apatite formation and burial in sediments from non-upwelling, continental margin environments. *Geochimica. Cosmochimica. Acta* 57, 991–1007. doi: 10.1016/0016-7037(93)90035-U

Schenau, S. J., and De Lange, G. J. (2000). A novel chemical method to quantify fish debris in marine sediments. *Limnol. Oceanogr.* 45, 963–971. doi: 10.4319/lo.2000.45.4.0963

Schmidt, M., and Eggert, A. (2016). Oxygen cycling in the northern benguela upwelling system: Modelling oxygen sources and sinks. *Prog. Oceanogr.* 149, 145–173. doi: 10.1016/j.pocean.2016.09.004

Scholz, F., Hensen, C., Noffke, A., Rohde, A., Liebetrau, V., and Wallmann, K. (2011). Early diagenesis of redox-sensitive trace metals in the Peru upwelling area – response to ENSO-related oxygen fluctuations in the water column. *Geochimica. Cosmochimica. Acta* 75, 7257–7276. doi: 10.1016/j.gca.2011.08.007

Schulz, H. N. (2006). *The genus thiomargarita*. in The Prokaryotes, eds M. D. S. Falkow, E. Rosenberg, K.-H. Schleifer and E. Stackebrandt (New York, NY: Springer) 1156–1163.

Schulz, H. N., Brinkhoff, T., Ferdelman, T. G., Mariné, M. H., Teske, A., and Jørgensen, B. B. (1999). Dense populations of a Large sulfur bacterium in Namibian shelf sediments. *Science* 284, 493–495. doi: 10.1126/science.284.5413.493

Schulz, H. N., and Jørgensen, B. B. (2001). Big bacteria. *Annu. Rev. Microbiol.* 55, 105–137. doi: 10.1146/annurev.micro.55.1.105

Schulz, H. N., and Schulz, H. D. (2005). Large Sulfur bacteria and the formation of phosphorite. *Science* 307, 416–418. doi: 10.1126/science.1103096

Schutte, C. A., Teske, A., MacGregor, B. J., Salman-Carvalho, V., Lavik, G., Hach, P., et al. (2018). Filamentous giant beggiatoaceae from guaymas basin are capable of both denitrification and dissimilatory nitrate reduction to ammonium (DNRA). *Appl. Environ. Microbiol.* 84, e2860–e2817. doi: 10.1128/AEM.02860-17

Slomp, C. P., and Van Cappellen, P. (2007). The global marine phosphorus cycle: sensitivity to oceanic circulation. *Biogeosciences* 4, 155–171. doi: 10.5194/bg-4-155-2007

Slomp, C. P., van der Gaast, S. J., and Van Raaphorst, W. (1996). Phosphorus binding by poorly crystalline iron oxides in north Sea sediments. *Mar. Chem.* 52, 55–73. doi: 10.1016/0304-4203(95)00078-X

Sommer, S., Chuang, P.-C., Fabian, J., Sabbaghzadeh, B., Schulz-Vogt, H. N., Zabel, M., et al (in prep.) *In situ* benthic solute exchange in the mud-belt ecosystem off Namibia (Benguela upwelling system). *Recent Dev. Oxygen Minimum Zones Biogeochem.*

Stookey, L. L. (1970) Ferrozine–a new spectrophotometric reagent for iron. *Anal. Chem.* 42, 779–781. doi: 10.1021/ac60289a016

Suess, E. (1981) Phosphate regeneration from sediments of the Peru continental margin by dissolution of fish debris. *Geochimica. Cosmochimica. Acta* 45, 577–588. doi: 10.1016/0016-7037(81)90191-5

Sweerts, J.-P.R.A., Beer, D. D., Nielsen, L. P., Verdouw, H., den Heuvel, J. C. V., Cohen, Y., et al. (1990). Denitrification by sulphur oxidizing beggiatoa spp. *mats Freshw. sediments. Nat.* 344, 762–763. doi: 10.1038/344762a0

Van Cappellen, P., and Berner, R. A. (1988). A mathematical model for the early diagenesis of phosphorus and fluorine in marine sediments; apatite precipitation. *Am. J. Sci.* 288, 289–333. doi: 10.2475/ajs.288.4.289

van der Plas, A. K., Monteiro, P. M. S., and Pascall, A. (2007). Cross-shelf biogeochemical characteristics of sediments in the central benguela and their relationship to overlying water column hypoxia. *Afr. J. Mar. Sci.* 29, 37–47. doi: 10.2989/AJMS.2007.29.1.3.68

Wakeham, S. G., Sinninghe Damsté, J. S., Kohnen, M. E. L., and De Leeuw, J. W. (1995). Organic sulfur compounds formed during early diagenesis in black Sea sediments. *Geochimica. Cosmochimica. Acta* 59, 521–533. doi: 10.1016/0016-7037(94)00361-O

Wallmann, K. (2010). Phosphorus imbalance in the global ocean? *Global Biogeochem. Cycles* 24. doi: 10.1029/2009GB003643

Wallmann, K., Schneider, B., and Sarnthein, M. (2016). Effects of eustatic sea-level change, ocean dynamics, and nutrient utilization on atmospheric pCO_2 and seawater composition over the last 130 000 years: a model study. *Clim. Past* 12, 339–375. doi: 10.5194/cp-12-339-2016

West, S., Jansen, J. H. F., and Stuut, J. B. (2004). Surface water conditions in the northern benguela region (SE Atlantic) during the last 450 ky reconstructed from assemblages of planktonic foraminifera. *Mar. Micropaleontol.* 51, 321–344. doi: 10.1016/j.marmicro.2004.01.004

Westrich, J. T., and Berner, R. A. (1984). The role of sedimentary organic matter in bacterial sulfate reduction: The G model tested1. *Limnol. Oceanogr.* 29, 236–249. doi: 10.4319/lo.1984.29.2.0236

Winkel, M., Salman-Carvalho, V., Woyke, T., Richter, M., Schulz-Vogt, H. N., Flood, B. E., et al. (2016). Single-cell sequencing of thiomargarita reveals genomic flexibility for adaptation to dynamic redox conditions. *Front. Microbiol.* 7. doi: 10.3389/fmicb.2016.00964

Zabel, M., Boetius, A., and Emeis, K. C. (2012). *PROSA - process studies in the Eastern south Atlantic: Cruise no. M76, April 12 - august 24,2008, cape town (South Africa - Walvis bay (Namibia)* (DFG-Senatskomm. f. Ozeanographie).

Zabel, M., Mohrholz, V., Schulz-Vogt, H., Sommer, S., and Zettler, M. (2019). *The benguela system under climate change effects of variability in physical forcing on carbon and oxygen budgets, cruise no. M157, 04.08.2019 - 16.09.2019, mindelo (Cape Verde) - Walvis bay (Namibia).*

Zoss, R., Medina Ferrer, F., Flood, B. E., Jones, D. S., Louw, D. C., and Bailey, J. (2019). Microbial communities associated with phosphogenic sediments and phosphoclast-associated DNA of the benguela upwelling system. *Geobiology* 17, 76–90. doi: 10.1111/gbi.12318

frontiers | Frontiers in Marine Science

TYPE Original Research
PUBLISHED 08 December 2022
DOI 10.3389/fmars.2022.902062

OPEN ACCESS

EDITED BY
Annie Bourbonnais,
University of South Carolina,
United States

REVIEWED BY
Karen L. Casciotti,
Stanford University, United States
Xin Zhou,
Guangdong Ocean University, China
Su Mei Liu,
Ocean University of China, China

*CORRESPONDENCE
Andrew W. Dale
adale@geomar.de

†PRESENT ADDRESS
Frederike Korth,
Institute of Agricultural Engineering,
University of Natural Resources and
Life Sciences, Wien, Austria

SPECIALTY SECTION
This article was submitted to
Marine Biogeochemistry,
a section of the journal
Frontiers in Marine Science

RECEIVED 22 March 2022
ACCEPTED 10 November 2022
PUBLISHED 08 December 2022

CITATION
Dale AW, Clemens D, Dähnke K,
Korth F, Wankel SD,
Schroller-Lomnitz U, Wallmann K and
Sommer S (2022) Nitrogen cycling in
sediments on the NW African margin
inferred from N and O isotopes in
benthic chambers.
Front. Mar. Sci. 9:902062.
doi: 10.3389/fmars.2022.902062

Nitrogen cycling in sediments on the NW African margin inferred from N and O isotopes in benthic chambers

Andrew W. Dale[1]*, David Clemens[1], Kirstin Dähnke[2], Frederike Korth[1†], Scott D. Wankel[3], Ulrike Schroller-Lomnitz[1], Klaus Wallmann[1] and Stefan Sommer[1]

[1]GEOMAR Helmholtz Centre for Ocean Research Kiel, Kiel, Germany, [2]Institute of Carbon Cycles, Helmholtz Centre Hereon, Geesthacht, Germany, [3]Department of Marine Chemistry and Geochemistry, Woods Hole Oceanographic Institution, Woods Hole, MA, United States

Benthic nitrogen cycling in the Mauritanian upwelling region (NW Africa) was studied in June 2014 from the shelf to the upper slope where minimum bottom water O_2 concentrations of 25 µM were recorded. Benthic incubation chambers were deployed at 9 stations to measure fluxes of O_2, dissolved inorganic carbon (DIC) and nutrients (NO_3^-, NO_2^-, NH_4^+, PO_4^{3-}, H_4SiO_4) along with the N and O isotopic composition of nitrate ($\delta^{15}N\text{-}NO_3^-$ and $\delta^{18}O\text{-}NO_3^-$) and ammonium ($\delta^{15}N\text{-}NH_4^+$). O_2 and DIC fluxes were similar to those measured during a previous campaign in 2011 whereas NH_4^+ and PO_4^{3-} fluxes on the shelf were 2 – 3 times higher and possibly linked to a long-term decline in bottom water O_2 concentrations. The mean isotopic fractionation of NO_3^- uptake on the margin, inferred from the loss of NO_3^- inside the chambers, was 1.5 ± 0.4 ‰ for $^{15/14}N$ ($^{15}\epsilon_{app}$) and 2.0 ± 0.5 ‰ for $^{18/16}O$ ($^{18}\epsilon_{app}$). The mean $^{18}\epsilon_{app}$:$^{15}\epsilon_{app}$ ratio on the shelf (< 100 m) was 2.1 ± 0.3, and higher than the value of 1 expected for microbial NO_3^-reduction. The $^{15}\epsilon_{app}$ are similar to previously reported isotope effects for NO_3^- respiration in marine sediments but lower than determined in 2011 at a same site on the shelf. The sediments were also a source of ^{15}N-enriched NH_4^+ (9.0 ± 0.7 ‰). A numerical model tuned to the benthic flux data and that specifically accounts for the efflux of ^{15}N-enriched NH_4^+ from the seafloor, predicted a net benthic isotope effect of N loss ($^{15}\epsilon_{sed}$) of 3.6 ‰; far above the more widely considered value of ~0‰. This result is further evidence that the assumption of a universally low or negligible benthic N isotope effect is not applicable to oxygen-deficient settings. The model further suggests that $^{18}\epsilon_{app}$:$^{15}\epsilon_{app}$ trajectories > 1 in the benthic chambers are most likely due to aerobic ammonium oxidation and nitrite oxidation in surface sediments rather than anammox, in agreement with published observations in the water column of oxygen deficient regions.

KEYWORDS

nitrogen isotopes, fractionation, particulate organic carbon (POC), continental margin, denitrification, anammox, NW Africa upwelling, marine sediments

1 Introduction

The Canary upwelling region along the north-western African coast is an important eastern boundary current system with regard to primary production (0.33 Gtons C yr^{-1}), second in magnitude only to the Benguela upwelling (Carr, 2001). Off Mauritania, high primary production is driven by upwelling of nutrient-rich South Atlantic Central Water (SACW) and huge dust inputs from the adjacent Sahara-Sahel region (Fischer et al., 2010). Subsurface waters off Mauritania are better ventilated than the Benguela system and the other large upwelling systems in the Eastern Tropical Pacific, with minimum bottom water dissolved O_2 levels on the margin of several tens of micromoles per liter (Hartmann et al., 1976; Dale et al., 2014; Thomsen et al., 2019). However, the SACW in the Eastern Tropical North Atlantic (ETNA) appears to be undergoing significant deoxygenation of ca. 0.5 µmol kg^{-1} yr^{-1} (Stramma et al., 2008), possibly due to a warming-induced decrease in solubility and biological O_2 consumption (Schmidtko et al., 2017). At this rate, subsurface waters on the Mauritanian margin are heading towards anoxia by the end of the 21st century.

In the Eastern Tropical Pacific and South Atlantic upwelling systems, the anoxic water column is a hotspot of microbially-mediated N loss, either by denitrification (nitrate reduction to N_2) and/or anammox (anaerobic oxidation of ammonium by nitrite to N_2) (Devol et al., 2006; Lam and Kuypers, 2011). Along with the Arabian Sea and Bay of Bengal, most fixed N loss in ocean waters occurs in these 'oxygen minimum zones (OMZ)' (Gruber, 2008). In sediments, by contrast, and with the possible exception of the oligotrophic deep-sea and euxinic basins, microbial transformation of fixed N to N_2 by microorganisms occurs almost everywhere (Middelburg et al., 1996). In the Mauritanian OMZ, where pelagic O_2 concentrations are consistently above the inhibition threshold for denitrification (ca. 5 µM), benthic denitrification/anammox is the only significant N loss pathway. Benthic denitrification rates measured using ^{15}N-labelling techniques range from around 4 mmol N m^{-2} d^{-1} on the shelf to 1 mmol N m^{-2} d^{-1} on the upper slope (Sokoll et al., 2016), and are toward the higher end for open-ocean continental margins. Anammox was found to be of minor importance (Sokoll et al., 2016).

Current understanding of the fixed N balance in the ocean is dependent on knowledge of the rates of N transformation pathways, both in the water column and in the sediment. To a large extent, this is achieved by balancing the marine inventory of stable N isotopes (^{14}N and ^{15}N) under steady state conditions (Brandes and Devol, 2002). This approach is possible because most microbial N transformation processes impart unique degrees of isotopic discrimination, or fractionation, of one isotope over another, expressed as a kinetic isotope effect (KIE), or ϵ (unit: ‰). (In this paper, $\epsilon = (\alpha - 1)\cdot 1000$, where α is the fractionation factor defined as ${}^{L}k/{}^{H}k$, and where k denotes the reaction rate constant of the heavy (H) and light (L) isotopologues). Studies in the water column and in the laboratory have revealed a wealth of information concerning N and O effects of microbial N cycling (e.g. Sigman et al., 2006; Casciotti and McIlvin, 2007; Granger et al., 2008; Buchwald and Casciotti, 2013; Gaye et al., 2013; Bourbonnais et al., 2015 and many others). For instance, the N and O isotope effects during the dissimilatory reduction of nitrate (NO_3^-) to nitrite (NO_2^-) are similar at ca. 15 – 30 ‰ in favor of the lighter isotopes (Voss et al., 2001; Kritee et al., 2012; Bourbonnais et al., 2015). Oxidation of NO_2^- to NO_3^-, in contrast, has an inverse isotope effect due to fractionation at the enzymatic level during N–O bond formation by nitrite oxidoreductase (Casciotti, 2009). NO_2^- oxidation leads to enrichment of ^{14}N and ^{16}O in the residual NO_2^- and an enrichment of ^{15}N and ^{18}O in the NO_3^- product (Casciotti, 2009). This divergence has led numerous investigators to conclude that a significant fraction of NO_2^- produced by reduction of NO_3^- in oxygen deficient waters is reoxidized to NO_3^- (Casciotti and McIlvin, 2007; Buchwald and Casciotti, 2013; Casciotti et al., 2013; Gaye et al., 2013; Bourbonnais et al., 2015; Casciotti, 2016; Granger and Wankel, 2016). Fewer studies have been carried out in sediments, although so far it appears that the microbial isotope effects observed in the water column are largely transferrable to the benthic environment (Lehmann et al., 2004; Lehmann et al., 2007; Alkhatib et al., 2012; Dale et al., 2014; Dale et al., 2019). The major difference between the water column and sediment rests with the much lower isotopic fractionation of NO_3^- uptake by sediments (hereafter benthic fractionation), arising from transport limitation of NO_3^- diffusion within the sediment (< 3 ‰; Brandes and Devol, 1997; Lehmann et al., 2004). Based on this assumption, it is understood that around two-thirds of the global oceanic fixed N loss takes place in the sediment and one-third in OMZ waters (Brandes and Devol, 2002; Somes et al., 2013). However, more recent studies suggest that the benthic N isotope effect may be higher, especially in sediments underlying oxygen-deficient bottom waters (Lehmann et al., 2007; Alkhatib et al., 2012; Dähnke and Thamdrup, 2013; Dale et al., 2014; Dale et al., 2019). Furthermore, it can be enhanced by the efflux of ^{15}N-enriched NH_4^+ from the sediment (Lehmann et al., 2007; Granger et al., 2011; Alkhatib et al., 2012). Accurate estimates of the total benthic N isotope effect that also includes NH_4^+ and other N species, and thus more relevant for the global N budget, require a deeper understanding of the rate of benthic N loss and associated N isotope transformations.

In this study, we deployed *in situ* benthic incubation chambers on the Mauritanian margin in 2014 during the transition from the strong to weak upwelling season (Thomsen et al., 2019). Fieldwork was conducted along a transect from the shallow shelf to the upper slope at 18 °N. Our objective was to determine the recycling rates and exchange fluxes of dissolved inorganic nitrogen (DIN: NO_3^-, NO_2^-, NH_4^+) between the sediment and water column and compare them to results from

an earlier campaign in 2011. We also measured the N and O isotopic composition of NO_3^- (δ^{15}N-NO_3^- and δ^{18}O-NO_3^-) and NH_4^+ (δ^{15}N-NH_4^+) inside the chambers. With this information, and with the help of a numerical model, we were able to calculate the total the benthic N isotope effect along with further information on benthic N turnover rates, sources and transformations.

2 Oceanographic setting

The study area lies within the Mauritanian upwelling region in the ETNA. The prominent water mass that upwells onto the margin at 18 °N is poleward-flowing and nutrient-rich SACW. Upwelling is strongest between January and April when the Intertropical Convergence Zone (ITCZ) migrates southwards (Mittelstaedt, 1983). It weakens when the ITZC moves northwards, leading to a decline in primary production on the shelf. Primary production nonetheless remains relatively high year-round at 80 – 200 mmol m^{-2} d^{-1} of C (Huntsman and Barber, 1977). Oceanographic data indicate that upwelling was active during the fieldwork (Thomsen et al., 2019). Dissolved O_2 levels below the surface mixed layer are dictated by SACW ventilation, vertical mixing, and respiration rates of organic carbon in the water column (Mittelstaedt, 1983; Schafstall et al., 2010; Thomsen et al., 2019). They present a deep minimum of 40 – 50 µM at 400 – 500 m water depth and a shallow minimum of 30 – 50 µM on the shelf at 50 - 100 m (Karstensen et al., 2008; Schroller-Lomnitz et al., 2019; Thomsen et al., 2019). The lowest O_2 levels on the shelf are usually encountered during upwelling relaxation in July and August due to combined effects of stratification and benthic respiration (Klenz et al., 2018). A detailed oceanographic overview of the study area during the fieldwork is described by Thomsen et al. (2019) and water column O_2 measurements at the sampling stations are presented by Schroller-Lomnitz et al. (2019).

The sediments on the margin at 18°N are classified as slightly sandy mud or muddy sand (Dale et al., 2014). They comprise 10 - 20% carbonates with organic C increasing from ~1% on the shelf to 3% at 1000 m water depth (Hartmann et al., 1976; Gier et al., 2017). Sediment reworking by turbulent mixing exports fine-grained particles down the slope (Fütterer, 1983; Schafstall et al., 2010). Consequently, sedimentation rates on the shelf determined by ^{210}Pb accumulation are low, and increase to 350 cm kyr^{-1} below the shelf break (Dale et al., 2014). Porewaters in the upper 20 cm are mostly ferruginous, becoming sulfidic on the shallow shelf (Dale et al., 2014; Gier et al., 2017; Schroller-Lomnitz et al., 2019). Benthic respiration rates on the shelf range from approximately 10 to 20 mmol m^{-2} d^{-1} of C (Dale et al., 2014; Schroller-Lomnitz et al., 2019). These values are typical for the average margin, but far smaller than those in the carbon-rich shelf sediments in the Peruvian and Benguelan upwelling systems (Brüchert et al., 2003; Dale et al., 2015).

3 Material and methods

Data presented here were mostly measured within the framework of the project "Climate – Biogeochemistry Interactions in the Tropical Ocean" (www.sfb754.de) on research campaign M107 (RV Meteor) from 30 May to 3 July 2014. A complete overview of sediment operations can be found in the cruise report (Sommer et al., 2015). Digital links to the data and a general overview of the project are provided by Krahmann et al. (2021).

3.1 Benthic flux measurements

In situ fluxes of O_2, dissolved inorganic carbon (DIC), NO_3^-, NO_2^-, NH_4^+, silicic acid (H_4SiO_4) and N/O isotopes of N species were measured in benthic chambers along an E-W transect at 18.1° N using autonomous Biogeochemical Observatories (BIGO; Sommer et al., 2008). A total of nine BIGO deployments were made at nine stations along a latitudinal transect across the shelf/slope covering a horizontal distance of 50 km from ~50 to ~1110 m water depth (Figure 1). Seven of the stations were revisited from an earlier cruise during March/April 2011, which coincided with the transition between the strong upwelling and weak upwelling seasons (Dale et al., 2014). Geographical coordinates for each station are listed in Schroller-Lomnitz et al. (2019). These workers reported mean PO_4^{3-} and DIC fluxes at each site for the same lander deployments.

The design and implementation of the BIGO landers has been discussed in detail previously (Krahmann et al., 2021). Each BIGO (I and II) contained two circular flux chambers (C1 and C2) with an internal diameter of 28.8 cm where the sediment was incubated for ~30 h. Discrete samples were taken using glass syringes (eight per chamber) at pre-programmed time intervals for chemical analysis. After BIGO recovery, the syringes were immediately transferred to the onboard cool room (4°C) for filtering (0.2 µm) and sub-sampling. Another six water samples were taken from inside each benthic chamber into quartz tubes for analysis of DIC.

Solute fluxes were calculated from the slope of the linear regression of the concentration data versus sampling time and the height of the water inside each chamber. Fluxes represent the net flux by diffusion/advection in addition to solute pumping by animals (bioirrigation). A total of 29 nutrient data points from the whole data set (n = 720) set were visually assigned as outliers and omitted from the calculations. Twelve DIC data were removed from 90 data points, mainly corresponding to the last syringe samples taken from the chambers on the shelf. For the calculation of the O_2 flux, equal to total oxygen uptake (TOU), the linear initial part of the O_2 time series recorded by optodes (see below) was used. Negative fluxes denote net uptake by the sediment and positive fluxes net release.

3.2 Sediment sampling

Sediment cores at each station were retrieved using a multiple-corer (MUC). Porewaters and particulates were extracted from the sediment as described by Schroller-Lomnitz et al. (2019) and Gier et al. (2017). Further details are provided in those publications.

3.3 Analytical methods

Nutrients in the benthic landers were analyzed on board with a Quaatro Autoanalyzer (Seal Analytic) using standard photometric approaches. Porewaters were analyzed for ferrous iron (Fe^{2+}), NO_3^-, NO_2^-, NH_4^+, PO_4^{3-}, H_4SiO_4, total alkalinity (TA) and hydrogen sulfide (H_2S). Analytical details can be found in Gier et al. (2017); Schroller-Lomnitz et al. (2019) and Sommer et al. (2015). Sediment samples were also stored refrigerated for analysis of solid phase constituents and physical properties at the home laboratory.

The O_2 concentration and temperature inside each chamber were measured using optodes. Bottom water O_2 values were taken from additional optodes mounted externally on the landers. DIC measurements were performed using a quadrupole membrane inlet mass spectrometer (MIMS, GAM200, In Process Instruments) following Sommer et al. (2015). The instrument was equipped with inline sample acidification to convert DIC to dissolved CO_2 gas for measurement at a mass-to-charge ratio of 44.

The particulate organic carbon (POC) content of freeze-dried and milled sediment samples was determined by flash combustion in a Carlo Erba Elemental Analyzer (NA 1500) with an analytical precision and detection limit of 0.04% (dry weight percent) and 0.05%, respectively. POC contents have been published previously (Schroller-Lomnitz et al., 2019). Samples were decarbonated with 0.25 N HCl prior to analysis. Carbonate (assumed to be $CaCO_3$) was determined by weight difference. The precision and detection limit of the carbonate analysis was 2% and 0.1%, respectively. Total particulate nitrogen was determined on the elemental analyzer with the same precision and detection limit as carbonate. We assumed that this is equal to particulate organic N (PON). Porosity was determined from the weight difference of the wet and freeze–dried sediment, assuming a sediment density of 2.5 g cm^{-3} and a seawater density of 1.023 g cm^{-3}.

During a separate field campaign in July 2019 (M156, Sommer et al., 2020), surface sediment close to St. 5 (182 m depth) was analyzed for $\delta^{15}N$ and $\delta^{13}C$ using a high sensitivity elemental analyzer (HSEA) connected to an isotope ratio mass spectrometer (DeltaPlus Advantage, Thermo Fisher Scientific) as described by Hansen and Sommer (2007). $\delta^{15}N$ and $\delta^{13}C$ values of the bulk particulate material (after removing carbonates) were calculated as:

$$\delta^{H}X = \left(\frac{\left({}^{H}X/{}^{L}X\right)_{Sample}}{\left({}^{H}X/{}^{L}X\right)_{Standard}} - 1 \right) \cdot 1000 \quad (1)$$

where $\delta^{H}X$ denotes the isotopic composition (‰) of X (C or N) and H and L are the heavy and light isotopologue of C (13) or N (15). The reference standards were V-PDB for C and N_2 in air for N. System calibration was implemented by the combustion of International Atomic Energy Agency (IAEA-N-1, IAEA-N-2, IAEA-NO-3) and National Institute of Standards and Technology (NBS-22 and NBS-600) compounds. Acetanilide was used as an internal standard after every sixth sample within each sample run. The overall standard deviation (SD) for the low measurement range 2.5 - 8 µg N and 5.0 - 80 µg C was ± 0.25 ‰ and ± 0.2 ‰, respectively. The overall SD for the higher measurement range 3 - 15 µg N and 10 - 140 µg C was ± 0.2 ‰ and ± 0.15‰, respectively.

Benthic lander samples were analyzed for the isotopic composition of nitrate ($\delta^{15}N\text{-}NO_3^-$ and $\delta^{18}O\text{-}NO_3^-$) and ammonium ($\delta^{15}N\text{-}NH_4^+$). Most of the samples were analyzed for $\delta^{15}N\text{-}NO_3^-$ and $\delta^{18}O\text{-}NO_3^-$ at GEOMAR (Kiel, Germany). At three stations (St. 1, 2 and 4), $\delta^{15}N\text{-}NO_3^-$ and $\delta^{18}O\text{-}NO_3^-$ were measured at the Helmholtz Center Hereon (Geesthacht, Germany). In both labs, nitrate dual isotopes were analyzed using the denitrifier method (Sigman et al., 2001; Casciotti et al., 2002). All samples for $\delta^{15}N\text{-}NH_4^+$ were analyzed at GEOMAR using the hypobromite/azide-method (Mcilvin and Altabet, 2005; Zhang et al., 2007). $\delta^{15}N\text{-}NH_4^+$ was only measured in benthic lander samples on the shelf where NH_4^+ concentrations were above the detection limit for a reliable isotope analysis (1 µM). Due to limited sample availability and low NO_2^- concentrations, $\delta^{15}N\text{-}NO_2^-$ could not be measured.

The denitrifier method and the hypobromite/azide-method are based on the isotopic analysis of nitrous oxide (N_2O). In the denitrifier method, NO_3^- and NO_2^- are quantitatively converted to N_2O by *Pseudomonas aureofaciens* (ATTC 13985). The hypobromite/azide-method is based on the chemical conversion of NH_4^+ to N_2O by a subsequent addition of a hypobromite and azide solution. For both methods, the sample volume was adjusted to a sample size of 10 nmol of N_2O. N_2O was extracted from the sample vials by purging with helium and measured with a GasBench II, coupled to an isotope ratio mass spectrometer (Delta Plus, Thermo Fisher Scientific, Germany). Each batch of samples using the denitrifier method included two international standards (USGS34: $\delta^{15}N$ = -1.8‰ vs N_2, $\delta^{18}O$ = -27.9‰ vs. VSMOW; IAEA-NO-3: $\delta^{15}N$ = 4.7‰ vs N_2, $\delta^{18}O$ = +25.6‰ vs. VSMOW) (Böhlke et al., 2003) and an internal standard. A bracketing correction (Sigman et al., 2009) was applied to the nitrate isotope data to correct for exchange with water. To calibrate $\delta^{15}N\text{-}NH_4^+$ measurements, three international standards (IAEA-N-1: $\delta^{15}N$ = 0.4‰, USGS25: $\delta^{15}N$ = -30.4‰, USGS26: $\delta^{15}N$ = 53.7‰) were used with each sample run. All measurements were replicated, with a typical reproducibility for $\delta^{15}N\text{-}NO_3^-$, $\delta^{18}O\text{-}NO_3^-$

and $\delta^{15}N\text{-}NH_4^+$ better than 0.2‰, 0.6‰ and 0.9‰, respectively. Since NO_2^- comprised on average 2% of the combined NO_2^- + NO_3^- pool, the contribution of NO_2^- interference to the reported $\delta^{15}N$ and $\delta^{18}O$ nitrate values was considered negligible.

N and O isotope ratios are reported in per mil (‰), relative to the analytical standards (N_2 in air for $\delta^{15}N$, and Vienna Standard Mean Ocean Water (VSMOW) for O) using Eq. (1).

3.4 C and N recycling rates

Depth-integrated rates (total rate per unit area) of POC oxidation to DIC ($RPOC_{TOT}$, mmol C m^{-2} d^{-1}), ammonification of particulate organic N (R_{AMF}, mmol N m^{-2} d^{-1}), nitrification of NH_4^+ to NO_3^- (R_{NIT}, mmol N m^{-2} d^{-1}) and denitrification of NO_3^- to N_2 (R_{DEN}, mmol N m^{-2} d^{-1}) were calculated using a mass balance of the fluxes (F) of O_2, NO_3^- and NH_4^+ measured in the benthic chambers (Dale et al., 2014):

$$RPOC_{TOT} = \frac{r_{CN}\,(2\,F_{NH4}\,r_{NO3} - F_{O2}\,r_{NO3} - F_{NH4}\,r_{O2} - F_{NO3}\,r_{O2})}{2\,r_{NO3} - r_{O2} + r_{CN}\,r_{NO3}\,r_{O2}} \quad (2)$$

$$R_{AMF} = \frac{RPOC_{TOT}}{r_{CN}} \quad (3)$$

$$R_{NIT} = \frac{-F_{O2}\,r_{NO3} - F_{NO3}\,r_{O2} - F_{NH4}\,r_{CN}\,r_{NO3}\,r_{O2}}{2\,r_{NO3} - r_{O2} + r_{CN}\,r_{NO3}\,r_{O2}} \quad (4)$$

$$R_{DEN} = \frac{-F_{O2} - F_{NH4}\,r_{CN}\,r_{O2} - 2\,F_{NO3} - F_{NO3}\,r_{CN}\,r_{O2}}{2\,r_{NO3} - r_{O2} + r_{CN}\,r_{NO3}\,r_{O2}} \quad (5)$$

where r_{CN} is the atomic C:N ratio in organic matter undergoing degradation, and r_{O2} and r_{NO3} are the molar ratios of O_2:POC and NO_3^-:POC, respectively, during aerobic respiration and denitrification of organic carbon. r_{O2} and r_{NO3} were previously defined as 118/106 and 94.4/106 (respectively) for organic matter with an oxidation state of -0.45 (Dale et al., 2014). These equations are only approximations because they ignore NO_2^- fluxes, yet which are equivalent to only a few percent of NO_3^- fluxes.

3.5 Isotope calculations

The loss of NO_3^- inside the chambers due to benthic respiration takes place within a closed system where there is no exchange of NO_3^- with the surrounding waters. Under these conditions, the apparent benthic fractionation of N ($^{15}\epsilon_{app}$) or O ($^{18}\epsilon_{app}$) was calculated using a closed system Rayleigh model (Marioitti et al., 1981; Prokopenko et al., 2013):

$$\delta^H X - \delta^H X_0 = {}^{-H}\epsilon_{app}\,ln\,f \quad (6)$$

where $\delta^H X$ and $\delta^H X_0$ denote the isotopic composition (‰) of X (N or O) during the incubation and at the start of the incubation, respectively, and f is the remaining fraction of NO_3^- in the chamber. $^H\epsilon_{app}$ is equal to the slope of the linear regression of a plot of $\delta^H X$ versus $\ln(f)$. Values of ϵ_{app} at each station were determined by pooling the data from both BIGO chambers. Only slopes that were significant (p value< 0.05) are reported, which eliminates the $^{15}\epsilon_{app}$ and $^{18}\epsilon_{app}$ data from the two deepest stations and also $^{18}\epsilon_{app}$ from St. 3 and 7. At these sites, the change in $\delta^H X$ is too small or scattered to calculate reliable ϵ_{app}.

$^H\epsilon_{app}$ is related to the $\delta^H X$ of the NO_3^- flux relative to the $\delta^H X$ of bottom water NO_3^-, $\delta^H X_{NO_{3BW}}$ (Alkhatib et al., 2012):

$${}^H\epsilon_{app} = \delta^H X_{NO_{3_{BW}}} - \delta_{F_{NO_3}} \quad (7)$$

Where

$$\delta_{F_{NO_3}} = \left(\frac{\left(F_{H_{NO_3}}/F_{L_{NO_3}}\right)}{\left({}^H\mathrm{N}/{}^L\mathrm{N}\right)_{\mathrm{Standard}}} - 1 \right) \cdot 1000 \quad (8)$$

and $F_{H_{NO3}}$ and $F_{L_{NO3}}$ are the benthic fluxes of the heavy and light isotopologues at the sediment surface, respectively (see Supplement).

4 Results

4.1 Particulate geochemistry across the margin

Mean POC content in the sediment cores retrieved by the MUC increased from < 1% on the shelf (< 200 m) to 2.9% at the deepest station (Table 1). $CaCO_3$ showed maximum values at St. 4 (37%) and decreased offshore. POC content was significantly and positively correlated with the particulate mud fraction (MF, %) reported by Dale et al. (2014), where POC = 28.1 MF – 13.3 (p< 0.05, data not shown) whereas $CaCO_3$ was not. The mean $\delta^{13}C$ and $\delta^{15}N$ of the particulate material close to St. 5 was -20.8 ± 0.2 ‰ and 3.7 ± 0.4 ‰, respectively (see Supplement). These $\delta^{13}C_{POC}$ fall within the range of -16 to -22 ‰ characteristic of marine organic matter (Meyers, 1994). The mean atomic ratio of POC to PON (r_{CN}, mol C (mol N)$^{-1}$) in each sediment core was mainly constant over the transect (~9 – 10), with a lower ratio at St. 4 of 7.6. These values are typical for marine algae (Burdige, 2006).

4.2 Seafloor recycling of biogenic matter

NO_3^- fluxes were directed into the sediment with highest values on the shelf (-2.9 mmol m^{-2} d^{-1}) (Table 2). NO_2^- effluxes were highest on the shelf (0.13 mmol m^{-2} d^{-1}) and at least a factor of 20 lower than the NO_3^- flux. NH_4^+ and H_4SiO_4 fluxes

10.3389/fmars.2022.902062

were also highest on the shelf and directed from the sediment to the bottom water (Figure S1). The ratio of Si fluxes relative to DIC was 0.5 ± 0.2 and higher than the diatomic Si:C ratio of 0.13 (Brzezinski, 1985), indicating preferential dissolution of opal compared to POC.

In situ fluxes of O_2, DIC and nutrients were highest on the shelf and lowest offshore (Table 2 and Figure 1A). DIC fluxes (F_{DIC}) decreased from 20.7 mmol m^{-2} d^{-1} at St. 1 to 3.5 mmol m^{-2} d^{-1} at St. 9. O_2 fluxes (= TOU) were on average 25% lower than F_{DIC}. The offshore decrease in F_{DIC} and TOU are consistent with a decrease in remineralization of labile organic matter with increasing water depth. $RPOC_{TOT}$ decreased from 18.2 mmol m^{-2} d^{-1} on the shelf to ~2 mmol m^{-2} d^{-1} at St. 9. $RPOC_{TOT}$ was equal to 82% of F_{DIC} for the margin as a whole (Figure 1B). The excess DIC flux over TOU is likely to be driven by carbonate dissolution induced by metabolically-produced CO_2 in surface sediment (Jahnke and Jahnke, 2004). This is further indicated by the respiratory quotient (RQ), determined as the ratio between DIC outflux and O_2 influx across the sediment surface. RQ was 1.5 ± 0.6 across the margin (Table 2). Whilst similar to other estimates using benthic chambers (Jørgensen et al., 2022), it is much higher than the expected value of 0.7 based on complete aerobic mineralization of organic matter with an average phytoplankton composition (Anderson, 1995).

The sediments acted as a net sink for DIN [NO_3^-+NO_2^-+NH_4^+)]. Denitrification rates (R_{DEN}) decreased from 3.6 mmol N m^{-2} d^{-1} on the shelf where $RPOC_{TOT}$ was highest, to < 1 mmol N m^{-2} d^{-1} at the deepest stations. These are consistent with those determined from ^{15}N labelling experiments (Sokoll et al., 2016). R_{DEN} accounted for 24% of $RPOC_{TOT}$ (Figure 1C). Nitrification (R_{NIT}) was apparently active at every station with rates that were 17% of R_{DEN} on average.

The loss of fixed N was further evident in the flux of the tracer N* (F_{N^*}) (Gruber and Sarmiento, 1997; Lehmann et al., 2004):

$$F_{N*} = F_{DIN} - 16\,F_{PO4} \quad (9)$$

TABLE 1 Mean contents of POC, $CaCO_3$ and the C:N ratio in the sediment cores recovered from each station along with mean bottom water O_2 concentrations recorded on the BIGO landers.

Station	Water depth (m)	O_2 (µM)	$CaCO_3$ (%)	POC (%)	r_{CN} (mol C mol N^{-1})
1	46	40	23	0.8	10.1
2	65	25	22	0.7	8.8
3	90	26	31	0.7	8.9
4	130	40	37	0.9	7.6
5	174	41	27	1.1	9.7
6	241	47	17	0.8	9.1
7	412	42	11	1.3	10.3
8	787	76	13	2.7	9.6
9	1100	116	13	2.9	9.2

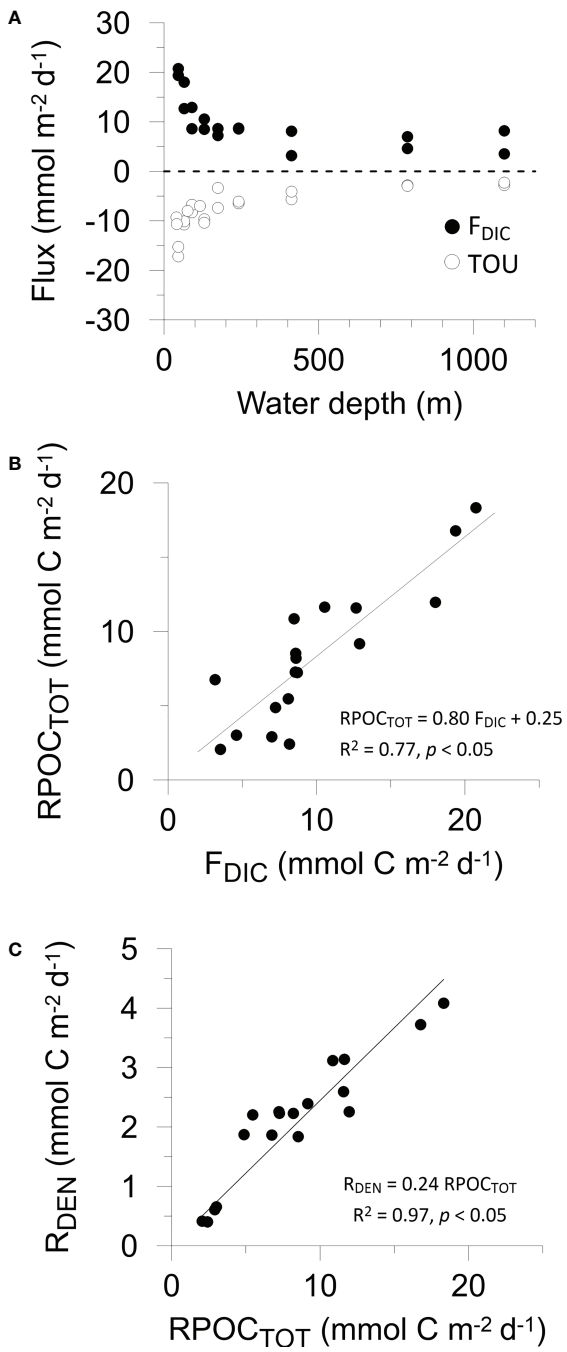

FIGURE 1
(A) Benthic fluxes of DIC (black symbols) and TOU (open symbols) versus water depth. Two data points per water depth correspond to the two benthic chambers in each BIGO lander. Cross plots of **(B)** organic carbon degradation versus measured DIC flux, and **(C)** denitrification versus organic carbon degradation, as determined by the mass balance. Denitrification rates (Table 2) have been converted to mmol C m^{-2} d^{-1} by dividing by r_{NO3}. The trendline in **(C)** has been forced through the origin so that R_{DEN} = 0 if $RPOC_{TOT}$ = 0. For **(B, C)**, Pearson correlation coefficients and *p* values are given.

TABLE 2 Benthic fluxes (F) measured in the individual benthic chambers (mmol m^{-2} d^{-1}) across the transect, the respiratory quotient (RQ, see text) and depth-integrated reaction rates, R [Eq. (2)-(5)].

Station	BIGO		Water depth (m)	F_{DIC}	F_{O_2}	F_{NO_3}	F_{NO_2}	F_{NH_4}	F_{Si}	F_{PO_4}	F_{N^*}	RQ	$RPOC_{TOT}$	R_{AMF}	R_{DEN}	R_{NIT}
1	BIGO 2-4	C1	46	20.7	-17.2	-3.0	0.12	1.14	11.8	0.17	-4.47	1.2	18.3	1.8	3.6	0.7
		C2	46	19.4	-15.3	-2.9	0.09	1.29	11.0	0.24	-5.47	1.3	16.8	1.7	3.3	0.4
2	BIGO 2-5	C1	65	18.0	-10.7	-2.0	0.13	1.39	8.5	0.21	-3.90	1.7	12.0	1.4	2.0	n.d
		C2	65	12.7	-10.1	-2.3	0.11	1.26	7.3	0.15	-3.24	1.3	11.6	1.3	2.3	0.1
3	BIGO 1-3	C1	90	12.9	-8.3	-1.8	0.11	0.66	4.4	0.05	-1.72	1.6	9.2	1.0	2.1	0.4
		C2	90	8.6	-6.8	-2.0	0.06	1.30	4.5	0.13	-2.78	1.3	8.5	1.0	1.6	n.d
4	BIGO 1-4	C1	130	8.5	-9.7	-2.2	0.03	0.89	5.9	0.15	-3.70	0.9	10.9	1.4	2.8	0.5
		C2	130	10.6	-10.4	-2.3	0.06	1.07	7.0	0.17	-3.97	1.0	11.6	1.5	2.8	0.5
5	BIGO 2-3	C1	174	8.6	-7.4	-1.6	0.03	0.47	4.2	0.11	-2.82	1.2	8.2	0.8	2.0	0.4
		C2	174	7.2	-3.4	-1.7	0.06	0.50	4.4	0.17	-3.87	2.2	4.9	0.5	1.7	0.0
6	BIGO 1-2	C1	241	8.6	-6.5	-1.6	0.04	0.37	3.5	0.06	-2.06	1.3	7.3	0.8	2.0	0.4
		C2	241	8.7	-6.1	-1.7	0.04	0.51	3.7	0.16	-3.74	1.4	7.2	0.8	2.0	0.3
7	BIGO 2-2	C1	412	3.2	-5.7	-1.6	0.05	0.55	3.0	0.11	-2.65	0.6	6.8	0.7	1.7	0.1
		C2	412	8.1	-4.1	-1.7	0.02	0.29	1.6	0.06	-2.41	2.0	5.5	0.5	2.0	0.2
8	BIGO 1-1	C1	787	7.0	-2.8	-0.4	0.00	0.18	1.7	0.04	-0.95	2.5	2.9	0.3	0.5	0.1
		C2	787	4.6	-2.9	-0.4	0.00	0.16	1.6	0.05	-1.09	1.6	3.0	0.3	0.6	0.2
9	BIGO 2-1	C1	1100	8.2	-2.8	-0.1	0.00	–	1.7	0.05	-0.74	3.0	2.4	0.3	0.4	0.3
		C2	1100	3.5	-2.3	-0.1	0.00	–	1.5	0.06	-1.37	1.5	2.1	0.2	0.4	0.2
			Mean	9.9	-7.3	-1.6	0.05	0.66	4.8	0.12	-2.83	1.5	8.3	0.9	1.9	0.3
			SD	4.9	4.2	0.8	0.04	0.48	3.1	0.06	1.29	0.6	4.5	0.5	0.9	0.2

Negative fluxes denote uptake by the sediment and vice versa. Negative N* fluxes indicate preferential loss of N relative to P. Mean values ± standard deviation are also given. Cases where the mass balance did not converge (only applicable for R_{NIT}) are listed as not defined (n.d).

where F_{PO4} is the PO_4^{3-} flux (Table 2) and the factor 16 stems from the Redfield composition of organic matter (N:P = 16:1). If organic N and P are completely remineralized, $F_{N^*} = 0$. F_{N^*} was negative at all sites because the sediments acted as a source of PO_4^{3-} and a sink of DIN, illustrating preferential loss of DIN relative to PO_4^{3-}. The most negative N* flux of -5.5 mmol m^{-2} d^{-1} was determined at St. 1 where R_{DEN} was highest. The highest F_{N^*} of -1 mmol m^{-2} d^{-1} was calculated for St. 9. Across the transect, the mean F_{N^*} was -2.8 ± 1.3 mmol m^{-2} d^{-1}.

4.3 N isotopes in benthic chambers

$\delta^{15}N\text{-}NO_3$ and $\delta^{18}O\text{-}NO_3$ inside the benthic chambers are illustrated in Figure 2. Bottom water $\delta^{15}N\text{-}NO_3$, taken as the first time point immediately after the chambers were closed, was approximately 5.0 ± 0.5 ‰. Enrichments in ^{15}N over time were generally observed in all chambers on the shelf and upper slope. $\delta^{15}N\text{-}NO_3$ increased by roughly 1 ‰ on the shelf and by <1 ‰ on the upper slope over the course of the incubations. At the two deepest sites, variations in $\delta^{15}N\text{-}NO_3$ and $\delta^{18}O\text{-}NO_3$ were within analytical precision. Bottom water $\delta^{18}O\text{-}NO_3$ was more variable than $\delta^{15}N\text{-}NO_3$. Enrichments in ^{18}O were stronger on the shelf compared to the slope.

The apparent fractionation of N ($^{15}\epsilon_{app}$) and O ($^{18}\epsilon_{app}$) accompanying NO_3^- loss inside the benthic chambers varied between 0.7 and 2.0 ‰ for $^{15}\epsilon_{app}$ and between 1.7 and 2.9 ‰ for $^{18}\epsilon_{app}$ with no clear trends across the transect (Figure 3A and Table S4). The average $^{15}\epsilon_{app}$ and $^{18}\epsilon_{app}$ were 1.5 ± 0.4 ‰ and 2.0 ± 0.5 ‰, respectively. For the shelf (< 100 m), $^{18}\epsilon_{app}$ was twice as high as $^{15}\epsilon_{app}$ (1.8 versus 0.9 ‰). The ratio of these numbers, $^{18}\epsilon_{app}$:$^{15}\epsilon_{app}$, varied from 2.0 to 2.3 at stations 1, 2 and 4. $^{18}\epsilon_{app}$:$^{15}\epsilon_{app}$ was 0.9 at St. 5 and 6 (Figure 3B). The mean $^{18}\epsilon_{app}$:$^{15}\epsilon_{app}$ ratio of the shelf stations was 2.1 ± 0.3.

$\delta^{15}N\text{-}NH_4$ inside the benthic chambers at St. 1 and 2 was between 9 and 10 ‰ whereas the values at St. 3 were more scattered (Figure S2). The $\delta^{15}N$ of the NH_4^+ flux out of the sediment to the bottom water (δF_{NH4}) for the shelf stations was calculated as the intercept of a linear regression of $\delta^{15}N\text{-}NH_4$ versus the inverse NH_4^+ concentration (Mortazavi and Chanton, 2004; Dale et al., 2019). Values of δF_{NH4} were similar and varied from 8 ± 1.8 ‰ at St. 1 to 9.6 ± 1.2 ‰ at St. 2 (Figure 3C and Table S4). The average δF_{NH4} of the three shelf sites was 9.0 ± 0.7 ‰.

5 Discussion

5.1 N cycling inferred from benthic chamber isotopes

The increase in $\delta^{15}N\text{-}NO_3$ and $\delta^{18}O\text{-}NO_3$ in the benthic incubation chambers, along with a decrease in NO_3^-

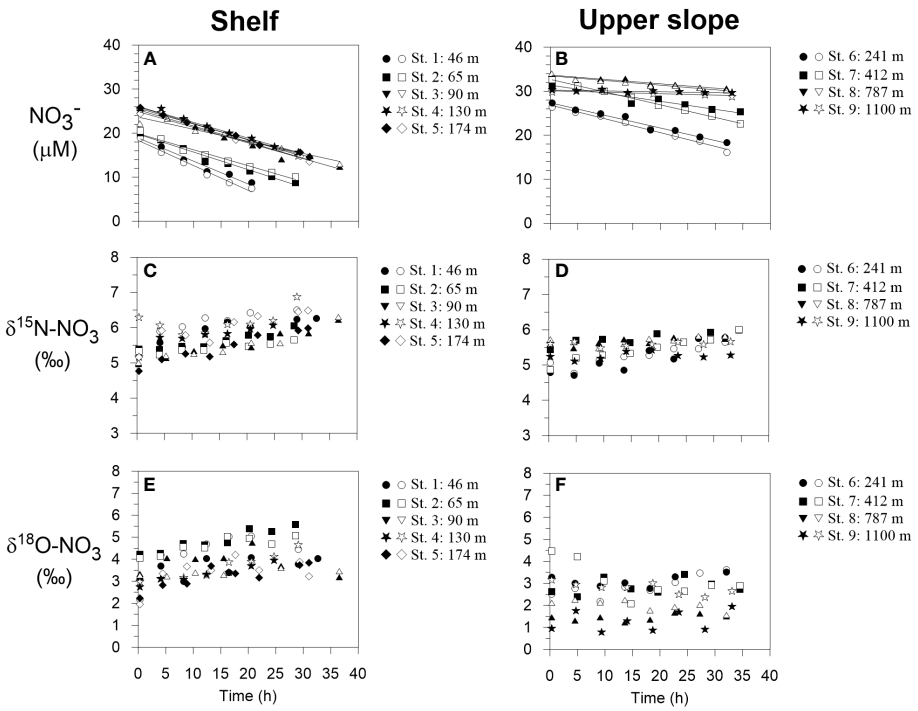

FIGURE 2
Benthic chamber incubation results for NO_3^- on the shelf and upper slope. **(A, B)** NO_3^- concentrations with linear regression curves from which the fluxes are calculated, **(C, D)** $\delta^{15}N\text{-}NO_3$ and **(E, F)** $\delta^{18}O\text{-}NO_3$. Filled and open symbols correspond to chamber 1 and 2 during each BIGO lander deployment, respectively.

concentrations, is attributed to dissimilatory reduction of NO_3^- to NO_2^- (Lehmann et al., 2004; Dale et al., 2014; Dale et al., 2019). Isotope effects for nitrate reduction estimated from $\delta^{15}N\text{-}NO_3$ distributions in the water column are ca. 15 – 30 ‰ (Voss et al., 2001; Kritee et al., 2012; Bourbonnais et al., 2015) for both ^{15}N and ^{18}O (Marioitti et al., 1981; Voss et al., 2001; Casciotti et al., 2002; Granger et al., 2008; Kritee et al., 2012). Thus, our data would appear to present two conflicts with the known isotopic fingerprint of dissimilatory NO_3^- reduction: (i) the apparent benthic fractionation factors, $^{15}\epsilon_{app}$ and $^{18}\epsilon_{app}$, are much lower than observed in the water column at all sites, and (ii) the ratio $^{18}\epsilon_{app}$:$^{15}\epsilon_{app}$ is higher than unity at St. 1, 2 and 4, but closer to unity at St. 5 and 6 (Figure 3).

On continental margins, including Mauritania, NO_3^- is typically exhausted within a few centimeters below the sediment surface due to high rates of respiration by microorganisms (Dale et al., 2014). The strong drawdown of NO_3^- leads to diffusive transport limitation of NO_3^- to the subsurface denitrifying layer, leading to complete consumption of NO_3^- that diffuses into the sediment (Brandes and Devol, 1997). This results in an under-expression of the isotope effect in the benthic NO_3^- flux and explains why larger isotope effects are observed in the water column (Brandes and Devol, 1997; Brandes and Devol, 2002; Lehmann et al., 2007; Alkhatib et al., 2012; Dale et al., 2019). The range of $^{15}\epsilon_{app}$ determined in this study is similar to that reported for other coastal sediments under oxygenated waters (Brandes and Devol, 2002; Lehmann et al., 2007; Alkhatib et al., 2012). ϵ_{app} may be larger in oxygen-deficient regions because the distance for molecules to diffuse between the seawater NO_3^- reservoir and the denitrification layer is smaller (Brandes and Devol, 1997; Lehmann et al., 2007). For instance, $^{15}\epsilon_{app}$ of 6 ± 2 ‰ were observed in sediments under hypoxic bottom waters in the Bering Sea (Lehmann et al., 2007). Sediments underlying anoxic waters in the Peruvian OMZ displayed even higher $^{15}\epsilon_{app}$ of 7.4 ± 0.7 ‰, decreasing to 2.5 ± 0.9 ‰ under oxygenated waters below the OMZ, with similar trends in $^{18}\epsilon_{app}$ (Dale et al., 2019). Dähnke and Thamdrup (2013) measured $^{15}\epsilon_{app}$ and $^{18}\epsilon_{app}$ of 18.9 ‰ and 15.8 ‰, respectively, in anoxic ex-situ incubations of organic-rich sediment. These results confirm observations and model predictions that nitrate isotope effects inferred from benthic flux data are under-expressed under oxic waters (Brandes and Devol, 1997; Lehmann et al., 2004; Lehmann et al., 2007). However, the assumption of a universally low or negligible benthic N isotope effect, as originally predicated in earlier studies, is not fully applicable to oxygen-deficient settings (Brandes and Devol, 1997; Lehmann et al., 2004).

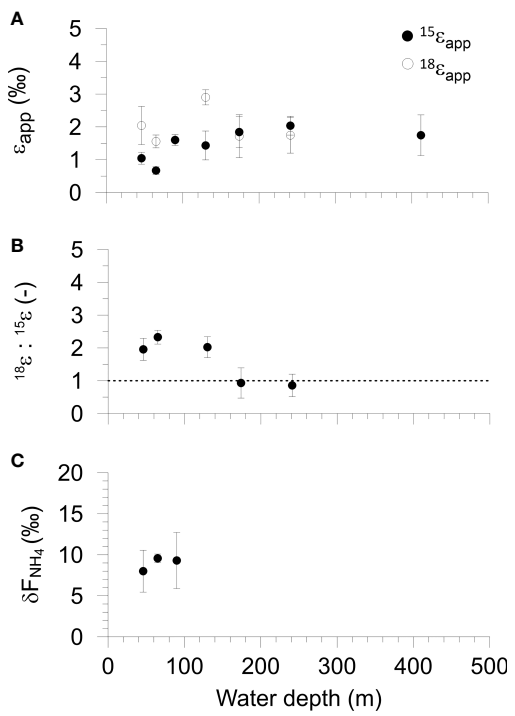

FIGURE 3
Benthic chamber isotope results versus water depth on the Mauritanian margin. **(A)** Fractionations of N-NO_3^- ($^{15}\epsilon_{app}$) and O-NO_3^- ($^{18}\epsilon_{app}$). **(B)** The ratio $^{18}\epsilon_{app}$: $^{15}\epsilon_{app}$, where the dashed line shows unity. **(C)** The $\delta^{15}N$ of the NH_4^+ flux from the sediment. Error bars represent the standard error of the regression slopes (see Methods). Data are tabulated in Table S1 in the Supplement.

$^{15}\epsilon_{app}$ and $^{18}\epsilon_{app}$ were substantially lower than the values of 8 and 14 ‰, respectively, determined in a single chamber at St. 1 in 2011 (Dale et al., 2014). While some temporal variability is to be expected, the difference between 2011 and 2014 is as much striking as it is puzzling, because the redox conditions and fluxes were not radically different. Lower O_2 levels in 2011 are unlikely to be the cause (see Section 5.3). $\delta^{15}N$-NO_3 and $\delta^{18}O$-NO_3 were measured in 2011 using the Cd-reduction/azide method with addition of NaCl (Ryabenko et al., 2009) and verified against the same international standards USGS34 and IAEA-NO-3. In 2011, the BIGO samples for isotope analysis were taken in quartz tubes whereas in 2014 the syringe samples were used (see Methods). The quartz tube samples were first analyzed on board for dissolved gases by passing the sample (without air contact) through the membrane inlet of a mass spectrometer prior to filtering and freezing. It is currently unclear whether this procedure significantly altered the isotopic composition of NO_3^-. Unfortunately, additional samples from the syringes were not analyzed during the 2011 campaign for comparison, and we are presently unable to resolve the inter-annual differences in $^{15}\epsilon_{app}$ and $^{18}\epsilon_{app}$.

A more realistic estimate of the total benthic N isotope effect on the oceanic N reservoir can be made from the flux of all fixed N species across the sediment-water interface, termed ϵ_{sed} by Lehmann et al. (2007). $^{15}\epsilon_{sed}$ can be higher than $^{15}\epsilon_{app}$ in continental margins if the sediment acts as a source of ^{15}N-enriched NH_4^+ to the water column, which in our setting has a $\delta^{15}N$ of ~9.0 ‰ (Figure 3C). Vertical mixing and oxidation of ^{15}N-enriched NH_4^+ higher up in the water column will then increase the $\delta^{15}N$ of the ocean NO_3^- reservoir. Mathematically, $^{15}\epsilon_{sed}$ can be calculated as:

$$^{15}\epsilon_{sed} = \delta^{15}N_{NO_{3_{BW}}} - \delta_{J_{Nreac}} = \delta^{15}N_{NO_{3_{BW}}} - \delta_{J_{N2}} \quad (10)$$

where $\delta_{J_{Nreac}}$ is the $\delta^{15}N$ of the net flux of reactive N species (NO_3^-, NO_2^-, NH_4^+, PON) and $\delta_{J_{N2}}$ is the $\delta^{15}N$ of all fixed N lost to N_2 ($\delta_{J_{N2}}$). This expression ignores dissolved organic nitrogen, which may be important in some settings (Alkhatib et al., 2012). Alkhatib et al. (2012) used a similar approach to determine $^{15}\epsilon_{app}$ based on NO_3^- fluxes (Eq. 7). Accurate estimations of $^{15}\epsilon_{sed}$ are hampered by the fact that $\delta_{J_{Nreac}}$ requires accurate isotope values for the fixed N fluxes including PON remineralization (Dale et al., 2019). Similarly, precise analytical determination of $\delta_{J_{N2}}$ is difficult due to the large background reservoir of N_2 in seawater (Brandes and Devol, 1997). In the following section, $^{15}\epsilon_{sed}$ is estimated using a numerical model of the benthic chamber incubation.

Deviations of $^{18}\epsilon_{app}$:$^{15}\epsilon_{app}$ above 1 are generally interpreted as the superimposition of the kinetic isotope effects of nitrification of NH_4^+ and denitrification (e.g. Lehmann et al., 2004; Dale et al., 2014). NH_4^+ is initially released to the porewater by the ammonification of PON with a small KIE of 1 – 2 ‰ (Möbius, 2013). The $\delta^{15}N$ of PON in the upper 30 cm of sediment on the margin is ~ 5 ‰ (Table S1). Hence, the $\delta^{15}N$ of NH_4^+ from ammonification should be close to this value. By contrast, nitrification of NH_4^+ to NO_2^- is associated with a large kinetic N isotope effect of 14 – 38 ‰ (Marioitti et al., 1981; Casciotti et al., 2003). The mass balance ($R_{NIT}/R_{AMF} < 1$) and the ^{15}N-enriched NH_4^+ effluxes indicate that NH_4^+ is only partially nitrified. If newly nitrified and ^{15}N-depleted NO_2^- is quantitatively oxidized to NO_3^-, the ^{15}N-depleted NO_3^- will dilute the ambient porewater NO_3^- pool with $^{14}NO_3^-$ and counteract the loss of $^{14}NO_3^-$ incurred through dissimilatory reduction (Lehmann et al., 2004; Lehmann et al., 2007). Nitrification does not lead to a similar behavior of $^{18}\epsilon_{app}$ because the $\delta^{18}O$ of newly nitrified NO_3^- is largely set by the $\delta^{18}O$ of seawater and is equal to ca. 0 ‰ (Buchwald and Casciotti, 2010; Casciotti et al., 2010; Buchwald et al., 2012). In other words, the $\delta^{15}N$ of NO_3^- in porewater subject to denitrification and partial nitrification will increase less quickly than its $\delta^{18}O$ signature, as long as the isotope effects for N and O by nitrate reduction are equivalent, leading to $^{18}\epsilon_{app}$:$^{15}\epsilon_{app}$.

The isotopic fingerprints of partial nitrification must be communicated back to the overlying chamber water in order

to bring about a change in observed $^{18}\epsilon_{app}$:$^{15}\epsilon_{app}$. This could take place directly by the injection of NO_3^- from the porewater into the chamber through flushing of animal burrows (Lehmann et al., 2004; Dale et al., 2014; Rooze and Meile, 2016), or indirectly by the alteration of the concentration gradients of NO_3^- isotopes at the sediment-water interface and subsequent changes in diffusive fluxes of individual isotopes (Bender, 1990; Brandes and Devol, 1997). All other things being equal, the combined effects of denitrification and partial nitrification ought to lead to $^{18}\epsilon_{app}$:$^{15}\epsilon_{app}$ values above 1 (Lehmann et al., 2004; Dale et al., 2014).

The turnover of NO_2^- adds an additional dimension to the N cycle that has received far more attention in the water column compared to sediments (Casciotti and McIlvin, 2007; Casciotti et al., 2013; Granger and Wankel, 2016). Reduction of NO_2^- occurs with a normal KIE (Casciotti et al., 2002), whereas NO_2^- oxidation occurs with an inverse KIE in both N and O, leaving residual NO_2^- depleted in ^{15}N and ^{18}O (Casciotti, 2009; Buchwald and Casciotti, 2010). Concurrent nitrate reduction and nitrite oxidation can lead to an enrichment of ^{15}N in the ambient NO_3^- pool and an enrichment of ^{14}N in NO_2^-. Several lines of evidence based on NO_2^- isotopes suggest that a significant fraction of NO_2^- produced by nitrate-reducing bacteria in oxygen deficient waters is reoxidized to NO_3^-, resulting in the $\delta^{15}N$ of NO_2^- being up to 60 ‰ lower than coexisting NO_3^- (Casciotti and McIlvin, 2007; Casciotti et al., 2013). A comprehensive box model of N and O isotope dynamics in the water column has since shown that the extent to which NO_3^- is produced relative to the fraction that is reduced plays a central role in determining the trajectories of $\delta^{15}N$-NO_3^- and $\delta^{18}O$-NO_3^- and hence $^{18}\epsilon_{app}$:$^{15}\epsilon_{app}$ (Granger and Wankel, 2016). The relevance of NO_2^- for benthic N fractionation and $^{18}\epsilon_{app}$:$^{15}\epsilon_{app}$ trajectories has been largely unexplored in benthic N isotope studies. In the following, we examine NO_2^- cycling in sediments more closely using a numerical model.

5.2 Insights from model simulations of a benthic chamber incubation experiment

5.2.1 Model set-up and calibration

In this section, we set up a multi-process numerical model of dual N and O isotope dynamics. The model consists of a 1-D, vertically-resolved, reaction-transport model of the surface sediment (upper 12 cm) coupled to a single box representative of a virtual benthic chamber, similar to the one described by Dale et al. (2019) for the Peruvian shelf. In this first step, the model is parameterized using data from St. 2 to constrain key model parameters and fractionations of the benthic N cycle for the Mauritanian shelf. In the second step, we apply the model more generally to explore the sensitivities of $^{18}\epsilon_{app}$:$^{15}\epsilon_{app}$ ratios toward different pathways of N turnover. We also interrogate the impact of the ^{15}N-enriched NH_4^+ efflux on the benthic N isotope effect on water column NO_3^-. Since most of the model structure and reaction network have been described elsewhere, we relegate the bulk of the corresponding model details to the Supplement, and here we only discuss the relevant aspects for this study (Bohlen et al., 2011; Dale et al., 2019).

The degradation of POC in the sediment drives the benthic N cycle, which in turn impacts the concentrations of N species and their isotopes in the benthic chamber. No N cycling is assumed to take place in the benthic chamber water, such that the measured chamber data act as passive tracers for the processes taking place in the sediment. The model includes most of the processes in the water column box model of Granger and Wankel (2016), including aerobic NH_4^+ oxidation (AMO), NO_3^- reduction (NAR), aerobic NO_2^- oxidation (NXR), and NO_2^- reduction to N_2 (NIR). In our model, NAR and NIR are coupled to the degradation of POC. Other electron acceptors for POC remineralization include O_2 and sulfate (SO_4^{2-}). The transition from one metabolic pathway to another during POC respiration depends on the relative concentrations of the terminal electron acceptors (TEA) and user-defined TEA threshold concentrations akin to half-saturation constants (Jourabchi et al., 2005). The TEAs are consumed in the order O_2: NO_2^-: NO_3^-: SO_4^{2-}, such that a high concentration of a TEA will inhibit less-favorable metabolic pathways. We also include ammonification of PON (AMF) that is linked to POC degradation through the atomic C:N ratio of organic matter. NH_4^+ and NO_2^- oxidation during AMO and NXR are defined as second-order reactions with rate constants k_{AMO} and k_{NXR}, respectively. At this stage, we do not consider anammox as it is a minor N loss pathway on the margin (Sokoll et al., 2016). We later relax this assumption for the sensitivity analysis. Solutes are able to diffuse through the porewater and across the sediment-water interface into and out of the benthic chamber depending on the reactions taking place in the sediment. Solute transport is also affected by bioirrigation, expressed mathematically as a simple non-local mixing function, and by bioturbation, expressed as a diffusion-like process.

The rate of organic matter degradation typically decreases with depth in the sediment as it becomes more recalcitrant over time (Middelburg, 1989). This can be constrained by the corresponding increase in NH_4^+ and total alkalinity concentrations (e.g. Berner, 1980). However, these analytes are of limited use to determine POC degradation on the Mauritanian shelf because porewaters are intensively irrigated with seawater by tube-dwelling animals (Gier et al., 2017). Therefore, following Stolpovsky et al. (2015), we used an empirical power law function to parameterize POC mineralization as function of sediment depth, x, termed RPOC(x):

$$\mathrm{RPOC}(x) = 0.5 \cdot (B_1 + x)^{B_2} \quad (11)$$

where RRPOC is the rain rate of POC to the seafloor (in mmol m^{-2} d^{-1}). Comparisons can be drawn between Eq. (11) and the power model proposed by Middelburg (1989) where the rate

constant for POC remineralization depends on the age of POC being degraded. If RRPOC provides an upper limit of the total amount of POC available for degradation, B1 can be defined as:

$$B_1 = (-2 \cdot (B_2 + 1) \cdot RRPOC)^{\frac{1}{1+B_2}} \quad (12)$$

The value of B2 was determined empirically by simulating a global dataset of benthic O_2 and NO_3^- fluxes (Stolpovsky et al., 2015):

$$B_2 = -3.73 \cdot RRPOC^{-0.17} \quad (13)$$

We assigned a value of 16.7 mmol m^{-2} d^{-1} to RRPOC, based partly on the measured TOU and partly on achieving a good fit to the benthic chamber NH_4^+ and NO_3^- fluxes. This gives B_1 and B_2 values of 0.76 cm and -2.3 (dimensionless), respectively.

The KIEs associated with nitrogen cycling (ϵ_{AMO}, ϵ_{NAR}, ϵ_{NIR}, ϵ_{NXR}), the TEA threshold NO_3^- and NO_2^- concentrations during NAR and NIR (K_{NAR}, K_{NIR}) and the rate constants k_{AMO} and k_{NXR} were mainly constrained by fitting the model to the benthic chamber data and, to a lesser extent, to the porewater data (see Supplement Figure S3). All other model parameters were fixed at reasonable values for fine grained shelf sediments, or values derived from field observations. Following Granger and Wankel (2016), we assumed that $^{15}\epsilon_{NAR} = {}^{18}\epsilon_{NAR}$, $^{15}\epsilon_{NIR} = {}^{18}\epsilon_{NIR}$, and $^{15}\epsilon_{NXR} \neq {}^{18}\epsilon_{NXR}$. The $\delta^{15}N$ of NH_4^+ produced from PON was assigned a value of 5 ‰, which is close to the mean $\delta^{15}N$ of oceanic NO_3^- (Brandes and Devol, 2002). The $\delta^{18}O$ of the NO_2^- produced by AMO was fixed (-2.3 ‰, see Supplement) and calculated as a function of the $\delta^{18}O$ of ambient H_2O and O_2, and the fractionation factors associated with their incorporation into NO_2^- (Casciotti et al., 2010). Similarly, the $\delta^{18}O$ of the NO_3^- produced by NXR was set by the inverse O isotope effect of NO_2^- oxidation ($^{18}\epsilon_{NXR}$) and the isotope effect of O incorporation into NO_2^- from water (Buchwald and Casciotti, 2010). In addition to NXR and NIR, the $\delta^{18}O$ of the NO_2^- pool is affected by the branching isotope effect of O atom extraction during NAR ($^{18}\epsilon_{NARBR}$), which was assigned a value of 25 ‰ (Granger and Wankel, 2016). In contrast to observations in the water column, we assumed that the O atoms in NO_2^- are not equilibrated with water (Buchwald and Casciotti, 2013). This is because the abiotic equilibration time is days to weeks (Buchwald and Casciotti, 2013), whereas the residence time of NO_2^- in shelf porewaters in our simulations is typically on the order of minutes. In deep-sea sediments, where NO_2^- turnover rates are far lower, abiotic equilibration must be considered (Buchwald et al., 2018).

As with most ecological models, ours is underdetermined with respect to the number of field observations available to constrain the unknown parameter values. The lack of $\delta^{15}N$ and $\delta^{18}O$ data for NO_2^- from the benthic chambers unfortunately compromises the accuracy of the model simulations. To reduce the margin of error, we ran the model using a Monte Carlo procedure to find the optimum fit to the chamber data by tuning the nine unknown parameters to the benthic chamber data. The model was run over an ensemble of 20 k iterations, in each case with a random set of parameter values chosen from typical ranges reported in the literature (Dale et al., 2014). The parameter values from simulations meeting a least squares criterion for the fit between the model and the benthic chamber data were then averaged. These are listed in Table 3 along with other model outputs of interest including ratios of depth-integrated rates and benthic isotope effects.

The optimized isotope effects for ϵ_{AMO} (35 ± 3 ‰), ϵ_{NAR} (9 ± 3 ‰), ϵ_{NIR} (14 ± 6 ‰), $^{15}\epsilon_{NXR}$ (-8 ± 5 ‰) and $^{18}\epsilon_{NXR}$ (-7 ± 5 ‰) are well-within ranges of previously-determined isotope effects in the water column (reviewed by Granger and Wankel, 2016) and sediments (Lehmann et al., 2007; Alkhatib et al., 2012; Dale et al., 2014; Dale et al., 2019). The best-fit model solutions (n = 54) of the chamber data agree well with the measured data (Figure 4). Modeled $\delta^{15}N$-NO_2^- and $\delta^{18}O$-NO_2^- are clearly sensitive to the set of best-fit parameters. This suggests that NO_2^- isotope data would help to narrow the parameter uncertainty in Table 3. It is interesting that the $\delta^{18}O$-NO_2^- flux is always positive (mean = 27 ± 6 ‰). This is explained by (i) the $\delta^{18}O$ of newly nitrified NO_2^- is set by the $\delta^{18}O$ of seawater, (ii) $^{18}\epsilon_{NIR} > {}^{18}\epsilon_{NXR}$, which enriches porewater NO_2^- in ^{18}O, and (iii) only a small fraction of NO_2^- is reoxidized to NO_3^- (NXR/NAR = 9%). In contrast, the $\delta^{15}N$ of newly nitrified NO_2^- (mean = -3 ± 5 ‰) can be positive or negative because it depends on ϵ_{AMO} and the fraction of NH_4^+ that is oxidized. The $\delta^{15}N$ of the NO_2^- flux is more sensitive to ϵ_{AMO} than any other model parameter (not shown), with higher ϵ_{AMO} leading to more ^{15}N-depleted NO_2^- fluxes.

The model predicts that 14% of NH_4^+ produced from PON is oxidized to NO_2^- (AMO/AMF). This is higher than predicted by the mass balance (RNIT/RAMF ~7%, Table 2), yet necessary in order to reproduce the efflux of ^{15}N-enriched NH_4^+. The disagreement with the model and mass balance may be rooted in the fact that the latter does not explicitly consider NO_2^-. A better agreement between the model and the mass balance was found for denitrification, with the model predicting a fixed N loss of 2.0 ± 0.1 mmol m^{-2} d^{-1}.

The N and O isotope effects for NO_3^- reduction ($^{15}\epsilon_{app}$ = 0.8 ± 0.3 ‰, $^{18}\epsilon_{app}$ = 1.2 ± 0.4 ‰) and the ratio $^{18}\epsilon_{app}$:$^{15}\epsilon_{app}$ (1.8 ± 0.8 ‰) are within the uncertainty of the observed values (Figure 3). In sediments, high $^{18}\epsilon_{app}$:$^{15}\epsilon_{app}$ are thus possible at low NXR/NAR, whereas in the water column elevated $^{18}\epsilon_{app}$:$^{15}\epsilon_{app}$ are associated with NXR/NAR of >50% (Casciotti et al., 2013; Granger and Wankel, 2016). This discrepancy probably arises from the abundance of NH_4^+ in porewaters produced by anaerobic remineralization pathways, mainly sulfate reduction, such that only a small amount of NH_4^+ oxidation with a high ϵ_{AMO} is needed to produce large $^{18}\epsilon_{app}$:$^{15}\epsilon_{app}$ trajectories. In the water column, NH_4^+ production is stoichiometrically constrained by organic matter remineralization using O_2, NO_2^- and NO_3^-, and elevated $^{18}\epsilon_{app}$:$^{15}\epsilon_{app}$ are only feasible with tightly coupled NO_2^- oxidation and NO_3^- reduction.

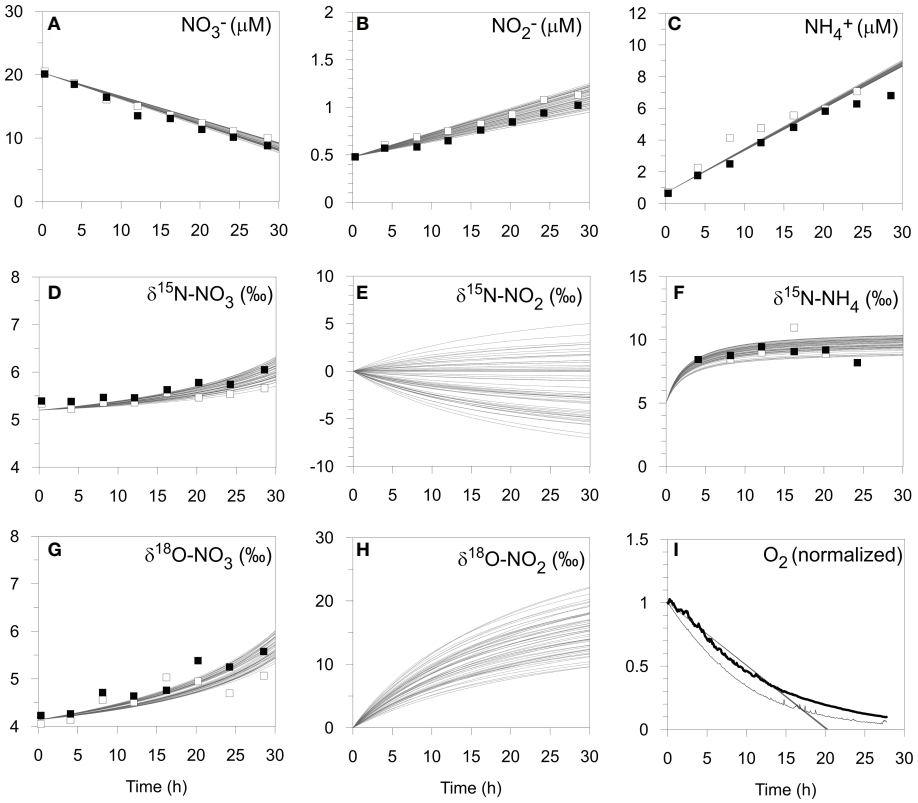

FIGURE 4
Model simulation results (curves, n = 54) of the benthic chamber incubation experiment at St. 2 on the shelf (BIGO 2-5) including **(A–C)** N concentrations, **(D–H)** N and O isotopes, and **(I)** O_2 concentrations (see text). Open and filled symbols correspond to chamber 1 and 2, respectively. For the O_2 optode data, chamber 1 and 2 are denoted by the thin and thick black lines, respectively, and have been normalized to the initial values.

TABLE 3 Key model results for the Mauritanian shelf [a].

Term	Description	Value
ϵ_{AMO}	N isotope effect for aerobic NH_4^+ oxidation, ‰	35 ± 3
$^{15}\epsilon_{NAR}$, $^{18}\epsilon_{NAR}$	N and O isotope effect for NO_3^- reduction, ‰	9 ± 3
$^{15}\epsilon_{NIR}$, $^{18}\epsilon_{NIR}$	N and O isotope effect for NO_2^- reduction, ‰	14 ± 6
$^{15}\epsilon_{NXR}$	N isotope effect for nitrite oxidation, ‰	-8 ± 5
$^{18}\epsilon_{NXR}$	O isotope effect for nitrite oxidation, ‰	-7 ± 5
$^{15}\epsilon_{app}$	Apparent benthic fractionation of N for NO_3^-, ‰	0.8 ± 0.3
$^{18}\epsilon_{app}$	Apparent benthic fractionation of O for NO_3^-, ‰	1.3 ± 0.4
$^{18}\epsilon_{app}$:$^{15}\epsilon_{app}$	Ratio of $^{18}\epsilon_{app}$ to $^{15}\epsilon_{app}$, –	1.7 ± 0.8
$^{15}\epsilon_{sed}$	Total benthic fractionation of N, ‰	3.6 ± 0.5
K_{NAR}	NO_3^- threshold concentration for NO_3^- reduction, μmol cm^{-3}	0.007 ± 0.005
K_{NIR}	NO_2^- threshold concentration for NO_2^- reduction, μmol cm^{-3}	0.006 ± 0.002
k_{AMO}	Rate constant for aerobic NH_4^+ oxidation, cm^3 μmol^{-1} yr^{-1}	$9\times10^5 \pm 1\times10^5$
k_{NXR}	Rate constant for aerobic nitrite oxidation, cm^3 μmol^{-1} yr^{-1}	$6\times10^6 \pm 3\times10^6$
NXR/NAR	NO_3^- production relative to reduction, %	9 ± 5
AMO/AMF	NH_4^+ oxidation relative to production, %	14 ± 1

[a]All model parameters are given in the Supplementary Information.

It is noteworthy that ϵ_{NAR} is much higher than $^{15}\epsilon_{app}$, confirming that the intrinsic cellular fractionation of NO_3^- reduction is not fully expressed in the benthic NO_3^- flux (Lehmann et al., 2007). ϵ_{NAR} is similar to 10 - 15 ‰ determined in pure cultures of denitrifying bacteria under typical marine conditions (Kritee et al., 2012) and to estimates from our previous box model of shelf sediments (~13 ‰, Dale et al., 2014). It also fits well with modelled data from the North Atlantic and Eastern Tropical North Pacific water column (14 ± 2 ‰, Granger and Wankel, 2016). Others have reported comparable values using model approaches that account for both closed and open system effects of NO_3^- reduction on ϵ_{NAR} (Deutsch et al., 2004; Altabet, 2007).

The total benthic N isotope effect, $^{15}\epsilon_{sed}$, calculated using Eq. (10), equals 3.6 ± 0.5 ‰. As expected, it is higher than $^{15}\epsilon_{app}$ because of the efflux of ^{15}N-enriched NH_4^+. The NO_2^- flux, although acting to decrease $^{15}\epsilon_{sed}$, hardly affects $^{15}\epsilon_{sed}$ in this setting since the flux is relatively small (Table 2). The modelled $^{15}\epsilon_{sed}$ is consistent with values of 2 – 6 ‰ determined from porewater gradients in the upper St. Lawrence Estuary where O_2 levels are below 100 µM (Alkhatib et al., 2012). It is also close to estimates of 4 – 7 ‰ reported by Lehmann et al. (2007) for the upper continental margin and with results from a global N isotope model (2 – 4 ‰; Somes et al., 2013).

The environmental controls on $^{15}\epsilon_{sed}$ are not well understood presently, and correlations between $^{15}\epsilon_{sed}$ and organic matter quality and bottom water O_2 levels have been discussed (Lehmann et al., 2007; Alkhatib et al., 2012; Dale et al., 2019). However, changes in organic matter quality and bottom water redox conditions are often intertwined (Cowie et al., 2014), and their individual contribution to $^{15}\epsilon_{sed}$ has not yet been investigated under laboratory conditions. Furthermore, the relationship between $^{15}\epsilon_{sed}$ and bioirrigation is highly non-linear and far more intricated than the simple mathematical expression of bioirrigation used in our model (Rooze and Meile, 2016). The contribution of dissolved organic N fluxes to $^{15}\epsilon_{sed}$ also deserves to be explored in future studies due to its significance in other organic-rich environments (Alkhatib et al., 2012). Despite these caveats, our results provide supporting evidence that benthic N fractionation on the continental margin exceeds previously assumed values of 0 – 2 ‰ for marine sediments (Brandes and Devol, 2002; Altabet, 2007).

5.2.2 Sensitivity of $^{15}\epsilon_{app}$, $^{18}\epsilon_{app}$:$^{15}\epsilon_{app}$ and ϵ_{sed} to N cycling pathways

We now apply the model to explore the sensitivity of ϵ_{app}, $^{18}\epsilon_{app}$:$^{15}\epsilon_{app}$ and $^{15}\epsilon_{Sed}$ to a broader range of N turnover rates, using the best-fit ϵ values in Table 3. To keep the procedure manageable, parameters associated with the physical environment (e.g. compaction, bioirrigation, boundary conditions) and RPOC(x) were left unchanged. Our primary interest here is on the internal interplay of the N cycle pathways in a continental shelf setting like the Mauritanian margin. Anammox (AMX) is now included to make the model more generic and to test the impact of AMX/AMF on the benthic isotope effect (see Supplement). Fractionations of 24 ‰ ($^{15}\epsilon_{AMXNH4}$) and 16 ‰ ($^{15}\epsilon_{AMXNO2}$) were assigned to NH_4^+ oxidation and NO_2^- reduction, respectively (Brunner et al., 2013). The ^{18}O isotope for NO_2^- reduction ($^{18}\epsilon_{AMXNO2}$) was set equal to $^{18}\epsilon_{NIR}$ (Granger and Wankel, 2016). During AMX, an additional 0.3 moles of NO_2^- are oxidized to NO_3^- per mole of NO_2^- reduced, which accounts for the reduction of inorganic carbon during production of biomass (Strous et al., 1999). NO_2^- oxidation by AMX has an inverse N isotope effect ($^{15}\epsilon_{AMXNO2ox}$) of around -30 ‰ and produces ^{15}N-enriched NO_3^- (Brunner et al., 2013). The $\delta^{18}O$ of the NO_3^- was defined analogously as described above for NXR, assuming that the O isotope effect of NO_2^- oxidation by AMX ($^{18}\epsilon_{AMXNO2ox}$) is equal to $^{18}\epsilon_{NXR}$ (Granger and Wankel, 2016).

Model results show linear and non-linear dependencies of ϵ_{app}, $^{15}\epsilon_{Sed}$ and $^{18}\epsilon_{app}$:$^{15}\epsilon_{app}$ on NXR, AMO and AMX (Figure 5). Over the ranges tested, $^{15}\epsilon_{app}$ is most sensitive to the proportion of NH_4^+ oxidized by AMO and AMX (Figure 5A). $^{15}\epsilon_{app}$ increases steadily with AMX (grey curve), which is due to the production of ^{15}N-enriched NO_3^- by the negative N isotope effect of NO_2^- oxidation. On the contrary, $^{15}\epsilon_{app}$ barely changes when NO_2^- oxidation by AMX is turned off (green curve). The production of ^{15}N-enriched NO_3^- by AMX enhances $^{15}\epsilon_{app}$ in the following way. Addition of $^{15}NO_3^-$ to the porewater slightly weakens the $^{15}NO_3^-$ concentration gradient at the sediment surface relative to $^{14}NO_3^-$, leading to an increase in porewater δ^{15}N-NO_3^- (Figure 6A). The flux of $^{15}NO_3^-$ into the sediment is reduced (relative to $^{14}NO_3^-$) and brings about a lowering of the δ^{15}N of the NO_3^- flux into the sediment (Figure 6B). As a consequence, $^{15}\epsilon_{app}$ increases (Eq. (7)). When NO_2^- oxidation by AMX is turned off, the substrates for AMX (NH_4^+ and NO_2^-) are permanently lost as N_2 with no effect on NO_3^-, which curtails any impact on $^{15}\epsilon_{app}$. A similar effect of AMX is observed for $^{18}\epsilon_{app}$ due to the negative O isotope effect of NO_2^- oxidation (grey curve, Figure 5B), which together with $^{15}\epsilon_{app}$ produces very little change in $^{18}\epsilon_{app}$:$^{15}\epsilon_{app}$ over the ranges of AMX tested (grey curve, Figure 5C). This finding is tentative, but agrees with studies in the water column where AMX fails to explain $^{18}\epsilon_{app}$:$^{15}\epsilon_{app}$ trajectories >1 (Granger and Wankel, 2016). Overall, the model suggests that observed $^{18}\epsilon_{app}$:$^{15}\epsilon_{app}$ trajectories > 1 on the Mauritanian shelf are not easily explainable by anammox alone.

AMO has a different impact on $^{15}\epsilon_{app}$ since NH_4^+ is recycled to NO_2^-, part of which can be oxidized to NO_3^-. At low AMO rates, nitrified NO_2^- is strongly depleted in ^{15}N due to the large N isotope effect, ϵ_{AMO}. The portion of this newly nitrified $^{14}NO_2^-$ that is oxidized to $^{14}NO_3^-$ causes a weakening of the $^{14}NO_3^-$ concentration gradient and a decrease in $^{15}\epsilon_{app}$ (blue curve, Figure 5A). As NH_4^+ becomes more quantitatively consumed (AMO/AMF > ~30%), newly nitrified NO_2^- and NO_3^- are increasingly ^{15}N-enriched, reversing the impact on the NO_3^- concentration gradients and

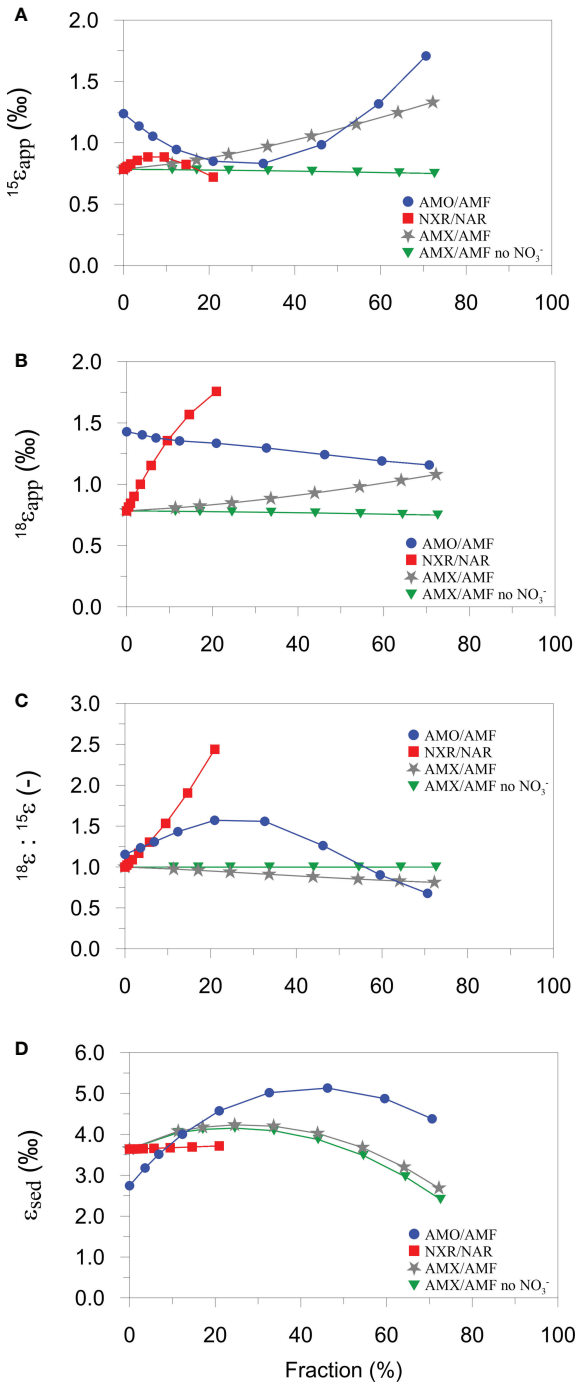

FIGURE 5
Model sensitivity analysis of **(A)** $^{15}\epsilon_{app}$, **(B)** $^{18}\epsilon_{app}$, **(C)** $^{18}\epsilon_{app}$:$^{15}\epsilon_{app}$, and **(D)** $^{15}\epsilon_{sed}$ towards AMO, AMX and NXR, given as percentage contributions to AMF or NAR. Blue, red and grey curves were generated by varying the rate constant for AMO (k_{AMO}), NXR (k_{NXR}), and AMX (k_{AMX}) stepwise between 0 and 2.6 × 10^7 cm^3 μmol^{-1} yr^{-1}. The green curves are the results for AMX/AMF without oxidation of NO_2^- to NO_3^-. All other parameter values in Table 3 and Table S2 are held constant.

producing an increase in $^{15}\epsilon_{app}$. By contrast, $^{18}\epsilon_{app}$ decreases by less than 0.5 ‰ for the full range of AMO/AMF because the $\delta^{18}O$ of newly nitrified NO_2^- is fixed (-2.3 ‰). The N and O effects of AMO combine to give a trajectory in $^{18}\epsilon_{app}$:$^{15}\epsilon_{app}$ that is highest at intermediate values of AMO/AMF (blue curve, Figure 5C). If AMO/AMF exceeds ~60%, $^{18}\epsilon_{app}$:$^{15}\epsilon_{app}$ even falls below 1. Thus, for the present model configuration, AMO can explain a wide range of $^{18}\epsilon_{app}$:$^{15}\epsilon_{app}$ ratios observed in the field.

In contrast to AMO/AMF, the fraction of NO_2^- that is oxidized relative to NO_3^- reduction (NXR/NAR) is important for $^{18}\epsilon_{app}$ but not for $^{15}\epsilon_{app}$ (red curves, Figures 5A, B). Following the reasoning based on diffusive gradients, the increase in $^{18}\epsilon_{app}$ with NXR can be explained by preferential production of $N^{18}O_3^-$ in the oxidized surface layers. This is conceivable because the $\delta^{18}O$ of newly nitrified NO_3^- is determined by the $\delta^{18}O$ of O_2 and H_2O and the inverse O isotope effect of NXR (ϵ_{NXR} = -7 ‰). Since newly produced NO_2^- has a $\delta^{18}O$ of -2.3 ‰ and is oxidized with an inverse isotope effect, the $\delta^{18}O$ of newly nitrified NO_3^- will always be higher than the $\delta^{18}O$ of NO_3^- reduced (ϵ_{NAR} = 9 ‰). $^{18}\epsilon_{app}$ rises sharply to 1.8 ‰ for NXR/NAR = 20%. (Higher ratios could not be simulated in the model due to diffusive constraints on the O_2 flux). This trend is carried through to the $^{18}\epsilon_{app}$:$^{15}\epsilon_{app}$ trajectory that also shows a steep increase (red curve, Figure 5C). NXR, therefore, is also a viable candidate for producing $^{18}\epsilon_{app}$:$^{15}\epsilon_{app}$ > 1 in benthic chambers, as proposed for the water column (Granger and Wankel, 2016).

The model results show that $^{15}\epsilon_{Sed}$ is more sensitive to AMO and AMX compared to NXR, largely due to escape of residual $^{15}NH_4^+$ from the sediment (Lehmann et al., 2007; Alkhatib et al., 2012). Although anammox also has a large N isotope effect of 24 ‰ for NH_4^+ oxidation, it does not present as similarly strong of a dynamic as AMO. Reasons for this are difficult to disentangle due to the tight coupling of the N turnover pathways, but the depth in the sediment where AMO and AMX take place may be important. Ammonium oxidation is restricted to the oxidized surface sediment that is only a few millimeters thick, which allows residual $^{15}NH_4^+$ to quickly escape to the bottom water. Anammox, in contrast, occurs over a greater depth interval where NO_3^- and NO_2^- are available (Dalsgaard et al., 2005), implying a greater path length for residual $^{15}NH_4^+$ to diffuse into the bottom water. We suggest that this raises the likelihood that residual $^{15}NH_4^+$ can be oxidized by AMO or AMX, thereby muting the intrinsic isotope fingerprint of AMX on $^{15}\epsilon_{Sed}$. High rates of AMX (and AMO) even tend to decrease $^{15}\epsilon_{Sed}$, presumably because the total flux of NH_4^+ leaving the sediment is reduced at higher consumption rates.

A final point of significance is that $^{15}\epsilon_{Sed}$ and $^{15}\epsilon_{app}$ display opposing trends with regards to AMO. At low rates, AMO is associated with a decrease in $^{15}\epsilon_{app}$, whilst simultaneously increasing $^{15}\epsilon_{Sed}$, and vice-versa at high rates (blue curves Figures 5A, D). $^{15}\epsilon_{app}$ is not, therefore, a reliable indicator of the total sediment N isotope effect, $^{15}\epsilon_{Sed}$. The interplay of the N

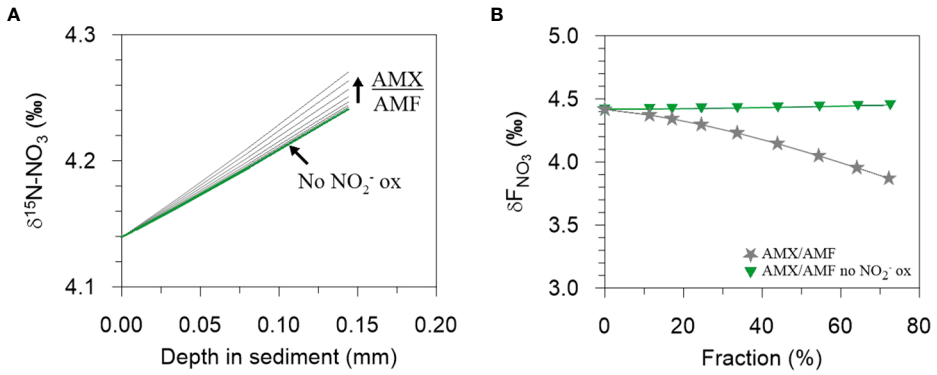

FIGURE 6
The effect on increasing AMX/AMF on **(A)** the δ^{15}N-NO_3 of porewater NO_3^- at the sediment surface and on **(B)** the δ^{15}N of the NO_3^- flux into the sediment. In **(A)**, an increase in AMX/AMF leads to a steepening of the δ^{15}N-NO_3 gradient and consequently, in **(B)**, to a decrease in $\delta_{F_{NO3}}$. Each curve in **(A)** has a corresponding symbol in **(B)**. The green lines in **(A)** are almost superimposed, reflecting a negligible change in δ^{15}N-NO_3 when NO_2^- oxidation by AMX is turned off. See Figure 5 for more details.

cycle leads to a difference between $^{15}\epsilon_{Sed}$ and $^{15}\epsilon_{app}$ that can be several ‰ at intermediate AMO/AMF values. This is a non-trivial amount considering that the oceanic N isotope balance is sensitive to small changes in the benthic N isotope effect (Brandes and Devol, 2002). For the continental margin, where most benthic denitrification takes place, the contribution of the NH_4^+ flux to the total benthic N isotope effect may be as important as NO_3^-. Consequently, δ^{15}N-NH_4 measurements in benthic chambers should be prioritized alongside δ^{15}N-NO_3.

5.3 Interannual variability of nutrient fluxes

As with most continental margins, benthic fluxes and N turnover pathways on the Mauritanian margin at 18°N reveal an intensification of nutrient recycling on the shelf and a sharp decrease offshore (Jahnke et al., 1990). This trend is driven by the increasingly recalcitrant nature of bulk sedimentary POC and POC rain rate with water depth (Dale et al., 2014).

The deposition flux of labile POC to the seafloor is positively correlated with benthic denitrification, and high rates of fixed N loss to N_2 are observed in both fine-grained and sandy continental shelves (Middelburg et al., 1996; Cook et al., 2006). The mean fraction of POC respired by denitrification on the Mauritanian margin (24%, Figure 1C) is higher than the global average of ≤10% (Middelburg et al., 1996). This can be explained by the amplification of denitrification in sediments underlying oxygen – deficient bottom waters due to less inhibition by O_2. The impact of denitrification is to raise the RQ since it produces DIC whilst not impacting TOU. If the 24% of POC that is remineralized by denitrification on the margin would instead be channeled through aerobic pathways, we might expect the TOU to increase by a similar amount with a corresponding decrease in RQ from 1.5 to 1.2. This is higher than the theorical value of 0.7 based on complete aerobic mineralization of organic matter with an average phytoplankton composition (Anderson, 1995) and supports the idea that benthic carbonate dissolution is driving an excess DIC flux across the margin.

The loss of fixed N relative to PO_4^{3-} generates N-depleted recycling fluxes (negative N*) compared to the standard phytoplankton N:P composition of ~16. If the calculated denitrification rates are added to F_{N^*}, the mean F_{N^*} increases from -2.8 to -1 mmol m^{-2} d^{-1}. indicating that N loss accounts for roughly two thirds of the negative N* flux. Enhanced PO_4^{3-} release under low-oxygen bottom waters probably accounts for the remaining third (Schroller-Lomnitz et al., 2019). Low or negative N* fluxes are characteristic of sediments under oxygen-deficient waters. Outside of these areas, where O_2 levels are > 100 µM, N-depleted fluxes are much more muted (Bohlen et al., 2012), partly due to more efficient sequestration of PO_4^{3-} by adsorption onto iron (oxyhydr)oxide minerals (Sundby et al., 1986). Mixing of low N:P waters from the benthic boundary layer into oxygen-poor water columns has the potential to enhance N_2 fixation, leading to a positive feedback between primary production, O_2 drawdown and benthic P release (Kemena et al., 2019).

On average, NH_4^+ and PO_4^{3-} fluxes on the shelf were 2 to 3 times higher in June 2014 compared to 2011 (Dale et al., 2014; Schroller-Lomnitz et al., 2019). NO_3^- and H_4SiO_4 fluxes were also elevated by 40 and 25%, respectively. Mean TOU in 2011 and 2014 was the same (ca. 10 mmol m^{-2} d^{-1}), and benthic carbon respiration rates on the shelf in 2014 were similar ($RPOC_{TOT}$ = 10 – 11 mmol m^{-2} d^{-1}). Given that the release of NH_4^+ and PO_4^{3-} from sediments is typically regulated by nitrification and adsorption by iron (oxyhydr)oxide minerals,

respectively (Sundby et al., 1986; Sloth et al., 1992), the higher NH_4^+ and PO_4^{3-} fluxes in 2014 suggest that the bottom waters might have become more reducing since 2011. Indeed, a long-term decline of O_2 concentrations in the ETNA has received much publicity (Stramma et al., 2008; Schmidtko et al., 2017). Our data corroborate these findings, with a decrease in minimum bottom water O_2 concentrations on the shelf from 42 µM in 2011 (Dale et al., 2014) to 25 µM in 2014 (Table 1).

One could conclude that the observed increase in NH_4^+ and PO_4^{3-} fluxes between 2011 and 2014 is caused by the long-term decrease in bottom water O_2. Yet, other contributing factors that are not easily quantifiable deserve careful consideration, such as (i) seasonal accumulation and depletion of nutrients in porewaters (e.g. Dale et al., 2013), (ii) changes in the faunal community structure and sediment reworking rates (Dale et al., 2013; Gier et al., 2017), (iii) low frequency changes in O_2 respiration close to the seabed associated with particle resuspension (Thomsen et al., 2019), and (iv) the episodic formation and export of oxygen-poor mesoscale eddies over the shelf on quasi-monthly time-scales (Thomsen et al., 2019). The magnitude of the O_2 decrease between 2011 and 2014 observed on the landers (17 µM) is also much higher than observed deoxygenation rates in the ETNA of ca. 0.5 µmol kg^{-1} yr^{-1} (Stramma et al., 2008). Long-term monitoring of sediment fluxes is needed to address this issue more precisely, preferably using autonomous methodologies such as bottom crawlers that can operate independently of costly ship-based surveys (Wenzhöfer et al., 2016). Until the technology to do so becomes more accessible, future projections of the nutrient budgets and the economic sustainability of fisheries in tropical upwelling regions will carry larger uncertainties (Wallmann et al., 2022).

6 Conclusions

This study presents *in situ* fluxes of O_2, DIC, nutrients and stable isotopes of dissolved inorganic nitrogen species in benthic chambers deployed on the Mauritanian margin in 2014. The aim was to quantify the recycling rates of biogenic debris with particular emphasis on the N cycle. The trends in benthic fluxes were generally similar to those measured in an earlier campaign to the region in 2011, and associated with a decrease in organic matter remineralization and denitrification rates with water depth. Notably, though, the fluxes of NH_4^+ and PO_4^{3-} on the shelf were 2 – 3 times higher in 2014. We were unable to pinpoint the cause of this increase from only two sets of field data. Long-term, or more frequent, monitoring of sediment-water interactions is needed to determine whether the seafloor is becoming more reducing and to elucidate possible linkages with the observed long-term decline in O_2 concentration in the tropical Atlantic. Elevated release of PO_4^{3-} from the standing stock of iron-bound P might stimulate the productivity of surface waters and continue to drive down subsurface O_2 levels, leading to a positive feedback between benthic PO_4^{3-} release and deoxygenation.

The mean isotopic fractionations of N ($^{15}\epsilon_{app}$) and O ($^{18}\epsilon_{app}$) accompanying benthic NO_3^- uptake were low and in good agreement with previously reported isotope effects for NO_3^- respiration in marine sediments. Analysis of the data using a numerical model showed that the overall benthic N isotope effect ($^{15}\epsilon_{sed}$) that includes the efflux of ^{15}N-enriched NH_4^+ from the seafloor, and the one that is of relevance to the global N isotope budget, bears no straightforward relationship with $^{15}\epsilon_{app}$. The model predicted $^{15}\epsilon_{Sed}$ = 3.6 ‰ for the Mauritanian shelf which, whilst lower than observed isotope effects of pelagic N loss in oxygen-deficient regions, adds to the growing body of evidence that the assumption of a universally low or negligible benthic N isotope effect is not applicable to oxygen-deficient settings.

The isotope model was used to constrain the relative rates of N turnover processes in the sediment. The model showed that observed trajectories in $^{18}\epsilon_{app}$:$^{15}\epsilon_{app}$ > 1 on the shelf were likely the result of aerobic ammonium oxidation and nitrite oxidation in surface sediments. Anammox has little influence on $^{18}\epsilon_{app}$:$^{15}\epsilon_{app}$ in this setting. This finding may be more widely applicable because the isotopic impact of anammox is less easily communicated to the water column than ammonium and nitrite oxidation. Anammox, however, tends to increase $^{15}\epsilon_{sed}$ if the fraction of NH_4^+ consumed is not too high. Our model suggests that NO_2^- isotope data from benthic chambers would help to constrain further the rates of N turnover in sediments, provided that the analytical challenge of low sample volumes from benthic chambers and low NO_2^- concentrations can be overcome.

Data availability statement

The datasets presented in this study can be found in online repositories. The names of the repository/repositories and accession number(s) can be found below: https://doi.pangaea.de/10.1594/PANGAEA.928206 https://doi.pangaea.de/10.1594/PANGAEA.941569.

Author contributions

AD conceived and wrote the paper. AD, DC, US-L and SS conducted fieldwork and chemical analyses. KD and FK performed isotope measurements. All authors contributed to the article and approved the submitted version.

Funding

This work is supported by the Sonderforschungsbereich 754 “Climate – Biogeochemistry Interactions in the Tropical Ocean”

(www.sfb754.de) financed by the Deutsche Forschungsgemeinschaft (DFG), and also by the German Federal Ministry of Education and Research (BMBF, funding ref. no. 03F0815A) through the research project REEBUS (Role of Eddies in the Carbon Pump of Eastern Boundary Upwelling Systems).

Acknowledgments

We thank A. Petersen, M. Türk, and S. Cherednichenko for their assistance in deploying the landers, and B. Domeyer, V. Thönissen, S. Trinkler, S. Kriwanek, A. Bleyer, R. Suhrberg, F. Jung geochemical analyses. We also thank Thomas Hansen (GEOMAR) for measuring the C and N isotopes in sediment samples and to Fabian Jung for assisting with the BIGO isotope measurements. We are grateful to the crew of RV Meteor and RV Maria S. Merian for their enthusiastic support. We express our gratitude to Annie Bourbonnais for editorial handling of the manuscript, and to the reviewers for their expertise and input that improved the finalized version.

Conflict of interest

The authors declare that the research was conducted in the absence of any commercial or financial relationships that could be construed as a potential conflict of interest.

Publisher's note

Supplementary material

The Supplementary Material for this article can be found online at: https://www.frontiersin.org/articles/10.3389/fmars.2022.902062/full#supplementary-material

References

Alkhatib, M., Lehmann, M. F., and del Giorgio, P. A. (2012). The nitrogen isotope effect of benthic remineralization–nitrification–denitrification coupling in an estuarine environment. *Biogeosciences* 9, 1633–1646. doi: 10.5194/bg-9-1633-2012

Altabet, M. A. (2007). Constraints on oceanic n balance/imbalance from sedimentary. *Biogeosciences* 4, 75–86. doi: 10.5194/bg-4-75-2007

Anderson, L. A. (1995). On the hydrogen and oxygen content of marine phytoplankton. *Deep-Sea Res. Part I-Oceanogr. Res. Pap.* 42, 1675–1680. doi: 10.1016/0967-0637(95)00072-E

Bender, M. L. (1990). The $\delta^{18}O$ of dissolved O_2 in seawater: A unique tracer of circulation and respiration in the deep sea. *J. Geophys. Res.* 95, 22243–22252. doi: 10.1029/JC095iC12p22243

Berner, R. A. (1980). *Early diagenesis–a theoretical approach. Princeton univ* (Princeton, N. J: Press).

Bohlen, L., Dale, A. W., Sommer, S., Mosch, T., Hensen, C., Noffke, A., et al. (2011). Benthic nitrogen cycling traversing the Peruvian oxygen minimum zone. *Geochim. Cosmochim. Acta* 75, 6094–6111. doi: 10.1016/j.gca.2011.08.010

Bohlen, L., Dale, A. W., and Wallmann, K. (2012). Simple transfer functions for calculating benthic fixed nitrogen losses and C:N:P regeneration ratios in global biogeochemical models. *Glob. Biogeochem. Cy.* 26, GB3029. doi: 10.1029/2011GB004198

Böhlke, J. K., Mroczkowski, S. J., and Coplen, T. B. (2003). Oxygen iso-topes in nitrate: new reference materials for18O :17O :16O mea-surements and observations on nitrate-water equilibration. *Rapid Commun. Mass Spectrom.* 17, 1835–1846. doi: 10.1002/rcm.1123

Bourbonnais, A., Altabet, M. A., Charoenpong, C. N., Larkum, J., Hu, H., Bange, H. W., et al. (2015). N-loss isotope effects in the Peru oxygen minimum zone studied using a mesoscale eddy as a natural tracer experiment. *Global Biogeochem. Cycles* 29, 793–811. doi: 10.1002/2014GB005001

Brandes, J. A., and Devol, A. H. (1997). Isotopic fractionation of oxygen and nitrogen in coastal marine sediments. *Geochim. Cosmochim. Acta* 61, 1793–1801. doi: 10.1016/S0016-7037(97)00041-0

Brandes, J. A., and Devol, A. H. (2002). A global marine-fixed nitrogen isotopic budget: Implications for Holocene nitrogen cycling *Global Biogeochem. Cycles* 16 (4), 1120. doi: 10.1029/2001GB001856

Brüchert, V., Jørgensen, B. B., Neumann, K., Riechmann, D., Schlösser, M., and Schulz, H. (2003). Regulation of bacterial sulfate reduction and hydrogen sulfide fluxes in the central namibian coastal upwelling zone. *Geochim. Cosmochim. Acta* 67, 4505–4518. doi: 10.1016/S0016-7037(03)00275-8

Brunner, B., Contreras, S., Lehmann, M. F., Matantseva, O., Rollog, M., Kalvelage, T., et al. (2013). Nitrogen isotope effects induced by anammox bacteria. *Proc. Natl. Acad. Sci. U.S.A.* 110, 18994–18999. doi: 10.1073/pnas.1310488110

Brzezinski, M. A. (1985). The Si:C:N ratio of marine diatoms: Interspecific variability and the effect of some environmental variables. *J. Phycol.* 21, 347–357. doi: 10.1111/j.0022-3646.1985.00347.x

Buchwald, C., and Casciotti, K. L. (2010). Oxygen isotopic fractionation and exchange during bacterial nitrite oxidation. *Limnol. Oceanogr.* 55, 1064–1074. doi: 10.4319/lo.2010.55.3.1064

Buchwald, C., and Casciotti, K. L. (2013). Isotopic ratios of nitrite as tracers of the sources and age of oceanic nitrite. *Nat. Geosci.* 6, 1–6. doi: 10.1038/ngeo1745

Buchwald, C., Homola, K., Spivack, A. J., Estes, E. R., Murray, R. W., and Wankel, S. D. (2018). Isotopic constraints on nitrogen transformation rates in the deep sedimentary marine biosphere. *Glob. Biogeochem. Cy.* 32, 1688–1702. doi: 10.1029/2018GB005948

Buchwald, C., Santoro, A. E., McIlvin, M. R., and Casciotti, K. L. (2012). Oxygen isotopic composition of nitrate and nitrite produced by nitrifying cocultures and natural marine assemblages. *Limnology Oceanography* 57, 1361–1375. doi: 10.4319/lo.2012.57.5.1361

Burdige, D. J. (2006). *Geochemistry of marine sediments* (Princeton: Princeton University Press), 609.

Carr, M.-E. (2001). Estimation of potential productivity in Eastern boundary currents using remote sensing. *Deep-Sea Res. Part II Top. Stud. Oceanogr.* 49, 59–80. doi: 10.1016/S0967-0645(01)00094-7

Casciotti, K. L. (2009). Inverse kinetic isotope fractionation during bacterial nitrite oxidation. *Geochim. Cosmochim. Acta* 73, 2061–2076. doi: 10.1016/j.gca.2008.12.022

Casciotti, K. L. (2016). Nitrite isotopes as tracers of marine n cycle processes. *Philos. Trans. R. Soc A* 374, 20150295. doi: 10.1098/rsta.2015.0295

Casciotti, K. L., Buchwald, C., and McIlvin, M. (2013). Implications of nitrate and nitrite isotopic measurements for the mechanisms of nitrogen cycling in the Peru oxygen deficient zone. *Deep-Sea Res. I* 80, 78–93. doi: 10.1016/j.dsr.2013.05.017

Casciotti, K. L., and McIlvin, M. R. (2007). Isotopic analyses of nitrate and nitrite from reference mixtures and application to Eastern tropical north pacific waters. *Mar. Chem.* 107, 184–201. doi: 10.1016/j.marchem.2007.06.021

Casciotti, K. L., McIlvin, M. R., and Buchwald, C. (2010). Oxygen isotopic exchange and fractionation during bacterial ammonia oxidation. *Limnol. Oceanogr.* 55, 753–762. doi: 10.4319/lo.2010.55.2.0753

Casciotti, K. L., Sigman, D. M., Galanter Hastings, M., and Böhlke, J. K. (2002). Measurement of the oxygen isotopic composition of nitrate in seawater and freshwater using the denitrifier method. *Analyt. Chem.* 74, 4905–4912. doi: 10.1021/ac020113w

Casciotti, K. L., Sigman, D. M., and Ward, B. B. (2003). Linking diversity and stable isotope fractionation in ammonia-oxidizing bacteria. *Geomicrobiol. J.* 20, 335–353. doi: 10.1080/01490450303895

Cook, P. L. M., Wenzhoefer, F., Rysgaard, S., Galaktionov, O. S., Meysman, F. J. R., Eyre, B. D., et al. (2006). Quantification of denitrification in permeable sediments: Insights from a two–dimensional simulation analysis and experimental data. *Limnol. Oceanogr. Meth.* 4, 294–307. doi: 10.4319/lom.2006.4.294

Cowie, G., Mowbray, S., Kurian, S., Sarkar, A., White, C., Anderson, A., et al. (2014). Comparative organic geochemistry of Indian margin (Arabian Sea) sediments: estuary to continental slope. *Biogeosciences* 11, 6683–6696. doi: 10.5194/bg-11-6683-2014

Dähnke, K., and Thamdrup, B. (2013). Nitrogen isotope dynamics and fractionation during sedimentary denitrification in boknis eck, Baltic Sea. *Biogeosciences* 10, 3079–3088. doi: 10.5194/bg-10-3079-2013

Dale, A. W., Bertics, V. J., Treude, T., Sommer, S., and Wallmann, K. (2013). Modeling benthic-pelagic nutrient exchange processes and porewater distributions in a seasonally-hypoxic sediment: evidence for massive phosphate release by *Beggiatoa*? *Biogeosciences* 10, 629–651. doi: 10.5194/bg-10-629-2013

Dale, A. W., Bourbonnais, A., Altabet, M., Wallmann, K., and Sommer, S. (2019). Isotopic fingerprints of benthic nitrogen cycling in the Peruvian oxygen minimum zone. *Geochim. Cosmochim. Acta* 245, 406–425. doi: 10.1016/j.gca.2018.10.025

Dale, A. W., Sommer, S., Lomnitz, U., Montes, I., Treude, T., Liebetrau, V., et al. (2015). Organic carbon production, mineralisation and preservation on the Peruvian margin. *Biogeosciences* 12, 1537–1559. doi: 10.5194/bg-12-1537-2015

Dale, A. W., Sommer, S., Ryabenko, E., Noffke, A., Bohlen, L., Wallmann, K., et al. (2014). Benthic nitrogen fluxes and fractionation of nitrate in the Mauritanian oxygen minimum zone (Eastern tropical north Atlantic). *Geochim. Cosmochim. Acta* 134, 234–256. doi: 10.1016/j.gca.2014.02.026

Dalsgaard, T., Thamdrup, B., and Canfield, D. E. (2005). Anaerobic ammonium oxidation (anammox) in the marine environment. *Res. Microbiol.* 156, 457–464. doi: 10.1016/j.resmic.2005.01.011

Deutsch, C., Sigman, D. M., Thunell, R. C., MEckler, A. N., and Haug, G. H. (2004). Isotopic constraints on glacial/interglacial changes in the oceanic nitrogen budget. *Glob. Biogeochem. Cy.* 18, GB4012. doi: 10.1029/2003GB002189

Devol, A. H., Uhlenhopp, A. G., Naqvi, S. W. A., Brandes, J. A., Jayakumar, D. A., Naik, H., et al. (2006). Denitrification rates and excess nitrogen gas concentrations in the Arabian Sea oxygen deficient zone. *Deep. Res. I* 53, 1533–1547. doi: 10.1016/j.dsr.2006.07.005

Fischer, G., Neuer, S., Davenport, R., Romero, O., Ratmeyer, V., Donner, B., et al. (2010). "The Northwest African margin, in: Carbon and nutrient fluxes in continental margins," in *A global synthesis*. Eds. K.-K. Liu, L. Atkinson, R. Quiñones and L. Talaue-McManus (Berlin: IGBP Book Series, Springer), 77–103.

Fütterer, D. K. (1983). "The modern upwelling record off northwest Africa, in coastal upwelling: Its sedimentary record, part b," in *Sedimentary records of ancient coastal upwelling*. Eds. J. Thiede and E. Suess (Plenum, New York: Springer), 105–121.

Gaye, B., Nagel, B., Dähnke, K., Rixen, T., and Emeis, K.-C. (2013). Evidence of parallel denitrification and nitrite oxidation in the ODZ of the Arabian Sea from paired stable isotopes of nitrate and nitrite. *Glob. Biogeochem. Cy.* 27, 1059–1071. doi: 10.1002/2011GB004115

Gier, J., Löscher, C. R., Dale, A. W., Sommer, S., Lomnitz, U., and Treude, T. (2017). Benthic dinitrogen fixation traversing the oxygen minimum zone off Mauritania (NW Africa). *Front. Mar. Sci.* 4. doi: 10.3389/fmars.2017.00390

Granger, J., Prokopenko, M. G., Sigman, D. M., Mordy, C. W., Morse, Z. M., Morales, L. V., et al. (2011). Coupled nitrification-denitrification in sediment of the eastern Bering Sea shelf leads to ^{15}N enrichment of fixed n in shelf waters. *J. Geophys. Res.* 116. doi: 10.1029/2010JC006751

Granger, J., Sigman, D. M., Lehmann, M. F., and Tortell, P. D. (2008). Nitrogen and oxygen isotope fractionation during dissimilatory nitrate reduction by denitrifying bacteria. *Limnol. Oceanogr.* 53, 2533–2545. doi: 10.4319/lo.2008.53.6.2533

Granger, J., and Wankel, S. D. (2016). Environmental overprinting of nitrate isotopes. *Proc. Nat. Acad. Sci.* 113 (42), E6391–E6400. doi: 10.1073/pnas.1601383113

Gruber, N. (2008). The marine nitrogen cycle and atmospheric CO_2.In: *Nitrogen in the Marine Environment* (*Second* Edition) DG Capone, DA Bronk, MR Mulholland and EJ Carpenter (Academic Press) 1–50. doi: 10.1016/B978-0-12-372522-6.00001-3

Gruber, N., and Sarmiento, J. (1997). Global patterns of marine nitrogen fixation and denitrification. *Glob. Biogeochem. Cy.* 11, 235–266. doi: 10.1029/97GB00077

Hansen, T., and Sommer, U. (2007). Increasing the sensitivity of $\delta^{13}C$ and $\delta^{15}N$ abundance measurements by a high sensitivity elemental analyser connected to an isotope ratio mass spectrometer. *Rapid Commun. Mass Spectrom.* 21, 314–318. doi: 10.1002/rcm.2847

Hartmann, M., Müller, P. J., Suess, E., and van der Weijden, C. H. (1976). Chemistry of late quaternary sediments and their interstitial waters from the NW African continental margin. *Meteor Forschungsergebnisse. Reihe C: Geologie und Geophysik* 24, 1–67.

Huntsman, S. A., and Barber, R. T. (1977). Primary production off northwest Africa: the relationship to wind and nutrient conditions. *Deep Sea Res.* 24, 25–33. doi: 10.1016/0146-6291(77)90538-0

Jahnke, R. A., and Jahnke, D. B. (2004). Calcium carbonate dissolution in deep sea sediments: Reconciling microelectrode, pore water and benthic flux chamber results. *Geochim. Cosmochim. Acta* 68, 47–59. doi: 10.1016/S0016-7037(03)00260-6

Jahnke, R. A., Reimers, C. E., and Craven, D. B. (1990). Organic matter recycling at the seafloor: intensification near ocean margins. *Nature* 348, 50–54. doi: 10.1038/348050a0

Jourabchi, P., Van Cappellen, P., and Reginer, P. (2005). Quantitative interpretation of pH distributions in aquatic sediments: A reaction-transport modeling approach. *Am. J. Sci.* 305, 919–956. doi: 10.2475/ajs.305.9.919

Jorgensen, B. B., Wenzh.fer, F., Egger, M, and Glud, R. N. (2022). Sediment oxygen consumption: Role in the global marine carbon cycle. *Earth-Science Reviews* 228, 103987. doi: 10.1016/j.earscirev.2022.103987

Karstensen, J., Stramma, L., and Visbeck, M. (2008). Oxygen minimum zones in the eastern tropical Atlantic and pacific oceans. *Prog. Oceanogr.* 77, 331–350. doi: 10.1016/j.pocean.2007.05.009

Kemena, T. P., Landolfi, A., Oschlies, A., Wallmann, K., and Dale, A. W. (2019). Ocean phosphorus inventory: large uncertainties in future projections on millennial timescales and their consequences for ocean deoxygenation. *Earth Syst. Dynam.* 10, 539–553. doi: 10.5194/esd-10-539-2019

Klenz, T., Dengler, M., and Brandt, P. (2018). Seasonal variability of the Mauritania current and hydrography at 18°N. *J. Geophys. Res. Oceans* 123, 8122–8137. doi: 10.1029/2018JC014264

Krahmann, G., Arévalo-Martínez, D. L., Dale, A. W., Dengler, M., Engel, A., Glock, N., et al. (2021). Climate-biogeochemistry interactions in the tropical ocean: data collection and legacy. *Front. Mar. Sci.* 8. doi: 10.3389/fmars.2021.723304

Kritee, K., Sigman, D. M., Granger, J., Ward, B. B., Jayakumar, A., and Deutsch, C. (2012). Reduced isotope fractionation by denitrification under conditions relevant to the ocean. *Geochim. Cosmochim. Acta* 92, 243–259. doi: 10.1016/j.gca.2012.05.020

Lam, P., and Kuypers, M. M. M. (2011). Microbial nitrogen cycling processes in oxygen minimum zones. *Ann. Rev. Mar. Sci.* 3, 317–345. doi: 10.1146/annurev-marine-120709-142814

Lehmann, M. F., Sigman, D. M., and Berelson, W. M. (2004). Coupling the $^{15}N/^{14}N$ and $^{18}O/^{16}O$ of nitrate as a constraint on benthic nitrogen cycling. *Mar. Chem.* 88, 1–20. doi: 10.1016/j.marchem.2004.02.001

Lehmann, M. F., Sigman, D. M., McCorkle, D. C., Granger, J., Hoffmann, S., Cane, G., et al. (2007). The distribution of nitrate $^{15}N/^{14}N$ in marine sediments and the impact of benthic nitrogen loss on the isotopic composition of oceanic nitrate. *Geochim. Cosmochim. Acta* 71, 5384–5404. doi: 10.1016/j.gca.2007.07.025

Marioitti, A., Germon, J. C., Hubert, P., Kaiser, P., Letolle, R., Tardieux, A., et al. (1981). Experimental determination of nitrogen kinetic isotope fractionation: Some principles; illustration for the denitrification and nitrification processes. *Plant Soil* 62, 413–430. doi: 10.1007/BF02374138

Mcilvin, M. R., and Altabet, M. A. (2005). Chemical conversion of nitrate and nitrite to nitrous oxide for nitrogen and oxygen isotopic analysis in freshwater and seawater. *Anal. Chem.* 77, 5589–5595. doi: 10.1021/ac050528s

Meyers, P. A. (1994). Preservation of elemental and isotopic source identification of sedimentary organic matter. *Chem. Geol.* 114, 289–302. doi: 10.1016/0009-2541(94)90059-0

Middelburg, J. J. (1989). A simple rate model for organic matter decomposition in marine sediments. *Geochim. Cosmochim. Acta* 53, 1577–1581. doi: 10.1016/0016-7037(89)90239-1

Middelburg, J. J., Soetaert, K., Herman, P. M. J., and Heip, C. H. R. (1996). Denitrification in marine sediments: A model study. *Glob. Biogeochem. Cy.* 10, 661–673. doi: 10.1029/96GB02562

Mittelstaedt, E. (1983). The upwelling area off Northwest Africa – a description of phenomena related to coastal upwelling. *Prog. Oceanogr.* 12, 307–331. doi: 10.1016/0079-6611(83)90012-5

Möbius, J. (2013). Isotope fractionation during nitrogen remineralization (ammonification): Implications for nitrogen isotope biogeochemistry. *Geochim. Cosmochim. Acta* 105, 422–432. doi: 10.1016/j.gca.2012.11.048

Mortazavi, B., and Chanton, J. P. (2004). Use of keeling plots to determine sources of dissolved organic carbon in nearshore and open ocean systems. *Limnol. Oceanogr.* 49, 102–110. doi: 10.4319/lo.2004.49.1.0102

Prokopenko, M. G., Hirst, M. B., De Brabandere, L., Lawrence, D. J. P., Berelson, W. M., Granger, J., et al. (2013). Nitrogen losses in anoxic marine sediments driven by *Thioploca*-anammox bacterial consortia. *Nature* 500, 194–198. doi: 10.1038/nature12365

Rooze, J., and Meile, C. (2016). The effect of redox conditions and bioirrigation on nitrogen isotope fractionation in marine sediments. *Geochim. Cosmochim. Acta* 184, 227–239. doi: 10.1016/j.gca.2016.04.040

Ryabenko, E., Altabet, M. A., and Wallace, D. W. R. (2009). Effect of chloride on the chemical conversion of nitrate to nitrous oxide for delta n–15 analysis. *Limnol. Oceanogr. Meth.* 7, 245–552. doi: 10.4319/lom.2009.7.545

Schafstall, J., Dengler, M., Brandt, P., and Bange, H. (2010). Tidal induced mixing and diapycnal nutrient fluxes in the Mauritanian upwelling region. *J. Geophys. Res.* 115, C10014. doi: 10.1029/2009JC005940

Schmidtko, S., Stramma, L., and Visbeck, M. (2017). Decline in global oceanic oxygen content during the past five decades. *Nature* 542, 335–339. doi: 10.1038/nature21399

Schroller-Lomnitz, U., Hensen, C., Dale, A. W., Scholz, F., Clemens, D., Sommer., S., et al. (2019). Dissolved benthic phosphate, iron and carbon fluxes in the Mauritanian upwelling system and implications for ongoing deoxygenation. *Deep-Sea Res. I* 143, 70–84. doi: 10.1016/j.dsr.2018.11.008

Sigman, D. M., Casciotti, K. L., Andreani, M., Barford, C., Galanter, M., and Böhlke, J. K. (2001). A bacterial method for the nitrogen isotopic analysis of nitrate in seawater and freshwater. *Anal. Chem.* 73, 4145–4153. doi: 10.1021/ac010088e

Sigman, D. M., DiFiore, P. J., Hain, M. P., Deutsch, C., Wang, Y., Karl, D. M., et al. (2009). The dual isotopes of deep nitrate as a constraint on the cycle and budget of oceanic fixed nitrogen. *Deep-Sea Res. I Oceanogr. Res. Pap.* 56, 1419–1439. doi: 10.1016/j.dsr.2009.04.007

Sigman, D. M., Granger, J., DiFiore, P. J., Lehmann, M. F., Ho, R., Cane, G., et al. (2006). Coupled nitrogen and oxygen isotope measurements of nitrate along the eastern north pacific margin. *Global Biogeochem. Cycles* 19, GB4022. doi: 10.1029/2005GB002458

Sloth, N. P., Nielsen, L. P., and Blackburn, T. H. (1992). Nitrification in sediment cores measured with acetylene inhibition. *Limnol. Oceanogr.* 37, 1108–1112. doi: 10.4319/lo.1992.37.5.1108

Sokoll, S., Lavik, G., Sommer, S., Goldhammer, T., Kuypers, M. M. M., and Holtappels, M. (2016). Extensive nitrogen loss from permeable sediments off north-West Africa. *J. Geophys. Res. Biogeosci.* 121, 1144–1157. doi: 10.1002/2015JG003298

Somes, C. J., Oschlies, A., and Schmittner, A. (2013). Isotopic constraints on the pre-industrial oceanic nitrogen budget. *Biogeosciences* 10, 5889–5910. doi: 10.5194/bg-10-5889-2013

Sommer, S., Adam, N., Becker, K., Dale, A. W., Hahn, J., Kampmeier, M., et al. (2020). *Role of eddies in the carbon pump of Eastern boundary upwelling systems, REEBUS, cruise no. M156, 03.07. – 01.08.2019 mindelo (Cap Verde) – mindelo* (Bonn: Meteor Berichte, M156. Gutachterpanel Forschungsschiffe), 53 pp. doi: 10.2312/cr_m156

Sommer, S., Dengler, M., and Treude, T. (2015). *Benthic element cycling, fluxes and transport of solutes across the benthic boundary layer in the Mauritanian oxygen minimum zone, (SFB754) - cruise no. M107, may 30 - July 03, 2014, fortaleza (Brazil) - las palmas (Spain). METEOR-berichte, M107* (Bremen: DFG-Senatskommission für Ozeanographie), 67 pp. doi: 10.2312/cr_m107

Sommer, S., Türk, M., Kriwanek, S., and Pfannkuche, O. (2008). Gas exchange system for extended *in situ* benthic chamber flux measurements under controlled oxygen conditions: First application – Sea bed methane emission measurements at captain arutyunov mud volcano. *Limnol. Oceanogr. Meth.* 6, 23–33. doi: 10.4319/lom.2008.6.23

Stolpovsky, K., Dale, A. W., and Wallmann, K. (2015). Toward a parameterization of global-scale organic carbon mineralization kinetics in surface marine sediments. *Glob. Biogeochem. Cy.* 29, 812–829. doi: 10.1002/2015GB005087

Stramma, L., Johnson, G. C., Sprintall, J., and Mohrholz, V. (2008). Expanding oxygen–minimum zones in the tropical oceans. *Science* 320, 655–658. doi: 10.1126/science.1153847

Strous, M., Fuerst, J. A., Kramer, E. H. M., Logemann, S., Muyzer, G., van de Pas-Schoonen, K. T., et al. (1999). Missing lithotroph identified as new planctomycete. *Nature* 400, 446–449. doi: 10.1038/22749

Sundby, B., Anderson, L. G., Hall, P. O. J., Iverfeldt, Å., van der Loeff, M. M. R., and Westerlund, S. F. G. (1986). The effect of oxygen on release and uptake of cobalt, manganese, iron and phosphate at the sediment-water interface. *Geochim. Cosmochim. Acta* 50 (6), 1281–1288. doi: 10.1016/0016-7037(86)90411-4

Thomsen, S., Karstensen, J., Kiko, R., Krahmann, G., Dengler, M., and Engel, A. (2019). Remote and local drivers of oxygen and nitrate variability in the shallow oxygen minimum zone off Mauritania in June 2014. *Biogeosciences* 16, 979–998. doi: 10.5194/bg-16-979-2019

Voss, M., Dippner, J. W., and Montoya, J. P. (2001). Nitrogen isotope patterns in the oxygen–deficient waters of the Eastern tropical north pacific ocean. *Deep–Sea Res. I* 48, 1905–1921. doi: 10.1016/S0967-0637(00)00110-2

Wallmann, K., José, Y. S., Hopwood, M. J., Somes, C. J., Dale, A. W., Scholz, F., et al. (2022). Biogeochemical feedbacks may amplify ongoing and future ocean deoxygenation: A case study from the Peruvian oxygen minimum zone. *Biogeochemistry* 159, 45–67. doi: 10.1007/s10533-022-00908-w

Wenzhöfer, F., Lemburg, J., Hofbauer, M., Lehmenhecker, S., and Färber, P. (2016). *TRAMPER – an autonomous crawler for long-term benthic oxygen flux studies in remote deep-sea ecosystems* (Monterey: OCEANS 2016 MTS/IEEE), 1–6.

Zhang, L., Altabet, M. A., Wu, T., and Hadas, O. (2007). Sensitive measurement of NH_4^+ $^{15}N/^{14}N$ (delta $^{15}NH_4^+$) at natural abundance levels in fresh and saltwaters. *Anal. Chem.* 79, 5297–5303. doi: 10.1021/ac070106d

frontiers | Frontiers in Marine Science

TYPE Review
PUBLISHED 27 April 2023
DOI 10.3389/fmars.2023.1122043

OPEN ACCESS

EDITED BY
Amal Jayakumar,
Princeton University, United States

REVIEWED BY
Amit Sarkar,
Kuwait Institute for Scientific Research, Kuwait
Helga Do Rosario Gomes,
Columbia University, United States
Arun Deo Singh,
Banaras Hindu University, India

*CORRESPONDENCE
Zouhair Lachkar
zouhair.lachkar@nyu.edu

RECEIVED 12 December 2022
ACCEPTED 16 March 2023
PUBLISHED 27 April 2023

CITATION
Lachkar Z, Lévy M, Hailegeorgis D and Vallivattathillam P (2023) Differences in recent and future trends in the Arabian Sea oxygen minimum zone: processes and uncertainties.
Front. Mar. Sci. 10:1122043.
doi: 10.3389/fmars.2023.1122043

Differences in recent and future trends in the Arabian Sea oxygen minimum zone: processes and uncertainties

Zouhair Lachkar[1]*, Marina Lévy[2], Derara Hailegeorgis[1] and Parvathi Vallivattathillam[1]

[1]Arabian Center for Climate and Environmental Sciences, New York University Abu Dhabi, Abu Dhabi, United Arab Emirates, [2]Sorbonne Université (CNRS/IRD/MNHN), LOCEAN-IPSL, Paris, France

The Arabian Sea is an exceptionally complex system that hosts a highly productive marine ecosystem. This intense productivity leads to high oxygen consumption at depth that maintains, together with the sluggish circulation, the world's thickest oxygen minimum zone (OMZ). While observations have been scarce in the region, evidence for a recent (1960-2020) decline in oxygen is emerging in the northern Arabian Sea. However, in the longer term (2050 to 2100) the future evolution of the OMZ is more uncertain, as the model projections that have been carried out are not consistent with each other. On the one hand, this reflects the limitations of current generation models that do not adequately represent key physical and biogeochemical processes, resulting in large O_2 biases in the region under present-day conditions. On the other hand, the inherent difficulty of predicting future O_2 conditions in the Arabian Sea is a consequence of the sensitivity of O_2 supply and consumption to local and remote changes that evolve on different timescales. Here we aim to synthesize current knowledge of the Arabian Sea OMZ in relation to important factors controlling its intensity and review its recent change and potential future evolution. In particular, we explore potential causes of the differences in recent and future O_2 trends in the region and identify key challenges to our ability to project future OMZ changes and discuss ideas for the way forward.

KEYWORDS

Arabian Sea oxygen minimum zone, ocean deoxygenation, oxygen trends, ocean ventilation and oxygenation, denitrification

1 Introduction

Ocean currents and mixing supply dissolved oxygen to water masses at depth while organic matter degradation consumes it. In the Arabian Sea, as in other oceanic regions where biological productivity is high and ventilation is weak, the inefficient replenishment of oxygen depleted by intense remineralization results in the presence of a poorly

oxygenated water body at depth, known as oxygen minimum zone (OMZ). While moderate oxygen deficits (hypoxia, usually defined as O_2 lower than 60 mmol m^{-3}) challenge the survival of higher trophic animals such as crustaceans and fishes (Vaquer-Sunyer and Duarte, 2008), near complete O_2 depletion (suboxia, defined here as O_2 lower than 4 mmol m^{-3}) favors denitrification, a type of anaerobic respiration where nitrate is used as an electron acceptor. This not only depletes the inventory of bio-available nitrogen, critical for phytoplankton growth, but also releases N_2O, a potent greenhouse gas (Codispoti et al., 2001; Bange et al., 2005; Gruber, 2008).

The warming of the ocean waters decreases dissolved O_2 solubility, enhances respiration-induced oxygen consumption and strengthens vertical stratification, thus weakening the oxygen replenishment of the ocean interior (Oschlies et al., 2018). These changes together cause the ocean to lose oxygen as it warms up, a process known as ocean deoxygenation (Keeling et al., 2010; Robinson, 2019). The ocean lost 2% of its O_2 between 1960 and 2010 (Ito et al., 2017; Schmidtko et al., 2017). Previous studies attribute most of this oxygen decline to changes in ocean ventilation and to a lesser extent reduced solubility, with biogeochemical processes playing a potentially significant role only in the low-latitude low O_2 regions (Bindoff et al., 2019; Couespel et al., 2019; Oschlies, 2019; Buchanan and Tagliabue, 2021). Deoxygenation is expected to accelerate in the future with the ocean losing about 3-4% of its O_2 inventory by 2100 under the high-emission scenario, with most of this loss concentrated in the upper 1000 m (Long et al., 2019). Even if the emissions were to stop, deoxygenation will continue over centuries in the deep ocean (Long et al., 2019) as the decline of O_2 committed by historical emissions is estimated to be 3 times larger than current O_2 loss (Oschlies, 2021). In the tropical thermocline, ocean deoxygenation has been shown to cause the expansion and shoaling of OMZs (Stramma et al., 2008; Stramma et al., 2010; Breitburg et al., 2018; Bindoff et al., 2019; Zhou et al., 2022). This can lead to a substantial reduction in habitat of sensitive marine organisms, including commercial fish species such as tunas and billfishes (Stramma et al., 2012b). Oxygen decline can also increase the frequency and severity of hypoxic conditions in the ocean, challenging the health of various ecosystems and causing important loss of marine biodiversity and shifts in the food web structure (Rabalais et al., 2002; Laffoley and Baxter, 2019; Hughes et al., 2020). Observational evidence suggests that even slight changes in dissolved oxygen can profoundly alter OMZ plankton community composition (Wishner et al., 2018; Goes et al., 2020).

In the Arabian Sea, observations as well as model simulations point toward a decline in oxygen in the region over the recent decades (Banse et al., 2014; Rixen et al., 2014; Piontkovski and Al-Oufi, 2015; Ito et al., 2017; Schmidtko et al., 2017; Queste et al., 2018; Buchanan and Tagliabue, 2021; Lachkar et al., 2021; Zhang et al., 2022; Hood et al., 2023). Yet, model-based future projections show insignificant future O_2 changes (and even oxygenation in the central and southern sectors) by the end of the century (2080-2100) (Bopp et al., 2013; Kwiatkowski et al., 2020). Thus, recent and future trends in O_2 in the region appear inconsistent for reasons that remain unclear. Here, we explore the important processes controlling the OMZ intensity as well as recent and future trends and discuss factors potentially contributing to this apparent conundrum. We also highlight and discuss the sources of major uncertainties tainting the future projections of the Arabian Sea OMZ. More specifically, in section 2, we overview the main factors controlling O_2 demand and supply in the Arabian Sea, and use a Lagrangian analysis to guide our discussion of the sources and timescales of the ventilation of the OMZ. In section 3, we review the recent changes in the Arabian Sea OMZ as inferred from recent observational and modeling studies. In section 4, we discuss the potential future changes in the Arabian Sea OMZ, while focusing on the key mechanisms controlling these changes as well as their timescales and the uncertainties around their relative importance and interaction. Finally, in section 5, we discuss the differences between recent and future O_2 trends and their potential causes and summarize the key challenges to our ability to predict future Arabian Sea OMZ changes as well as explore ideas for a way forward.

2 The Arabian Sea oxygen minimum zone

The Arabian Sea hosts the world's thickest OMZ thanks to a combination of large remineralization fluxes associated with intense summer and winter blooms together with a sluggish circulation, particularly in the northern and eastern portions of the basin. Suboxia at the Arabian Sea OMZ core favors intense denitrification fluxes representing up to 20-30% of global pelagic nitrogen loss despite occupying less than 2% of the World Ocean area (Dueser et al., 1978; Naqvi et al., 1982; Gupta and Naqvi, 1984; Naqvi, 1987; Bange et al., 2005; Hood et al., 2023). As the intensity of the Arabian Sea OMZ is set by the magnitude of oxygen demand (remineralization) and supply (ventilation) in the region, we next explore the main factors controlling the two terms of this balance (Figure 1).

2.1 Factors controlling O_2 demand in the Arabian Sea OMZ

O_2 consumption in the Arabian Sea OMZ is affected by various factors. Here we review the role of four major mechanisms, namely: (i) the magnitude of seasonal blooms, (ii) the lateral advection of organic matter and nutrients from the productive western Arabian Sea to the central and eastern sectors, (iii) the depth of remineralization and (iv) the intensity of denitrification (Figure 1).

The summer southwesterly winds drive upwelling along the coasts of Oman and Somalia whereas the winter northeasterly winds induce convective mixing in the northern Arabian Sea. Both mechanisms transport nutrients from the deep layers into the well-lit upper ocean, causing two seasonal phytoplankton blooms (Banse and McClain, 1986; Madhupratap et al., 1996; Wiggert et al., 2005; Lévy et al., 2007; Resplandy et al., 2012; Lachkar et al., 2018). Although previous studies suggest that nitrogen is generally the most limiting nutrient of biological

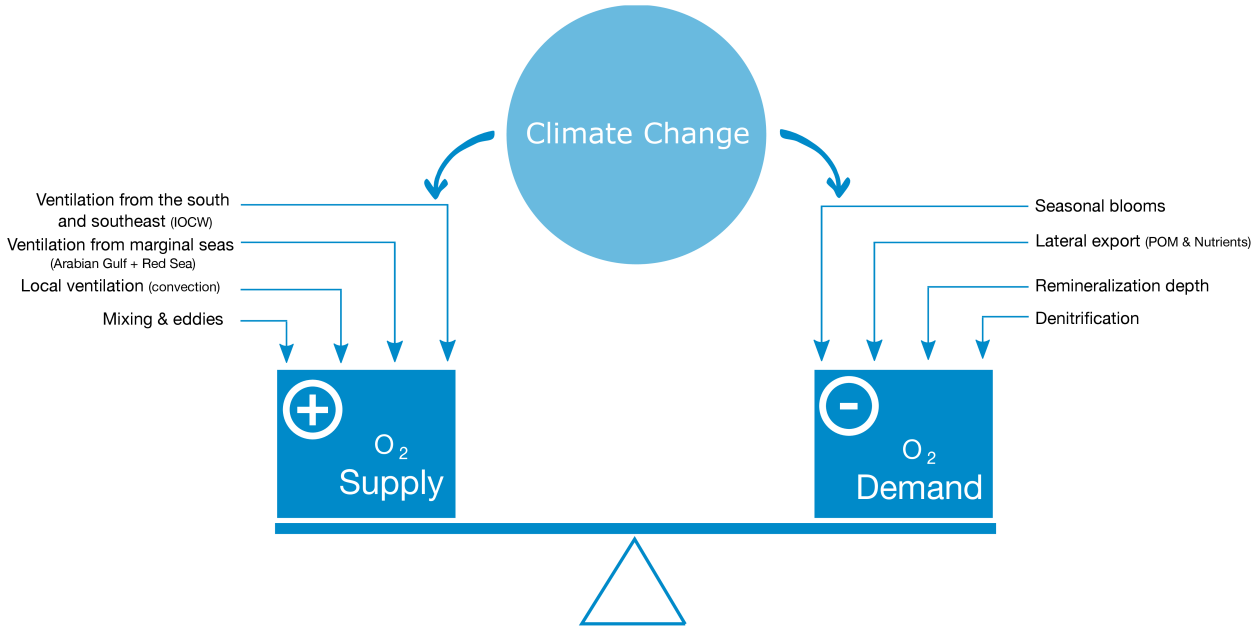

FIGURE 1
Factors controlling the Arabian Sea OMZ intensity. Main factors controlling the O_2 supply (left pan of the balance) and demand (right pan of the balance) under the influence of climate change that may offset the balance, favoring deoxygenation or oxygenation.

productivity in the Arabian Sea, silicate and more importantly iron have also been suggested to limit productivity locally (Naqvi et al., 2002; Wiggert et al., 2006; Moffett et al., 2007; Wiggert and Murtugudde, 2007; Koné et al., 2009; Naqvi et al., 2010; Resplandy et al., 2011; Moffett et al., 2015; Chinni and Singh, 2022). Indeed, previous works indicate that the region off the coasts of Somalia and Oman is prone to iron limitation during both summer and winter monsoon seasons (Wiggert et al., 2006; Wiggert and Murtugudde, 2007; Moffett and Landry, 2020). A recent modeling study by Guieu et al. (2019) suggests that around half of summer primary production in the Arabian Sea is dependent on iron supply through aeolian dust deposition, confirming the critical role that iron may play in limiting biological production in the Arabian Sea. Iron limitation was also suggested to contribute to the weak and delayed response of diatoms to upwelling (Moffett and Landry, 2020). Finally, interannual variability in dust driven iron fluxes was hypothesized to contribute to interannual variability in Arabian Sea productivity (Moffett and Landry, 2020).

The lateral advection of organic matter and unutilized nutrients from the upwelling zone into the central sectors of the Arabian Sea have been shown to affect the intensity of the OMZ there (McCreary et al., 2013; Moffett and Landry, 2020). For instance, McCreary et al. (2013) investigated the role of lateral advection and transport of organic matter in controlling the oxygen distribution in the Arabian Sea. Their modeling work highlights the importance of lateral transport of organic matter from the western Arabian Sea into the central and eastern sectors of the Arabian Sea, where it enhances remineralization and contributes to lowering O_2 levels to below suboxic thresholds. A recent analysis of back-scatter data in the northern Arabian Sea also supports that cross-shelf transport of organic matter is linked to the intensification of the OMZ in the eastern Arabian Sea (Sarma et al., 2020). This transport is likely dominated by eddies. Indeed, mesoscale eddies and submesoscale filaments have been shown to play a critical role in advecting nutrients from the coastal upwelling region into the oligotrophic central Arabian Sea (e.g. Koné et al., 2009; Resplandy et al., 2011).

The depth of remineralization, defined as the depth at which sinking organic matter is decomposed back to inorganic carbon and nutrients (Kwon et al., 2009; Cavan et al., 2017), is an additional factor modulating the Arabian Sea OMZ intensity. For instance, early observational studies showed evidence that the aggregation of organic matter with lithogenic particles from rivers increases the efficiency of the export fluxes in the Bay of Bengal relative to the Arabian Sea (Nair et al., 1989; Ittekkot et al., 1991; Rao et al., 1994). In a modeling study, Al Azhar et al. (2016) have demonstrated that the shallower remineralization depth in the Arabian Sea relative to the Bay of Bengal (driven by relatively slower particle sinking speeds in the former) contributes to enhancing the OMZ there. Indeed, the absence of a major source of ballast minerals similar to the one associated with the large riverine input in the Bay of Bengal decreases the particle sinking speed, thus increasing the organic matter residence time in the OMZ layer, and hence enhancing oxygen consumption there.

Finally, the biological consumption of O_2 is reduced at low-O_2 levels as anaerobic respiration (canonical denitrification and anaerobic ammonium oxidation) is favored over aerobic respiration (Oschlies et al., 2019; Rixen et al., 2020). Thus, increasing denitrification (in case of the expansion of the OMZ suboxic core) can act as a relative source of O_2 that stabilizes the OMZ and limits its intensification (negative feedback) (Lachkar et al., 2016; Lachkar et al., 2019). An additional mechanism through which denitrification acts on O_2 is *via* its impact on nitrogen

inventory. Indeed, denitrification generates deficits in bio-available nitrogen that may not be compensated by N_2 fixation on short timescales (Naqvi, 2008; Oschlies et al., 2019). This can lead to a reduction in biological productivity and respiration, thus limiting O_2 consumption (Altabet et al., 1995). Under such conditions, an eventual expansion of the volume of suboxic waters in the OMZ core can be accompanied by a reduction of the volume of hypoxic waters (Deutsch et al., 2011; Lachkar et al., 2016).

2.2 O_2 supply to the Arabian Sea OMZ: sources and timescales

The ventilation of the Arabian Sea OMZ is sensitive to both basin-scale circulation as well as to local mixing processes (Figure 1). Previous studies point to the Indian Ocean Central Water (IOCW) and the Persian (Arabian) Gulf Water (PGW) as two major sources of ventilation of the OMZ (Wyrtki et al., 1971; Gupta and Naqvi, 1984; Resplandy et al., 2012; McCreary et al., 2013; Acharya and Panigrahi, 2016; Lachkar et al., 2019). IOCW forms through convective mixing as Subantarctic Mode Water in the southern Indian Ocean and is advected northward into the OMZ as a part of the Somali Current. The relatively oxygen-rich PGW subducts in the northern Arabian Sea after its outflow from the Gulf and is exported into the Arabian Sea OMZ (Rixen et al., 2005; Lachkar et al., 2019; Schmidt et al., 2020; Schmidt et al., 2021). Moreover, waters from both the Red Sea and the Indonesian throughflow have been suggested to influence properties of the Arabian Sea thermocline (McCreary et al., 2013; Lachkar et al., 2019). Finally, winter convective mixing in the northern Arabian Sea is a well-known mechanism of local ventilation of the upper OMZ (Resplandy et al., 2012; McCreary et al., 2013).

Here we present the results of a quantitative analysis of the sources and timescales of the Arabian Sea OMZ ventilation based on a Lagrangian particle tracking approach (Supplementary Information). OMZ water particles are traced back to five ventilation source entries: namely the southern entry at 5°S (south), the south-eastern entry at 78° E (southeast), the Bab El Mendeb (Red Sea), the Strait of Hormuz (Arabian Gulf) and the base of the winter mixed layer (local ventilation) (Figure 2). This analysis confirms that the ventilation of the OMZ is dominated by the inflow of IOCW from the south as nearly $\frac{3}{4}$ of OMZ water parcels originate from the southern source (Figure 2A). The analysis of the east-west distribution of particles at the southern entry section (5°S) further indicates that they are mostly associated with waters advected along the western Arabian Sea (west of 42°E) (Figure S1 in Supplementary Information). The remaining sources (southeastern, local ventilation and marginal seas) play a substantially smaller role. However, when considering the upper OMZ only (100-300 m), the contribution of the southwestern source to the OMZ ventilation becomes considerably smaller (45%). Conversely, the contributions of the remaining ventilation sources are twice to three times larger (Figure 2A). The analysis of the depth profiles of the source waters at their original locations as well as when they enter the OMZ reveals that the dominance of the southwestern source is established mostly for the deeper layers of the OMZ (300-1500 m), whereas in the upper layer (100-300m) the contribution of the remaining sources is of comparable magnitude (Figures 2B, C). Furthermore, the analysis of ventilation timescales associated with the different sources reveal that despite its relatively smaller contribution in terms of water volume, the Arabian Gulf has a ventilation timescale (a few months) that is around two orders of magnitude shorter than that associated with the inflow of IOCW from the south (a few decades) (Figure 2D). Thus, despite its modest contribution to the ventilation on decadal timescales, the Arabian Gulf is a more efficient source of ventilation on shorter timescales (months to years). This implies that the Arabian Sea OMZ is likely to respond more rapidly to changes in the Arabian Gulf water properties (e.g., changes in O_2 or water density) than to changes involving the transport of IOCW or its O_2 content (Table 1).

Because of the enhanced ventilation of the western Arabian Sea from the IOCW and the PGW, the Arabian Sea OMZ is more intense in the eastern portion of the basin despite the productivity being highest along the western side (Morrison et al., 1999; Resplandy et al., 2012; McCreary et al., 2013; Rixen et al., 2014; Acharya and Panigrahi, 2016; Zhang et al., 2022). This feature, previously referred to as the eastward shift of the AS OMZ is also presumably aided by eddy-driven lateral transport of organic matter and unutilized nutrients from the western to the central Arabian Sea that contributes to enhancing respiration and lowering O_2 concentrations there below suboxic thresholds (McCreary et al., 2013). Moreover, intense vertical and lateral eddy mixing in the western Arabian Sea (Resplandy et al., 2012; McCreary et al., 2013; Lachkar et al., 2016) play a crucial role in supplying O_2 to the western Arabian Sea.

Finally, isopcynal and diapycnal mixing have been shown to strongly contribute to OMZ ventilation (Gnanadesikan et al., 2012; Lévy et al., 2022). In the Arabian Sea, model simulations suggest that in the absence of oxygen supplied by eddy mixing, the volume of the Arabian Sea OMZ would double (Lachkar et al., 2016). Changes in mixing have also been shown to dominate future projected deoxygenation in global models (Couespel et al., 2019; Lévy et al., 2022).

3 Past changes in the Arabian Sea OMZ

3.1 Past variability in the Arabian Sea OMZ from paleo-records

Paleo-reconstructions suggest important past changes in the intensity of the Arabian Sea OMZ over different periods and on timescales ranging from decades to millennia (Altabet et al., 1995; Altabet et al., 1999; Altabet et al., 2002; Gupta et al., 2003; Singh et al., 2011). For instance, Altabet et al. (1999) suggested that denitrification in the Arabian Sea was greatest during interglacial periods and probably ceased during most glacial phases. Additionally, evidence from paleo-records suggests an intensification of the OMZ core from the mid to late Holocene (Das et al., 2017). Previous studies attributed this to both large-scale ventilation changes as well as increased monsoon intensity and export fluxes (Schulz et al., 1998; Pichevin et al., 2007; Böning and Bard, 2009; Rixen et al., 2014; Das et al., 2017;

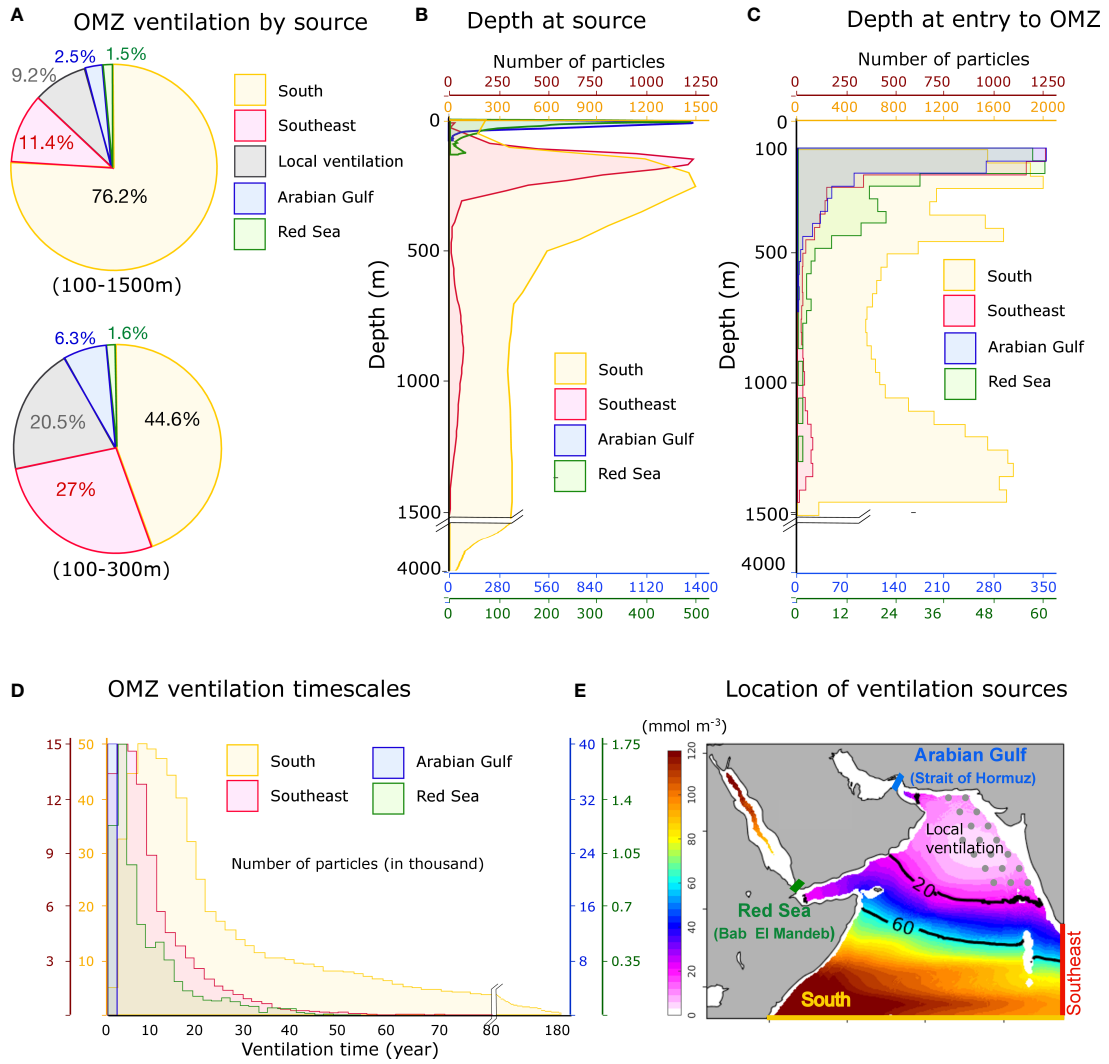

FIGURE 2
Arabian Sea OMZ ventilation sources and timescales. **(A)** Contributions of different source waters to the ventilation of the Arabian Sea OMZ (100-1500 m) and its upper part (100-300 m). The OMZ waters are linked through Lagrangian tracking to five potential sources associated with five sections shown in **(E)**: south (at 5°N), southeast (at 78°E), the Arabian Gulf (Strait of Hormuz), the Red Sea (Bab El Mandeb) and the local ventilation (winter convection). **(B, C)** Particle depth at source **(B)** and at entry to the OMZ **(C)** associated with different remote sources. **(D)** Frequency distribution of OMZ ventilation timescales (in year) associated with different remote sources. Note that given the differences in the number of particles associated with each source, different sources are shown on different vertical axes in **(B–D)**. **(E)** Location of the entry sections where source particles are intercepted. Grey circles indicate the area of local ventilation (where the OMZ core gets in contact with the winter mixed layer). Color shading shows annual mean O_2 (in mmol m^{-3}) averaged between 250 and 700 m.

Gaye et al., 2018; Joshi et al., 2021). On shorter timescales, Altabet et al. (2002) established a strong correspondence between changes in denitrification (and OMZ intensity) in the Arabian Sea and century-scale Dansgaard–Oeschger events during the last glacial period, with denitrification increasing during warm periods concurrently with the summer monsoon and productivity intensification, and decreases during cold phases. Other studies linked past OMZ intensity changes to changes in winter monsoon wind intensity y (Reichart et al., 1998; Reichart et al., 2004; Klöcker and Henrich, 2006). For instance, Reichart et al. (1998) reconstructed the fluctuations of the Arabian Sea OMZ over the past 225,000 years using multiple paleo-proxies and found the lowest O_2 concentrations to correlate with maxima in productivity and weak winter mixing. On the basis of an analysis of sediment samples collected off Pakistan in the northern Arabian Sea, Klöcker and Henrich (2006) attributed the weakening (strengthening) of the OMZ during the stadials (interstadials, Late Holocene) to enhanced (reduced) winter monsoons resulting in an invigorated (weakened) ventilation at intermediate depths. Similarly, Reichart et al. (2004) linked the intensification of the Arabian Sea OMZ during interstadials to enhanced stratification in the northern Arabian Sea during these warm periods leading to reduced winter mixing.

3.2 Recent changes in the Arabian Sea OMZ

More recently, the analysis of historical O_2 observations in the Arabian Sea over the last few decades documents trends dominated by

TABLE 1 Potential perturbations affecting O_2 in the Arabian Sea region under future climate.

Perturbation source	Perturbation mechanism	Likely mpact on O_2	Affected region	Response timescale	Location of forcing	Confidence level	References
O_2 consumption (biology)	N supply to surface (upwelling/mixing)	+	NAS, SAS	Short	Local	Low	B13, L18, K20, Lo19
	Dust deposition	?	NAS, SAS	Short	Local	Low	G19, ML20, I16
	Denitrification	?	NAS	Short	Local	Low	L16, L18, O19
	Terrestrial N input	–	NAS	Short	Local	Low	N00, G21,
	Community composition	?	NAS, SAS	Short	Local	Low	H21
O_2 supply (ventilation)	Solubility	–	NAS, SAS	Short	Local	High	B13, Lo19 K20
	Winter convection	–	NAS	Short	Local	High	L21, K20
	O_2 supply (AG)	–	NAS	Short	Local	High	M13, L19 YN19, L21
	O_2 supply (South)	+	SAS	Intermediate/ Long	Remote	Medium	B17, Lo19
	O_2 supply (East)	+	SAS	Intermediate/ Long	Remote	Medium	B17, Lo19 S21
Local O_2 gradients	Mixing	?	NAS, SAS	Short	Local	High	B19, L22
	Remineralization	?	NAS, SAS	Short	Local	High	A17

The mechanisms, timescales and uncertainties around potential future O_2 changes in the Arabian Sea region. NAS and SAS refer to the northern (north of 15°N) and southern (south of 15°N) Arabian Sea, respectively. Perturbations expected to more likely increase (decrease) O2 are labelled with + (-) symbols. Poorly known processes or perturbations with unclear net effect on O2 are indicated with '?' symbol. Abbreviations used in the References column are defined as follows: B13: Bopp et al. (2013), L18: Lachkar et al. (2018), K20: Kwiatkowski et al. (2020), Lo19: Long et al. (2019)), G19: Guieu et al. (2019), G21: Gupta et al. (2021), ML20: Moffett and Landry (2020), I16: Ito et al. (2016), H21: Henson et al. (2021), L16: Lachkar et al. (2016), O19: Oschlies et al. (2019), L21: Lachkar et al. (2021), M13: McCreary et al. (2013), L19: Lachkar et al. (2019), L21: Lachkar et al. (2021), N00: Naqvi et al. (2000), B17: Bopp et al. (2017), S21: Schmidt et al. (2021), L22: Lévy et al. (2022), A17: Al Azhar et al. (2016), YN19: Al-Yamani and Naqvi (2019).

a decline in most of its northern sector and inconsistent changes in the central and southern parts (Rixen et al., 2020) (Figure 3). For example, the analysis of global historical oxygen observations by Schmidtko et al. (2017) reveals a moderate O_2 decline in the subsurface of the Arabian Sea between 1960 and 2010. Similarly, O_2 trend analysis by (Schmidtko et al., 2017) indicates a drop in oxygen in the northern and western Arabian Sea as well as along the west coast of India over the same period. Using over 2000 O_2 profiles collected between 1960 and 2008 off the coast of Oman, Piontkovski and Al-Oufi (2015) reported a decline in O_2 in the upper 300 m in the northern and northwestern Arabian Sea, attributed to increased thermal stratification and a shoaling of the oxycline between the 1960s and 2000s. In an analysis of sea glider data and historical profiles, Queste et al. (2018) also reported an intensification of the suboxic conditions at depth in the Sea of Oman over the recent decades. Banse et al. (2014) analyzed historical O_2 measurements collected in the Arabian Sea in the 150-500 m layer between 1959 and 2004. They found no clear systematic trend across the entire basin, although O_2 was found to decline in most of the central Arabian Sea and slightly increase in the northeastern Arabian Sea and in the southern Arabian Sea (Figure 3). Nitrite (NO_2^-) is an intermediate product formed during nitrification and denitrification. Due to the lack of oxygen required for nitrification in the upper part of the Arabian Sea OMZ, the accumulation of nitrite known as the secondary nitrite maximum (SNM) is assumed to be caused primarily by denitrification (Gupta et al., 1976; Naqvi, 1991). Banse et al. (2014) also analyzed historical trends in nitrite (NO_2^-) concentrations in the subsurface. They found inconsistent trends in different locations with a dominance of profiles indicating an increase in nitrite over time, suggesting a potential intensification of denitrification over the observation period. Similarly, Rixen et al. (2014) analyzed trends in nitrite in the Arabian Sea from the Joint Global Ocean Flux Study (JGOFS) measurements in 1995 and from published data prior to 1993. They found an expansion of the SNM in 1995 relative to the pre-JGOFS data with an increase in western and southern sectors, indicating a potential increase in denitrification. However, these changes could also be linked to interannual variability characterizing denitrification in the region (Lachkar et al., 2021), rather than reflecting long-term trends (Naqvi, 2019). A recent analysis of historical observations by Zhou et al. (2022) has revealed an expansion of the area occupied by all major OMZs, including the Arabian Sea OMZ, over the last 3 to 4 decades. Goes et al. (2020) reported evidence of increased winter stratification (and reduced winter convection) in the northern Arabian Sea, together with a decrease in the N:P ratios, indicative of an increase in denitrification over the recent decades. These changes were suggested to create a niche favorable for the mixotroph Noctiluca scintillans in the northern Arabian Sea (do Rosário Gomes et al., 2014; Goes et al., 2020). Finally, preliminary observations suggest recent O_2 decline in the Arabian marginal seas (i.e., the Red Sea and the Gulf) with the emergence of summertime hypoxia in the Gulf (Al-Ansari et al., 2015; Al-Yamani and Naqvi, 2019; Saleh et al., 2021; Lachkar et al., 2022) and ongoing deoxygenation in the northern Red Sea (Naqvi, 2019).

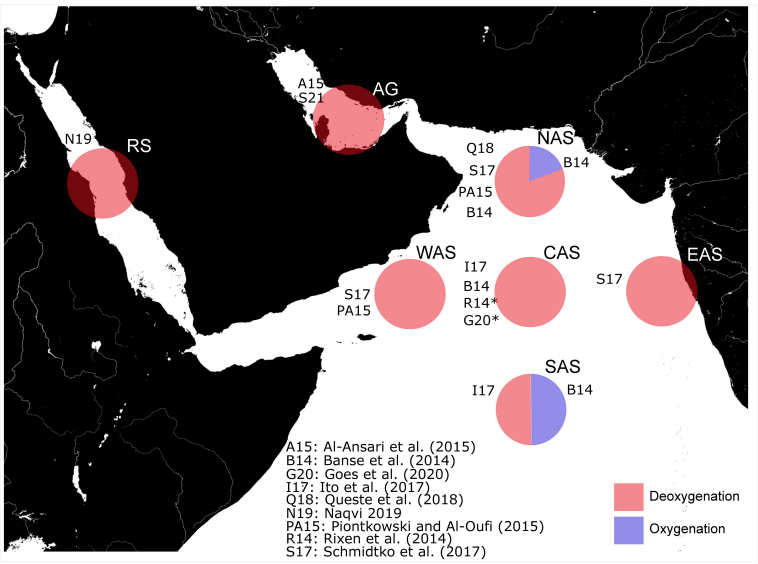

FIGURE 3
Observational studies reporting recent O_2 changes in the Arabian Sea. Observational studies documenting recent O_2 trends in the northern (NAS), central (CAS), southern (SAS), eastern (EAS) and western (WAS) Arabian Sea, as well as in the Arabian Gulf (AG) and Red Sea (RS). In each subregion, the proportion of studies suggesting deoxygenation (red) vs. oxygenation (blue) is indicated with a pie chart. Deoxygenation trends in studies labeled with (*) are inferred from relevant proxy data and are not based on direct measurements of oxygen.

Recent modelling works have reproduced declining O_2 trends in the Arabian Sea region and investigated their potential drivers. For instance, historical deoxygenation trends were simulated in the mesopelagic zone (200-1000 m) in the northern and northwestern Arabian Sea in a global hindcast simulation covering the period between 1958 and 2014 (Buchanan and Tagliabue, 2021). The study further suggests that this O_2 loss is driven by changes in apparent oxygen utilization (AOU), likely associated with ventilation changes. These conclusions were also supported by the analysis of O_2 trends in the Arabian Sea region over the period from 1975 and 2014 using the latest Coupled Model Intercomparison Project (CMIP6) model simulations (Buchanan and Tagliabue, 2021). Finally, a strong deoxygenation in the northern Arabian Sea in the 100-1000 m subsurface layer was reported in a recent regional modeling study of the Indian Ocean covering the period from 1982 to 2010 (Lachkar et al., 2021). Causing an important intensification of the OMZ core and a significant increase in denitrification there, this O_2 loss was attributed to increased stratification and reduced ventilation as a result of the recent fast warming in the northern Arabian Sea and the Gulf (Lachkar et al., 2021).

4 Future changes in the Arabian Sea OMZ

4.1 Mechanisms and timescales

The Arabian Sea OMZ is vulnerable to various potential future changes affecting O_2 demand and supply terms (Table 1 and Figure 4). More specifically, increases in stratification are expected to lead to a significant reduction in productivity and export under future climate change (Bopp et al., 2013; Long et al., 2019; Kwiatkowski et al., 2020). While a few previous works suggested a potential future intensification of summer upwelling-favorable winds in the northern Arabian Sea (Sandeep and Ajayamohan, 2015; deCastro et al., 2016; Praveen et al., 2016), other studies indicate a future weakening of winter monsoon winds that could cause a reduction in convective mixing in the northern Arabian Sea and decrease productivity there (Vallivattathillam et al., 2017). Additionally, a weakening of the summer Walker circulation was also suggested to lead to summer productivity decline in the southern Arabian Sea (e.g., Vallivattathillam et al., submitted). Lachkar et al. (2018) highlighted that changes in OMZ intensity associated with productivity changes can develop over relatively short timescales (Table 1). Although both CMIP5 and CMIP6 multi-model averages point to a future reduction in productivity in the region, individual models show important discrepancies and project changes that go in both directions (Bopp et al., 2013; Kwiatkowski et al., 2020). Additionally, these models generally do not take into account potential changes in dust deposition or effects of changes in denitrification on productivity. For instance, Guieu et al. (2019) have shown that almost half of the Arabian Sea productivity is dependent on iron supply *via* dust deposition. Thus, changes in this source of iron due to wind changes for instance can have a dramatic impact on productivity and OMZ (Moffett and Landry, 2020). Lachkar et al., (2016) demonstrated that a weakening of denitrification can lead to a significant increase in productivity and export, with implications for the OMZ volume.

Additional mechanisms can affect the O_2 demand in the Arabian Sea region such as the increase in nutrient loading associated with major river runoff and changes in the plankton community composition (Table 1). Early studies (e.g., Naqvi et al., 2000) suggested that eutrophication associated with increased nutrient loading resulting from agricultural and urban coastal

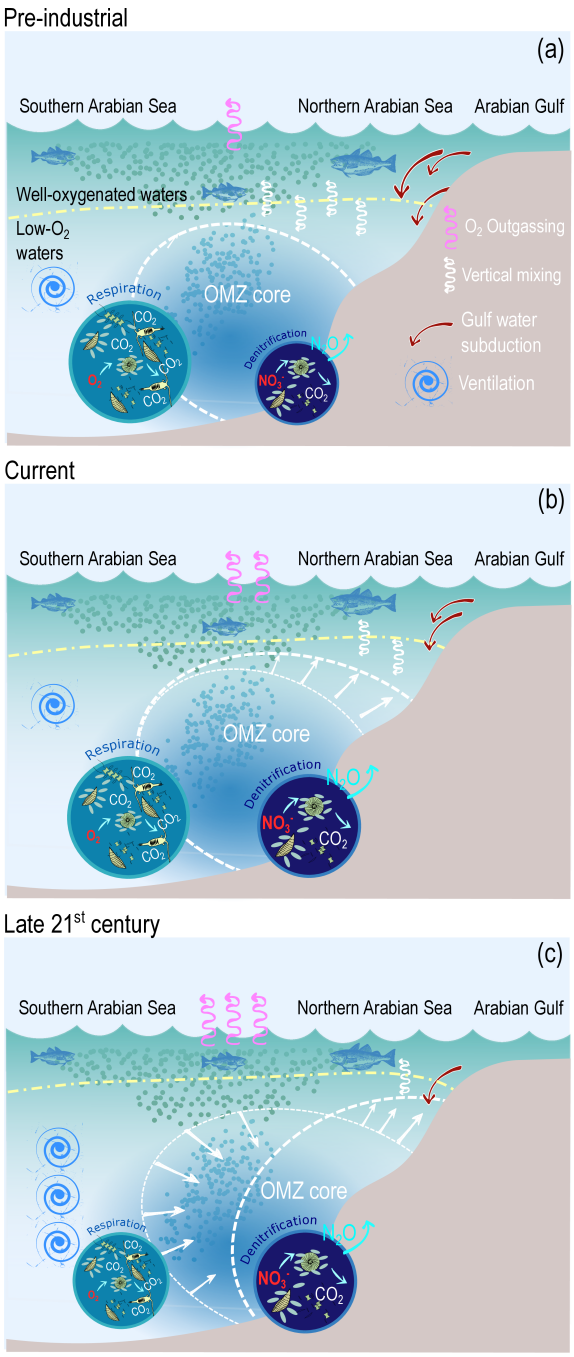

FIGURE 4
Summary of recent and potential future changes in Arabian Sea OMZ. This schematic summarizes the recent and main potential future changes in the Arabian Sea OMZ as well as their drivers and implications. **(A)** Pre-industrial conditions: cool conditions favor strong O_2 solubility in the seawater and weak outgassing. Well-oxygenated waters (O_2 > 100 mmol m^{-3}) occupy a thick upper layer overlaying the OMZ. Strong winter convection and subduction of Gulf waters in the north ventilate the upper OMZ, thus maintaining its denitrifying suboxic core contained at depth. **(B)** Present-day conditions: weaker O_2 solubility in the seawater causes moderate outgassing. A weaker winter convection and subduction of Gulf waters in the north cause an expansion of the upper OMZ and an increase of denitrification. **(C)** Future conditions: warmer conditions further lower O_2 solubility in the water and enhance outgassing. Moreover, enhanced stratification limits the vertical penetration of well-oxygenated waters, contained in a thinner layer (compressing potential habitat). Reduction in winter convection and Gulf water subduction causes a weakening of the ventilation of the upper OMZ in the northern Arabian Sea and a shoaling of the OMZ core, potentially leading to enhanced denitrification there. However, in the central and southern Arabian Sea, enhanced ventilation as well as reduced productivity and respiration lead to important oxygenation at depth, causing a substantial shrinking of the OMZ core.

pollution may have contributed to reported intensification of the hypoxic zone along the western continental shelf of India during summer and autumn. Nevertheless, more recent work by Gupta et al. (2021) tends to imply that the anoxic zone along the west coast of India is essentially formed through the upwelling of deoxygenated waters during the summer season and is little affected by riverine input of nutrients or sewage discharge from Indian megacities. These authors argue that acute oxygen deficiency was reported in areas where no major rivers exist, and far from the major cities on the west coast of India. They also noted that hypoxia intensity has remained relatively stable in the region despite a substantial increase in anthropogenic nutrient input over the last five decades (Gupta et al., 2016; Gupta et al., 2021). Finally, changes in the size and composition of phytoplankton dominant groups can affect the efficiency of particle export and hence alter the remineralization depth and the intensity of the OMZ. For instance, the reported recent shift in the composition of winter phytoplankton blooms in the northern Arabian Sea from diatoms to Noctiluca scintillans can have repercussions on the export fluxes, as these mixotrophs are essentially grazed on by salps, which typically produce large and rapidly sinking fecal pellets (do Rosário Gomes et al., 2014). Yet, predicting future changes in plankton community structure is challenging because of the complexity and the uncertainty around the mechanisms controlling the diversity within the plankton functional groups (Henson et al., 2021). Nevertheless, recent model projections suggest a future increase in the dominance of smaller phytoplankton groups, which could imply a reduced export efficiency and hence a shallower remineralization depth under warmer climate (Henson et al., 2021).

Potential future changes in the O_2 supply terms entail changes in solubility or ventilation terms. Surface warming is expected to increase outgassing, causing a loss of O_2 that is particularly important near the surface (Figure 4). In the ocean interior, changes in the intensity of ventilation can lead to changes in the OMZ intensity. For instance, an increase in winter stratification is predicted to inhibit convection and hence limit winter ventilation of the upper OMZ in the northern Arabian Sea (Figure 4). This mechanism has been suggested to contribute to recent OMZ intensification in the region (Goes et al., 2020; Lachkar et al., 2021). Furthermore, the warming of the Arabian Gulf is predicted to lead to a reduction in the subduction of the Gulf water in the northern Arabian Sea (Lachkar et al., 2019; Lachkar et al., 2021). Additionally, declining levels of O_2 in the Gulf waters (Saleh et al., 2021; Lachkar et al., 2022) and potentially increasing semi-labile total organic carbon (TOC) in the Gulf may further contribute to lowering O_2 in the upper layers of the OMZ in the northern Arabian Sea (Al-Yamani and Naqvi, 2019).

In the central and southern Arabian Sea, as well as in the deeper layers of the northern Arabian Sea, water ventilation is mostly associated with the inflow of the IOCW from the south along the western Arabian Sea (Figure 2; Schmidt et al., 2020; Schmidt et al., 2021). Thus, an increase in the O_2 content of these water masses is expected to lead to a weakening of the OMZ, particularly in the southern Arabian Sea (Vallivattathillam et al., in review) (Table 1 and Figure 4). The enhanced O_2 content of the equatorial Indian Ocean thermocline is relatively robust in most CMIP5 and CMIP6 models (Bopp et al., 2013; Kwiatkowski et al., 2020) and is likely associated with an increase in the ventilation of the tropical thermocline (Bopp et al., 2017; Oschlies et al., 2017; Oschlies et al., 2018) aided with a decrease in O_2 biological consumption.

Finally, changes that affect O_2 gradients without changing the regional O_2 inventory can also lead to changes in the volume and intensity of the Arabian Sea OMZ. For instance, a change in mixing driven by changes in eddy activity (e.g., Beech et al., 2022) in the region could alter the intensity of the OMZ (Lachkar et al., 2016; Lévy et al., 2022). Furthermore, changes in the remineralization depth associated with changes in the particle sinking speed or remineralization rate (for instance due to warming or changes in the community composition) can also affect the depth and intensity of the Arabian Sea OMZ as has been demonstrated by previous studies (e.g., Al Azhar et al., 2016) (Table 1).

4.2 Emergence of climate change driven O_2 changes and uncertainties around future trends

The northern sector of the Arabian Sea is among the few rare oceanic regions where forced O_2 trends emerge from noise already in the present-day (2005-2014) (Rodgers et al., 2015). This is particularly true for the upper layers (200-300 m) of the northern Arabian Sea where forced negative O_2 trends, associated with an increase in water age, can already be detected (Long et al., 2016). The time of emergence of the climate change driven signal varies spatially and for different depth layers and occurs later in the central Arabian Sea (Long et al., 2016; Gong et al., 2021). Furthermore, as hypoxic and suboxic water volumes display stronger interannual variability than O_2 concentrations (Deutsch et al., 2011), the forced climate change signal is likely to emerge later for the OMZ volume and intensity.

Global model future projections suggest that while the northern Arabian Sea is likely to undergo significant deoxygenation, the central and southern parts will be affected by a weak oxygenation signal that has low detectability due to strong natural variability (Bopp et al., 2017). The deoxygenation in the northern Arabian Sea appears to be driven by an increase in AOU, induced by an important increase in the water age (Long et al., 2019). In contrast, a decrease in water age is expected in the southern Arabian Sea (as in most of the equatorial Indian Ocean). This factor, together with reduced export, is predicted to lead to an increase in O_2 levels (Long et al., 2019) (Figure 4).

Nevertheless, these projections come with important uncertainties stemming from global models' persistent misrepresentation of oxygen in the tropics in general (Oschlies, 2019), and in the Arabian Sea in particular (Schmidt et al., 2021). For instance, observations suggest a decline of O_2 in the tropics over the last 50 years, whereas global models simulate non-significant (or even positive) oxygen trends (Stramma et al., 2012a; Oschlies et al., 2017). In addition to poorly constrained biogeochemical processes, different hypotheses were proposed to explain this mismatch such as excessive diapycnal mixing, ill-represented equatorial jets and natural variability in winds not properly represented in models

(Stramma et al., 2012a; Oschlies et al., 2017). In the Arabian Sea, the inaccurate representation of the OMZ in global models was linked to several factors, including an imprecise representation of marginal seas (the Arabian Gulf and the Red Sea) and an overestimation of O_2 in the IOCW source regions in the Southern Ocean (Schmidt et al., 2021). Despite an improvement in resolution and biogeochemical complexity, the biases reported in CMIP5 models are also present in CMIP6 models with the exception of two models that show significant improvement (Séférian et al., 2020). Furthermore, the projected O_2 trends in the Arabian Sea show a strong sensitivity to the employed lateral mixing coefficient with low mixing models showing a strong O_2 decline and strong mixing models displaying weak O_2 trends (Bahl et al., 2019).

5 Summary and discussion

Dissolved oxygen is important for marine life and for structuring ecosystems and biogeochemistry. Climate change driven ocean warming leads to global deoxygenation through various mechanisms (i.e., reduced solubility, reduced ventilation, enhanced respiration). This has been consistently reproduced by models and is consistent with recent observations. Global deoxygenation will continue and amplify in the future in response to projected additional ocean warming. It is well established that declining dissolved O_2 levels detrimentally affect marine life, alter microbial processes and biogeochemical cycling of key nutrients, potentially enhancing greenhouse gas emissions, thus affecting the Earth's climate. However, deoxygenation effects on ecosystems and biogeochemistry strongly depend on crossing critical thresholds, and hence are a function of the local O_2 levels, and more generally the local chemical (pH, pCO_2, macro- and micro-nutrients) and physical (e.g., temperature) environment. Therefore, although driven by global warming, deoxygenation is most relevant at the local and regional scales, where its ecological, biogeochemical and climatic impacts are most prominent.

Future deoxygenation is robust across Earth system models in the surface and the deep oceans as well as in the thermocline of the mid and high latitudes (Bopp et al., 2017). Yet, there is no clear theoretical basis for projecting future deoxygenation in the tropical thermocline. Indeed, models show inconsistent trends in the tropics where OMZs are located as the thermal (solubility) and non-thermal (ventilation and respiration) effects oppose each other (Bopp et al., 2017; Long et al., 2019). Although O_2 solubility is expected to decrease in response to future climate warming, models project a concomitant decrease in the AOU, mostly driven by a stronger ventilation at thermocline depth (Bopp et al., 2017), attributed to various mechanisms such as a shoaling and thinning of thermocline (Deutsch et al., 2011; Bopp et al., 2017), changes in equatorial undercurrents, and changes in relative contributions of surface and deep waters (Stramma et al., 2012a; Bopp et al., 2017). Projected future reduction in productivity may contribute to reduce oxygen utilization in the tropics. However, quantifying the role of respiration in future oxygen trends remains elusive due to the poor representation of biogeochemical processes in models (Oschlies et al., 2018). This is not only because the complexity of microbial respiration is often overly simplified in models (Laufkötter et al., 2017; Robinson, 2019), but also as key biogeochemical feedbacks involving iron, N_2 fixation and denitrification (that can either accelerate O_2 decline or oppose it) are still neither well understood nor properly represented in current generation models (Ulloa et al., 2012; Oschlies et al., 2019; Moffett and Landry, 2020; Wallmann et al., 2022). In the Arabian Sea, our ability to predict future changes is further hindered by additional uncertainties emanating from the poorly known and quantified role of marginal seas, as well as the uncertainty around the potential future changes in the Indian monsoon winds, and poorly understood regional processes such as the role of dust deposition, iron limitation or benthic processes.

The future (2050-2100) oxygenation projected by global models (Bopp et al., 2013; Long et al., 2019; Kwiatkowski et al., 2020) in the central and southern Arabian Sea contrasts with the observed recent (1960-2020) oxygen decline in the region (Zhou et al., 2022). We hypothesize that this apparent inconsistency is a consequence of the differences in timescales associated with local and remote perturbations driving recent and future O_2 changes and their relative importance (Table 1). On the one hand, the reduction of upper OMZ ventilation associated with the impacts of local warming in the northern Arabian Sea (i.e., reduced winter convective mixing and weakened Gulf water subduction) involves shorter timescales than those associated with the slower ventilation of the deeper layers *via* the IOCW. On the other hand, the limited changes in biological productivity over the recent decades in the Arabian Sea in particular and the Indian Ocean in general contrast with the more significant decline projected by the end of the century (Roxy et al., 2016; Kwiatkowski et al., 2020). Thus, in the longer term, O_2 increase in the equatorial thermocline or in the IOCW source waters in the Southern Ocean, combined with a more significant decline in O_2 demand can act to reverse recent deoxygenation trends in the region.

The strong natural variability in O_2 time series challenges the detection and attribution of observed trends to climate change (Bindoff et al., 2019). Furthermore, it remains unclear how low O_2 waters will be impacted by deoxygenation, nor how the Arabian Sea ecosystem may respond to O_2 changes. For instance, (Bahl et al., 2019) found an expansion of hypoxia in simulations showing the weakest global deoxygenation (low mixing models) and a contraction of the OMZ volume in simulations projecting the strongest global deoxygenation (high-mixing models). This is because O_2 depends on a subtle balance between supply and consumption processes, both depending on local and global climate change, making it difficult to predict in which direction this balance may shift (Fu et al., 2018; Resplandy, 2018; Lévy et al., 2022). Therefore, studies addressing future deoxygenation need to go beyond assessing changes in O_2 inventories and consider changes in O_2 distributions. Moreover, suitable observational strategies ensuring an adequate sampling of the Arabian Sea are needed in order to enhance our ability to detect long-term O_2 changes in the region and help with their attribution to the climate perturbation.

Finally, the representation of key physical and biogeochemical processes in models need to be improved in order to reduce inconsistencies among projected future O_2 changes in the region. In

this regard, regional downscaling of global model simulations can help reduce uncertainties associated with model misrepresentation of present-day condition (Figure 5). For instance, Vallivattathillam et al. (in review) have shown that downscaling CMIP5 simulations using a pseudo global warming approach (Xu et al., 2019) that corrects for systematic biases in the representation of physical circulation and biogeochemistry under current climate reduces inter-model discrepancies in future projections and yields more robust O_2 trends in the Arabian Sea region under future climate change. More generally, improved representation of key processes in models through refined parameterizations and increased resolution, jointly with enhanced coverage of oxygen observations in space and time, is vital to detect ongoing oxygen changes in the Arabian Sea region and predict the future of its OMZ.

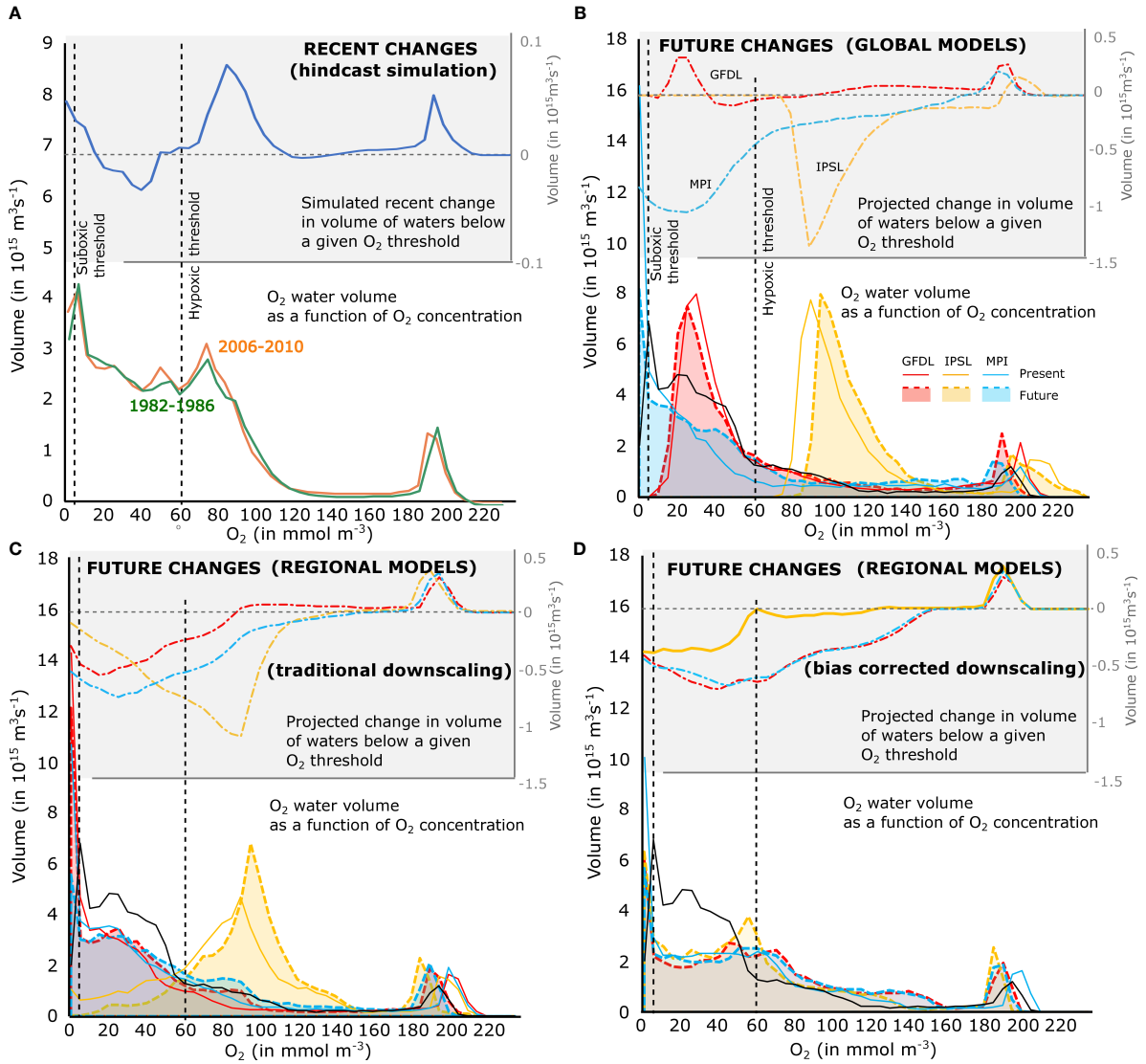

FIGURE 5
Recent and future changes in O_2 frequency distribution in the Arabian Sea. **(A)** O_2 frequency distribution in the Arabian Sea as simulated in the early 1980s (green) and the late 2000s (orange) as well as the cumulative frequency of simulated O_2 change over the 1982-2010 period (blue, right axis) from (Lachkar et al., 2021). Note the expansion of poorly oxygenated waters (O_2 < 100 mmol m^{-3}) as well as waters with extreme O_2 depletion (O_2 < 10 mmol m^{-3}). **(B–D)** O_2 frequency distribution in the Arabian Sea in the present-day (solid line) and in the future (dashed filled area) as well as cumulative frequency of future O_2 change (dash-dotted line, right axis) as simulated by **(B)** three global models (MPI, GFDL and IPSL) and a regional model (ROMS) forced with the three global models using traditional **(C)** and bias-corrected **(D)** downscaling approaches. Traditional downscaling consists in forcing the regional model with boundary conditions simulated by the global model, whereas bias-corrected downscaling (also known as pseudo global warming) consists in constructing regional model lateral boundary conditions by adding global model projected changes onto observational data. **(B–D)** Note the reduction in model discrepancies in future O_2 projections in the downscaled experiments, particularly when using the bias-correction approach, relative to the global simulations. Adapted from Vallivattathillam et al. (in review).

Author contributions

ZL conceived the review and wrote the manuscript with contributions from all authors. DH performed the Lagrangian analysis. All authors contributed to the article and approved the submitted version.

Acknowledgments

Support for this research has come from the Arabian Center for Climate and Environmental Sciences (ACCESS), through the New York University Abu Dhabi (NYUAD) Research Institute Grant CG009. Computations were performed at the High Performance cluster (HPC) of NYUAD, Dalma. We thank the NYUAD HPC team for technical support. The authors are also grateful to the editor Amal Jayakumar and to reviewers: Amit Sarkar, Helga Do Rosario Gomes, and Arun Deo Singh, for their constructive comments that helped improve the paper. The model code can be accessed online at http://www.crocoocean.org/.

Conflict of interest

The authors declare that the research was conducted in the absence of any commercial or financial relationships that could be construed as a potential conflict of interest.

Publisher's note

Supplementary material

The Supplementary Material for this article can be found online at: https://www.frontiersin.org/articles/10.3389/fmars.2023.1122043/full#supplementary-material

References

Acharya, S. S., and Panigrahi, M. K. (2016). Eastward Shift and maintenance of Arabian Sea oxygen minimum zone: Understanding the paradox. *Deep Sea Res. Part I: Oceanogr. Res. Papers* 115, 240–252.

Al-Ansari, E. M., Rowe, G., Abdel-Moati, M., Yigiterhan, O., Al-Maslamani, I., Al-Yafei, M., et al. (2015). Hypoxia in the central Arabian Gulf Exclusive Economic Zone (EEZ) of Qatar during summer season. *Estuarine Coast. Shelf Sci.* 159, 60–68. doi: 10.1016/j.ecss.2015.03.022

Al Azhar, M., Temimi, M., Zhao, J., and Ghedira, H. (2016). Modeling of circulation in the a rabian g ulf and the s ea of o man: Skill assessment and seasonal thermohaline structure. *J. Geophys. Res.: Oceans* 121, 1700–.

Altabet, M. A., Francois, R., Murray, D. W., and Prell, W. L. (1995). Climate-related variations in denitrification in the Arabian Sea from sediment 15N/14N ratios. *Nature* 373, 506–509. doi: 10.1038/373506a0

Altabet, M. A., Higginson, M. J., and Murray, D. W. (2002). The effect of millennial-scale changes in Arabian Sea denitrification on atmospheric CO_2. *Nature* 415, 159–162. doi: 10.1038/415159a

Altabet, M. A., Murray, D. W., and Prell, W. L. (1999). Climatically linked oscillations in Arabian Sea denitrification over the past 1 my: Implications for the marine n cycle. *Paleoceanography* 14, 732–743. doi: 10.1029/1999PA900035

Al-Yamani, F., and Naqvi, S. (2019). Chemical oceanography of the Arabian Gulf. *Deep Sea Res. Part II: Topical Stud. Oceanogr.* 161, 72–80.

Bahl, A., Gnanadesikan, A., and Pradal, M.-A. (2019). Variations in ocean deoxygenation across earth system models: isolating the role of parameterized lateral mixing. *Global Biogeochemical Cycles* 33, 703–724. doi: 10.1029/2018GB006121

Bange, H. W., Naqvi, S. W. A., and Codispoti, L. (2005). The nitrogen cycle in the Arabian Sea. *Prog. Oceanogr.* 65, 145–158. doi: 10.1016/j.pocean.2005.03.002

Banse, K., and McClain, C. R. (1986). Winter blooms of phytoplankton in the Arabian Sea as observed by the coastal zone color scanner. *Mar. Ecol. Prog. Ser.* 34, 201–211. doi: 10.3354/meps034201

Banse, K., Naqvi, S., Narvekar, P., Postel, J., and Jayakumar, D. (2014). Oxygen minimum zone of the open Arabian Sea: variability of oxygen and nitrite from daily to decadal timescales. *Biogeosciences* 11, 2237–2261. doi: 10.5194/bg-11-2237-2014

Beech, N., Rackow, T., Semmler, T., Danilov, S., Wang, Q., and Jung, T. (2022). Long-term evolution of ocean eddy activity in a warming world. *Nat. Climate Change* 12, 1–8. doi: 10.1038/s41558-022-01478-3

Bindoff, N. L., Cheung, W. W., Kairo, J. G., Arístegui, J., Guinder, V. A., Hallberg, R., et al. (2019). "Changing ocean, marine ecosystems, and dependent communities," in *IPCC special report on the ocean and cryosphere in a changing climate* (Cambridge, UK and New York, NY, USA: Cambridge University Press), 477–587.

Böning, P., and Bard, E. (2009). Millennial/centennial-scale thermocline ventilation changes in the Indian Ocean as reflected by aragonite preservation and geochemical variations in Arabian Sea sediments. *Geochimica Cosmochimica Acta* 73, 6771–6788. doi: 10.1016/j.gca.2009.08.028

Bopp, L., Resplandy, L., Orr, J. C., Doney, S. C., Dunne, J. P., Gehlen, M., et al. (2013). Multiple stressors of ocean ecosystems in the 21st century: projections with CMIP5 models. *Biogeosciences* 10, 6225–6245. doi: 10.5194/bg-10-6225-2013

Bopp, L., Resplandy, L., Untersee, A., Le Mezo, P., and Kageyama, M. (2017). Ocean (de) oxygenation from the last glacial maximum to the twenty-first century: insights from earth system models. *Philos. Trans. R. Soc. A: Mathematical Phys. Eng. Sci.* 375, 20160323.

Breitburg, D., Levin, L. A., Oschlies, A., Grégoire, M., Chavez, F. P., Conley, D. J., et al. (2018). Declining oxygen in the global ocean and coastal waters. *Science* 359. doi: 10.1126/science.aam7240

Buchanan, P. J., and Tagliabue, A. (2021). The regional importance of oxygen demand and supply for historical ocean oxygen trends. *Geophys. Res. Lett.* 48, e2021GL094797. doi: 10.1029/2021GL094797

Cavan, E. L., Trimmer, M., Shelley, F., and Sanders, R. (2017). Remineralization of particulate organic carbon in an ocean oxygen minimum zone. *Nat. Commun.* 8, 14847. doi: 10.1038/ncomms14847

Chinni, V., and Singh, S. K. (2022). Dissolved iron cycling in the Arabian Sea and sub-tropical gyre region of the Indian Ocean. *Geochimica Cosmochimica Acta* 317, 325–348. doi: 10.1016/j.gca.2021.10.026

Codispoti, L., Brandes, J. A., Christensen, J., Devol, A., Naqvi, S., Paerl, H. W., et al. (2001). The oceanic fixed nitrogen and nitrous oxide budgets: Moving targets as we enter the anthropocene? *Scientia Marina* 65, 85–105. doi: 10.3989/scimar.2001.65s285

Couespel, D., Lévy, M., and Bopp, L. (2019). Major contribution of reduced upper ocean oxygen mixing to global ocean deoxygenation in an earth system model. *Geophys. Res. Lett.* 46, 12239–12249. doi: 10.1029/2019GL084162

Das, M., Singh, R. K., Gupta, A. K., and Bhaumik, A. K. (2017). Holocene Strengthening of the oxygen minimum zone in the northwestern Arabian Sea linked to changes in intermediate water circulation or indian monsoon intensity? *Palaeogeogr. Palaeoclimatol. Palaeoecol.* 483, 125–135. doi: 10.1016/j.palaeo.2016.10.035

deCastro, M., Sousa, M., Santos, F., Dias, J., and Gómez-Gesteira, M. (2016). How will somali coastal upwelling evolve under future warming scenarios? *Sci. Rep.* 6, 1–9.

Deutsch, C., Brix, H., Ito, T., Frenzel, H., and Thompson, L. (2011). Climate-forced variability of ocean hypoxia. *science* 333, 336–339. doi: 10.1126/science.1202422

do Rosário Gomes, H., Goes, J. I., Matondkar, S. P., Buskey, E. J., Basu, S., Parab, S., et al. (2014). Massive outbreaks of noctiluca scintillans blooms in the Arabian Sea due to spread of hypoxia. *Nat. Commun.* 5, 1–8. doi: 10.1038/ncomms5862

Dueser, W., Ross, E., and Mlodzinska, Z. (1978). Evidence for and rate of denitrification in the Arabian Sea. *Deep Sea Res.* 25, 431–445. doi: 10.1016/0146-6291(78)90551-9

Fu, W., Primeau, F., Keith Moore, J., Lindsay, K., and Randerson, J. T. (2018). Reversal of increasing tropical ocean hypoxia trends with sustained climate warming. *Global Biogeochemical Cycles* 32, 551–564. doi: 10.1002/2017GB005788

Gaye, B., Böll, A., Segschneider, J., Burdanowitz, N., Emeis, K.-C., Ramaswamy, V., et al. (2018). Glacial–interglacial changes and holocene variations in Arabian Sea denitrification. *Biogeosciences* 15, 507–527. doi: 10.5194/bg-15-507-2018

Gnanadesikan, A., Dunne, J., and John, J. (2012). Understanding why the volume of suboxic waters does not increase over centuries of global warming in an earth system model. *Biogeosciences* 9, 1159–1172. doi: 10.5194/bg-9-1159-2012

Goes, J. I., Tian, H., do Rosario Gomes, H., Anderson, O. R., Al-Hashmi, K., deRada, S., et al. (2020). Ecosystem state change in the Arabian Sea fuelled by the recent loss of snow over the himalayan-tibetan plateau region. *Sci. Rep.* 10, 1–8. doi: 10.1038/s41598-020-64360-2

Gong, H., Li, C., and Zhou, Y. (2021). Emerging global ocean deoxygenation across the 21st century. *Geophys. Res. Lett.* 48, e2021GL095370. doi: 10.1029/2021GL095370

Gruber, N. (2008). The marine nitrogen cycle: overview and challenges. *Nitrogen Mar. Environ.* 2, 1–50.

Guieu, C., Al Azhar, M., Aumont, O., Mahowald, N., Lévy, M., Éthé, C., et al. (2019). Major impact of dust deposition on the productivity of the Arabian Sea. *Geophys. Res. Lett.* 46, 6736–6744. doi: 10.1029/2019GL082770

Gupta, A. K., Anderson, D. M., and Overpeck, J. T. (2003). Abrupt changes in the asian southwest monsoon during the holocene and their links to the north atlantic ocean. *Nature* 421, 354–357. doi: 10.1038/nature01340

Gupta, G., Jyothibabu, R., Ramu, C. V., Reddy, A. Y., Balachandran, K., Sudheesh, V., et al. (2021). The world's largest coastal deoxygenation zone is not anthropogenically driven. *Environ. Res. Lett.* 16, 054009. doi: 10.1088/1748-9326/abe9eb

Gupta, R. S., and Naqvi, S. (1984). Chemical oceanography of the Indian Ocean, north of the equator. *Deep Sea Res. Part A. Oceanogr. Res. Papers* 31, 671–706. doi: 10.1016/0198-0149(84)90035-9

Gupta, R. S., Rajagopal, M., and Qasim, S. (1976). Relationship between dissolved oxygen and nutrients in the north-western Indian Ocean. *J Mar. Sci* 5, 201–211.

Gupta, G., Sudheesh, V., Sudharma, K., Saravanane, N., Dhanya, V., Dhanya, K., et al. (2016). Evolution to decay of upwelling and associated biogeochemistry over the southeastern Arabian Sea shelf. *J. Geophys. Res.: Biogeosciences* 121, 159–175. doi: 10.1002/2015JG003163

Henson, S. A., Cael, B., Allen, S. R., and Dutkiewicz, S. (2021). Future phytoplankton diversity in a changing climate. *Nat. Commun.* 12, 5372. doi: 10.1038/s41467-021-25699-w

Hood, R. R., Rixen, T., Levy, M., Hansell, D. A., Coles, V. J., and Lachkar, Z. (2023). Oxygen, carbon and ph variability in the Indian Ocean (Elsevier).

Hughes, D. J., Alderdice, R., Cooney, C., Kühl, M., Pernice, M., Voolstra, C. R., et al. (2020). Coral reef survival under accelerating ocean deoxygenation. *Nat. Climate Change* 10, 296–307. doi: 10.1038/s41558-020-0737-9

Ito, T., Minobe, S., Long, M. C., and Deutsch, C. (2017). Upper ocean o2 trends: 1958–2015. *Geophys. Res. Lett.* 44, 4214–4223. doi: 10.1002/2017GL073613

Ito, T., Nenes, A., Johnson, M., Meskhidze, N., and Deutsch, C. (2016). Acceleration of oxygen decline in the tropical pacific over the past decades by aerosol pollutants. *Nat. Geosci.* 9, 443–447. doi: 10.1038/ngeo2717

Ittekkot, V., Nair, R., Honjo, S., Ramaswamy, V., Bartsch, M., Manganini, S., et al. (1991). Enhanced particle fluxes in Bay of Bengal induced by injection of fresh water. *Nature* 351, 385–387. doi: 10.1038/351385a0

Joshi, G. P., Naik, S. S., and Banakar, V. (2021). Last 10000 years variation in the intensity of OMZ-core reconstructed from sediment of the eastern Arabian Sea. *J. Geological Soc. India* 97, 243–248. doi: 10.1007/s12594-021-1673-7

Keeling, R. F., Körtzinger, A., and Gruber, N.. (2010). Ocean deoxygenation in a warming world. *Annu. Rev. Mar. Sci.* 2, 199–229. doi: 10.1146/annurev.marine.010908.163855

Klöcker, R., and Henrich, R. (2006). Recent and late quaternary pteropod preservation on the pakistan shelf and continental slope. *Mar. Geol.* 231, 103–111. doi: 10.1016/j.margeo.2006.05.014

Koné, V., Aumont, O., Lévy, M., and Resplandy, L. (2009). Physical and biogeochemical controls of the phytoplankton seasonal cycle in the Indian Ocean: A modeling study. *Indian Ocean Biogeochemical Processes Ecol. Variability* 185, 350. doi: 10.1029/2008GM000700

Kwiatkowski, L., Torres, O., Bopp, L., Aumont, O., Chamberlain, M., Christian, J. R., et al. (2020). Twenty-first century ocean warming, acidification, deoxygenation, and upper-ocean nutrient and primary production decline from cmip6 model projections. *Biogeosciences* 17, 3439–3470. doi: 10.5194/bg-17-3439-2020

Kwon, E. Y., Primeau, F., and Sarmiento, J. L. (2009). The impact of remineralization depth on the air–sea carbon balance. *Nat. Geosci.* 2, 630–635. doi: 10.1038/ngeo612

Lachkar, Z., Lévy, M., and Smith, S. (2018). Intensification and deepening of the Arabian Sea oxygen minimum zone in response to increase in indian monsoon wind intensity. *Biogeosciences* 15, 159–186. doi: 10.5194/bg-15-159-2018

Lachkar, Z., Lévy, M., and Smith, K. (2019). Strong intensification of the Arabian Sea oxygen minimum zone in response to Arabian Gulf warming. *Geophys. Res. Lett.* 46, 5420–5429. doi: 10.1029/2018GL081631

Lachkar, Z., Mehari, M., Al Azhar, M., Lévy, M., and Smith, S. (2021). Fast local warming is the main driver of recent deoxygenation in the northern Arabian Sea. *Biogeosciences* 18, 5831–5849. doi: 10.5194/bg-18-5831-2021

Lachkar, Z., Mehari, M., Lévy, M., Paparella, F., and Burt, J. A. (2022). Recent expansion and intensification of hypoxia in the Arabian Gulf and its drivers. *Front. Mar. Sci.* 9, 1616. doi: 10.3389/fmars.2022.891378

Lachkar, Z., Smith, S., Lévy, M., and Pauluis, O. (2016). Eddies reduce denitrification and compress habitats in the Arabian Sea. *Geophys. Res. Lett.* 43, 9148–9156. doi: 10.1002/2016GL069876

Laffoley, D. D., and Baxter, J. (2019). *Ocean deoxygenation: Everyone's problem-causes, impacts, consequences and solutions* (Gland, Switzerland: IUCN).

Laufkötter, C., John, J. G., Stock, C. A., and Dunne, J. P. (2017). Temperature and oxygen dependence of the remineralization of organic matter. *Global Biogeochemical Cycles* 31, 1038–1050. doi: 10.1002/2017GB005643

Lévy, M., Resplandy, L., Palter, J. B., Couespel, D., and Lachkar, Z. (2022). The crucial contribution of mixing to present and future ocean oxygen distribution. *Ocean mixing*, 329–344. doi: 10.1016/B978-0-12-821512-8.00020-7

Lévy, M., Shankar, D., André, J.-M., Shenoi, S., Durand, F., and de Boyer Montégut, C. (2007). Basin-wide seasonal evolution of the Indian Ocean's phytoplankton blooms. *J. Geophys. Res.: Oceans* 112.

Long, M. C., Deutsch, C., and Ito, T. (2016). Finding forced trends in oceanic oxygen. *Global Biogeochemical Cycles* 30, 381–397. doi: 10.1002/2015GB005310

Long, M., Ito, T., and Deutsch, C. (2019). *Oxygen projections for the future. ocean deoxygenation: Everyone's problem* Vol. 562 (Gland, Switzerland: IUCN).

Madhupratap, M., Kumar, S. P., Bhattathiri, P., Kumar, M. D., Raghukumar, S., Nair, K., et al. (1996). Mechanism of the biological response to winter cooling in the northeastern Arabian Sea. *Nature* 384, 549–552. doi: 10.1038/384549a0

McCreary, J. P., Yu, Z., Hood, R. R., Vinaychandran, P., Furue, R., Ishida, A., et al. (2013). Dynamics of the indian-ocean oxygen minimum zones. *Prog. Oceanogr.* 112, 15–37. doi: 10.1016/j.pocean.2013.03.002

Moffett, J. W., Goepfert, T. J., and Naqvi, S. W. A. (2007). Reduced iron associated with secondary nitrite maxima in the Arabian Sea. *Deep Sea Res. Part I: Oceanogr. Res. Papers* 54, 1341–1349.

Moffett, J. W., and Landry, M. R. (2020). Grazing control and iron limitation of primary production in the Arabian Sea: Implications for anticipated shifts in southwest monsoon intensity. *Deep Sea Res. Part II: Topical Stud. Oceanogr.* 179, 104687.

Moffett, J. W., Vedamati, J., Goepfert, T. J., Pratihary, A., Gauns, M., and Naqvi, S. (2015). Biogeochemistry of iron in the a rabian s ea. *Limnol. Oceanogr.* 60, 1671–1688. doi: 10.1002/lno.10132

Morrison, J. M., Codispoti, L., Smith, S. L., Wishner, K., Flagg, C., Gardner, W. D., et al. (1999). The oxygen minimum zone in the Arabian Sea during 1995. *Deep Sea Res. Part II: Topical Stud. Oceanogr.* 46, 1903–1931.

Nair, R., Ittekkot, V., Manganini, S., Ramaswamy, V., Haake, B., Degens, E., et al. (1989). Increased particle flux to the deep ocean related to monsoons. *Nature* 338, 749–751. doi: 10.1038/338749a0

Naqvi, S. (1987). Some aspects of the oxygen-deficient conditions and denitrification in the Arabian Sea. *J. Mar. Res.* 45, 1049–1072. doi: 10.1357/002224087788327118

Naqvi, W. (1991). Geographical extent of denitrification in the Arabian Sea in relation to some physical processes. *Oceanologica Acta* 14, 281–290.

Naqvi, S. (2008). The Indian Ocean. *Nitrogen Mar. Environ.* 2, 631–681. doi: 10.1016/B978-0-12-372522-6.00014-1

Naqvi, S. (2019). "Evidence for ocean deoxygenation and its patterns: Indian ocean," in *Ocean deoxygenation: Everyone's problem*. Eds. D. Laffoley and J. M. Baxter (Gland, Switzerland: IUCN).

Naqvi, S., Jayakumar, D., Narvekar, P., Naik, H., Sarma, V., D'souza, W., et al. (2000). Increased marine production of n2o due to intensifying anoxia on the indian continental shelf. *Nature* 408, 346–349. doi: 10.1038/35042551

Naqvi, S., Moffett, J., Gauns, M., Narvekar, P., Pratihary, A., Naik, H., et al. (2010). The Arabian Sea as a high-nutrient, low-chlorophyll region during the late southwest monsoon. *Biogeosciences* 7, 2091–2100. doi: 10.5194/bg-7-2091-2010

Naqvi, S. W. A., Noronha, R. J., and Reddy, C. G. (1982). Denitrification in the Arabian Sea. *Deep Sea Res. Part A. Oceanogr. Res. Papers* 29, 459–469. doi: 10.1016/0198-0149(82)90070-X

Naqvi, S., Sarma, V., and Jayakumar, D. (2002). Carbon cycling in the northern Arabian Sea during the northeast monsoon: Significance of salps. *Mar. Ecol. Prog. Ser.* 226, 35–44. doi: 10.3354/meps226035

Oschlies, A. (2019). *Ocean deoxygenation from climate change* (Gland, Switzerland: IUCN).

Oschlies, A. (2021). A committed fourfold increase in ocean oxygen loss. *Nat. Commun.* 12, 1–8. doi: 10.1038/s41467-021-22584-4

Oschlies, A., Brandt, P., Stramma, L., and Schmidtko, S. (2018). Drivers and mechanisms of ocean deoxygenation. *Nat. Geosci.* 11, 467–473. doi: 10.1038/s41561-018-0152-2

Oschlies, A., Duteil, O., Getzlaff, J., Koeve, W., Landolfi, A., and Schmidtko, S. (2017). Patterns of deoxygenation: sensitivity to natural and anthropogenic drivers. *Philos. Trans. R. Soc. A: Mathematical Phys. Eng. Sci.* 375, 20160325.

Oschlies, A., Koeve, W., Landolfi, A., and Kähler, P. (2019). Loss of fixed nitrogen causes net oxygen gain in a warmer future ocean. *Nat. Commun.* 10, 1–7. doi: 10.1038/s41467-019-10813-w

Pichevin, L., Bard, E., Martinez, P., and Billy, I. (2007). Evidence of ventilation changes in the Arabian Sea during the late quaternary: Implication for denitrification and nitrous oxide emission. *Global Biogeochemical Cycles* 21. doi: 10.1029/2006GB002852

Piontkovski, S., and Al-Oufi, H. (2015). The omani shelf hypoxia and the warming Arabian Sea. *Int. J. Environ. Stud.* 72, 256–264. doi: 10.1080/00207233.2015.1012361

Praveen, V., Ajayamohan, R., Valsala, V., and Sandeep, S. (2016). Intensification of upwelling along oman coast in a warming scenario. *Geophys. Res. Lett.* 43, 7581–7589. doi: 10.1002/2016GL069638

Queste, B. Y., Vic, C., Heywood, K. J., and Piontkovski, S. A. (2018). Physical controls on oxygen distribution and denitrification potential in the north west Arabian Sea. *Geophys. Res. Lett.* 45, 4143–4152. doi: 10.1029/2017GL076666

Rabalais, N. N., Turner, R. E., and Wiseman, ,. W. J.Jr (2002). Gulf of mexico hypoxia, aka "the dead zone". *Annu. Rev. Ecol. Systematics* 33, 235–263. doi: 10.1146/annurev.ecolsys.33.010802.150513

Rao, C., Naqvi, S., Kumar, M. D., Varaprasad, S., Jayakumar, D., George, M., et al. (1994). Hydrochemistry of the bay of bengal: possible reasons for a different water-column cycling of carbon and nitrogen from the Arabian Sea. *Mar. Chem.* 47, 279–290. doi: 10.1016/0304-4203(94)90026-4

Reichart, G.-J., Brinkhuis, H., Huiskamp, F., and Zachariasse, W. J. (2004). Hyperstratification following glacial overturning events in the northern Arabian Sea. *Paleoceanography* 19. doi: 10.1029/2003PA000900

Reichart, G.-J., Lourens, L., and Zachariasse, W. (1998). Temporal variability in the northern Arabian Sea oxygen minimum zone (OMZ) during the last 225,000 years. *Paleoceanography* 13, 607–621. doi: 10.1029/98PA02203

Resplandy, L. (2018). Climate change and oxygen in the ocean. *Nature: Int. Weekly J. Sci* 557, 314–315.

Resplandy, L., Lévy, M., Bopp, L., Echevin, V., Pous, S., Sarma, V., et al. (2012). Controlling factors of the oxygen balance in the Arabian Sea's omz. *Biogeosciences* 9, 5095–5109. doi: 10.5194/bg-9-5095-2012

Resplandy, L., Lévy, M., Madec, G., Pous, S., Aumont, O., and Kumar, D. (2011). Contribution of mesoscale processes to nutrient budgets in the Arabian Sea. *J. Geophys. Res.: Oceans* 116.

Rixen, T., Baum, A., Gaye, B., and Nagel, B. (2014). Seasonal and interannual variations in the nitrogen cycle in the Arabian Sea. *Biogeosciences* 11, 5733–5747. doi: 10.5194/bg-11-5733-2014

Rixen, T., Cowie, G., Gaye, B., Goes, J., do Rosário Gomes, H., Hood, R. R., et al. (2020). Reviews and syntheses: Present, past, and future of the oxygen minimum zone in the Northern Indian Ocean. *Biogeosciences* 17, 6051–6080. doi: 10.5194/bg-17-6051-2020

Rixen, T., Guptha, M., and Ittekkot, V. (2005). Deep ocean fluxes and their link to surface ocean processes and the biological pump. *Prog. Oceanogr.* 65, 240–259. doi: 10.1016/j.pocean.2005.03.006

Robinson, C. (2019). Microbial respiration, the engine of ocean deoxygenation. *Front. Mar. Sci.* 5, 533. doi: 10.3389/fmars.2018.00533

Rodgers, K. B., Lin, J., and Frölicher, T. L. (2015). Emergence of multiple ocean ecosystem drivers in a large ensemble suite with an earth system model. *Biogeosciences* 12, 3301–3320. doi: 10.5194/bg-12-3301-2015

Roxy, M. K., Modi, A., Murtugudde, R., Valsala, V., Panickal, S., Prasanna Kumar, S., et al. (2016). A reduction in marine primary productivity driven by rapid warming over the tropical Indian Ocean. *Geophys. Res. Lett.* 43, 826–833. doi: 10.1002/2015GL066979

Saleh, A., Abtahi, B., Mirzaei, N., Chen, C.-T. A., Ershadifar, H., Ghaemi, M., et al. (2021). Hypoxia in the persian Gulf and the strait of hormuz. *Mar. pollut. Bull.* 167, 112354. doi: 10.1016/j.marpolbul.2021.112354

Sandeep, S., and Ajayamohan, R. (2015). Poleward shift in indian summer monsoon low level jetstream under global warming. *Climate Dynamics* 45, 337–351. doi: 10.1007/s00382-014-2261-y

Sarma, V., Bhaskar, T. U., Kumar, J. P., and Chakraborty, K. (2020). Potential mechanisms responsible for occurrence of core oxygen minimum zone in the north-eastern Arabian Sea. *Deep Sea Res. Part I: Oceanogr. Res. Papers* 165, 103393.

Schmidt, H., Czeschel, R., and Visbeck, M. (2020). Seasonal variability of the Arabian Sea intermediate circulation and its impact on seasonal changes of the upper oxygen minimum zone. *Ocean Sci.* 16, 1459–1474. doi: 10.5194/os-16-1459-2020

Schmidt, H., Getzlaff, J., Löptien, U., and Oschlies, A. (2021). Causes of uncertainties in the representation of the Arabian Sea oxygen minimum zone in CMIP5 models. *Ocean Sci.* 17, 1303–1320. doi: 10.5194/os-17-1303-2021

Schmidtko, S., Stramma, L., and Visbeck, M. (2017). Decline in global oceanic oxygen content during the past five decades. *Nature* 542, 335–339. doi: 10.1038/nature21399

Schulz, H., von Rad, U., Erlenkeuser, H., and von Rad, U. (1998). Correlation between Arabian Sea and greenland climate oscillations of the past 110,000 years. *Nature* 393, 54–57. doi: 10.1038/31750

Séférian, R., Berthet, S., Yool, A., Palmieri, J., Bopp, L., Tagliabue, A., et al. (2020). Tracking improvement in simulated marine biogeochemistry between cmip5 and CMIP6. *Curr. Climate Change Rep.* 6, 95–119. doi: 10.1007/s40641-020-00160-0

Singh, A. D., Jung, S. J., Darling, K., Ganeshram, R., Ivanochko, T., and Kroon, D. (2011). Productivity collapses in the Arabian Sea during glacial cold phases. *Paleoceanography* 26. doi: 10.1029/2009PA001923

Stramma, L., Johnson, G. C., Sprintall, J., and Mohrholz, V. (2008). Expanding oxygen-minimum zones in the tropical oceans. *science* 320, 655–658. doi: 10.1126/science.1153847

Stramma, L., Oschlies, A., and Schmidtko, S. (2012a). Mismatch between observed and modeled trends in dissolved upper-ocean oxygen over the last 50 yr. *Biogeosciences* 9, 4045–4057. doi: 10.5194/bg-9-4045-2012

Stramma, L., Prince, E. D., Schmidtko, S., Luo, J., Hoolihan, J. P., Visbeck, M., et al. (2012b). Expansion of oxygen minimum zones may reduce available habitat for tropical pelagic fishes. *Nat. Climate Change* 2, 33–37. doi: 10.1038/nclimate1304

Stramma, L., Schmidtko, S., Levin, L. A., and Johnson, G. C. (2010). Ocean oxygen minima expansions and their biological impacts. *Deep Sea Res. Part I: Oceanogr. Res. Papers* 57, 587–595.

Ulloa, O., Canfield, D. E., DeLong, E. F., Letelier, R. M., and Stewart, F. J. (2012). Microbial oceanography of anoxic oxygen minimum zones. *Proc. Natl. Acad. Sci.* 109, 15996–16003. doi: 10.1073/pnas.1205009109

Vallivattathillam, P., Iyyappan, S., Lengaigne, M., Ethé, C., Vialard, J., Levy, M., et al. (2017). Positive Indian Ocean dipole events prevent anoxia off the west coast of india. *Biogeosciences* 14, 1541–1559. doi: 10.5194/bg-14-1541-2017

Vallivattathillam, P., Lachkar, Z., and Levy, M. Robust shrinking of the Arabian Sea oxygen minimum zone with climate change projected with a downscaled model. *Front. Mar. Sci.*

Vallivattathillam, P., Suresh, I., Lengaigne, M., Vialard, J., Izumo, T., Sadhvi, K., et al. (2019). Mechanisms of the Southern Arabian Sea summer primary productivity weakening in response to anthropogenic forcing in CMIP5 models. *J. Geophys. Res. Biogeosciences*. 21:1-1. 1p.

Vaquer-Sunyer, R., and Duarte, C. M. (2008). Thresholds of hypoxia for marine biodiversity. *Proc. Natl. Acad. Sci.* 105, 15452–15457. doi: 10.1073/pnas.0803833105

Wallmann, K., José, Y. S., Hopwood, M. J., Somes, C. J., Dale, A. W., Scholz, F., et al. (2022). Biogeochemical feedbacks may amplify ongoing and future ocean deoxygenation: a case study from the peruvian oxygen minimum zone. *Biogeochemistry* 159, 45–67. doi: 10.1007/s10533-022-00908-w

Wiggert, J. D., Hood, R., Banse, K., and Kindle, J. (2005). Monsoon-driven biogeochemical processes in the Arabian Sea. *Prog. Oceanogr.* 65, 176–213. doi: 10.1016/j.pocean.2005.03.008

Wiggert, J. D., and Murtugudde, R. G. (2007). The sensitivity of the southwest monsoon phytoplankton bloom to variations in aeolian iron deposition over the Arabian Sea. *J. Geophys. Res.: Oceans* 112.

Wiggert, J., Murtugudde, R., and Christian, J. (2006). Annual ecosystem variability in the tropical Indian Ocean: Results of a coupled bio-physical ocean general circulation model. *Deep Sea Res. Part II: Topical Stud. Oceanogr.* 53, 644–676. doi: 10.1016/j.dsr2.2006.01.027

Wishner, K. F., Seibel, B. A., Roman, C., Deutsch, C., Outram, D., Shaw, C. T., et al. (2018). Ocean deoxygenation and zooplankton: Very small oxygen differences matter. *Sci. Adv.* 4, eaau5180. doi: 10.1126/sciadv.aau5180

Wyrtki, K., Bennett, E. B., and Rochford, D. J.. (1971). *Oceanographic atlas of the international Indian ocean expedition* Vol. 531 (Washington, DC: National Science Foundation).

Xu, Z., Han, Y., and Yang, Z. (2019). Dynamical downscaling of regional climate: A review of methods and limitations. *Sci. China Earth Sci.* 62, 365–375. doi: 10.1007/s11430-018-9261-5

Zhang, Z., Ma, W., and Chai, F. (2022). Role of ocean circulation and settling of particulate organic matter in the decoupling between the oxygen minimum zone and the phytoplankton productive zone in the Arabian Sea: A modeling study. *Front. Mar. Sci.* 9, 1960. doi: 10.3389/fmars.2022.927921

Zhou, Y., Gong, H., and Zhou, F. (2022). Responses of horizontally expanding oceanic oxygen minimum zones to climate change based on observations. *Geophys. Res. Lett.* 49, e2022GL097724. doi: 10.1029/2022GL097724

frontiers | Frontiers in Marine Science

TYPE Original Research
PUBLISHED 12 May 2023
DOI 10.3389/fmars.2023.1137064

OPEN ACCESS

EDITED BY
Sanjeev Kumar,
Physical Research Laboratory, India

REVIEWED BY
Damian L. Arévalo-Martínez,
Radboud University, Netherlands
Sohiko Kameyama,
Hokkaido University, Japan

*CORRESPONDENCE
Annie Bourbonnais
abourbonnais@seoe.sc.edu

RECEIVED 03 January 2023
ACCEPTED 31 March 2023
PUBLISHED 12 May 2023

CITATION
Bourbonnais A, Chang BX, Sonnerup RE, Doney SC and Altabet MA (2023) Marine N_2O cycling from high spatial resolution concentration, stable isotopic and isotopomer measurements along a meridional transect in the eastern Pacific Ocean.
Front. Mar. Sci. 10:1137064.
doi: 10.3389/fmars.2023.1137064

Marine N_2O cycling from high spatial resolution concentration, stable isotopic and isotopomer measurements along a meridional transect in the eastern Pacific Ocean

Annie Bourbonnais[1]*, Bonnie X. Chang[2], Rolf E. Sonnerup[2], Scott C. Doney[3] and Mark A. Altabet[4]

[1]School of the Earth, Ocean and Environment, University of South Carolina, Columbia, SC, United States, [2]Cooperative Institute for Climate, Ocean, and Ecosystem Studies, University of Washington, Seattle, WA, United States, [3]Department of Environmental Sciences, University of Virginia, Charlottesville, VA, United States, [4]School for Marine Science and Technology, University of Massachusetts, Dartmouth, MA, United States

Nitrous oxide (N_2O) is a potent greenhouse gas and ozone depleting substance, with the ocean accounting for about one third of global emissions. In marine environments, a significant amount of N_2O is produced by biological processes in Oxygen Deficient Zones (ODZs). While recent technological advances are making surface N_2O concentration more available, high temporal and spatial resolution water-column N_2O concentration data are relatively scarce, limiting global N_2O ocean models' predictive capability. We present a N_2O concentration, stable isotopic composition and isotopomer dataset of unprecedently large spatial coverage and depth resolution in the broader Pacific, crossing both the eastern tropical South and North Pacific Ocean ODZs collected as part of the GO-SHIP P18 repeat hydrography program in 2016/2017. We complement these data with dissolved gases (nitrogen, oxygen, argon) and nitrate isotope data to investigate the pathways controlling N_2O production in relation to apparent oxygen utilization and fixed nitrogen loss. N_2O yield significantly increased under low oxygen conditions near the ODZs. Keeling plot analysis revealed different N_2O sources above the ODZs under different oxygen regimes. Our stable isotopic data and relationships between the N_2O added by microbial processes (ΔN_2O) and dissolved inorganic nitrogen (DIN) deficit confirm increased N_2O production by denitrification under low oxygen conditions near the oxycline where the largest N_2O accumulations were observed. The slope for $\delta^{18}O$-N_2O versus site preference (SP, the difference between the central (α) and outer (β) N atoms in the linear N_2O molecule) in the eastern tropical North Pacific ODZ was lower than expected for pure N_2O reduction, likely because of the observed decrease in $\delta^{15}N^{\beta}$. This trend is consistent with prior ODZ studies and attributed to concurrent production of N_2O from nitrite with a low $\delta^{15}N$ or denitrification with a SP >0‰. We estimated

10.3389/fmars.2023.1137064

apparent isotope effects for N_2O consumption in the ETNP ODZ of 3.6‰ for $^{15}N^{bulk}$, 9.4‰ for $^{15}N^{\alpha}$, -2.3‰ for $^{15}N^{\beta}$, 12.0‰ for ^{18}O, and 11.7‰ for SP. These values were generally within ranges previously reported for previous laboratory and field experiments.

KEYWORDS

nitrous oxide, greenhouse gas, stable isotopes, isotopomers, oxygen deficient zones, eastern South Pacific Ocean, eastern North Pacific Ocean, Southern Ocean

1 Introduction

Nitrous oxide (N_2O) is mainly produced by microbial processes and contributes to climate change as a tropospheric greenhouse gas approximately 275 times more potent than CO_2 on a per molecule basis (Forster et al., 2021). N_2O produced at the Earth's surface has a long atmospheric residence time of more than 100 years and is the main source of ozone-depleting nitric-oxide radicals in the stratosphere (Nevison and Holland, 1997; Ravishankara et al., 2009). Biogeochemical models estimate that the ocean accounts for about one third of global N_2O emissions (Freing et al., 2012; Ciais et al., 2013; Tian et al., 2020; Forster et al., 2021) with a global oceanic flux estimate of 4.2 ± 1.0 Tg N y^{-1} (Yang et al., 2020). Coastal upwelling systems associated with Oxygen Deficient Zones (ODZs) account for up to 35% of the oceanic N_2O total emissions (Bakker et al., 2014; Arévalo-Martínez et al., 2015; Yang et al., 2020), yet temporal variability from these productive coastal waters is still not well quantified.

N_2O is produced in oxic ocean waters as a by-product of nitrification through the oxidation of hydroxylamine (NH_2OH), an intermediate during ammonia (NH_3) oxidation to nitrite (NO_2^-) by both archaeal and bacterial nitrifiers (Caranto and Lancaster, 2017) (Figure 1). Under low oxygen (O_2)-conditions, ammonia oxidizing bacteria (AOB) produce N_2O by nitrifier-denitrification, the sequential NO_2^- reduction to N_2O during respiration (Goreau et al., 1980; Wrage et al., 2001; Frame and Casciotti, 2010). N_2O is also produced by ammonia oxidizing archaea (AOA) following a hybrid pathway where one atom in the N_2O molecule is derived from NH_3 (e.g., NH_2OH) and the other from NO_2^- (Trimmer et al., 2016). N_2O production by nitrification leads to strong positive correlations between Apparent Oxygen Utilization (AOU) and ΔN_2O (i.e., the difference between N_2O measured and at atmospheric equilibrium) and nitrate (NO_3^-) concentrations (Yoshinari and Knowles, 1976; Cohen and Gordon, 1979; Nevison et al., 2003). N_2O production yield per NO_2^- generated during nitrification by either AOA or AOB is generally low, varying from 0 to 2% of NO_3^- production (Yoshida et al., 1989; Frame and Casciotti, 2010; Santoro et al., 2010; Santoro et al., 2011; Löscher et al., 2012; Ryabenko et al., 2012) but is generally higher for AOB (Hink et al., 2017a; Hink et al., 2017b) and enhanced under low-O_2 conditions according to both culture and field observations (up to 10% at low O_2; Goreau et al., 1980; Ji et al., 2015).

Under anoxic conditions, denitrification, the sequential reduction of NO_3^-, NO_2^-, and NO to N_2O, both produces and consumes N_2O. Enhanced N_2O production occurs under low-O_2 conditions (generally below 10 µmol kg^{-1}; Frey et al., 2020) due to different O_2 sensitivities for the different steps involved in denitrification, with nitrous oxide reductase being inhibited by even nanomolar O_2 concentrations (Dalsgaard et al., 2014). N_2O produced by incomplete denitrification significantly accumulates in low-O_2 conditions near the upper oxycline in the eastern tropical North Pacific (ETNP) and eastern tropical South Pacific (ETSP) ODZs (e.g., Ji et al., 2015; Kock et al., 2016; Bourbonnais et al., 2017; Casciotti et al., 2018; Frey et al., 2020; Kelly et al., 2021; Monreal et al., 2022). High N_2O accumulations of up to 1 µmol L^{-1} were observed in surface waters off the Peru coast, where anoxic waters from the ETSP ODZ are continuously upwelled (Arévalo-Martínez et al., 2015). N_2O accumulation is caused by a decoupling between N_2O production and its reduction to N_2 by denitrification, the latter process being less O_2 tolerant (Dalsgaard et al., 2014). N_2O is generally completely reduced to non-bioavailable N_2 in anoxic waters. ODZs are thus generally net N_2O sinks, with concentrations near or below atmospheric equilibrium concentrations (Bange et al., 2001; Yamagishi et al., 2007; Kock et al., 2016).

Natural stable isotopes are broadly used as tracers of N-cycle processes in the ocean which integrate over space and time (e.g., Sigman et al., 2005; Altabet, 2006; Bourbonnais et al., 2009;

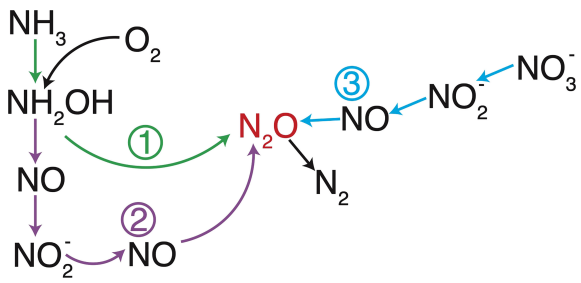

FIGURE 1
N_2O production and consumption processes. N_2O is produced by hydroxylamine oxidation (1, green) or nitrifier-denitrification (2, purple) during ammonia oxidation and denitrification (3, light blue) by bacteria and archaea. Modified from Bourbonnais et al. (2021).

Bourbonnais et al., 2015). The N_2O molecule contains both bulk ($\delta^{15}N$ and $\delta^{18}O$) and, given its asymmetric arrangement of atoms, ^{15}N site specific signatures that are valuable for identifying production and consumption processes. Bulk $\delta^{15}N$ and $\delta^{18}O$ are expressed as:

$$\delta^{15}N \text{ or } \delta^{18}O = ((R_{sample}/R_{reference} - 1) \times 1000 \quad \text{(eq. 1)}$$

Units are in parts per thousand or per mil (‰) and R is the ratio of $^{15}N/^{14}N$ or $^{18}O/^{16}O$. Reference materials are atmospheric N_2 for N (scale AIR-N_2) and mean ocean water for O (scale Vienna Standard Mean Ocean Water, V-SMOW). The bulk isotopic composition ($\delta^{15}N$ and $\delta^{18}O$) of N_2O depends in part on the isotopic composition of its substrates. For instance, for hydroxylamine oxidation, bulk N_2O $\delta^{15}N$ and $\delta^{18}O$ depend on the $\delta^{15}N$ of the source NH_3 and $\delta^{18}O$ of dissolved O_2. Conversely for nitrifier-denitrification and denitrification, N_2O $\delta^{15}N$ and $\delta^{18}O$ is dependent on the $\delta^{15}N$ and $\delta^{18}O$ of source NO_3^- and/or NO_2^- (Ostrom and Ostrom, 2012). Additionally, significant O exchange usually occurs between NO_2^- and H_2O during N_2O production by nitrifier-denitrification or denitrification (Buchwald and Casciotti, 2010; Kool et al., 2011), which acts to decouple the $\delta^{18}O$ values of source and product.

Isotopic fractionation during nitrification and denitrification is the other major influence on the $\delta^{15}N$ and $\delta^{18}O$ of N_2O. Kinetic isotope fractionation occurs as the molecules containing the lighter isotopes (e.g., ^{14}N, ^{16}O) react more quickly leaving the residual substrate enriched in heavier isotopes (e.g., ^{15}N and ^{18}O). The isotope effect (ε) is defined by:

$$\varepsilon(‰) = ((k_2/k_1) - 1) \times 1000 \quad \text{(eq. 2)}$$

where k_1 and k_2 are the specific reaction rates for the lighter and heavier isotope, respectively. N and O isotope effects ($^{15}\varepsilon$, $^{18}\varepsilon$) during N_2O production and consumption vary substantially in laboratory culture as well as in the environment (Bourbonnais et al., 2017 and references therein).

In contrast to bulk isotope values, N_2O Site Preference (SP) is independent of initial isotopic composition of the substrate (Toyoda et al., 2002; Schmidt et al., 2004; Sutka et al., 2006). Thus, SP is generally process-dependent and can be used as a tracer to identify the source of N_2O. SP is calculated from the difference in $\delta^{15}N$ between the central (α) and outer (β) N atoms in the linear, asymmetrical N_2O molecule (NNO):

$$SP = \delta^{15}N^{\alpha} - \delta^{15}N^{\beta} \quad \text{(eq. 3)}$$

Non-zero SP arises from the differential biochemical bond making and breaking experienced by each of the two N atoms as a consequence of their different molecular positions. Low SP isotopic signatures (-11 to 0‰) are associated with N_2O production *via* NO_2^- reduction by nitrifier-denitrification or denitrification. Much higher SP values are indicative of abiotic N_2O formation (Heil et al., 2014) or production by hydroxylamine oxidation (30-36‰) (Sutka et al., 2006; Frame and Casciotti, 2010). N_2O isotopic signatures have consequently been classified into distinct compositional fields used to evaluate the relative contribution from different processes (e.g., Wankel et al., 2017 and reference therein). However, SP does increase as a result of isotope fractionation during consumption by denitrification as discussed above (Yamagishi et al., 2005; Ostrom et al., 2007; Yamagishi et al., 2007).

The main objectives of this study are to better understand nitrous oxide (N_2O) distribution and production mechanisms along the meridional P18 transect in the eastern Pacific sampled as part of the U.S. GO-SHIP program (Figure 2). We sampled at an unprecedently high spatial resolution to investigate how N_2O dynamics respond to changes in O_2 concentrations and dissolved inorganic nitrogen (DIN) loss. We then evaluated pathways responsible for N_2O production in sub-oxic waters (O_2 > 5 µmol kg^{-1}) overlying the ETNP and ETSP ODZs as well as deep waters using stable isotopes and isotopomers and Keeling plot analysis. We also investigated N_2O cycling within the ETNP ODZ and estimated apparent isotope effects for N_2O consumption.

2 Methods

The U.S. GO-SHIP Program conducted a hydrographic survey along the P18 section in 2016/2017 (Figure 2). Core physical and biogeochemical data from the cruise (e.g., temperature and salinity, O_2 and nutrient concentrations, transient tracers, radiocarbon) are publicly available at https://cchdo.ucsd.edu/cruise/33RO20161119. Samples for N_2/Ar were collected every ~2 degrees latitude during leg 1 at 25 stations in total. N_2O stable isotope and isotopomer samples were collected at 44 stations, every ~2 degrees latitude during leg 1 and every 3 to 4 degrees during leg 2, except between 3°

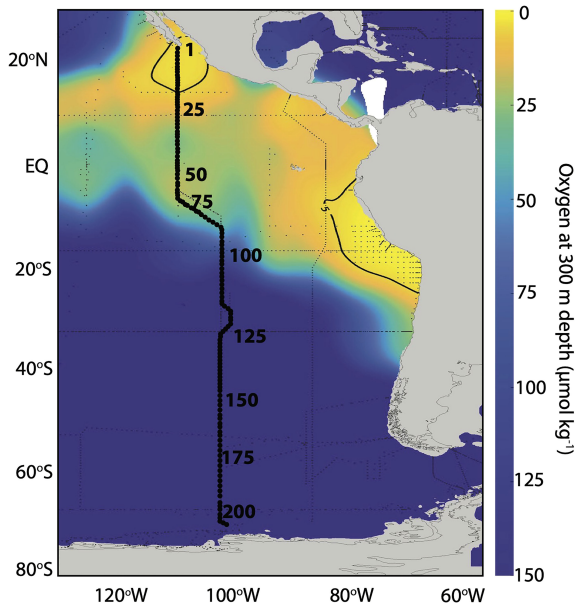

FIGURE 2
Stations sampled as part of the U.S. GO-SHIP Program along the P18 section in 2016/2017. Representative station numbers (every 25 stations) are shown along the transect. Colors indicate O_2 concentration at 300 m depth from the Global Ocean Data Analysis Project (GLODAPv2.2022). The 5 µmol kg^{-1} O_2 contour is shown.

N and 3°S where the resolution was increased to ~1 degree. Samples for $\delta^{15}N$ of NO_3^- analysis were collected during leg 1 at every degree of latitude, but only analyzed at station 32 in the ETNP and stations 53, 55, 62, 68, 74, 78, 90, 92, 96, 100, 104, 108 and 112 near the equator and the ETNP. We usually collected water column profiles from the surface to 2000 m depth, with deeper profiles at 3 stations.

2.1 N_2/Ar

N_2/Ar and $\delta^{15}N_2$ samples were collected and preserved as in Charoenpong et al. (2014) and analyzed at the University of Massachusetts Dartmouth (UMass Dartmouth). In total, approximately 600 samples were collected in 60 mL serum bottles. Water samples were pumped, at 5 to 10 ml min^{-1}, through a continuous sparger which transfers dissolved gases quantitatively to a continuous flow of helium (He) carrier gas. Analysis time was about 10 minutes. Carrier gas was passed through water, carbon dioxide (CO_2), and software selectable hot-copper O_2 traps before admittance *via* an open split to an isotope-ratio mass spectrometer (IRMS). The GV IsoPrime IRMS was fitted with collectors for simultaneous measurement of N_2 (masses 28 and 29), O_2 (masses 32, 33, and 34), and Ar (mass 40). Gas and isotopic ratios were measured against artificial compressed gas mixtures of N_2, O_2, and Ar close to expected dissolved gas ratios. Reproducibility of N_2/Ar measurements were better than 0.5‰. Daily calibration against an atmosphere reference (water equilibrated with air) was carried out at precisely controlled temperatures of 10.0 and 20.0°C. Excess (biogenic) N_2 was calculated against equilibrium values expected from *in situ* temperature and salinity as in Charoenpong et al. (2014). Subtraction of the background N_2 excess was done as in Bourbonnais et al. (2015) using N_2/Ar values in source waters near the equator.

2.2 N_2O concentrations, stable isotopes and isotopomers

Samples for dissolved N_2O were collected in a similar fashion as for dissolved O_2/N_2/Ar samples. Tygon tubing was attached to the Niskin bottle and a 165 mL serum glass bottle was filled and overflowed with seawater at least 2 times before capping with a butyl stopper and crimp sealed with aluminum. This procedure was executed underwater in a plastic container to avoid air bubbles. After collection, 0.2 mL of a saturated $HgCl_2$ solution was injected to prevent biological activity. In total, approximately 800 samples were collected.

Samples were analyzed at UMass Dartmouth using a GV IsoPrime Continuous Flow, MultiCollector, IRMS (CF-MC-IRMS) coupled to an automated gas extraction as described in Bourbonnais et al. (2017). The collector configuration included masses 30, 31 for the NO^+ fragment of N_2O (used for the determination of $\delta^{15}N^{\alpha}$) and 44, 45, and 46 (used for the determination of $\delta^{15}N^{bulk}$ and $\delta^{18}O$). Briefly, dissolved N_2O was pumped through a gas extractor, completely extracted through bubbling with a continuous flow of He and concentrated and purified in a purge-trap system. CO_2 and H_2O vapor were removed using chemical and cryogenic traps. N_2O was cryo-focused with two liquid N_2 traps and passed through a capillary gas chromatography (GC) column prior to IRMS analysis. Results were reproducible even at low N_2O concentration (down to ~5 nmol L^{-1}). N_2O concentrations in our samples were calculated from relative peak heights between the samples and a seawater standard of known N_2O concentration equilibrated with seawater at 5°C (12.5 nmol L^{-1} at salinity 34 as calculated using the Weiss and Price (1980) equation). Equilibrium N_2O concentrations at depth were calculated using historical reconstructions of atmospheric N_2O and water mass age distributions estimated from chlorofluorocarbon and sulfur hexafluoride tracers as described in section 2.4.

The N_2O concentrations measured with our IRMS agreed well with those measured independently using gas chromatography and an electron capture detector (ECD) at sea during the same research expedition (data available at https://cchdo.ucsd.edu/cruise/33RO20161119).

The reproducibility of $\delta^{15}N^{bulk}$, the average of $\delta^{15}N^{\alpha}$ and $\delta^{15}N^{\beta}$, $\delta^{18}O$ and SP as well as any instrumental drift were determined from measurements of the 5°C seawater standard distributed throughout an analytical run. We calibrated measurements and corrected for scrambling between the α and β positions (Westley et al., 2007) using four N_2O standards covering a large range of SP (as well as $\delta^{15}N^{bulk}$ and $\delta^{18}O$) composition (see Mohn et al., 2014). These standards were analyzed in duplicate for each run to quantify the scrambling effect and potential offsets, and we iteratively solved for the different calibration parameters as described in Frame and Casciotti (2010) and Mohn et al. (2014). Correction for isobaric interference from ^{17}O was included in these procedures. Standard deviations for triplicate measurements of our N_2O standards were typically below 0.1‰ for $\delta^{15}N^{bulk}$ N_2O, 0.1‰ for $\delta^{18}O$-N_2O and 1.0‰ for SP, which were comparable to values reported by Mohn et al. (2014).

2.3 Nitrate isotopes

The $\delta^{15}N$ of NO_3^- was measured using the Ti (III) reduction method for nitrate conversion to N_2O (Altabet et al., 2019). The product N_2O was purified and analyzed at UMass Dartmouth using a GV Isoprime continuous flow IRMS equipped with a custom purge trap extraction system and a PAL autosampler. Target sample size was 10 nmoles. Samples were standardized using a three-point correction with the international standards IAEA-N3 ($\delta^{15}N$ = 4.7‰ *vs* AIR), USGS-34 ($\delta^{15}N$ = -1.8‰ *vs* AIR) and USGS-35 (2.7‰ *vs* AIR). The isotope ratios are expressed in δ (‰) relative to AIR for N. The average standard deviation for duplicate samples was better than ± 0.3‰ for $\delta^{15}N$.

2.4 Calculation of N_2O at equilibrium using transit time distributions

In the same water parcel as N_2O, three transient tracers [chlorofluorocarbon (CFC)-11, CFC-12, and sulfur hexafluoride (SF_6)] were measured, each of which are affected by mixing

differently due to their differing atmospheric histories. This concurrence provides a means of estimating, from multiple tracer ages, the impact of mixing on the ages. To estimate mean ventilation timescales, age distributions, otherwise known as transit-time distributions (TTDs), were approximated using the inverse Gaussian form:

$$G(t) = \sqrt{\frac{\Gamma^3}{4\pi\Delta^2 t^3}} \exp\left[-\frac{\Gamma(t-\Gamma)^2}{4\Delta^2 t}\right] \quad \text{(eq. 4)}$$

where Γ is the mean age and Δ is the width, or standard deviation, of the distribution (Waugh et al., 2003).

Each water sample's measured CFC-11, CFC-12, and SF_6 were matched to a TTD lookup table (Stanley et al., 2012; Sonnerup et al., 2015) that allowed for Δ/Γ to range, in 0.1 increments, from 0.3 up to 1.8, the range that can be constrained by those three tracers (Stöven et al., 2015), and included each TTD's atmospheric N_2O, below. The matching criterion was within ± 3 σ of the combined tracer measurement and tracer saturation level uncertainties. The saturation levels dominate the uncertainty. Saturation levels of CFC-11, CFC-12, and SF_6 were estimated from the outcropping region of the respective isopycnals.

2.4.1 N_2O atmospheric history

The N_2O atmospheric history post-1800 was estimated using the polynomial fit presented in Freing et al. (2009), updated to the present using annual global mean N_2O atmospheric mixing ratios from the NOAA Earth System Research Laboratory (ESRL) Global Monitoring Division (https://www.esrl.noaa.gov/gmd/hats/combined/N2O.html). Pre-1800, a constant N_2O mixing ratio of 274.81 ppb was used.

2.4.2 Using TTDs to constrain biogenic N_2O

The total N_2O in a water parcel (N_2O_{obs}) is the sum of N_2O from two different sources: 1) equilibrated from the atmosphere at the time it was last at the surface (N_2O_{bkg}) and 2) added from microbial processes (ΔN_2O or N_2O_{prod}):

$$\Delta N_2O = [N_2O]_{prod} = [N_2O]_{obs} - [N_2O]_{bkg} \quad \text{(eq. 5)}$$

$$[N_2O]_{bkg} = X_{N2O} \times P \times F_{T,S} \quad \text{(eq. 6)}$$

where X_{N2O} is the atmospheric mixing ratio of N_2O, P is the atmospheric pressure, and $F_{T,S}$ is the temperature and salinity dependent solubility of N_2O in seawater (Weiss and Price, 1980). The N_2O mixing ratio of the TTDs for each water parcel were calculated using the atmospheric history of N_2O. The TTDs' N_2O mixing ratio were used to calculate the N_2O concentration at atmospheric equilibrium (N_2O_{bkg}) for each water sample. For values where the CFC-11 was below detection (< 0.001 pmol kg^{-1}), an atmospheric N_2O mixing ratio of 274.81 ppb was used.

2.5 Keeling plot analysis

In order to determine the sources of high ΔN_2O near the oxycline in the ETNP and ETSP ODZs, the isotopic and isotopomer compositions of the N_2O produced within given water masses and at different O_2 concentrations were estimated using Keeling plot analysis (Keeling, 1961; Pataki et al., 2003; Yamagishi et al., 2007; Fujii et al., 2013; Casciotti et al., 2018). The isotopic composition of source N_2O was determined using equation 5 and:

$$\delta_{obs} \times [N_2O]_{obs} = \delta_{bkg} \times [N_2O]_{bkg} + \delta_{prod} \times [N_2O]_{prod} \quad \text{(eq. 7)}$$

where the obs, prod and bkg subscripts refer to N_2O measured, newly produced and at equilibrium, respectively.

Rearranging equations 5 and 7 gives:

$$\delta_{obs} = 1/[N_2O]_{obs} \times (\delta_{bkg} - \delta_{prod} \times [N_2O]_{bkg} + \delta_{prod} \quad \text{(eq. 8)}$$

The intercepts of the linear regression between the inverse of measured N_2O concentration and the $\delta^{15}N^{bulk}$, $\delta^{15}N^{\alpha}$, $\delta^{15}N^{\beta}$, $\delta^{18}O$ and SP thus represents the isotopic composition of produced N_2O.

2.6 Isotope effects during N_2O consumption

We estimated isotope effects associated with N_2O consumption in the ETNP ODZ using a closed-system Rayleigh model (Mariotti et al., 1981). Only data in the ETNP ODZ at $[O_2]$ < 5 µmol kg^{-1} where N_2O consumption occurs were selected for this analysis.

$$\delta N_2O = \delta N_2O_{initial} - \varepsilon \ln([N_2O]_{obs}/[N_2O]_{initial}) \quad \text{(eq. 9)}$$

where $\delta^{15}N_2O$ is the $\delta^{15}N^{bulk}$, $\delta^{15}N^{\alpha}$, $\delta^{15}N^{\beta}$, $\delta^{18}O$ or SP for samples at O_2 < 5 µmol kg^{-1} (mostly in the ETNP ODZ), and the subscript refers to N_2O measured and initial concentrations and isotopic values before the onset of N_2O consumption. The isotope effects were estimated as the slopes of the linear regressions between δN_2O versus -ln$[N_2O]$, -ln$[N_2O]$ being an approximation of the $[N_2O]_{obs}/[N_2O]_{initial}$ term.

3 Results

3.1 Water mass characterization

Water masses were characterized according to Emery (2001). The main surface water (0 – 500 m depth) masses along the P18 transects, listed from north to south with potential temperature and absolute salinity ranges in brackets, were Eastern North Pacific Central Water (ENPCW; 12.0-20°C; 34.2-35.0), Eastern North Pacific Transition Water (ENPTW; 11.0-20.0°C, 33.3-34.3), Pacific Equatorial Water (PEW; 7.0-23.0°C, 34.5-36.0), Eastern South Pacific Central Water (ESPCW; 8.0-24°C; 34.4-36.4), Eastern South Pacific Transition Water (ESPTW; 14.0-20.0°C; 34.6-35.2), and Antarctic Surface Water (AASW; -1.0-1.0°C, 34.0-34.6). Intermediate water masses (500 – 1500 m depth) include Eastern South Pacific Intermediate Water (ESPIW; 10.0–12.0°C, 34.0-34.3) and Antarctic Intermediate Water (2-10°C, 33.8-34.5). Circumpolar Deep Water (CDW; 0.1-2.0°C, 34.62-34.73) was observed below 1500 m depth (Figure 3).

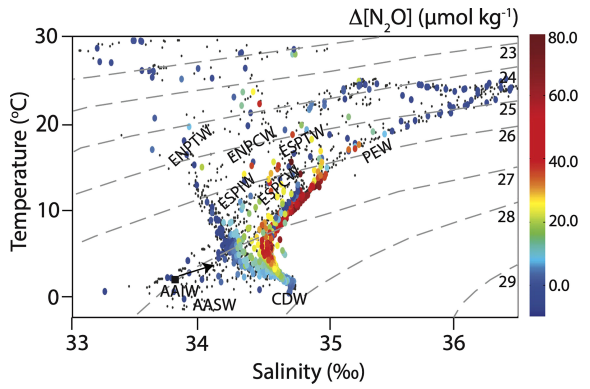

FIGURE 3
Potential temperature-absolute salinity plot showing the main water masses along the P18 transect from discrete water samples and ΔN_2O values as the color of the symbols (color bar). Smaller black dots indicate samples for which ΔN_2O was not measured. The different water masses abbreviations are for deep waters: Circumpolar Deep Water (CDW), intermediate waters: Eastern South Pacific Intermediate Water (ESPIW), and Antarctic Intermediate Water (AAIW), and surface waters: Pacific Equatorial Water (PEW), Eastern South Pacific Transition Water (ESPTW), Eastern South Pacific Central Water (ESPCW), Eastern North Pacific Central Water (ENPCW), Eastern North Pacific Transition Water (ENPTW), and Antarctic Surface Water (AASW). Lines of equal potential density (sigma-theta (σ_θ)) are shown (dashed grey lines).

3.2 Distribution of O_2, nutrient concentrations, NO_3^- isotopes, DIN deficit and biogenic N

The P18 transects crossed the ETNP ODZ and the fringe of the ETSP ODZ. O_2 concentrations decreased to < 5 μmol kg^{-1} between 120 m and 845 m depth in the northernmost part of the transect in the ETNP ODZ. In the ETSP, O_2 concentrations generally remained > 5 μmol kg^{-1}, except at few stations/depths between 4.5°S and 9.7°S and 195 and 495 m depth. The oxycline depth varied between 70 m at 10.5°N to 285 m at 16°S (Figure 4A).

Nitrite concentrations were generally low (<2.7 μmol kg^{-1}), with highest concentrations between 13°N and 16°N and 110 m to 285 m depth in the ETNP ODZ. Nitrite also accumulated at the fringe of the ETSP ODZ, with maximum concentrations between 7.5°S and 16.5°S near 100 m depth. Modest nitrite accumulations (<0.5 μmol kg^{-1}) were also observed in the upper 200 m from 34°S to 60°S (Figure 4B). Nitrate concentrations were generally depleted in surface waters, with the deepest maximum nitracline found at 350 m depth in the oligotrophic subtropical South Pacific from 21°S to 31.5°S (Figure 4C). A high $\delta^{15}N$ of NO_3^- of up to ~15‰ was observed in surface waters (Figure 4D), as expected following fractionation during NO_3^- assimilation by phytoplankton (Altabet, 2001; Granger et al., 2004). Nitrate concentrations were

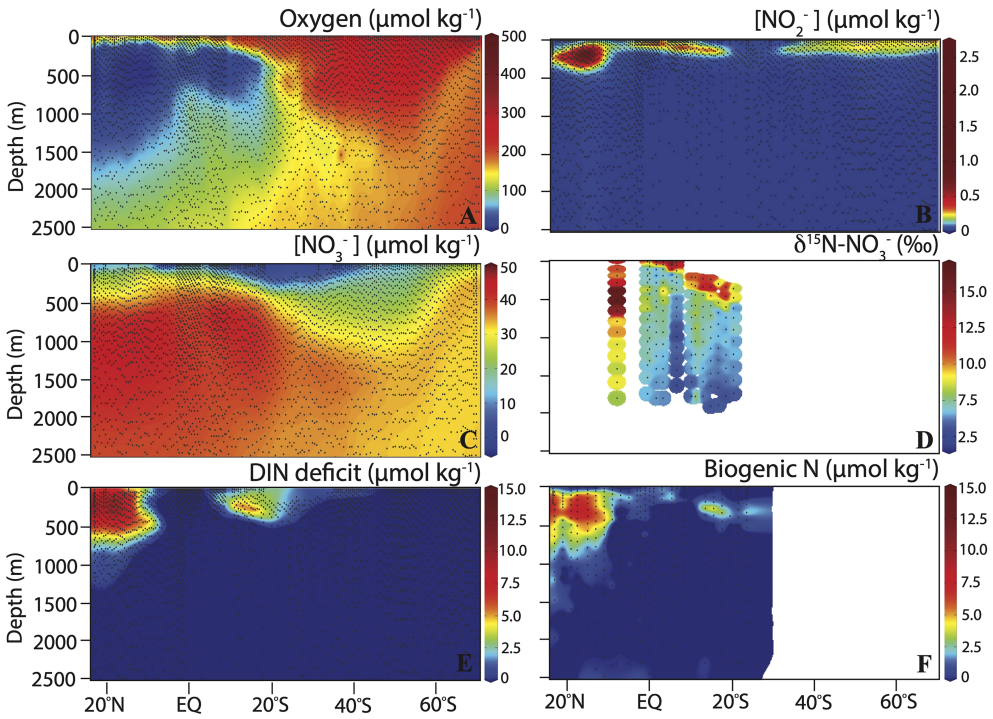

FIGURE 4
Section plots showing **(A)** dissolved O_2 concentration, **(B)** NO_2^- concentration, **(C)** NO_3^- concentration, **(D)** $\delta^{15}N$-NO_3^-, **(E)** DIN deficit calculated from nutrient concentrations, and **(F)** biogenic N (calculated from N_2/Ar measurements) along the P18 transect in 2016/2017.

moderate in the upper 500 m of the ETNP ODZ (minimum $[NO_3^-]$ of 21 μmol kg^{-1}), corresponding to ENPCW. The $\delta^{15}N$ of NO_3^- was also elevated in the ODZ (up to 16.7‰ at 8.5°N and 425 m depth), consistent with fractionation during denitrification (Cline and Kaplan, 1975; Granger et al., 2008). Nitrate accumulation of up to 45 μmol kg^{-1}were observed between 625 and 1750 m depth and was more pronounced in the ETNP. Nitrate concentrations remained relatively constant below 2000 m depth, with higher concentrations (~38 μmol kg^{-1}) in the northern portion of the transect compared to the South (~33 μmol kg^{-1}) (Figures 4C, D).

The DIN deficit (Howell et al., 1997) was calculated using the following equations:

$$\text{DIN deficit} = \text{DIN}_{exp} - \text{DIN}_{obs} \quad \text{(eq. 10)}$$

$$\text{DIN}_{exp} = m \times [PO_4^{3-}]_{obs} + b \quad \text{(eq. 11)}$$

where DIN_{exp} is the concentrations of dissolved inorganic nitrogen expected assuming Redfield stoichiometry (typically 16N:1P), DIN_{obs} is the concentration of nitrate plus nitrite measured and m and b are the slope and intercept, respectively, of the relationship between DIN and phosphate (PO_4^{3-}) concentrations for source waters outside of the ETNP and ETSP ODZs. DIN_{exp} was calculated according to Chang et al. (2010; Chang et al., 2012). DIN deficit was particularly elevated (up to 13.75 μmol kg^{-1}) between 50 and 580 m depth in the ETNP ODZ. DIN deficit was also elevated at the fringes of the ETSP ODZ, with values of up to 12.4 μmol kg^{-1} at 9.7°S and 205 m depth. Biogenic N derived from N_2/Ar data (as μmol N kg^{-1}) were generally comparable to DIN deficit, although generally a bit lower. Discrepancy between these two measurements could be caused by collection (N_2/Ar was not a prioritized gas sample during the P18 cruise) and/or storage effects for the N_2/Ar samples (Figures 4E, F).

3.3 ΔN_2O, N_2O stable isotopes and isotopomers

The largest ΔN_2O accumulation of 75.7 nmol kg^{-1} at $[O_2]$ < 5 μmol kg^{-1} was observed at a depth of 95 m (σ_θ = 25.65), near the oxycline in the ENPCW water mass in the ETNP ODZ (14.5°N) (Figure 5A). High ΔN_2O of up to 73 nmol kg^{-1} were also observed under low-O_2 conditions (15 μmol kg^{-1}) at the fringe of the ETSP ODZ (7-9°S) at 180-195 m depth (σ_θ = 26.4), which corresponds to the PEW water mass (Figures 3, 5). Overall, elevated ΔN_2O concentrations (>30 nmol kg^{-1} were observed from the northern portion of the P18 transect to about 20°S, clearly associated with low-O_2 waters from the ETNP and ETSP ODZs. In contrast, slightly negative ΔN_2O (undersaturation) (~-1 nmol kg^{-1}) values were observed in surface waters at the southern part of the transect associated with the subduction of AASW forming AAIW (Emery, 2001). Rapid cooling and sinking of surface water, with insufficient time for re-equilibration with the atmosphere, is likely causing the observed N_2O undersaturation in near surface waters in this region. A slight increase in ΔN_2O (up to ~20 nmol kg^{-1}) was observed from

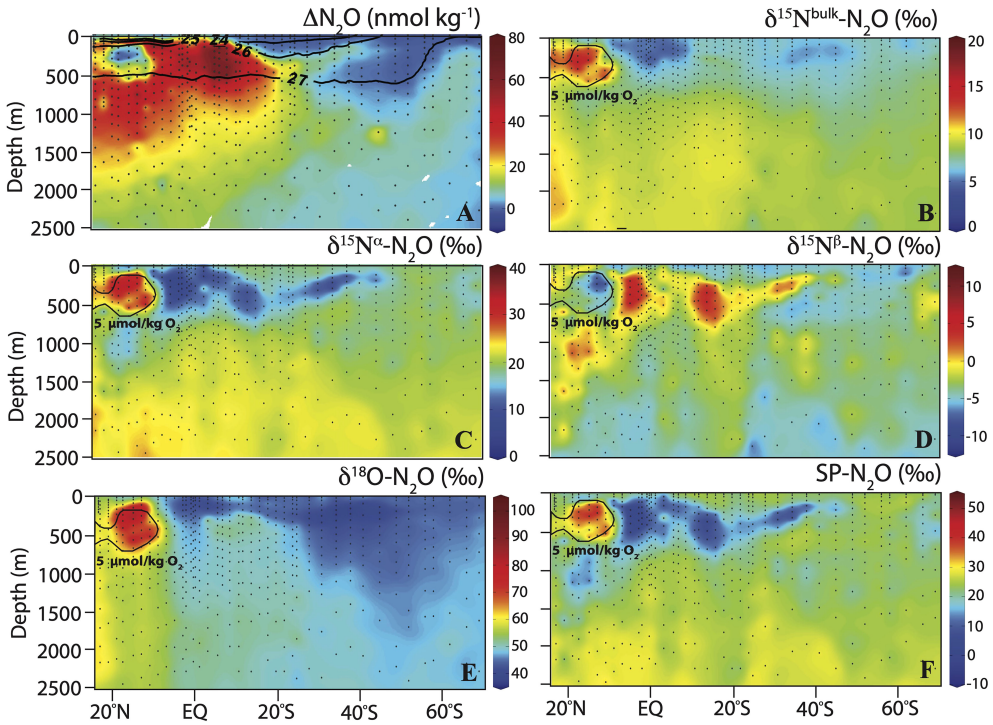

FIGURE 5
Section plots of **(A)** ΔN_2O with sigma-theta (σ_θ; kg m^{-3}) in overlay, **(B)** $\delta^{15}N^{bulk}$-N_2O, **(C)** $\delta^{15}N^{\alpha}$-N_2O, **(D)** $\delta^{15}N^{\beta}$-N_2O, **(E)** $\delta^{18}O$-N_2O, and **(F)** SP-N_2O along the P18 transect. The 5 μmol kg^{-1} O_2 contour in the ETNP is shown in **(B–F)**.

60°S to 20°S in AAIW waters. Negative ΔN_2O (minimum of ~-5 nmol kg^{-1}) were observed within the anoxic zone (O_2 < 5 µmol kg^{-1}) of the ETNP (Figure 5A).

The $\delta^{15}N^{bulk}$-N_2O was lowest in the first 500 m depth near the equator, with values less than 5‰, indicating production (Figure 5B). The highest $\delta^{15}N^{bulk}$-N_2O values (up to 18‰) were observed within the ETNP ODZ, consistent with the observed low ΔN_2O and indicating net consumption (Ostrom et al., 2007). $\delta^{15}N^{bulk}$-N_2O remained approximately 8 to 10‰ in waters deeper than 1000 m depth. The $\delta^{15}N^{\alpha}$-N_2O nearly followed the same distribution pattern as $\delta^{15}N^{bulk}$-N_2O, with overall higher values (up to 42.5‰) in the ETNP ODZ (Figure 5C). The $\delta^{15}N^{\beta}$-N_2O contrasted with the $\delta^{15}N^{bulk}$-N_2O and $\delta^{15}N^{\alpha}$-N_2O distributions, with highest values (up to 9.4‰) within the first 500 m flanking the equator and lowest values (minimum of -11.3‰) in the ETNP ODZ (Figure 5D). The $\delta^{18}O$-N_2O decreased along the north-south gradient of the P18 transect, with highest values (up 100‰) in the ETNP ODZ (Figure 5E). $\delta^{18}O$-N_2O remained fairly constant below 2000 m depth and increased from ~48 to 56‰ in CDW from south to north along the P18 transect. SP distribution was similar to that of $\delta^{15}N^{\alpha}$-N_2O, with lowest values (minimum of -6.1‰) in low O_2 waters (>5 µmol kg^{-1}) in the upper 500 m near the equator and highest values (up to 49‰) in the ETNP ODZ (Figure 5F). In AASW and AAIW at the southern portion of the transect near Antarctica, $\delta^{15}N^{bulk}$, $\delta^{15}N^{\alpha}$, $\delta^{15}N^{\beta}$, $\delta^{18}O$ and SP were close to atmospheric N_2O values (6.2‰ for $\delta^{15}N^{bulk}$, 15.8‰ for $\delta^{15}N^{\alpha}$, -3.4‰ for $\delta^{15}N^{\beta}$, 44.3‰ for $\delta^{18}O$ and 19.2‰ for SP; Kelly et al., 2021). The isotopic signatures of N_2O, together with the observed slight N_2O undersaturation, indicate no N_2O production in this region.

3.4 Relationships between ΔN_2O, AOU and N deficit

The ratio between ΔN_2O/AOU, indicative of cumulative N_2O production yield, increased at low O_2 concentration to 0.3 (Figure 6A). Other high ΔN_2O/AOU ratios observed at higher O_2 concentrations were clearly influenced by the contrasting effect of photosynthesis on AOU, as indicated by higher pH at these shallower isopycnal ranges (Supplementary materials, Figure S1). The lowest SPs were observed at highest ΔN_2O and ΔN_2O/AOU ratios (Figure 6B). Positive relationships between ΔN_2O and AOU were observed in surface waters σ_θ < 26 kg m^{-3} in the ETNP and ETSP (Supplementary materials, Figure S2). No significant relationship between ΔN_2O and AOU was observed at 26 < σ_θ < 27 kg m^{-3} where highest ΔN_2O values were generally observed.

Significant positive relationships between ΔN_2O and DIN deficit were observed in the ETNP (18.5°N – Equator), with an increased slope toward deeper isopycnals where highest ΔN_2O were

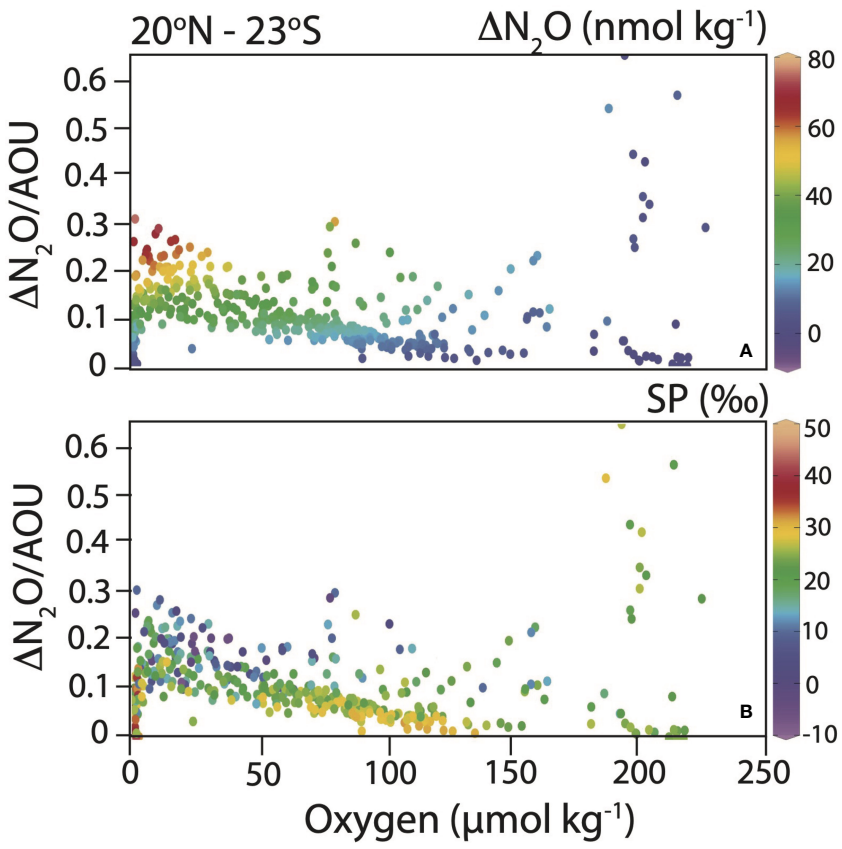

FIGURE 6
ΔN_2O/AOU versus O_2 concentration showing increased N_2O production yield (associated with low SP) under low O_2 conditions. ΔN_2O **(A)** and SP **(B)** are shown as the color of the symbols (see color bars).

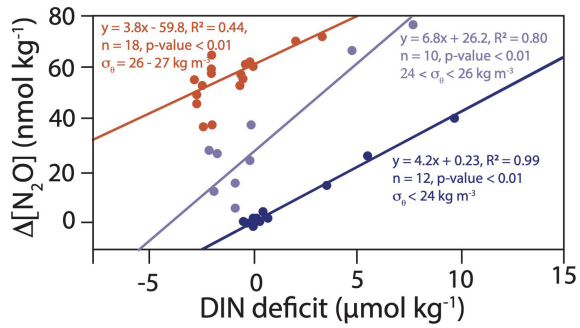

FIGURE 7
DIN deficit versus ΔN_2O for the ETNP (18°N – Equator) (blue dots and lines) and ETSP (Equator – 13S) (red dots and line). In the ETNP, the light and dark blue dots and lines represent different isopycnal ranges.

observed. A significant positive relationship between ΔN_2O and DIN deficit was also observed in the ETSP (Equator – 13°S) for the isopycnal range $26 < \sigma_\theta < 27$ kg m^{-3}. No such relationship was observed in the ETSP surface waters ($\sigma_\theta < 26$ kg m^{-3}) (Figure 7).

4 Discussion

4.1 Sources of the highest ΔN_2O accumulations near the oxycline in the ETNP and ETSP

We observed relatively high N_2O concentrations of up to 84 nmol kg^{-1} (940% supersaturation) near the upper oxycline in offshore waters along the P18 section crossing the ETNP ODZ and the fringe of the ETSP ODZ. High N_2O concentrations of up to ~100 nmol kg^{-1} were also observed offshore near the oxycline in the ETNP ODZ (Trimmer et al., 2016; Kelly et al., 2021). At offshore stations in the ETSP ODZ, Casciotti et al. (2018) observed N_2O concentrations were up to ~70 nmol kg^{-1}, comparable to observations along the P18 line. In contrast, Bourbonnais et al. (2017) observed much higher N_2O concentrations of up to ~190 nmol kg^{-1} in coastal surface waters off Peru in the ETSP ODZ. Differences in N_2O accumulation observed between these different studies appear to mostly relate to productivity (e.g., coastal versus offshore), but there is also evidence for dynamic N_2O cycling at offshore stations. For instance, the El Niño-Southern Oscillation and mesoscale processes such as eddies have been shown to influence N_2O distribution (e.g., Arévalo-Martínez et al., 2016; Ji et al., 2019; Babbin et al., 2020; Monreal et al., 2022)

Yield of N_2O from nitrification increased toward lower $[O_2]$, as also observed in previous studies (e.g., Ryabenko et al., 2012; Ji et al., 2015; Ji et al., 2018; Frey et al., 2020) (Figure 6). If we assume that 138 moles of O_2 are reduced for 16 moles of NH_4^+ nitrified (Ward, 2008), a yield of up to 0.5% N-N_2O mol produced per mol NH_4^+ oxidized is obtained considering the highest ΔN_2O/AOU slope of 0.3. A 0.5% yield falls in the range observed in the Pacific Ocean (Yoshida et al., 1989), but is lower than the maximum N_2O production yield for nitrification reported for ^{15}N-labeled incubation studies (up to ~3% in the ETSP ODZ) (Ji et al., 2018; Frey et al., 2020). However, while nitrification is clearly occurring in surface waters along the P18 transect, as shown by correlations between ΔN_2O and AOU, the data deviate from this relationship on isopycnals where the highest ΔN_2O were observed near the ODZ oxycline (Supplementary materials, Figure S2).

Two different sources of N_2O were observed from the Keeling plot analysis in both the ETNP and ETSP for $[O_2] > 5$ µmol kg^{-1} and $\sigma_\theta < 27$ kg m^{-3} (Figures 8, 9). A break-point analysis was performed in R using the package "segmented" (Muggeo, 2003; Muggeo and Muggeo, 2017) as described in Kelly et al. (2021). The breakpoint was around 33 nmol kg^{-1} ($1/[N_2O] = 0.03$) in both regions. Coincidentally, this analysis divided the data into two main O_2 regimes: 5 µmol kg^{-1} < $[O_2]$ < 100 µmol kg^{-1} and $[O_2] > 100$ µmol kg^{-1} (Table 1). It should be noted that highest ΔN_2O in the ETNP were observed at $[O_2]$ below 5 µmol kg^{-1} and were thus not included in the Keeling plot analysis. Kelly et al. (2021) found a clear relationship between distinct N_2O sources and $[NO_2^-]$, with highest N_2O accumulation at elevated $[NO_2^-]$ (up to ~1 µmol kg^{-1}) in the ETNP. In contrast to Kelly et al. (2021), no such relationship was observed when restricting the dataset to the same isopycnal range ($\sigma_\theta \leq 25$ kg m^{-3}).

The $\delta^{15}N^{bulk}$ of source N_2O varied from 4.0 to 7.2‰ (Table 1). $\delta^{15}N^{bulk}$ is affected by the $\delta^{15}N$ of the substrate and fractionation effects during N_2O production (e.g., Sutka et al., 2006; Frame et al., 2014; Bourbonnais et al., 2017). Similar $\delta^{15}N^{bulk}$ values for source N_2O were reported in the ETSP (Casciotti et al., 2018). These values fall within the expected range for the $\delta^{15}N$ of remineralized NH_4^+, the substrate for nitrification, assuming a $\delta^{15}N$ of sinking particulate matter of 3-15‰ (Altabet et al., 1999; Altabet, 2001; Berelson et al., 2015) in the eastern Pacific and a modest isotope effect during ammonification (Altabet, 1988). N_2O could also be produced by denitrification as the $\delta^{15}N$ of NO_3^- observed in this study (4.5-15.4‰) was also similar to observed $\delta^{15}N^{bulk}$-N_2O values. However, the upper range in $\delta^{15}N$ values for these substrates is needed to reproduce the observed $\delta^{15}N^{bulk}$-N_2O during nitrification and denitrification as both processes are expected to add a lower $\delta^{15}N$ due to isotopic fractionation, unless the substrate is completely consumed, or the reaction is diffusion limited (see Table 1 in Bourbonnais et al., 2017 for a compilation of ε associated with these processes and Ostrom and Ostrom, 2012; Frame et al., 2014).

A high $\delta^{18}O$ (52.3‰) and relatively low $\delta^{15}N^{\alpha}$ (2.7‰) and SP (-9.0‰) were estimated for source N_2O in the ETNP just above the ODZ corresponding to highest ΔN_2O accumulations. In contrast, $\delta^{15}N^{bulk}$, $\delta^{15}N^{\alpha}$, $\delta^{15}N^{\beta}$, $\delta^{18}O$ and SP of source N_2O in surface waters ($[O_2]$ higher than 100 µmol kg^{-1}) were more comparable to atmospheric signatures (Table 1). In the ETSP, the $\delta^{15}N^{\alpha}$ (11.0‰), $\delta^{18}O$ (55.7‰) and SP (9.5‰) of source N_2O were higher than in the ETNP near the oxycline and the SP in oxic surface waters (11.3‰) was significantly lower. The isotopic values of source N_2O observed in surface waters overlying the ODZ in the ETSP contrasted with the values estimated by Casciotti et al. (2018). For instance, the $\delta^{18}O$ was significantly lower and the SP was higher than the values reported by Casciotti et al. (2018) (Table 1). These differences were likely caused by spatial and/or temporal heterogeneity. Moreover, P18 only crossed the fringe of the ETSP ODZ, with $[O_2]$ generally higher than 5 µmol kg^{-1}, except at a few stations/depths.

10.3389/fmars.2023.1137064

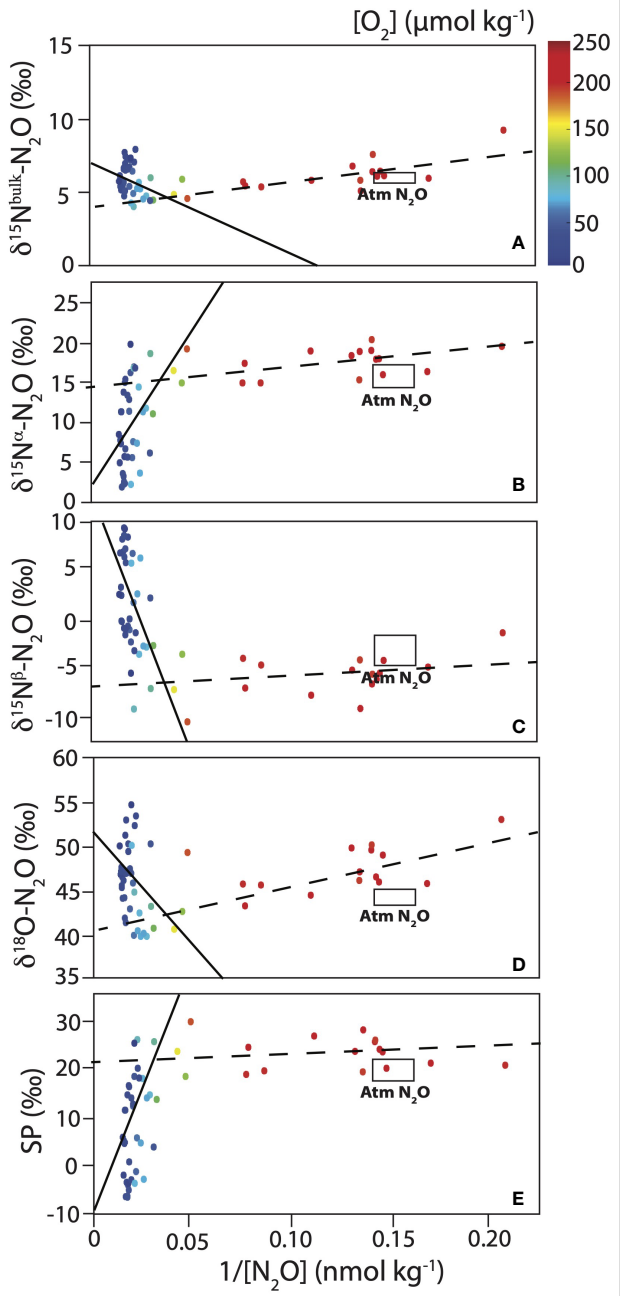

FIGURE 8
Keeling plot analysis for the ETNP (18°N – Equator) for **(A)** $\delta^{15}N^{bulk}$, **(B)** $\delta^{15}N^{\alpha}$, **(C)** $\delta^{15}N^{\beta}$, **(D)** $\delta^{18}O$ and **(E)** SP of N_2O (in ‰). Black lines are linear regressions (full line: 5 µmol kg^{-1} < $[O_2]$ < 100 µmol/kg and dashed line: $[O_2]$ > 100 µmol kg^{-1}). O_2 concentrations are shown as the color of the symbols (see color bar in top panel). Atmosphere N_2O isotopic values are shown as a rectangle (from Kelly et al., 2021). See Table 1 for intercept, R^2 and p-value for the linear regressions.

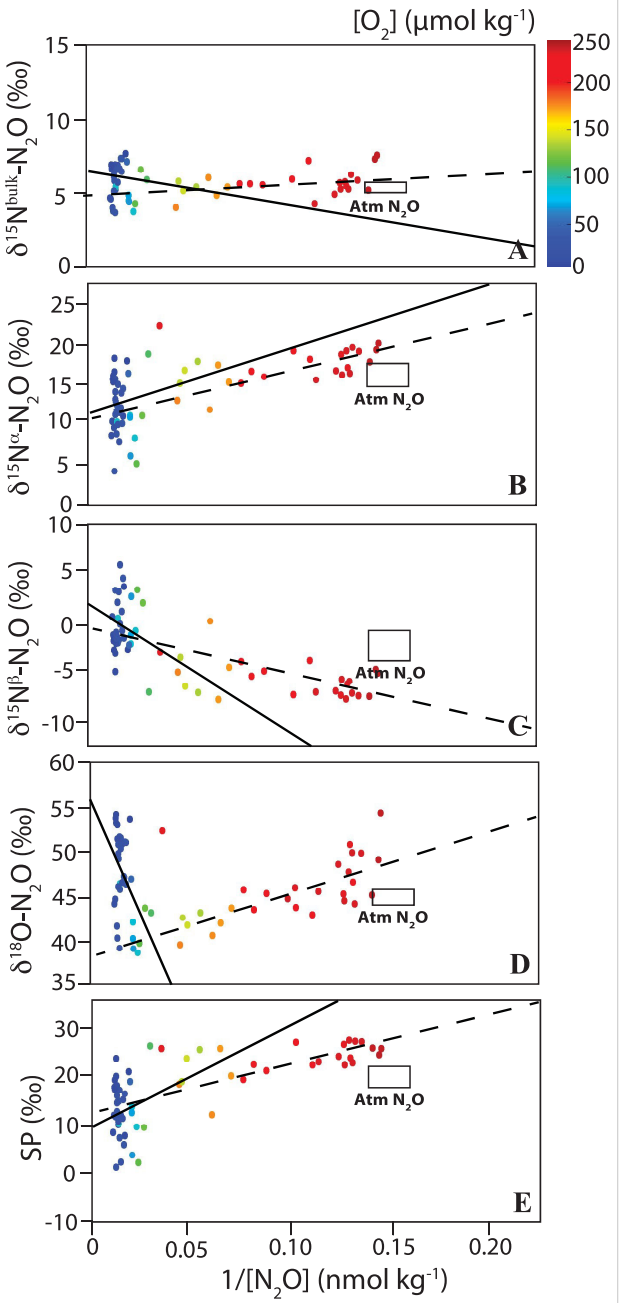

FIGURE 9
Keeling plot analysis for the ETSP (Equator – 13°S) for **(A)** $\delta^{15}N^{bulk}$, **(B)** $\delta^{15}N^{\alpha}$, **(C)** $\delta^{15}N^{\beta}$, **(D)** $\delta^{18}O$ and **(E)** SP of N_2O (in ‰). Black lines are linear regressions (full line: 5 µmol kg^{-1} < $[O_2]$ < 100 µmol kg^{-1} and dashed line: $[O_2]$ > 100 µmol kg^{-1}). O_2 concentrations are shown as the color of the symbols (see color bar in top panel). Atmosphere N_2O isotopic values are shown as a rectangle (from Kelly et al., 2021). See Table 1 for intercept, R^2 and p-value for the linear regressions.

The stable isotopic and isotopomer signatures observed at the highest ΔN_2O and lowest $[O_2]$ near the oxycline in both the ETNP and ETSP are consistent with production from denitrification or nitrifier-denitrification. SP is particularly useful for differentiating N_2O production processes as it is mainly pathway dependent and independent of the isotopic composition of the substrate (Schmidt et al., 2004; Sutka et al., 2004). For instance, formation of N_2O during bacterial denitrification occurs by combining two NO molecules following a *trans* mechanism (Toyoda et al., 2005; Magyar, 2017). This mechanism involves the asymmetrical intermediate *trans*-hyponitrite (-ONNO-) bridging two iron centers; the α N atom and the O comes from NO bonded to Fe_{heme} and the β N atom comes from NO bonded to Fe_B. If the precursor NO molecules are derived from the same substrate, this

10.3389/fmars.2023.1137064

TABLE 1 Intercept (in ‰), R^2, and p-values of linear regressions for Keeling plot analysis under different O_2 regimes and regions/water masses along the P18 line.

	$\delta^{15}N^{bulk}$-N_2O	$\delta^{15}N^{\alpha}$-N_2O	$\delta^{15}N^{\beta}$-N_2O	$\delta^{18}O$-N_2O	SP
ETNP (18.5°N – EQ)					
100 µmol kg^{-1} > $[O_2]$ > 5 µmol kg^{-1} (27 > σ_θ > 23.3 kg m^{-3}) (n = 37)					
Intercept	7.2 ± 0.8	2.7 ± 4.0	11.7 ± 3.5	52.3 ± 3.2	-9.0 ± 7.3
R^2	0.079	0.086	0.19	0.10	0.14
p-value	0.09	0.08	**<0.01**	0.06	0.02
$[O_2]$ > 100 µmol kg^{-1}(surface, σ_θ < 25.7 kg m^{-3}) (n = 18)					
Intercept	4.0 ± 0.4	12.3 ± 14.7	-6.5 ± 1.4	40.8 ± 1.4	20.7 ± 2.5
R^2	0.59	0.038	0.045	0.54	0.06
p-value	**<0.01**	0.4	0.4	**<0.01**	0.3
Deep waters, σ_θ > 27.3 kg m^{-3} (n = 47)					
Intercept	9.1 ± 5.0	16.8 ± 1.1	1.4 ± 0.9	52.7 ± 1.7	15.4 ± 2.0
R^2	0.01	0.39	0.46	0.020	0.45
p-value	0.6	**<0.01**	**<0.01**	0.4	**<0.01**
ETSP (13°S – EQ)					
100 µmol kg^{-1} > $[O_2]$ > 5 µmol kg^{-1}(27 > σ_θ > 26 kg m^{-3}) (n = 34)					
Intercept	6.3 ± 0.9	11.0 ± 2.6	1.6 ± 2.0	55.7 ± 3.3	9.5 ± 4.3
R^2	0.0056	0.0084	0.035	0.17	0.020
p-value	0.7	0.6	0.3	**0.01**	0.4
$[O_2]$ > 100 µmol kg^{-1} (surface waters, σ_θ < 26 kg m^{-3}) (n = 26)					
Intercept	4.9 ± 0.4	10.6 ± 1.2	-0.7 ± 1.2	38.3 ± 1.2	11.3 ± 2.2
R^2	0.12	0.54	0.37	0.59	0.49
p-value	0.08	**<0.01**	**<0.01**	**<0.01**	**<0.01**
Deep waters, σ_θ > 27 kg m^{-3} (n = 26)					
Intercept	7.0 ± 0.2	17.0 ± 0.9	-3.0 ± 1.0	45.5 ± 0.7	20.0 ± 1.8
R^2	0.67	0.34	0.0068	0.41	0.14
p-value	**<0.01**	**<0.01**	0.5	**<0.01**	**<0.01**
AAIW					
Intercept	9.4 ± 0.3	18.1 ± 0.8	0.8 ± 0.6	52.5 ± 0.6	17.2 ± 1.4
R^2	0.42	0.020	0.42	0.67	0.19
p-value	**<0.01**	0.2	**<0.01**	**<0.01**	**<0.01**
Casciotti et al. (2018) - ETSP					
Surface	6.1 ± 1.4	na	na	53.0 ± 3.1	5.4 ± 4.4
Oxycline	7.5 ± 2.2	na	na	50.7 ± 3.6	9.3 ± 2.4
Deep	6.6 ± 0.6	na	na	54.3 ± 0.6	20.1 ± 0.5
Kelly et al. (2021) – ETNP					
Surface	na	6.6 ± 0.5	0.6 ± 0.5	46.3 ± 0.5	6.6 ± 2.3
Oxycline	na	2.9 ± 1.4	-3.8 ± 0.9	53.1 ± 1.3	5.9 ± 0.8

(Continued)

TABLE 1 Continued

	$\delta^{15}N^{bulk}$-N_2O	$\delta^{15}N^{\alpha}$-N_2O	$\delta^{15}N^{\beta}$-N_2O	$\delta^{18}O$-N_2O	SP
Deep	6.2 ± 1.0	16.8 ± 0.	-4.5 ± 0.6	57.3 ± 0.8	21.3 ± 1.0
Atmosphere-equilibrated seawater (Kelly et al., 2021)	6.2 ± 0.4	15.8 ± 1.4	-3.4 ± 1.6	44.3 ± 0.8	19.2 ± 2.9

Standard error of the intercept is reported. P-value associated with a confidence level >90% are in bold. Atmospheric values are from Kelly et al. (2021). na means non available. AAIW temperature and salinity ranges are defined as in Emery (2001) (section 3.1).

mechanism causes little difference between the $\delta^{15}N$ of the α and β N atoms, resulting in a low SP (see Magyar, 2017 for more detail). In contrast, during N_2O formation according to a *cis* mechanism, a first NO molecule binds to one or the other iron center with the second NO molecule binding directly to the first NO, forming a symmetrical intermediate. Cleavage of ^{14}N-O bond is preferred over ^{15}N-O bond, leading to enrichment of the α position and a higher SP. Thus, N_2O produced by nitrification, either by archaea and bacteria, is generally associated with a high SP of 30-38‰ consistent with a *cis*-formation mechanism (Sutka et al., 2003; Sutka et al., 2004; Frame and Casciotti, 2010; Santoro et al., 2011; Löscher et al., 2012) whereas denitrification and nitrifier-nitrification are associated with much lower SPs (~ - 10 to 0‰) (Sutka et al., 2003; Sutka et al., 2004; Toyoda et al., 2005; Frame and Casciotti, 2010).

N_2O produced by denitrification is associated with a low SP of ~ -5 to 0‰ and adds a relatively low $\delta^{15}N$ (especially at the α position) with an isotope effect ($^{15}\varepsilon$) ranging from 13-37‰ (Barford et al., 1999; Sutka et al., 2003; Sutka et al., 2004; Toyoda et al., 2005; Sutka et al., 2006; Frame and Casciotti, 2010). On the other hand, branching fractionation, i.e., the preferential loss of ^{16}O relative to ^{18}O during NO_3^- reduction to N_2O, is expected to lead to high $\delta^{18}O$-N_2O values (Casciotti et al., 2002; Frame et al., 2014). The $\delta^{18}O$-N_2O is affected by both the branching isotope effects ($^{18}\epsilon$) of 25-30‰ for NO_3^- reduction to NO_2^- and 10-12‰ during NO_2^- reduction to N_2O during denitrification as well as the equilibration of NO_2^- O isotope with water (Casciotti et al., 2007; Casciotti and Buchwald, 2012). Nitrifier-denitrification is associated with a SP of -10-0‰ and adds a lower $\delta^{15}N$ compared to denitrification due to a larger $^{15}\varepsilon$ ranging from 31-58‰. Furthermore, an effective O isotope effect ($^{18}\epsilon$) of 8-12‰ was reported for NO_2^- reduction to N_2O during nitrifier denitrification (Sutka et al., 2003; Sutka et al., 2004; Sutka et al., 2006; Frame and Casciotti, 2010). Newly produced $\delta^{18}O$-N_2O values during nitrification and nitrifier denitrification are thus generally lower (13-35‰; Snider et al., 2012). Accordingly, low source $\delta^{18}O$-N_2O values were observed at $[O_2] > 100$ μmol kg^{-1} in the ETNP and ETSP whereas higher values were observed at deeper isopycnal ranges overlying the ODZs (Table 1), consistent with the dominance of N_2O production by nitrification in surface waters and denitrification at lower O_2 concentrations near the oxycline.

Kelly et al. (2021) similarly observed two distinctive sources of N_2O in the ETNP above the $\sigma_\theta < 25$ kg m^{-3} isopycnal. SPs of 6-8‰ were observed. Based on an isotopic mass balance and assuming that the SPs for N_2O produced during nitrification and denitrification are 30-38‰ and 0‰, respectively (Sutka et al., 2003; Sutka et al., 2004; Toyoda et al., 2005; Frame and Casciotti, 2010; Santoro et al., 2011; Löscher et al., 2012), about 80% of the N_2O production was attributed to denitrification or nitrifier-denitrification. Bourbonnais et al. (2017) and Casciotti et al. (2018) also observed low SPs (-3 to 10‰) corresponding to large ΔN_2O accumulation near the oxycline above the ETSP ODZ. The much lower SP observed in the ETNP in this study (-9‰) preclude any contribution from nitrification. The higher SP (9.5‰) for source N_2O observed at low $[O_2]$ near the fringe of the ETSP ODZ suggests a relatively minor contribution from nitrification (~1/3) and is consistent with the value reported by Casciotti et al. (2018). However, hybrid N_2O formation by archaea, where one atom is derived from nitric oxide (NO; from NO_2^-) and the other from hydroxylamine (NH_2OH; from NH_4^+) was shown to be an important production pathway in marine environments and could possibly contribute to endmember signatures estimated from the Keeling plot analysis (Stieglmeier et al., 2014; Kozlowski et al., 2016; Trimmer et al., 2016; Frame et al., 2017). Frey et al. (2020) showed that hybrid N_2O production accounts for 70-85% of the total N_2O production from NH_4^+ oxidation using ^{15}N-labeled incubation experiments in the ETSP. SP may, in part, reflect the relative $\delta^{15}N$ of the substrates for the α and β positions during hybrid archaeal N_2O production rather than being indicative of a particular pathway (Casciotti et al., 2018). Therefore, if lower SP could be produced by archaeal hybrid N_2O production, the fraction of denitrification needed to explain low SP signatures associated with high N_2O supersaturations observed above or in the ODZs in this and previous studies would further decrease (Bourbonnais et al., 2017; Casciotti et al., 2018; Kelly et al., 2021).

The observed relationships between ΔN_2O and DIN deficit at isopycnals $\sigma_\theta < 26$ kg m^{-3} and the absence of clear relationships between ΔN_2O and $[NO_2^-]$ further support a role for denitrification (rather than nitrifier-denitrification) as the dominant N_2O production pathway in both the ETSP and the ETNP. The decreased slope for the ΔN_2O versus DIN deficit relationship toward surface isopycnal ranges observed in the ETNP suggests decreased N_2O yield at higher $[O_2]$ concentrations or mixing/dilution of N_2O produced by denitrification advected from below, especially for upwelling waters near the equator. The $\delta^{15}N$ of NO_3^- provides more insights into N_2O sources yet these measurements were mostly available at ETSP stations. A plot of SP versus $\Delta^{15}N$ ($\delta^{15}N$-NO_3^- - $\delta^{15}N$-N_2O) showed that some of the highest ΔN_2O datapoint indeed fell within the expected compositional fields for N_2O production by bacterial denitrification ($\Delta\delta^{15}N$= 0-35‰, SP: -5-0‰) (Wankel et al. (2017) and references therein, Supplementary Figure S3). Some high ΔN_2O were associated with relatively high SPs (> 10‰), showing the overprinting effect of N_2O consumption during denitrification (Ostrom et al., 2007). Compositional field analysis (Figure S3) also suggests production by either archaeal and bacterial ammonia oxidation at higher $[O_2]$

and lower ΔN_2O. Bourbonnais et al. (2017) also invoked incomplete denitrification as a major pathway for extreme N_2O accumulation in newly upwelled surface waters off Peru based on the absence of a relationship between ΔN_2O and apparent O_2 utilization and significant relationships between NO_3^- and N_2O isotopes. The dominance of denitrification for N_2O production near the oxycline is also supported by ^{15}N-tracer incubation studies in the ETSP ODZ. N_2O production rates were indeed one order of magnitude higher for denitrification compared to ammonia oxidation under low-O_2 conditions at the ΔN_2O maximum just above the ETSP ODZ (Ji et al., 2015; Frey et al., 2020).

4.2 Sources of N_2O below the ETNP and ETSP ODZs and in AAIW

N_2O sources in deep ETNP and ETSP were also investigated using Keeling plot analysis (Supplementary materials, Figure S4 and Table 1). A deeper isopycnal range (σ_θ > 27.3 kg $m^{-3}$was selected for the ETNP due to the deeper ODZ at this location as in a previous study (Kelly et al., 2021). An isopycnal range with σ_θ > 27 kg m^{-3} was selected for the ETSP comparable to the σ_θ range in Casciotti et al. (2018). N_2O source values of 9.1‰ ($\delta^{15}N^{bulk}$), 16.8‰ ($\delta^{15}N^{\alpha}$), 1.4‰ ($\delta^{15}N^{\beta}$), 52.7‰ ($\delta^{18}O$) and 15.4‰ (SP) were estimated below the ETNP ODZ (Table 1). In the ETSP, the Keeling plot analysis revealed values of 7.0‰ ($\delta^{15}N^{bulk}$), 17.0‰ ($\delta^{15}N^{\alpha}$), -3.0‰ ($\delta^{15}N^{\beta}$), 45.5‰ ($\delta^{18}O$) and 20.0‰ (SP). The generally higher $\delta^{15}N^{\beta}$ as well as lower $\delta^{18}O$ and SP compared to prior studies (Casciotti et al., 2018; Kelly et al., 2021) might be the result of a lesser influence from N_2O production and consumption in the ODZ since our analysis also included equatorial waters. Overall, these isotopic signatures suggest the dominance of N_2O production by nitrification in deeper waters below the ETNP and ESTP ODZs. In fact, our results are more in line with a N_2O source from nitrification as a relatively low $\delta^{18}O$ is expected for this process (i.e., 13-35‰; Snider et al., 2012).

The sources of N_2O were investigated by restricting the Keeling plot analysis for the absolute salinity/potential temperature ranges characteristic of AAIW as described in section 3.1. The analysis was restricted to 60°S to 20°S, even if the northernmost extent of AAIW is found below the ETNP, to eliminate possible effects of the ETNP and ETSP ODZs on N_2O production in this water mass.

ΔN_2O clearly increased from -0.89 nmol kg^{-1} (-7.4% supersaturation) at 52°S to up to 20.6 nmol kg^{-1} (180% supersaturation) in the intermediate water mass AAIW (Figure 5), which is comparable to values observed by Carrasco et al. (2017). Keeling plot analysis revealed a N_2O source with a $\delta^{15}N^{bulk}$ = 9.4‰, $\delta^{15}N^{\alpha}$ = 18.1‰, $\delta^{15}N^{\beta}$ = 0.8‰, $\delta^{18}O$ = 52.5‰, and SP = 17.2‰ (Table 1). The relatively high SP suggests that N_2O is mainly derived from nitrification, consistent with previous studies (Casciotti et al., 2018; Toyoda et al., 2019; Kelly et al., 2021). The positive significant relationship observed between ΔN_2O and AOU in the AAIW water mass observed in this study and Carrasco et al. (2017) further supports this interpretation (Supplementary materials, Figure S2). The lower $\delta^{15}N^{\beta}$ and higher $\delta^{18}O$ and SP might reflect the influence of N_2O consumption in the ODZs in these prior studies.

4.3 Isotopic signatures of N_2O consumption in the ETNP

High values of $\delta^{15}N^{\alpha}$, $\delta^{18}O$ and SP and low or negative ΔN_2O were observed at $[O_2]$ < 5 µmol kg^{-1} in the ETNP ODZ, which are clear signatures of N_2O consumption (Figure 5). During N_2O reduction to N_2 gas, the N-O bond is broken, leaving the remaining substrate (N_2O) enriched in ^{15}N and ^{18}O. The α position in N_2O is preferentially enriched in ^{15}N compared to the β position since it is directly attached to the O atom being cleaved (e.g., Popp et al., 2002; Toyoda et al., 2002). Thus, ε for the α N atom (6.6-9.1‰) and $\delta^{18}O$ (10.9-15‰) are relatively large with only a small or negligible ε for β N atom (Ostrom et al., 2007). Notably, while $\delta^{15}N^{\alpha}$ and $\delta^{18}O$ increased in the ODZ, $\delta^{15}N^{\beta}$ generally decreased, as also observed in previous ETNP and ETSP ODZ studies (Bourbonnais et al., 2017; Casciotti et al., 2018; Kelly et al., 2021) (Figure 5). This trend is not expected during pure N_2O consumption.

The slope for the relationship between $\delta^{18}O$ versus and $\delta^{15}N^{\alpha}$ (1.6 ± 0.1) was indistinguishable from the expected slope (i.e., 1.7) during N_2O consumption in soils and pure denitrifier cultures (Ostrom et al., 2007). However, the observed slope for $\delta^{18}O$-N_2O versus SP (0.8 ± 0.1) clearly deviated from the expected value of 2.2 for pure N_2O reduction (Ostrom et al., 2007) (Figure 10). A wider

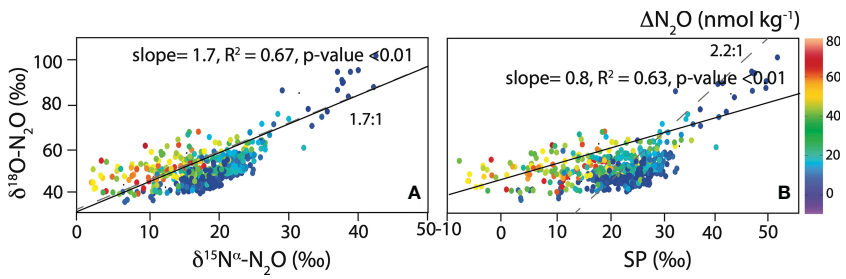

FIGURE 10
$\delta^{18}N$-N_2O versus **(A)** $\delta^{15}N^{\alpha}$-N_2O, and **(B)** SP. The slope expected for pure denitrification is indicated with dashed grey lines (Ostrom et al., 2007). ΔN_2O concentrations are shown as the color of the symbols (see color bar in top panel). Linear regressions for O_2 < 5 µmol kg^{-1} are shown with black lines.

range of 1.3-3.3 for $\delta^{18}O$ versus SP during consumption by denitrification was also reported for soil mesocosms, which is still higher than the slope observed in this study (Lewicka-Szczebak et al., 2017). This observation is consistent with previous studies in marine ODZs, reporting slopes for $\delta^{18}O$ versus SP ranging between (0.9-1.8) (Bourbonnais et al., 2017; Casciotti et al., 2018; Kelly et al., 2021). For instance, in the ODZ off Peru, the slope for increase in $\delta^{18}O$-N_2O versus SP deviates from what is expected during pure denitrification, mostly due to a decrease in $\delta^{15}N^{\beta}$ within the ODZ (Bourbonnais et al., 2017; Casciotti et al., 2018). This trend showing a decreasing $\delta^{15}N^{\beta}$ associated with high $\delta^{18}O$-N_2O has also been observed in other ODZs and marine anoxic environments (Yamagishi et al., 2005; Westley et al., 2006; Yamagishi et al., 2007; Farías et al., 2009; Kelly et al., 2021). The cause for the decreasing $\delta^{15}N^{\beta}$ in the ODZ will be further discussed below.

In this study, apparent isotope effects (ε_{app}) were derived for all isopycnal ranges within the ETNP ODZ at $[O_2]$ < 5 µmol kg^{-1}, where N_2O consumption is known to occur (Dalsgaard et al., 2014). This approach was used in Casciotti et al. (2018) to further investigate if a decrease in $\varepsilon^{18}O$ or increase in εSP could explain the deviation from the expected slope for $\delta^{18}O$-N_2O versus SP during pure N_2O consumption in the ETSP ODZ. Apparent isotope effects calculated for all isopycnal ranges were 3.6‰ for $^{15}N^{bulk}$, 9.4‰ for $^{15}N^{\alpha}$, -2.3‰ for $^{15}N^{\beta}$, 12.0‰ for ^{18}O and 11.7‰ for SP (Table 2 and Figure 11). The ε_{app} for $^{15}N^{bulk}$ was slightly lower than the range reported for pure culture by Ostrom et al. (2007). Yet, the

TABLE 2 Apparent isotope effects for N_2O consumption (in ‰) calculated using a closed system Rayleigh model for $^{15}N^{bulk}$, $^{15}N^{\alpha}$, $^{15}N^{\beta}$, ^{18}O and SP for the ETNP.

	This study	Ostrom et al. (2007) Pure culture	Casciotti et al. (2018) ETSP ODZ	Kelly et al. (2021) ETNP ODZ
$\epsilon^{15}N^{bulk}$	3.6 ± 0.4 R^2 = 0.65, P < 0.01	4.1 – 6.6	na	na
$\epsilon^{15}N^{\alpha}$	9.4 ± 0.9 R^2 = 0.66, P < 0.01	6.6 – 9.1	na	11.8 ± 2.5
$\epsilon^{15}N^{\beta}$	-2.3 ± 0.6 R^2 = 0.20, P < 0.01	1.6 – 2.2	na	-2.0 ± 2.0
$\epsilon^{18}O$	12.0 ± 1.3 R^2 = 0.60, P < 0.01	10.9 – 15.0	14.5 – 25.6	20.2 ± 6.1
εSP	11.7 ± 1.4 R^2 = 0.57, P < 0.01	5.0 - 6.8	11.6 – 17.5	na
$\epsilon^{18}O/\epsilon^{15}N^{bulk}$	3.4 ± 0.5 R^2 = 0.91, P < 0.01	2.5 ± 0.2	na	na
$\epsilon^{18}O/\epsilon SP$	1.0 ± 0.2	2.2	0.9 – 1.5	na

Only samples with $[O_2]$ < 5 µmol kg^{-1} were considered. Isotope effects observed in pure laboratory culture and field studies in the ETNP and ETSP ODZs are also listed (Ostrom et al., 2007; Casciotti et al., 2018; Kelly et al., 2021). Standard error of the slope is shown. na means non available.

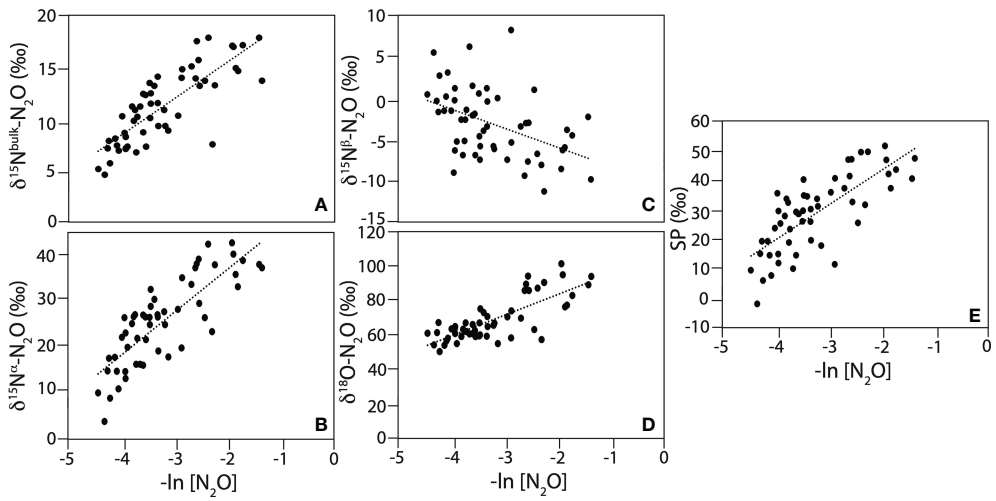

FIGURE 11
Apparent isotope effects for **(A)** $\delta^{15}N^{bulk}$-N_2O, **(B)** $\delta^{15}N^{\alpha}$-N_2O, **(C)** $\delta^{15}N^{\beta}$-N_2O, **(D)** $\delta^{18}O$-N_2O, and **(E)** SP calculated for $[O_2]$ < 5 µmol kg^{-1}. Black lines are linear regressions. Linear regression outputs are reported in Table 2.

ε_{app} for $^{15}N^{\alpha}$ and $^{15}N^{\beta}$ were comparable to values (11.8‰ and -2‰, respectively) estimated by Kelly et al. (2021) in the ETNP ODZ. Notably, the negative isotope effect for $^{15}N^{\beta}$ indicates a decrease in $\delta^{15}N^{\beta}$ as N_2O is reduced to N_2 within the ODZ. The ε for ^{18}O calculated in this study was significantly lower than the values (14.5 – 20.2‰) estimated in other ODZ marine field studies (Casciotti et al., 2018; Kelly et al., 2021), but comprised within the range observed for pure culture (10.9 – 15‰) (Ostrom et al., 2007). The ε for SP was higher than for pure culture (5.0 – 6.8‰) but comparable to values estimated in the ETSP ODZ (11.6 – 17.5‰) (Casciotti et al., 2018). Casciotti et al. (2018) observed different apparent isotope effects at different isopycnal ranges within the ETSP ODZ. They observed a decrease in the $\varepsilon^{18}O$ within the ODZ (from 25.6‰ in the upper, to 19.6‰ in the middle and 14.5‰ in the lower ODZ) while the εSP increased slightly and then decreased (17.5‰ in the upper to 21.7‰ in the middle to 11.6‰ in the lower ODZ). A more detailed analysis by isopycnal ranges (upper, middle, and lower ODZ) could however not reproduce observed trends in Casciotti et al. (2018) for the P18 transect. For instance, ε_{app} for ^{18}O (13.9‰ in the upper ODZ to 11.4‰ in the middle, and 16.2‰ in the lower ODZ) and SP (14.2‰ in the upper ODZ to 7.5‰ in the middle, and 17.9‰ in the lower ODZ) both decreased toward the middle ODZ and then increased in the deeper ODZ (Supplementary materials, Figure S5). The slope for $\varepsilon^{18}O$ versus εSP also gradually decreased from 1.6 to 0.65 instead of being lowest in the middle ODZ. Irrespective of the observed trends, using a modeling approach and isotope values of substrates (NO_3^- and $N^{18}O_2^-$) during denitrification, previous studies attributed the lower $\varepsilon^{18}O$:εSP to an increase in SP due to a decrease in $\delta^{15}N^{\beta}$ rather than a decrease in $\varepsilon^{18}O$ or increase in εSP in both the ETNP and ESTP ODZs (Casciotti et al., 2018; Kelly et al., 2021).

Several hypotheses have been proposed to explain the decreasing $\delta^{15}N^{\beta}$ in ODZ waters, including concurrent N_2O production *via* denitrification of NO_3^- with a site preference >0‰ (Schmidt et al., 2004; Casciotti et al., 2018; Kelly et al., 2021). Rate experiments as well as prior stable abundance isotopic studies suggest concurrent N_2O production and consumption as well as a rapid N_2O turnover in the ODZ (Farías et al., 2009; Babbin et al., 2015; Ji et al., 2015; Bourbonnais et al., 2017; Casciotti et al., 2018; Frey et al., 2020; Kelly et al., 2021). Casciotti et al. (2018) modeled N_2O cycling at steady-state in the ODZ using both $\delta^{15}N$ and $\delta^{18}O$ of substrate molecules (NO_2^- and NO_3^-) during denitrification. N_2O isotopic signatures were only reproduced when NO_3^- was used as the substrate and implying a site preference >0‰ (i.e., greater fractionation at the $^{15}N^{\beta}$ position relative to the $^{15}N^{\alpha}$) during N_2O production by denitrification. This suggests that an internal (rather than ambient) pool of NO_2^- is used during denitrification as further discussed in Casciotti et al. (2018). Accordingly, a relatively long residence time was estimated for ambient NO_2^- (in the order of months) in the primary NO_2^- maximum and low-O_2 waters based on rates of abiotic O isotope exchange between nitrite and water (Buchwald and Casciotti, 2013; Bourbonnais et al., 2015). In another modeling study, a non-steady-state N_2O cycling as well as an ambient NO_2^- substrate source (with a $\delta^{15}N$ as low as -30‰) or a SP of ~25‰ during concurrent N_2O production by denitrification were required to explain the observed low $\delta^{15}N^{\beta}$ values in the ETNP ODZ (Kelly et al., 2021). The low $\delta^{15}N^{\beta}$ of N_2O could also result from an alternate mechanism in the ODZ, such as N_2O production from AO archaea and bacteria, which is associated with a high SP (30-38‰; Sutka et al., 2003; Sutka et al., 2004; Frame and Casciotti, 2010; Santoro et al., 2011; Löscher et al., 2012). For instance, an archaeal AO isolated from ODZs (*Nitrosopumilus maritimus*) produced both N_2 and O_2 under dark anaerobic conditions, following a pathway that involves N_2O as an intermediate (Kraft et al., 2022). Yet, N_2O production rates from AO based on ^{15}N-labeled experiments were relatively low (up to 0.1 nmol L^{-1} d^{-1}) and generally at least one order of magnitude lower than N_2O production rates from NO_3^- (denitrification) under anoxic conditions in the ETSP ODZ (Frey et al., 2020).

The idea of denitrification with a site preference >0‰ is not new (i.e., see Schmidt et al., 2004). Several studies invoked N_2O production during denitrification with a site preference >0‰ in the ETNP and ETSP ODZs and Canadian Arctic bottom waters influenced by sedimentary processes (Casciotti et al., 2018; Lehmann et al., 2019; Kelly et al., 2021). Some variability in the SP of N_2O produced by denitrification was reported for different bacterial strains. For instance, Toyoda et al. (2005) observed a high SP of 22 to 24‰ for N_2O production during denitrification by *Pseudomonas fluorescens*, suggesting a symmetrical intermediate (i.e., *cis* formation mechanism). These observations for denitrifying bacteria are analogous to the wide range of SPs (15.8 – 37.1‰) that have been reported for different fungal species and strains (Maeda et al., 2015; Lazo-Murphy et al., 2022). These data challenge the conventional view that fungal denitrification fits into narrow compositional fields with relatively high SP values. Similarly, it is possible that denitrifying microbial consortia thriving under different O_2 regimes are associated with variable SPs, but this hypothesis remains to be verified.

5 Concluding remarks

This study presents oceanic N_2O concentration, stable isotope and isotopomer data of unprecedently high spatial resolution along the P18 line in the eastern Pacific sampled in 2016/2017. Highest ΔN_2O accumulations (up to 940% supersaturation) were observed close to the oxycline in both the ETNP and the fringe of the ETSP ODZ. N_2O yield from AOU increased at lower [O_2], consistent with previous studies. Keeling plot analysis identified two distinct sources of N_2O at different [O_2] regimes. At lower [O_2] concentrations close to the oxycline in both ODZs, where highest ΔN_2O were observed, SP of source N_2O was relatively low, suggesting production from denitrification (or nitrifier-denitrification). Relationships between ΔN_2O and DIN deficit and the isotopic composition of $\delta^{15}N$ of the substrate (NO_3^-) further suggest that denitrification is the dominant process at low [O_2] concentrations. SP generally increased in more oxygenated surface waters, suggesting a greater contribution from nitrification. The isotopic composition of source N_2O in deeper waters of the ETNP and ETSP as well as in AAIW also suggested that nitrification was the main pathway for N_2O formation.

The $\delta^{18}O$ versus $\delta^{15}N^{\alpha}$ relationship showed a slope characteristic of N_2O consumption during denitrification in low O_2 waters. Isotope

effects calculated for N_2O consumption were consistent with previous field and laboratory studies (Ostrom et al., 2007; Casciotti et al., 2018; Kelly et al., 2021). Yet, $\delta^{15}N^{\beta}$ decreased (rather than the predicted no change or slight increase during denitrification) in the ODZ, which was also observed by previous studies (e.g., Bourbonnais et al., 2017; Casciotti et al., 2018; and Kelly et al., 2021). These signatures are best explained by concurrent N_2O production (from NO_3^- or NO_2^-) with a site preference >0‰, an ambient NO_2^- source with a low $\delta^{15}N$ and non-steady-state conditions (e.g., Kelly et al., 2021). Clearly, more research is needed to elucidate the SP and its variability for diverse denitrifying bacterial strains living in marine ODZs as current values are mostly from terrestrial environments (e.g., Toyoda et al., 2005). Some contribution from an alternative N_2O production pathway is also possible, for example anaerobic AO (see Kraft et al., 2022).

This study establishes a benchmark against which to evaluate changes in N_2O cycling for future decadal occupations of the P18 line. ODZ are currently expanding (Stramma et al., 2013), with unknown impacts on N_2O cycling. The vertical expansion of ODZs not only increases the volume of low-O_2 waters where N_2O is potentially produced but also increases N_2O exchange with the atmosphere. However, co-occurring warming causes stronger stratification, which could reduce mixing and N_2O outgassing to the atmosphere. At this point, it is unclear which mechanism will dominate. Thus, more observational data is needed to evaluate the impacts of ODZs expansion on marine N_2O cycling and atmospheric emissions.

Data availability statement

The datasets presented in this study can be found in online repositories. The names of the repository/repositories and accession number(s) can be found below: https://cchdo.ucsd.edu/cruise/33RO20161119.

Author contributions

AB, SD, and MA designed the study. AB analyzed stable isotope and isotopomer samples. BC analyzed N_2O concentration and CFC/SF_6 samples and RS calculated the transit time distributions. AB wrote the manuscript with input from all co-authors. All authors contributed to the article and approved the submitted version.

Funding

This study was funded through a GO-SHIP National Science Foundation (NSF) postdoctoral Fellowship to AB (NSF OCE-1437015) and NSF OCE-2023545 that covered publication costs. MA and SD acknowledge support from NSF (OCE-1851361 and OCE-1947822). BC and RS were supported by the National Oceanic and Atmospheric Administration's Global Ocean Monitoring and Observations program.

Acknowledgments

We thank the captain and crew of the NOAA R/V Ronald Brown for their support during the P18 research expedition. We also thank the scientific party, especially Brendan Carter, chief scientist during leg 1 of P18 and Alexander Sidelev for collecting N_2O stable isotope and isotopomer samples during leg 2.

Conflict of interest

The authors declare that the research was conducted in the absence of any commercial or financial relationships that could be construed as a potential conflict of interest.

Publisher's note

Supplementary material

The Supplementary Material for this article can be found online at: https://www.frontiersin.org/articles/10.3389/fmars.2023.1137064/full#supplementary-material

References

Altabet, M. A. (1988). Variations in nitrogen isotopic composition between sinking and suspended particles: Implications for nitrogen cycling and particle transformation in the open ocean. *Deep Sea Res. Part A. Oceanographic Res. Papers* 35 (4), 535–554. doi: 10.1016/0198-0149(88)90130-6

Altabet, M. A. (2001). Nitrogen isotopic evidence for micronutrient control of fractional NO_3^- utilization in the equatorial pacific. *Limnol. Oceanogr.* 46 (2), 368–380. doi: 10.4319/lo.2001.46.2.0368

Altabet, M. A. (2006). "Isotopic tracers of the marine nitrogen cycle: present and past," in *Marine organic matter: Chemical and biological markers. the handbook of environmental chemistry*. Ed. J. Volkman (Berlin: Springer-Verlag), pp251–pp293.

Altabet, M. A., Pilskaln, C., Thunell, R., Pride, C., Sigman, D., Chavez, F., et al. (1999). The nitrogen isotope biogeochemistry of sinking particles from the margin of the Eastern north pacific. *Deep Sea Res. Part I: Oceanographic Res. Papers* 46 (4), 655–679. doi: 10.1016/S0967-0637(98)00084-3

Altabet, M. A., Wassenaar, L. I., Douence, C., and Roy, R. (2019). A Ti (III) reduction method for one-step conversion of seawater and freshwater nitrate into N2O for stable isotopic analysis of $^{15}N/^{14}N$, $^{18}O/^{16}O$ and $^{17}O/^{16}O$. *Rapid Commun. Mass Spectrometry* 33 (15), 1227–1239. doi: 10.1002/rcm.8454

Arévalo-Martínez, D. L., Kock, A., Löscher, C. R., Schmitz, R. A., and Bange, H. W. (2015). Massive nitrous oxide emissions from the tropical south pacific ocean. *Nat. Geosci.* 8 (7), 530–533. doi: 10.1038/ngeo2469

Arévalo-Martínez, D. L., Kock, A., Löscher, C. R., Schmitz, R. A., Stramma, L., and Bange, H. W. (2016). Influence of mesoscale eddies on the distribution of nitrous oxide in the eastern tropical south pacific. *Biogeosciences* 13 (4), 1105–1118. doi: 10.5194/bg-13-1105-2016

Babbin, A. R., Bianchi, D., Jayakumar, A., and Ward, B. B. (2015). Rapid nitrous oxide cycling in the suboxic ocean. *Science* 348 (6239), 1127–1129. doi: 10.1126/science.aaa8380

Babbin, A. R., Boles, E. L., Mühle, J., and Weiss, R. F. (2020). On the natural spatio-temporal heterogeneity of south pacific nitrous oxide. *Nat. Commun.* 11 (1), 1–9. doi: 10.1038/s41467-020-17509-6

Bakker, D. C., Bange, H. W., Gruber, N., Johannessen, T., Upstill-Goddard, R. C., Borges, A. V., et al. (2014). Air-sea interactions of natural long-lived greenhouse gases (CO_2, N_2O, CH_4) in a changing climate. *Ocean-Atmosphere Interactions of Gases and Particles*. (Switzerland AG: Springer Nature), pp113–169.

Bange, H. W., Andreae, M. O., Lal, S., Law, C. S., Naqvi, S. W. A., Patra, P. K., et al. (2001). Nitrous oxide emissions from the Arabian Sea: A synthesis. *Atmospheric Chem. Phys.* 1 (1), 61–71. doi: 10.5194/acp-1-61-2001

Barford, C. C., Montoya, J. P., Altabet, M. A., and Mitchell, R. (1999). Steady-state nitrogen isotope effects of N_2 and N_2O production in paracoccus denitrificans. *Appl. Environ. Microbiol.* 65 (3), 989–994. doi: 10.1128/AEM.65.3.989-994.1999

Berelson, W. M., Haskell, W. Z.II, Prokopenko, M., Knapp, A. N., Hammond, D. E., Rollins, N., et al. (2015). Biogenic particle flux and benthic remineralization in the Eastern tropical south pacific. *Deep Sea Res. Part I: Oceanographic Res. Papers* 99, 23–34. doi: 10.1016/j.dsr.2014.12.006

Bourbonnais, A., Altabet, M. A., Charoenpong, C. N., Larkum, J., Hu, H., Bange, H. W., et al. (2015). N-loss isotope effects in the Peru oxygen minimum zone studied using a mesoscale eddy as a natural tracer experiment. *Global Biogeochemical Cycles* 29 (6), 793–811. doi: 10.1002/2014GB005001

Bourbonnais, A., Lehmann, M. F., Waniek, J. J., and Schulz-Bull, D. E. (2009). Nitrate isotope anomalies reflect N_2 fixation in the Azores front region (subtropical NE Atlantic). *J. Geophys. Res.: Oceans* 114 (C3). doi: 10.1029/2007JC004617

Bourbonnais, A., Letscher, R. T., Bange, H. W., Echevin, V., Larkum, J., Mohn, J., et al. (2017). N_2O production and consumption from stable isotopic and concentration data in the Peruvian coastal upwelling system. *Global Biogeochemical Cycles* 31 (4), 678–698. doi: 10.1002/2016GB005567

Bourbonnais, A., Frey, C., Sun, X., Bristow, L. A., Jayakumar, A., Ostrom, N. E., et al. (2021). Protocols for assessing transformation rates of nitrous oxide in the water column. *Front. Mar. Sci.* 8, 611937. doi: 10.3389/fmars.2021.611937

Buchwald, C., and Casciotti, K. L. (2010). Oxygen isotopic fractionation and exchange during bacterial nitrite oxidation. *Limnol. Oceanogr.* 55 (3), 1064–1074. doi: 10.4319/lo.2010.55.3.1064

Buchwald, C., and Casciotti, K. L. (2013). Isotopic ratios of nitrite as tracers of the sources and age of oceanic nitrite. *Nat. Geosci.* 6(4), 308–313.

Caranto, J. D., and Lancaster, K. M. (2017). Nitric oxide is an obligate bacterial nitrification intermediate produced by hydroxylamine oxidoreductase. *Proc. Natl. Acad. Sci.* 114 (31), 8217–8222. doi: 10.1073/pnas.1704504114

Carrasco, C., Karstensen, J., and Farias, L. (2017). On the nitrous oxide accumulation in intermediate waters of the eastern south pacific ocean. *Front. Mar. Sci.* 4, 24. doi: 10.3389/fmars.2017.00024

Casciotti, K. L., Böhlke, J. K., McIlvin, M. R., Mroczkowski, S. J., and Hannon, J. E. (2007). Oxygen isotopes in nitrite: Analysis, calibration, and equilibration. *Analytical Chem.* 79 (6), 2427–2436. doi: 10.1021/ac061598h

Casciotti, K. L., and Buchwald, C. (2012). Insights on the marine microbial nitrogen cycle from isotopic approaches to nitrification. *Front. Microbiol.* 3, 356. doi: 10.3389/fmicb.2012.00356

Casciotti, K. L., Forbes, M., Vedamati, J., Peters, B. D., Martin, T. S., and Mordy, C. W. (2018). Nitrous oxide cycling in the Eastern tropical south pacific as inferred from isotopic and isotopomeric data. *Deep Sea Res. Part II: Topical Stud. Oceanogr.* 156, 155–167. doi: 10.1016/j.dsr2.2018.07.014

Casciotti, K. L., Sigman, D. M., Hastings, M. G., Böhlke, J. K., and Hilkert, A. (2002). Measurement of the oxygen isotopic composition of nitrate in seawater and freshwater using the denitrifier method. *Analytical Chem.* 74 (19), 4905–4912. doi: 10.1021/ac020113w

Chang, B. X., Devol, A. H., and Emerson, S. R. (2010). Denitrification and the nitrogen gas excess in the eastern tropical south pacific oxygen deficient zone. *Deep Sea Res. Part I: Oceanographic Res. Papers* 57 (9), 1092–1101. doi: 10.1016/j.dsr.2010.05.009

Chang, B. X., Devol, A. H., and Emerson, S. R. (2012). Fixed nitrogen loss from the eastern tropical north pacific and Arabian Sea oxygen deficient zones determined from measurements of N_2: Ar. *Global Biogeochem. Cycles* 26 (3). doi: 10.1029/2011GB004207

Charoenpong, C. N., Bristow, L. A., and Altabet, M. A. (2014). A continuous flow isotope ratio mass spectrometry method for high precision determination of dissolved gas ratios and isotopic composition. *Limnol. Oceanogr.: Methods* 12 (5), 323–337. doi: 10.4319/lom.2014.12.323

Ciais, P., Sabine, C., Bala, G., Bopp, L., Brovkin, V., Canadell, J., et al. (2013). Carbon and Other Biogeochemical Cycles. In: Climate Change 2013: *The Physical Science Basis. Contribution of Working Group I to the Fifth Assessment Report of the Intergovernmental Panel on Climate Change* [T. F. Stocker, D. Qin, G.-K. Plattner, M. Tignor, S. K. Allen, J. Boschung, et al (eds.)]. Cambridge University Press, Cambridge, United Kingdom and New York, NY, USA, pp465, pp570.

Cline, J. D., and Kaplan, I. R. (1975). Isotopic fractionation of dissolved nitrate during denitrification in the eastern tropical north pacific ocean. *Mar. Chem.* 3 (4), 271–299. doi: 10.1016/0304-4203(75)90009-2

Cohen, Y., and Gordon, L. I. (1979). Nitrous oxide production in the ocean. *J. Geophys. Res.: Oceans* 84 (C1), 347–353. doi: 10.1029/JC084iC01p00347

Dalsgaard, T., Stewart, F. J., Thamdrup, B., De Brabandere, L., Revsbech, N. P., Ulloa, O., et al. (2014). Oxygen at nanomolar levels reversibly suppresses process rates and gene expression in anammox and denitrification in the oxygen minimum zone off northern Chile. *MBio* 5 (6), e01966–e01914. doi: 10.1128/mBio.01966-14

Emery, W. J. (2001). Water types and water masses. *Encyclopedia ocean Sci.* 6, 3179–3187. doi: 10.1006/rwos.2001.0108

Farías, L., Castro-González, M., Cornejo, M., Charpentier, J., Faúndez, J., Boontanon, N., et al. (2009). Denitrification and nitrous oxide cycling within the upper oxycline of the eastern tropical south pacific oxygen minimum zone. *Limnol. Oceanogr.* 54 (1), 132–144. doi: 10.4319/lo.2009.54.1.0132

Forster, P., Storelvmo, T., Armour, K., Collins, W., Dufresne, J.-L., Frame, D., et al. (2021). "The earth's energy budget, climate feedbacks, and climate sensitivity," in *Climate change 2021: The physical science basis. contribution of working group I to the sixth assessment report of the intergovernmental panel on climate change*. Eds. V. [Masson-Delmotte, P. Zhai, A. Pirani, S. L. Connors, C. Péan, S. Berger, N. Caud, Y. Chen, L. Goldfarb, M. I. Gomis, M. Huang, K. Leitzell, E. Lonnoy, J. B. R. Matthews, T. K. Maycock, T. Waterfield, O. Yelekçi, R. Yu and B. Zhou (Cambridge, United Kingdom and New York, NY, USA: Cambridge University Press), pp923–p1054. doi: 10.1017/9781009157896.009

Frame, C. H., and Casciotti, K. L. (2010). Biogeochemical controls and isotopic signatures of nitrous oxide production by a marine ammonia-oxidizing bacterium. *Biogeosciences* 7 (9), 2695–2709. doi: 10.5194/bg-7-2695-2010

Frame, C. H., Deal, E., Nevison, C. D., and Casciotti, K. L. (2014). N_2O production in the eastern south Atlantic: Analysis of N_2O stable isotopic and concentration data. *Global Biogeochemical Cycles* 28 (11), 1262–1278. doi: 10.1002/2013GB004790

Frame, C. H., Lau, E., Nolan, E. J.IV, Goepfert, T. J., and Lehmann, M. F. (2017). Acidification enhances hybrid N_2O production associated with aquatic ammonia-oxidizing microorganisms. *Front. Microbiol.* 7, 2104. doi: 10.3389/fmicb.2016.02104

Freing, A., Wallace, D. W., and Bange, H. W. (2012). Global oceanic production of nitrous oxide. *Philos. Trans. R. Soc. B: Biol. Sci.* 367 (1593), 1245–1255. doi: 10.1098/rstb.2011.0360

Freing, A., Wallace, D. W. R., Tanhua, T., Walter, S., and Bange, H. W. (2009). North Atlantic production of nitrous oxide in the context of changing atmospheric levels. *Global Biogeochemical Cycles* 23, 13. doi: 10.1029/2009gb003472

Frey, C., Bange, H. W., Achterberg, E. P., Jayakumar, A., Löscher, C. R., Arévalo-Martínez, D. L., et al. (2020). Regulation of nitrous oxide production in low-oxygen waters off the coast of Peru. *Biogeosciences* 17 (8), 2263–2287. doi: 10.5194/bg-17-2263-2020

Fujii, A., Toyoda, S., Yoshida, O., Watanabe, S., Sasaki, K. I., and Yoshida, N. (2013). Distribution of nitrous oxide dissolved in water masses in the eastern subtropical north pacific and its origin inferred from isotopomer analysis. *J. Oceanogr.* 69 (2), 147–157. doi: 10.1007/s10872-012-0162-4

Goreau, T. J., Kaplan, W. A., Wofsy, S. C., McElroy, M. B., Valois, F. W., and Watson, S. W. (1980). Production of NO_2^- and N_2O by nitrifying bacteria at reduced concentrations of oxygen. *Appl. Environ. Microbiol.* 40 (3), 526–532. doi: 10.1128/aem.40.3.526-532.1980

Granger, J., Sigman, D. M., Lehmann, M. F., and Tortell, P. D. (2008). Nitrogen and oxygen isotope fractionation during dissimilatory nitrate reduction by denitrifying bacteria. *Limnol. Oceanogr.* 53 (6), 2533–2545. doi: 10.4319/lo.2008.53.6.2533

Granger, J., Sigman, D. M., Needoba, J. A., and Harrison, P. J. (2004). Coupled nitrogen and oxygen isotope fractionation of nitrate during assimilation by cultures of marine phytoplankton. *Limnol. Oceanogr.* 49 (5), 1763–1773. doi: 10.4319/lo.2004.49.5.1763

Heil, J., Wolf, B., Brüggemann, N., Emmenegger, L., Tuzson, B., Vereecken, H., et al. (2014). Site-specific ^{15}N isotopic signatures of abiotically produced N_2O. *Geochimica Cosmochimica Acta* 139, 72–82. doi: 10.1016/j.gca.2014.04.037

Hink, L., Lycus, P., Gubry-Rangin, C., Frostegård, Å., Nicol, G. W., Prosser, J. I., et al. (2017a). Kinetics of NH_3-oxidation, NO-turnover, N_2O-production and electron flow during oxygen depletion in model bacterial and archaeal ammonia oxidisers. *Environ. Microbiol.* 19 (12), 4882–4896. doi: 10.1111/1462-2920.13914

Hink, L., Nicol, G. W., and Prosser, J. I. (2017b). Archaea produce lower yields of N_2O than bacteria during aerobic ammonia oxidation in soil. *Environ. Microbiol.* 19 (12), 4829–4837.

Howell, E. A., Doney, S. C., Fine, R. A., and Olson, D. B. (1997). Geochemical estimates of denitrification rates for the Arabian Sea and bay of Bengal during WOCE. *Geophys. Res. Lett.* 24, 2549–2552. doi: 10.1029/97GL01538

Ji, Q., Altabet, M. A., Bange, H. W., Graco, M. I., Ma, X., Arévalo-Martínez, D. L., et al. (2019). Investigating the effect of El niño on nitrous oxide distribution in the eastern tropical south pacific. *Biogeosciences* 16 (9), 2079–2093. doi: 10.5194/bg-16-2079-2019

Ji, Q., Babbin, A. R., Jayakumar, A., Oleynik, S., and Ward, B. B. (2015). Nitrous oxide production by nitrification and denitrification in the Eastern tropical south pacific oxygen minimum zone. *Geophys. Res. Lett.* 42 (24), 10–755. doi: 10.1002/2015GL066853

Ji, Q., Buitenhuis, E., Suntharalingam, P., Sarmiento, J. L., and Ward, B. B. (2018). Global nitrous oxide production determined by oxygen sensitivity of nitrification and

denitrification. *Global Biogeochemical Cycles* 32 (12), 1790–1802. doi: 10.1029/2018GB005887

Keeling, C. D. (1961). The concentration and isotopic abundances of carbon dioxide in rural and marine air. *Geochimica Cosmochimica Acta* 24 (3-4), 277–298. doi: 10.1016/0016-7037(61)90023-0

Kelly, C. L., Travis, N. M., Baya, P. A., and Casciotti, K. L. (2021). Quantifying nitrous oxide cycling regimes in the Eastern tropical north pacific ocean with isotopomer analysis. *Global Biogeochemical Cycles* 35 (2), e2020GB006637. doi: 10.1029/2020GB006637

Kock, A., Arévalo-Martínez, D. L., Löscher, C. R., and Bange, H. W. (2016). Extreme N_2O accumulation in the coastal oxygen minimum zone off Peru. *Biogeosciences* 13 (3), 827–840. doi: 10.5194/bg-13-827-2016

Kool, D. M., Dolfing, J., Wrage, N., and Van Groenigen, J. W. (2011). Nitrifier denitrification as a distinct and significant source of nitrous oxide from soil. *Soil Biol. Biochem.* 43 (1), 174–178. doi: 10.1016/j.soilbio.2010.09.030

Kozlowski, J. A., Stieglmeier, M., Schleper, C., Klotz, M. G., and Stein, L. Y. (2016). Pathways and key intermediates required for obligate aerobic ammonia-dependent chemolithotrophy in bacteria and thaumarchaeota. *ISME J.* 10 (8), 1836–1845. doi: 10.1038/ismej.2016.2

Kraft, B., Jehmlich, N., Larsen, M., Bristow, L. A., Könneke, M., Thamdrup, B., et al. (2022). Oxygen and nitrogen production by an ammonia-oxidizing archaeon. *Science* 375 (6576), 97–100. doi: 10.1126/science.abe6733

Lazo-Murphy, B. M., Larson, S., Staines, S., Bruck, H., McHenry, J., Bourbonnais, A., et al. (2022). Nitrous oxide production and isotopomer composition by fungi isolated from salt marsh sediments. *Front. Mar. Sci.* 9, 2645. doi: 10.3389/fmars.2022.1098508

Lehmann, N., Kienast, M., Granger, J., Bourbonnais, A., Altabet, M. A., and Tremblay, J.É. (2019). Remote western Arctic nutrients fuel remineralization in deep Baffin bay. *Global Biogeochemical Cycles* 33 (6), 649–667. doi: 10.1029/2018GB006134

Lewicka-Szczebak, D., Augustin, J., Giesemann, A., and Well, R. (2017). Quantifying N_2O reduction to N_2 based on N_2O isotopocules–validation with independent methods (helium incubation and ^{15}N gas flux method). *Biogeosciences* 14 (3), 711–732. doi: 10.5194/bg-14-711-2017

Löscher, C. R., Kock, A., Könneke, M., LaRoche, J., Bange, H. W., and Schmitz, R. A. (2012). Production of oceanic nitrous oxide by ammonia-oxidizing archaea. *Biogeosciences* 9 (7), 2419–2429. doi: 10.5194/bg-9-2419-2012

Maeda, K., Spor, A., Edel-Hermann, V., Heraud, C., Breuil, M. C., Bizouard, F., et al. (2015). N_2O production, a widespread trait in fungi. *Sci. Rep.* 5 (1), 9697. doi: 10.1038/srep09697

Magyar, P. M. (2017). *Insights into pathways of nitrous oxide generation from novel isotopologue measurements*. Dissertation (Ph.D.), California Institute of Technology, 119 pp. doi: 10.7907/Z93776RJ

Mariotti, A., Germon, J. C., Hubert, P., Kaiser, P., Letolle, R., Tardieux, A., et al. (1981). Experimental determination of nitrogen kinetic isotope fractionation: some principles; illustration for the denitrification and nitrification processes. *Plant Soil* 62 (3), 413–430. doi: 10.1007/BF02374138

Mohn, J., Wolf, B., Toyoda, S., Lin, C. T., Liang, M. C., Brüggemann, N., et al. (2014). Interlaboratory assessment of nitrous oxide isotopomer analysis by isotope ratio mass spectrometry and laser spectroscopy: current status and perspectives. *Rapid Commun. Mass Spectrometry* 28 (18), 1995–2007. doi: 10.1002/rcm.6982

Monreal, P. J., Kelly, C. L., Travis, N. M., and Casciotti, K. L. (2022). Identifying the sources and drivers of nitrous oxide accumulation in the eddy-influenced Eastern tropical north pacific oxygen-deficient zone. *Glob. Biogeochem. Cycles* 36 (6), e2022GB007310. doi: 10.1007/BF02374138

Muggeo, V. M. (2003). Estimating regression models with unknown break-points. *Stat. Med.* 22(19), 3055–3071. doi: 10.1002/sim.1545

Muggeo, V. M., and Muggeo, M. V. M. (2017). Package 'segmented'. *Biometrika* 58 (525-534), 516.

Nevison, C., Butler, J. H., and Elkins, J. W. (2003). Global distribution of N_2O and the ΔN_2O-AOU yield in the subsurface ocean. *Global Biogeochemical Cycles* 17 (4). doi: 10.1029/2003GB002068

Nevison, C., and Holland, E. (1997). A reexamination of the impact of anthropogenically fixed nitrogen on atmospheric N_2O and the stratospheric O_3 layer. *J. Geophys. Res.: Atmospheres* 102 (D21), 25519–25536. doi: 10.1029/97JD02391

Ostrom, N. E., and Ostrom, P. H. (2012). "The isotopomers of nitrous oxide: analytical considerations and application to resolution of microbial production pathways," in *Handbook of environmental isotope geochemistry* (Berlin, Heidelberg: Springer), pp453–pp476. doi: 10.1029/2006JG000287

Ostrom, N. E., Pitt, A., Sutka, R., Ostrom, P. H., Grandy, A. S., Huizinga, K. M., et al. (2007). Isotopologue effects during N_2O reduction in soils and in pure cultures of denitrifiers. *J. Geophys. Res.: Biogeosciences* 112 (G2). doi: 10.1029/2006JG000287

Pataki, D. E., Ehleringer, J. R., Flanagan, L. B., Yakir, D., Bowling, D. R., Still, C. J., et al. (2003). The application and interpretation of keeling plots in terrestrial carbon cycle research. *Global Biogeochem. Cycles* 17 (1). doi: 10.1029/2001GB001850

Popp, B. N., Westley, M. B., Toyoda, S., Miwa, T., Dore, J. E., Yoshida, N., et al. (2002). Nitrogen and oxygen isotopomeric constraints on the origins and sea-to-air flux of N_2O in the oligotrophic subtropical north pacific gyre. *Global Biogeochemical Cycles* 16 (4), 12–11. doi: 10.1029/2001GB001806

Ravishankara, A. R., Daniel, J. S., and Portmann, R. W. (2009). Nitrous oxide (N_2O): the dominant ozone-depleting substance emitted in the 21st century. *Science* 326 (5949), 123–125. doi: 10.1126/science.1176985

Ryabenko, E., Kock, A., Bange, H. W., Altabet, M. A., and Wallace, D. W. R. (2012). Contrasting biogeochemistry of nitrogen in the Atlantic and pacific oxygen minimum zones. *Biogeosciences* 9, 203–215. doi: 10.5194/bg-9-203-2012

Santoro, A. E., Buchwald, C., McIlvin, M. R., and Casciotti, K. L. (2011). Isotopic signature of N_2O produced by marine ammonia-oxidizing archaea. *Science* 333 (6047), 1282–1285. doi: 10.1126/science.1208239

Santoro, A. E., Casciotti, K. L., and Francis, C. A. (2010). Activity, abundance and diversity of nitrifying archaea and bacteria in the central California current. *Environ. Microbiol.* 12 (7), 1989–2006. doi: 10.1111/j.1462-2920.2010.02205.x

Schmidt, H. L., Werner, R. A., Yoshida, N., and Well, R. (2004). Is the isotopic composition of nitrous oxide an indicator for its origin from nitrification or denitrification? a theoretical approach from referred data and microbiological and enzyme kinetic aspects. *Rapid Commun. Mass Spectrometry* 18 (18), 2036–2040. doi: 10.1002/rcm.1586

Sigman, D. M., Granger, J., DiFiore, P. J., Lehmann, M. M., Ho, R., Cane, G., et al. (2005). Coupled nitrogen and oxygen isotope measurements of nitrate along the eastern north pacific margin. *Global Biogeochemical Cycles* 19 (4). doi: 10.1029/2005GB002458

Snider, D. M., Venkiteswaran, J. J., Schiff, S. L., and Spoelstra, J. (2012). Deciphering the oxygen isotope composition of nitrous oxide produced by nitrification. *Global Change Biol.* 18 (1), 356–370. doi: 10.1111/j.1365-2486.2011.02547.x

Sonnerup, R. E., Mecking, S., Bullister, J. L., and Warner, M. J. (2015). Transit time distributions and oxygen utilization rates from chlorofluorocarbons and sulfur hexafluoride in the southeast pacific ocean. *J. Geophys. Res. Ocean.* 120, doi:10.1002/2015JC010781. doi: 10.1002/2015JC010781

Stanley, R. H. R., Doney, S. C., Jenkins, W. J., and Lott, D. E. (2012). Apparent oxygen utilization rates calculated from tritium and helium-3 profiles at the Bermuda Atlantic time-series study site. *Biogeosciences* 9 (6), 1969–1983. doi: 10.5194/bg-9-1969-2012

Stieglmeier, M., Mooshammer, M., Kitzler, B., Wanek, W., Zechmeister-Boltenste. rn, S., Richter, A., et al. (2014). Aerobic nitrous oxide production through n-nitrosating hybrid formation in ammonia-oxidizing archaea. *ISME J.* 8 (5), 1135–1146. doi: 10.1038/ismej.2013.220

Stöven, T., Tanhua, T., Hoppema, M., and Bullister, J. L. (2015). Perspectives of transient tracer applications and limiting cases. *Ocean Sci.* 11 (5), 699–718. doi: 10.5194/os-11-699-2015

Stramma, L., Bange, H. W., Czeschel, R., Lorenzo, A., and Frank, M. (2013). On the role of mesoscale eddies for the biological productivity and biogeochemistry in the eastern tropical Pacific Ocean off Peru. *Biogeosciences* 10 (11), 7293–7306. doi: 10.5194/bg-10-7293-2013

Sutka, R. L., Ostrom, N. E., Ostrom, P. H., Breznak, J. A., Gandhi, H., Pitt, A. J., et al. (2006). Distinguishing nitrous oxide production from nitrification and denitrification on the basis of isotopomer abundances. *Appl. Environ. Microbiol.* 72 (1), 638–644. doi: 10.1128/AEM.72.1.638-644.2006

Sutka, R. L., Ostrom, N. E., Ostrom, P. H., Gandhi, H., and Breznak, J. A. (2003). Nitrogen isotopomer site preference of N_2O produced by nitrosomonas europaea and methylococcus capsulatus bath. *Rapid Commun. Mass Spectrometry* 17 (7), 738–745. doi: 10.1002/rcm.968

Sutka, R. L., Ostrom, N. E., Ostrom, P. H., and Phanikumar, M. S. (2004). Stable nitrogen isotope dynamics of dissolved nitrate in a transect from the north pacific subtropical gyre to the Eastern tropical north pacific. *Geochimica Cosmochimica Acta* 68 (3), 517–527. doi: 10.1016/S0016-7037(03)00483-6

Tian, H., Xu, R., Canadell, J. G., Thompson, R. L., Winiwarter, W., Suntharalingam, P., et al. (2020). A comprehensive quantification of global nitrous oxide sources and sinks. *Nature* 586, 248–256. doi: 10.1038/s41586-020-2780-0

Toyoda, S., Mutobe, H., Yamagishi, H., Yoshida, N., and Tanji, Y. (2005). Fractionation of N_2O isotopomers during production by denitrifier. *Soil Biol. Biochem.* 37 (8), 1535–1545. doi: 10.1016/j.soilbio.2005.01.009

Toyoda, S., Yoshida, N., Miwa, T., Matsui, Y., Yamagishi, H., Tsunogai, U., et al. (2002). Production mechanism and global budget of N_2O inferred from its isotopomers in the western north pacific. *Geophys. Res. Lett.* 29 (3), 7–1. doi: 10.1029/2001GL014311

Toyoda, S., Yoshida, O., Yamagishi, H., Fujii, A., Yoshida, N., and Watanabe, S. (2019). Identifying the origin of nitrous oxide dissolved in deep ocean by concentration and isotopocule analyses. *Sci. Rep.* 9 (1), 1–9. doi: 10.1038/s41598-019-44224-0

Trimmer, M., Chronopoulou, P. M., Maanoja, S. T., Upstill-Goddard, R. C., Kitidis, V., and Purdy, K. J. (2016). Nitrous oxide as a function of oxygen and archaeal gene abundance in the north pacific. *Nat. Commun.* 7 (1), 1–10. doi: 10.1038/ncomms13451

Wankel, S. D., Ziebis, W., Buchwald, C., Charoenpong, C., de Beer, D., Dentinger, J., et al. (2017). Evidence for fungal and chemodenitrification based N_2O flux from nitrogen impacted coastal sediments. *Nat. Commun.* 8 (1), 1–11. doi: 10.1038/ncomms15595

Ward, B. B. (2008). "Nitrification in marine systems," in *Nitrogen in the marine environment*. Eds. D. G. Capone, D. A. Bronk, M. R. Mulholland and E. J. Carpenter (Elsevier, San Diego, California: Academic Press), pp199–pp261.

Waugh, D. W., Hall, T. M., and Haine, T. W. N. (2003). Relationships among tracer ages. *J. Geophys. Research-Oceans* 108 (C5), 16. doi: 10.1029/2002jc001325

Weiss, R. F., and Price, B. A. (1980). Nitrous oxide solubility in water and seawater. *Mar. Chem.* 8 (4), 347–359. doi: 10.1016/0304-4203(80)90024-9

Westley, M. B., Popp, B. N., and Rust, T. M. (2007). The calibration of the intramolecular nitrogen isotope distribution in nitrous oxide measured by isotope ratio mass spectrometry. *Rapid Commun. Mass Spectrometry* 21 (3), 391–405. doi: 10.1002/rcm.2828

Westley, M. B., Yamagishi, H., Popp, B. N., and Yoshida, N. (2006). Nitrous oxide cycling in the black Sea inferred from stable isotope and isotopomer distributions. *Deep Sea Res. Part II: Topical Stud. Oceanogr.* 53, 1802–1816. doi: 10.1016/j.dsr2.2006.03.012

Wrage, N., Velthof, G. L., Van Beusichem, M. L., and Oenema, O. (2001). Role of nitrifier denitrification in the production of nitrous oxide. *Soil Biol. Biochem.* 33 (12-13), 1723–1732. doi: 10.1016/S0038-0717(01)00096-7

Yamagishi, H., Westley, M. B., Popp, B. N., Toyoda, S., Yoshida, N., Watanabe, S., et al. (2007). Role of nitrification and denitrification on the nitrous oxide cycle in the eastern tropical north pacific and gulf of California. *J. Geophys. Res.: Biogeosciences* 112 (G2). doi: 10.1029/2006JG000227

Yamagishi, H., Yoshida, N., Toyoda, S., Popp, B. N., Westley, M. B., and Watanabe, S. (2005). Contributions of denitrification and mixing on the distribution of nitrous oxide in the north pacific. *Geophys. Res. Lett.* 32 (4). doi: 10.1029/2004GL021458

Yang, S., Chang, B. X., Warner, M. J., Weber, T. S., Bourbonnais, A. M., Santoro, A. E., et al. (2020). Global reconstruction reduces the uncertainty of oceanic nitrous oxide emissions and reveals a vigorous seasonal cycle. *Proc. Natl. Acad. Sci.* 117 (22), 11954–11960. doi: 10.1073/pnas.1921914117

Yoshida, N., Morimoto, H., Hirano, M., Koike, I., Matsuo, S., Wada, E., et al. (1989). Nitrification rates and ^{15}N abundances of N_2O and NO_3^- in the western north pacific. *Nature* 342 (6252), 895–897.

Yoshinari, T., and Knowles, R. (1976). Acetylene inhibition of nitrous oxide reduction by denitrifying bacteria. *Biochem. Biophys. Res. Commun.* 69 (3), 705–710. doi: 10.1016/0006-291X(76)90932-3

frontiers | Frontiers in Marine Science

TYPE Original Research
PUBLISHED 31 May 2023
DOI 10.3389/fmars.2023.1123739

OPEN ACCESS

EDITED BY
Sudheesh Valliyodan,
Central University of Kerala, India

REVIEWED BY
Vinu Valsala,
Indian Institute of Tropical Meteorology (IITM), India
Haimanti Biswas,
Council of Scientific and Industrial Research (CSIR), India

*CORRESPONDENCE
Parvathi Vallivattathillam
pv32@nyu.edu

RECEIVED 14 December 2022
ACCEPTED 10 May 2023
PUBLISHED 31 May 2023

CITATION
Vallivattathillam P, Lachkar Z and Lévy M (2023) Shrinking of the Arabian Sea oxygen minimum zone with climate change projected with a downscaled model. *Front. Mar. Sci.* 10:1123739. doi: 10.3389/fmars.2023.1123739

Shrinking of the Arabian Sea oxygen minimum zone with climate change projected with a downscaled model

Parvathi Vallivattathillam[1]*, Zouhair Lachkar[1] and Marina Lévy[2]

[1]Arabian Center for Climate and Environmental Sciences, New York University Abu Dhabi, Abu Dhabi, United Arab Emirates, [2]Sorbonne Université (CNRS/IRD/MNHN), LOCEAN-IPSL, Paris, France

In Arabian Sea (AS), land-locked northern boundary and strong seasonal productivity lead to the formation of one of the most intense open ocean Oxygen Minimum Zones (OMZs). Presence of this perennial OMZ has significant consequences on adjacent coastal fisheries and ecosystem. Simulations from CMIP5 suggest significant weakening of both monsoonal winds and productivity under high emission scenario. But the fate of AS OMZ in this scenario - whether it will expand or shrink - still remains elusive, mainly due to poor representation of extent and strength of AS OMZ in CMIP5 present-day simulations. To address this, we analyze the distribution of O_2 in AS from a subset of three contrasted CMIP5 simulations, and complemented with a set of regional downscaled model experiments which we forced at surface and open boundaries using information from those three CMIP5 models. We tested two regional downscaling approaches - with and without correction of CMIP5 biases with respect to observations. Using a set of sensitivity experiments, we disentangle the contributions of local (atmospheric) forcing vs. remote (at the lateral boundaries) forcing in driving the future projected O_2 changes. While CMIP5 projects either shrinking or expansion of the AS OMZ depending on the model, our downscaling experiments consistently project a shrinking of AS OMZ. We show that projected O_2 changes in OMZ layer are affected by both local and remote processes. In the southern AS, the main response to climate change is oxygenation that originates from the boundaries, and hence downscalled and CMIP5 model responses are similar. In contrast, in northern AS, downscaling yields a substantial reduction in O_2 projection discrepancies because of a minimal influence of remote forcing there leading to a stronger sensitivity to improved local physics and improved model representation of present-day conditions. We find that when corrected for present-day biases, projected deoxygenation in the northern AS is shallower. Our findings indicate the importance of downscaling of global models in regions where local forcing is dominant, and the need for correcting global model biases with respect to observations to reduce uncertainties in future O_2 projections.

KEYWORDS

Arabian Sea, climate change, oxygen minimum zone, downscaling, CMIP5, ocean modeling

1 Introduction

A land-locked northern boundary and limited ventilation to the north, combined with intense surface seasonal blooms lead to the formation and maintenance of one of the thickest, open ocean Oxygen Minimum Zones (OMZs) in the Arabian Sea (AS; Figures 1A, F). As dissolved O_2 is crucial for sustenance of most marine animal life, the presence of low-oxygen mesopelagic zones can potentially impart stress on the marine life (Bopp et al., 2013), resulting in significant reduction in the marine biodiversity in OMZs as compared with well oxygenated regions (Stramma et al., 2012).

The OMZs also play crucial role in the cycling of gases (e.g., CO_2, N_2O, CH_4), and elements (e.g., nitrogen, sulfur and carbon) that have direct implications for the Earth's climate. For instance, the emission of potent greenhouse gases (such as nitrous oxide, methane, etc.) resulting from the anaerobic metabolism in the OMZs (Dileep, 2006) can exacerbate the greenhouse warming

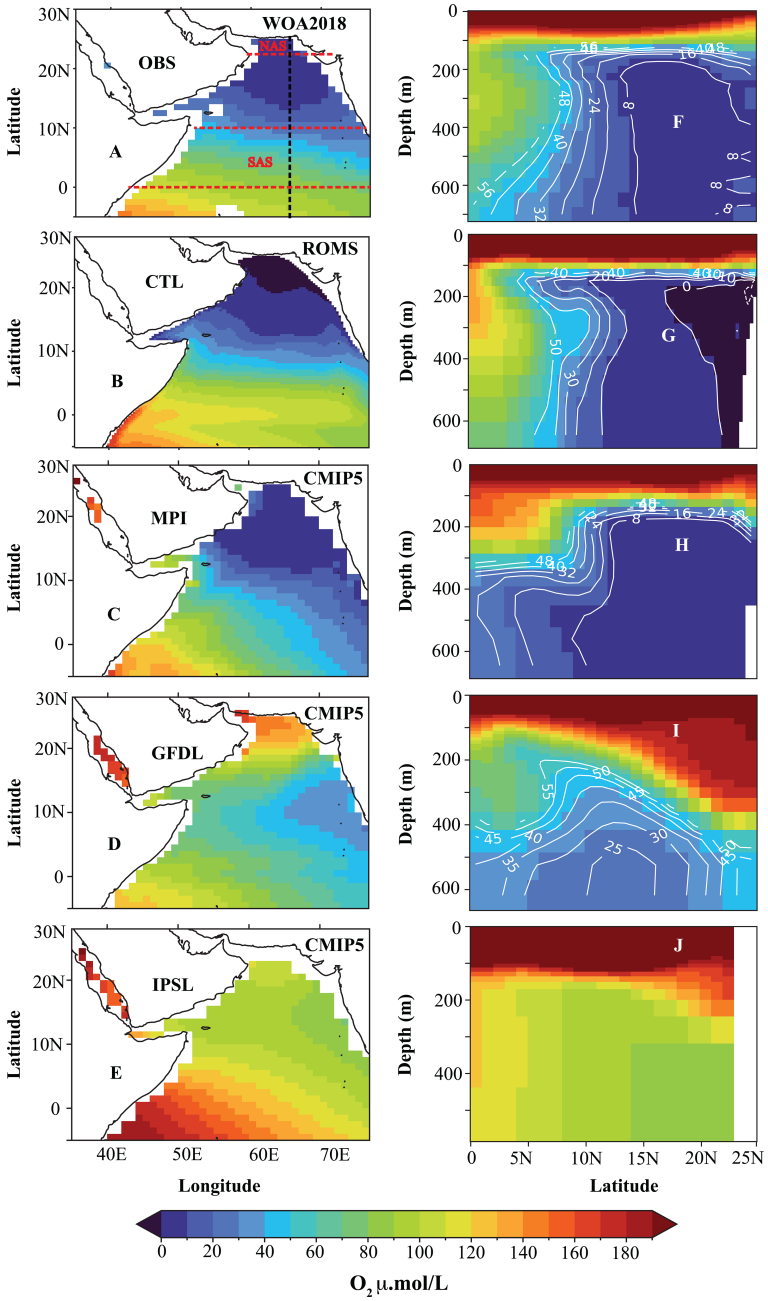

FIGURE 1
Evaluation of modelled present day O_2 against Word Ocean Atlas observations. The left column shows the O_2 inventory averaged over the layer 200-700m, the right column shows the meridional section at 65°E (indicated by black dashed lines on panel A) with white contours indicating the hypoxic regions (O2< 60 µmol/L). **(A-F)** WOA observations (WOA 2018); **(B–G)** downscalled experiment (ROMS_CTL); **(C–E, H–J)** the three CMIP5 models (MPI, GFDL, IPSL) over the present-day period (CMIP5_HIST simulations, averaged from years 1986 to 2005). The northern Arabian Sea (NAS) and southern Arabian Sea (SAS) regions are delimited by red dashed lines on panel **(A)**.

and the associated climate change (Naqvi & Noronha, 1991; Codispoti et al., 2001; Chronopoulou et al., 2017). In addition to this, the denitrification and anaerobic ammonium oxidation (anammox) in the OMZs lead to fixed nitrogen loss in the pelagic ocean (Stief et al., 2017), limiting the inventory of bioavailable oceanic nitrogen (Falkowski, 1997). This can potentially inhibit the marine productivity, and hence affect the marine food web. Another important concern arises from the direct interaction of open ocean OMZs with the neighboring coastal regions. For instance, the upwelling along west coast of India during boreal summer triggers the development of largest natural seasonal hypoxic (O_2< 60 µmol/L) events, causing frequent major fish-kill events there (Naqvi et al., 2009; Parvathi et al., 2017a; Pearson et al., 2022). On the other hand, the seasonal upwelling in this region bears a large sector of the Indian economy by supporting the pelagic fisheries during the summer monsoons (Vivekanandan et al., 2005). The recurring seasonal hypoxia and their sporadic intensification thus adversely affects the ecosystem and fisheries stock in this region and forms a direct threat to the Indian economy (Naqvi et al., 2009).

Despite the strong seasonal modulation of both atmospheric forcing and oceanic productivity, the AS OMZ is reported to have no pronounced seasonal changes (Resplandy et al., 2012). In the present-day climate, this has reportedly been maintained through the subtle balance that exists between supply of oxygen through dynamical processes (i.e., transport through western boundary currents, mixing and advection by mesoscale eddies and convective mixing), and the biological demand resulting from seasonal blooms (Sarma, 2002; Resplandy et al., 2012; McCreary et al., 2013). However, a recent modeling study by Lachkar et al. (2018) have demonstrated that both the source (dynamical supply) and sink (biological demand) of oxygen in the AS OMZ are highly sensitive to the monsoonal winds. In addition to this, the future projections from CMIP5 simulations indicate significant changes in both the dynamical forcing (atmospheric circulation) and associated biological productivity in response to climate change (Sandeep & Ajayamohan, 2015; Praveen et al., 2016; Roxy et al., 2016; Parvathi et al., 2017b). Moreover, the steady and heterogenous warming of AS reported at decadal to multi-decadal time-scales (Han et al., 2014; Roxy et al., 2016; Gopika et al., 2020; Lachkar et al., 2021) has the potential to reduce the solubility of O_2, and also strengthen the oceanic stratification, thus weakening the vertical mixing and limiting the supply of O_2 to the sub-surface layers. Additionally, the shallow marginal seas in the neighborhood of AS play a crucial role in controlling the extent of sub-surface OMZ (e.g., Naqvi et al., 2009; McCreary et al., 2013; Lachkar et al., 2019). The ongoing warming increases the buoyancy of the shallow Arabian Gulf (also known as Persian Gulf) water, preventing its subduction into the northern AS, and weakening one of the ventilation pathways of the AS OMZ leading to an expansion of its core (Lachkar et al., 2019; Lachkar et al., 2021). Despite all of the above facts, there is no clear consensus on the impact of climate change on the AS OMZ. The complex interaction between physical and biological processes and their differential responses to the climate sensitivity pose a major constraint for the accurate anticipation of projected response in the OMZ under climate change. However, most of the earlier findings indicate that despite its occurrence throughout the geological time-period (Fennel & Testa, 2019), the recent intensification of the global OMZs (both coastal and open ocean) is vastly due to the dominance of anthropogenic climate change (Breitburg et al., 2018). The important role of oxygen in maintaining a healthy ecosystem, diverse fisheries, and hence the economy of the highly populated coastal belt along the western India calls for a thorough assessment of the impact of climate change on the AS OMZ.

Climate simulations from the Earth System Models (ESMs) have widely been utilized to study the impact of climate change on a broad range of physical-biogeochemical systems as well as for making policies that help to mitigate the adverse impacts. While the ESM simulations performed under CMIP5 bring great opportunity to explore future projections of both atmospheric and oceanic processes, they also possess biases that can potentially alias the interpretation of climate change driven future projections (Lachkar et al, 2021; Gopika et al., 2020). Moreover, the biases are generally reported to be larger (in comparison to the physical parameters for instance) for biogeochemical variables, and particularly for oxygen (Bopp et al., 2013; Cocco et al., 2013; Schmidt et al., 2021). Earlier studies focusing on the north Indian Ocean/AS have indicated the cascading effects of misrepresentation of key processes in bringing huge biases in the mean-state of both atmospheric and oceanic simulated fields. For example, the misrepresentation of main water masses leads to the biases in depth of mixed layer/thermocline in the northern AS, which in turn affects the present-day simulations of Indian monsoons in the CMIP5 models (Nagura et al., 2018). The misrepresentation of water masses in the CMIP5 models have also been identified as the main reason for the biases in the AS OMZ simulations by Schmidt et al. (2021). The ill-represented AS OMZ mean state in the CMIP5 prevents utilizing the ensemble of these simulations alone to draw meaningful conclusions in a regional context (Schmidt et al., 2021).

Another important contribution for the supply of oxygen to the interior of the ocean and hence the ventilation of open ocean OMZs comes from the mixing (both vertical and horizontal transport; Lévy et al., 2021). The OMZ in the AS is largely influenced by the strong mixing in its western boundary arising from energetic mesoscale eddies (McCreary et al., 2013). Hence, the simulation of present-day mean state distribution of oxygen in the AS demands an accurate representation of the mesoscale spectrum, either through increasing grid resolution or though choosing accurate parameterization schemes (Resplandy et al., 2012; Lachkar et al., 2016). The computational cost and the global coverage prevent the ESM under CMIP5 to account for such great details in the regional basins. In order to overcome some of the biases of global CMIP5 simulations possibly arising from the above factors, and gain some insight about the robust patterns of projected changes in AS OMZ in response to climate change, along with its driving processes, the present study, attempts a regional downscaling approach. Such downscaling methods have been used to understand the physical-biogeochemical interaction in the future climate change scenario elsewhere in the global oceans (Echevin et al., 2020; Buil et al., 2021), but not yet in the Indian Ocean.

Hence in the present study, we specifically address the following questions: (1) Will the AS OMZ expand or shrink in response to

climate change? (2) What are the contributions of local vs. remote forcing in driving the projected O_2 changes? (3) How sensitive are future response patterns to the model representation of the present-day state? To this end, we performed a set of simulations with an eddy-permitting (1/3°) regional configuration of the physical-biogeochemical model ROMS over the AS domain, using atmospheric fields and oceanic boundary conditions taken from observed climatologies and from CMIP5 model projections. We have designed a set of specific sensitivity experiments to identify the evolution of key physical and biogeochemical processes that maintain the present-day balance of the AS OMZ. Finally, we show the potential and the limits of regional downscaling to enhance our ability to predict future OMZ changes and more generally improve our understanding of the key biogeochemical processes in the regional basins.

The paper is organized as follows: Section 2 is dedicated to provide the details of the methodology. In particular, this section includes the details of the CMIP5 simulations, regional model experiments with ROMS, and observations. Section 3 describes the main results of our study. In section 4, we provide a discussion of the lessons learnt and the limitations of the study. Finally, section 5 provides the main conclusions of the study.

2 Methods

In this section, we introduce the three selected CMIP5 models and the associated downscaled eddy-permitting ROMS experiments, followed by details of our downscaling approach. A summary of these details is provided in Tables 1, 2.

2.1 CMIP5 simulations

The CMIP5 archive contains global coupled simulations performed with Earth System Models (ESM). These simulations cover the present-day "historical" period (denoted as CMIP5 _HIST_modelname in this study), where the coupled model is forced by observed atmospheric composition changes of greenhouse gases during the industrial period (mid-nineteenth century to near present). They are followed by future projection simulations, known as Representative Concentration Pathway (RCP), which are forced with atmospheric composition changes consistent with varying degrees of greenhouse gas emission scenarios (denoted as CMIP5 _RCP_modelname in this study). The RCP experiments are named based on the amount of radiative forcing added to the experiment. Here, we used the unmitigated high emission scenario RCP8.5 wherein the radiative forcing increases throughout the 21st century before reaching a level of 8.5 W m^{-2} at the end of the century (Taylor et al., 2012; Bopp et al., 2013).

We focus our analysis on a subset of simulations from the CMIP5 archive, based on three ESM, i.e., MPI-ESM-LR, GFDL-ESM2M, and IPSL-CM5A-MR (Table 1, here onwards we refer them as MPI, GFDL and IPSL). These three ESM are based on different ocean general circulation models, along with different mixing schemes and resolutions (both horizontal and vertical), and on different biogeochemical models, with various degrees of complexity. They also differ in representing the influence of marginal seas, particularly of the Arabian Gulf (AG). For instance, the MPI model includes the AG water explicitly, and uses the Pacanowski and Philander (1981) mixing scheme. In the GFDL model, the impact of AG water is parameterized by enhanced cross-land mixing. The GFDL model uses the KPP mixing scheme. The IPSL model does not include the effect of AG water explicitly nor does it represent its impact through restoring temperature or salinity to observation. The mixing scheme used in the IPSL model is Blanke and Delecluse (1993) (A detailed discussion on this can be found in Huang et al., 2014 and Nagura et al., 2018).

These differences explain in part the different mean states of the OMZ represented in the historical simulations (Figure 1). In fact, this subset of three CMIP5 models was actually selected (out of 9 available) because it covers contrasted representations of the present-day OMZ (Figure 1). CMIP5_HIST_MPI (Figures 1C, H) has the closest

TABLE 1 Description of the three CMIP5 models used in the present study.

Experiment	Model name	Modeling Group	Physical model	Biogeochemical model	Horizontal resolution (Lon X Lat in degrees)	Number of vertical levels	Exchange of Gulf water with northern AS	Future response
CMIP5	MPI-ESM-LR	Max Planck Institute (MPI) for Meteorology	MPIOM	HAMOCC5	0.82 X 0.45	40	Likely directly determined	(RCP8.5 – HIST) *
	GFDL-ESM2M	National Oceanic and Atmospheric Administration (NOAA)/ Geophysical Fluid Dynamics Laboratory (GFDL)	MOM	COBALTv2	1.0 X 1.0	50	Parameterized using Griffies (2004) cross-land mixing scheme	
	IPSL-CM5A-MR	L'Institut Pierre-Simon Laplace (IPSL)	NEMO	PISCES	1.25 X 2.5	31	No representation of Gulf water exchange	

*The difference between averages over last 20 years from both RCP8.5 (2081-2100) and the Historical (2005-1986) simulations.

TABLE 2 Description of the regional, downscalled simulations of the Arabian Sea performed with the ROMS model, and of their forcings.

Simulation period	Experiment name	Description	Surface forcing fields	Lateral boundary conditions	Future response assessment
present day (1980-2005)	ROMS_CTL	ROMS control simulation	Observation (COADS (heat fluxes), Pathfinder (SST), QuickSCOW (winds))	Observation (WOA +SODA)	
	ROMS_HIST*	Downscaled CMIP5 historical simulations	CMIP5 fields during historical period (2000s)	CMIP5 fields during historical period	
Future conditions (2081-2100)	ROMS_DD*	Direct downscaling (DD) of future RCP8.5 CMIP5 simulations	CMIP5 RCP8.5 fields	CMIP5 RCP8.5 fields	ROMS_DD – ROMS_HIST (Climate change impact assessed with DD approach)
	ROMS_BCD*	Bias corrected downscaling (BCD) of future RCP8.5 CMIP5 simulations	Observation + CMIP5 anomaly between 2100s and 2000s	Observation + CMIP5 anomaly between 2000s and 2100s	ROMS_BCD – ROMS_CTL (Climate change impact assessed with BCD approach)
Future conditions (2081-2100) (includes present day boundary conditions)	ROMS_BCD$_{LOC}$*	BCD of future RCP8.5 CMIP5 simulations forced with present-day boundary conditions (only local atmospheric forcing varies in the future)	Observation + CMIP5 anomaly between 2100s and 2000s	Observation (WOA +SODA)	ROMS_BCD$_{LOC}$ - ROMS_CTL (Climate change impact associated with local forcing)
	ROMS_BCD$_{PHY}$*	BCD of future RCP8.5 CMIP5 simulations forced with present-day biogeochemical boundary conditions (only physical conditions vary in the future)	Observation + CMIP5 anomaly between 2100s and 2000s	NO_3 & O_2: WOA, all other variables: WOA + CMIP5 anomaly between 2000s and 2100s	ROMS_BCD$_{PHY}$ – ROMS_BCD$_{LOC}$ (Climate change impact associated with remote physical changes) ROMS_BCD – ROMS_BCD$_{PHY}$ (Climate change impact associated with remote biogeochemical changes)

Table legend: Different assessments of future climate change impact are derived from multiple pairs of simulations as described in the last column. Cells are shaded in gray when not applicable. Experiments indicated with (*) correspond to groups of 3 simulations forced with outputs from the three CMIP5 models described in Table 1.

agreement with observations (Figures 1A, F), CMIP5_HIST_GFDL (Figures 1D, I) has intermediate skill and CMIP5_HIST_IPSL (Figures 1E, J) completely fails at capturing the observed subsurface depletion of oxygen in the AS, however has lesser O_2 in the sub-surface layers compared to the surface (Figure 1J). The representation of the OMZ in each simulation is quantified more accurately by comparing the volume fraction of the OMZ (defined as the volume of hypoxic waters, i.e. where O2<60 µmol/L in the region north of Equator and comprised between 0 and 1000 m depth) and of the core of the OMZ (defined as the volume of suboxic waters, i.e. where O2<4 µmol/L in the same region) in the simulations with climatological observations (Figure 2). Such quantitative assessments are important to determine the reliability of model's skill in representing the observed variables. Our analysis reveals that, CMIP5_HIST_MPI, which best captures the volume of the OMZ, does it at the expense of a strong overestimation of the volume of suboxic waters (which was not very clear from the qualitative maps), while the CMIP5_HIST_GFDL does not have any suboxic waters, and the CMIP5 _HIST_IPSL does not even represent hypoxic waters (Figure 2).

2.2 Regional simulations

2.2.1 Model configuration

We used the Regional Ocean Modeling System Adaptive Grid Refinement in Fortran (ROMS-AGRIF; http://www.croco-ocean.org/; here onwards mentioned as ROMS) with an embedded biogeochemical model to simulate the dynamics of the AS-OMZ (Lachkar et al., 2016). ROMS has terrain following sigma coordinates and solves the primitive equations with Boussinesq and Hydrostatic approximations. (Shchepetkin and McWilliams, 2005). To reduce spurious mixing, ROMS includes a rotated-split third-order upstream biased algorithm for the advection of tracers (Marchesiello et al., 2009). The subgrid vertical mixing is represented by including non-local K-profile parameterization (KPP) scheme (Large et al., 1994).

The embedded biogeochemical model has previously been used in ROMS simulations of the AS OMZ (Lachkar et al., 2016; Lachkar et al., 2018; Lachkar et al., 2021) and is fully described therein. It includes nitrate, ammonium, one class of phytoplankton, one class

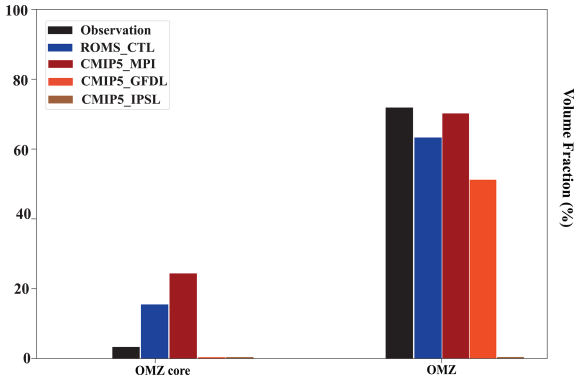

FIGURE 2
Quantitative evaluation of modelled present day OMZ against Word Ocean Atlas observations. Volume fraction occupied by suboxic water masses (OMZ_core, O2< 4 µmol/L) and by hypoxic water masses (OMZ, O2<60 µmol/L) in the 0 – 1000 m top layer of the Arabian Sea, in Word Ocean Atlas observations (WOA 2018, black), in CMIP5 historical simulations (shades of red: CMIP5_HIST_MPI, CMIP5_HIST_GFDL, CMIP5_HIST_IPSL), and in the downscalled ROMS present-day simulation (ROMS_CTL, in blue). Note that the only CMIP5 model that simulates OMZ_core waters is the MPI model, and that the IPSL CMIP5 model does not even simulate OMZ waters.

of zooplankton, two classes of detritus, a dynamic chlorophyll-to-carbon ratio and a module that describes the evolution of O_2, with anaerobic respiration below a fixed threshold (O_2< 4µmol/L) and benthic denitrification.

Our regional configuration covers the AS meridionally from 5° S to 30° N and zonally from 33° E to 78° E, with lateral open boundaries at 5° S and 78°E. The model is forced at the surface with wind, air-temperature, humidity, SST and atmospheric heat fluxes, and with temperature, salinity and currents at lateral boundaries. Apart from the above, the oxygen and nitrate initial and boundary conditions were also provided for the biogeochemistry. Depending on the experiment, the surface forcing and lateral boundary fields were either constructed from observations or from CMIP5 outputs (details are provided in the subsequent sections). Experiments were performed using an eddy-permitting 1/3° horizontal grid resolution with 32 sigma layers. This allowed a significant improvement in the representation of the Arabian Sea OMZ relative to the CMIP5 models (Figures 1, 2). Using the downscaled model at higher horizontal resolutions (1/6° and 1/12°) brought about less changes in terms of the simulated present day OMZ than changes associated with the model (CMIP5 vs ROMS, Figure SI 1). Therefore, for computational efficiency and to be able to run multiple sensitivity simulations, we decided to use this same resolution (1/3°) for all regional downscaling experiments presented in this study. The sensitivity to model resolution of the response of the OMZ to future climate change will be the topic of a follow-up study. Contrary to CMIP5 projections, we have the same base model for all the downscaled experiments, which is one of the main advantages of our downscaling approach. Hence, this approach will allow us to examine the susceptibility of future projections to model's representation of the present-day state and the contributions of local and remote forcing to projected changes.

2.2.2 Control present-day experiment (ROMS_CTL)

The control simulation (denoted as ROMS_CTL throughout the paper) is forced with observation-based climatologies, and thus represents the present-day (equivalent to CMIP5 historical) period. The atmospheric forcing fields for heat and freshwater fluxes are constructed from COADS monthly climatology, and we used monthly wind stress climatology based on QuikSCAT - derived Scatterometer Climatology of Ocean Winds (SCOW; Risien and Chelton, 2008). Temperature, salinity, oxygen, and nitrate were initialized and forced at the open boundaries using monthly climatology from World Ocean Atlas (2018). Currents were initialized and laterally forced at the open boundaries from Simple Ocean Data Assimilation (SODA) at monthly frequency. For all our simulations, we applied a restoring of surface temperature and salinity using kinematic flux corrections described in Barnier et al. (1995). The ROMS_CTL experiments were run for 50 years. The model was spun-up until a steady state was reached (45 years) and the last 5 years were used for analysis (Figure SI 2).

The overall evaluation of physical and biogeochemical properties in summer and winter in the ROMS_CTL experiment is shown in Figures SI 3-5. The main features of the model solution are the signature of seasonal upwelling along the coasts of Somalia, Oman and western India comparable with observations, with however a slight overestimation of surface chlorophyll in the Great Whirl region. The winter convective mixing in the northern AS is also reasonably captured as can be inferred from the cooling of SST (Figure SI 3), along with nutrient injection (Figure SI 4) and enhanced surface chlorophyll (Figure SI 5). Our model also captures the main circulation patterns and its seasonal modulations in the AS domain (not shown). However, from the water mass analysis shown in Figure SI 6A, E), we also notice that, the ROMS_CTL do not simulate the high salinity tongue - indicating the underestimation of Gulf water intrusion in the northern AS (our model domain includes the Arabian Gulf). This underestimation was already reported in Lachkar et al. (2018), and could be due to the model limitations arising from the lack of realistic forcing data in the Gulf region or the model grid resolution (Lachkar et al., 2018).

Despite the above factors, the comparison of the volume fractions of OMZ and OMZ_core in the AS from the ROMS_CTL experiment with observation reveals better skills of the ROMS_CTL experiment at capturing the AS OMZ, both its core and total volume, compared to the set of CMIP5_HIST simulations (Figure 2).

2.2.3 Regional downscaling experiments

2.2.3.1 Direct downscaling (DD)

In direct downscaling (DD) approach, we use CMIP5 model simulations to initialize and force our regional AS simulations with no correction of the CMIP5 model biases (with respect to observations). We applied DD to both historical (denoted as ROMS_HIST) and future (referred to as ROMS_DD) simulations. For historical simulations, we used monthly climatologies from historical CMIP5 simulations (i.e., CMIP5_HIST) computed over 1986-2005 as forcing and boundary (for physical variables as well as biogeochemical tracers) fields. Similarly, for future simulations, we used monthly climatologies from future CMIP5 simulations (i.e., CMIP5_RCP8.5) averaged over 2081 to 2100. As for ROMS_CTL, both historical and future climate downscaled experiments were run for total 50 years with a spin-up-up of 45 years. We used the last 5 years for the analysis presented here.

2.2.3.2 Bias corrected downscaling (BCD)

An additional downscaling approach, denoted as Bias-Corrected Downscaling (BCD) and similar to the Pseudo Global Warming downscaling method discussed in earlier regional climate studies (Xu et al., 2019), is used here. In this approach we correct the present-day biases in CMIP5 models with respect to observations before using this data to force the future regional projections (referred to as ROMS_BCD). More concretely, we added future anomalies from CMIP5 models to observational climatologies (used to force ROMS_CTL and denoted OBS) to construct the forcing and boundary fields (i.e., (CMIP5_RCP - CMIP5_HIST) + OBS) used to initialize and force the future regional AS simulations (i.e., ROMS_BCD). The monthly averages of CMIP5 future anomalies were computed by subtracting the last 20 years averages of ESM simulated variables for present-day (i.e., 1986-2005, CMIP5_HIST) from the future simulations (i.e., 2081-2100, CMIP5_RCP; Figure SI 7, 8, only O_2, and NO_3 are shown). As for the experiments mentioned in previous sections, these downscaling experiments were also run for 50 years, where the model was spun-up for 45 years and, the last 5 years were used for the analysis. In both DD and BCD, when the monthly outputs were not available (for O_2 & NO_3), we repeated the annual values to construct the monthly cycle.

2.2.3.3 Quantification of the contributions of local vs remote forcing to Ochanges:

To disentangle the roles of local vs. remote forcing in controlling the future evolution of the AS OMZ, we performed a first set of sensitivity downscaling experiments (referred to $ROMS\_BCD_{LOC}$) where the prescribed atmospheric forcing is similarly based on bias-corrected future conditions (similar to ROMS_BCD runs) while lateral boundary conditions are maintained at the current conditions (similar to ROMS_CTL). Additionally, to explore the role of physical vs. biogeochemical forcing we performed a second set of twin simulations (denoted $ROMS\_BCD_{PHY}$), where only biogeochemical boundary conditions (i.e., O_2, NO_3) are maintained at current conditions (similar to ROMS_CTL) whereas both atmospheric and physical boundary conditions (i.e., T, S, u, v) are based on future conditions (similar to ROMS_BCD runs).

Using our sensitivity simulations, we linearly decompose the downscaled projected O_2 changes obtained by subtracting the control simulation ROMS_CTL from the bias-corrected downscaled experiment (Total changes = ROMS_BCD – ROMS_CTL) into the sum of three contributions: (i) local forcing, (ii) remote physical forcing and (iii) remote biogeochemical forcing.

$$\overbrace{ROMS\_BCD - ROMS\_CTL}^{Total\ O_2\ changes}$$

$$= \overbrace{ROMS\_BCD_{LOC} - ROMS\_CTL}^{Local\ forcing}$$

$$+ \overbrace{ROMS\_BCD_{PHY} - ROMS\_BCD_{LOC}}^{Remote\ physical\ forcing}$$

$$+ \overbrace{ROMS\_BCD - ROMS\_BCD_{PHY}}^{Remote\ biogeochemical\ forcing}$$

While the effect of changes in local forcing on future O_2 changes (LOC_{FRC}) can be assessed by simply subtracting the ROMS_CTL from the bias-corrected downscaled experiment forced with present-day boundary conditions (i.e., $ROMS\_BCD_{LOC} - ROMS\_CTL$), the impact of changes in physical conditions at the lateral boundaries can be evaluated by subtracting the BCD experiments forced with present-day boundary conditions ($ROMS\_BCD_{LOC}$) from the BCD experiments forced with present-day biogeochemical boundary conditions ($ROMS\_BCD_{PHY}$). Finally, the contribution of changes in biogeochemical conditions at the lateral boundaries (REM_{BGC}) can be assessed by subtracting the BCD experiments forced with present-day biogeochemical boundary conditions from the BCD experiments forced with future conditions (i.e., $ROMS\_BCD - ROMS\_BCD_{PHY}$).

Following earlier studies (e.g., Lachkar et al., 2020), we assessed the impact of thermal and non-thermal drivers on the total O_2 changes from both CMIP5 and downscaled simulations. For this, we decomposed the total O_2 changes into O_2 saturation (O_2Sat), accounting the thermal effects, and Apparent Oxygen Utilization (AOU), accounting the non-thermal effects (i.e., ventilation as well as biological components, Kwiatkowski et al., 2020).

$$\triangle O_2 = \triangle O_2\mathrm{Sat} - \triangle AOU$$

3 Results

3.1 Future O_2 changes in the AS OMZ

We analyze the impact of climate change on the AS OMZ (O_2 averaged over 200-700m layer) by contrasting the future projections from both CMIP5 and downscaled simulations (Figure 3). All CMIP5

models consistently project future oxygenation (positive anomaly, Figures 3A–C) of the sub-surface layer in the southern AS (SAS, Equator to ~10°N) in agreement with earlier studies (e.g., Bopp et al., 2013; Cocco et al., 2013; Bianchi et al., 2018). A similar oxygenation projected from all 3 models in two regional downscaled approaches further strengthens the reliability of this O_2 future response pattern (Figures 3A.1-C.1, A.2–C.2). In contrast to this, both the magnitude and sign of projected O_2 in the northern AS (NAS, north of ~20°N) exhibits a strong sensitivity to the choice of CMIP5 model (Figures 3A–C). The deoxygenation is stronger and encompasses larger area over the NAS in CMIP5_GFDL (Figure 3B) compared to much weaker deoxygenation seen in both CMIP5_MPI (Figure 3A) and CMIP5_IPSL (Figure 3C). These differences may in part reflect differences in the representation of local physics and biogeochemistry in these models. To explore this hypothesis, we contrast regional downscaled models with their parent CMIP5 model. Using a common physical-biogeochemical model (ROMS-NPZD), the DD projections expectedly display slightly weaker model discrepancies (associated with differences in parent model present-day conditions) relative to those in CMIP5 models. This is particularly true in the NAS where the strongly contrasting O_2 changes simulated by the three CMIP5 models are significantly reduced in the DD experiments (Figure 3). However, despite using a common physical and biogeochemical model, these simulations still display substantial differences in their projected O_2 changes in both NAS and SAS. This indicates that, despite the higher regional model resolution and the likely improved representation of local physics and biogeochemistry in the regional simulations, other factors and biases inherent to the parent models such as the representation of present-day conditions and their projected large-scale physical and environmental changes strongly influence the downscaled O_2 projections.

3.2 Sensitivity of future oxygen projections to model representation of present-day conditions

The DD and the BCD simulations differ only by their initial state, as they are conducted with a common (ROMS-NPZD) model, and are forced with the same CMIP5 anomalies at the boundaries.

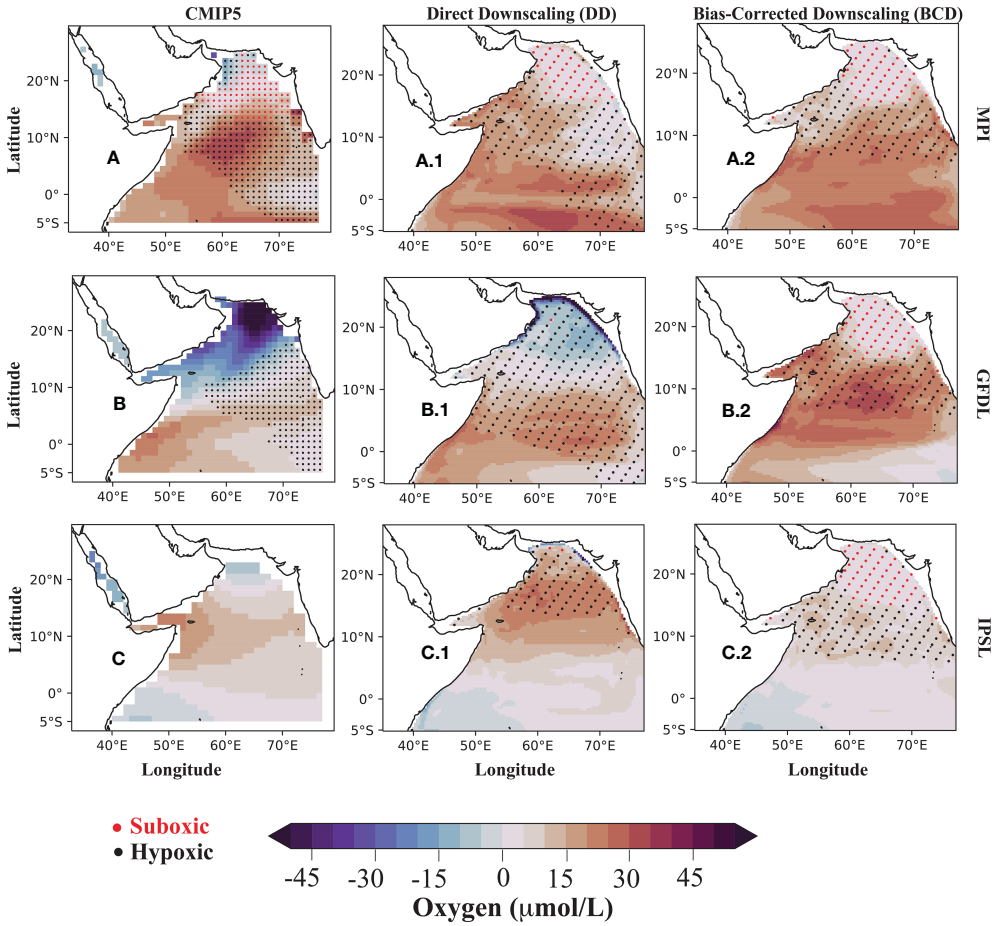

FIGURE 3
Projected oxygen changes in the OMZ layer (200-700m). **(A–C)** with the 3 CMIP5 experiments; **(A.1–C.1)** with the corresponding Direct Downscalling ROMS experiments; **(A.2–C.2)** with the corresponding Bias-Corrected Downscalling ROMS experiments. Oxygen losses (deoxygenation) appear in blue shading, and oxygen gain (oxygenation) in red shading. Red dots show the location of anoxic waters (OMZ core) and black dots show the location of hypoxic waters (OMZ) in the corresponding present-day simulations (CMIP5_HIST for CMIP5, ROMS_HIST for DD, ROMS_CTL for BCD). By construction, the present-day experiment (ROMS_CTL) is the same for the three BCD experiments, and the BCD experiments are the best estimates.

Therefore, contrasting the projections computed from these experiments allows us to quantify the sensitivity of the future oxygen projections to model representation of present-day conditions. The comparison between the BCD and DD projections indeed reveals significant differences in the OMZ layer in NAS, particularly with models that are associated with large biases in their representation of the present-day OMZ, such as the GFDL and IPSL (Figure 3). However, when corrected for the present-day biases, the spread in the projected patterns in the NAS reduces substantially among the three models in BCD experiments relative to the DD simulations (Figure 3). Indeed, the three BCD simulations consistently project a slight oxygenation in the NAS in opposition with the conflicting trends in the DD and CMIP5 simulations. In contrast to this, the inter-model differences are maintained and remain similar between the DD and BCD experiments in the SAS (Figure 3). These differences can also be seen in the vertical profiles of the projected O_2 anomalies presented in Figure 4. By removing the present-day biases in their initial state, the 3 models agree on the simulated changes throughout the water column in the NAS (Figure 4C). Moreover, in contrast to both CMIP5 (Figure 4A) and DD (Figure 4B) simulations, the layer of maximum deoxygenation is much shallower in the BCD experiments in the NAS (Figure 4C). In the SAS, however, the model discrepancies rather than the experiment strategies remain important among the BCD experiments and are similar to those simulated in the CMIP5 and DD runs (Figure 4). This indicates that the sensitivity of the O_2 projections to model representation of present-day conditions is much more important in the NAS relative to the SAS. It also suggests that downscaling following the BCD approach can help reduce model discrepancies and narrow down uncertainties in projected future O_2 changes in the NAS, while it adds little value in the SAS. Our quantitative analysis (Figure 5) further reveals that, the consistent oxygenation of the sub-surface layers in SAS leads to a future shrinking of AS OMZ under the climate change.

In the next section, we examine the role of local vs. remote forcing in causing O_2 changes in both NAS and SAS regions.

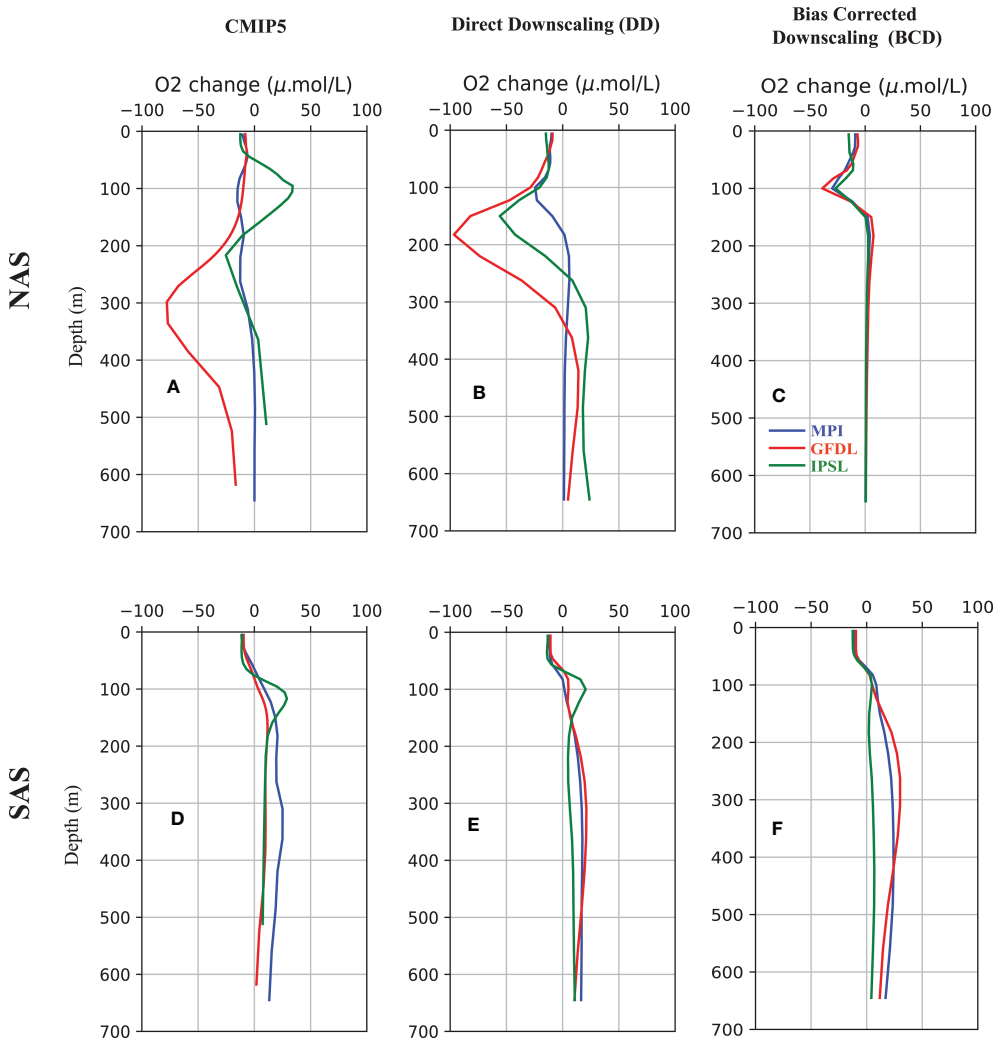

FIGURE 4
Projected changes in O2 vertical profiles. O2 response profiles averaged over the northern (NAS) and southern (SAS) Arabian Sea **(A, D)** with the three CMIP5 experiments, **(B, E)** with the corresponding Direct Downscaling ROMS experiments and **(C, F)** with the corresponding Bias-Corrected Downscaling ROMS experiments (MPI in blue, GFDL in red and IPSL in green). The NAS and SAS zones are shown in Figure 1A.

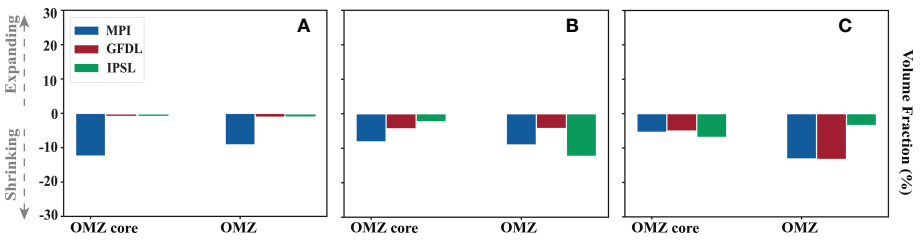

FIGURE 5
Projected changes in OMZ volume. Projected changes in the Volume fraction occupied by suboxic water masses (OMZ_core, O2 < 4 µmol/l) and by hypoxic water masses (OMZ, O2 <60 µmol/l) in the 0 – 1000 m top layer of the Arabian Sea, **(A)** in the three CMIP5 experiments, **(B)** in the corresponding Direct Downscaling experiments and **(C)** in the corresponding Bias-Corrected Downscaling experiments (MPI in blue, GFDL in red and IPSL in green). The OMZ volume is shrinking in all experiments.

3.3 Contribution of local vsremote forcing to projected future Ochanges

As both local and remote forcings play major role in controlling the coastal and open-ocean biogeochemistry in AS (Currie et al., 2013; Parvathi et al., 2017a; Pearson et al., 2022), we further use our downscaled model to disentangle their respective contributions to the future projected OMZ response. In Figure 6, we decompose the total projected O_2 response in the OMZ layer in to that resulting from local atmospheric changes, and remote physical and biogeochemical changes. This decomposition reveals that, each process contributes significantly to the total O_2 changes in the AS OMZ layer, depending on the region and the model (Figure 6). In the SAS, local forcing is leading to a weak deoxygenation along the Indian west coast and oxygenation over the rest, consistently among all models (Figures 6A.1-C.1). In all the models, the oxygenation along the west coast of India (region within SAS) is driven by both remote physical and biogeochemical processes, while it is dominated by the remote biogeochemical forcing in the rest of SAS (Figures 6A.2–C.2, A.3–C.3).

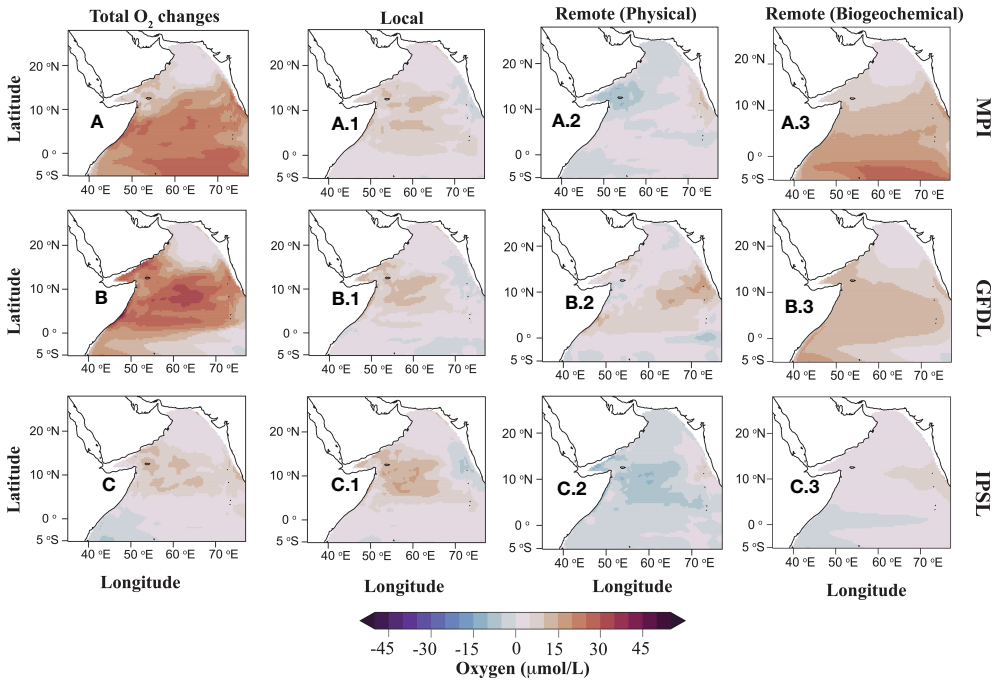

FIGURE 6
Projected oxygen changes in the OMZ layer (200-700m) **(A–C)** The impact of climate change on the ASOMZ computed from the 3 Bias-Corrected Downscalled ROMS experiments (ROMS_BCD – ROMS_CTL), **(A.1–C.1)** with a set of sensitivity experiments with which the impact of changes in surface forcing is isolated ($ROMS\_BCD_{LOC}$ – ROMS_CTL), **(A.2–C.2)** with a set of sensitivity experiments with which the role of changes in physical lateral boundary condition is isolated ($ROMS\_BCD_{PHY}$ – $ROMS\_BCD_{LOC}$), **(A.3–C.3)** with a set of sensitivity experiments the impact of changes in biogeochemical lateral boundary conditions are isolated (ROMS_BCD – $ROMS\_BCD_{PHY}$). Oxygen losses (deoxygenation) appear in blue shading, and oxygen gain (oxygenation) in red shading. Differences between experiments reveal the respective contribution of local and remote forcings to the total projected change in O2.

3.4 Mechanisms driving the future OMZ changes

In the subsequent analysis, we separated out the contribution from thermal and non-thermal components on the O_2 changes (Figure 7). The nearly compensating influence of thermal and non-thermal components in the sub-surface layer of NAS leads to weaker OMZ changes in all 3 BCD projections (Figure 7). In contrast, in the SAS the non-thermal component, i.e., AOU, drives most of the sub-surface oxygenation (Figure 7). As the AOU is affected by both ventilation and biological changes (Kwiatkowski et al., 2020), the oxygenation (deoxygenation) signal can be indicative of either an increase (decrease) in dynamical supply or decline (increase) in biological demand. Within the scope of current study, we test the dominant driver for OMZ changes by analyzing the future projected annual productivity simulations from both CMIP5 and downscaling experiments (Figure 8). In agreement with earlier studies (e.g., Praveen et al., 2016; Roxy et al., 2016), all the models from CMP5 and regional downscaling project a consistent weakening of annual productivity in large parts of the AS under the climate change. The consistent weakening of biological demand arising from this decline in productivity in SAS (Figure 8) along with the larger supply of O_2 (Figure SI 7) at the southern boundaries, lead to a future oxygenation of the SAS under climate change. Whereas, in the NAS, the projected annual productivity response from both CMIP5 and regional downscaling is highly sensitive to the model.

4 Discussion

4.1 Lessons learnt from the regional downscaling:

(a) Will the AS OMZ expand or shrink under the climate change?

The subtle balance between the dynamical ventilation and biological demand is reported to maintain the AS OMZ with no pronounced seasonality in the present-day climate (Sarma, Sarma, 2002; Resplandy et al., 2012 and the references therein). Previous studies based on CMIP5 simulations have exhibited the potential impact of climate change on both atmospheric circulation and the oceanic primary productivity (Sandeep & Ajayamohan, 2015; Praveen et al., 2016; Roxy et al., 2016; Parvathi et al., 2017b).

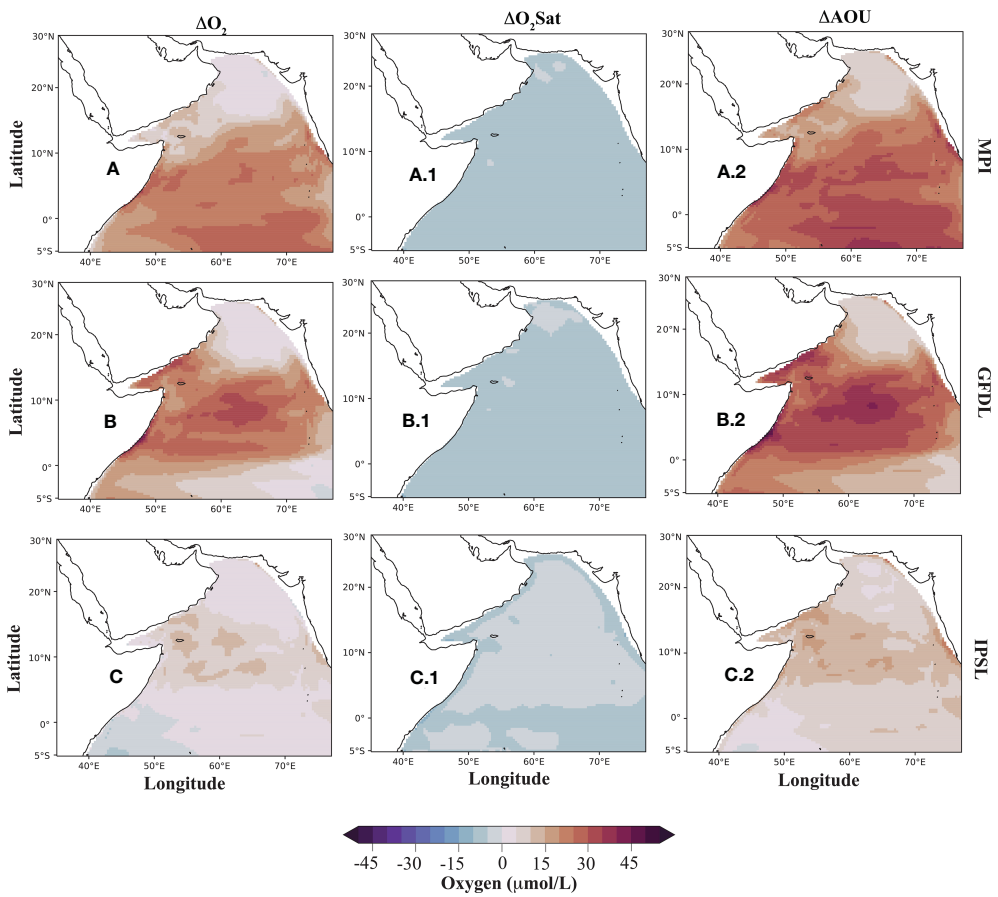

FIGURE 7
Contribution from thermal and non-thermal components to the projected OMZ changes. **(A-C)** Projected changes in O2 averaged over the 200-700m layer in the Arabian Sea in the 3 Bias-Corrected Downscaling ROMS experiments, decomposed into their thermal (**A.1-C.1**; ΔO2sat) and non-thermal (**A.2-C.2**; - ΔAOU) components.

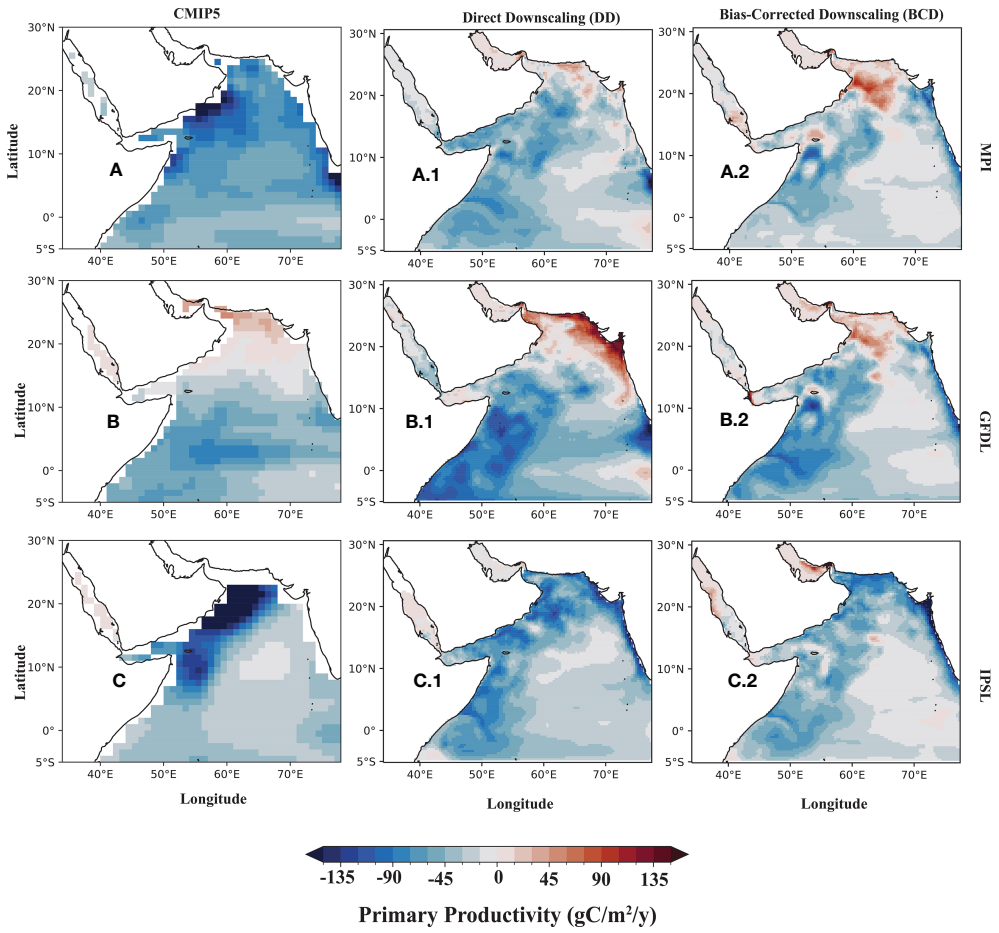

FIGURE 8
Drivers of oxygenation at the SAS. **(A–C)** Projected changes in the annual net primary productivity from 3 CMIP5 experiments; **(A.1–C.1)** with the corresponding Direct Downscalling ROMS experiments; **(A.2–C.2)** with the corresponding Bias-Corrected Downscalling ROMS. A future weakening appears in blue shading, and strengthening in red shading.

Those projected changes have the potential to impact the AS OMZ in future. Using regional downscaling of a subset of ESMs under CMIP5, we find a consistent oxygenation in the sub-surface (200-700m) layer of the SAS, that potentially leads to shrinking of the AS OMZ (Figure 5) under climate change. This is strikingly different compared to other low-oxygen zones of the global oceans, which are reported to expand under the climate change (e.g., Keeling et al., 2010).

(b)How does the model representation of present-day conditions influence the future projections?

The convective mixing driven by northeast (boreal winter) monsoon winds acts as a ventilation pathway for the perennial AS OMZ (Morrison et al., 1999). This density driven overturning is highly influenced by the influx of high saline water from the Arabian Gulf. Moreover, the Arabian Gulf water itself acts as a ventilation pathway for the AS OMZ (Naqvi et al., 2009; Lachkar et al., 2019; Lachkar et al., 2021).

Our analyses indicate that misrepresentation of the main water masses and mixing in the northern AS in CMIP5 models has led to intense deoxygenation in those biased models. For instance, overestimation of inflow of the high saline Gulf water and the Arabian Sea High Salinity Water results in a very weak stratification in both GFDL and IPSL models (Figure 9). This weak stratification leads to anomalous mixing and hence deepening of the mixed layer, allowing intrusion of high oxygenated water into greater depths in the northern AS (Figure 1). However, the basin-wide warming (~4°C, calculated from 3 CMIP5 models) and the reduced winter monsoonal circulation (Parvathi et al., 2017a) under climate change act to weaken the vertical mixing, leading to intense deoxygenation in the future projections of GFDL. The above present-day misrepresentations have led to inconsistent future projections in the NAS. On the other hand, we have consistent response in the NAS when corrected for the present-day biases (Figures 3, 4). When the background stratification is very strong (Figure 9, the pattern is very similar even with salinity or density), even if we force the regional (ROMS_DD GFDL) model with biased surface and boundary fields, the projected deoxygenation in the north remains much weaker compared to the its parent CMIP5 model (Figure 3). This clearly indicates the sensitivity of mean state of model in determining the future projections of OMZ in the northern AS. When corrected for the present-day biases in regional models, we find that the layer of deoxygenation has shown significant shift and

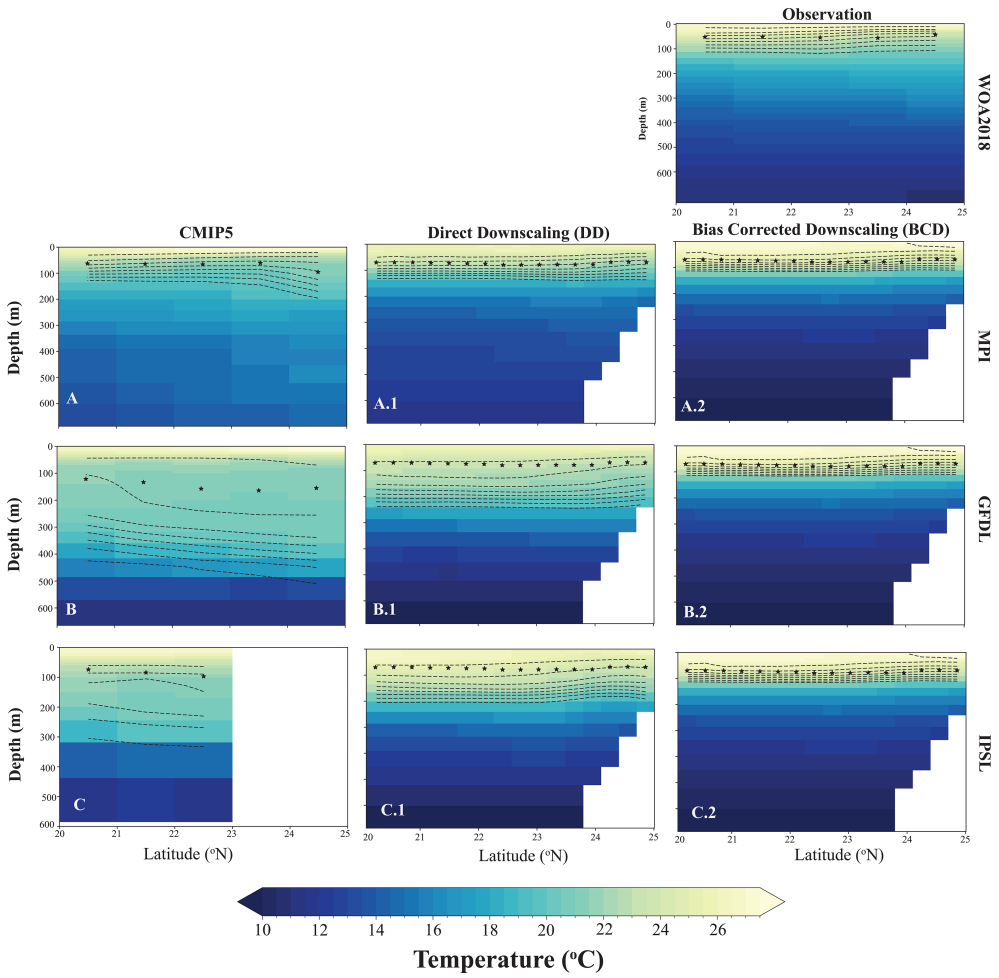

FIGURE 9
Role of background stratification in determining the vertical distribution. Vertical section of annual temperature (°C; in color shading), dissolved oxygen (µmol/L; dashed contours from 80 µmol/L and above concentration) along with winter mixed layer (m; asterisks) averaged in the northern Arabian Sea from observation (upper top, WOA2018), **(A–C)** the three CMIP5 models (MPI, GFDL, IPSL) over the present-day period (CMIP5_HIST simulations, averaged from years 1986 to 2005); **(A.1–C.1)** the corresponding (to CMIP5_HIST) Direct Downscalling ROMS experiments; and **(A.2–C.2)** from the corresponding (to CMIP5_HIST) Bias-Corrected Downscalling ROMS experiments.

agreement amongst the models (Figure 4). This is particularly important as the deoxygenation and the associated shoaling of low oxygen water are known to impart stress on the ecosystem leading to habitat compression – a major negative impact of climate change as reported in many earlier studies (Eg., Köhn et al., 2022).

(c) What drives the robust oxygenation in the southern Arabian Sea?

Earlier studies have shown the importance of southern boundary in ventilating the AS OMZ and thereby preventing its extension to the south (Sarma, 2002; Resplandy et al., 2012; McCreary et al., 2013). Using specific sensitivity experiments, we investigated the importance of southern boundary for the future evolution of AS OMZ under climate change. Our analysis revealed that, the oxygenation in the sub-surface layers of southern AS is largely driven by the remote processes influencing the southern and eastern boundaries. The reduced demand resulting from weaker primary productivity overwhelms the weaker dynamical supply under the climate change. With specific sensitivity experiments, we also demonstrate that the transport of O_2 from the southern Indian Ocean is important even under the climate change.

(d) How important is it to do regional downscaling for future projection of OMZs?

Unlike many parts of the global ocean, climate change induces an oxygenation of the southern boundary of AS that can potentially lead to a future shrinking of AS OMZ. From our downscaling experiments, we find that regional downscaling of global models is relevant only where local forcing is dominant, away from boundaries. For instance, in regions like northern AS, where there are many controlling factors for the present-day state, it is important to account for the mean-state biases. A correction of such biases can bring completely new insights, and also improve the inter-model agreement. The subtle balance between the source and sink can be highly sensitive to the layer and the region which we consider. With present study, we also learnt that, the commonly accepted practice of considering multi-model mean from CMIP5 can potentially mislead, as some of the models with anomalous response pattern can completely alias the mean response patterns.

Hence, one has to practice caution while interpreting the impact of climate change on the dissolved O_2 from global coupled models.

4.2 Limitations of the study

The present study while bringing insights to the impact of climate change on the AS OMZ, also possesses some unavoidable limitations. One of the main limitations arises from the simplicity of our biogeochemical model. The NPZD coupled with ROMS is based only on nitrogen and do not represent any other limiting nutrients. This can potentially lead to the biases in the representation of phytoplankton in the regions such as western AS, where nutrients other than nitrate may be a limiting factor (Naqvi et al., 2009). However, the productivity in a large part of AS is limited by nitrate (Koné et al., 2009) and hence the choice of our biogeochemical component should not affect the main conclusions of the study. We also find an underestimation of the intrusion of the Gulf water in the northern AS that introduces strong stratification there. This has already been noticed in the earlier studies with same configuration (Lachkar et al., 2018) and is attributed to inaccurate forcing fields in the Gulf region, that does not allow the correct representation of circulation and the outflow of the Gulf water into AS. However, compared to the highly biased CMIP5 models, our configuration captures the main patterns of key physical and biogeochemical patterns in the AS basin including their seasonal modulations, indicating the above factors do not necessarily limit exploiting the regional model for current attempt.

5 Conclusions

We utilize simulations from a subset of 3 selected Coupled Model Intercomparison Project Phase 5 (CMIP5) along with a set of regional downscaled experiments using ROMS configured for the Arabian Sea (AS) domain to assess the impact of climate change on the AS Oxygen Minimum Zone (OMZ), and to investigate its main drivers. The regional downscaling approach allows us to design and perform various sensitivity experiments with the same base model for the selected parent CMIP5 model. Thus, the sensitivity to the model representation of present-day conditions, as well as the contributions of local and remote forcing can be isolated. Moreover, the regional downscaling approach also allows us to correct the biases in the earth system models.

Overall, our analysis reveals a robust oxygenation in the southern AS that can potentially lead to a shrinking of the AS OMZ under the climate change. The sensitivity experiments clearly reveal the dominance of remote processes in driving this oxygenation through a combination of weaker dynamical supply and reduced biological demand. The influence of local and remote processes is highly sensitive to the layer that we consider. While the local warming dominates in the upper 100m (not shown), the role of local and remote processes shows meridional heterogeneity in the sub-surface (200-700m), with local (remote) forcing driving trends in the northern (southern) AS. Using our downscaling experiments, we also show the importance of model's present-day biases in determining the layer of deoxygenation in the northern AS. Finally, contrasting downscaling approaches with and without correction of model biases with respect to observations revealed a strong sensitivity of future O_2 projections to model simulated current conditions. Therefore, improving the representation of present-day conditions in global models is needed to reduce uncertainties in downscaled future O_2 projections.

Data availability statement

The raw data supporting the conclusions of this article will be made available by the authors, without undue reservation.

Author contributions

All the authors contributed towards forming the objectives of current study and designing the regional downscaled experiments. PV performed the simulations and analysis, wrote the manuscript with the help of ZL and ML. All authors contributed to the article and approved the submitted version.

Funding

This research was fully funded by the research grants from Center for Prototype Climate Modeling (CPCM) and Arabian Center for Climate and Environmental ScienceS (ACCESS) at New York University Abu Dhabi (NYUAD). Both PV and ZL were supported by Tamkeen through research grant CG009 to NYUAD's ACCESS research center.

Acknowledgments

We thank the support from the Arabian Center for Climate and Environmental ScienceS (ACCESS) at New York University Abu Dhabi (NYUAD) for providing the financial support for carrying out this research work. We thank the NYUAD for facilitating high-performance computing (HPC) resources, where our downscaling experiments and the analysis were performed. We thank Benoit Marchand, Muataz Al Barwani and the whole NYUAD HPC team for technical support. We thank the ROMS/CROCO team for giving access to the model and simulations respectively. We acknowledge the World Climate Research Programme's Working Group on Coupled Modelling, which is responsible for CMIP, and we thank the climate modeling groups (listed in Table 1 of this paper) for producing and making available their model output. For CMIP the U.S. Department of Energy's Program for Climate Model Diagnosis and Intercomparison provides coordinating support and led development of software infrastructure in partnership with the Global Organization for Earth System Science Portals. We thank Shafer Smith (NYU, New York) for the constant encouragement and support. PV thanks Alain De Verneil and Michael Mehari (NYUAD) for fruitful discussions. PV also thanks Suresh Iyyappan (CSIR-NIO, Goa) for helping to shape the initial project proposal.

Conflict of interest

The authors declare that the research was conducted in the absence of any commercial or financial relationships that could be construed as a potential conflict of interest.

Publisher's note

All claims expressed in this article are solely those of the authors and do not necessarily represent those of their affiliated organizations, or those of the publisher, the editors and the reviewers. Any product that may be evaluated in this article, or claim that may be made by its manufacturer, is not guaranteed or endorsed by the publisher.

Supplementary material

The Supplementary Material for this article can be found online at: https://www.frontiersin.org/articles/10.3389/fmars.2023.1123739/full#supplementary-material

References

Barnier, B., Siefridt, L., and Marchesiello, P. (1995). Thermal forcing for a global ocean circulation model using a three-year climatology of ECMWF analyses. *J. Mar. Syst.* 6 (4), 363–380. doi: 10.1016/0924-7963(94)00034-9

Bianchi, D., Weber, T. S., Kiko, R., and Deutsch, C. (2018). Global niche of marine anaerobic metabolisms expanded by particle microenvironments. *Nat. Geosci* 11, 263–268. doi: 10.1038/s41561-018-0081-0

Bopp, L., Resplandy, L., Orr, J. C., Doney, S. C., Dunne, J. P., Gehlen, M., et al. (2013). Multiple stressors of ocean ecosys- tems in the 21st century: projections with CMIP5 models. *Biogeosciences* 10, 6225–6245. doi: 10.5194/bg-10-6225-2013

Breitburg, D., Levin, L. A., Oschlies, A., Grégoire, M., Chavez, F. P., Conley, D. J., et al. (2018). Declining oxygen in the global ocean and coastal waters. *Science* 359, eaam7240. doi: 10.1126/science.aam7240

Buil, P. M., Jacox, M. G., Fiechter, J., Alexander, M. A., Bograd, S., Curchitser, E. N., et al. (2021). A dynamically downscaled ensemble of future projections for the California current system. *Front. Mar. Sci.* 8, 612874. doi: 10.3389/fmars.2021.612874

Chronopoulou, P. M., Shelley, F., Pritchard, W., Maanoja, S. T., and Trimmer, M. (2017). Origin and fate of methane in the Eastern tropical north pacific oxygen minimum zone. *ISME J.* 11, 1386–1399. doi: 10.1038/ismej.2017.6

Cocco, V., Joos, F., Steinacher, M., Froölicher, T. L., Bopp, L., Dunne, J., et al. (2013). Oxygen and indicators of stress for marine life in multi-model global warming projections. *Biogeosciences* 10, 1849–1868. doi: 10.5194/bg-10-1849-2013

Codispoti, L. A., Brandes, J. A., Christensen, J. P., Devol, A. H., Naqvi, S. W. A., Paerl, H. W., et al. (2001). The oceanic fixed nitrogen and nitrous oxide budgets: moving targets as we enter the anthropocene? *Sci. Mar.* 65, 85–105. doi: 10.3989/scimar.2001.65s285

Currie, J. C., Lengaigne, M., Vialard, J., Kaplan, D. M., Aumont, O., Naqvi, S. W. A., et al. (2013). Indian Ocean dipole and El Niño/Southern oscillation impacts on regional chlorophyll anomalies in the Indian ocean. *Biogeosciences* 10, 6677–6698. doi: 10.5194/bg-10-6677-2013

Dileep, K. (2006). *Biogeochemitry of north Indian ocean, IGBP-WCRP-SCOPE report series: 1*. Indian National Science Academy).

Echevin, V., Gévaudan, M., Espinoza-Morriberón, D., Tam, J., Aumont, O., Gutierrez, D., et al. (2020). Physical and biogeochemical impacts of RCP8.5 scenario in the Peru upwelling system. *Biogeosciences* 17, 3317–3341. doi: 10.5194/bg-17-3317-2020

Falkowski, P. (1997). Evolution of the nitrogen cycle and its influence on the biological sequestration of CO2 in the ocean. *Nature* 387, 272–275. doi: 10.1038/387272a0

Fennel, K., and Testa, J. M. (2019). Biogeochemical controls on coastal hypoxia. *Annu. Rev. Mar. Sci.* 11, 105–130. doi: 10.1146/annurev-marine-010318-095138

Gopika, S., Izumo, T., Vialard, J., Lengaigne, M., Suresh, I., and Kumar, M. R. R. (2020). Aliasing of the Indian ocean externally-forced warming spatial pattern by internal climate variability. *Climate Dynamics* 54 (1–2), 1093–1111. doi: 10.1007/s00382-019-05049-9

Han, W., Vialard, J., McPhaden, M. J., Lee, T., Masumoto, Y., Feng, M., et al. (2014). Indian Ocean decadal variability: a review. *Bull. Am. Meteorological Soc.* 95 (11), 1679–1703. doi: 10.1175/BAMS-D-13-00028.1

Huang, C. J., Qiao, F., and Dai, D. (2014). Evaluating CMIP5 simulations of mixed layer depth during summer. *J. Geophys. Res. Oceans* 119, 2568–2582. doi: 10.1002/2013JC009535

Keeling, R. F., Körtzinger, A., and Gruber, N. (2010). Ocean deoxygenation in a warming world. *Annu. Rev. Mar. Sci.* 2, 199–229. doi: 10.1146/annurev.marine.010908.163855

Köhn, E. E., Münnich, M., Vogt, M., Desmet, F., and Gruber, N. (2022). Strong habitat compression by extreme shoaling events of hypoxic waters in the Eastern pacific. *J. Geophysical Research: Oceans* 127, e2022JC018429. doi: 10.1029/2022JC018429

Koné, V., Aumont, O., Lévy, M., and Resplandy, L. (2009). Physical and biogeochemical controls of the phytoplankton seasonal cycle in the Indian Ocean: A modeling study. *Indian Ocean Biogeochemical Processes Ecol. Variability* 185, 350. doi: 10.1029/2008GM000700

Kwiatkowski, L., Torres, O., Bopp, L., Aumont, O., Chamberlain, M., Christian, J. R., et al. (2020). Twenty-first century ocean warming, acidification, deoxygena- tion, and upper-ocean nutrient and primary production decline from CMIP6 model projections. *Biogeosciences* 17, 3439–3470. doi: 10.5194/bg-17-3439-2020

Lachkar, Z., Lévy, M., and Smith, S. (2018).). intensification and deepening of the Arabian Sea oxygen minimum zone in response to increase in Indian monsoon wind intensity. *Biogeosciences* 15, 159–186. doi: 10.5194/bg-15-159-2018

Lachkar, Z., Lévy, M., and Smith, K. S. (2019). Strong intensification of the Arabian Sea oxygen minimum zone in response to Arabian gulf warming. *Geophys. Res. Lett.* 46, 5420–5429. doi: 10.1029/ 2018GL081631

Lachkar, Z., Mehari, M., Al Azhar, M., Lévy, M., and Smith, S. (2021). Fast local warming is the main driver of recent deoxygenation in the northern Arabian Sea. *Biogeosciences* 18, 5831–5849. doi: 10.5194/bg-18-5831-2021

Lachkar, Z., Smith, S., Lévy, M., and Pauluis, O. (2016). Eddies reduce denitrification and compress habitats in the Arabian Sea. *Geophys. Res. Lett.* 43, 9148–9156. doi: 10.1002/2016GL069876

Large, W. G., McWilliams, J. C., and Doney, S. C. (1994). Oceanic vertical mixing: a review and a model with a nonlocal boundary layer parameterization. *Rev. Geophys.* 32, 363–403. doi: 10.1029/94RG01872

Lévy, M., Resplandy, L., Palter, J. B., Couespel, D., and Lachkar, Z. (2021). The crucial contribution of mixing to present and future ocean oxygen distribution: Chapter 13. A. C. Naveira Garabato and M. P. Meredith. *Ocean Mixing, 1st* edition, Elsevier, Ocean Mixing, 9780128215135. doi: 10.1016/B978-0-12-821512-8.00020-7ff

Marchesiello, P., Debreu, L., and Couvelard, X. (2009). Spurious diapycnal mixing in terrain-following coordinate models: the problem and a solution. *Ocean Modell.* 26, 156–169. doi: 10.1016/j.ocemod.2008.09.004

McCreary, J. P.Jr., Yu, Z., Hood, R. R., Vinaychandran, P. N., Fu- rue, R., Ishida, A., et al. (2013). And Dynamics of the Indian- ocean oxygen minimum zones, prog. *Oceanogr. 112/113* 15–, 37.

Morrison, J. M., Codispoti, L. A., Smith, S. L., Wishner, K., Flagg, C., Gardner, W. D., et al. (1999). And gundersen, J The oxygen minimum zone in the Arabian Sea during 1995 – overall seasonal and geographic patterns, and relationship to oxygen gradients. *S.Deep-Sea Res. Pt. II* (doi:10.1016/S0967-0645(99)00048- X) 46, 1903–1931. doi: 10.1016/S0967-0645(99)00048-

Nagura, M., McCreary, J., and Annamalai, H. (2018). Origins of coupled model biases in the Arabian Sea climatological state. *J. ofClimate* 31 (5), 2005–2029. doi: 10.1175/JCLI-D-17-0417.1

Naqvi, S. W. A., Naik, H., Jayakumar, D. A., Pratihary, A. K., Narvenkar, G., Kurian, S., et al. (2009). Seasonal anoxia over the Western in- dian continental shelf. *Geoph. Monog. Ser.* 185, 333–345. doi: 10.1029/2008GM000745

Naqvi, S. W. A., and Noronha, R. J. (1991). Nitrous oxide in the Arabian Sea. *Deep Sea Res. Part A* 38, 871–890, 38. doi: 10.1016/0198-0149(91)90023-9

Parvathi, V., Suresh, I., Lengaigne, M., Ethe, C., Vialard, J., Levy, M., et al. (2017a).). positive Indian ocean dipole events prevent anoxia along the west coast of India. *Biogeosciences* 14 (6), 1541–1559. doi: 10.5194/bg-14-1541-2017

Parvathi, V., Suresh, I., Lengaigne, M., Izumo, T., and Vialard, J. (2017b). Robust projected weakening of winter mon- soon winds over the Arabian Sea under climate change. *Geophysical Res. Lett.* 44. doi: 10.1002/2017GL075098

Pearson, J., Resplandy, L., and Poupon, M. (2022). Coastlines At risk of hypoxia from natural variability in the northern Indian ocean. *Global Biogeochem. Cycles* 36, e2021GB007192. doi: 10.1029/2021GB007192

Praveen, V., Ajayamohan, R., Valsala, V., and Sandeep, S. (2016). Intensification of upwelling along Oman coast in a warming scenario. *Geophys. Res. Lett.* 43, 7581–7589. doi: 10.1002/2016GL069638

Resplandy, L., Lévy, M., Bopp, L., Echevin, V., Pous, S., Sarma, V. V. S. S., et al. (2012). Controlling factors of the oxygen balance in the Arabian sea's OMZ. *Biogeosciences* 9, 5095–5109. doi: 10.5194/bg-9-5095-2012

Risien, C. M., and Chelton, D. B. (2008). A global climatology of surface wind and wind stress fields from eight years of QuikSCAT scat- terometer data. *J. Phys. Oceanogr.* 38, 2379–2413. doi: 10.1175/2008JPO3881.1

Roxy, M. K., Modi, A., Murtugudde, R., Valsala, V., Panickal, S., and Prasanna Kumar, S. (2016). A reduction in marine primary productivity driven by rapid warming over the tropical Indian ocean. *Geophysical Res. Lett.* 43, 826–833. doi: 10.1002/2015GL066979

Sandeep, S., and Ajayamohan, R. S. (2015). Poleward shift in Indian summer monsoon low level jetstream under global warming. *ClimateDynamics* 45, 337–351. doi: 10.1007/s00382-014-2261-y

Sarma, V. V. S. S. (2002). An evaluation of physical and biogeochemical processes regulating perennial suboxic conditions in the water column of the Arabian Sea. *Global Biogeochem. Cy.* 16, 1082. doi: 10.1029/2001GB001461

Schmidt, H., Getzlaff, J., Löptien, U., and Oschlies, A. (2021). Causes of uncertainties in the representation of the Arabian Sea oxygen minimum zone in CMIP5 models. *Ocean Sci.* 17, 1303–1320. doi: 10.5194/os-17-1303-2021

Shchepetkin, A. F., and McWilliams, J. C. (2005). The regional oceanic modeling system (ROMS): a split-explicit, free-surface, topography-following-coordinate oceanic model. *Ocean Mod- ell.* 9, 347–404. doi: 10.1016/j.ocemod.2004.08.002

Stief, P., Lundgaard, A. S. B., Morales-Ramírez, Á., Thamdrup, B., and Glud, R. N. (2017). Fixed-nitrogen loss associated with sinking zooplankton carcasses in a coastal oxygen minimum zone (Golfo dulce, Costa Rica). *Front. Mar. Sci.* 4. doi: 10.3389/fmars.2017.00152

Stramma, L., Prince, E. D., Schmidtko, S., Luo, J., Hoolihan, J. P., Visbeck, M., et al. (2012). Expansion of oxygen minimum zones may reduce available habitat for tropical pelagic fishes. *Nat. Climate Change* 2, 33–37. doi: 10.1038/nclimate1304

Taylor, R. J, and Meehl, G. A. (2012). An overview of CMIP5 and the experimentdesign bull. *Am. Meteorol. Soc* 93 (4), 485–498. doi: 10.1175/BAMS-D-11-00094.1

Vivekanandan, E., Srinath, M., and Kuriakose, S. (2005). Fishing the marine food web along the Indian coast. *Fish. Res.* 72, 241–252. doi: 10.1016/j.fishres.2004.10.009

Xu, Z., Han, Y., and Yang, Z. (2019). Dynamical downscaling of regional climate: a review of methods and limitations. *Sci. China Earth Sci.* 62, 365–375. doi: 10.1007/s11430-018-9261-5

frontiers | Frontiers in Marine Science

TYPE Original Research
PUBLISHED 12 June 2023
DOI 10.3389/fmars.2023.1134851

OPEN ACCESS

EDITED BY
Claire Mahaffey,
University of Liverpool, United Kingdom

REVIEWED BY
Wei-Jen Huang,
National Sun Yat-sen University, Taiwan
Samuel T. Wilson,
University of Hawaii at Manoa, United States
Clara A. Fuchsman,
University of Maryland, College Park, United States

*CORRESPONDENCE
Craig L. McNeil
cmcneil@uw.edu

RECEIVED 31 December 2022
ACCEPTED 15 May 2023
PUBLISHED 12 June 2023

CITATION
McNeil CL, D'Asaro EA, Altabet MA, Hamme RC and Garcia-Robledo E (2023) Autonomous observations of biogenic N_2 in the Eastern Tropical North Pacific using profiling floats equipped with gas tension devices.
Front. Mar. Sci. 10:1134851.
doi: 10.3389/fmars.2023.1134851

Autonomous observations of biogenic N_2 in the Eastern Tropical North Pacific using profiling floats equipped with gas tension devices

Craig L. McNeil[1]*, Eric A. D'Asaro[1], Mark A. Altabet[2], Roberta C. Hamme[3] and Emilio Garcia-Robledo[4]

[1]Applied Physics Laboratory, University of Washington, Seattle, WA, United States, [2]School for Marine Science and Technology, University of Massachusetts Dartmouth, New Bedford, MA, United States, [3]School of Earth and Ocean Sciences, University of Victoria, Victoria, BC, Canada, [4]Department of Biology, University of Cadiz, Cadiz, Spain

Oxygen Deficient Zones (ODZs) of the world's oceans represent a relatively small fraction of the ocean by volume (<0.05% for suboxic and<5% for hypoxic) yet are receiving increased attention by experimentalists and modelers due to their importance in ocean nutrient cycling and predicted susceptibility to expansion and/or contraction forced by global warming. Conventional methods to study these biogeochemically important regions of the ocean have relied on well-developed but still relatively high cost and labor-intensive shipboard methods that include mass-spectrometric analysis of nitrogen-to-argon ratios (N_2/Ar) and nutrient stoichiometry (relative abundance of nitrate, nitrite, and phosphate). Experimental studies of denitrification rates and processes typically involve either *in-situ* or *in-vitro* incubations using isotopically labeled nutrients. Over the last several years we have been developing a Gas Tension Device (GTD) to study ODZ denitrification including deployment in the largest ODZ, the Eastern Tropical North Pacific (ETNP). The GTD measures total dissolved gas pressure from which dissolved N_2 concentration is calculated. Data from two cruises passing through the core of the ETNP near 17 °N in late 2020 and 2021 are presented, with additional comparisons at 12 °N for GTDs mounted on a rosette/CTD as well as modified profiling Argo-style floats. Gas tension was measured on the float with an accuracy of< 0.1% and relatively low precision (< 0.12%) when shallow (P< 200 dbar) and high precision (< 0.03%) when deep (P > 300 dbar). We discriminate biologically produced N_2 (ie., denitrification) from N_2 in excess of saturation due to physical processes (e.g., mixing) using a new tracer – 'preformed excess-N_2'. We used inert dissolved argon (Ar) to help test the assumption that preformed excess-N_2 is indeed conservative. We used the shipboard measurements to quantify preformed excess-N_2 by cross-calibrating the gas tension method to the nutrient-deficit method. At 17 °N preformed excess-N_2 decreased from approximately 28 to 12 μmol/kg over $\sigma_{0\ =}$ 24–27 kg/m^3 with a resulting precision of ±1 μmol N_2/kg; at 12 °N values were similar except in the potential density range of 25.7< σ_0< 26.3 where they were lower by 1 μmol N_2/kg due likely to being composed of different source waters. We then applied these results to gas tension and O_2 (< 3 μmol O_2/kg) profiles measured by the nearby float to obtain

the first autonomous biogenic N_2 profile in the open ocean with an RMSE of ± 0.78 μM N_2, or ± 19%. We also assessed the potential of the method to measure denitrification rates directly from the accumulation of biogenic N_2 during the float drifts between profiling. The results suggest biogenic N_2 rates of ±20 nM N_2/day could be detected over >16 days (positive rates would indicate denitrification processes whereas negative rates would indicate predominantly dilution by mixing). These new observations demonstrate the potential of the gas tension method to determine biogenic N_2 accurately and precisely in future studies of ODZs.

KEYWORDS

denitrification, biogenic nitrogen, oceanographic floats, gas tension device, argon

1 Introduction

ODZ's are important in ocean nutrient cycling, typically are in close proximity to large fisheries, and are susceptibile to change linked to global warming (Engel et al., 2022). Occurring primarily on the eastern edge of ocean basins, ODZ's are a recognized source of the potent greenhouse gas nitrous-oxide (N_2O) to the atmosphere and an oceanic sink of nitrogen-based nutrients (nitrate and nitrite) as a consequence of microbial processes (denitrification and anammox) requiring the near absence of O_2 (Codispoti et al., 2001). Nitrogen cycling activity levels of ODZ microbial communities thus overall have a positive response to the supply of organic matter and a negative response to oxygen despite varying individual responses. The tolerance of anaerobic microbes to trace levels (nM) of dissolved oxygen (O_2) has been the focus of many prior laboratory and field studies due to its importance in modeling and prediction. The simplest model (exponential-type inhibition kinetics) assumes a threshold of O_2 at or below a few hundred nM O_2 (~0.1% of background outside the ODZ) above which denitrification processes resulting in the the accumulation of N_2 gas in the mesopelagic stop (Dalsgaard et al., 2014). There is considerable uncertainty associated with this threshold O_2 concentration and even the applicability of such a simplified model since microbes can adapt and respond to O_2 forcing, so a deeper knowledge of sub-threshold O_2 responses is required (Bristow et al., 2016; Garcia-Robledo et al., 2017; Zakem and Follows, 2017; Penn et al., 2019; Berg et al., 2022). Identification of ODZ waters is more commonly based on denitrification activity, rather than oxygen concentration, through removal of NO_3^- (**N deficit**), the presence of a secondary NO_2^- maximum (Banse et al., 2017), or the appearance of biogenic N_2 produced by denitrification. These waters have also been termed 'functionally anoxic' having O_2 concentrations of<10's nM (Revsbech et al., 2009; Tiano et al., 2014).

From an experimental viewpoint focused on dissolved gas cycling, the study of ODZ biogeochemistry requires measuring trace level changes in O_2 and N_2 correlated in time and space with likely forcings. Prior studies of open ocean ODZs have measured water column biogenic-N_2 and denitrification rates (ie., the production rate of biogenic-N_2) using a combination of mass-spectrometric or gas-chromatographic analysis of dissolved N_2 in discrete water samples (Chang et al., 2010; Chang et al., 2012; Fuchsman et al., 2018) or *in vitro* incubations using automated nutrient analysis for elemental stoichiometry and spiking with ^{15}N-labeled substrates to distinguish denitrification and anaerobic ammonium oxidation (anammox) processes (e.g., Babbin et al., 2014; Dalsgaard et al., 2014). Although these types of measurements are generally highly precise and accurate, they are both costly due to the requirement for specialized collection, storage, and analysis of seawater samples at a shoreside laboratory and limited in time and space. Consequently, large research gaps have developed because of the limited types, quantity, and distribution of oceanographic data provided by existing methods. A few prior studies have investigated spatial variability in ocean denitrification rates and found evidence that eddies can be significant hotspots for denitrification (Callbeck et al., 2017; Altabet and Bourbonnais, 2019) but more statistics are needed to better understand how important eddies really are in ODZ biogeochemistry. Although short term variability in denitrification rates can be measured during a several week-long cruise, investigation of seasonal cycles in N_2 using sparse existing data sets collected using conventional approaches is far out of reach. New *in situ* methods are needed that can be deployed on moorings, floats, and gliders to allow measurement of denitrification at revelvant spatial and temporal scales.

Over the last several years we have been developing new approaches for studying denitrification in the Eastern Tropical North Pacific (**ETNP**, see Figure 1), the largest of the three major ODZs. Our approach was motivated by the need to autonomously observe long-term changes in dissolved gas cycling within ODZs that have been observed (Horak et al., 2016; Ito et al., 2017), or are predicted (e.g., Deutsch et al., 2014), to occur due to the impacts of global warming on ODZ biogeochemistry. We use a membrane-based dissolved gas sensor known as a Gas Tension Device (**GTD**), which was originally developed (McNeil et al., 1995) for studying air-sea gas exchange rates and processes in oxic waters, to measure total dissolved air pressure. With the intent of providing enough

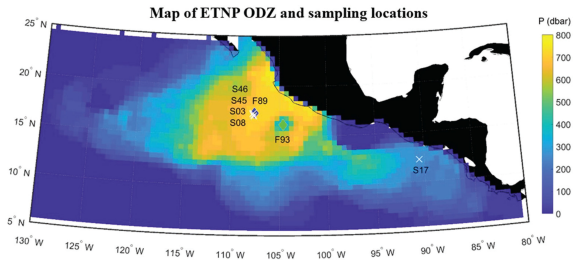

FIGURE 1
Map of the ETNP showing the thickness (color scale) of the ODZ layer from the reanalysis by Kwiecinski and Babbin (2021) overlaid with the shipboard CTD stations (white crosses labeled with 'Station#' from Table 1) and location of the float sampling ('F89' – filled blue diamond, 'F93' – filled light green diamond).

detail so other researchers can employ these methods for themselves, and likely improve upon them, we describe the dissolved gas sensors and adaptations for the sampling platforms we used, and the assumptions and data processing steps involved in calculating N_2 concentrations, biogenic-N_2, and even denitrification rates. A limitation of our approach, based on measuring N_2 in situ, is that we cannot distinguish different processes that produce N_2 gas as other methods, such as labeled-incubations with GC-MS analysis, can and so we cannot distinguish denitrification and annamox processes (unless perhaps these processes are known to occur in different regions of the water column or under different environmental conditions).

We present and discuss vertical profiles of GTD-derived biogenic-N_2 made using data collected in the core waters of the ETNP near 17 °N. The data highlights that real-time biogenic-N_2 can now be measured at sea by ships and BGC-Argo-style profiling floats and therefore this new method offers the possibility to map important oceanographic regions (e.g., ODZ boundary) or study oceanographic features of interest (e.g., eddies) within the ODZ. These data also motive the need to better understand subtler long-term changes in ODZ biogeochemistry through a combination of combined observational and modeling campaigns.

2 Materials and methods

2.1 Overview

To better study ODZ biogeochemistry our sampling objectives were: 1) to measure biogenic-N_2 profiles that result from microbial decomposition of nitrogen-based nutrients (nitrate, nitrite, ammonia) in anoxic waters at approximately the same location in the ocean (ie., **Eulerian approach**), and 2) to measure the time rate of change of biogenic-N_2, or the denitrification rate, within the same subsurface water mass moving with the mean flow (ie., **Lagrangian approach**). The Eulerian approach uses a GTD, mounted either on the ship's CTD or a profiling float, held at various depths or isopycnals for sufficient time (< 1 day) to equilibrate the sensors and obtain a vertical profile. The Lagrangian approach can be used to estimate *in situ* denitrification rates by making repeat measurements on a freely drifting float at the same isopycnal to ensure sensors stay in the same water mass for sufficient time (>10 days) to detect a change in biogenic N_2. In the ODZ core region where horizontal currents are weak, vertical gradients in biogenic-N_2 are much larger than horizontal gradients and a simple 1-D budget model for N_2 (see Figure 2) can be used to interpret both sampling approaches. A complication when applying such a simplistic N_2 budget is the need to separate biogenic and non-biogenic components (e.g., physical processes including mixing). This complication holds for any technique that budgets N_2, regardless of the method used to measure N_2 in seawater. For example, Chang et al. (2012) encountered this same issue interpreting N_2 measurements made in the ETNP ODZ using mass-spectrometric measurements of N_2 and solved the problem by referencing their N_2 measurements made inside the ODZ region to background measurements at the same density made outside the ODZ. Their technique further benefited from using measured N_2/Ar ratios (the raw measurements of the mass spectrometer) since inert Ar provides essentially an intrinsic reference for abiotic-N_2. We adopt and extend this same approach by considering the different source waters to the ODZ core region as importing their own preformed excess-N_2 to the ODZ and mixing vertically and horizontally along their pathways to the core of the ODZ. Rather

TABLE 1 Details on time, location, and depth range of GTD sampling by ship and float.

Cruise or Float ID [Station#, Event#]	Date [dd-mm-yyyy]	Time [GMT]	Latitude [°N]	Longitude [°W]	Depth range [dbar]
SR2011[S03, E12]	22-Dec-2020	17:37	17.289	107.775	29–859
SR2011[S08, E03]	29-Dec-2020	20:03	17.079	107.739	28–1009
SR2114[S45, E04]	14-Jan-2022	17:57	16.980	107.700	84–1010
SR2114[S46, E01]	15-Jan-2022	01:42	17.202	107.815	59–858
SR2114[S17, E05]	29-Dec-2021	01:39	12.217	90.543	83–859
F89 Drift:	01-Jan-2021	05:12	17.288	107.634	15–706 (242 ± 4)
F93	18-Apr-2022	15:06	16.119	104.613	17–1019

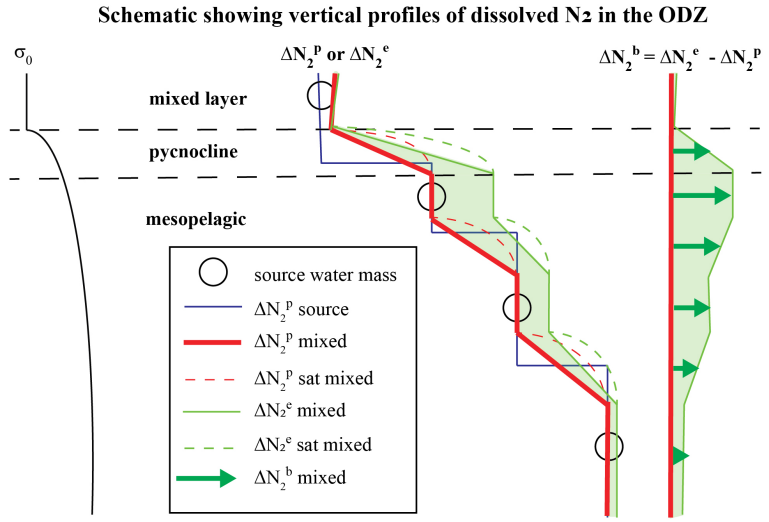

FIGURE 2
An idealized 1-D schematic of the upper ocean in the ETNP ODZ showing: (left) a vertical profile of potential density σ_0, (middle) vertical profiles of preformed excess-N_2 (ΔN_2^p) and measured excess-N_2 (; ΔN_2^e) in layered mixtures of discrete source water masses (circles) that feed the ODZ, and (right) biogenic-N_2 (ΔN_2^b) in each layer calculated using Eqn. (4). Discrete source waters (circles) of the ODZ with initial ΔN_2^p (blue line), set by air-sea gas exchange in the water masses where their isopycnals outcrop and any prior denitrification, mix with each other in the ODZ where they yield a mixed ΔN_2^p profile (red line). Non-linearity of solubility contributes to supersaturations (see 'N_2 sat' in legend) of the water mass mixtures. Once a layer becomes functionally anoxic, ΔN_2^b accumulates in that layer.

than having to measure dissolved gas levels outside the ODZ as Chang et al. did, we calibrate our biogenic N_2 to a concurrent but independent measurement based on nutrient stoichiometry to obtain vertical profiles of preformed excess-N_2 in the water mixtures at the ODZ core. The validity of the 1-D model is assessed using conservative mixing lines for independently measured argon.

We used the *in-situ* gas tension method as an alternative approach to measuring N_2 in seawater since it can be measured autonomously, is relatively easy, reliable, and inexpensive compared to conventional techniques. In the anoxic seawater layer found at the core of the ODZ, the gas tension method has increased accuracy due to the elimination of measurement errors associated with dissolved O_2. One prior study used this same advantage to study aerobic/anoxic N_2 cycling in the Baltic Sea (Loeffler et al., 2011). A disadvantage of the gas tension method alone is that argon levels are usually assumed, and therefore no compensatory information on abiotic processes is measured. We, however, used an advanced isotope dilution mass-spectrometric technique developed to measure absolute Ar concentrations to high accuracy. The Ar samples were drawn from the same rosette CTD used for gas tension sampling. The drawbacks of the isotope dilution technique method are high per-sample analysis cost and there are only a few laboratories that can do it, but this disadvantage is somewhat offset by the fact that argon is expected to vary predictably and smoothly (Ito et al., 2011) by conservative mixing away from boundary sources so only targeted sampling of ODZ source waters was required. We used independent shipboard measurements of biogenic N_2 from nutrient stoichiometry with concurrent gas tension derived estimates of biogenic N_2 to determine N_2 variability due solely to physical processes. We used the Ar measured by isotope dilution techniques to check our assumption that this 'preformed' excess-N_2 followed expected conservative mixing curves. We applied the preformed excess-N_2 profiles measured in the ODZ core during the cruise to profiles of gas tension measured after the cruise by autonomous profiling floats deployed in the same vicinity to obtain the first autonomous biogenic N_2 profiles in an ODZ. Derived denitrification rates require a quantifiable increase of biogenic N_2 within the same water mass over a known period of time; this period will be longer for regions or isopycnals with lower microbial activity.

2.2 Field campaigns

Biogenic N_2 was measured in the ETNP near 17 °N (see Figure 1) during two cruises on the RV *Sally Ride* (CruiseID = SR2011 during 16-Dec-2020 to 06-Jan-2021m; CruiseID = SR2114 during 21-Dec-2021 to 21-Jan-2022). A GTD was mounted on the rosette CTD to measure vertical profiles of gas tension, along with O_2 (by SBE-43), temperature (T) and salinity (S). Water samples were taken for nutrients (nitrate, nitrite and phosphate). A Switchable Trace amount OX-ygen (**STOX**) sensor (Revsbech et al., 2011) was used to reference the SBE-43 O_2 data to anoxia (± 50 nM) in the ODZ core waters. Autonomous floats, also with GTD sensors, were deployed. Table 1 lists sampling details for the data presented here.

2.3 Gas tension devices

New versions of Gas Tension Devices (GTDs manufactured by Pro-Oceanus Systems, Inc., Bridgewater, NS, Canada) were used to

measure gas tension on the floats and the ship's CTD in this study. Unlike older versions of the GTD (McNeil et al., 1995; McNeil et al., 2006), the new sensor has only a weak hydrostatic response, due primarily to the use of the relatively incompressible Teflon AF 2400 gas permeable membrane introduced by Reed et al. (2018). The new GTD has the same external mechanical design as the profiling GTD developed for use on the ship's CTD (McNeil et al., 2018, see figures on pages 88 and 96) but was modified at APL/UW internally to: 1) improve the electronics, and 2) allow the sensor's pressure sensor to be easily replaced at sea even in the event of a flooded membrane. The novelty of the profiling GTD design lies in the use of a miniature pressure sensor (type Micro Electrical Mechanical System- or **MEMS**) with a very small (approximately 40 µL) gas sensing volume. Since this pressure sensing volume contributes to the total sample volume behind the membrane that must exchange through the membrane, the response time of the new GTD is small: In separate laboratory tests conducted using similar high-flow pumps and plenums the characteristic (e-folding) response times were approximately 1 minute at 20°C and 3 minutes at 5 °C. The response time of any GTD varies with seawater temperature because of the temperature dependence of gas diffusivity and solubility in the GTD's membrane. The new GTD was mounted onto a rosette 911 SBE CTD system that had a serial RS-232 ('Data Uplink') capability for real-time data and a spare SBE 5T pump running at approximately 50% of maximum capacity (ie., 0.5 A at 12 V, or 6 W); the pump flushed the GTD's membrane using a plenum attachment as described in McNeil et al. (2018). The GTD had an operating-depth rating of 1000 m.

The time required to equilibrate the new GTD to an acceptable level (e.g.,<1 mbar of absolute) when profiled through strong temperature and dissolved gas gradients is not simply a function of the isothermal response time of the sensor found in the laboratory, it also depends on the prior history of exposure of the sensor during the profile and geophysical noise such as the passage of internal waves. Since GTD measurements took many hours on station, it was necessary to minimize the wait time at each sampling

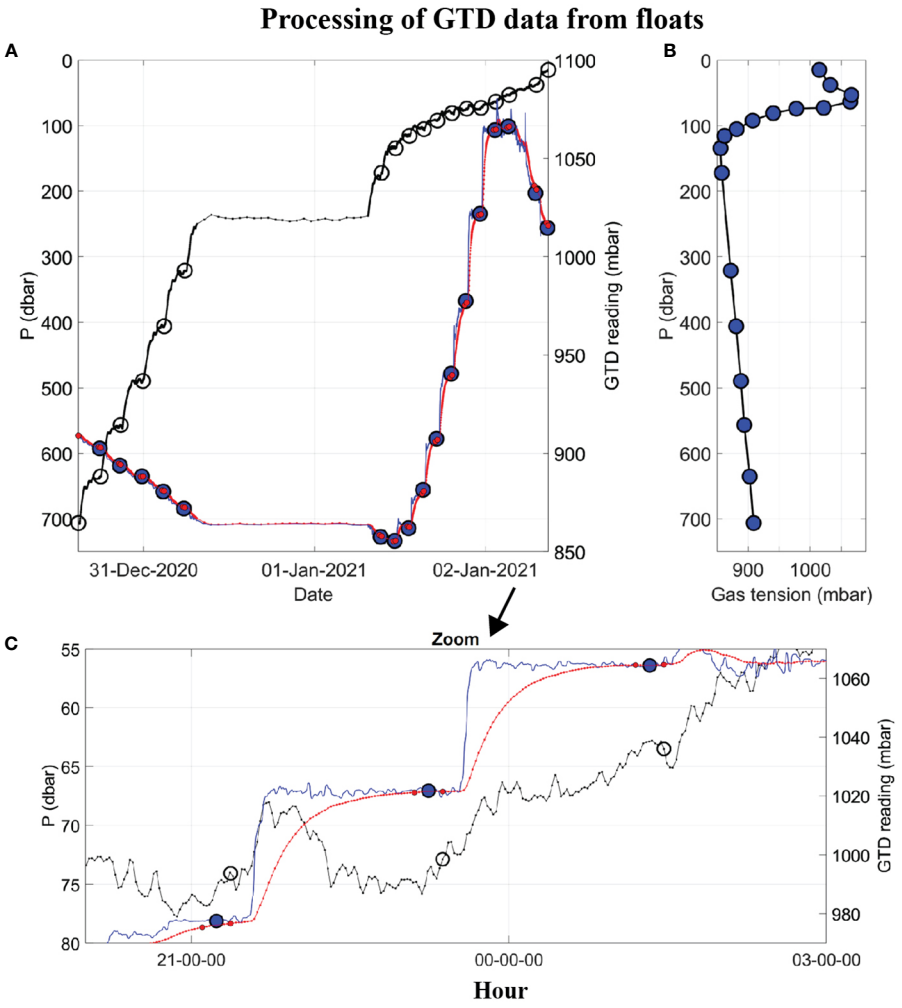

FIGURE 3
Example of raw and processed float data, from F89, showing: **(A)** Time series of hydrostatic pressure (left axis, black line) with time marks showing when the GTD is fully equilibrated (left axis, black circles), raw GTD reading (right axis, red line), and deconvolved GTD data (right axis, blue line), with time marks (small red dots) over which the mean equilibrated gas tension is calculated (large blue dot); **(B)** Vertical profile of gas tension (large blue dots); and **(C)** Zoom-in of the upper plot for three equilibrations, starting at 20:00 on 01-Jan-2021.

depth and provide a straightforward procedure for CTD operators to follow. At-sea trials of the new GTD on the ship's CTD were performed at the start of the cruise to determine the minimum wait-time required to equilibrate the GTD in temperature and gas before moving the CTD to the next sampling-depth. A wait-time of 10 minutes at each sampling-depth found to be sufficient except in the thermocline where the wait-time was increased to 15 minutes. Equilibrated data were chosen based on averages over the last few minutes of data prior to moving the CTD to the next depth.

2.4 Autonomous floats

As part of a larger distributed array designed to capture relevant temporal and spatial variability in denitrification rates and processes in the ETNP, a total of 10 modified Argo-style floats were deployed on the two cruises and data from two of those floats deployed in the ODZ core region are examined here. Floats (model **ALTO**) manufactured by Marine Robotics Systems (**MRV**) were modified in collaboration with MRV to carry one or more GTD sensors and two Seabird-63 optode oxygen sensors. The float's new GTD and optode membranes were flushed using a low flow rate SBE-5M pump to reduce power consumption, the trade-off being a significantly longer equilibration time of approximately 20 minutes for the GTD (ie., approximately 20 times slower than the fastest laboratory equilibrations). One of the two optodes measured the water; the other measured in a saturated sodium sulfite solution and acted as an anoxic reference solution subject to the same temperature and pressure as the water optode. The standard optode calibration equation is not accurate at concentrations below a few µmol/kg as it does not account for temperature and pressure dependences of the optode response at zero oxygen. Here, oxygen was computed both from the difference between the water and reference optodes corrected for a linear pressure trend and by reformulating the calibration equation with the appropriate pressure and temperature variations. The ODZ core was clearly apparent as a minimum in oxygen concentration several hundred meters thick, with values of a few µmol/kg or less and a linear variation of oxygen with depth of a few hundred nmol/kg. The pressure coefficient was adjusted to make oxygen constant in this region; an offset was adjusted to center this on zero. The STOX sensor on the ship's CTD, when available, was used to check the optode derived profiles. A detailed description is beyond the scope of this paper and will be reported elsewhere.

The float mission was modified from that of a standard Argo float. After an initial dive to 800–1000 m and a few hours to allow the sensors to settle, the float profiled upward in a stairstep profile (Figure 3), moving upward 50–100 m, then settling at a nearly fixed depth and isopycnal for 1–2 hours to allow the GTD to equilibrate, then moving upward again. The float then drifted for up to 10 days in the OMZ just below the oxycline, about 200 m, before continuing the stair-step profile upward, surfacing, communicating, and repeating the cycle. Occasional glitches resulted in the float profiling to as deep as 1500 m with no apparent issues.

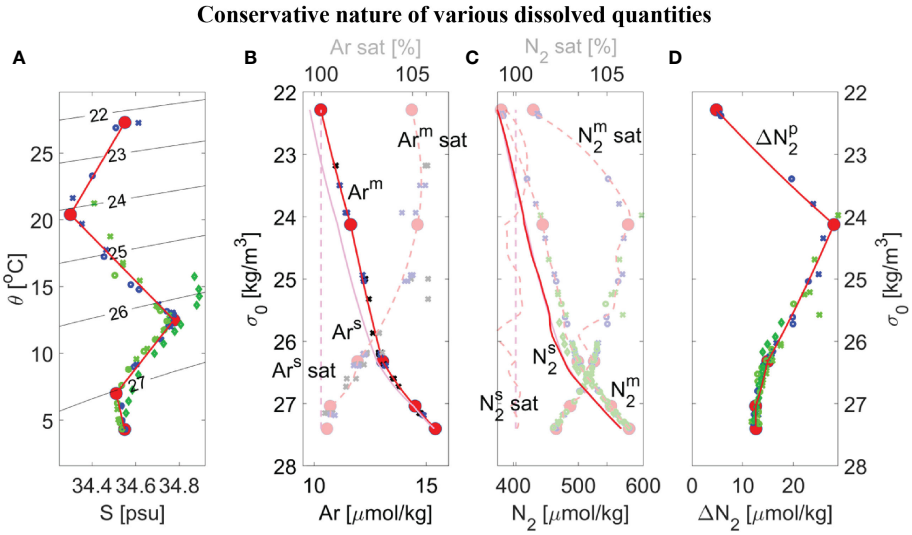

FIGURE 4
Overview of dissolved gas measurements made during duplicate casts (#1 as small circles, #2 as small crosses, and consistent with Legend shown in Figure 5B) and modeling results (red lines) for either conservative properties (opaque markers and lines) or non-conservative properties (semi-transparent markers and lines) within the ETNP ODZ core near 17°N from SR2011 (blue) or SR2114 (light green) and 12 °N from SR2114 (dark green), showing: **(A)** Potential temperature θ versus salinity S with contours of potential density σ_0; **(B)** Dissolved argon concentration Ar^m that is either measured (blue/green symbols) or is a best-fit or mixing-model result (red solid lines), equilibrium solubility Ar^s (magenta lines), and corresponding saturation level Ar sat (dashed lines) versus potential density σ_0; **(C)** Similar to panel B but GTD-measured nitrogen N_2^m and best fit (semi-transparent red line) using a smoothing spline with a residual rms of ±0.15% to maintain consistency with errors in solubility coefficients; **(D)** Preformed excess nitrogen ΔN_2^p versus σ_0 calculated using Eqn. (8). Five distinct water masses (large red dots) were chosen from panel A for the mixing model and all properties were determined by interpolating on potential density to the data. For comparison purposes, corresponding θ/S/ΔN_2^p at 12 °N from SR2114 were added to panels **(A, D)** (dark green diamonds) and additional argon data at 14–15.5 °N from SR2011 were added to panel **(B)** (black markers).

Data from two floats are reported here. The first float (F89) was deployed in the ODZ core close to the location of four CTD stations (S46, S45, S03, S08) occupied during our two cruises (see Figure 1). Only shipboard data, not all concurrent, were used to calibrate our new method for determining biogenic N_2. After calibrations, our new method was then applied to the float data to provide the first test of the new method when applied to autonomously collected data delivered by satellite. Since the first float and CTD data were collected at the same location within the ODZ, the comparison is designed to provide information on the accumulated errors when applying our new method to float data. To demonstrate our overall goal of a long-term distributed float-based sensing observational system, we applied our new method to data from a second float (F93) chosen to be nearby and longafter the shipboard calibrations work.

2.5 Dissolved N_2 from gas tension

Definitions - Dissolved N_2 partial pressure (pN_2) was calculated by the gas tension method using:

$$pN_2 = P_T - pO_2 - pH_2O - pTrace \qquad \text{Eqn. (1)}$$

where P_T is the total gas tension, and pO_2 and pH_2O are the partial pressure of oxygen and water vapor, respectively. The trace gas partial pressure ($pTrace$) is mostly argon with a small contribution from pCO_2, is relatively small, and can be accounted for in the calculations with little error (using Table 1 from Reed et al., 2018 we expect $pTrace$ = 9.6 – 10.9 (± 0.9) mbar for P = 0 – 400 dbar, which is equivalent to an uncertainty of ± 16% in an assumed biogenic N_2 signal of 10 mbar). It should be possible to reduce uncertainties associated with pCO_2 further (we did not measure it) by estimating it from either Apparent Oxygen Utilization (**AOU**) or climatological empirical relationships for carbonate system parameters within the ODZ (i.e., TAlk and DIC versus temperature and sailinity) along with the standard seawater carbonate system calculators (e.g., CO2SYS program). We have not attempted to include any corrections here since our initial focus was understanding large scale variability in pN_2 associated with variability in actual preformed N_2. We refer to the calculated dissolved nitrogen concentration using Henry's Law and Equ. (1) as the **'*measured*' nitrogen (N_2^m)**:

$$N_2^m = (P_T - pO_2 - pH_2O - pTrace) \times S_{N2}^{(P,T,S)} \qquad \text{Eqn. (2)}$$

where gas specific Henry's Law solubility coefficients (S_H) are known functions of water temperature (T), salinity (S), and hydrostatic pressure (P). Unique to the ODZ is a functionally anoxic core layer where $pO_2 = 0$. Outside of this anoxic layer small changes in O_2 are accounted for in Eqn. (2) with little error in determined N_2 by referencing the O_2 sensor data from the ship's CTD to a precise zero-point using a STOX sensor (more details below - see also Supplement in Tiano et al., 2014). We refer to **nitrogen '*solubility*' (N_2^s)** as the value in seawater in equilibrium with one standard atmosphere of moist tropospheric air (Hamme and Emerson, 2004). All Henry's Law solubilities are calculated using MATLAB solubility calculators (Emerson and Hamme, 2022).

We define other nitrogen quantities as well, specifically **'*excess*' nitrogen (ΔN_2^e)** as:

$$\Delta N_2^e = N_2^m - N_2^s \qquad \text{Eqn. (3)}$$

and **'*biogenic*' nitrogen (ΔN_2^b)** as:

$$\Delta N_2^b = \Delta N_2^e - \Delta N_2^p \qquad \text{Eqn. (4)}$$

where the **'*preformed*' excess nitrogen (ΔN_2^p)** is the portion of excess N_2 associated with all processes that alter source water N_2 *prior* to it entering the ODZ, and include: 1) physical (abiotic) processes, such as air-sea gas exchange of the water masses during formation, and 2) denitrification in anoxic micro-environments of sinking organic matter (Bianchi et al., 2018) or continental shelf sediments (Devol, 2015). Since each source water mass to the ODZ will have its own value of ΔN_2^p with likely small interannual variability since the water formation regions are remote, we can expect mixing of the source waters within the ODZ to create stronger spatial than temporal variability in ΔN_2^p throughout the ODZ. Conservative mixing of two source waters that have different T and ΔN_2^p raises the N_2 saturation level of the mixture, a consequence of the non-linearity in the temperature dependence of Henry's Law solubility coefficients (rather than production of N_2) and must be accounted for in all mixing calculations.

Deconvolutions – To determine equilibrium values of measured quantities on the floats, which have a much slower response GTD than used on the ship CTD due to available power, we used a deconvolution model similar to Reed et al. (2018) with a suitable intrinsic (e-folding) response time scale determined by inspection of the raw data. We applied this deconvolution model to determine both raw quantities (e.g., gas tension) and derived parameters (e.g., ΔN_2^b). Initial transients can result from the fact that O_2 rapidly leaves the GTD after it was lowered into the deeper anoxic waters from the equilibrated sea surface while at the same time N_2 entered the GTD because N_2 was supersaturated in the deeper anoxic core waters due to denitrification processes making modeling of the float data difficult. To accurately deconvolve all the raw gas tension signal required use of a multiple response time deconvolution model that separately tracked equilibration of each gas. Although we developed and tested this more complex deconvolution approach, we avoided using it by simply neglecting initial transients in the derived quantities (manifest as overshoots in the raw data) and determining equilibrium values for the later phase of equilibration since the additional complexity in the end added no value to the results based on the goal of determining equilibrium end-points. However, we add this information here to document that more complex details GTD equilibration in the ODZ can be understood if, for some reason, that were an objective of the analysis. By design, the thermal equilibration time of the GTD is smaller than the gas diffusion equilibration time scales (for N_2 and O_2) so thermal transients mostly relax quickly. This much simpler approach worked well under most circumstances, except during profiling across the strongest part of the thermocline and the only solution to that problem was to hold the sensors for longer at those depths

before moving the sensor to the next sampling depth as described above.

2.6 Biogenic N_2 from nutrient deficit

We use the **nutrient deficit (N_{def})** method (Codispoti and Richards, 1976; Codispoti et al., 2001) to calculate an independent ***'nutrient'*** (ΔN_2^n) based on the stoichiometry of microbial N_2 production from nitrate. N_{def} is the difference between measured and expected dissolved inorganic nitrogen (**DIN**) concentrations with DIN as the sum of measured NO_3^- and NO_2^- as NH_4^+ is typically undetectable in the open ODZ:

$$N_{def} = DIN_{exp} - (NO_3^- + NO_2^-) \quad \text{Eqn. (5)}$$

$$\Delta N_2^n = N_{def}/\alpha \quad \text{Eqn. (6)}$$

where the divisor α accounts for conversion to di-nitrogen (N_2) gas using appropriate stoichiomentry.

DIN_{exp} is commonly estimated from PO_4^{3-} given its strong linear relationship with NO_3^- outside of ODZ's. Here we use regression coefficients to estimate DIN_{exp} derived from data in the GLODAP V2 database for regions adjacent to the western Mexico EDZ:

$$DIN_{exp} = 14.58 \times (PO_4^{3-} - 0.14)\,. \quad \text{Eqn. (7)}$$

The slope and intercept for Eqn. 7 was determined through linear regression of data from the GLODAP database (Garcia et al., 2014) for the ETNP region excluding points with evidence of denitrification with results similar to Chang et al. (2012). For these calculations we used α = 2.0. NO_3^-, NO_2^-, and PO_4^{3-} were measured on board using a SEAL AQ 400 nutrient analyzer using standard methods. PO_4^{3-} was also estimated *via* a linear regression with AOU data also using the GLODAP database. This approach was applied to the 12°N station, and one station at 17 °N, as data quality problems with the directly measured PO_4^{3-} data was evident. For those calculations, α = 1.712 was used following the stoichiometry of Richard's equation: $(CH_2O)_{106}(NH_3)_{16}H_3PO_4$ + 94.4 HNO_3 = 106 CO_2 + 55.2 N_2 + 177.2 H_2O + H_3PO_4 (Richards, 1965).

2.7 Conservative preformed excess N_2

Equating the measured biogenic-N_2 derived from the GTD-method (i.e., ΔN_2^b from Eq. 4) to that measured by the nutrient-method (i.e., ΔN_2^n from Eqn. 6) using our CTD station data - even if the CTD stations were from inside of the ODZ region as will be discussed in Section 2.9 - we obtain a measurement-based estimate of the preformed excess-N_2 from:

$$\Delta N_2^p = N_2^m - N_2^s - \Delta N_2^n\,. \quad \text{Eqn. (8)}$$

By interpolating (on density) the shipboard measurements to common density levels, we derived vertical profiles of ΔN_2^p at the ODZ core. Measurements were made at approximately the same latitude (17 °N), in duplicate casts, and repeated one year later (see Table 1) to assess interannual variability. Argon and nutrients were typically measured at the same CTD station on the prior or next cast that the GTD measurements were made due to sampling limitations but Argon data are only available here for the first cruise (samples were collected during the second cruise but analysis is not yet complete).

In the deeper stratified waters of the ODZ, which is unaffected by air-sea gas exchange processes, we expect ΔN_2^p to be a conservative quantity. We also expect latitudinal variability in ΔN_2^p since the ODZ core is fed by multiple northern and southern sources, and each source water having been formed in different regions of the ocean will likely have different ΔN_2^p. An objective is to reliably predict ΔN_2^p across the entire ODZ based on circulation and conservative mixing of ODZ source waters then use those predicted distributions along with measured profiles of gas tension, temperature, salinity and oxygen to predict, using Eqn. (4), biogenic N_2 at the floats. We assess latitudinal variability in ΔN_2^p comparing estimates made in the ODZ core at 17 °N to measurements made at 12 °N which are strongly influenced by the southern sources. Since these two stations capture a large fraction of the variability in the ETNP ODZ hydrography, we expect the comparison to provide a first look at how variable ΔN_2^p is within the ETNP ODZ for different source water masses. Finding no differences in the deeper water masses below the active denitrification zone would be a good internal-consistency check of our methods, noting that we cannot independently verify our method without a second independent measurement of ΔN_2^p.

2.8 *In situ* denitrification rates

Measurements of N_2 made on a float following a subsurface water mass (Lagrangian) in theory allow *in situ* production (or consumption) rates to be determined by measurement of dN_2/dt if horizontal (isopycnal) and vertical (diapycnal) mixing effects are fully compensated. However, floats do not follow water masses perfectly, especially if the water mass properties change over time due to vertically sheared mixing which will dilute over time the original water mass under study with the surrounding waters. Notwithstanding these complications, local **denitrification rates (DNR)** along the float track-line can be estimated from the production of biogenic N_2 at the float using:

$$DNR = d(\Delta N_2^b)/dt\,. \quad \text{Eqn. (9)}$$

Note that for a perfectly Lagrangian float with negligible vertical fluxes of biogenic N_2 or preformed biogenic N_2, the term ΔN_2^b in Eqn. (9) could be replaced by ΔN_2^m.

2.9 Argon measurements and assumptions

Although argon is a small component of the gas tension signal and assumptions for argon have little impact on the biogenic N_2 error analysis (see Section 2.4), argon still plays a significant role in

our work as a proxy measurement of inert-N_2 which, theoretically, would be a fully conservative quantity in the ODZ mesopelagic. Since we cannot measure conservative ΔN_2^p everywhere in the ODZ, we use argon to help predict distributions of ΔN_2^p based on the stirring and mixing of source waters within the ODZ. We capitalize on the fact that argon, like potential temperature and salinity, is a third conservative tracer and therefore expect Ar and ΔN_2^p to co-vary.

Source waters for the ODZ were last at the ocean surface outside the ODZ, likely during periods of strong air-sea interaction. During water mass formation, local atmospheric pressure may be several percent different from one atmosphere and rapid cooling may have caused further disequilibrium in gas saturation levels, but these processes affect N_2 and Ar similarly (Stanley and Jenkins, 2013; Hamme et al., 2019). Dissolution of bubbles from breaking waves also creates gas supersaturation, at nearly twice the rate for nitrogen as for argon due to their differences in solubility. However, given that both preformed excess N_2 and argon are inert and conservative, we expect variability in these quantities within the ODZ to be relatively small and to vary smoothly over large spatial and temporal scales in similar ways. Precise Ar concentrations can only be measured using advanced mass-spectrometric techniques (e.g., isotope dilution, see Section 2.9) and there are only a few existing measurements in the ETNP. Prior studies did not specifically target measurements in the ODZ source waters.

One particularly relevant study of the ETNP region (Chang et al., 2012) derived a relationship for the gas concentration ratio Ar:N_2, which is much easier to measure than argon alone, as a function of potential density and geographically separated into 'inside' and 'outside' of the ODZ. Their analysis was based on a difference approach, subtracting 'inside' from 'outside' measurements at the same isopycnal to get estimates of the ODZ impact as a function of density. Extending their approach to consider our definition of ΔN_2^p, it is unclear how Ar:N_2 ratios should vary inside the ODZ, as mass spectrometry cannot discriminate ΔN_2^p from ΔN_2^b, and would imply that ΔN_2^p can only be inferred from gas ratio measurements if those measurements are taken 'outside' of the ODZ. This argument is fine but breaks down if the measurements made in waters 'outside' of the ODZ were previously exported from the ODZ, which is somewhat unavoidable when sampling unless close attention is paid to currents and the history of the current pathway is known when sampling. Also, Chang et al.'s data were collected mostly in the northern waters, which contains information on only half of the ODZ region. Further, their smoothed density relationship derived from 'outside' ODZ measurements blurs important information related to mixing of source waters (ie., 'spice') which is important evidence for an analysis based on conservative mixing. Combining and replotting all available argon concentration data from Chang et al. (2012) and Fuchsman et al. (2018) showed very clear linear mixing lines, similar to T/S, which convinced us that there was potential for better parameterizations of ΔN_2^p rather than density alone. Here we argue that the Chang et al.'s approach can be fundamentally improved by focusing attention on the handful of northern and southern source waters to the ODZ, rather than 'outside' ODZ waters, and how these source waters get mixed within the ODZ to form 'inside' waters. Our approach essentially intensifies the geographical constraints of the problem to the source waters, and demands new data in the southern waters. Our cruises tracks specifically targeted sampling of northern and southern water mass sources to the ODZ and measured argon in them. Most importantly, our improved approach does not require the measurement over all density ranges of 'outside' ODZ waters because our conservative mixing model can recreate 'inside' and 'outside' ODZ mixtures from water mass fractional composition analysis of source waters.

Our argon concentrations were measured by isotope dilution on discrete water samples (Hamme and Severinghaus, 2007; Hamme et al., 2017) collected on the first 2020 cruise. Briefly, glass flasks with a ~180-mL volume and a double-O-ring Louwers-Hapert valve were evacuated to a high vacuum prior to shipping to the field site. The necks of the flasks were kept evacuated by a rough vacuum pump on a large manifold at sea to prevent air leaking into the flasks. Duplicate water samples were introduced from Niskin bottles into the evacuated flasks through tubing pre-flushed with CO_2 until the flasks were half-full. Back on shore, flasks were weighed, the headspace and water were equilibrated and then the water was removed. Headspace gases were flowed through ~90°C ethanol to remove water vapor, gettered to remove all except noble gases, an aliquot of ^{38}Ar added, frozen into a tube immersed in liquid helium, and brought to higher pressure with a balance gas of helium. Argon isotopes were analyzed on a dual-inlet MAT 253 Isotope Ratio Mass Spectrometer at the University of Victoria against a standard of similar composition. The standard and ^{38}Ar aliquot amount were calibrated relative to air measurements. The pooled standard deviation of the duplicates for Ar on this cruise was 0.21%.

2.10 Linear Mixing model

To aid interpretation of our station data at 17 °N in the core waters of the ODZ, a linear mixing model was developed based on the five major water types for that region. The model was initialized using shipboard observations of the three conservative tracers, namely potential temperature, salinity and argon concentration. Although argon saturation level is not conservative, it's strong sensitivity to the choice of water types values helps fine tune the model to best match the observations – this sensitivity comes from the temperature and salinity dependence of the Henry's Law solubility coefficients. Unlike argon, nitrogen gas is non-conservative in the ODZ due to N_2 production by microbial activity in functionally anoxic waters. The abiotic component of N_2, which is equivalent to the red line in Figure 2, cannot be measured directly but can be modeled using the calibrated mixing model with conservative preformed excess N_2 from Eqn. 8 as inputs.

To determine conservative property values for each water type, a **'broken-stick' best fit model** was initially applied to the TS data and then to argon concentration. A segmented linear regression (or 'broken-stick') routine called SML (Shape Language Modeling) and developed in MATLAB was used with unconstrained setting (ie., 'free knots') to find the location in T-S space of the four water type values. These values were then used in the linear mixing model. The

process was repeated for argon and salinity then water type values for each conservative property were further refined by tuning the model to fit all observations, including argon saturation levels, simultaneously. The entire process proved too complicated to fully automate, so the values reported here are approximations derived ultimately by visual best fit between the model and the data.

Once the model is best fit to the observations, the model provides a convenient way to determine smoothed versions of any quantity (e.g., of ΔN_2^p or ΔN_2^b) versus potential density that satisfies the model's conceptual framework (ie., dilution of 5 water types). The results at 17 °N were then compared to results at 12 °N.

3 Results

3.1 Gas tension

An example of raw and processed time series data from an early float (Table 1, F89) mission are shown in Figure 3A. After the float sunk to its maximum depth (700 m) it slowly ascended to the sea surface, stopping at many (17) targeted depths (or isopycnals) to equilibrate the GTD. The wait time at each targeted depth was 2 hours but this was extended to 24 hours at the 'Lagrangian drift' depth (242 ± 4 m) on this dive. The total submerged time was approximately 2 days. Data were reported by satellite after surfacing. A constant e-folding response time of 20 minutes was used to deconvolve these raw GTD data (see Figures 3A, C and compare red and blue lines). This is a factor of 10–20 times slower than the fastest response of the sensor achievable using a fast flow rate pump but draws little energy from the float's batteries since it uses a small flow rate pump. The equilibrated gas tension values at each hold-depth used a 15-minute average of the deconvolved time series just before the float is moved to the next hold-depth. The standard deviation, SD, of the data during the 15 min averaging period provides a good indicator of uncertainty. We found for P > 300 dbar that SD< 0.03% and for P< 200 dbar that SD< 0.12% (see Figure S1 in Supplementary Materials). Internal waves in the strongly stratified thermocline of the ODZ were the leading cause of geophysical noise.

Processing of the shipboard data was much simpler and didn't require deconvolving the raw data because the hold time of the GTD at any depth (10–15 minutes) was chosen to be much longer than the sensor response time (2–3 minutes, using the high flow rate pump). The noise level of the raw ship GTD data was better than ±0.2 mbar and the end-point detection typically within ±0.5 mbar assessed by variability from steady readings (see Figure S2 in Supplementary Materials).

To summarize, vertical profiles of gas tension (see Eqn. 1), temperature, salinity and dissolved O_2 were made at 12 °N and 17 °N by ship and floats during two cruises. Additional processing produced estimates of dissolved N_2 (see Eqn. 2), the results of which are described next.

3.2 Regional water mass analysis

Shipboard measured θ, S, Ar, and GTD-derived N_2 at the ODZ core near 17 °N are shown in Figure 4. Five regional water types are readily identified on the conservative θ-S diagram (Figure 4A, red dots) as 'break-points', defined where the slope of the plot changes rapidly. In theory, any water mass, or layer in this stratified system, that lies between two water types on the θ-S diagram can be

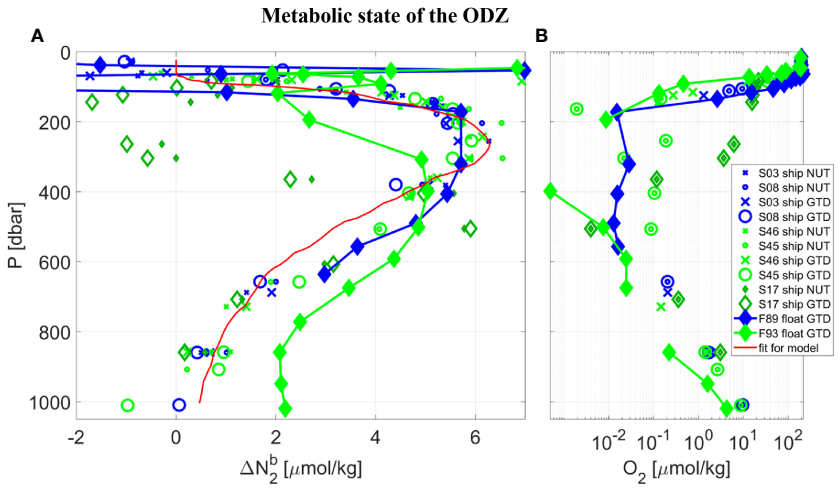

FIGURE 5
Vertical profiles taken in the core of the ETNP near 17 °N, from SR2011 (blue) and SR2114 (green), of: **(A)** biogenic N_2, and **(B)** dissolved O_2 using a logarithmic scale. Following Table 1 and the Legend, data collected at CTD Station ('S') by ship or float ('F') used either the traditional nutrient method ('NUT') or the new gas tension method ('GTD') to measure biogenic N_2. Note that all data labeled 'ship NUT' are used to calculate the best fit of $\Delta N_2^p(\sigma_o)$ so the resulting data labelled 'ship GTD' are calibrated and therefore must agree. Data labelled 'float GTD' also use $\Delta N_2^p(\sigma_o)$ but their gas tension and oxygen are independent. Since 'F89 float GTD' data were taken during the cruise and in the vicinity of the float the good agreement serves to validate the GTD method. The 'F93 float GTD' data were measured autonomously 2 months after the cruise and much further east (see Figure 1) with significantly different hydrography and are not expected to necessarily agree with 'F89 float GTD' data. A second order Gaussian best-fit curve (red line) to the shipboard nutrient data is used for mixing-model calculations.

described as a mixture of two adjacent water types. The linear mixing model (see Section 2.10) recreates all possible mixtures of water types that could occur between adjacent water types to produce the model result (Figure 4A, red line). The model can only produce straight lines between water types when quantities are conservative, such as θ, S, and Ar. The model easily reproduces the same 'broken stick' shape for conservative Ar (Figure 4B, solid red line) that matches the shipboard data. Derived model quantities that are non-conservative can also be calculated from the conservative model output. Gas saturation levels are one such calculation. Since Henry's Law solubility coefficients are non-linear functions of θ and S, a model Ar saturation level is calculated using the modeled θ, S, and Ar. Since Ar saturation level is non-conservative, the model produces curved lines between water types on a conservative plot and also on density (see Figure 2). The model Ar saturation level reproduces the observed Ar saturation level curved-shape (Figure 4B, semi-transparent red dashed line) and, as mentioned in Section 2.10, is sensitive to the choice of end-member values and provides an additional constraint for tuning the model to the data.

The now calibrated model is used to test the assumption that excess pre-formed N_2 derived from the GTD-measured N_2 (Figure 4C) is conservative. The model ΔN_2^P versus σ_0 (Figure 4D, red lines) shows breakpoints in density that correspond well with equivalent breakpoints on both θ-S and Ar curves which used both 2021 and 2022 station data due to the limited amount of calibrated data available. These broad similarities provide corroborating evidence that preformed excess N_2 is indeed conservative and values for each conservative property can be estimated for each water type. Based on this result, the water type values can be further refined so that preformed excess N_2 also is included in the optimization approach to determine water type properties. Our best estimate of water properties for all five water types is summarized in Table 2 and compared to previously published values (Evans et al., 2020). As previously noted, our results do not use an automated 'broken stick' detection algorithm and hence errors in the fits are not fully quantified.

For comparison purposes, additional argon data at 14–15.5 °N from cruise SR2011 were added to Figure 4B to help expand the limited information on argon beyond the site. In addition, corresponding θ/S/ΔN_2^P at 12 °N from SR2114 were added to Figures 4A, D to provide some additional testing of these new methods. On closer inspection, lower values of ΔN_2^P, by up to 1 μmolN_2/kg, were observed at 12 °N in the potential density range of $25.7 < \sigma_0 < 26.3$ compared to those values at 17 °N indicating water masses (or mixtures of water types) at 12 °N that were not found at 17 °N. Additional evidence is seen on the θS plot (see Figure 4A, dark green diamonds) where these same water at 12 °N are found to have higher salinity than any waters near the same density range at 17 °N. Since it is impossible for the mixing model calibrated at 17 °N to reproduce water masses at 12 °N that have higher salinity than water types found at 17 °N, the anomaly is understandable. Application of the model calibrated to 17 °N to data at 12 °N manifests as a latitudinal dependence to ΔN_2^P. Considering the regional water masses identified in prior work (Evans et al., 2020), a likely explanation is that we are seeing purer 13CW water at 12 °N than at 17 °N. The obvious solution is to expand the analysis to other latitudes to cover all θ-S space in the ODZ.

In general, all additional data compare favorably with the main results from 17 °N to provide additional confidence that these methods are not simply unique to the core region and have broader applicability over the entire ODZ region, as we would expect given the model framework is based on conservative mixing.

3.3 Biogenic N_2 and O_2

The model's best fit of ΔN_2^P (σ_0) at 17 °N (Figure 4D, red line) was then used to determine GTD-derived estimates of ΔN_2^b using

TABLE 2 Comparison of water types and properties of the ETNP identified by Evans et al. (2020) and water types or water mass mixtures identified in this work (bold text) at 17 °N: Upper Circumpolar Deep Water (UCDW), Antarctic Intermediate Water (AAIW), North Equatorial Pacific Intermediate Water (NEPIW), 13°C Water (13CW), Pacific Subarctic Upper Water (PSUW), Equatorial Surface Water (ESW), and Tropical Surface Water (TSW).

	Evans et al. (2020)			This work			
Row	Source Water Type or Water Mass Mixture	Theta (°C)	S (psu)	Theta (°C)	S (psu)	ΔN_2^P (μmol/kg)	Ar (μmol/kg)
1	UCDW	1.42	34.87	-	-	–	–
2	**mix of UCDW + AAIW**	**3.725**	**34.785**	**4.31**	**34.55**	**12.60**	**15.40**
3	AAIW	6.03	34.7	-	-	–	–
4	**mix of AAIW + NEPIW**	**7.795**	**34.75**	**7.0**	**34.51**	**12.55**	**14.50**
5	NEPIW	9.56	34.8	-	-	–	–
6	**13CW**	**12.81**	**34.965**	**12.5**	**34.77**	**14.91**	**13.06**
7	mix of NEPIW + PSUW	12.94	34.465	-	-	–	–
8	PSUW	16.32	34.13	-	-	–	–
9	**ESW**	**22.27**	**34.5**	**20.4**	**34.3**	**28.0**	**11.63**
10	**TSW**	**26.95**	**34.06**	**27.3**	**34.55**	**4.78**	**10.30**

10.3389/fmars.2023.1134851

Eqn. 4. This conveniently ensures that any water mass composed of a mixture of two adjacent water types uses the correct and smoothed mixed water mass value for ΔN_2^b. The results for biogenic N_2 alongside O_2 are shown in Figure 5. The biogenic N_2 peaks at just below the oxycline (within 100 m) at 17 °N. Note that since ΔN_2^P (σ_0) was derived by matching the ship GTD-derived biogenic N_2 estimates to the nutrient-derived estimates at 17 °N, the shipboard nutrient and GTD results must agree and the residuals simply provide information on the errors in the data and analysis procedure. A regression fit to a double Gaussian that is constrained to zero at the surface and deepest waters (see Figure 5A, red line) shows an R-squared of 0.96 and RSME of 0.54 µM N_2. The first independent float-based measurements of ΔN_2^b using the same method applied to gas tension and oxygen data from Float 89 within 26 km of the shipboard station generally agrees with the shipboard calibration measurements over 130< P< 630 dbar or O_2< 3 uM: Density interpolated measurements show a mean (n=7) difference of -0.42 (± 0.78 RMSE) µM N_2, or 10 (± 19) %. This result provides a first quantitative assessment of fully autonomous measurements of biogenic N_2 using GTD-equipped floats. ODZ core water O_2 near Float 89 was uniform over 160< P< 700 dbar and assumed anoxic since shipboard STOX O_2 was ±25 nmol/kg and float optode O_2 was likewise near zero and uniform (after correcting for the anoxic optode pressure and temperature coefficients).

For comparison to the results from the first float, we present additional measurements made by a second float (see Table 1, float F93) several months after the end of the second cruise and located approximately 350 km to the southeast of the core station. The second float showed lower O_2 and higher biogenic N_2 in the deeper waters (see Figure 5, float F93 results in light green filled diamonds) consistent with expected higher denitrification rates in less oxygenated waters but less biogenic N_2 at comparable O_2 in the shallower waters. This could indicate slightly different hydrography between the two locations, with the deeper waters being older at the second float, or variations in denitrification forcing, we don't know. We also have no independent comparison of Float 93 optode-derived O_2 to shipboard STOX due to the fact that the second float data were collected several months after the ship left the region, but expect the absolute value of oxygen is uncertain to several hundred nmol/kg or more. The ΔN_2^b and O_2 profiles from both floats are otherwise fairly consistent which independently supports the results from the first float.

For additional observations with which to compare and contrast with the first float, which was located near 17 °N in the ODZ core, we look to shipboard data from lower latitudes and specifically southern waters which will have different histories of biological processing than those in the core region. Indeed, the largest deviations were observed were near 12 °N where the upper oxycline was much deeper than at the core station with distinctly different water mass properties (see Figure 4A, dark green non-filled diamonds). Remarkably, the same characteristic of biogenic N_2 peaking just below the oxycline was reproduced at 12 °N even though the oxycline at 12 °N was approximately 200 m deeper than at 17 °N. Most important, the apparently low ΔN_2^b values at P = 265 and 305 dbar correspond with significantly high CTD measured O_2 (3.6< O_2< 6.2 µmol/kg) compared to other mesopelagic waters during the same cast (ie., it likely isn't a measurement error as the CTD O_2 goes well below 1 µM during the same cast) along with observed low and near zero ΔN_2^b. Since these hypoxic waters are typically considered well above the threshold for functional anoxia, we would not expect these waters to have previously hosted denitrification processes leading to N_2 production, leading us to believe these hypoxic waters are the southern source waters we had set out to find. The remaining oxygen in the waters (4.9 ± 1.3 µmol/kg) would need to be lost to respiration processes before becoming functionally anoxic and capable of hosting a robust denitrifying microbial community. This rather exciting discovery also lends support to our overall approach. We also note, however, that no truly independent measurement of biogenic N_2 has yet been made at either location and hope to make those measurements in the future.

3.4 Lagrangian drift

An example of various estimates of dissolved N_2 variability measured during a 20 hour drift period of a float at a mean potential density of 26.474 kg/m^3 are shown in Figure 6. Variability in dissolved N_2 (Figure 6, blue line) measured by the gas tension technique is very small, about 1 µmol/kg, or 0.18%. This is comparable to the uncertainty in Henry's Law solubility coefficients. Variability in biogenic N_2 (thick red line) is even smaller, at<250 nmol/kg or<0.05%. The impact of excluding dissolved O_2 in the calculation of biogenic N_2 is nearly undetectable given that measured O_2 variability is at the limit of

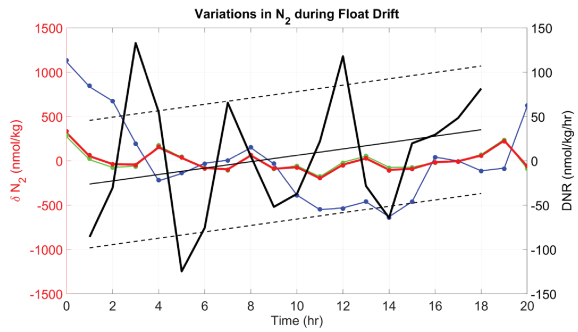

FIGURE 6
Deviations in water mass N_2 from the mean (δN_2) during the Lagrangian drift of a float on mean isopycnal of 26.474 kg/m^3 and P = 242 ± 4 dbar (F89 starting 31-Dec-2020 at 09:00 GMT). Different calculations of δN_2, using a specified ΔN_2 and O_2, are shown: 1) ΔN_2^b with measured O_2 (red line), 2) ΔN_2^e with measured O_2 (green line), 3) N_2^m with measured O_2 (blue line), and 4) similar calculations as (1) – (3) but assuming anoxia (dots, using same color code). Note that since the plots show deviations from the mean, the mean values of δN_2 zero. The Lagrangian rate of change of ΔN_2^b is shown (left), calculated as local denitrification rate DNR (thick black line) using Eqn. 9, with corrections based on the local vertical gradient. A linear regression fit (thin black line) highlights slowly varying changes in the rates, with ±1 std deviation of the points (black dashed lines) as an indicator of variability. Notice that DNR is negative during the first half of the time series and changes to positive values during the second half of the time series.

detection (LOD) and indistinguishable from anoxic conditions. Calculation of rates (Figure 6, black lines) allow trends in ΔN_2^b to be detected at ±100 nMN_2/day: Positive rates would imply active denitrification after compensating for mixing effects and slippage of the float into different waters (which would explain negative rates). These rates and trends seem to be well above the LOD for ΔN_2^b since internal wave effects with periods of approximately 2 hr are well resolved, implying that longer term averaging (assuming Gaussian distribution) over 16.5 days could reduce these uncertainties to ±20 nM N_2/day. This would be suitable for detection of active denitrification in coastal waters of the ETNP where rates of up to 20 nM N_2/day have been reported (Babbin et al., 2020), but further resolution would be required to detect active denitrification in the offshore waters with reported rates of up to 4 nM N_2/day (Babbin et al., 2020).

4 Discussion

The amplitude (6 ± 1 $\mu molN_2/kg$), profile shape, and depth distribution of the biogenic N_2 with a peak at 300 m just below the oxycline agree very well with the prior detailed study of Fuchsman et al. (2018) for the ETNP ODZ core. This same study also noted significant and unexplained mismatches in excess and biogenic N_2 of 1–2 $\mu molN_2/kg$ near 15 °N. The authors hypothesized that water mass mixing did not following their empirical 'background' (or 'outside ODZ') values. Similarly, we found these anomalies at lower latitudes, specially 12 °N, but our water mass mixing approach provides a path toward resolving them. Southern source waters to the ODZ have different preformed excess N_2 values at the same density range as waters further north around 17 °N yet span the same density range. A simple density parameterization of 'background' excess N_2 is thus not sufficient to explain all variability across the entire ODZ. Our approach to reconstruct the equivalent abiotic excess N_2 from a mixture of various water types with different preformed excess N_2 values should ultimately provide improved biogenic N_2 estimates at all latitudes by either method. The relatively small latitudinal dependence of ΔN_2^p we found by comparing our method applied at 17 °N to observations from 12 °N is expected to be resolved by properly accounting of all water types in the model at 12 °N. Correctly predicting ΔN_2^p over the entire ETNP ODZ based on a linear mixing model of different water types is an overarching goal.

Our primary nutrient-based estimates of biogenic N_2 were used in calibrating our novel gas tension-based estimates, and so a current weakness is the lack of a second independent estimate for comparison. Since many more hydrocasts were taken during both cruises that are not yet fully analyzed, we plan on using these shipboard data at other stations to both calibrate (ie., quantify preformed excess N_2) and validate (ie., quantify absolute accuracy). Accuracy and calibration drift is not expected to be limited by the raw measurement of gas tension, although dissolved O_2 could introduce comparable errors at either high O_2 levels or if the O_2 sensor has a significant zero reading offset (>2 μM). To perform the extended analysis over the entire ETNP ODZ and synthesize all our observations, we want to step back and refine a procedure that identifies water types and their values from the 'broken stick' analysis of multi-conservative parameter data. Work is in progress to fully automate this procedure with the expectation that the water types and property values can be determined with quantified confidence intervals, a non-trivial task given the fitting needs to be done on scattered data in multi-dimensions with many unconstrained break-points. An alternative approach would be to use a regional numerical model of the ODZ that includes dissolved Ar and a representation of abiotic N_2, conservatively redistributes these quantities within the model domain, and is tuned to the observations inside and outside the anoxic core. This would facilitate inclusion of N_2/Ar measurements and make better connections between this method and those of Fuchsman et al. (2018) and Chang et al. (2012). The water masses created by mixing of source water types would be subject to parameterization of diapycnal and isopycnal mixing in the model.

Regarding the potential of floats to directly measure *in situ* denitrification rates (DNR), our first attempt amounts to a test of the procedure given the paucity of the data presented here and the low denitrification rates of the offshore region. It seems clear, however, that improved mapping of ΔN_2^b and understanding of mixing at the float are prerequisites to inspecting additional data we have collected for scientifically interesting results. There will likely be tradeoffs while trying to reduce uncertainty by using longer averaging periods versus the potential for the float to slip out of the water mass under study and into a different water mass of similar density during the drift. Analysis of longer duration float-drift data is clearly required, but the initial results are encouraging since they suggest that the higher denitrification rates typical of the more productive coastal waters of the ETNP (up to 20 $nmolN_2/kg/day$) should be resolvable using this method by extending the float drift period to more than 16 days. This is a great start.

Lastly, regarding our experiences using the shipboard GTD at sea, we note that each hydrocast took approximately 2.5 hrs longer due to the time required to equilibrate the GTD at the 12 sampling depths – this could be reduced to approximately 1 hr if analysis relied upon deconvolution of the data but more time would need to be spent determining the response time characteristics of the mounted GTD. The same ship's GTD used on cruise SR2011 was used on the first half of the cruise SR2114 but succumbed to a small crustacean that got trapped in the plenum against the thin membrane and punctured it and had to be swapped out for a spare.

5 Summary

We report for the first time direct autonomous vertical profile measurements of gaseous dissolved biogenic N_2 and dissolved O_2 made on two profiling floats. The profiles were collected near 17 °N in the ETNP ODZ. The data show peaks in biogenic N_2 just below the oxycline in the mesopelagic and continues to decrease until oxygen begins to increase in the deeper intermediate waters. Our measurements are the result of a new method (calculated using Eqn. 4) we have developed to autonomously determine biogenic N_2 on floats, and potentially other oceanographic platforms, based on measurement of N_2 by the gas tension method. Conservative 'linear-mixing' of multiple water types is used to predict abiotic dissolved N_2 in

a mixed water mass (i.e., a mixture of several source water types). We have defined, measured, and used a new conservative quantity which we call 'preformed excess N_2'. We calibrated our method (see Eqn. 8) at 17 °N in the anoxic core region using shipboard measured gas tension, temperature, salinity, dissolved oxygen, and nutrients, and used argon as a constraint. The RMSE of the new method was assessed at ±19%. The method can be improved by reducing and quantifying uncertainty in how water types and their conservative preformed N_2 are determined. Our shipboard sampling targeted and successfully found northern and southern source waters to the ETNP ODZ. The southern waters near 12 °N had not been sampled before for argon, gas tension or preformed excess N_2 and were found to contain very low O_2 (5 ± 1.3 µmol/kg) and near zero biogenic N_2. Our new method can also be applied to Lagrangian isopycnal data to determine *in situ* biogenic N_2 production rates. Our first attempt shows that our new method has a signal-to-noise ratio that should be useful for assessing productive nearshore waters of the ETNP ODZ but needs improvement for offshore waters with significantly lower denitrification rates.

Data availability statement

The original contributions presented in the study are included in the article/Supplementary Material. Further inquiries can be directed to the corresponding author.

Author contributions

The first three authors have worked equally to formulate the methods and apply them to the data. All authors have collaborated over the last 6-8 years to measure dissolved gases in the ETNP during three cruises. CM was responsible for gas tension derived N_2, EAD for floats with O_2, MA for nutrients and at sea mass-spectrometry as well as being Chief Scientist on the cruises, RH for Ar, and EG-R for STOX O_2. Each have contributed to data planning, collection, processing, and QC of their data and sharing for this manuscript. All authors contributed to the article and approved the submitted version.

Funding

This work was funded by NSF under grants OCE-1153295/1154741/1851210/1851361. EG-R was supported by the Ramon y Cajal Program (RYC2019-027675-I) and project number PID2020-117340RA-I00 from the Spanish Ministry of Science.

Acknowledgments

We are grateful to: Nick Michel-Hart and Kevin Zack (APL/UW) who significantly improved the production GTD for this project; Robert Daniels and Trina Litchendorf (APL/UW) for float preparations and field support; and Mark Barry and Bruce Johnson (Pro-Oceanus Systems, Inc.); employees of MRV Inc. for customizing their floats throughout the pandemic. We thank the water sampling teams during the cruises who enabled the collection of the data: Valentina Giunta, Darcy Perin, Neeharika Verma, Siddhant Kerhalkar, Alanna Mnich, Jenn Crandall, and Sergio Cambronero and C. Erinn Raftery for Ar analysis. We thank Steve Riser and Dana Swift (UW) who helped get earlier versions of GTD-equipped float deployed, Andrew Reed (WHOI) who during his PhD worked on estimating bioN_2 from the first float data and Figure 2 modified from his thesis (Reed, 2018); Bonnie Chang (CICOES/UW) and Clara Fuchsman (UMCES) for sharing their earlier ETNP argon data. We thank the reviewers for significantly improving the manuscript. We also thank the Captain and crew of the RV *Sally Ride* for taking us to the ETNP ODZ twice.

Conflict of interest

CM is a co-founder and Vice President of the company Pro-Oceanus Systems, Inc. PSI who manufactures the GTDs used in this work – his potential conflict of interest is managed by a plan developed by the UW's Office of Research Compliance.

The remaining authors declare that the research was conducted in the absence of any commercial or financial relationships that could be construed as a potential conflict of interest.

Publisher's note

Supplementary material

The Supplementary Material for this article can be found online at: https://www.frontiersin.org/articles/10.3389/fmars.2023.1134851/full#supplementary-material

References

Altabet, M. A., and Bourbonnais, A. (2019). N-loss stoichiometry in a Peru ODZ eddy. *J. Mar. Res.* 77 (2), 169–189. doi: 10.1357/002224019828474269

Babbin, A. R., Buchwald, C., Morel, F. M., Wankel, S. D., and Ward, B. B. (2020). Nitrite oxidation exceeds reduction and fixed nitrogen loss in anoxic pacific waters. *Mar. Chem.* 224, 103814. doi: 10.1016/j.marchem.2020.103814

Babbin, A. R., Keil, R. G., Devol, A. H., and Ward, B. B. (2014). Organic matter stoichiometry, flux, and oxygen control nitrogen loss in the ocean. *Science* 344 (6182), 406–408. doi: 10.1126/science.1248364

Banse, K., Naqvi, S. W. A., and Postel, J. R. (2017). A zona incognita surrounds the secondary nitrite maximum in open-ocean oxygen minimum

zones. *Deep Sea Res. Part I: Oceanographic Res. Pap.* 127, 111–113. doi: 10.1016/j.dsr.2017.07.004

Berg, J. S., Ahmerkamp, S., Pjevac, P., Hausmann, B., Milucka, J., and Kuypers, M. M. (2022). How low can they go? aerobic respiration by microorganisms under apparent anoxia. *FEMS Microbiol. Rev.* 46 (3), fuac006. doi: 10.1093/femsre/fuac006

Bianchi, D., Weber, T. S., Kiko, R., and Deutsch, C. (2018). Global niche of marine anaerobic metabolisms expanded by particle microenvironments. *Nat. Geosci.* 11 (4), 263–268. doi: 10.1038/s41561-018-0081-0

Bristow, L. A., Dalsgaard, T., Tiano, L., Mills, D. B., Bertagnolli, A. D., Wright, J. J., et al. (2016). Ammonium and nitrite oxidation at nanomolar oxygen concentrations in oxygen minimum zone waters. *Proc. Natl. Acad. Sci.* 113 (38), 10601–10606. doi: 10.1073/pnas.1600359113

Callbeck, C. M., Lavik, G., Stramma, L., Kuypers, M. M., and Bristow, L. A. (2017). Enhanced nitrogen loss by eddy-induced vertical transport in the offshore Peruvian oxygen minimum zone. *PloS One* 12 (1), e0170059. doi: 10.1371/journal.pone.0170059

Chang, B. X., Devol, A. H., and Emerson, S. R. (2010). Denitrification and the nitrogen gas excess in the eastern tropical south pacific oxygen deficient zone. *Deep Sea Res. Part I: Oceanographic Res. Pap.* 57 (9), 1092–1101. doi: 10.1016/j.dsr.2010.05.009

Chang, B. X., Devol, A. H., and Emerson, S. R. (2012). Fixed nitrogen loss from the eastern tropical north pacific and Arabian Sea oxygen deficient zones determined from measurements of N_2: ar. *Global Biogeochemical Cycles* 26 (3). doi: 10.1029/2011GB004207

Codispoti, L. A., Brandes, J. A., Christensen, J. P., Devol, A. H., Naqvi, S. W. A., Paerl, H. W., et al. (2001). The oceanic fixed nitrogen and nitrous oxide budgets: moving targets as we enter the anthropocene? *Scientia Marina* 65 (S2), 85–105. doi: 10.3989/scimar.2001.65s285

Codispoti, L. A., and Richards, F. A. (1976). An analysis of the horizontal regime of denitrification in the eastern tropical north pacific 1. *Limnol. Oceanogr.* 21 (3), 379–388. doi: 10.4319/lo.1976.21.3.0379

Dalsgaard, T., Stewart, F. J., Thamdrup, B., De Brabandere, L., Revsbech, N. P., Ulloa, O., et al. (2014). Oxygen at nanomolar levels reversibly suppresses process rates and gene expression in anammox and denitrification in the oxygen minimum zone off northern Chile. *MBio* 5 (6), e01966–e01914. doi: 10.1128/mBio.01966-14

Deutsch, C., Berelson, W., Thunell, R., Weber, T., Tems, C., McManus, J., et al. (2014). Centennial changes in north pacific anoxia linked to tropical trade winds. *Science* 345 (6197), 665–668. doi: 10.1126/science.1252332

Devol, A. H. (2015). Denitrification, anammox, and N2 production in marine sediments. *Annu. Rev. Mar. Sci.* 7, 403–423. doi: 10.1146/annurev-marine-010213-135040

Emerson, S. R., and Hamme, R. C. (2022). *Chemical oceanography: element fluxes in the Sea* (Cambridge: Cambridge University Press).

Engel, A., Kiko, R., and Dengler, M. (2022). Organic matter supply and utilization in oxygen minimum zones. *Annu. Rev. Mar. Sci.* 14, 355–378. doi: 10.1146/annurev-marine-041921-090849

Evans, N., Boles, E., Kwiecinski, J. V., Mullen, S., Wolf, M., Devol, A. H., et al. (2020). The role of water masses in shaping the distribution of redox active compounds in the Eastern tropical north pacific oxygen deficient zone and influencing low oxygen concentrations in the eastern pacific ocean. *Limnol. Oceanogr.* 65 (8), 1688–1705. doi: 10.1002/lno.11412

Fuchsman, C. A., Devol, A. H., Casciotti, K. L., Buchwald, C., Chang, B. X., and Horak, R. E. (2018). An N isotopic mass ballance of the Eastern tropical north pacific oxygen deficient zone. *Deep Sea Res. Part II: Topical Stud. Oceanogr.* 156, 137–147. doi: 10.1016/j.dsr2.2017.12.013

Garcia, H. E., Locarnini, R. A., Boyer, T. P., Antonov, J. I., Baranova, O. K., Zweng, M. M., et al. (2014). *World ocean atlas 2013, volume 4: dissolved inorganic nutrients (phosphate, nitrate, silicate)*. Ed. S. Levitus, 25, A. Mishonov Technical Ed. (Natl. Cent. Environ. Inf.:Silver Spring, MD)

Garcia-Robledo, E., Padilla, C. C., Aldunate, M., Stewart, F. J., Ulloa, O., Paulmier, A., et al. (2017). Cryptic oxygen cycling in anoxic marine zones. *Proc. Natl. Acad. Sci.* 114 (31), 8319–8324. doi: 10.1073/pnas.1619844114

Hamme, R. C., and Emerson, S. R. (2004). The solubility of neon, nitrogen, and argo in distilled water and seawater. *Deep-Sea Res. I* 51, 1517–1528. doi: 10.1016/j.dsr.2004.06.009

Hamme, R. C., Emerson, S. R., Severinghaus, J. P., Long, M. C., and Yashayaev, I. (2017). Using noble gas measurements to derive air-sea process information and predict physical gas saturations. *Geophys. Res. Lett.* 44, 1–9. doi: 10.1002/2017GL075123

Hamme, R. C., Nicholson, D. P., Jenkins, W. J., and Emerson, S. R. (2019). Using noble gases to assess the ocean's carbon pumps. *Annu. Rev. Mar. Sci.* 11, 75–103. doi: 10.1146/annurev-marine-121916-063604

Hamme, R. C., and Severinghaus, J. P. (2007). Trace gas disequilibria during deep-water formation. *Deep Sea Res. I* 54, 939–950. doi: 10.1016/j.dsr.2007.03.008

Horak, R. E., Ruef, W., Ward, B. B., and Devol, A. H. (2016). Expansion of denitrification and anoxia in the eastern tropical north pacific from 1972 to 2012. *Geophys. Res. Lett.* 43 (10), 5252–5260. doi: 10.1002/2016GL068871

Ito, T., Hamme, R. C., and Emerson, S. (2011). Temporal and spatial variability of noble gas tracers in the north pacific. *J. Geophys. Res.: Oceans* 116 (C8). doi: 10.1029/2010JC006828

Ito, T., Minobe, S., Long, M. C., and Deutsch, C. (2017). Upper ocean O2 trends: 1958–2015. *Geophys. Res. Lett.* 44 (9), 4214–4223. doi: 10.1002/2017GL073613

Kwiecinski, J. V., and Babbin, A. R. (2021). A high-resolution atlas of the eastern tropical pacific oxygen deficient zones. *Global Biogeochemical Cycles* 35 (12), e2021GB007001. doi: 10.1029/2021GB007001

Loeffler, A., Schneider, B., Schmidt, M., and Nausch, G. (2011). Estimation of denitrification in Baltic Sea deep water from gas tension measurements. *Mar. Chem.* 125 (1-4), 91–100. doi: 10.1016/j.marchem.2011.02.006

McNeil, C., D'Asaro, E., Johnson, B., and Horn, M. (2006). A gas tension device with response times of minutes. *J. Atmos. Oceanic Technol.* 23 (11), 1539–1558. doi: 10.1175/JTECH1974.1

McNeil, C. L., D'Asaro, E. A., Reed, A., Altabet, M. A., Bourbonnais, A., and Beaverson, C. (2018). Innovative nitrogen sensor maps the north pacific oxygen minimum zone. – 31 (91), 96.

McNeil, C. L., Johnson, B. D., and Farmer, D. M. (1995). *In-situ* measurement of dissolved nitrogen and oxygen in the ocean. *Deep Sea Res. Part I: Oceanographic Res. Pap.* 42 (5), 819–826. doi: 10.1016/0967-0637(95)97829-W

Penn, J. L., Weber, T., Chang, B. X., and Deutsch, C. (2019). Microbial ecosystem dynamics drive fluctuating nitrogen loss in marine anoxic zones. *Proc. Natl. Acad. Sci.* 116 (15), 7220–7225. doi: 10.1073/pnas.1818014116

Reed, A. (2018). *A gas tension device & method for denitrification studies in oxygen minimum zones* (School of Oceanography at University of Washington). PhD Thesis.

Reed, A., McNeil, C., D'Asaro, E., Altabet, M., Bourbonnais, A., and Johnson, B. (2018). A gas tension device for the mesopelagic zone. *Deep Sea Res. Part I: Oceanographic Res. Pap.* 139, 68–78. doi: 10.1016/j.dsr.2018.07.007

Revsbech, N. P., Larsen, L. H., Gundersen, J., Dalsgaard, T., Ulloa, O., and Thamdrup, B. (2009). Determination of ultra-low oxygen concentrations in oxygen minimum zones by the STOX sensor. *Limnol. Oceanogr.: Methods* 7 (5), 371–381. doi: 10.4319/lom.2009.7.371

Revsbech, N. P., Thamdrup, B., Dalsgaard, T., and Canfield, D. E. (2011). "Construction of STOX oxygen sensors and their application for determination of O2 concentrations in oxygen minimum zones," in *Methods in enzymology*, vol. 486. (Academic Press), 325–341).

Richards, F. A. (1965). "Anoxic basins and fjords," in *Chemical oceanography*, vol. 1. Eds. J. P. Riley and G. Skirrow (New York:Academic Press) 611–645.

Stanley, R. H., and Jenkins, W. J. (2013). "Noble gases in seawater as tracers for physical and biogeochemical ocean processes," in *The noble gases as geochemical tracers* (Berlin, Heidelberg: Springer), 55–79.

Tiano, L., Garcia-Robledo, E., Dalsgaard, T., Devol, A. H., Ward, B. B., Ulloa, O., et al. (2014). Oxygen distribution and aerobic respiration in the north and south eastern tropical pacific oxygen minimum zones. *Deep Sea Res. Part I: Oceanographic Res. Pap.* 94, 173–183. doi: 10.1016/j.dsr.2014.10.001

Zakem, E. J., and Follows, M. J. (2017). A theoretical basis for a nanomolar critical oxygen concentration. *Limnol. Oceanogr.* 62 (2), 795–805. doi: 10.1002/lno.10461

frontiers | Frontiers in Marine Science

TYPE Original Research
PUBLISHED 04 July 2023
DOI 10.3389/fmars.2023.1155932

OPEN ACCESS

EDITED BY
Sudheesh Valliyodan,
Central University of Kerala, India

REVIEWED BY
Jianing Wang,
Chinese Academy of Sciences (CAS), China
Damian L. Arévalo-Martínez,
Radboud University, Netherlands

*CORRESPONDENCE
Matías Pizarro-Koch
matiaspizarro@udec.cl

RECEIVED 01 February 2023
ACCEPTED 16 May 2023
PUBLISHED 04 July 2023

CITATION
Pizarro-Koch M, Pizarro O, Dewitte B, Montes I, Paulmier A, Garçon V, Sepulveda HH, Corredor-Acosta A, Aguirre C and Ramos M (2023) On the interpretation of changes in the subtropical oxygen minimum zone volume off Chile during two La Niña events (2001 and 2007).
Front. Mar. Sci. 10:1155932.
doi: 10.3389/fmars.2023.1155932

On the interpretation of changes in the subtropical oxygen minimum zone volume off Chile during two La Niña events (2001 and 2007)

Matías Pizarro-Koch[1,2,3]*, Oscar Pizarro[3,4,5], Boris Dewitte[5,6,7,8], Ivonne Montes[9,10], Aurélien Paulmier[11], Véronique Garçon[11], Hector Hito Sepulveda[4], Andrea Corredor-Acosta[12], Catalina Aguirre[1,2,13,14] and Marcel Ramos[7,8]

[1]Escuela de Ingeniería Civil Oceánica, Facultad de Ingeniería, Universidad de Valparaíso, Valparaíso, Chile, [2]Millennium Nucleus Understanding Past Coastal Upwelling Systems and Environmental Local and Lasting Impacts (UPWELL), Coquimbo, Chile, [3]Millennium Institute of Oceanography, Concepción, Chile, [4]Department of Geophysics, University of Concepcion, Concepcion, Chile, [5]CECI, Université de Toulouse, CERFACS/CNRS, Toulouse, France, [6]Centro de Estudios Avanzados en Zonas Áridas (CEAZA), Coquimbo, Chile, [7]Departamento de Biología Marina, Facultad de Ciencias del Mar, Universidad Católica del Norte, Coquimbo, Chile, [8]Centro de Ecología y Manejo Sustentable de Islas Oceánicas, Universidad Católica del Norte, Coquimbo, Chile, [9]Instituto Geofísico del Perú, Lima, Peru, [10]Universidad de Ingeniería y Tecnología (UTEC), Lima, Peru, [11]Laboratoire d'Études en Géophysique et Océanographie Spatiales (LEGOS), Université de Toulouse, CNRS/IRD/UT3/CNES, Toulouse, France, [12]Centro FONDAP de Investigación en Dinámica de Ecosistemas Marinos de Altas Latitudes (IDEAL), Valdivia, Chile, [13]Center for Climate and Resilience Research (CR)2, Santiago, Chile, [14]Centro de Observación Marino para Estudios de Riesgos del Ambiente Costero (COSTAR), Valparaíso, Chile

Oxygen minimum zones (OMZs) are extended oceanic regions for which dissolved oxygen concentration is extremely low. They are suspected to be expanding in response to global warming. However, currently, the mechanisms by which OMZ varies in response to climate variability are still uncertain. Here, the variability of the subtropical OMZ off central Chile of a regional coupled physical–biogeochemical regional model simulation was analyzed for the period 2000–2008, noting that its fluctuations were significant despite the relatively weak amplitude of the El Niño/Southern Oscillation (ENSO). In particular, the interannual variability in the OMZ volume (OMZ_{VOL}, defined as the volume with dissolved oxygen concentration (DO) ≤ 45μM) was approximately 38% larger than that of the seasonal cycle, with maximum and minimum anomalies of OMZ_{VOL} taking place during two cold La Niña (LN) years (2001 and 2007). The model analyses further reveal that these anomalies resulted from a combined effect of changes in (1) the oxygen-poor waters poleward transport by the Peru–Chile undercurrent (PCUC), (2) the intensity of quasi-zonal jets influencing the transport of water to and from the OMZ, and (3) the zonal DO transport related to mesoscale eddy activity. Specifically, the interannual variability of the PCUC modulated primarily the DO contents of the OMZ core [(DO) ≤ 20μM] and secondarily the OMZ_{VOL}, while cross-shore DO transport by the zonal jets and the eddy fluxes played a major role in ventilating and shaping the offshore extent of the OMZ. When the OMZ_{VOL} was maximum (minimum), the PCUC transport was slightly increased (reduced), which was

associated with a reduction (increase) in the ventilation of the OMZ through negative (positive) anomalies of zonal advection and DO eddy fluxes. Our results demonstrate that significant natural interannual variability in the subtropical OMZ off Chile originates from the interplay between oceanic equatorial teleconnection (PCUC transport) and local non-linear dynamics (the zonal jets and mesoscale eddies).

KEYWORDS

subtropical Eastern Pacific, oxygen minimum zone, ENSO (El Niño/Southern Oscillation), Peru-Chile undercurrent, mesoscale eddy flux

1 Introduction

In the present and projected global warming scenario, both model and observations indicate that the ocean is currently losing oxygen (Bopp et al., 2013; Schmidtko et al., 2017; Grégoire et al., 2021) and the deoxygenation trend will continue through the twenty-first century (e.g., Bindoff et al., 2019). This condition involves negative effects on marine ecosystems and the biogeochemical cycles (e.g., carbon, nitrogen, and many others) in regions where dissolved oxygen (DO) concentration is already low (Keeling et al., 2010; Breitburg et al., 2018; Pitcher et al., 2021), such as the oxygen minimum zones (OMZ) formed in Eastern Boundary Upwelling Systems (EBUS) (Karstensen et al., 2008; Paulmier and Ruiz-Pino, 2009; Garçon et al., 2019). Consensus among simulations participating in the Coupled Model Intercomparison Project (CMIP) has remained low in terms of the oxygen long-term trend in the OMZs (Cabré et al., 2015; Oschlies et al., 2018; Kwiatkowski et al., 2020), pointing out the limitations of the global low-resolution Earth System Model simulations in accounting for the non-linear upwelling dynamics in EBUS (Gruber, 2011) and a certainly important role of natural climate variability in these regions.

The sparse observational data suggests that natural climate variability in oxygen is certainly obscuring the long-term trend associated with external forcing of anthropogenic sources (Frölisher et al., 2009; Gilbert et al., 2010; Long et al., 2016; Graco et al., 2017; Ito et al., 2017). Therefore, a better understanding of the drivers related to the OMZ variability at the range of frequencies associated with basin-scale natural climate modes, such as the ENSO, is needed (Frischknecht et al., 2015; Mogollón and Calil, 2017; Espinoza-Morriberón et al., 2019). Among the EBUS experiencing a significant variability of the OMZ associated with the interannual to decadal timescales, the Humboldt Current System (HCS) is an archetype. This system is under the influence of the tropical Pacific climate variability through the efficient oceanic teleconnections pathways at different timescales (Pizarro et al., 2002; Ramos et al., 2008; Dewitte et al., 2012; Vergara et al., 2017; Sprintall et al., 2020). In addition, the HCS hosts one of the most intense and relatively shallow OMZ in the world (Huyer et al., 1987; Fuenzalida et al., 2009; Albert et al., 2010), which makes it an ideal laboratory for a better understanding of the OMZ climate variability despite the scarcity in long-term data sets (García-Reyes et al., 2015; Breitburg et al., 2018). Moreover, due to the large latitudinal extent of the OMZ in the HCS (from the equator to the subtropical region ~40°S), several physical and biogeochemical mechanisms interact heterogeneously over its spatial and temporal variability (Paulmier et al., 2006; Pitcher et al., 2021), which also undergo significant natural climate variability at a wide range of frequencies from intraseasonal to interannual and decadal time scales (Duteil et al., 2018; Duteil, 2019). Currently, a greater focus has been placed on the ENSO-OMZ relationship in the Northern HCS (Peruvian coast) from both observations (Gutiérrez et al., 2008; Graco et al., 2017; José et al., 2019) and model simulations (Mogollón and Calil, 2017; Espinoza-Morriberón et al., 2019), but less is known about the interannual fluctuations of the OMZ in the subtropical HCS off the Chilean coasts.

Previous modeling studies have shown the importance of the advective and eddy cross-shore (mainly zonal in our study region) fluxes in the seasonal variability of the OMZ off Peru and Chile. For example, Bettencourt et al. (2015) showed two key roles of the mesoscale eddies at the oceanic OMZ boundary between 380 and 600 m depth off Peru. On the one hand, the trajectory and mean position of the turbulent fluxes delimit and maintain the OMZ boundaries, and on the other hand, the high-frequency variability of these fluxes injects DO into the OMZ, being larger than the mean advective flux. Subsequently, Vergara et al. (2016) suggested the existence of distinct seasonal regimes for the ventilation of the Peruvian OMZ by eddies at its boundaries, whereas Espinoza-Morriberón et al. (2019) showed the impact of the enhanced mesoscale variability over the OMZ ventilation during the warm ENSO phase through the interaction between the horizontal and vertical eddy fluxes. Along with these mechanisms, the Peru–Chile undercurrent (PCUC) has been recognized as the main poleward transport pathway of the oxygen depleted Equatorial Subsurface Water (ESSW) mass along the Peruvian and Chilean coasts, extending southward the OMZ (e.g., Wooster & Gilmartin, 1961; Silva and Neshyba, 1979; Silva et al., 2009). Therefore, the variability of the OMZ features is associated with the PCUC variability (e.g., Hormazábal et al., 2006). Pizarro-Koch et al. (2019) showed a close relationship between the variability of the PCUC transport with the seasonal cycle of the OMZ in the extra-tropical region, where an intense southward transport by the PCUC is related to a larger OMZ volume off central Chile. However, this modulation is not

homogeneous alongshore due to simultaneous processes, such as disturbances in the PCUC transport by the meridionally alternating jets [so-called striations; cf., Belmadani et al. (2017)] and mesoscale eddy activity. The latter suggests that these zonal jets and the mean eddy flux also shape the offshore boundary of the OMZ modulating its cross-shore extension, even when they are lower than the mean seasonal flux. In this study, we analyze the interannual fluctuations of the OMZ volume of the subtropical HCS off central Chile (30°S–38°S) in a regional simulation of a coupled physical–biogeochemical model. This simulation was analyzed in a previous study focusing on the seasonal cycle (Pizarro-Koch et al., 2019). This latter study showed that the seasonal variations of the OMZ off Central Chile can be interpreted as resulting from the interplay of mean and (mesoscale) eddy-induced transports of DO. We extend here the analysis to the investigation of interannual fluctuations first observing that they are as large as that of the seasonal cycle despite a relatively low variance in tropical forcing over the period of study (2000–2008). Our motivation is thus to better understand the mechanisms associated with natural variability in the OMZ volume. Natural variability refers here to changes not linearly related to ENSO, which manifests in this simulation as opposite variations in OMZ volume during two cold La Niña years (2001 and 2007). This marked asymmetry is in response to ENSO forcing calls for revisiting this simulation (Pizarro-Koch et al., 2019) focusing on interannual timescales. This also complements previous studies that focused on the response of the OMZ to warm El Niño events (Mogollón and Calil, 2017; Garçon et al., 2019).

The rest of the paper is organized as follows: In *Section 2*, we present a brief description of the coupled model setup and its validation and details in the methods and diagnostics. In *Section 3*, we diagnosed processes (DO budget, PCUC transport fluctuations, and eddy flux) behind the interannual variability of the subtropical OMZ contrasting in particular the years 2001 and 2007. Finally, discussion and concluding remarks are presented in *Section 4*.

2 Model description and methods

2.1 Model

2.1.1 High-resolution coupled physical–biogeochemical regional model setup

The Regional Ocean Model System (ROMS) AGRIF version of the hydrodynamical model was used and coupled to the BioEBUS biogeochemical model. ROMS is a split-explicit (i.e., the barotropic and baroclinic momentum equations are resolved separately using different time steps), free surface oceanic model, which solves the rotating primitive equations, based on the Boussinesq approximation and the hydrostatic vertical momentum balance (Shchepetkin and McWilliams, 2003; Shchepetkin and McWilliams, 2005; Penven et al., 2006). ROMS is discretized using curvilinear coordinates in the horizontal and terrain-following (or sigma levels) coordinate transformations in the vertical. BioEBUS is a nitrogen-based biogeochemical model derived from the $N_2P_2Z_2D_2$ model of Koné et al. (2005), specially developed for EBUS (Gutknecht et al., 2013). BioEBUS provides an estimate of 10 nitrogen state variables associated with six compartments, having two size classes for phytoplankton (small—flagellate, large—diatoms), zooplankton (small—ciliates, large—copepods), and detritus (small and large size). Furthermore, four other compartments include dissolved organic nitrogen (DON) and three dissolved inorganic nitrogen (DIN) compartments represented by nitrate (NO_3^-), nitrite (NO_2^-), and ammonium (NH_4^+). In addition to nitrification, BioEBUS considers specific microbial OMZ processes interacting within the DIN pool, such as denitrification and anammox. Initial and boundary conditions for nitrate and DO are provided by the CARS-2009 climatology (Dunn and Ridgway, 2002; Ridgway et al., 2002). For NO_2^-, NH_4^+, and DON, the initial and lateral boundary conditions are established using constant (in time) profiles similar to those described by Koné et al. (2005). The reader is referred to Gutknecht et al. (2013) for more detailed information about the BioEBUS biogeochemical model.

The configuration used in this study (hereafter referred to as PCCC12) is based on the hydrodynamical solution of Dewitte et al. (2012) coupled to the BioEBUS model setup of Montes et al. (2014). This latter study tuned the BioEBUS model so as to realistically simulate the OMZ off Peru [see also Bettencourt et al. (2015)]. The parameter values of the model are provided in Appendix A of Montes et al. (2014). The model domain extends from the North Equatorial Pacific (12°N) to eastern South Pacific (40°S), and from the South American coast to 95°W, with 37 sigma levels and a horizontal resolution of 1/12°. The model was originally run for 50 years (1958–2008); however, here, we use only the last 9 years (2000–2008), which corresponds to the period when there is a larger confidence in the realism of the atmospheric forcing. The latter is based on the statistical downscaling of the low-resolution (2.5° × 2.5°) NCEP-NCAR dataset using QuikSCAT data that covers the period 2000–2008, implying a better skill of the statistical model for that period (Goubanova et al., 2011; Cambon et al., 2013). PCCC12 has been also analyzed extensively over that period, indicating that it is skillful in simulating many aspects of the mean and seasonal circulation and OMZ (Vergara et al., 2016; Vergara et al., 2017; Pizarro-Koch et al., 2019). The following provides new material to evaluate the realism of the simulation for interannual timescales.

2.1.2 Model validation

We focus here on the validation of the model variability at interannual timescale over the period 2000–2008 considering that the model simulation was previously validated for the mean circulation and seasonal cycle (Dewitte et al., 2012; Vergara et al., 2016; Vergara et al., 2017; Pizarro-Koch et al., 2019; Conejero et al., 2020). We take advantage of a monthly ship-based time series of DO from the University of Concepcion at 36°30′S over the continental shelf (~90 m depth) for the period 2003–2008 (see Sobarzo et al. (2007) and Escribano et al. (2012) for more details) and current observations from the subsurface mooring located over the continental slope at 30°S. From this mooring, two Aanderaa current meters (RCM 8) at 220 and 480 m depth were used. Finally, satellite-derived (level-3 products of the Moderate Resolution Imaging Spectro-radiometer-MODIS-Aqua mission) sea surface

temperature (SST) and chlorophyll-a (Chl-a) concentration available from the National Aeronautics and Space Administration Jet Propulsion Laboratory PO.DAAC (https://podaac.jpl.nasa.gov/) are used (see Appendix).

The results of the comparison between model and observations indicate that the model simulates with some realism both the amplitude and the pattern of the observed SST (see Figures A1A, B) and Chl-a (see Figures A1D, E) variability, although there is a tendency for the model to have a lower variability, which is more pronounced for primary production than for SST. Figure A2 indicates that the model has also some skill in simulation DO variability. The correlation between observed and model oxycline depth reaches in particular 0.60 ($p< 0.05$). The variability of the model and observation has also a comparable amplitude, although the model tends to yield a weaker value (see Table A1). The statistics for meridional current are provided in Tables A1, indicating that the model has also some skill in accounting for the interannual variations in the circulation. In particular, at the depth corresponding to the PCUC core (220m), the correlation between model and observation reaches 0.48 ($p<0.05$). This complementary validation with respect to previous works supports the expectation that the model can account for fluctuations of the OMZ characteristics at interannual timescales.

2.2 Methods

2.2.1 DO budget analysis

The evolution of the DO in BioEBUS is determined by the advection–diffusion equation (Gutknecht et al., 2013). In this regard, the DO budget is performed at interannual timescales by estimating the anomalies (deviation from the mean climatology) of the tendency terms in Equation (1) for the rate of DO change.

$$\frac{\partial DO}{\partial t} = -\nabla\cdot(\vec{v}DO) + K_h\nabla^2 DO + \frac{\partial}{\partial z}\left(K_z\,\partial\frac{DO}{\partial z}\right) + SMS(DO) \quad (1)$$

On the right-hand side, the first three terms represent DO advection (with $\vec{v}$ the velocity vector); K_h and $K_z$are the horizontal and vertical eddy diffusion coefficient, respectively [K_h is equal to 100 m^2s^{-1} in our model, and $K_z$is calculated based on the K-profile parameterization mixing scheme; Large et al. (1994)]. Note that the hydrodynamic model also has numerical diffusion associated with inherent spurious diapycnal mixing of the numerical scheme, so that K_h is empirically adjusted. The *SMS*(sources minus sinks) term includes all biogeochemical processes considered by the model that act as sources and sinks, in this case, for DO. The total physical term (named *PHYS* below) is the summed up of the advective term ($ADV = -\nabla\cdot(\vec{v}DO)$) and the horizontal ($K_h\nabla_h^2 DO$) and vertical ($\frac{\partial}{\partial z}(K_z\frac{\partial DO}{\partial z})$) mixing, hereafter called *Hmix* and *Vmix*, respectively. Note that *ADV* also contains diffusion (through numerical diffusion) and non-linear advection that can be interpreted as mixing (like that generated by mesoscale eddies), so that *Hmix* is not the "full" mixing that is taking place in the model (cf., Vergara et al., 2017). The *ADV* can also be represented separately through its contributions related to the different components as: the zonal ($Xadv = -u\partial(DO)/\partial x$), meridional ($Yadv = -v\partial(DO/\partial y$) and vertical ($Zadv = -w\partial(DO)/\partial z$) advection, where u, v, and w are the zonal, meridional, and vertical velocity components, respectively.

2.2.2 Estimation of the subtropical OMZ volume and PCUC transport

The OMZ volume (hereafter OMZ_{VOL}) was estimated following the methodology by Pizarro-Koch et al. (2019), choosing the water volume with a DO level limit ≤ 45 µM (~1 ml L^{-1}) between 30°S and 38°S. This threshold is used, since it characterizes the hypoxic waters (e.g., Naqvi et al., 2010), which impact mostly the ecosystems far from the anoxic center of the ESP-OMZ off Peru. Here, the variability of the OMZ was analyzed using the OMZ_{VOL} and the mean DO inside this volume (OMZ intensity, denoted by OMZ_{DO}). In our analysis, both OMZ_{VOL} and OMZ_{DO} monthly anomaly time series were low-pass filtered using a 7-month running mean.

The transport associated with the Peru–Chile undercurrent (hereafter $PCUC_{TR}$) was estimated through spatially averaging the southward flow (only velocities with absolute values higher than 0.02 m s^{-1}) in a rectangular box with a cross-shelf extension spanning from the coast to ~100 km and between 80 and 800 m depth (vertical extension). This corresponds approximately to the location of the mean PCUC in the range of latitudes corresponding to our region of interest (see Figure 3 in Pizarro-Koch et al., 2019). The southward flow corresponds here to the negative meridional component of the currents. The PCUC anomalies were 7-month low-pass filtered similarly as the OMZ time series described above. In addition, the mean DO inside the region encompassed by the mean position of the PCUC (for values of mean meridional velocity higher than −0.02 m s^{-1}) was also estimated. It is referred to hereafter as $PCUC_{DO}$.

2.2.3 Remote and local forcing

Since the remote equatorial forcing is composed of Kelvin waves having different characteristics (vertical structure, energy, and phase speed), it is important to consider the waves that have the most energy with clear propagating characteristics. In the far eastern Pacific, these correspond to the wave of the gravest vertical modes (1–3) (Dewitte et al., 1999). We thus derive the contribution of the Kelvin waves of the first three baroclinic modes to sea level anomalies based on a vertical mode decomposition of the SODA Reanalysis. The method consists in projecting the pressure and zonal current fields onto the vertical modes derived from the mean vertical stratification at each grid point along the equator. We further projected the obtained quantities on the theoretical meridional structures of the equatorial waves in order to derive the equatorial Kelvin waves' amplitude (in equivalent sea level). Here, we will consider a time series of the Kelvin wave amplitude at 90°W along the equator for the summed-up contribution of the first three baroclinic modes, which corresponds to the longitude of the open boundary of the regional model.

The zonal (*Taux*) and meridional (*Tauy*) wind stress (hereafter ZWS and MWS, respectively) are from the model forcing, which is based on the Fairall et al. (2003) bulk parameterization using wind speed as inputs. Interannual variability of the wind stress was estimated in a coastal band spanning 210 km. In addition, the wind stress curl (hereafter WSC) was estimated in this coastal band excluding the five grid points close to the coast due to the limitation of the QuickSCAT data to account realistically for the wind drop-off (Astudillo et al., 2017).

2.2.4 Estimation of the DO eddy fluxes

In order to further interpret the processes at work, we estimated the DO eddy fluxes. In particular, the mean non-linear advection that is part of *PHYS* can be interpreted as the divergence of the DO eddy flux. The latter corresponds to the flux associated to the interannual fluctuations in DO and currents. It writes as follows: $(\langle \widetilde{DO}.\tilde{u} \rangle, \langle \widetilde{DO}.\tilde{v} \rangle)$, where the tilde refers to monthly mean anomalies relative to the climatological seasonal cycle.

We also estimated the mesoscale DO eddy flux that is associated with mesoscale eddy activity assumed to be dominated by energy in the range of frequencies higher than ~3 months. These fluxes can also be experienced interannual variations, which is estimated as the covariance between horizontal velocity fluctuations (u', v') and DO', i.e., $\langle u'DO' \rangle$3-m and $\langle v'DO' \rangle$3-m, where "$\langle\rangle$3-m" stands for a 3-month moving average, and the prime refers to the intraseasonal anomalies calculated as the departure from 3-month running mean of the total fields like in Pizarro-Koch et al. (2019).

2.2.5 ENSO indices

Over the period of interest, ENSO variability can be characterized by an index accounting for Central Pacific SST variability. This index, named the C index, is obtained from the decomposition in Empirical Orthogonal Function (EOF) of the SST anomalies in the tropical Pacific (120°E–80°W; 11°S–11°N) following Takahashi et al. (2011). SST is from HadISST v1.1. data set (Rayner et al., 2003). The C index accounts for both warm CP El Niño events (C>0) and La Niña events (C<0). Defining CP events when the C index in DJF is above 1 (1 standard deviation), one finds two CP El Niño (03/2002, 05/2004) and three La Niña events (1999/2000, 2000/2001, and 2007/2008). Note that an El Niño event also took place in 2006/2007, but this event had its peak SST in the eastern Pacific and was classified as an Eastern Pacific (EP) El Niño event (Yu et al., 2012). To characterize the variability in the region of influence of this type of event, we will use the E index that is obtained similarly as the C index [see Takahashi et al. (2011)]. Despite the relatively low variance of the E index over the period of interest, it still informs on equatorial Kelvin wave activity in the eastern Pacific because SST is sensitive to vertical advection processes there. Note that any historical ENSO indices can be approximated by the linear combination of the E and C indices (Takahashi et al., 2011). In particular, the ONI index (SST anomalies averaged over the region (170°W–120°W; 5°S–5°N) can be approximated by 0.52E + 0.62C through bilinear regression analysis. The mechanisms modulating the OMZ at ENSO timescales are numerous (Pitcher et al., 2021), so that the interpretation of the relationship between the ENSO indices and the OMZ metrics defined here is not straightforward. Still, we find a significant correlation between them and the C index in particular, with the C index ahead by a few months, confirming the key role of CP El Niño and La Niña variability in modulating the OMZ properties over this period.

3 Results

3.1 Variability of the subtropical OMZ (a study case: 2001 versus 2007)

The 9-year (2000–2008) mean value of the subtropical OMZ_{VOL} off central Chile (30°S–38°S) was ~4.5×10^4 km^3, with a thickness and offshore extension decreasing southward (Figures 1A, B). The core of the OMZ in this region was located over the continental slope centered at ~300 m depth (see shading blue color Figure 1B), and the mean OMZ_{DO} for the whole period was 32 µM. The OMZ_{DO} time series showed a large variability and was significatively anti-correlated with the OMZ_{VOL} at 95% confidence level (Figure 1C; r =−0.62 at 3-months lag) with the OMZ_{DO} ahead of the OMZ_{VOL} by 3 months. The OMZ_{VOL} time series also showed an interannual variability during the study period with maximum and minimum values during 2001 and 2007, respectively (Table 1; Figure 1C). Even though changes related to the ENSO cycles—in both the model and observed ENSO indices—were weak during 2000–2008 with a standard deviation of about 0.6°C, meanwhile, the historical series (1950–2020) of the ONI index showed a slightly larger standard deviation (0.8°C). During 2000–2008, the interannual changes in the OMZ_{VOL} were larger than those associated with the typical seasonal variability (Figure 2A; Table 1). In particular, the OMZ_{VOL} in 2001 is 38% larger than the mean value. Two other relative maxima with positive anomalies were observed in 2006 and 2008, but< 5% over the mean value. In fact, the OMZ_{VOL} showed mostly negative anomalies during the period 2003–2008 with a minimum during 2007 that was 23% smaller than the mean value. The OMZ 3D structure during these 2 years (2001 and 2007) with maximum/minimum anomalies is shown in Figures 2B, C, which illustrates the drastic change in OMZ_{VOL} when these years are compared, being 3 (1.7) times larger in 2001 than in 2007 when a threshold of 20 (45) µM is used (Table 1).

With regards to the water column structure, T-S-DO diagram and alongshore sections of averaged DO over the first 80 km from the coast for 2001 and 2007 are presented in Figures 3A–D, along with their difference in Figure 3F. Together with this, the water masses proportion (in %) as a function of latitude from the surface to 1,500 m depth was also estimated following the definition by Silva et al. (2009) (Figure 3G). The larger differences in DO concentration were observed in the core of the OMZ and around the upper oxycline, mainly south of 34°S. During 2007, the ESSW showed a reduced proportion inside the OMZ—consistent with a large increase of OMZ_{DO} observed this year—particularly important south of 34°S, while the AAIW and SAAW showed an increase (Figure 3G). In contrast, in 2001, when the

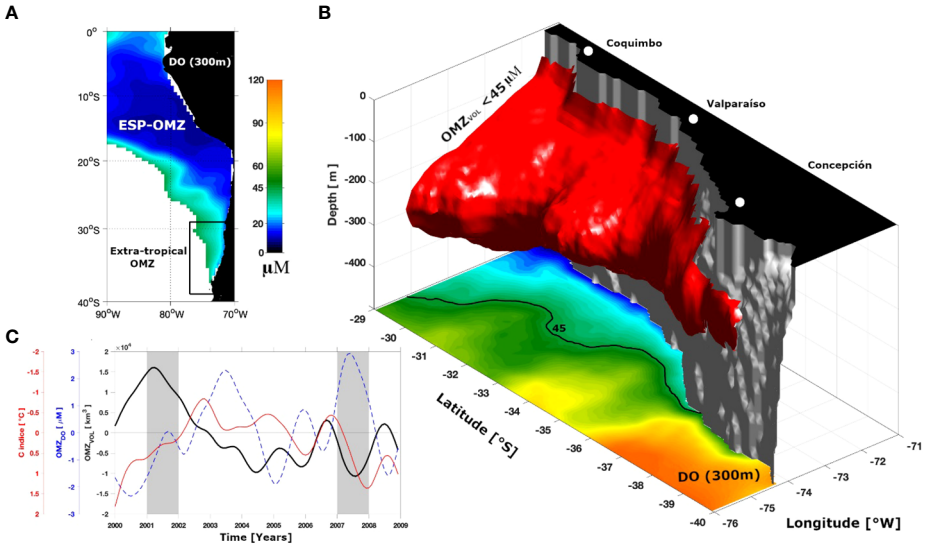

FIGURE 1
Climatological mean of the dissolved oxygen (DO) at 300 m depth in the eastern South Pacific Oxygen Minimum Zone (ESP-OMZ) obtained from CARS 2009 climatology **(A)**. The area of study defined here such as the extra-tropical region of ESP-OMZ is located between 30°S - 38°S and 76° W – and the coast (black square). A 3-D annual mean volume of the extra-tropical OMZ modeled defined here as the region with 9-year (2000-2008) mean DO < 45 µM (red isosurface) **(B)**. The shading color represents the spatial DO distribution modeled at 300m depth. The interannual anomalies of the OMZ volume (black line; OMZ_{VOL}), the DO within OMZ (blue dashed line; OMZ_{DO}) obtained from the model, and the Central El Niño indice (C indice; red line) **(C)**. The shaded area corresponds to the years 2001 and 2007.

OMZ_{VOL} was much larger (and OMZ_{DO} relatively low; Figure 2B), the proportions of the water masses showed only slight changes compared to their mean values. Figure 1C also shows that some fluctuations of the $OMZ_{\_DO}$ are not related to changes in the $OMZ_{\_VOL}$, suggesting internal redistribution of DO (below<45 µM).

3.2 DO budget analysis

To analyze the drivers of DO inside the OMZ off central Chile, we used the advection-diffusion Equation (1). Here, we followed a similar methodology as in Pizarro-Koch et al. (2019) who analyzed the seasonal variability for the same region. Table 2 shows the average values and the RMS values for the different terms that make up this equation for the entire period (2000–2008). The different terms were averaged inside the mean volume conforming the OMZ (i.e., the fixed volume with a mean DO value lower than 45 µM, as shown in Figure 2B). The anomalies of the different terms for the mean OMZ_{VOL} involved in the balance (1) are shown in Figure 4. It is worth mentioning that a linear regression indicates a slight negative (positive) trend of the DO rate of change (DO) of ~ −1.62 m s^{-1} µM (1µM) observed during the studied period (2000–2008; Figure 4A), which may be related to low-frequency variability like, e.g., decadal changes (not analyzed in this study). According to the physical terms, the three components of advective anomalies are of the same order of magnitude (Figure 4B), whereas the terms involving small-scale (subgrid) mixing are lower by two orders of magnitude (Figure 4C). This implies that *PHYS* anomalies, which represent all the physical terms in Equation (1), are mainly dominated by the advection terms (*ADV*) and is significantly (95% confidence) correlated with them (particularly, the correlations between *PHYS* and each of the advection anomalies components are: r = 0.64 with *Xadv*, r = -0.51 with *Yadv*, and r = 0.77 with *Zadv*). Additionally, *PHYS* anomalies (dashed red line in Figure 4B) is highly correlated (r = 0.8) with ∂DO/∂t at zero lag (red line in Figure 4A). The horizontal advection terms, *Xadv* and *Yadv* (magenta and blue lines, respectively in Figure 4B), are inversely correlated (r=-0.9) compensating each other and suggesting that over this period, the *Zadv* anomalies largely

TABLE 1 Root mean square (RMS) and descriptive statistics of the seasonal and interannual variability of the OMZ_{VOL} (in km^3) and OMZ_{DO} (µM).

	Seasonal RMS	Interannual RMS	2001 Average	2007 Average	[2000–2008] Average	Max	Min
OMZ_{VOL} (≤ 45 µM)[a]	2.30E+03	7.50E+03	5.50E+04	3.20E+04	4.00E+04	6.30E+04	2.60E+04
OMZ_{VOL} (≤ 20 µM)[b]	1.80E+04	3.70E+03	1.50E+04	4.90E+03	1.10E+04	2.20E+04	1.20E+03
OMZ_{DO} [a]	0.7	1.4	28.1	31	28.4	33	24
OMZ_{DO} [b]	0.6	0.8	12	14	12.2	17	9

Superscript "a" denotes the complete volume of the oxygen minimum zone (OMZ) that is encompassed by the dissolved oxygen (DO) threshold of ≤ 45 µM. Superscript "b" represents the OMZ core volume represented by the DO threshold of ≤20 µM

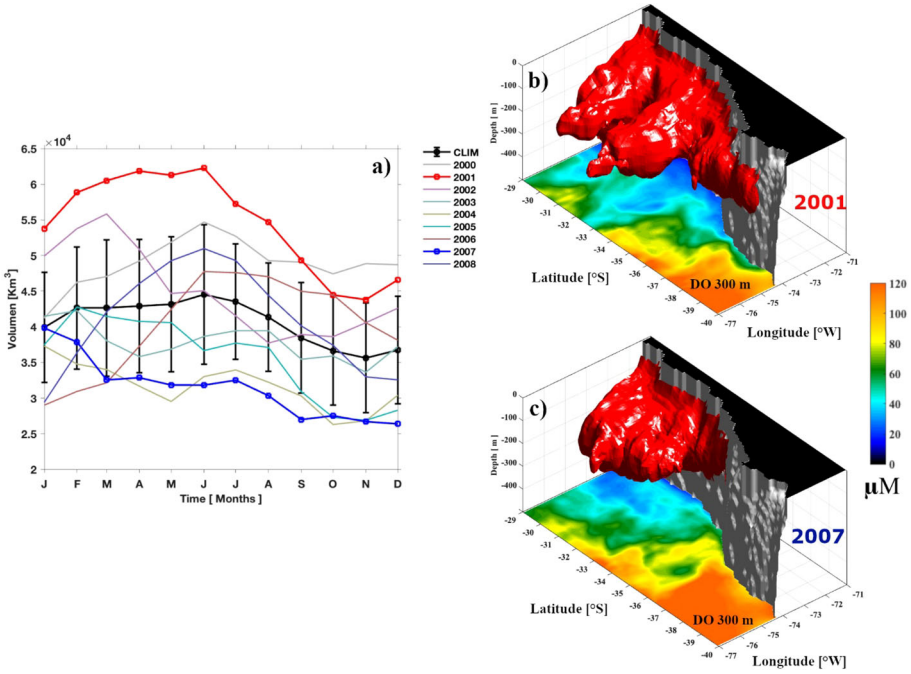

FIGURE 2
Seasonal cycles (black square-line) and monthly time series between of the extratropical OMZ volume between 2000-2008 years **(A)**. The 2001 and 2007 years are represented by red and blue square-line, respectively. The climatological seasonal cycle and its standard deviation of the volume are shown by black square-line and error bar. Panels **(B, C)** show 3-D distributions of the annual mean extratropical OMZ volume for the years 2001 and 2007, respectively, represented by red isosurfaces.

govern *PHYS* anomalies. Note that this does not imply that horizontal advection is not important for explaining DO variability along a vertical section or at particular depths within the OMZ (see *Section 3.4*).

During 2001, *PHYS* anomalies were slightly positive, while in 2007, they were slightly negative. In both cases the previous year (i.e., 2000 and 2006), *PHYS* showed positive anomalies, while *Xadv* term showed an inverse phase during 2000 (negative anomalies) and 2007 (positive anomalies). Due to the different terms involved in the balance being spatially averaged in the whole OMZ volume, there is little difference between 2001 and 2007 regarding the magnitude of these terms, although both years show large differences in OMZ_{VOL}. On the other hand, interannual anomalies of the *SMS* was less than that of *PHYS* with an RMS value reaching 5.8×10^{-8} µM s^{-1}, which contribute approximately 30% of the DO rate of change ($\partial DO/\partial t$). The main processes that governed the *SMS* term were the oxic decomposition and nitrification processes (Figure 4D). Only a large negative anomaly of oxic decomposition processes was observed during 2007 associated with the contraction of the OMZ. For comparison, the RMS of the seasonal cycle for all the above terms and their mean values for 2001 and 2007 years are indicated in Table 2. Additionally, Figure 5 shows the seasonal evolution of OMZ_{DO} and DO rate of change ($\partial DO/\partial T$) during 2001 and 2007, which are contrasted with the climatological seasonal cycle. We also display the evolution of the *PHYS* and *SMS* terms. Consistently, both *PHYS* and $\partial DO/\partial t$ time series show similar seasonal variability, which emphasizes the prominent role of physical processes in controlling the averaged seasonal variability of DO inside the OMZ. Overall, *PHYS* shows a larger (smaller) annual and semi-annual amplitude of the seasonal cycle in 2001 (2007) with respect to the climatological mean, with a maximum during the austral winter season (Figure 5C). Meanwhile, the *SMS* shows a similar magnitude for both years (2001 and 2007) and climatological mean, but during 2001, a phase shift by 2 months of the seasonal cycle was observed (Figure 5D).

3.3 Physical OMZ drivers

In this section, we analyze the physical drivers described by Pizarro-Koch et al. (2019) for the seasonal cycle of the OMZ in order to evaluate if they operate at interannual timescales and if they can explain the asymmetry of the response of the OMZ between the two La Niña events of 2001 and 2007. These include the poleward flow (i.e., Peru–Chile undercurrent) that represents the conduit by which the OMZ off Chile is connected to the tropical OMZ off Peru, the local wind forcing (meridional wind stress (MWS) and wind stress curl (WSC)), and the equatorial Kelvin forcing. In addition, the DO transport associated with mesoscale activity (i.e., the eddy fluxes and zonal jets) with the OMZ extent will also be evaluated.

3.3.1 Peru–Chile undercurrent

First, the $PCUC_{TR}$ and $PCUC_{DO}$ anomalies at different latitudes were assessed (see Figure 6). In general, for the entire period, a reduction in $PCUC_{TR}$ was associated with an increase in $PCUC_{DO}$ ($r = -0.6$, significant at 95% confidence level) with the larger changes in $PCUC_{TR}$ between 2004 and 2008 over the entire

10.3389/fmars.2023.1155932

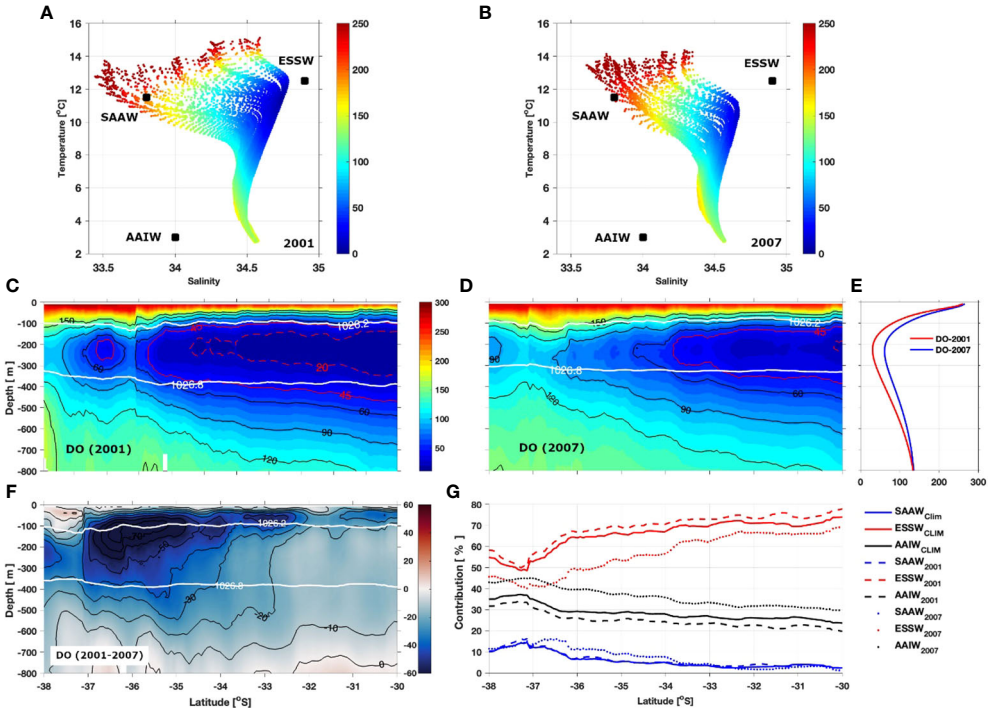

FIGURE 3
T-S-DO diagrams obtained from a meridional section during 2001 **(A)** and 2007 **(B)** for the coastal band (Only water encompassing the region within the first 80 km from the coast and from the surface to 1500 m depth in the whole domain were considered). Annual mean of the DO meridional section during 2001 **(C)** and 2007 **(D)**. The vertical mean of the DO sections **(E)** and the difference between both periods **(F)**. Background color in (μM) and the isopycnals of 1026.2 and 1026.8 kgm^{-3} are shown overlaid in white. Water masses percentage estimated between 1026.2 and 1026.8 kgm^{-3} isopycnals **(G)**. The water masses are Subantarctic Water, (SAAW; 11.5°C, 33.8), Equatorial Subsurface Water (ESSW; 12.5°C, 34.9) and Antarctic Intermediate Water (AAIW; 3°C, 34). The water mass and their thermohaline indices (T, S) indicated above were obtained from Silva et al., 2009 and were used here to compute the water mass proportions.

TABLE 2 Root mean square (RMS) of the seasonal and interannual variability of the DO concentration and the different terms of the DO budget in a fixed volume defined as the region with 9-year (2000–2008) mean DO ≤ 45 μM, as shown in Figure 1B.

DO Budget Terms	Seasonal RMS	Interannual RMS	Mean [2000–2008] Average	2001 %	2007 %
DO	3.2	5.1	32	−19	28
∂DO/∂t	5.40E−07	2.21E−07	−2.80E−08	−283	160
PHYS	1.02E−06	1.02E−06	1.78E−06	19	29
Xadv	1.60E−06	1.59E−06	−4.43E−06	22	−58
Yadv	6.00E−07	1.40E−06	3.85E−06	6	−41
Zadv	4.80E−07	9.20E−07	2.35E−06	46	−21
Hmix	7.40E−09	8.90E−09	−2.86E−08	18	−39
Vmix	1.01E−08	8.90E−09	4.76E−08	17	15
SMS	2.21E−07	9.53E−08	−1.45E−06	3	14
Photosynthetic production	1.95E−09	5.20E−10	6.86E−09	−4	2
Oxic decomposition	1.48E−07	1.18E−07	−7.32E−07	−6	42
Excretion	2.54E−08	7.73E−09	−1.02E−07	3	4
Nitrification	1.00E−07	8.48E−07	−6.60E−06	14	−17

The mean (2000–2008) and annual mean to 2001 and 2007 for DO and each term of the DO budget is also presented. Note that annual mean values for 2001 and 2007 are expressed as a percentage relative to 2000–2008 mean. The physical term (*PHYS*) is the summed-up contribution of all advection and mixing terms to the rate of change of DO (∂DO/∂t). The advection terms are the zonal (*Xadv*), meridional (*Yadv*), and vertical (*Zadv*) advections. The subgrid mixing terms are the summed-up contribution of the horizontal diffusion (*Hmix*) and vertical diffusivity (*Vmix*). The biogeochemical fluxes (*SMS*) represent the "source-minus-sink" contribution to the ∂DO/∂t due to biogeochemical processes. The *SMS* term is decomposed in photosynthetic production, oxic decomposition, excretion, and nitrification. The DO is in μM and DO budget terms are in μM s^{-1}.

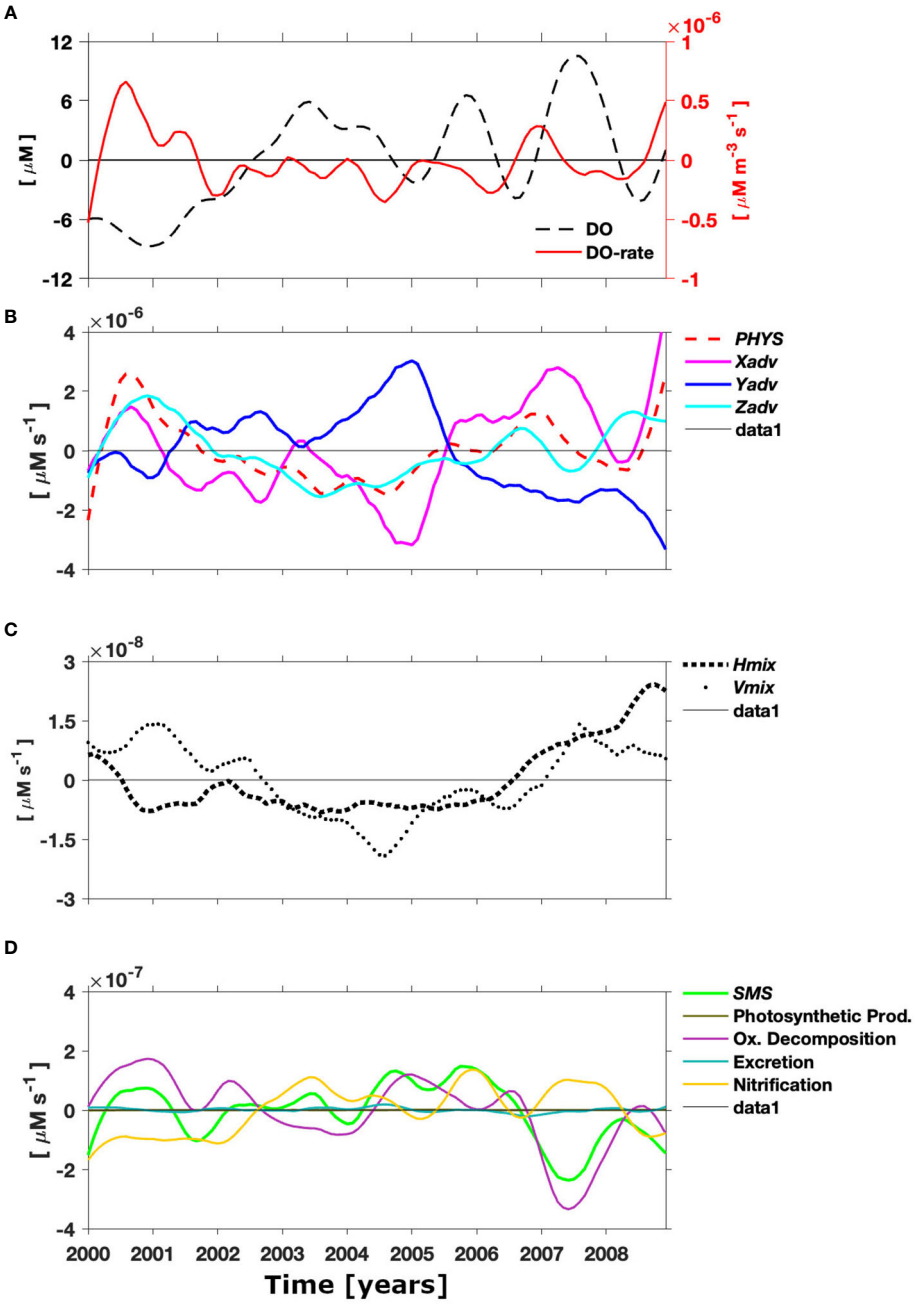

FIGURE 4
Interannual DO budget within the mean OMZ volume (see Figure 1B). Interannual anomalies of DO and DO rate of change ($\partial DO/\partial T$) **(A)**. The different terms of the right-hand side of Equation (1) are also shown **(B)** the physical term (*PHYS* red dashed line) is the summed-up contribution of advection and mixing. The advection term (*ADV*) is composed, in turn, by zonal (*Xadv*, magenta line), meridional (*Yadv*, blue line), and vertical (*Zadv*, cyan line) advections. The mixing terms are the summed-up contribution of the horizontal diffusion (*Hmix*; gray line) and vertical diffusivity (*Vmix*, dark green line) **(C)**. The biogeochemical fluxes (*SMS*, light green line) represent the "source-minus-sink" contribution to the DO rate of change due to biogeochemical processes; among them are photosynthetic production (dark-green line), oxic decomposition (dark-magenta line), excretion (skyline), and nitrification (yellow line) **(D)**.

region. In particular, a significant weakening (positive anomalies) of the $PCUC_{TR}$ was observed during 2007, consistent with the minimum OMZ_{VOL} and the increase in $PCUC_{DO}$. In contrast, a slight increase in the $PCUC_{TR}$ during 2001 was observed to be associated with a negative anomaly of $PCUC_{DO}$ (Figure 6). The Pearson's correlation between $PCUC_{TR}$ and OMZ_{VOL} was rather small with a maximum value for correlation of −0.4 (significant at 95% confidence level) reached at 3–4 months lags ($PCUC_{TR}$ ahead OMZ_{VOL}), while the magnitude of the correlation between $PCUC_{TR}$ and OMZ_{DO} peaked at 0.75 at 3–4 months lags (significant at the 95% confidence level), indicating that the $PCUC_{TR}$ variability plays a more important role over the OMZ_{DO} than over the whole OMZ_{VOL}. Note that using a threshold of DO< 20 μM for accounting for the OMZ core, the correlation between the

10.3389/fmars.2023.1155932

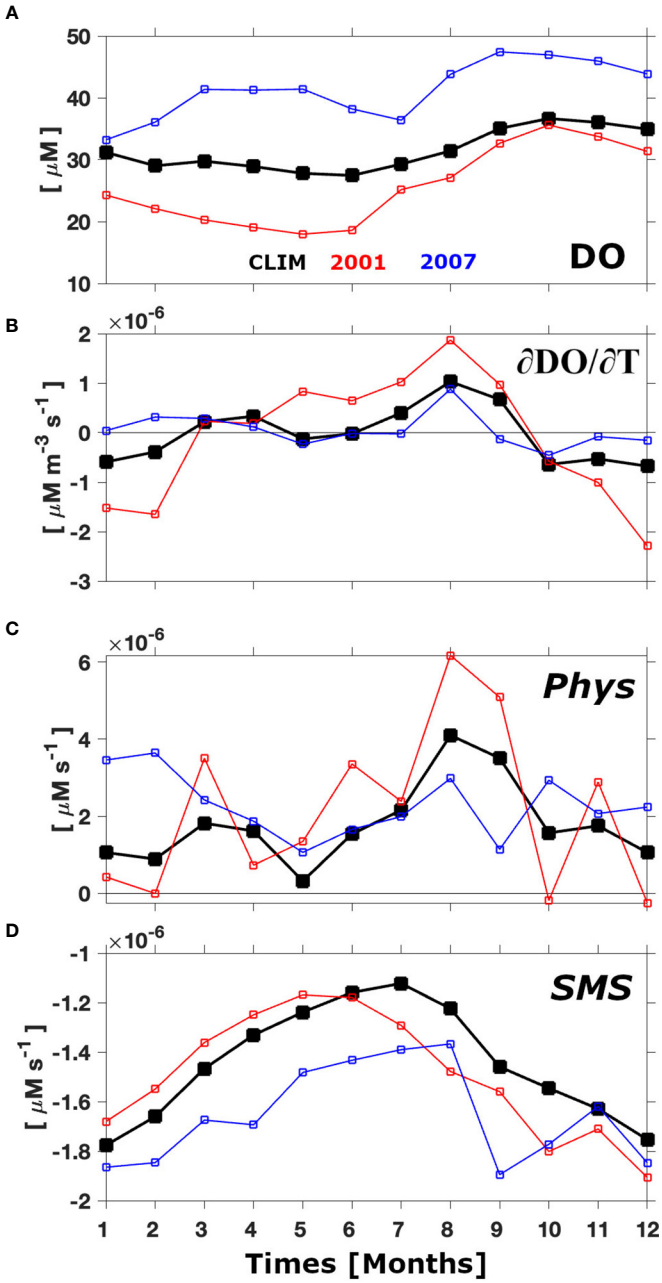

FIGURE 5
Seasonal cycle of OMZ_{DO} **(A)** and DO rate of change **(B)**; ($\partial DO/\partial T$) during 2001 (red line) and 2007 (blue line) CLIM correspond to the climatology seasonal cycle (in this case, the OMZ is considered as fixed volume defined as the region with 9-year (2000-2008) mean DO ≤ 45 μM; see Figure 1B). The seasonal DO Budget is represented by the summed-up contribution of *PHYS* **(C)** and *SMS* **(D)**. *PHYS* is the summed-up contribution of advection plus mixing, and *SMS* represents the "source-minus-sink" contribution to the $\partial DO/\partial T$ due to biogeochemical processes; among them are photosynthetic production, oxic decomposition, excretion, and nitrification.

OMZ_{VOL20} (OMZ_{DO20}) and the $PCUC_{TR}$ increases to r = −0.6 (r = 0.8) at zero-lag and becomes significant at the 95% confidence level. These results indicate that the PCUC modulates the OMZ mostly over the continental slope, where the PCUC and OMZ cores are located, but its fluctuations cannot explain the variability of the whole OMZ volume.

We now consider three metrics associated with local and remote forcings of the PCUC: the equatorial Kelvin wave (EKW) and the local wind forcing accounted for here by MWS and WSC. Using a multilinear regression analysis, we assess the relationship between the PCUC variability and these forcings in an alongshore-average (between 30° and 38°S) cross-shore section (see time series in Figure 7A). In the multilinear regression analysis, the $PCUC_{TR}$ is the predictand, whereas the local forcings (MWS and WSC) and remote forcing (EKW) are the predictor variables taken at zero lag. The results indicate that the $PCUC_{TR}$ variability is dominantly accounted for by MWS having the largest contribution of 40% (r^2 = 0.43), compared to 22% and 19% for EKW and WSC,

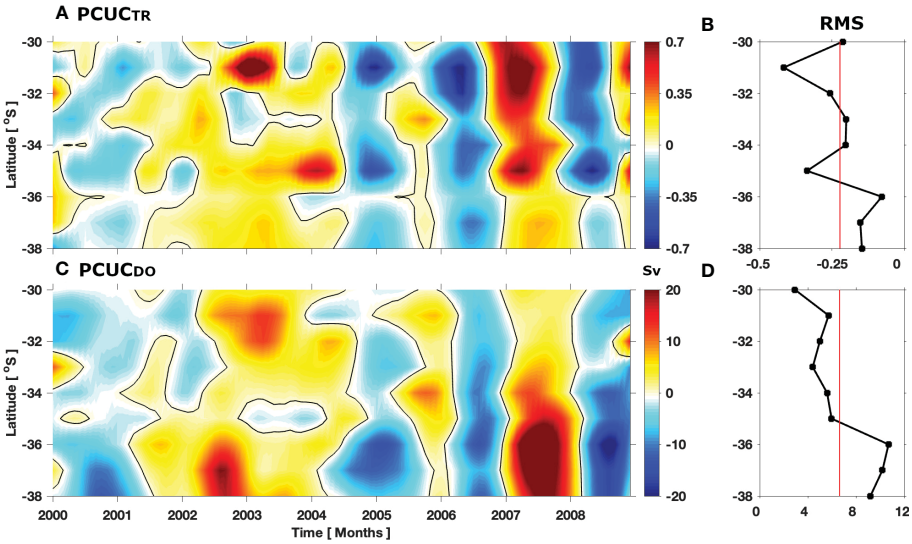

FIGURE 6
Interannual anomalies of the alongshore southward transport associated to the PCUC modeled (in Sv, 1 Sv = 10^6 m^3s^{-1}) **(A)** and mean DO inside the PCUC defined by the isopleth of −0.02 m s^{-1} in the first 100 km from the coast and between 80 and 800 m depth **(C)**. Positive anomalies in $PCUC_{TR}$ and $PCUC_{DO}$ indicate a weakening of the PCUC and ventilation, respectively. The root mean square (RMS) of the interannual variability of $PCUC_{TR}$ and $PCUC_{DO}$ is shown in panels **(B, D)**, respectively. Note that for panel **(A)**, positive (negative) values indicate weak (strong) southward transport.

respectively. This series can be interpreted as the coastal sea level (or pycnocline depth near the coast) variability, which for very low frequency (interannual periods) varies in phase along the coast of South America (e.g., Pizarro et al., 2001). These fluctuations then propagate offshore as a long Rossby wave. Then, when the coastal EKW series is decreasing after a maximum we can expect that the maximum has propagated offshore, generating an eastward pressure gradient force which is in geostrophic balance with a northward flow, that is with a weakening of the PCUC. This weakening of the PCUC after a maximum in the EKW series is consistent with that observed in Figure 7A. There, the current was weaker in 2007 (positive $PCUC_{TR}$ anomalies, black line) several months after the maximum of the EKW series (red line). The negative correlation between EKW and PCUCTR indicates that the PCUC is ahead of EKW, within about only 3-month. These results may be influenced for relatively high-frequency fluctuations when the interannual variability is weaker or the impact of atmospheric ENSO teleconnection over the $PCUC_{TR}$ over this period. During 2001 associated with a slightly strengthened $PCUC_{TR}$, the WSC showed a weak amplitude and MWS anomalies reached values around -0.01 N m^2 while these atmospheric forcings were twice larger during 2007. Contrary, the EKW showed smaller anomalies (upwelling) during 2007 than 2001 (Figure 7). In summary, the interannual variability of the $PCUC_{TR}$ results from both equatorial and local forcing and both can be modulated by the ENSO cycles. Longer simulations are required to clarify the $PCUC_{TR}$ dynamics at interannual time scales and how it is locally and remotely modulated. This case study focused on 2 peculiar events suggests that the $PCUC_{TR}$ dynamics at interannual time scales could also act as a driver of the low-frequency OMZ variability.

3.3.2 Eddy and advective oxygen fluxes

The meridional and zonal components of the DO fluxes in the oxygen minimum layer—averaged between the isopycnal surfaces 26.6 and 26.8 kg m^{-3}—are shown in Figure 8. The spatial structure

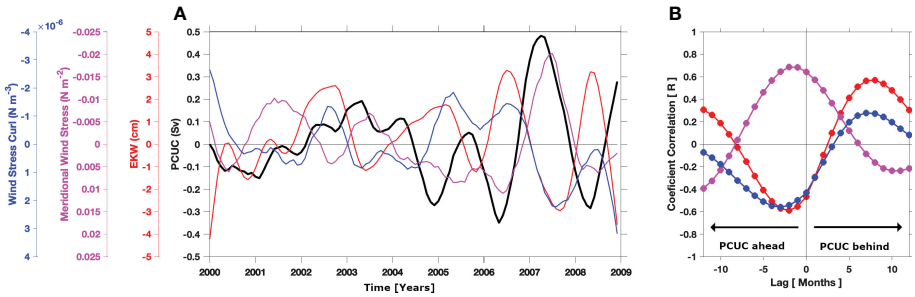

FIGURE 7
(A) Interannual anomalies of the alongshore mean PCUC transport modeled (black line; in Sv, 1 Sv = 10^6 m^3 s^{-1}). Additionally Equatorial Kelvin Wave at 90°W; −0.25°S (EKW in cm; red line), meridional wind stress (MWS in N m^{-2}; magenta line), and wind stress curl (WSC in N m^{-3}, blue line). **(B)** Lagged correlation between PCUC anomalies and EKW, MWS, and WSC, respectively. Note that lag is in months.

of the meridional component DO-eddy fluxes (hereafter, MEF) and DO-advective flux (hereafter, MAF) shows high spatial coherence with a predominant southward flux (negative) in a coastal band (Figures 8A–F). However, the MAFs represented approximately ~88% of alongshore DO fluxes with mean (maximum) value approximately 1 (4) m s^{-1} µM near the slope. Overall, during 2001, MEF and MAF showed a similar spatial pattern than that observed in mean conditions. Meanwhile, during 2007, MEF and MAF had a large bias respect to the annual mean, both in magnitude and direction. On the other hand, we observe that the zonal component of the DO-eddy fluxes (hereafter, ZEFs) was lower than the mean DO-advective fluxes (hereafter, ZAFs), but still with amplitudes of the same order of magnitude (Figures 8G–L). Over the whole study region, the spatial structure of ZEFs showed a predominant eastward (positive) flux being a ventilating mechanism for the OMZ (Figure 8G), while in ZAFs, meridionally confined bands of positive (onshore) and negative (offshore) flux can be observed. These bands may be related to the presence of meridionally alternating zonal jets or striations observed in the eastern South Pacific (cf., Belmadani et al., 2017). The location and intensity of these ZAF bands changed between 2001 and 2007, which was more pronounced and intense during 2007 (Figures 8J–L). Specifically, during 2001, when the OMZ_{VOL} was maximum, the spatial annual mean of the ZAFs decreased ~30% compared with the 9-year mean (2000–2008), whereas during 2007, when the OMZ_{VOL} was minimum, the ZAF values were slightly higher and positive (onshore flux) than climatological mean.

The OMZ oceanic boundary was evaluated through a meridional section with a center at 74°W, spanning a depth range of 50–500 m, for the annual means of 2001 and 2007. The cross-shore component of both ZEF and ZAFs were analyzed (see Figure 9) integrated between 50–500 m depth and its vertical mean section. It is worth mentioning that ZAFs and ZEFs were of the same order of magnitude during both years (2001 and 2007), but the spatial patterns of the DO fluxes were different (Figures 9A, B). Overall, ZAFs showed marked positive (onshore) and negative (offshore) bands along the section with maximum values approximately ~5 m s^{-1} µM between 50 and 150m depth and negative net fluxes upper ~300m. Meanwhile, ZEF is mainly positive between 50 to 500 m depth, indicating the ventilation role over the oceanic OMZ_{VOL}. In this sense, the large positive advective transport of DO (ZAFs) locate between 35.5°S and 37.5°S could be contributing to the ventilation of the southern part of the OMZ and to the associated reduction of the OMZ_{VOL} observed during 2007 (Figures 2C, 3B). In contrast, during 2001, the mean ZEF was reduced (Figure 9B) mainly between 200 and 500m depth, showing that changes in the ZEF are consistent with the reduction (increase) in the whole OMZ volume.

In summary, during 2007, the PCUC transport decreased significantly, leading to a reduced southward oxygen-poor water, which also involves weak MEFs. Simultaneously, the zonal currents (ZAFs) and mesoscale turbulence DO fluxes (ZEFs) increased eastward (to the coast) transporting oceanic oxygen-rich water to the OMZ. These anomalies of the eddy fluxes seem to be responsible for the rapid reduction in OMZ_{VOL} and the increasing OMZ_{DO}

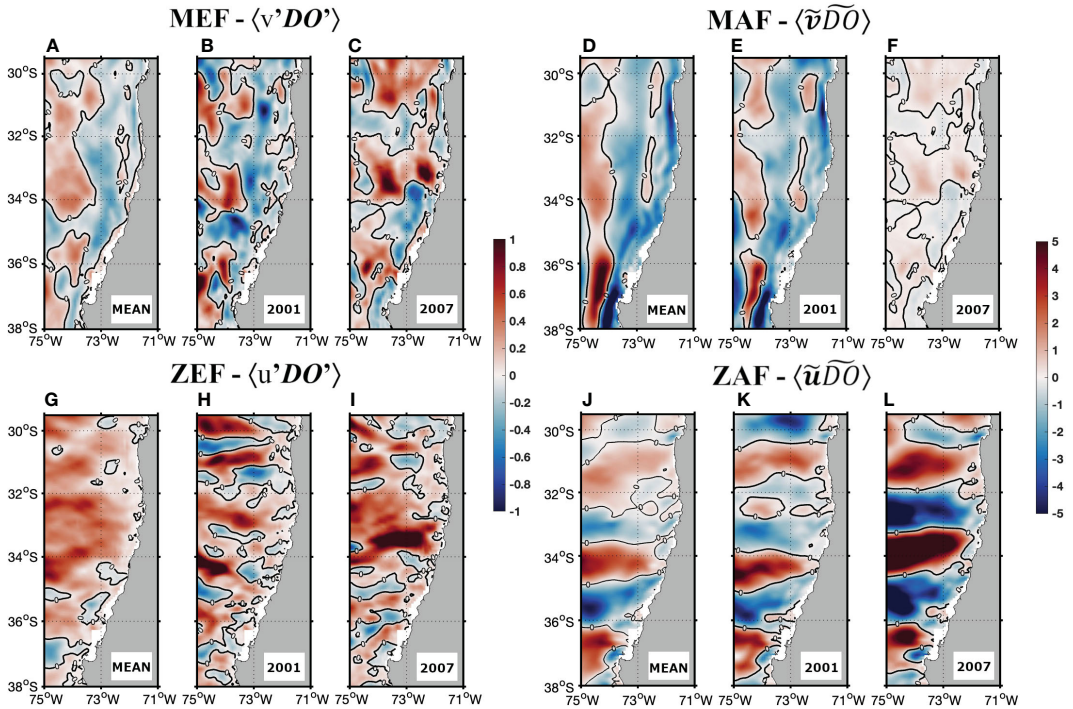

FIGURE 8
Climatological and annual mean DO Fluxes in 2001 and 2007 integrated between the 26.4 and 26.8 kg m^{-3} Isopycnals. The meridional (zonal) eddy fluxes are depicted in panels **(A–C, G–I)**, while the meridional (zonal) advective fluxes are depicted in panels **(D–F, J–L)**. The magnitude of fluxes is represented by the background color (in m s^{-1} µM). Note that positive (negative) values indicate east (west) and north (south) direction.

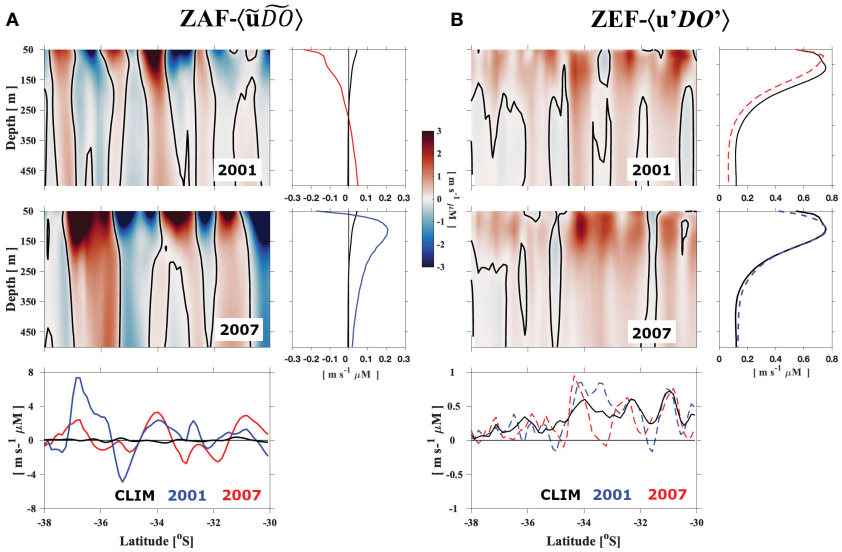

FIGURE 9
Annual mean of the zonal DO transport along meridional section at 74°W between 30° and 38°S during 2001 and 2007 periods represented separately by the sum between the mean zonal advective fluxes (ZAF; **A)** and the zonal mesoscale eddy fluxes (ZEF; **B)**. The shading color represented eastward (red) and westward (blue) flux (in m s^{-1} μM). The inset at the right and bottom of each main panel shows the vertical mean section and integrated between 50–500m depth, respectively. Note that the black line represent the climatological mean, respectively.

observed during 2007. In contrast, during 2001, while the $PCUC_{TR}$ and MEFs had values close to their climatological mean, the ZEFs that contribute to ventilating the OMZ were abnormally smaller than its mean value; meanwhile, the ZAFs were slightly negative, indicating a large westward (offshore) DO transport.

4 Discussion and concluding remarks

In this work, we have focused on understanding the opposite response of OMZ metrics [i.e., OMZ volume (OMZ_{VOL}) and intensity (OMZ_{DO})] during two cold events in the tropical Pacific in a high-resolution coupled physical/biogeochemical model simulation. These two metrics are shown to be moderately anti-correlated between them, i.e., lower values of OMZ_{DO} are not necessarily related to larger values of OMZ_{VOL} and vice versa, suggesting a combination of processes controlling the DO budget and its internal re-distribution within DO 45 μM isopleth. Our motivation was also to evaluate if processes controlling OMZ variability at seasonal timescales (Pizarro-Koch et al., 2019) can also operate at interannual timescales, observing furthermore that the OMZ variability over the period of interest (2000–2008) was as large as that of the seasonal cycle despite the relatively low ENSO variance (i.e., absence of extreme events). The analysis reveals that a distinct feature of the two cold events is that the first one (2001) marks the late stage of evolution of La Niña, while the latter marks the onset of a cold event in 2007. In particular, the 2001 La Niña belongs to a prolonged cool period (~3 years) that followed the strong 1997/1998 EP El Niño, so that the OMZ has been anomalously replenished with deoxygenated waters during 1999 and 2000. On the other hand, the 2007 La Niña followed the weak 2006 mixed-type El Niño, implying that the OMZ is close to its climatological state when the 2007 La Niña event starts to develop. Our results indicate that this opposite response can be understood in terms of the interplay of both local and remote oceanic processes including the southward transport of oxygen-poor waters (mainly ESSW) through the PCUC and the subsurface mesoscale circulation.

In 2007, the abnormal southerly position of the South Pacific Subtropical High resulted in increased equatorward alongshore winds off central Chile, intensifying the coastal upwelling and cooling of the entire shelf water column (Schneider et al., 2017). As a consequence, the PCUC experienced a substantial reduction in the presence of large positive anomalies of MWS and an intense negative WSC, which were in phase with the passage of a downwelling intraseasonal EKW, a remote forcing mechanism. This anomalous weakening of the PCUC led to an increase in the DO content inside the OMZ, a marked decline of the OMZ_{VOL}, and changes over the ESSW distribution in the study region. Concurrently, an increase in the DO fluxes was observed in the cross-shore direction across the oceanic boundary of the OMZ, primarily attributable to the intensification of the meridional alternating zonal jets in the eastward direction (DO advection) and, secondarily, to the eddy fluxes. In contrast, during 2001, a positive anomaly of the OMZ_{VOL} was observed; however, it was not directly related to an increase in the $PCUC_{TR}$. In general, the poleward transport exhibited a minimum (negative) anomaly during the year 2000, while during 2001, it approached the 9-year (2000–2008) mean state. In terms of local forcings, the MWS and

WSC were small, while the remote forcing (EKW) exhibited a weaker amplitude compared to that in 2007 and out-of-phase with the $PCUC_{TR}$. In addition, the cross-shore DO advection was associated with large negative fluxes transporting oxygen-poor waters westward (offshore) together with an expanding OMZ_{VOL}. Furthermore, the zonal DO eddy fluxes, which permanently contribute to ventilate the OMZ, were abnormally low.

Accordingly, the present study suggests the interannual variability of the PCUC primarily modulates the DO contents (intensity) of the OMZ core and secondarily the whole OMZ_{VOL}. Thus, indirectly, the PCUC through its instabilities plays a key role promoting the generation of subsurface mesoscale eddies (Colas et al., 2012; Thomsen et al., 2016; Frenger et al., 2018; Contreras et al., 2019), impacting the cross-shore DO transport represented by the zonal jets and the eddy fluxes, which are important in ventilating and shaping the offshore extent of the OMZ_{VOL} (Pizarro-Koch et al., 2019). In addition, the role of the subsurface mesoscale circulation is important to explain the large interannual OMZ variations found in this study, even when the mesoscale circulation off Central Chile is not linearly modulated by ENSO (Conejero et al., 2020). Therefore, the interplay between the PCUC dynamics and the mesoscale activity may significantly contribute to modulate the interannual intrinsic variability of the OMZ off central Chile regardless to ENSO dynamics.

Although the impacts of ENSO on ocean temperature and productivity have been investigated extensively in previous studies (Barber and Chavez, 1983; Philander, 1983; Escribano et al., 2004; McPhaden, 2012), their effects on the OMZ have only recently received more attention, as demonstrated by a limited number of studies comprising both observational (Morales et al., 1999; Escribano et al., 2004) and modeling approaches (Llanillo et al., 2013; Mogollón and Calil, 2017; Espinoza-Morriberón et al., 2019). Despite this, previous studies related to OMZ-ENSO have focused on strong EP events near to the Peruvian coast (Graco et al., 2017; Mogollón and Calil, 2017; Espinoza-Morriberón et al., 2019) with a main focus on biogeochemical processes and nutrient cycling and the general response of the OMZ characteristics to strong ENSO events. Therefore, this study is the first to characterize changes in the physical mechanisms controlling the spatiotemporal variability of the southern tip eastern Pacific OMZ during two moderate cold La Niña events. In this sense, our results have implications for understanding the natural variability of the OMZ off Chile, highlighting the importance of the PCUC not only for the southward transport (advect) of deoxygenated waters from the Peru upwelling system but also in the ability to modulate the eddy subsurface activity along the coast through baroclinic instabilities, inducing DO eddy fluxes. Both processes are influenced by the tropical variability, but having a stochastic component considering the PCUC dynamics is partly controlled by local winds.

The weak ENSO amplitude over 2000–2008 can be understood in terms of the sole occurrence of CP El Niño and La Niña, or mixed-type events (2006) that have a much weaker amplitude than extreme EP El Niño events of 1982–1983 and 1997–1998. The CP events are associated with a weaker oceanic teleconnection than the strong EP El Niño (Dewitte et al., 2012) but can modulate significantly the upwelling favorable winds off Chile south of 30°S through atmospheric teleconnection during the development of ENSO (Cai et al., 2020; Dewitte et al., 2023). This explains the overall large correlation between the C index and the OMZ metrics and the direction of the phase-lagged relationship (C index ahead OMZ metrics) (see Table 3). It is worth mentioning that for this period the PCUC transport was also highly correlated with the E index near lag zero (not shown), suggesting that the equatorial oceanic teleconnection is also operating despite the relatively weak amplitude of the E index. This can be understood in terms of the efficient propagation of intraseasonal Kelvin waves along the coast (Clarke and Shi, 1991).

Our results have implications for understanding the natural variability of the OMZ off Chile, and we now discuss perspectives of this work. First, we note the key role of the PCUC dynamics for understanding the OMZ interannual variability off Central Chile even during a period of low ENSO variance. While this is alike to what takes place at seasonal timescale (Pizarro-Koch et al., 2019), it also suggests that the details in the oceanic and atmospheric teleconnections during weak to moderate ENSO events certainly matters to drive the OMZ variability. In particular, the PCUC cannot only transport (advect) deoxygenated waters from the Peru upwelling systems, but it has also the ability to modulate eddy activity along the coast through baroclinic instabilities, inducing DO eddy flux. Both processes are influenced by tropical variability, but they also have a stochastic component considering that the PCUC dynamics is partly controlled by local winds, implying the natural variability in the OMZ core evidenced here. While our analysis supports such a hypothesis for the source of OMZ natural variability, the relatively short span of the simulation used here is certainly a limitation to reach a firm conclusion in this respect. As a perspective, we thus plan to run the model for repeated periods of low ENSO variance to further document the non-linear relationship between the OMZ volume and La Niña events suggested here. Documenting the physical forcing of the

TABLE 3 Maximum lag correlation between the ENSO indexes and both OMZ_{VOL} and OMZ_{DO}.

	ENSO Indices		
	ONI	C	E
OMZ_{VOL} (≤ 45 μM)[a]	−0.58 (8)	−0.59 (9)	0.44 (0)
OMZ_{VOL} (≤ 20 μM)[b]	−0.62 (7)	−0.56 (6)	0.52 (0)
OMZ_{DO} [a]	0.57 (7)	0.52 (6)	−0.47 (−1)
OMZ_{DO} [b]	0.57 (6)	0.50 (5)	−0.51 (−2)

The whole OMZ volume is represented by the DO threshold of ≤ 45 mM, while the OMZ core is represented by 20 ≤ μM. Parenthesis represent time lags in months. Note that negative (positive) lag indicates that the OMZ property is ahead (behind) the ENSO indices. ENSO indexes are represented by the ONI (Oceanic Niño Index), CP (Central Pacific El Niño index), and EP (Eastern Pacific El Niño).
Superscript "a" denotes the complete volume of the oxygen minimum zone (OMZ) that is encompassed by the dissolved oxygen (DO) threshold of ≤ 45 μM. Superscript "b" represents the OMZ core volume represented by the DO threshold of ≤20 μM.

subtropical OMZ off Chile during low-amplitude ENSO forcing has thus relevance for extending our view of the diversity in mechanisms at work in OMZ.

Data availability statement

ROMS model code is available at https://www.croco-ocean.org/. Raw model data are available upon request through BD and processed data files presented in this paper are available upon request through the corresponding author. The University of Concepcion and the "Fondo de Investigación Pesquera" (FIP; MOBIO-BIO program) provided in situ data. MODIS-Aqua SST and chlorophyll satellite data are available at http://oceancolor.gsfc.nasa.gov; AVISO for altimeter products (http://marine.copernicus.eu); CARS for climatological data (www.marine.csiro.au/~dunn/cars2009/). Data used for model validation are freely available under request to the Chilean National Center for Hydrographic and Oceanographic Data (Centro Nacional de Datos Hidrográficos y Oceanográficos de Chile; http://www. shoa.cl/n_cendhoc/).

Author contributions

Conceptualization: MP-K, BD and OP. Modelling setup: VG, BD, IM and AP. Data and statistical analysis: MP-K, BD, OP, HS, AC-A, CA and MR. Manuscript writing, MP-K. with input from all co-authors. All authors contributed to the article and approved the submitted version.

Funding

This work was funded by the Chilean Agency for Research and Development (FONDECYT Postdoctoral Project No. 3220768. This study was carried out under FONDECYT projects 1181872 led by OP. This study received support from FONDECYT 1190276 (led by BD), FONDECYT 1140845 (led by MR) and FONDECYT 11171163 (led by CA), Millennium Nucleus Understanding Past Coastal Upwelling Systems and Environmental Local and Lasting Impacts (UPWELL), Coquimbo, Chile, Anillo BiodUCCT ATE220044, Millennium Institute of Oceanography, Chile (ICM grant IC 120019), COPAS Coastal (FB210021), ANID (Anillo Eclipse ACT210071 and Concurso de Fortalecimiento al Desarrollo Científico de Centros Regionales 2020-R20F0008), and CRN3070-IAI (US National Science Foundation; grant GEO-11280040). MP-K thanks the financial support for internships at LEGOS and IGP from the REDOC.CTA (Red Doctoral en Ciencia, Tecnología y Ambiente, University of Concepción, Chile) and CONICYT, respectively. BD acknowledges support from the French National program LEFE (Les Enveloppes Fluides et l'Environnement), the CE2COAST project, and the EU H2020 FutureMares project (Theme LC-CLA-06-2019, Grant Agreement No. 869300). This work was granted access to the HPC resources of CALMIP supercomputing center at the Toulouse University under the allocations 2019-1044.

Conflict of interest

The authors declare that the research was conducted in the absence of any commercial or financial relationships that could be construed as a potential conflict of interest.

Publisher's note

References

Albert, A., Echevin, V., Lévy, M., and Aumont, O. (2010). Impact of nearshore wind stress curl on coastal circulation and primary productivity in the Peru upwelling system. *J. Geophys. Res.* 115 (C12). doi: 10.1029/2010jc006569

Astudillo, O., Dewitte, B., Mallet, M., Frappart, F., Rutllant, J. A., Ramos, M., et al. (2017). Surface winds offPeru-Chile: observing closer to the coast from radar altimetry. *Remote Sens. Environ.* 191, 179–196. doi: 10.1016/j.rse.2017.01.010

Barber, R. T., and Chavez, F. P. (1983). Biological consequences of El ni~no. *Science* 222 (4629), 1203–1210. doi: 10.1126/science.222.4629.1203

Belmadani, A., Concha, E., Donoso, D., Chaigneau, A., Colas, F., Maximenko, N. A., et al. (2017). Striations and preferred eddy tracks triggered by topographic steering of the background flow in the eastern south pacific. *J. Geophys. Res.-Oceans* 122, 2847–2870. doi: 10.1002/2016JC012348

Bettencourt, J. H., López, C., Hernández-García, E., Montes, I., Sudre, J., Dewitte, B., et al. (2015). Boundaries of the Peruvian oxygen minimum zone shaped by coherent mesoscale dynamics. *Nat. Geosci.* 8, 937–940. doi: 10.1038/ngeo2570

Bindoff, N. L., Cheung, W. W. L., Kairo, J. G., Arístegui, J., Guinder, V. A., Hallberg, R., et al. (2019). "Changing ocean, marine ecosystems, and dependent communities," in *IPCC special report on the ocean and cryosphere in a changing climate*. Eds. H.-O. Pörtner, D.C. Roberts, V. Masson-Delmotte, P. Zhai, M. Tignor, E. Poloczanska, et al (Cambridge, UK and New York, NY, USA,: Cambridge University Press). pp. 447–587. doi: 10.1017/9781009157964.007

Bopp, L., Resplandy, L., Orr, J. C., Doney, S. C., Dunne, J. P., Gehlen, M., et al. (2013). Multiple stressors of ocean ecosystems in the 21st century: projections with CMIP5 models. *Biogeosciences* 10, 6225–6245. doi: 10.5194/bg-10-6225-2013

Breitburg, D., Levin, L. A., Oschlies, A., Grégoire, M., Chavez, F. P., Conley, D. J., et al. (2018). Declining oxygen in the global ocean and coastal waters. *Science* 359 (6371), eaam 7240. doi: 10.1126/science.aam7240

Cabré, A., Marinov, I., Bernardello, R., and Bianchi, D. (2015). Oxygen minimum zones in the tropical pacific across CMIP5 models: mean state differences and climate change trends. *Biogeosciences* 12, 5429–5454. doi: 10.5194/bg-12-5429-2015

Cai, W., McPhaden, M. J., Grimm, A. M., Rodrigues, R., Taschetto, A. S., Garreaud, R., et al. (2020). Climate impacts of the El niño–southern oscillation on south America. *Nat. Rev. Earth Environ.* 1, 215–231. doi: 10.1038/s43017-020-0040-3

Cambon, G., Goubanova, K., Marchesiello, P., Dewitte, B., Illig, S., and Echevin, V. (2013). Assessing the impact of downscaled winds on a regional ocean model simulation of the Humboldt system. *Ocean Model.* 65, 11–24. doi: 10.1016/j.ocemod.2013.01.007

Clarke, A. J., and Shi, C. (1991). Critical frequencies at ocean boundaries. *J. Geophys. Res.* 96 (C6), 10731–10738. doi: 10.1029/91JC00933

Colas, F., McWilliams, J. C., Capet, X., and Kurian, J. (2012). Heat balance and eddies in the Peru-Chile current system. *Climate Dyn.* 39, 509–529. doi: 10.1007/s00382-011-1170-6

Conejero, C., Dewitte, B., Garçon, V., Sudre, J., and Montes, I.. (2020). ENSO diversity driving low-frequency change in mesoscale activity off Peru and Chile. *Sci. Rep.* 10 (1), 1–13. doi: 10.1038/s41598-020-74762-x

Contreras, M., Pizarro, O., Dewitte, B., Sepulveda, H. H., and Renault, L. (2019). Subsurface mesoscale eddy generation in the ocean off central Chile. *J. Geophys. Res. Oceans* 124 (8), 5700–5722. doi: 10.1029/2018JC014723

Dewitte, W., Chiappetta, A., Azmi, A., Witters, E., Strnad, M., Rembur, J., et al. (1999). Dynamics of cytokinins in apical shoot meristems of a day-neutral tobacco during floral transition and flower formation. *Plant Physiol.* 119 (1), 111–122. doi: 10.1104/pp.119.1.111

Dewitte, B., Concha, E., Saavedra, D., Pizarro, O., Martinez- Villalobos, C., Gushchina, D., et al. (2023). The ENSO-induced south pacific meridional mode. *Front. Climate* 4, 1080978. doi: 10.3389/fclim.2022.1080978

Dewitte, B., Vazquez-Cuervo, J., Goubanova, K., Illig, S., Takahashi, K., Cambon, G., et al. (2012). Change in El niño flavours over 1958– 2008: implications for the long-term trend of the upwelling off Peru. *Deep Sea Res. Part II: Topical Stud. Oceanogr.* 77-80, 143–156. doi: 10.1016/j.dsr2.2012.04.011

Dunn, J. R., and Ridgway, K. R. (2002). Mapping ocean properties in regions of complex topography. *Deep Sea Res. I Oceanogr. Res.* 49 (3), 591–604. doi: 10.1016/S0967-0637(01)00069-3

Duteil, O. (2019). Wind synoptic activity increases oxygen levels in the tropical pacific ocean. *Open Access Geophys. Res. Lett.* 46, (5). doi: 10.1029/2018GL081041

Duteil, O., Oschlies, A., and Böning, C. W. (2018). Pacific decadal oscillation and recent oxygen decline in the eastern tropical pacific ocean. *Open Access Biogeosci. (BG)* 15, 7111–7126. doi: 10.5194/bg-15-7111-2018

Escribano, R., Daneri, G., Farías, L., Gallardo, V. A., González, H. E., Gutiérrez, D., et al. (2004). Biological and chemical consequences of the 1997–1998 El niño in the Chilean coastal upwelling system: a synthesis. *Deep Sea Res. Part II: Topical Stud. Oceanogr.* 51 (20-21), 2389–2411. doi: 10.1016/j.dsr2.2004.08.011

Escribano, R., Hidalgo, P., Fuentes, M., and Donoso, K. (2012). Zooplankton time series in the coastal zone off Chile: variation in upwelling and responses of the copepod community. *Prog. Oceanogr.* 97-100, 174–186. doi: 10.1016/j.pocean.2011.11.006

Espinoza-Morriberón, D., Echevin, V., Colas, F., Tam, J., Gutierrez, D., Graco, M., et al. (2019). Oxygen variability during ENSO in the tropical south Eastern pacific. *Front. Mar. Sci.* 5, 1638. doi: 10.3389/fmars.2018.00526

Fairall, C. W., Bradley, E. F., Hare, J. E., Grachev, A. A., and Edson, J. B.. (2003). "Bulk parameterization of air–sea fluxes: updates and verification for the COARE algorithm.". *J. Climate* 16 (4), 571–591. doi: 10.1175/1520-0442(2003)016<0571:BPOASF>2.0.CO;2

Frenger, I., Bianchi, D., Sührenberg, C., Oschlies, A., Dunne, J., Deutsch, C., et al. (2018). Biogeochemical role of subsurface coherent eddies in the ocean: tracer cannonballs, hypoxic storms, and microbial stewpots. *Global Biogeochem. Cycles* 32, 226–249. doi: 10.1002/2017GB005743

Frischknecht, M., Münnich, M., and Gruber, N. (2015). Remote versus local influence of enso on the california current system. *J. Geophys. Res.: Oceans* 120 (2), 1353–1374. doi: 10.1002/2014JC010531

Fuenzalida, R., Schneider, W., Garces, J., Bravo, L., and Lange, C. (2009). Vertical and horizontal extension of the oxygen minimum zone in the eastern south pacific ocean. *Deep Sea Res. Part II: Topical Stud. Oceanogr.* 56, 992–1003. doi: 10.1016/j.dsr2.2008.11.001

Frölisher, T., Joos, F., Plattner, G.-K., Steinacher, M., and Doney, S. C. (2009). Natural variability and anthropogenic trends in oceanic oxygen in a coupled carbon cycle-climate model ensemble. *Global Biogeochem. Cy.* 23, GB1003. doi: 10.1029/2008GB003316

García-Reyes, M., Sydeman, W. J., Schoeman, D. S., Rykaczewski, R. R., Black, B. A., Smit, A. J., et al. (2015). Under pressure: climate change, upwelling, and eastern boundary upwelling ecosystems. *Front. Mar. Sci.* 2, 109. doi: 10.3389/fmars.2015.00109

Garçon, V., Dewitte, B., Montes, I., and Goubanova, K. (2019). "Land-Sea-Atmosphere interactions exacerbating ocean deoxygenation in Eastern boundary upwelling systems (EBUS)," in *Ocean deoxygenation: everyone's problem- causes, impacts, consequences and solutions, gland*, vol. 562 . Eds. D. Laffoley and J. M. Baxter (Switzerland: IUCN), 155–170.

Gilbert, D., Rabalais, N. N., Díaz, R. J., and Zhang, J. (2010). Evidence for greater oxygen decline rates in the coastal ocean than in the open ocean. *Biogeosciences* 7, 2283–2296. doi: 10.5194/bg-7-2283-2010

Goubanova, K., Echevin, V., Dewitte, B., Codron, F., Takahashi, K., Terray, P., et al. (2011). Statistical downscaling of sea-surface wind over the Peru–Chile upwelling region: diagnosing the impact of climate change from the IPSL-CM4 model. *Climate Dyn.* 36 (7–8), 1365–1378. doi: 10.1007/s00382-010-0824-0

Graco, M., Purca, S., Dewitte, B., Castro, C. G., Moron, O., Ledesma, J., et al. (2017). The OMZ and nutrients features as a signature of interannual and low frequency variability off the Peruvian upwelling system. *Biogeosciences* 14, 4601–4617. doi: 10.5194/bg-14-4601-2017

Grégoire, M., Garçon, V., Garcia, H., Breitburg, D., Isensee, K., Oschlies, A., et al. (2021). A global ocean oxygen database and atlas for assessing and predicting deoxygenation and ocean health in the open and coastal ocean. *Front. Mar. Sci.* 8. doi: 10.3389/fmars.2021.724913

Gruber, N. (2011). Warming up, turning sour, losing breath: ocean biogeochemistry under global change. *Philos. Trans. R. Soc. A: Mathematical Phys. Eng. Sci.* 369 (1943), 1980–1996. doi: 10.1098/rsta.2011.0003

Gutiérrez, D., Enríquez, E., Purca, S., Quipúzcoa, L., Marquina, R., Flores, G., et al. (2008). Oxygenation episodes on the continental shelf of central Peru: remote forcing and benthic ecosystem response. *Prog. Oceanogr.* 79, 177–189. doi: 10.1016/j.pocean.2008.10.025

Gutknecht, E., Dadou, I., Le Vu, B., Cambon, G., Sudre, J., Garçon, V., et al. (2013). Coupled physical/biogeochemical modeling including O2-dependent processes in Eastern boundary upwelling systems: application in the benguela. *Biogeosciences* 10 (1), 1–22. doi: 10.5194/bg-10-1-2013

Hormazábal, S., Shaffer, G., Silva, N., and Navarro, E. (2006). The perú-Chile undercurrent and the oxygen minimum zone variability off central Chile. *Gayana* 70 (1), 37–45. doi: 10.4067/S0717-65382006000300009

Huyer, A., Smith, R. L., and Paluszkiewicz, T. (1987). Coastal upwelling off Peru during normal and El niño times 1981–1984. *J. Geophys. Res.: Oceans* 92 (C13), 14297–14307. doi: 10.1029/JC092iC13p14297

Ito, T., Minobe, S., Long, M. C., and Deutsch, C. (2017). Upper ocean O2 trends: 1958–2015. *Geophys. Res. Lett.* 44 (9), 4214–4223. doi: 10.1002/2017GL073613

José, Y. S., Stramma, L., Schmidtko, S., and Oschlies, A. (2019). ENSO-driven fluctuations in oxygen supply and vertical extent of oxygen-poor waters in the oxygen minimum zone of the Eastern tropical south pacific. *Biogeosci. Discussions*. [preprint], 1–20. doi: 10.5194/bg-2019-155

Karstensen, J., Stramma, L., and Visbeck, M. (2008). Oxygen minimum zones in the eastern tropical atlantic and pacific oceans. *Prog. Oceanography* 77, 331–350. doi: 10.1016/j.pocean.2007.05.009

Keeling, R. F., Körtzinger, A., and Gruber, N. (2010). Ocean deoxygenation in a warming world. *Annu. Rev. Mar. Sci.* 2, 199–229. doi: 10.1146/annurev.marine.010908.163855

Koné, V., Machu, E., Penven, P., Garçon, V., Freon, P., and Demarcq, H. (2005). Modeling the primary and secondary productions of the southern benguela upwelling system: a comparative study through two biogeochemical models. *Global Biogeochem. Cycles* 19, GB4021. doi: 10.1029/2004GB002427

Kwiatkowski, L., Torres, O., Bopp, L., Aumont, O., Chamberlain, M., Christian, J. R., et al. (2020). Twenty-first century ocean warming, acidification, deoxygenation, and upper-ocean nutrient and primary production decline from CMIP6 model projections. *Biogeosciences* 17 (13), 3439–3470. doi: 10.5194/bg-17-3439-2020

Large, W., McWilliams, J. C., and Doney, S. (1994). Oceanic vertical mixing: a review and model with a nonlocal boundary layer parame- terization. *Rev. Geophys.* 32, 363–403. doi: 10.1029/94RG01872

Llanillo, P. J., Karstensen, J., Pelegrí, J. L., and Stramma, L. (2013). Physical and biogeochemical forcing of oxygen and nitrate changes during El Niño/El viejo and la Niña/La vieja upper-ocean phases in the tropical eastern south pacific along 86° W. *Biogeosciences* 10, 6339–6355. doi: 10.5194/bg-10-6339-2013

Long, M. C., Deutsch, C., and Ito, T. (2016). Finding forced trends in oceanic oxygen. *Global Biogeochem. Cycles* 30 (2), 381–397. doi: 10.1002/2015GB005310

McPhaden, M. J. (2012). A 21st century shift in the relationship between ENSO SST and warm water volume anomalies. *Geophys. Res. Lett.* 39 (9). doi: 10.1029/2012GL051826

Mogollón, R., and Calil, P. H. R. (2017). On the effects of ENSO on ocean biogeochemistry in the northern Humboldt current system (NHCS): a modeling study. *J. Mar. Syst.* 172, 137–159. doi: 10.1016/j.jmarsys.2017.03.011

Montes, I., Dewitte, B., Gutknecht, E., Paulmier, A., Dadou, I., Oschlies, A., et al. (2014). High-resolution modeling of the Eastern tropical pacific oxygen minimum zone: sensitivity to the tropical oceanic circulation. *J. Geophys. Res. Oceans* 119, 5515–5532. doi: 10.1002/2014JC009858

Morales, C. E., Hormazábal, S., and Blanco, J. L. (1999). Interannual variability in the mesoscale distribution of the depth of the upper boundary of the oxygen minimum layer off northern Chile (18–24S): implications for the pelagic system and biogeochemical cycling. *J. Mar. Res.* 57, 909–932. doi: 10.1357/002224099321514097

Naqvi, S. W. A., Bange, H. W., Farias, L., Monteiro, P. M. S., Scraton, M. I., and Zhang, J. (2010). Marine hypoxia/anoxia as a source of CH4 and N2O. *Biogeosciences* 7, 2159–2190. doi: 10.5194/bg-7-2159-2010

Oschlies, A., Brandt, P., Stramma, L., and Schmidtko, S. (2018). Drivers and mechanisms of ocean deoxygenation. *Nat. Geosci.* 11 (7), 467–473. doi: 10.1038/s41561-018-0152-2

Paulmier, A., and Ruiz-Pino, D. (2009). Oxygen minimum zones (OMZs) in the modern ocean. *Prog. Oceanogr.* 80 (3–4), 113–128. doi: 10.1029/j.pocean.2008.08.001

Paulmier, A., Ruiz-Pino, D., Garçon, V., and Farias, L. (2006). Maintaining ofthe east south pacific oxygen minimum Zone(OMZ) off chile. *Geophys.l Res. Lett.* 33, L20601. doi: 10.1029/2006GL026801

Penven, P., Debreu, L., Marchesiello, P., and McWilliams, J. C. (2006). Evaluation and application of the ROMS 1-way embedding procedure to the central california upwelling system. *Ocean Model.* 12 (1-2), 157–187. doi: 10.1016/j.ocemod.2005.05.002

Philander, S. G. H. (1983). El Nino southern oscillation phenomena. *Nature* 302 (5906), 295–301. doi: 10.1038/302295a0

Pitcher, G. C., Aguirre-Velarde, A., Breitburg, D., Cardich, J., Carstensen, J., Conley, D. J., et al. (2021). System controls of coastal and open ocean oxygen depletion. *Prog. Oceanogr.* 197, 102613. doi: 10.1016/j.pocean.2021.102613

Pizarro, O., Clarke, A. J., and Van Gorder, S. (2001). El Niño sea level and currents along the South American coast: comparison of observations with theory. *J. Phys. Oceanogr.* 31, 1891–1903. doi: 10.1175/1520-0485(2001)031<1891:ENOSLA>2.0.CO;2

Pizarro, O., Shaffer, G., Dewitte, B., and Ramos, M. (2002). Dynamics of seasonal and interannual variability ofthe Peru-Chile undercurrent. *Geophys. Res. Lett.* 29 (12), 1581. doi: 10.1029/2002GL014790

Pizarro-Koch, M., Pizarro, O., Dewitte, B., Montes, I., Ramos, M., Paulmier, A., et al. (2019). Seasonal variability of the southern tip of the oxygen minimum zone in the Eastern south pacific (30°-38°S): a modeling study. *J. Geophys. Res. Oceans.* 124, 8574–8604. doi: 10.1029/2019JC015201

Ramos, M., Dewitte, B., Pizarro, O., and Garric, G. (2008). Vertical propagation of extratropical rossby waves during the 1997–1998 El nin ˜o off the west coast of south America in a medium-resolution OGCM simulation. *Geophys. Res. Lett.* 113, C08041. doi: 10.1029/2007JC004681

Rayner, N. A. A., Parker, D. E., Horton, E. B., Folland, C. K., Alexander, L. V., Rowell, D. P., et al. (2003). Global analyses of sea surface temperature, sea ice, and night marine air temperature since the late nineteenth century. *J. Geophys. Res.: Atmos.* 108, D14. doi: 10.1029/2002JD002670

Ridgway, K. R., Dunn, J. R., and Wilkin, J. L. (2002). Ocean interpolation by four-dimensional least squares -application to the waters around Australia, j. atmos. *Ocean. Tech.* 19 (9), 1357–1375. doi: 10.1175/1520-0426(2002)019<1357:OIBFDW>2.0.CO;2

Schmidtko, S., Stramma, L., and Visbeck, M. (2017). Decline in global oceanic oxygen content during the past five decades. *Nature* 542, 335–339. doi: 10.1038/nature21399

Schneider, W., Donoso, D., Garcés-Vargas, J., and Escribano, R. (2017). Water-column cooling and sea surface salinity increase in the upwelling region off central-south Chile driven by a poleward displacement of the south pacific high. *Prog. Oceanogr.* 151, 38–48. doi: 10.1016/j.pocean.2016.11.004

Shchepetkin, A. F., and McWilliams, J. C. (2003). A method for computing horizontal pressure-gradient force in an oceanic model with a nonaligned vertical coordinate. *J. Geophys. Res. Oceans* 108 (C3). doi: 10.1029/2001JC001047

Shchepetkin, A., and McWilliams, J. C. (2005). The regional oceanic modeling system (ROMS): a split-explicit, free-surface, topography- following- coordinate oceanic model. *Ocean Model.* 9, 347–404. doi: 10.1016/j.ocemod.2004.08.002

Silva, N., and Neshyba, S. (1979). On the southernmost extension of the Peru-Chile undercurrent. *Deep Sea Res. Part I. Oceanogr. Res. Pap.* 26, 1387–1393. doi: 10.1016/0198-0149(79)90006-2

Silva, N., Rojas, N., and Fedele, A. (2009). Water masses in the Humboldt current system: properties, distribution, and the nitrate deficit as a chemical water mass tracer for equatorial subsurface water off Chile. *Deep Sea Res. Part II: Topical Stud. Oceanogr.* 56, 1004–1020. doi: 10.1016/j.dsr2.2008.12.013

Sobarzo, M., Bravo, L., Donoso, D., Garcés-Vargas, J., and Schneider, W. (2007). Coastal upwelling and seasonal cycles that influence the water column over the continental shelf off central Chile. *Prog. Oceanogr.* 75, 363–382. doi: 10.1016/j.pocean.2007.08.022

Sprintall, J., Cravatte, S., Dewitte, B., Du, Y., and Gupta, A. S. (2020). ENSO oceanic teleconnections. *El Niño South. Oscillation changing Climate* 4, 337–359. doi: 10.1002/9781119548164.ch15

Takahashi, K., Montecinos, A., Goubanova, K., and Dewitte, B. (2011). ENSO regimes: reinterpreting the canonical and modoki El niño. *Geophys. Res. Lett.* 38, L10704. doi: 10.1029/2011GL047364

Thomsen, S., Kanzow, T., Colas, F., Echevin, V., Krahmann, G., and Engel, A. (2016). Do submesoscale frontal processes ventilate the oxygen minimum zone off peru? *Geophys. Res. Lett.* 43 (15), 8133–8142. doi: 10.1002/2016GL070548

Vergara, O., Dewitte, B., Montes, I., Garçon, V., Ramos, M., Paulmier, A., et al. (2016). Seasonal variability of the oxygen minimum zone off Peru in a high-resolution regional coupled model. *Biogeosciences* 13, 4389–4410. doi: 10.5194/bg-13-4389-2016

Vergara, O., Dewitte, B., Ramos, M., and Pizarro, O. (2017). Vertical energy flux at ENSO time scales in the subthermocline of the southeastern pacific. *J. Geophys. Res. Oceans* 122. doi: 10.1002/2016JC012614

Wooster, W. S., and Gilmartin, M. (1961). The Peru–Chile undercurrent. *J. Mar. Res.* 19, 97–122.

Yu, J. Y., Zou, Y., Kim, S. T., and Lee, T. (2012). The changing impact of el nino on US winter temperatures. *Geophys. Res. Lett.* 39 (15). doi: 10.1029/2012GL052483

10.3389/fmars.2023.1155932

Appendix A: model validation

In this section, we provide additional validation of the model variability at interannual timescales to complement previous studies (Dewitte et al., 2012; Vergara et al. 2016, 2017; Pizarro-Koch et al. 2019; Conejero et al., 2020). The oxycline depth (in m), the subsurface meridional current variability (PCUC in cm s^{-1} and the coastal upwelling associated with cold water (SST in °C), and high primary production (Chl-a in mg m^{-3}) were compared between the model and the observations.

TABLE A1 Root mean square (RMS) for interannual anomalies of the oxygen (in µM) averaged from surface to 60 m depth, oxycline depth (in m) over the continental shelf at ~36.5°S, meridional current (PCUC; 30°S) at 220 m and 480 m (in cm s^{-1}) for both model and in-situ data.

	RMS In-situ	RMS Model	RMS Difference	r ($p < 0.05$)	Period
Oxycline (m)	33.7	22.5	19.2	0.63	2003-2008
DO anomalies (µM)	23.0	34.9	36.9	0.24	2003-2008
SST (°C)	0.7	0.5	0.7	0.99	2003-2008
Clh-a (mg m-3)	0.3	0.2	0.4	0.87	2003-2008
PCUC-220m (cm s-1)	4.8	8.2	2.6	0.48	2000-2008
PCUC-480m (cm s-1)	3.9	4.9	1.3	0.22	2000-2008

Note the RMS of both Sea surface temperature (SST, in °C) and chlorophyll-a (Chl-a in mg m^{-3}) were estimated in a coastal band (first 80 km) extending from 30°S to 38°S. The oxycline depth was estimated from the depth of the maximum vertical gradient in DO. Pearson's correlation between model and in situ data is represented by r at 95% confidence. The bias was estimated as the RMS difference between the model and observation.

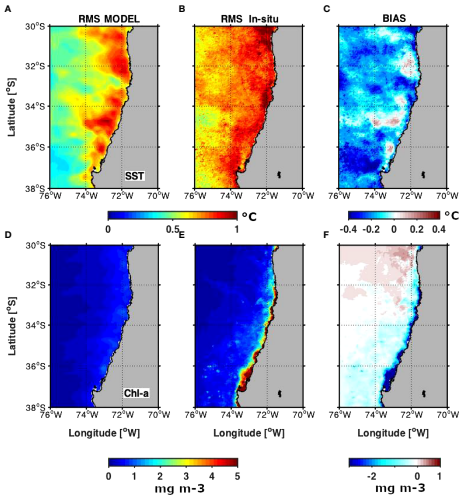

FIGURE A1
Root mean square (RMS) of the interannual anomalies of Sea Surface Temperature (SST in °C) for both model **(A)** and MODIS-Aqua **(B)** based on the 2003-2008 period. The RMS values of chlorophyll-a (Chl-a in mg m-3) are displayed in panels **(D, E)**, respectively. The bias of SST **(C)** and Chl-a **(F)** represent the difference between RMS modeled and in-situ observation.

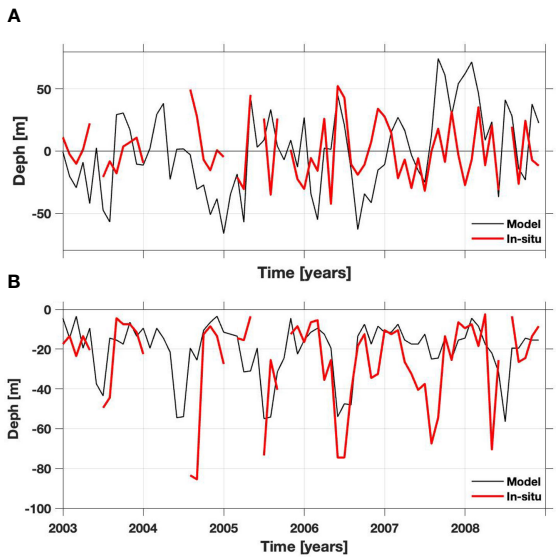

FIGURE A2
Interannual anomalies of the oxygen (DO in µM) averaged from surface to 60 m depth **(A)** and oxycline depth (in m) variability over the continental shelf at ~36.5°S (**B**; based from a monthly ship-based time series from the University of Concepcion at 36°30'S over the continental shelf (~90 m depth) for the period 2003–2008 (see Sobarzo et al. (2007) and Escribano et al. (2012) for more details) for both model (black line) and in situ data (red line). The oxycline depth **(B)** was estimated from the maximum vertical DO gradient.

frontiers | Frontiers in Marine Science

TYPE Original Research
PUBLISHED 18 July 2023
DOI 10.3389/fmars.2023.1134164

OPEN ACCESS

EDITED BY
Gireesh Kumar T R,
Council of Scientific and Industrial Research (CSIR), India

REVIEWED BY
Ejin George,
National Centre for Polar and Ocean Research (NCPOR), India
Alberto Sánchez-González,
National Polytechnic Institute (IPN), Mexico

*CORRESPONDENCE
Praxedes Muñoz
praxedes@ucn.cl

RECEIVED 04 January 2023
ACCEPTED 08 June 2023
PUBLISHED 18 July 2023

CITATION
Muñoz P, Castillo A, Valdés J and Dewitte B (2023) Oxidative conditions along the continental shelf of the Southeast Pacific during the last two millennia: a multiproxy interpretation of the oxygen minimum zone variability from sedimentary records.
Front. Mar. Sci. 10:1134164.
doi: 10.3389/fmars.2023.1134164

Oxidative conditions along the continental shelf of the Southeast Pacific during the last two millennia: a multiproxy interpretation of the oxygen minimum zone variability from sedimentary records

Praxedes Muñoz[1,2,3]*, Alexis Castillo[4,5,6], Jorge Valdés[7] and Boris Dewitte[1,2,3,8]

[1]Universidad Católica del Norte, Departamento de Biología Marina, Coquimbo, Chile, [2]Centro de Estudios Avanzados en Zonas Áridas, CEAZA, Coquimbo, Chile, [3]Núcleo Milenio de Ecología y Manejo Sustentable (ESMOI), Facultad de Ciencias del Mar, Departamento de Biología Marina, Universidad Católica del Norte, Coquimbo, Chile, [4]Centro de Investigación y Estudios Avanzados del Maule, Vicerrectoría de Investigación y Posgrado, Universidad Católica del Maule, Campus San Miguel, Talca, Chile, [5]J'EAI-CHARISMA, UMNG-Cajicá, Cajicá, Colombia, [6]ANID-Millennium Science Initiative Program Núcleo Milenio UPWELL, La Serena, Chile, [7]Laboratorio de Sedimentología y Paleoambientes, Instituto de Cs Naturales Alexander von Humboldt, Facultad de Ciencias del Mar y de Recursos Biológicos, Universidad de Antofagasta, Antofagasta, Chile, [8]CECI, Université de Toulouse, CERFACS/CNRS, Toulouse, France

The oxygen minimum zone (OMZ) is an essential feature along the Pacific margin, extensively studied for its influence on benthic fauna, acquiring relevance in coastal zones due to its impact on aquaculture species, marine-managed areas, and marine-protected areas. The most evident temporal variability beyond seasonal timescales observed for the OMZ was related to inter-annual variability associated with El Niño, when warmer and more oxygenated waters arrive at shallower zones and the OMZ becomes deeper. However, the impact of oxygen-deficient water that appears sporadically over the shelf is not yet understood. This study provides an integrated view of the oceanographic and climatic conditions behind bottom oxygen conditions along the Chilean continental margin, considering the temporal variability in the South East (SE) Pacific during the last ~2000 years. We organized the information on redox-sensitive metals and $\delta^{15}N$ from sedimentary cores obtained from shelf zones from 23°S to 36°S at water depths lower than 100 m. The results demonstrate the variability in the upper part of the OMZ over the shelf, which seems to respond to climatic oscillations. The element distribution indicated in particular a more intense OMZ was developed over the shelf before 1400 AD, followed by more oxygenated bottom conditions afterward, except between 1925 and 1970 off 36°S when the OMZ was intensified, a condition that was not observed at the northern sites. This period mostly coincided with a low Pacific Decadal Oscillation amplitude and reduced El Niño Southern Oscillation (ENSO)

activity. In the last 50 years, the proxy data suggests less intense suboxic environment along the Chilean margin. This weakening of the upper boundary of the OMZ in the last decades is interpreted as resulting from the accumulative effect of ventilation processes at different time scales.

KEYWORDS

oxygen minimum zone, denitrification, sensitive redox metals, enso, late holocene, eastern boundary upwelling system

Introduction

An essential feature of the eastern margins is the development of zones with low oxygen concentrations or oxygen minimum zones (OMZ), resulting from a high rate of oxygen consumption and limited ventilation. The eastern Pacific (EP) hosts one of the most extended OMZ of the planet that is embedded into the so-called Eastern Boundary Upwelling Systems (EBUS) in which nutrients are brought to the surface by the process of upwelling, making them among the most productive regions of the planet (Pauly and Christensen, 1995; Kämpf and Chapman, 2016). The high biological production associated with a complex nutrient cycle sustained by upwelling induces a significant oxygen consumption mainly through remineralizing organic matter, which, along the weak thermocline ventilation (Luyten et al., 1983) maintains a strong OMZ off Peru and the northern areas of Chile (Helly and Levin, 2004; Paulmier et al., 2006). There dissolved oxygen concentration can be as low as 0.5 mL L^{-1} (< 22 μM) with a maximum meridional extension of ~3000 km. Off central Peru (15°S), the upper boundary (25–50 m) is shallower and diminishes gradually in thickness and intensity toward the southern areas. Around 37°S, which corresponds to the southern tip of the Southeastern Pacific (SEP) OMZ, it is described as a thin band with a deeper upper boundary (> 100 m) (Schneider et al., 2006; Fuenzalida et al., 2009) (Figure 1).

Along the Chilean margin, the OMZ is composed of equatorial subsurface waters (ESSW), which are rich in nutrients and deficient in O_2 concentrations, transported southward by the Peru-Chile Undercurrent (PCUC) until ~48°S (Silva and Neshyba, 1979; Pizarro-Koch et al., 2019). It is located above the more oxygenated Antarctic intermediate water (AAIW) formed in the southern regions and moves northward, producing a distinct oxygen front around ~30°S. Nevertheless, the OMZ has limited ventilation because the South Pacific intermediate water (ESPIW) stabilizes the upper part of the water column (Schneider et al., 2003). It has been observed that this zone is highly impacted by remotely forced Kelvin waves originating from the equatorial region and propagating along the coast (Pizarro et al., 2002; Dewitte et al., 2012), which modulates the upwelling and OMZ extension, thereby changing the biogeochemical cycles in the water column and shelf sediments (Gutiérrez et al., 2008; Graco et al., 2017). Thus, the leading causes of their vertical and temporal variability over the contemporary period are tightly linked to the oceanic equatorial teleconnection (Sprintall et al., 2020).

On the other hand, sedimentary records along the SEP suggest that OMZ variability is related to the main atmospheric forcings at secular, decadal, and inter-annual scales (Salvatteci et al., 2014; Srain et al., 2015; Castillo et al., 2017; Ortega et al., 2019; Muñoz et al., 2020; Valdés et al., 2021). The Pacific Decadal Oscillation (PDO) and the Southern Annular Mode (SAM) have established regional cold/warm periods that are indirectly related to changes in bottom oxygenation due to the interaction of upwelling with primary productivity and ventilation. These periods are associated with changes in the position and strength of the westerlies, affecting the winter precipitation and intensity of the upwelling (Quintana and Aceituno, 2012; Ancapichún and Garcés-Vargas, 2015).

These climatic patterns can emulate ENSO-like conditions that affect the primary oceanographic features of the region (upwelling, OMZ, temperature, and productivity). They can exacerbate or weaken the effects of inter-annual variability, which depends on whether the decadal and inter-annual variability is in/out-of-phase (cold/warm). This has been described for the western North Pacific, where the PDO plays a relevant role in the intensity of ENSO (Yang and Oh, 2020). In particular, the cold (positive) phase of PDO (La Niña-like) tends to reduce ENSO variability by favoring a more northward Intertropical Convergence Zone (ITCZ) position and stronger cold tongue in the eastern equatorial Pacific (Hu and Fedorov, 2018). For instance, the northward position of the Intertropical Convergence Zone (ITCZ) was shown to allowed favorable conditions for upwelling and productivity in the early Holocene (Koutavas et al., 2006; Kaiser et al., 2008; Lamy et al., 2010), which in turn can favor a stronger OMZ along the SEP (Salvatteci et al., 2016). Afterward, the mid-Holocene warm period was interrupted by a weakening of ENSO around 6–7 ka when freshwater melting counteracted the insolation regime (Braconnot et al., 2012), driving cold periods associated with active upwelling and increased productivity for the central-Chilean margin (Carré et al., 2012; Carré et al., 2014; Muñoz et al., 2020). In addition, low ENSO activity at 4–5 ka for the Central Pacific, as evidenced by SST proxy from corals and fossil shells, was consistent with precessional forcing (Cobb et al., 2013; Carré et al., 2014). Such a reduced ENSO activity was also consistent with the small increases of diatoms and opal observed in sedimentary records of the north and central Chilean margin that suggested the maintenance of upwelling conditions over this period (Muñoz et al., 2012; Muñoz et al., 2020). However, during that period, the Peruvian margin did not evidence a stronger OMZ, which was explained by an intensification

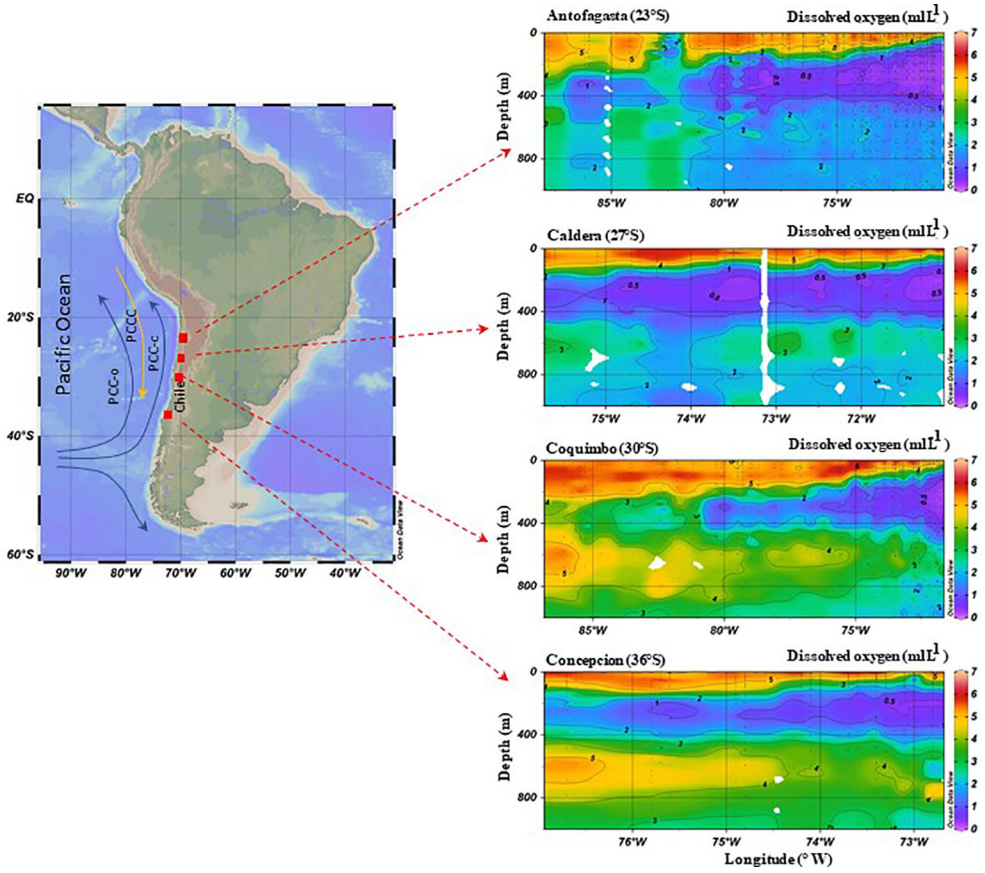

FIGURE 1
An overview map of South America (left) showing the areas of the cores recovered from the Chilean margin off Antofagasta (23°S; Mejillones Bay), Caldera (27°S; Inglesa Bay), Coquimbo (30°S; Guanaqueros and Tongoy Bay) and Concepcion (36°S; Concepcion shelf). For cores' information, see Table 1. The main oceanic surface currents are indicated with arrows: the Peru-Chile Current (PCC) coast(c), oceanic(o) branches, and the Peru-Chile Counter Current (PCCC). Dissolved oxygen (DO) concentrations in a transect in front of the study areas show the position of the oxygen minimum zone (OMZ) corresponding to concentrations lower than 0.5 ml L^{-1}. Data were obtained from Auger et al. (2020a); Auger et al. (2020b).

of equatorial subsurface countercurrents (Equatorial undercurrent, South Intermediate current, and Southern subsurface countercurrents) that introduced more oxygenated water and intensifying vertical mixing (Salvatteci et al., 2016; Mollier-Vogel et al., 2019). Recently, an expansion of the OMZ off central Peru was established after 1820 AD (Gutiérrez et al., 2009), while off northern Chile over the same period, the OMZ strengthened and reached shallower depths (Vargas et al., 2007; Valdés et al., 2021). On the other hand, for the central Chilean margin, the OMZ intensity was maintained through the mid-Holocene but experienced a strong reduction over the last 2000 years (Muñoz et al., 2020). The bottom oxygenation suggested by Muñoz et al. (2020) could have been associated with changes in equatorial variability favoring the atmospheric teleconnection off Central Chile. In particular there is a transition zone around 30°S for the ENSO atmospheric teleconnection: to the South of 30°S, upwelling favorable winds tend to reduce during El Niño (Dewitte et al., 2023).

The variability in the OMZ intensity during the late Holocene has been explained by changes in the expansion/contraction of the South Pacific Anticyclone (SPA) and the strength of the Walker Circulation for the Tropical SE Pacific, which determines the intensity of wind and upwelling (Salvatteci et al., 2016; Castillo et al., 2017). However, it has had different effects on the OMZ along the SE Pacific margin, owing to other ventilation mechanisms or local processes (Pitcher et al., 2021). Thus, there is currently still much uncertainty about the mechanisms at play to explain the variability of the SEP OMZ over the last millennia, which calls for revisiting existing proxy data in an integrative way. In this study, we take advantage of sedimentary geochemical records collected at four main upwelling zones in the northern and central Chilean continental shelf, where the OMZ intercepts the bottom: off Antofagasta (23°S), Caldera (27°S), Coquimbo (30°S), and Concepcion (36°S) (Figure 1 and Table 1), to establish the temporal evolution of the OMZ in the SE Pacific over the last 2000 years and discuss the possible processes involved.

Regional settings

The Chilean continental margin has distinct topographical, climatic, and oceanographic characteristics, modulating the primary productivity and chemical composition of the water column. This zone has been characterized as having several sites of high primary production (0.5–9.3 g C m^{-2} d^{-1}; González et al.,

TABLE 1 General information on the selected cores from the Chilean continental margin.

Locality	ID Core	Column water depth (m)	Core length (cm)	Temporal scale (yr)	Dating method	References
Mejillones del Sur Bay (23°S)	Mej2009	87	54	700 AD	^{210}Pb-^{14}C	Guiñez et al. (2014); Valdés et al. (2021)
Inglesa Bay (27°S)	BIAC072014	90	53	1500 AD	^{210}Pb-^{241}Am-^{14}C	Castillo et al. (2017)
Guanaqueros Bay (30°S)	BGGC5	89	126	7990 (CalBP)	^{210}Pb-^{14}C (Clam 2.2)	Muñoz et al. (2020)
Tongoy Bay (30°S)	BTGC8	85	98	8012 (CalBP)	^{210}Pb-^{14}C (Clam 2,2)	Muñoz et al. (2020)
Concepcion (36°S)	ST18 (short core) VG06-2 Long core)	88	30 220	1818 AD 2024* (CalBP)	^{210}Pb-^{14}C (Clam 2.2)	Muñoz et al. (2012); Srain et al. (2015)

(*) 79 cm, corresponding to the last radiocarbon age.

1998; Daneri et al., 2000; Thomas et al., 2001) off Iquique (21°S), Antofagasta (23°S), Coquimbo (30°S) and Concepción (36°S), produced by the influx of waters enriched in nutrients forced by local winds. Differences can be established latitudinally. Upwelling is semi-permanent in the North of Chile (18–30°S) and seasonal in the south (Montecino and Lange, 2009). This productivity occurs close to the coast above the narrow continental shelf in the north, which allows the development of relevant fisheries (Escribano et al., 2004 and references therein). Toward the south, the continental shelf is wider (~36–37°S). The upwelling sustains high primary productivity rates (9.9–19.9 g C m^{-2} d^{-1}) during the spring-summer period (Bernal et al., 1989; Fossing et al., 1995; Dellarosa, 1998; Daneri et al., 2000).

To the north (at 21°S) and off Peru, the OMZ is permanently present and can extend into the euphotic zone. In the case of northern Chile and southern Peru, it does not interface significantly with the benthic environment because of a narrow continental shelf (Helly and Levin, 2004). Off Central Peru (~11-14°S) and northern Chile (21-23°S), the OMZ extends over the shelf. It has been reported that during the 1997–98 warm ENSO event (El Niño), the appearance of the sediments was less reduced, in some cases, up to a depth of 10 cm, with positive redox potential values at the surface (Muñoz et al., 2004). The most evident response of the benthic fauna was a switch in species composition, deeper penetration of the fauna into the sediments, and increased body size of the organisms (Gutiérrez et al., 2006; Sellanes et al., 2007; Gutiérrez et al., 2008). Following this El Niño, the dissolved oxygen decreased gradually to reach normal low concentrations (< 0.5 ml L^{-1}), dropping well below 0.25 ml L^{-1} due to repeatedly La Niña events during 1999, 2000, and 2001, reaching considerably lower oxygen concentrations than values reported in previous years (Gonzalez et al., 2007). The oxygen rise at the bottom directly affects biogeochemical cycles that can be observed several months after the event (Ulloa et al., 2001; Escribano et al., 2004).

Methods

Sedimentary records

We reanalyzed previously published information from six sedimentary records at four sites along the Chilean margin: Mejillones del Sur Bay (23°S), Inglesa Bay (27°S), Coquimbo Bay (30°S; Guanaqueros and Tongoy Bay), and Concepcion Bay (36°S) (Muñoz et al., 2012; Guiñez et al., 2014; Srain et al., 2015; Castillo et al., 2017; Muñoz et al., 2020; Valdés et al., 2021). The cores have been dated using short-lived radioisotopes (^{210}Pb, ^{241}Am) by gamma and alpha counting combined with AMS radiocarbon measurements. In the case of Concepción Bay, the geochronology obtained with lineal regression (Muñoz et al., 2012) was updated using the Clam 2.2 software. The background information for each sedimentary record is presented in Table 1.

Cores description

The sedimentological characteristics of the selected cores are summarized below for a better approach to proxy interpretation.

The core located at the northern site (23°S, Mejillones del Sur Bay) was composed of silts (11–15%) and clays (> 70%), presenting an increase in clays in recent times (~90%). The total organic (TOC) content was high, between ~4% in the base of the core, increasing to the surface, reaching 5.5–7%. The sediments were described as olive green, with low stratifications, only visible with X-Rays, and were recognized three sedimentary facies based on color and thickness. Therefore, low bioturbation was observed. The age lower limits for the units were 1880 and 1600 AD, respectively (Guiñez et al., 2014; Valdés et al., 2021).

At 27°S off Inglesa Bay, the sediments also exhibited laminations of alternating light and dark color bands, the latter corresponding to hemipelagic organic material. Four units were recognized based on these laminations. The age lower limits were 1826, 1311, and 1009 AD, with slumps between the last three units. The TOC content was between 4% and 7%, with decreasing values toward the present (Castillo et al., 2017).

The cores retrieved from the southern sites did not show lamination. Off ~30°S (Guanaqueros and Tongoy Bays) were composed of very fine sand and silt, with evidence of weak laminations and low bioturbation. They also contain debris from fish vertebrates and shells, commonly observed in sediments from the northern Chilean shelf areas (Milessi et al., 2005). The sediment colors varied between bays. Guanaqueros exhibited accentuated olive-green colors, whereas Tongoy displayed colors in the range of

very dark grayish-brown to dark olive green. In this core, a slight increase in the mean grain size occurred in the last 1000 years owing to a major continental input, which also explains the colors found. In agreement with this, the TOC (%) was lower (1–1.5%) than that in Guanaqueros (< 5%) (Muñoz et al., 2020).

The cores from the shelf of Concepcion (36°S) were composed of dark olive green hemipelagic mud at the surface, followed by distinctive olive green layers alternating with grey clayey mud layers. Differences in colors were related to their composition; olive-green corresponded to low bulk density and higher TOC content, between 1% and 2%, while the gray layers were low in TOC and showed higher bulk densities. This composition is similar to that of the Coquimbo shelf, but the core of Concepcion has a thin gray layer at ~79 cm, corresponding to hemipelagic sediments. These sediments exhibited moderate bioturbation and were not typically laminated (Srain et al., 2015; Muñoz et al., 2020).

The rationale for the selection of proxies $\delta^{15}N$

Water column denitrification has been indirectly inferred from $\delta^{15}N$ in sedimentary organic materials (Altabet, 2005; Robinson et al., 2014). Under low subsurface oxygen in the water column (< 2 µmol O_2 L^{-1}), the partial NO_3 uptake and denitrification process resulted in increased values of $\delta^{15}N$-nitrate, imprinting higher $\delta^{15}N$ in sinking organic particles. This signal has been used as a proxy for changes in oxic conditions at the bottoms (Lam et al., 2009; Farmer et al., 2021). Global $\delta^{15}N$ variation has been associated with glacial cooling. It is described as a less intense suboxia in denitrification zones due to oxygen supply to the thermocline zone or reduced oxygen consumption due to reduced export production (Robinson et al., 2007 and references therein). This process marks periods of reduced denitrification associated with lower $\delta^{15}N$ values during glacial periods and higher values during interglacial periods. This variability has been observed along the SE Pacific in shallower and deeper zones, establishing denitrification zones and their regional variations in surface sediments (De Pol-Holz et al., 2006; Robinson et al., 2007; De Pol-Holz et al., 2009; Mollier-Vogel et al., 2012). Here, we used this tool as a proxy for denitrification intensity, which describes the subsurface variability of oxygen content over the continental shelf.

Redox-sensitive metals (Mo, U)

A few redox-sensitive metals have been used to reconstruct the redox conditions of depositional environments. Under oxygen-deficient subsurface water conditions (reducing conditions), metals show a higher enrichment compared with normoxic conditions (Tribovillard et al., 2006; Bennett and Canfield, 2020; Sánchez et al., 2022). However, the availability of reactive organic material in the column may also control the accumulation and enrichment of redox-sensitive metals on the seafloor (Nameroff et al., 2002; McManus et al., 2006; Algeo and Li, 2020). In the SE Pacific, redox-sensitive metals, such as Mo, Re, and U, have demonstrated moderate to strong enrichment behavior, especially in coastal areas associated with the OMZ (Böning et al., 2004; Böning et al., 2005; Böning et al., 2009; Muñoz et al., 2012; Salvatteci et al., 2014; Valdés et al., 2014; Castillo et al., 2019; Valdés et al., 2021; Muñoz et al., 2022). Here, we used redox-sensitive elements (U and Mo) to interpret the oxidative changes on the bottoms related to oxygen availability, using TOC and stable isotope distribution for complementary interpretations.

Results

$\delta^{15}N$ and TOC distribution

The latitudinal distribution of $\delta^{15}N$ does not describe a clear pattern (Figure 2). The values vary between ~1.2 and ~13‰, being higher in northern areas (23–27°S). The range of variability of the isotope was narrow for Mejillones and Coquimbo cores, while the cores at 27°S and 36°S showed more variability. In the case of Concepcion, the period of lowest values is concomitant with that of the lowest values for TOC (i.e., ~400 AD), corresponding to sandy sediment below the gray layer. Off-Mejillones (23°S), the maximum values were at the oldest periods (~1400 AD), and in Inglesa Bay, the maxima were around 900–1100 AD. Meanwhile, at the southern sites (30°S–36°S), $\delta^{15}N$ values peak during the recent period (~9‰–10‰).

Similarly, TOC content did not exhibit a clear latitudinal pattern. The maximum TOC values were in Mejillones (21°S) with high variability, showing an increasing trend in recent times; from 1950 to 2000, the TOC reached 6.5% (~0.5%/decade). Off Coquimbo (30°S), the TOC values were lower and similar amongst the different cores, ~1% and 3% in Tongoy and Guanaqueros Bay, respectively. Other sites showed maximum values between 1000 and 1400 AD, around 6% and 3% off Inglesa Bay and Concepcion, respectively. After this age, the TOC content tended to diminish (~3% and ~1%, respectively) by ~1950–1960. After this date, most sites evidence an increase, except for Inglesa Bay (27°S), which indicates a gradual decrease in the recent period from ~1500 AD.

For a better approach, $\delta^{15}N$ related to the denitrification process was standardized to establish its variability at each site (Figure 3). Standardization consisted of estimating the variability around the mean value at each core according to (value-average)/standard deviation. This approach resulted in positive and negative values that helped visualize the intensity of the processes at each site, independently of the latitudinal differences in the proxy concentrations. Figure 3 indicates that, between 0 and 500 AD in Concepcion (36°S), the standardized $\delta^{15}N$ evolved from low positive to higher negative values, corresponding to less intense denitrification. In contrast, Coquimbo (30°S) showed high negative values that grew to small positive values, which means that the denitrification was increasing, being slightly more intense at the end of the period. There is no information to compare to northern sites.

Between 500 and 1100 AD, Inglesa Bay (27°S) and Concepcion (36°S) displayed a similar trend. The $\delta^{15}N$ evolved from strongly negative or "neutral" to positive values; both sites indicated increasing denitrification, peaking at ~900–1000 AD.

Between 1100 and 1500 AD, denitrification was more intense in Mejillones (23°S, only data from ~1300 AD) and Inglesa Bay (27°S),

10.3389/fmars.2023.1134164

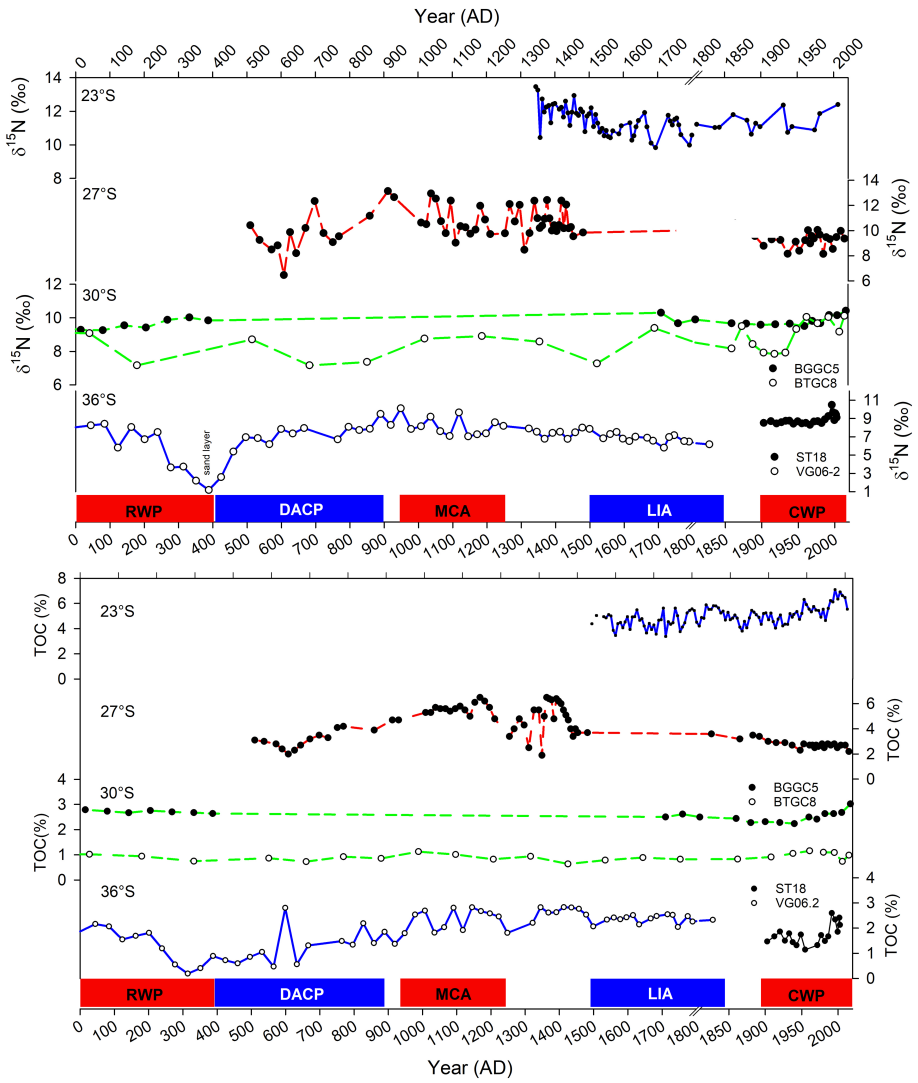

FIGURE 2
Comparison of $\delta^{15}N$ and total organic carbon (TOC%) records along the Chilean margin (23–36°S). The records correspond to the cores indicated in Table 1; Core MEJ2009 (23°S), core BIAC072014 (27°S), core BGGC5 (black dots, 30°S), core BTGC8 (unfilled dots, 30°S), core ST18 (black dots, 36° S) and core VG06-2 (unfilled dots, 36°S). Cold (blue) and warm (red) periods are indicated on the x-axis: RWP (0-400 AD), DACP (400-800 AD), MCA (9501250 AD), LIA (1500-1850 AD) and CWP (> 1900 AD).

diminishing to the southern sites (36°S) during the same period (there is a gap in information from Coquimbo). The cores of Concepcion showed low variability, low positive values around the mean value. On the other hand, the intensity in denitrification decreased toward 1500 AD in Mejillones, while in Inglesa Bay, this is less clear due to a gap of information in this period, only few data indicated small negative values occurred around 1500 AD, suggesting less intensity in this process.

Between 1500 AD and ~1900 AD, Mejillones showed the lowest intensity in denitrification (higher negative values). Similar to Coquimbo, mostly negative values indicated a diminishing denitrification process; however, only a few pieces of data were available for this period. For Concepcion, the values were also negative but close to the mean intensity. No information is available at Inglesa Bay for this period.

After 1900 AD, Mejillones (23°S) showed alternating positive and negative values with a magnitude similar to the other sites, indicating high variability in the intensity of denitrification. In Inglesa Bay (27°S), they were consistently negative or less intense denitrification. On the other hand, in Coquimbo (30°S), both cores showed an increasing trend to higher positive values indicating an intensified denitrification. Concepcion (36°S) evolved from negative values until ~1970 to very high positive values at the current time.

TOC and metal relationship

We further explored the relationship between Mo and TOC (Figure 4) since Mo indicates reduced conditions closely related to organic matter remineralization in zones with high productivity.

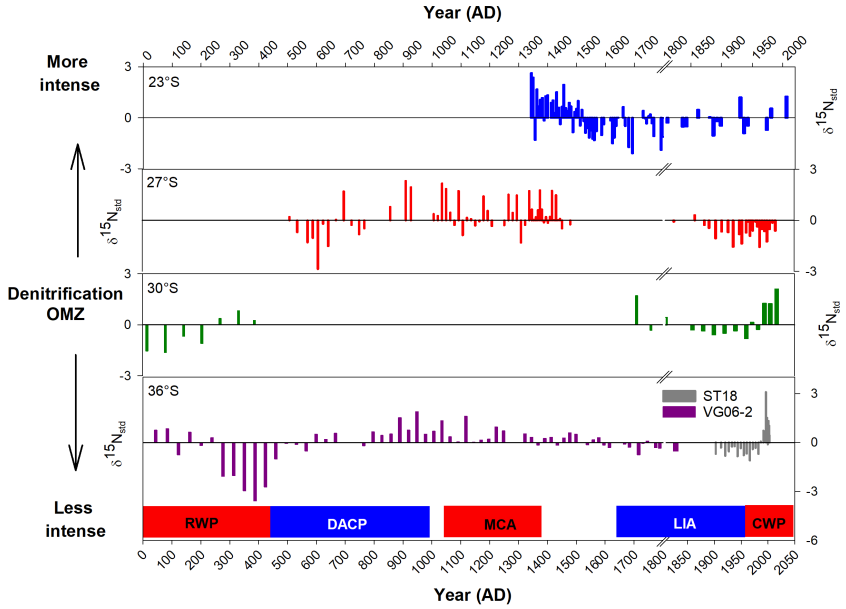

FIGURE 3
Comparison of standardized isotopic records ($\delta^{15}N_{std}$) along the Chilean margin. The core information is indicated in Table 1. (23°S: core Mej2009; 27°S: coreBIAC072014; 30°S: BGGC5 core; 36°S: ST18 and VG06-2 cores).

Also, we analyzed the relationship between U and Mo (Figure 5) in order to characterize the flux of organic particles. There is a clear linear relationship between U and Mo, independent of the temporal scale of each core (see Table 1). This relationship was more robust in the northern zones (23–27°S; r2 = 0.78–0.81; $p < 0.0001$) and decreased towards the southern sites, where the relationship between U and Mo weakens but still remains significant (36°S; r^2 = 0.24–0.33). TOC was higher in Mejillones (23°S) with maximum values reaching 6–7%, and the relationship with Mo showed a negative correlation (r^2 = 0.45). To the south, the TOC values decreased to 3% at Concepción with a positive relationship with Mo (Figure 4), but with a weaker value of correlation (36°S; r^2 = 0.13 −0.26), probably caused by an increase in detrital inputs that spoilt the relationship between sedimented organic matter and metal precipitation.

These EFs were reported as the amount of metal over the crustal concentrations determined in each location (Muñoz et al., 2012; Castillo et al., 2017; Castillo et al., 2019; Valdés et al., 2021) (Table 2). The use of enrichment factors considering local detrital supply has been criticized because several processes in sediment transport may reduce detrital sedimentation. It has been proposed that Me/Al is a better approach (Bennett and Canfield, 2020). However, after reanalyzing the data, the Mo/Al ratio (in $\mu g\ g^{-1}/\%$) showed similar behavior to using the EFs, reaching higher values in Mejillones (20–70) and decreasing in southern areas (< 3). Considering the standard EF calculation, the enrichments were high in Mejillones (23°S), one order of magnitude higher (~50–300) than at the southern sites, which was accompanied by a decrease in TOC content. South of 23°S, the EF values peaked to ~25 in Coquimbo and were as low as 3 in Inglesa Bay. This enrichment is probably underestimated because it was calculated using a very high detrital value measured in aeolian dust, enriched in metals by the presence of phosphorites in the zone (Table 2 and Figure 4).

This study used metal ratios to estimate the variability at each site, showing changes that resulted from the redox condition variability at the bottom over time along the margin.

Metal distribution

Similar to $\delta^{15}N$, the metal concentrations were standardized. This information is not complete for all sites (Figure 6), but a similar palpable trend of lower concentrations (below the mean value) of U and Mo was observed from ~1400 AD to the present, suggesting less suboxic conditions, except for Concepcion (36°S) at the southern tip of our study area where the OMZ was more intense between 1900 and 1970 AD, which was not observed in the northern areas. Between 1400 and 1600 AD, significant anoxic conditions in the north sites (23–27°S) were not observed at 36°S, indicating a less intense OMZ. The few data points off Coquimbo also reveals a less severe suboxic environment. Between 800 and 1400 AD, these suboxic conditions were somewhat variable. In the case of 27°S, less intense suboxic conditions covered the period spanning between around 1300 to 600 AD. Both elements suggest less anoxic conditions. Before 800 AD, only the Concepcion site benefits from the complete data. They indicate less intense suboxic conditions between 100 and 600 AD, peaking between 300 and 500 AD. A few data available in Coquimbo 30°S) suggest that this condition was the opposite in this period because U continued to show moderate intensification although mostly negative values of Mo, implying that the sulfidic conditions necessary for Mo precipitation were weak.

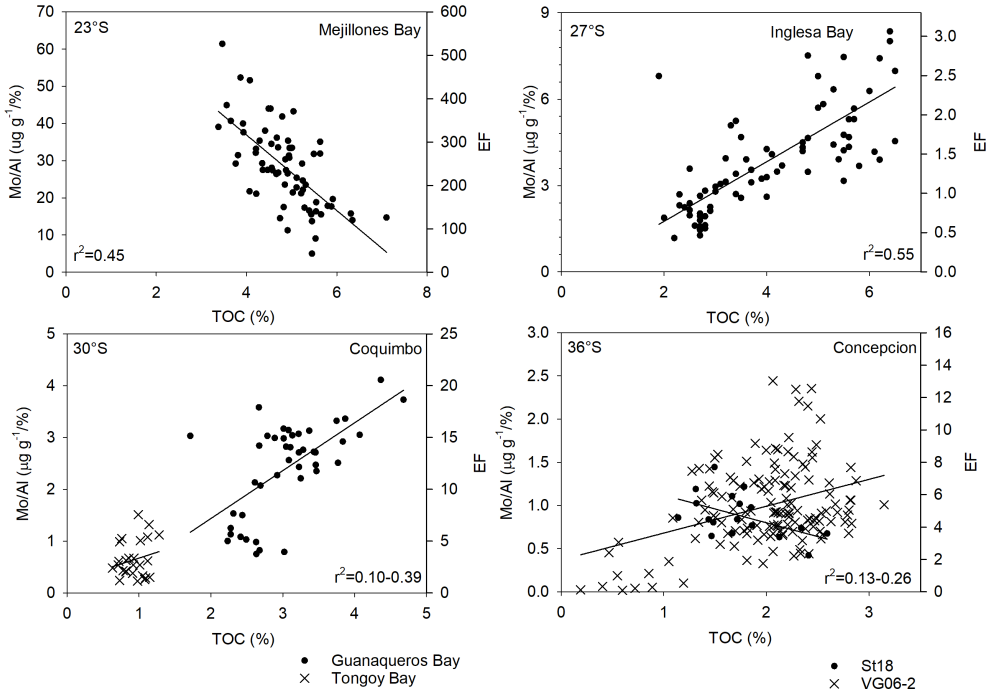

FIGURE 4
The TOC(%), enrichment factor (EF), and Mo/Al relationship are shown for each core. It considers the complete records of each core (see details in Table 1). r^2 = 0.45 at 23°S; r^2 = 0.55 at 27°S; r^2 = 0.39 at 30°S; r^2 = 0.13–0.26 at 36°S, p < 0.0001. The EF values were from Valdés et al. (2021); Muñoz et al. (2012), and Castillo et al. (2017); Castillo et al. (2019).

Discussion

$\delta^{15}N$ and TOC distribution

Differences in $\delta^{15}N$ were established between the northern and southern sites of the Chilean margin, showing a slight latitudinal decrease to the south (Figure 2). The variability in temporal scale at the northern sites (23°S-27°S) were ~3-4‰, in a similar range to that observed in Peru, with a maximum reaching 8–9‰ and a minimum of ~5‰ (Gutiérrez et al., 2009). At the southern sites, the $\delta^{15}N$ was lower, between 10‰ and−5‰, except in the sand layer in the core off Concepcion (<3‰), establishing a latitudinal decreasing trend of $\delta^{15}N$ toward higher latitudes. This trend could be interpreted as a dilution effect by the increasing input of organic matter from rivers, characterized by low $\delta^{15}N$ (2–3‰)(Meyers, 1997; Calvert et al., 2001), which would be absent in the north (23–27°S). However, the organic matter in sediments along the SE Pacific has been described as predominantly marine (De Pol-Holz et al., 2009; Mollier-Vogel et al., 2012). The continental effect would be relevant only in the period corresponding to the sand layer of Concepcion´s core. A better explanation of this light latitudinal gradient may lie from differences in nitrate concentrations and the uptake and assimilation of this nutrient by phytoplankton along the margin (Robinson et al., 2007; De Pol-Holz et al., 2009; Sánchez et al., 2022). The denitrification process domain at shallower depths and any variability could be caused by differences in the utilization

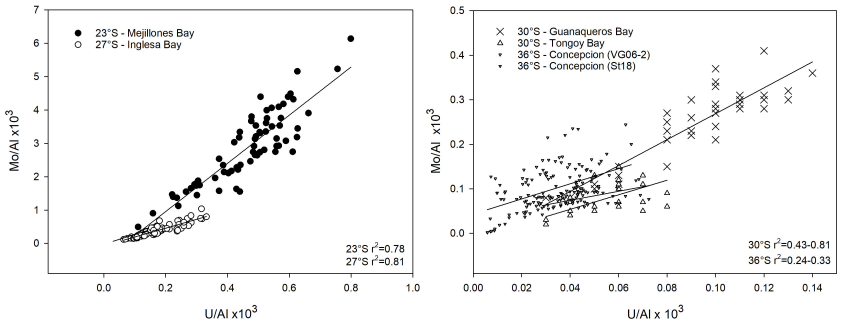

FIGURE 5
U/Al and Mo/Al relationships, considering the complete record of each core. Cores details are shown in Table 1. r^2 = 0.78 at 23°S; r^2 = 0.81 at 27°S; r^2 = 0.43–0.81 at 30°S; r^2 = 0.24–0.33 at 36°S, p < 0.0001.

TABLE 2 Metal concentrations in detrital sources.

	Metal Background				
Metal (mg kg^{-1})	B. Mejillones (23°S)[a]	B. Inglesa (27°S)[a]	B. Tongoy-Guanaqueros (30°S)[b]	Concepcion (36°S)*,[c]	Average shale
Mo	0.58	8.2	1.3	0.9*	1.3
U	3.47	2.0	1.3	0.9	3.0
Al (%)	5.18	3.04	6.7	5.8	8.9
Reference	Valdés et al. (2014)	unpublished data	Muñoz et al. (2012)	Muratli et al. (2010) ; Muñoz et al. (2012)	Wedepohl (1971)

[a]Aeolian dust from unpopulated area.
[b]Surface sediment from undegraded wetland zone in Tongoy Bay.
[c]Mean concentration value in the BioBio and Itata River suspended particles. *Mo data unpublished.

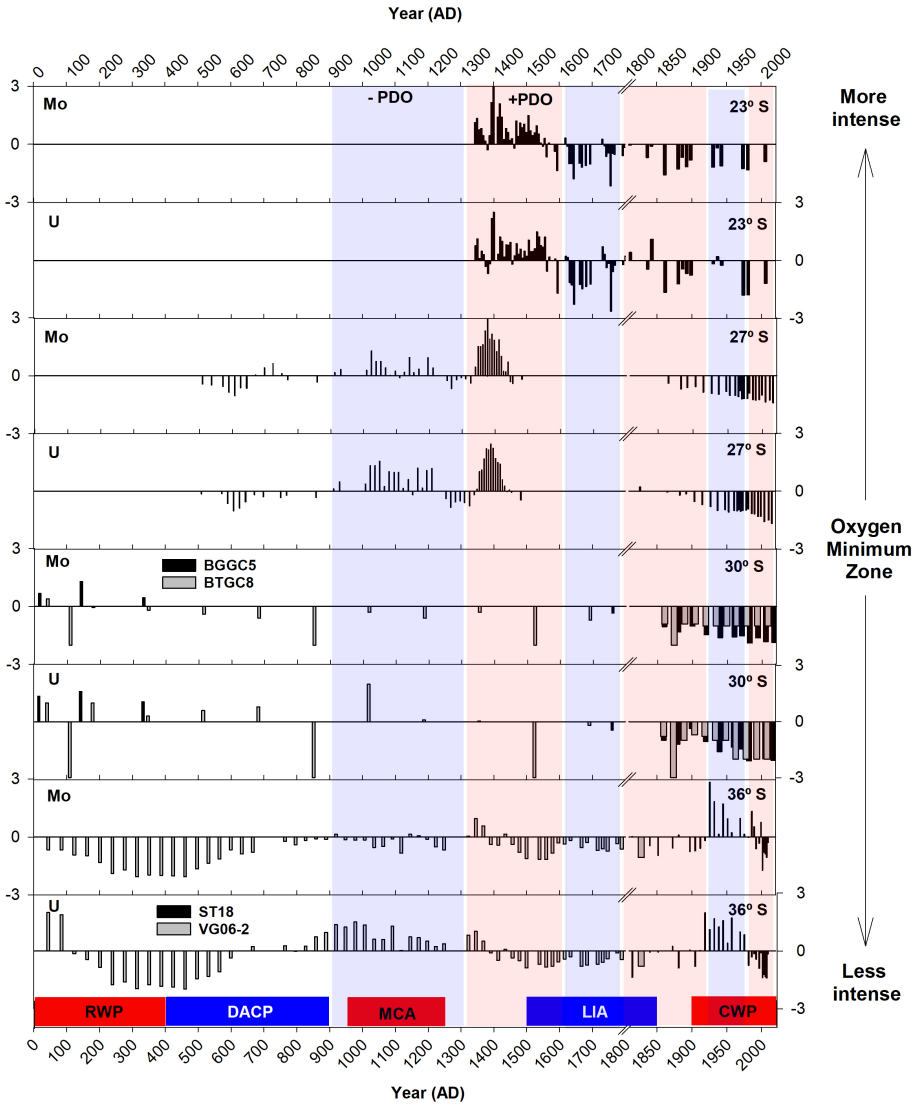

FIGURE 6
Standardized data records of Mo and U in Mejillones Bay (23°S), Inglesa Bay (27°S), Coquimbo Bay (30°S; Guanaqueros and Tongoy bays), and Concepcion Bay (36°S). Cold (blue) and warm (red) periods are indicated on the x-axis: RWP (0-400 AD), DACP (400-800 AD), MCA (9501250 AD), LIA (1500-1850 AD) and CWP (> 1900 AD). Periods of low (purple) and high (pink) amplitude PDO are indicated by shading. The periods are selected based on the MacDonald and Case (2005)'s reconstructed index (see their Figure 2).

of nitrate, such that, north of ~30°S, this nitrate consumption is complete compared with the southern sites, where it could be partial (De Pol-Holz et al., 2009). This signal is translated to the sediments, where the shelf sediments represent the composition of the sinking organic matter favored by the high sedimentation rates (0.24 – 0.15 cm/yr; Muñoz et al., 2004). Therefore, diagenetic alterations would not be relevant for $\delta^{15}N$, this being a robust proxy in sedimentary records to reconstruct denitrification intensity (Robinson et al., 2007; De Pol-Holz et al., 2009). On the other hand, latitudinal increases from Peru to northern Chile were attributed to differences in upwelling and progressive $\delta^{15}N$ enrichment associated with the southward flux by the PCUC, which explained the increased values from Peru to Mejillones Bay (23°S) (Vargas et al., 2007; Sifeddine et al., 2008; Gutiérrez et al., 2009). In contrast, the southern sites of Chile showed a decreasing trend that could be attributed to a change in the upwelling pattern, being seasonal off 36°S and almost permanent north of Coquimbo. Therefore, the influence of the denitrification zone would be reduced in the southern sites (Vargas et al., 2007; Sánchez et al., 2012).

Similarly, the TOC content (Figure 2) slightly decreased at the southern sites. The highest values (4–6%) were found in Mejillones, dropping to 3–4% in Inglesa Bay and Coquimbo and off Concepcion, with values ranging between 2% and 3%, except in the sand layer (< 1%). This observation suggests differences in the continental runoff over the shelves, particularly along the coast of Concepcion. The rivers off Concepcion are the primary particle sources that reduce the TOC in the bulk content. However, this contradicts previous analysis of $\delta^{13}C$, which indicates that the organic carbon source is controlled by marine productivity (Hebbeln et al., 2000; De Pol-Holz et al., 2009). However, it has increased the influence of freshwater species on the diatom compositions preserved in sediments in recent times (Sánchez et al., 2012).

The sedimentation rates (SR) estimated in the sediment cores of this study were in the range of values reported previously. Off Concepcion, it is higher (0.27 cm/yr) than the north of 30°S (0.04 and 0.11 cm/yr, in Mejillones and Coquimbo, respectively). However, the organic carbon accumulation rate shows an opposite trend. Off the Mejillones Bay, the value is ~105 gC/cm^{2}yr, and in the southern sites, it is ~38.9 – 24.50 gC/m^{2}yr. Therefore, the differences in organic carbon (OC) accumulation at our sites could result from differences in the detrital runoff. However, it could also respond to enhanced organic preservation in the north because the OMZ is thicker and less affected by seasonal variability (Valdés et al., 2004; Valdés et al., 2009). The buried OC results from organic matter that escapes oxidation referred to as burial efficiency (Middelburg et al., 1993), which depends on oxygen availability and sedimentation. Here, differences in SR should not be enough to explain differences in OC accumulation. Therefore, the differences in its accumulation could be attributed to oxygen availability and primary productivity fluxes at the bottom. Other factors relevant to C preservation include surface area reactivity, grain size composition, and organic carbon reactivity (Burdige, 2007; Katsev and Crowe, 2015), which should be considered but have not been evaluated. The OC content variability over time followed similar patterns at all sites. Considering a larger timescale (> 2000 cal BP) for Coquimbo and Concepcion (Muñoz et al., 2012; Muñoz, et al. 2020), the TOC content showed a slowly decreasing trend after 1400 AD toward the beginning of the Common Era. However, after the 1970s (Figure 2), it rapidly increased, being markedly high in Mejillones and Concepcion, corresponding to the north and south ends of our study area. This change is coincident with the climate shift of the 1970s (Jacques–Coper and Garreaud, 2014), described as a warming shift on the east coast of South America concomitant with a weakening of the subtropical South Pacific High (SPSH). It would be condusive of a decreased organic flux by diminished primary productivity. Notwithstanding, an intensification of coastal upwelling was described for Mejillones (Vargas et al., 2007) and the Peruvian continental margin (Gutiérrez et al., 2011; Salvatteci et al., 2014), explaining the enhanced TOC trend, although others identified this trend earlier, around 1878 (Flores-Aqueveque et al., 2015). These studies identified enhanced wind stress in particular years, suggesting an interplay between inter-annual and decadal variability, which also had an incidence in the manifestation of the 1970s shift (Jacques–Coper and Garreaud, 2014) and would also explain the increased TOC off Concepcion. Even with increased runoff with low metabolizable organic material contributing to enhancing the organic content of these sediments, the $\delta^{13}C$ still indicates a marine phytoplankton source (Sánchez et al., 2012). These authors state that the increased river inputs would be a nutrient source that overcompensates for the diminished nutrient inputs from the impoverished upwelling.

Denitrification

The range of the mass accumulation rates was not highly dissimilar. Despite the contribution of rivers in the south that support fresh organic C (highly reactive matter) to shallow depths, phytoplankton sedimentation dominates. Therefore, they maintain the isotopic composition of the settled organic material. The $\delta^{15}N$ in the sediments is related to denitrification, linked to the available oxygen content over the bottom. The standardized $\delta^{15}N$ data show better the variability of this process over the shelf despite the narrow range of the isotopic values (Figures 2, 3). In general, less intense denitrification, peaking at 300 and 600 AD off Concepción (36°S) and Inglesa Bay, respectively, occurred predominantly in a cold period (Dark Age Cold Period, DACP). However, lower values were also observed in the previous warm period (Roman Warm Period, RWP). Thus less intense denitrification was set before 800 AD; afterward, all sites exhibited enhancement of denitrification (more positive values), peaking during ~1100-1400 AD. The maximum values corresponded predominantly to a warm climate in the medieval climate anomaly (MCA) and the current warm period, while minimum values were during the cold period between 1600 and 1750 AD when the little ice age (LIA) arose. During this cold period, denitrification was less intense, except off Coquimbo (30°S), which has remained positive but more intense in the current time. Previous periods (< 1400 AD) at 23°S were insufficient for comparison. Thus, attenuation of the denitrification process during warmer periods (after 1400 AD) and a less intense OMZ was

observed, implying a higher variability of oxygen conditions in the bottom waters. In the last 50 years, the data indicated a more intense denitrification, suggesting a more reduced environment, similar to most sites along the Chilean margin (except at 27°S). These conditions agree with the increase in C accumulation in recent sediments and more reduced conditions on the shelf caused by the intensification of the OMZ, promoting also intensified denitrification. Thus, changes in denitrification could be related to the variability in the upper limit of the OMZ.

Trace metals distribution

U and Mo enrichments (authigenic precipitations) in reduced sediments have been widely used to interpret past redox conditions. U accumulation rate is highly correlated with the organic flux to the ocean bottom, where the precipitation of this element within the sediments could be microbially mediated (Zheng et al., 2002). Still, a substantial fraction can also be lost to the water column during sediment perturbations that affect the redox conditions and release U in the porewater. The U cycling would be similar to Fe cycling, having a similar redox reduction boundary (Zheng et al., 2002). Instead, Mo precipitation requires a sulfidic environment with concentrations >11 μM (Erickson and Helz, 2000). However, in sediments below suboxic waters, Mo-sulfide and Fe-sulfide coprecipitate at very low sulfide concentrations ~ 0.1 μM (Zheng et al., 2000), producing authigenic metal precipitation. Otherwise, Mo could also form intermediate complexes with dissolved organic matter in the bottom waters and sediments in suboxic conditions, contributing to sequestering Mo during early diagenesis (Wagner et al., 2017). This process could be relevant in places where the high primary productivity promotes higher organic flux to the bottoms, as described for the HCS; thus, several pathways can enhance Mo concentrations over the lithogenic background within the sediments. Instead of Mo, for U authigenic enrichment, an oxygen penetration of < 1 cm is necessary to maintain suboxic conditions within the sediments and U in a precipitated form (Morford and Emerson, 1999). Therefore both elements help determine the intensity of the redox changes, establishing suboxic and anoxic conditions.

In the Chilean margin, higher EFs were estimated for Mo over U concentrations, which showed a positive and significative correlation (Figures 4, 5), except at Concepcion, probably due to enhanced input of detrital material (r^2 = 0.24-0.33). This situation indicates that the sulfide concentrations were sufficient for Mo precipitation, which are between < 10 and 30 μM off Concepcion (36°S; Muñoz et al., 2012b), and reports for Coquimbo (30°S) indicate similar values of ~10 μM and ~80 μM (Muñoz, unpublished data). There are no sulfide records off Mejillones (23°S) and Inglesa Bay (27°S); however, in both sites, the correlation between metal enrichment and sulfate reduction intensity is poor, and the intensity of this process does not control the metal enrichment by itself (Valdés et al., 2014; Castillo et al., 2019). Thioploca mats on the bottoms probably reduce sulfide availability, diminishing metal-sulfide formation (Valdés et al., 2014). Instead, the metal transport during the Fe reduction/oxidation cycle has been proposed as a relevant mechanism for Mo enrichment (Valdés et al., 2014). Off-Perú, models of Fe shuttle for Mo enrichments would apply for the Chilean margin, even in shallower zones, where Fe has a crucial control over metal accumulation below a nitrogen-rich OMZ (Scholz et al., 2017; Scholz, 2018). The relationship between Mo and U enrichment is presented in Figure 7. It is based on the scheme proposed by Algeo and Tribovillard (2009) that establishes the range for metal enrichment in sulfidic, anoxic, and suboxic conditions. The U/Mo relation exceeds three times the seawater values in Mejillones, indicating a crucial particulate shuttle for metal enrichment here, but not in the other sites, which mostly fall in the suboxic condition area ruled by oxygen content in the bottoms and organic fluxes.

The organic fluxes measured in sediments are highly dependent on primary productivity and constitute an essential carrier phase for metal accumulation in surface sediments in the Chilean margin and Peru in deeper zones (McManus et al., 2006; Scholz, 2018). This relationship is negative in Mejillones and positive in the southern sites (Figure 4), suggesting enhanced organic carbon preservation and reduced detrital siliciclastic input in Mejillones. In restricted basins, authigenic enrichment can limit Mo accumulation because the dissolved phase is determined by circulation. This situation diminishes Mo precipitation, producing a lower Mo/Al value related to higher TOC content within the sediments (Tribovillard et al., 2012), explaining the negative correlation. However, this would not apply to upwelling zones; instead, the negative relationship between TOC and Mo in Mejillones (23°S) could result from increased oxygenation. The presence of Fe oxides promotes Mo accumulation during the recycling of oxides, as discussed earlier, and reduces the organic content by remineralization (Figure 4). Besides, it is essential to note that the

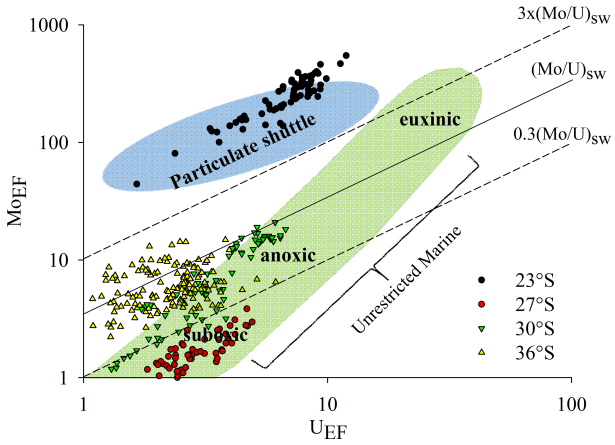

FIGURE 7
Model adapted from Tribovillard et al. (2012) to interpret the relationship of MoEF vs. UEF of the sedimentary records of the study area (both axes on logarithmic scale): Mejillones del Sur Bay (23°S, black circle), Inglesa Bay (27°S, red circle), Coquimbo (30°S, green triangle), and Concepcion (36°S, yellow triangle). Segmented line identifies Mo/U molar ratios equal to the seawater value (1xSW) and fractions thereof (0.3xSW, 3xSW). The light blue and green sections represent main redox conditions, and the accumulation mechanisms for Mo and U.

concentrations of Mo and EFs are very high in Mejillones compared with the bays south of 23°S. Therefore, although the exact mechanism of this metal enrichment has not been established yet, the Fe shuttle is a plausible explanation (Valdés et al., 2014; Castillo et al., 2019).

The temporal evolution of U and Mo (Figure 6) suggests that in Mejillones Bay (23°S), an increasing trend of oxygenation was sustained from ~1600 AD to 1900 AD. While at the southern sites, the trend has been maintained since 1400 AD. No records were obtained at 23°S before 1300 AD. Therefore, while the southern sites (30–36°S) showed cycles of more or less extended periods of suboxic conditions of ~600 years, in the northern areas (23–27°S), this periodicity would be reduced to ~400 years. On the other hand, a reducing condition is observed in all cores but diminishes over time.

Comparing the standardized data of metals and $\delta^{15}N$ records, they were relatively in phase until ~1900 AD, suggesting more or less intensity in the OMZ and denitrification. Following this period, an increase in oxygenation does not imply a decrease in denitrification. For example, after 1970, in most sites (except for Inglesa Bay), the less intense OMZ coincided with an intensified denitrification, which appears contradictory. In that case, other variables as the mixing of water mass properties can be considered relevant to adjust the frequency and seasonality of the OMZ upper limit, consistent with the increased occurrence of strong El Niño events after the climate shift of the 70s (Capotondi and Sardeshmukh, 2017).

Temporal variability of OMZ influence above shallows zones

Period 0-800 AD

Before 800 AD, a substantial impact of oxygenation on the southern tip of the study area was observed; metal enrichment was low in Concepcion, peaking around 400 AD, corresponding to the end stage of the RWP, followed by the DACP. To the northern sites, the metal enrichment showed consistently higher oxygenation off Inglesa Bay and Coquimbo (30°). Thus, the less intense OMZ in this period was accompanied by less severe denitrification around 400 AD, except at Coquimbo (30°S), where a moderate intensification of the OMZ and denitrification was observed. The southern position of the westerlies before 400 AD established dryer conditions on northern Patagonia (41-44°S), followed by a northward migration around 600 AD, which determined an intensification of the westerlies, an enhanced runoff by the precipitation, and a northward migration of cooler waters (Mohtadi et al., 2008). It would have a significant impact around 36°S, diminishing toward the northern sites (<30°), establishing the temporal and latitudinal differences at the centennial scale (Figures 3, 6).

Period 800 – 1200 AD

Around 1000–1200 AD, a more intense OMZ was observed, corresponding to the MCA peak that fell during a mostly weaker negative PDO amplitude developed during an extended period (993–1300; MacDonald and Case, 2005). The effects of these environmental conditions in South America have been described based on marine and continental records (Lüning et al., 2019). Marine proxies suggest an intensification of upwelling off Peru and northern Chile concomitant with an intensification of denitrification during this warm period (Salvatteci et al., 2016; Castillo et al., 2017), but others suggest a higher frequency of El Niño episodes in agreement with warmer climatic conditions (Moy et al., 2009, Conroy et al., 2008). A global analysis discussed by Graham et al. (2011) stated that during MCA, the zonal gradient of sea surface temperatures increased in the Tropical Pacific, with cooler conditions in the eastern Pacific and warmer conditions in the western Pacific. This would be in agreement with the intensified upwelling on the eastern side. This situation led to increased metal enrichment in the northern Chilean shelf, as observed at 27°S, related to a rise in organic sedimentation and agreement with denitrification intensification (Figure 3). Conversely, at the southern locations (30 – 36°S), less Mo enrichment was observed. However, U was still higher, indicating less sulfidic conditions but suboxic and less intense denitrification (Figures 3, 6). Therefore, during the MCA period, differences can be established between sites located north and south of 30°S.

Period 1200 – 1600 AD

On decadal scale, cold/warm periods commonly relate to conditions such as La Niña/El Niño-like, intense/reduced upwelling, and more/less reduced conditions would agree with more/less denitrification intensity. However, this cannot be generalized throughout the Chilean margin. During part of the MCA-LIA transitional period and early LIA (1500–1600), denitrification was more intense in northern sites, especially off Mejillones, and marked differences between northern and southern sites were observed (Figure 3). In this period, a mean positive PDO was set up, which implies positive anomalies of SST along the coast and more stratification intensifying the denitrification. In northern sites (23-27°S), the enhanced reduced conditions at the bottoms, resulting in an intensified OMZ, agreed with intensified denitrification (Figures 3, 6). However, south of 30°S, the Mo and U enrichments became opposite to the northern sites (around 1400–1600 AD), suggesting less reduced conditions at the bottoms, less intense OMZ but only minor changes in the denitrification that was still positive (Figures 3, 6).

Period 1600 – 1800 AD

During this cold period, weakened reduced environmental conditions and less intense denitrification were maintained along the Chilean margin but were stronger in the northern sites (Mejillones and Inglesa Bay, 23 – 27°S) (Figure 6). A weakened OMZ and denitrification would be related to the ventilation of subsurface waters, which has been explained by a greater influence of the ESPIW (Eastern South Pacific Intermediate Water) during the northward position of the SPSH. Thermocline ventilation has been proposed as a main mechanism to control the OMZ dynamics at low frequency, highlighting the role of the ESPIW (De Pol-Holz et al., 2006). It has been described for Mejillones ~1870 AD

(Gutiérrez et al., 2009) and Inglesa Bay in the last century (Castillo et al., 2017). Thus, the northward migration of westerlies would reduce the latitudinal differences in the sediment redox conditions along the Chilean margin, ventilating the subsurface waters and diminishing the intensity of the OMZ.

Period 1800 AD –recent time

In general, enhanced suboxic conditions have evolved to a less suboxic environment along the Chilean margin in the last century. However, discrepancies with the denitrification process occur after the 1900s. Off Concepcion (36°S), a more intense OMZ deduced from higher Mo and U enrichment was set with less severe denitrification before 1970, which would be explained by enhanced ventilation. The mixing and ventilation of subsurface waters could reduce the denitrification process but enhance the metal accumulation through Mn/Fe oxide transport in the water-sediment interphase (Algeo and Li, 2020; Bennett and Canfield, 2020). However, the Mn-Fe oxide shuttle that increases the metal accumulation does not seem to operate at 36°S (Figure 7). This process has been described in the Arabian Sea OMZ by Kessarkar et al. (2018), explaining that this is valid for other OMZs like the Peruvian margin where the oxides shuttle process occurs under suboxic, not sulfidic conditions (Scholz et al., 2017); but at Concepcion the Mo enrichment still does not reach high enough values to consider this process. Enhanced upwelling was reported in a short period between 1935 and 1970 (Srain et al., 2015), reinforcing the suboxic conditions through intensified vertical advection over the shelf during the negative PDO phase. Others reported for Concepcion a decreasing trend of diatoms in sedimentary records from 1920, accompanied by an increased contribution of warm-temperate and freshwater groups and an increased SST of ~0.7°C (Sánchez et al., 2012). This situation could reduce the denitrification due to a decreased primary productivity, or the $\delta^{15}N$ records is showing the continental influence over the shelf at Concepcion (36°S), because it does not match with intensified reduced conditions at bottoms before 1960–70.

Afterward, enhanced denitrification corresponded with a weakened OMZ along the Chilean margin deduced for the lower metal accumulation. It would result from increased stratification but more frequent oxygenation events produced by El Niño. During these events, change the oxide-reduction limits within sediments (Gutiérrez et al., 2000) and reduce the porewaters' U and Mo content. Additionally, reduced primary productivity would reduce the metal transport to the bottoms and oxygen consumption. In the northern areas, this condition has been variable in recent times; but it showed oxygenation too (Figure 6). This trend was concomitant with intensified denitrification (Figure 3). However, it was not observed in Inglesa Bay, probably due to local differences in the upwelling intensity and the OMZ position (Figure 1). From 1950 to the present, the increased denitrification observed off Mejillones (23°S) and Concepcion (36°S) (Figure 3) was not consistent with the increase in SST (~1°C) established after this date (Vargas et al., 2007; Sánchez et al., 2012). Notwithstanding, a decreased temperature was deduced for Coquimbo (30°S) (Ortega et al., 2019), which would agree with the intensified denitrification due to the OMZ influence over the narrow shelf. Additionally, the upwelling seems to have been intensified, which could be due to local air-sea interaction (e.g. enhanced marine boundary layer mixing and momentum entrainment due to the warmer SST), which promotes phytoplankton development and later oxygen consumption.

Recent evidence suggests that positive ENSO and PDO phases predominated over the last 50 years (Perez et al., 2021), and after the 1970s, an intensified frequency of inter-annual variability (El Niño events) (MacDonald and Case, 2005; Wam et al., 2019). Strong El Niño events induced bottom oxygenations detected from southern Peru to southern Chile at 36°S (Sellanes et al., 2007; Gutiérrez et al., 2008; Graco et al., 2017), supporting oxygen variability in the upper limit of the OMZ that affected the metal records in the last 50 years. Our records indicate that all sites, except for Inglesa Bay (27°S), responded similarly after the 1970s, with intensified denitrification. Although Inglesa Bay showed a slight return to less negative values of denitrification, suggesting a slight intensification of the upwelling. However, they corresponded with a weaker OMZ, which would agree with increased events of ventilation caused by inter-annual variability, producing a cumulative effect of oxygenation over the bottoms.

Latitudinal differences along the Chilean margin can be produced by differences in the hydrographic conditions that allow the ventilation of the OMZ; in the southern regions, the meridional position of the subtropical front and the intensity of the SPSH, which modulates the winds alongshore (Pitcher et al., 2021 and references therein) can modulate the OMZ. Additionally, during the negative phase of the PDO (la Niña-like), the intensity of the inter-annual variability in the EP is reduced; therefore, suboxic conditions would be less affected at the southern tip of our study area, where weakened El Niño causes fewer effects through oceanic teleconnection (at 36°S). Conversely, during the positive phase of the PDO and current global warming, the interannual variability would be intensified, and these latitudinal differences could be reduced.

In the past, the higher/lower denitrification and metal accumulations seem to respond to, probably, by more/less intense primary productivity. It maintains low oxygen concentrations and sulfidic conditions, which have been changing gradually in agreement with the climatic shifts that control the ventilation of subsurface waters. Thus, the current interpretations would be related to a higher stratification and intensified OMZ, in disagreement with higher metal accumulation due to increased oxygenation events.

Conclusions

The suboxic environment settled above the shelf bottoms along the Chilean margin has experienced increased oxygenation over the last 2000 years in response to decadal and inter-annual variability in the circulation in the Pacific. The lowest variability before 1400 AD was highlighted. In this period, denitrification intensified along with the intensification of suboxic conditions. The reconstructed PDO

index from 993 (AD) (MacDonald and Case, 2005) indicates that negative anomalies (cold periods) were more common for extended periods before 1300 AD when reduced denitrification and intense OMZ were established. Afterward, positive anomalies with enhanced variability dominated (MacDonald and Case, 2005), which allowed the maintenance of an enhanced denitrification intensity but contributed to diminishing the reduced conditions and OMZ intensity. It showed a decreasing trend toward current times deduced from metal accumulation. The magnitude of the suboxic condition related to more/less OMZ intensity in the upper boundary is affected by remote-forcing oceanic waves that work on different timescales. The effect of this variability is coupled with the inter-annual and decadal variability, whose intensity and periodicity have increased. These processes promote changes in the redox conditions above the bottom of the shelf, leaving less reduced environments. Besides their value for validation purposes, our result challenges projections of current-generation climate models that still indicate a low consensus in the fate of the SEP OMZs in the 21st century (Cabré et al., 2015; Kwiatkowski et al., 2020).

Data availability statement

The original contributions presented in the study are included in the article/Supplementary Material. Further inquiries can be directed to the corresponding author.

Author contributions

PM prepared the manuscript with contributions from all co-authors. All authors drafted the database used in this manuscript. All data used in this manuscript is the result of different projects belonging to the authors of this manuscript. The analysis of this information was discussed with the contribution of all authors of this paper. All authors contributed to the article and approved the submitted version.

Funding

The authors are grateful for the financial support provided by the Anillo Project ACT210071, Fondecyt 1200390 granted to (JV), Núcleo Milenio UPWELL (NCN19_153), and the CLAP program (Concurso de Fortalecimiento al Desarrollo Científico de Centros Regionales 2020-R20F0008-CEAZA). We also extend our gratitude to COPAS Sur-Austral ANID AFB170006 and COPAS COASTAL FB210021, who contributed to the completion of this study.

Conflict of interest

The authors declare that the research was conducted in the absence of any commercial or financial relationships that could be construed as a potential conflict of interest.

Publisher's note

Supplementary material

The Supplementary Material for this article can be found online at: https://www.frontiersin.org/articles/10.3389/fmars.2023.1134164/full#supplementary-material

References

Algeo, T., and Li, C. (2020). Redox classification and calibration of redox thresholds in sedimentary systems. *Geochim. Cosmochim. Ac.* 287, 8–26. doi: 10.1016/j.gca.2020.01.055

Algeo, T. J., and Tribovillard, N. (2009). Environmental analysis of paleoceanographic systems based on molybdenum-uranium covariation. *Chem. Geology* 268, 211–225. doi: 10.1016/j.chemgeo.2009.09.001

Altabet, M. A. (2005). "Isotopic tracers of the marine nitrogen cycle: present and past," in *Marine organic matter: biomarkers, isotopes and DNA. the handbook of environmental chemistry*, vol. 2N . Ed. J. K. Volkman (Berlin, Heidelberg: Springer). doi: 10.1007/698_2_008

Ancapichún, S., and Garcés-Vargas, J. (2015). Variability of the southeast pacific subtropical anticyclone and its impact on sea surface temperature off north-central Chile cienc. *Mar* 41 (1), 1–20. doi: 10.7773/cm.v41i1.2338

Auger, P.-A., Bento, J. P., Hormazabal, S., Morales, C. E., and Bustamante, A. (2020a). Temperature, salinity, density and dissolved oxygen profiles from the world ocean database and argo floats in the eastern south pacific over the 1928-2018 period. *SEANOE*. doi: 10.17882/74336

Auger, P.-A., Bento, J. P., Hormazabal, S., Morales, C. E., and Bustamante, A. (2020b). Mesoscale variability in the boundaries of the oxygen minimum zone in the eastern south pacific: influence of intrathermocline eddies. *J. Geophys. Res. Oceans*. doi: 10.1029/2019JC015272

Bennett, W., and Canfield, D. (2020). Redox-sensitive trace metals as paleoredox proxies: a review and analysis of data from modern sediments. *Earth Sci. Rev.* 204, 103175. doi: 10.1016/j.earscirev.2020.103175

Bernal, P., Ahumada, R., González, H., Pantoja, S., and Troncoso, A. (1989). Carbon flux in a pelagic trophic model for concepción bay, Chile. *Biología Pesquera* 18, 5–14.

Böning, P., Brumsack, H.-J., Böttcher, M. E., Schnetger, B., Kriete, C., Kallmeyer, J., et al. (2004). Geochemistry of Peruvian near-surface sediments. *Geochim. Cosmochim. Ac.* 68, 4429–4451. doi: 10.1016/j.gca.2004.04.027

Böning, P., Brumsack, H.-J., Schnetger, B., and Grunwald, M. (2009). Trace element signatures of Chilean upwelling sediments at 36°S. *Mar. Geol.* 259, 112–121. doi: 10.1016/j.margeo.2009.01.004

Böning, P., Cuypers, S., Grunwald, M., Schnetger, B., and Brumsack, H.-J. (2005). Geochemical characteristics of Chilean upwelling sediments at 36°S. *Mar. Geol.* 220, 1–21. doi: 10.1016/j.margeo.2005.07.005

Braconnot, P., Luan, Y., Brewer, S., and Zheng, W. (2012). Impact of earth's orbit and freshwater fluxes on Holocene climate mean seasonal cycle and ENSO characteristics. *Clim. Dyn.* 38, 1081–1092. doi: 10.1007/s00382-011-1029-x

Burdige, D. (2007). Preservation of organic matter in marine sediments: controls, mechanisms, and an imbalance in sediment organic carbon budgets? *Chem. Rev.* 107, 467–485.

Cabré, A., Marinov, I., Bernardello, R., and Bianchi, D. (2015). Oxygen minimum zones in the tropical pacific across CMIP5 models: mean state differences and climate change trends. *Biogeosciences* 12 (18), 5429–5454. doi: 10.5194/bg-12-5429-2015

Calvert, S. E., Pedersen, T. F., and Karlin, R. E. (2001). Geochemical and isotopic evidence for postglacial palaeoceanographic changes in saanich inlet, British Columbia. *Mar. Geol.* 174, 287–305. doi: 10.1016/S0025-3227(00)00156-0

Capotondi, A., and Sardeshmukh, P. D. (2017). Is El niño really changing? *Geophysical Res. Lett.* 44 (16), 8548–8556. doi: 10.1002/2017GL074515

Carré, M., Azzoug, M., Bentaleb, I., Chase, B. M., Fontugne, M., Jackson, D., et al. (2012). Mid-Holocene mean climate in the south eastern pacific and its influence on south America. *Quat. Int.* 253, 55–66. doi: 10.1016/j.quaint.2011.02.004

Carré, M., Sachs, J. P., Purca, S., Schauer, A. J., Braconnot, P., Falcón, R. A., et al. (2014). Holocene History of ENSO variance and asymmetry in the eastern tropical pacific. *Science* 345, 1045–1048. doi: 10.1126/science.1255768

Castillo, A., Valdés, J., Sifedine, A., Reyss, J.-L., Bouloubassi, I., and Ortlieb, L. (2017). Changes in biological productivity and ocean-climatic fluctuations during the last ~1.5 kyr in the Humboldt ecosystem off northern Chile (27°S): a multiproxy approach. *Palaeogeogr. Palaeocl.* 3, 798–815.b. doi: 10.1016/j.palaeo.2017.07.038

Castillo, A., Valdés, J., Sifedine, A., Vega, S.-E., Diaz-Ochoa, J., and Marambio, Y. (2019). Evaluation of redox-sensitive metals in marine surface sediments influenced by the oxygen minimum zone of the Humboldt current system, northern Chile. *Int. J. Sediment Res.* 179, 2–14. doi: 10.1016/j.ijsrc.2018.08.005

Cobb, K. M., Westphal, N., Sayani, H. R., Watson, J. T., Di Lorenzo, E., Cheng, H., et al. (2013). Highly variable El niño-southern oscillation throughout the Holocene. *Science* 339 (6115), 67-70. doi: 10.1126/science.1228246

Conroy, J., Overpeck, J., Cole, J. E., Shanahan, T. M., and Steinitz-Kannan, M. (2008). Holocene Changes in eastern tropical pacific climate inferred from a galápagos lake sediment records. *Quat. Sci. Rev.* 27, 1166–1180.

Crusius, J., and Thomson, J. (2000). Comparative behavior of authigenic re, U, and Mo during reoxidation and subsequent long-term burial in marine sediments. *Geochim. Cosmochim Ac.* 64, 2233–2242. doi: 10.1016/S0016-7037(99)00433-0

Daneri, G., Dellarossa, V., Quiñones, R., Jacob, B., Montero, P., and Ulloa, O. (2000). Primary production and community respiration in the Humboldt current system off Chile and associated oceanic areas, mar. *Ecol. Prog. Ser.* 197, 41–49. doi: 10.3354/meps197041

Dellarosa, V. (1998). *Producción primaria anual en sistemas de alta producción biológica (Doctoral dissertation, tesis escuela de graduados* (Concepción, Chile: Universidad de Concepción), 149.

De Pol-Holz, R., Robinson, R. S., Hebbeln, D., Sigman, D. M., and Ulloa, O. (20092009). Controls on sedimentary nitrogen isotopes along the Chile margin. *Deep-Sea Res.* II 56, 1042–1054. doi: 10.1016/j.dsr2.2008.09.014

De Pol-Holz, R., Ulloa, O., Dezileau, L., Kiser, J., Lamy, F., and Hebbeln, D. (2006). Melting of the Patagonian ice sheet and deglacial perturbations of the nitrogen cycle in the eastern south pacific. *Geophys. Res. Lett.* 33, L04704. doi: 10.1029/2005GL024477

Dewitte, B., Concha, E., Saavedra, D., Pizarro, O., Martinez-Villalobos, C., Gushchina, D., et al. (2023). The ENSO-induced south pacific meridional mode. *Front. Clim.* 4, 143–156. doi: 10.3389/fclim.2022.1080978

Dewitte, B., Vazquez-Cuervo, J., Goubanova, K., Illig, S., Takahashi, K., Cambon, G., et al. (2012). Change in El niño flavours over 1958-2008: implications for the long-term trend of the upwelling off Peru. *Deep Sea Res. II*. doi: 10.1016/j.dsr2.2012.04.011

Erickson, B. E., and Helz, G. R. (2000). Molybdenum(VI) speciation in sulfidic waters: stability and lability of thiomolybdates. *Geochim. Cosmochim. Acta* 64 (7), 1149–1158. doi: 10.1016/S0016-7037(99)00423-8

Escribano, R., Daneri, G., Farías, L., Gallardo, V. A., González, H., Gutiérrez, D., et al. (2004). Biological and chemical consequences of the 1997–1998 El ni˜no in the Chilean coastal upwelling system: a synthesis. *Deep Sea Res. Part II Top. Stud. Oceanogr.* 51, 2389–2411. doi: 10.1016/j.dsr2.2004.08.011

Farmer, J. R., Hertsberg, J. E., Cardinal, D., Fletz, S., Hendry, K., S., L., et al. (2021). Assessment of c, n, and Si isotopes as tracers of past ocean nutrient and carbon cycling. *Global Biochem. Cy.* 35. doi: 10.1029/2020GB006775

Flores-Aqueveque, V., Alfaro, S., Vargas, G., Rutllant, J. A., and Caquineau, S. (2015). Aeolian particles in marine cores as a tool for quantitative high-resolution reconstruction of upwelling favorable winds along coastal atacama desert, northern Chile. *Progr. Oceanogr*. 244–255. doi: 10.1016/j.pocean.2015.02.003

Fossing, H., Gallardo, V. A., Jørgensen, B. B., Hüttel, M., Nielsen, L. P., Schulz, H., et al. (1995). Concentration and transport of nitrate by the matforming sulphur bacterium thioploca. *Nature* 374, 713–715. doi: 10.1038/374713a0

Fuenzalida, R., Schneider, W., Garcés-Vargas, J., Bravo, L., and Lange, C. (2009). Vertical and horizontal extensión of the oxygen minimum zone in the eastern south pacific ocean. *Deep-Sea Res. Pt.II* 56, 992–1003. doi: 10.1016/j.dsr2.2008.11.001

González, H., Daneri, G., Figueroa, D., Iriarte, J. L., Pizarro, G., Quiñones, R., et al. (1998). Primary production and its fate in the pelagic food web and deep-sea, and ocean-atmosphere CO2 exchange in the northern Humboldt current (23°S): possible effects of the 1997–1998 El niño in Chile. *Rev. Chil. Hist. Nat.* 71, 429–458.

Gonzalez, H., Menschel, E., Aparicio, C., and Barría, C. (2007). Spatial and temporal variability of microplankton and detritus, and their export to the shelf sediments in the upwelling area off concepción, Chile (36°S), during 2002–2005. *Prog. Oceanogr.* 75, 435–451. doi: 10.1016/j.pocean.2007.08.025

Graco, M., Purca, S., Dewitte, B., Castro, C. G., Moron, O., Ledesma, J., et al. (2017). The OMZ and nutrients features as a signature of interannual and low frequency variability off the Peruvian upwelling system. *Biogeosciences* 14, 4601–4617. doi: 10.5194/bg-14-4601-2017

Graham, N. E., Ammann, C. M., Fleitmann, D., Cobb, K. M., and Luterbacher, J. (2011). Support for global climate reorganization during the "Medieval climate anomaly". *Clim. Dyn.* 37, 1217–1245.

Guiñez, M., Valdés, J., Sifedine, A., Boussafir, M., and Dávila, P. (2014). Anchovy population and ocean-climatic fluctuations in the Humboldt current system during the last 700 years and their implications. *Palaeogeogr. Palaeocl.* 415, 210–224. doi: 10.1016/j.palaeo.2014.08.026

Gutiérrez, D., Gallardo, V. A., Mayor, S., Neira, C., Vásquez, C., Sellanes, J., et al. (2000). Effects of dissolved oxygen and fresh organic matter on the bioturbation potential of macrofauna in sublittoral bottoms off central Chile, duringthe 1997–98 El niño. *Mar. Ecol. Prog. Ser.* 202, 81–99. doi: 10.3354/meps202081

Gutiérrez, D., Bouloubassi, I., Sifeddine, A., Purca, S., Goubanova, K., Graco, M., et al. (2011). Coastal cooling and increased productivity in the main upwelling zone off Peru since the mid-twentieth century. *Geophys. Res. Lett.* 38, L07603. doi: 10.1029/2010GL046324

Gutiérrez, D., Enríquez, E., Purca, S., Quipuzcoa, L., Marquina, R., Flores, G., et al. (2008). Oxygenation episodes on the continental shelf of central Peru: remote forcing and benthic ecosystem response, prog. *Oceanography* 79, 177–189.

Gutiérrez, D., Sifeddine, A., Field, D. B., Ortlieb, L., Vargas, G., Chavez, F., et al. (2009). Rapid reorganization in ocean biogeochemistry off Peru towards the end of the little ice age. *Biogeosciences* 6, 835–848. doi: 10.5194/bg-6-835-2009

Gutiérrez, D., Sifeddine, A., Reyss, J. L., Vargas, G., Velazco, F., Salvatteci, R., et al. (2006). Anoxic sediments off central Peru record interannual to multidecadal changes of climate and upwelling ecosystem during the last two centuries. *Adv. Geosci.* 6, 119–125. doi: 10.5194/adgeo-6-119-2006

Hebbeln, D., Marchant, M., Freudenthal, T., and Wefer, G. (2000). Surface distribution along the Chilean continental slope related to upwelling and productivity. *Mar. Geol.* 164, 119–137. doi: 10.1016/S0025-3227(99)00129-2

Helly, J., and Levin, L. (2004). Global distribution of naturally occurring marine hypoxia on continental margin. *Deep-Sea Res. Pt. I* 51, 1159–1168. doi: 10.1016/j.dsr.2004.03.009

Hu, S., and Fedorov, A. V. (2018). Cross-equatorial winds control El niño diversity and change. *Nat Clim Change* 8 (9), 798–802. doi: 10.1038/s41558-018-0248-0

Jacques–Coper, M., and Garreaud, R. (2014). Characterization of the 1970s climate shift in south America. *Int. J. Climatol*. doi: 10.1002/joc4120

Kaiser, J., Schefuß, E., Lamy, F., Mohtadi, M., and Hebbeln, D. (2008). Glacial to Holocene changes in sea surface temperature and coastal vegetation in north central Chile: high versus low latitude forcing, quat. *Sci. Rev.* 27, 2064–2075. doi: 10.1016/j.quascirev.2008.08.025

Kämpf, J., and Chapman, P. (2016). "Upwelling systems of the world," in *A scientific journey to the most productive marine ecosystems* (Springer). doi: 10.1007/978-3-319-42524-5

Katsev, S., and Crowe, S. (2015). Organic carbon burial efficiencies in sediments: the power law of mineralization revisited. *Geology* 43, 607–610. doi: 10.1130/G36626.1

Kessarkar, P. M., Naqvi, S. W. A., Thamban, M., Fernandes, L. L., Siebert, C., Rao, V. P., et al. (2018). Variations in denitrification and ventilation within the Arabian Sea oxygen minimum zone during the Holocene. *Geochem. Geophys. Geosystems* 19, 2179–2193. doi: 10.1029/2017GC007286

Koutavas, A., de Menocal, P. B., Olive, G. C., and Lynch-Stieglitz, J. (2006). Mid-Holocene El niño–southern oscillation (ENSO) attenuation revealed by individual foraminifera in eastern tropical pacific sediments. *Geology* 34, 993–996. doi: 10.1130/G22810A.1

Kwiatkowski, L., Torres, O., Bopp, L., Aumont, O., Chamberlain, M., Christian, J. R., et al. (2020). Twenty-first century ocean warming, acidification, deoxygenation, and upper-ocean nutrient and primary production decline from CMIP6 model projections. *Biogeosciences* 17, 3439–3470. doi: 10.5194/bg-17-3439-2020

Lam, P., Lavik, G., Jensen, M. M., van de Vossenberg, J., Schmid, M., Woebken, D., et al. (2009). Revising the nitrogen cycle in the Peruvian oxygen minimum zone. *Proc. Natl. Acad. Sci. USA* 106, 4752–4757. doi: 10.1073/pnas.0812444106

Lamy, F., Kilian, R., Arz, H. W., Francois, J.-P., Kaiser, J., Prange, M., et al. (2010). Holocene Changes in the position and intensity of the southern westerly wind belt. *Nat. Geosci.* 3, 695–699. doi: 10.1038/ngeo959

Lüning, S., Gałka, M., Bamont, F. P., García, F., and Vahrenholt, F. (2019). The medieval climate anomaly in south America. *Quat. Int.* 508, 70–87. doi: 10.1016/j.quaint.2018.10.041

Luyten, J. R., Pedlosky, J., and Stommel, H. (1983). The ventilated thermocline. *J. Phys. Oceanogr.* 13, 292–309. doi: 10.1175/1520-0485(1983)013<0292:TVT>2.0.CO;2

MacDonald, G., and Case, R. (2005). Variations in the pacific decadal oscillation over the past millennium. *Geophys. Res. Lett.* 32, L08703. doi: 10.1029/2005GL022478

McManus, J., Berelson, W. M., Severmann, S., Poulson, R. L., Hammond, D. E., Klinkhammer, G. P., et al. (2006). Molybdenum and uranium geochemistry in continental margin sediments: paleoproxy potential. *Geochim. Geochim. Cosmochim. Ac.* 70, 4643–4662. doi: 10.1016/j.gca.2006.06.1564

Meyers, P. A. (1997). Organic geochemical proxies of paleoceanographic, paleolimnologic, and paleoclimatic processes. *Org. Geochem.* 27, 213–250. doi: 10.1016/S0146-6380(97)00049-1

Middelburg, J., Vlug, T., Jaco, F., and van der Nat, W. A. (1993). Organic matter mineralization in marine systems. *Glob. Planet. Change* 8, 47–58. doi: 10.1016/0921-8181(93)90062-S

Milessi, A. C., Sellanes, J., Gallardo, V. A., and Lange, C. B. (2005). Osseous skeletal material and fish scales in marine sediments under the oxygen minimum zone off northern and central Chile. *Estuar. Coast. Shelf Sci.* 64 (2–3), 185–190. doi: 10.1016/j.ecss.2005.02.013

Mohtadi, M., Rossel, P., Lange, C. B., Pantoja, S., Böning, P., Repeta, D., et al. (2008). Deglatial pattern of circulation and marine productivity in the upwelling region off central-south Chile. *Earth Planet. Sci. Lett.* 272, 221–230. doi: 10.1016/j.epsl.2008.04.043

Mollier-Vogel, E., Martinez, P., Blanz, T., Robinson, R., Desprat, S., Etourneau, J., et al. (2019). Mid-Holocene deepening of the southeast pacific oxycline, glob. *Planet. Change* 172, 365–373. doi: 10.1016/j.gloplacha.2018.10.020

Mollier-Vogel, E., Ryabenko, E., Martinez, P., Wallace, D., Altabet, M., and Schneider, R. (2012). Nitrogen isotope gradients off Peru and Ecuador related to upwelling, productivity, nutrient uptake and oxygen deficiency. *Deep-Sea Re. Pt.I* 70, 14–25. doi: 10.1016/j.dsr.2012.06.003

Montecino, V., and Lange, C. (2009). The Humboldt current system: ecosystem omponents and processes, fisheries, and sediment studies. *Prog. Oceanogr.* 83, 65–75. doi: 10.1016/j.pocean.2009.07.041

Montero-Serrano, J., Martínez-Santana, M., Tribovillard, N., Riboulleau, A., and Garbán, G. (2009). Geochemical behavior of molybdenum and its isotopes in the sedimentary environment – a bibliographic review. *Rev. Biol. Mar. Oceanogr.* 44 (2), 263–275.

Morford, J., and Emerson, S. (1999). The geochemistry of redox sensitive trace metals in sediments, geochim. *Cosmochim. Ac.* 63, 1735–1750. doi: 10.1016/S0016-7037(99)00126-X

Moy, C., Moreno, P., Dunbar, R., Kaplan, M., Francois, J.-P., Villalba, R., et al. (2009). "Past climate variability in south America and surrounding regions," in *Climate change in southern south America during the last two millennia. chapter 15*. Ed. F. Vimeux (Springer), 353–393.

Muñoz, P., Dezileau, L., Lange, C., Cárdenas, L., Sellanes, J., Salamanca, M., et al. (2012). Evaluation of sediment trace metal records as paleoproductivity and paleoxygenation proxies in the upwelling center off concepción, Chile (36° s). *Prog. Oceanogr.* 92–95, 66–80. doi: 10.1016/j.pocean.2011.07.010

Muñoz, P., Lange, C. B., Gutiérrez, D., Hebbeln, D., Salamanca, M. A., Dezileau, L, et al. (2004). Recent sedimentation and mass accumulation rates based on 210Pb along the Peru-Chile continental margin. *Deep Sea Res. Pt. II*, 2523–2541.

Muñoz, P., Rebolledo, L., Dezileau, L., Maldonado, A., Mayr, C., C´ardenas, P., et al. (2020). Reconstructing past variations in environmental conditions and paleoproductivity over the last ~8000 years off north-central Chile (30°S). *Biogeosciences* 17, 5763–5785. doi: 10.5194/bg-17-5763-2020

Muñoz, P., Hevia-Hormazabal, V., Araya, K., Maldonado, A., and Salamanca, A. (2022). Metal enrichment evolution in marine sediments influenced by oxygen-deficient waters in a mineral loading zone, atacama, Chile (27°S). *Mar. Environ. Res.* 177, 105619. doi: 10.1016/j.marenvres.2022.105619

Muratli, J. M., Chase, Z., Mix, A. C., and McManus, J. (2010). Increased glacial-age ventilation of the Chilean margin by antarctic intermediate water. *Nat. Geosci.* 3, 2326. doi: 10.1038/NGEO715

Nameroff, T., Balistrieri, L., and Murray, W. (2002). Suboxic trace metals geochemistry in the eastern tropical north pacific. *Geochim. Cosmochim. Ac.* 66, 1139–1158. doi: 10.1016/S0016-7037(01)00843-2

Ortega, C., Vargas, G., Rojas, M., Rutllant, J. A., Mu¯noz, P., Lange, C. B., et al. (2019). Extreme ENSO-driven torrential rainfalls at the southern edge of the atacama desert during the late Holocene and their projection into the 21th century. *Glob. Planet. Change* 175, 226–237. doi: 10.1016/j.gloplacha.2019.02.011

Paulmier, A., Ruiz-Pino, D., Garçon, V., and Farías, L. (2006). Maintaining of the East south pacific oxygen minimum zone (OMZ) off Chile. *Geophys. Res. Lett.* 33 (6), L20601. doi: 10.1029/2006GL026801

Pauly, D., and Christensen, V. (1995). Primary production required to sustain global fisheries. *Nature* 374, 255–257. doi: 10.1038/374255a0

Perez, L., Barreiro, M., Etchevers, I., Crisci, C., and García-Rodríguez, F. (2021). Centennial hydroclimatic and anthropogenic processes of south East south America modulate interannual and decadal river discharge. *Sci. Total Environ.* 781, 146733. doi: 10.1016/j.scitotenv.2021.146733

Pitcher, G. C., Aguirre-Velarde, A., Breitburg, D., Cardich, J., Carstensen, J., Conley, D. J, et al. (2021). System controls of coastal and open ocean oxygen depletion. *Progr. Oceanogr.* doi: 10.1016/j.pocean.2021.102613

Pizarro, O., Shaffer, G., Dewitte, B., and Ramos, M. (2002). Dynamics of seasonal and interannual variability of the Peru-Chile undercurrent. *Geophys. Res. Lett.* 29, 28–31. doi: 10.1029/2002GL014790

Pizarro-Koch, M., Pizarro, O., Dewitte, B., Montes, I., Ramos, M., Paulmier, A., et al. (2019). Seasonal variability of the southern tip of the oxygen minimum zone in the Eastern south pacific (30°-38°S): a modeling study. *J. Geophys. Res.-Oceans*. doi: 10.1029/2019JC015201

Quintana, J. M., and Aceituno, P. (2012). Changes in the rainfall regime along the extratropical west coast of south America (Chile): 30–43 s. *Atmosfera* 25, 1–22.

Ramos, M., Dewitte, B., Pizarro, O., and Garric, G. (2008). Vertical propagation of extratropical rossby waves during the 1997–1998 El niño off the west coast of south America in a mediumresolution OGCM simulation. *J. Geophys. Res.* 113, C08041. doi: 10.1029/2007JC004681

Ramos, M., Pizarro, O., Bravo, L., and Dewitte, B. (2006). Seasonal variability of the permanent thermocline off northern Chile. *Geophys. Res. Lett.* 33, L09608. doi: 10.1029/2006GL025882

Robinson, R., Etourneau, J., Martinez, P., and Schneider, R. (2014). Expansion of pelagic denitrification during early pleistocene cooling. *Earth Planet. Sci. Lett.* 389, 52–61. doi: 10.1016/j.epsl.2013.12.022

Robinson, R. S., Mix, A., and Martinez, P. (2007). Southern ocean control on the extent of denitrification in the southeast pacific over the last 70 ka quaternary. *Sci. Rev.* 26, 201–212. doi: 10.1016/j.quascirev.2006.08.005

Salvatteci, R., Gutiérrez, D., Field, D., Sifeddine, A., Ortlieb, L., Bouloubassi, I., et al. (2014). The response of the Peruvian upwelling ecosystem to centennial-scale global change during the last two millennia. *Clim. Past* 10, 1–17. doi: 10.5194/cp-10-715-2014

Salvatteci, R., Gutiérrez, D., Sifedine, A., Ortlieb, L., Druffel, E., Boussafir, M., et al. (2016). Centennial to millennial-scale changes in oxygenation and productivity in the Eastern tropical south pacific during the last 25000 years. *Quat. Sci. Rev.* 131, 102–117. doi: 10.1016/j.quascirev.2015.10.044

Sánchez, G., Lange, C., González, H., Vargas, G., Muñoz, P., Cisternas, C., et al. (2012). Siliceous microorganisms in the upwelling center off concepción, Chile (36°S): preservation in surface sediments and downcore fluctuations during the past ~150 years. *Prog. Oceanogr.* 92–95, 50–65. doi: 10.1016/j.pocean.2011.07.014

Sánchez, A., Shumilin, E., and Rodríguez-Figueroa, G. (2022). Trace elements V, Ni, Mo and U: a geochemical tool to quantify dissolved oxygen concentration in the oxygen minimum zone of the north-eastern pacific. *J. Mar. Syst.* 230, 103732. doi: 10.1016/j.jmarsys.2022.103732

Schneider, W., Fuenzalida, R., Garcés-Vargas, J., Bravo, L., and Lange, C. (2006). Vertical and horizontal extensión of the oxygen mínimum zone in the eastern south pacific ocean. *Gayana* 70, 79–82. doi: 10.4067/S0717-65382006000300016

Schneider, W., Fuenzalida, R., Rodríguez-Rubio, E., and Garcés-Vargas, J. (2003). Characteristics and formation of Eastern south pacific intermediate water. *Geophys. Res. Lett.* 30, 158. doi: 10.1029/2003GL017086

Scholz, F. (2018). Identifying oxygen minimum zone-type biogeochemical cycling in earth history using inorganic geochemical proxies. *Earth. Sci. Rev.* 184, 29–45. doi: 10.1016/j.earscirev.2018.08.002

Scholz, F., Siebert, C., Dale, A. W., and Frank, M. (2017). Intense molybdenum accumulation in sediments underneath a nitrogenous water column and implications for the reconstruction of paleo-redox conditions based on molybdenum isotopes. *Geochim. Cosmochim. Ac.* 213, 400–417. doi: 10.1016/j.gca.2017.06.048

Sellanes, J., Quiroga, E., Neira, C., and Gutiérrez, D. (2007). Changes of macrobenthos composition under different ENSO cycle conditions on the continental shelf off central Chile. *Continent. Shelf Res.* 27, 1002–1016. doi: 10.1016/j.csr.2007.01.001

Sifeddine, A., Gutiérrez, D., Ortlieb, L., Boucher, H., Velazco, F., Field, D., et al. (2008). Laminated sediments from the central Peruvian continental slope: a 500 year record of upwelling system productivity, terrestrial runoff and redox conditions. *Prog. Oceanogr.* 79, 190–197. doi: 10.1016/j.pocean.2008.10.024

Silva, N., and Neshyba, S. (1979). On the southern most extension of the Peru–Chile undercurrent. *Deep-Sea Res.* 26A, 1387–1393.

Sprintall, J., Cravatte, S., Dewitte, B., Du, Y., and Sen Gupta, A. (2020). *Oceanic teleconnections, chapter 15 in "El nino in a changing climate" AGU book*. 528, ISBN: Available at: https://agupubs.onlinelibrary.wiley.com/doi/abs/10.1002/9781119548164.ch15.

Srain, B., Pantoja, S., Sepúlveda, J., Lange, C. B., Muñoz, P., Summons, R. E., et al. (2015). Interdecadal changes in intensity of the oxygen minimum zone off concepción, Chile (_36_ s), over the last century. *Biogeosciences* 12, 6045–6058. doi: 10.5194/bg-12-6045-2015

Thomas, A. C., Blanco, J. L., Carr, M. E., Strub, P. T., and Osses, J. (2001). Satellite-measured chlorophyll and temperature variability off northern Chile during the 1996–1998 la niña and El niño. *J. Geophys. Res.* 106, 899–915. doi: 10.1029/1999JC000052

Tribovillard, N., Algeo, T. J., Baudin, F., and Riboulleau, A. (2012). Analysis of marine environmental conditions based onmolybdenum–uranium covariation–applications to mesozoic paleoceanography. *Chem. Geol.* 324-325, 46–58. doi: 10.1016/j.chemgeo.2011.09.009

Tribovillard, N., Algeo, T., Lyons, T., and Riboulleau, A. (2006). Trace metals as paleoredox and paleoproductivity proxies: an update. *Chem. Geol.* 232, 12–32. doi: 10.1016/j.chemgeo.2006.02.012

Ulloa, O., Escribano, R., Hormazabal, S., Quiñones, R. A., Gonzalez, R., and Ramos, M. (2001). Evolution and biological effects of the 1997–98 E1 niño in the upwelling ecosystem off northern Chile, geophys. *Res. Lett.* 28, 1591–1594. doi: 10.1029/2000GL011548

Valdés, J., Sifeddine, A., Boussafir, M., and Ortlieb, L. (2014). Redox conditions in a coastal zone of the Humboldt system (Mejillones,23° s). influence on the preservation of redox-sensitive metals. *J. Geochem. Explor.* 140, 1–10. doi: 10.1016/j.gexplo.2014.01.002

Valdés, J., Sifeddine, A., Lallier-Verges, E., and Ortlieb, L. (2004). Petrographic and geochemical study of organic matter in surficial sediments from an upwelling system

(Mejillones del sur bay, northern Chile). *Org. Geochem.* 35 (5), 881–894. doi: 10.1016/j.orggeochem.2004.02.009

Valdés, J., Sifedine, A., Guiñez, M., and Castillo, A. (2021). Oxygen minimum zone variability during the last 700 years in a coastal upwelling area of the Humboldt system (Mejillones, 23° s, chile). a new approach from geochemical signature. *Prog. Oceanogr.* 193, 102520. doi: 10.1016/j.pocean.2021.102520

Valdés, J., Sifedine, A., Ortlieb, L., and Pierre, C. (2009). Interplay between sedimentary organic matter and dissolved oxygen availability in a coastal zone of the Humboldt current system; mejillones bay, northern Chile. *Mar. Geol.* 265, 157–166. doi: 10.1016/j.margeo.2009.07.004

Vargas, G., Pantoja, S., Rutllant, J., Lange, C., and Ortlieb, L. (2007). Enhancement of coastal upwelling and interdecadal ENSO-like variability in the Peru-Chile current since late 19th century. geophys. *Res. Lett.* 34, L13607. doi: 10.1029/2006GL028812

Wagner, M., Chappaz, A., and Lyons, T. W. (2017). Molybdenum speciation and burial pathway in weakly sulfidic environments: insights from XAFS. *Geochim. Cosmochim. Acta* 206, 18–29. doi: 10.1016/j.gca.2017.02.018

Wam, B., Luo, X., Yang, Y.-M., Sun, W., Cane, M., Cai, W., et al. (2019). Historical change of El niño properties sheds light on future changes of extreme El niño. *PNAS* 116 (5), 22512–22517. doi: 10.1073/pnas.191113011

Wedepohl, K. (1971). "Environmental influences on the chemical composition of shales and clays," in *Physics and chemistry of the earth*. Eds. L. Ahrens, F. Press, S. Runcorn and H. Urey(Oxford: Pergamon), 8, 307–333. doi: 10.1016/0079-1946(71)90020-6

Yang, S., and Oh, J.-H. (2020). Effects of modes of climate variability on wave power during boreal summer in the western north pacific. *Sci. Rep.* 10 (5187), 1–10. doi: 10.1038/s41598-020-62138-0

Zheng, Y., Anderson, R., Van Geen, A., and Fleisher, M. Q. (2002). Remobilization of authigenic uranium in marine sediments by bioturbation. *Geochim. Cosmichim. Acta* 66, 1759–1772.

Zheng, Y., Anderson, R., Van Geen, A., and Kuwabara, J. (2000). Authigenic molybdenum formation in marine sedimentys: a link to porewater sulfide in the Santa Barbara basin. *Geochim. Cosmochim. Acta* 64, 4165–4178.

Frontiers in Marine Science

Explores ocean-based solutions for emerging global challenges

The third most-cited marine and freshwater biology journal, advancing our understanding of marine systems and addressing global challenges including overfishing, pollution, and climate change.

Discover the latest Research Topics

See more →

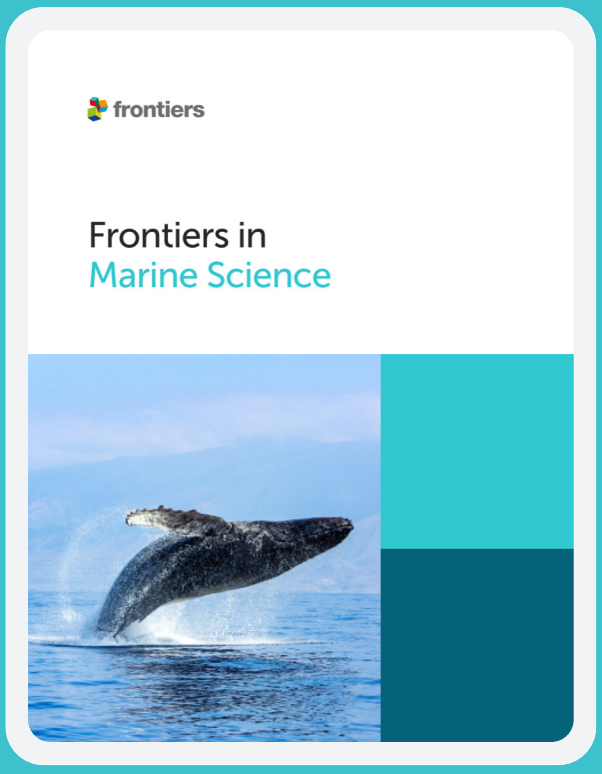

Frontiers

Avenue du Tribunal-Fédéral 34
1005 Lausanne, Switzerland
frontiersin.org

Contact us

+41 (0)21 510 17 00
frontiersin.org/about/contact